

# PROJECT REPORT

## ASTEROSEISMOLOGY OF SOLAR-TYPE OSCILLATORS

NAME: SHATANIK BHATTACHARYA

Roll no.: PHUG/198/17

E-Mail: [shatanik2@gmail.com](mailto:shatanik2@gmail.com)

DEPARTMENT OF PHYSICS

RAMAKRISHNA MISSION RESIDENTIAL COLLEGE (AUTONOMOUS),  
NARENDRAPUR, KOLKATA-700103

GUIDED and SUPERVISED BY:

Dr. ANWESH MAZUMDAR,  
ASSOCIATE PROFESSOR,

HOMI BHABHA CENTRE FOR SCIENCE EDUCATION --  
TATA INSTITUTE OF FUNDAMENTAL RESEARCH

V.N. Purav Marg, Mankhurd,  
Mumbai-400088

E-Mail: [anwesh@tifr.res.in](mailto:anwesh@tifr.res.in)

~~~~~



**Ramakrishna Mission Residential College (Autonomous)**

**Vivekananda Centre for Research**

**Ramakrishna Mission Ashrama**

(A Branch Centre of Ramakrishna Mission, Belur Math, Howrah-711202)

**Narendrapur, Kolkata - 700 103, West Bengal, India**

A Scientific Industrial Research Organisation, Recognised by DST, Govt. of India

College with Potential for Excellence (CPE), Re-accredited by NAAC - 'A' (CGPA 3.56 out of 4)

---

## **DEPARTMENT OF PHYSICS**

### **Certificate**

This is to certify that SHATANIK BHATTACHARYA, a student of B. Sc has successfully completed the project of UG curriculum entitled "ASTEROSEISMOLOGY OF SOLAR-TYPE OSCILLATORS" in the period from January to May, 2020.

Malay Purkait  
.....  
30.06.2020.

**Signature Of HOD**

**Dept. of Physics**

**Dr. Malay Purkait**

Associate Prof. & Head

Department of Physics

Ramakrishna Mission Residential College  
(Autonomous)

Narendrapur, Kolkata-700 103, (W.B.)



# ACKNOWLEDGEMENTS

SHATANIK BHATTACHARYA

6th Semester Student,  
Department of Physics,  
RAMAKRISHNA MISSION RESIDENTIAL COLLEGE (AUTONOMOUS)  
Narendrapur, Kolkata-700103  
shatanik2@gmail.com

I, Shatanik Bhattacharya, 6th Semester student of Ramakrishna Mission Residential College (Autonomous), am indebted to a number of personalities who have at various stages, helped and motivated me to bring out my project titled "**ASTEROSEISMOLOGY OF SOLAR-TYPE OSCILLATORS**".

I would like to thank my project supervisor Dr. Anwesh Mazumdar of Homi Bhabha Centre for Science Education-TIFR, Mankhurd, Mumbai and Prof. H.M. Antia of Tata Institute of Fundamental Research, Colaba, Mumbai for guiding me through the project by giving me valuable suggestions and helping me out with necessary resources. I would like to acknowledge support (in the form of funds and resources) from the NIUS Programme of HBCSE-TIFR and the staff of HBCSE-TIFR which enabled me to carry this project out efficiently. I would also like to thank NASA's Kepler and KASOC team for making the pre-processed data available to us.

I am grateful to the faculty and staff of my parent institution:

Ramakrishna Mission Residential College (Autonomous) for providing me help in many ways including access to computational resources for the sake of my project. Finally, I thank my family members who have given me immense support and motivation for these past months.

*Shatanik Bhattacharya*

SHATANIK BHATTACHARYA



# INDEX

| <u>SECTION NO.</u> | <u>TOPIC</u>                                                               | <u>PAGE NO.</u> |
|--------------------|----------------------------------------------------------------------------|-----------------|
|                    | <b>AIM</b>                                                                 | 1               |
| <b>I</b>           | <b><i>Basics of Asteroseismology</i></b>                                   |                 |
| A                  | Introduction to Asteroseismology                                           | 1               |
| B                  | Theory of the Solar-Like Oscillations                                      | 1               |
| C                  | Spatial Response of Observations                                           | 2               |
| D                  | Fourier Analysis of Time Series Data                                       | 4               |
| E                  | Nature of the Frequencies in the Power Spectrum                            | 5               |
|                    |                                                                            |                 |
| <b>II</b>          | <b><i>Determination of mode parameters from Asteroseismic analysis</i></b> |                 |
| A                  | Generating the Power Spectrum to be used for Analysis                      | 7               |
| B                  | Creating the model to be fitted                                            | 7               |
| C                  | Maximum Likelihood Function                                                | 8               |
| D                  | Broyden-Fletcher-Goldfarb-Shanno (B.F.G.S.) Algorithm                      | 9               |
| E                  | Output                                                                     | 11              |
| F                  | Results Obtained                                                           | 11              |
|                    |                                                                            |                 |
| <b>III</b>         | <b>PYTHON PACKAGES USED</b>                                                | 14              |
| <b>IV</b>          | <b>CONCLUSION</b>                                                          | 14              |
| <b>V</b>           | <b>ACKNOWLEDGEMENTS</b>                                                    | 14              |
| <b>VI</b>          | <b>BIBLIOGRAPHY</b>                                                        | 14              |

In this project, we have developed a python code to fit the model of the solar-like oscillations to the power spectral density profile of a target star and thereby deduce the eigenfrequencies of oscillations and other relevant properties like rotational splittings, the inclination of its rotational axis with respect to the our line of sight, etc..

We will first introduce ourselves to the basics of solar-like oscillations and then discuss how the theoretical model in the frequency domain is developed. Finally, we will present the concepts used to develop the code and then discuss the results obtained with the G-type star 16 Cyg A (KIC 12069424).

## I: BASICS OF ASTEROSEISMOLOGY:

### I.A: INTRODUCTION TO ASTEROSEISMOLOGY:

Asteroseismology is the branch of astrophysics that deals with the oscillations (stellar “quakes”) occurring inside stars that are direct consequences of their basic physical constituency. Precise and accurate measurements of these oscillations with high resolution telescopes help in observing these oscillations, thus enabling us to draw out conclusions regarding stellar interiors. One very common technique used to study asteroseismic properties of stars is photometry- the measurement of flux of a certain band of electromagnetic radiation received on detectors from astronomical objects. With the advent of very high precision photometry in telescopes like CoRoT, *Kepler*, TESS, etc. it is possible to detect the very minute oscillations (usually in the order of parts per million) of the stars over a long period of time. The signal received on performing fourier analysis enables us to identify the eigenfrequencies of oscillations which carry information regarding the internal structure of the star.

### I.B: THEORY OF THE SOLAR-LIKE OSCILLATONS:

Solar-like oscillations, the stochastically excited (by turbulent convection) and intrinsically damped resonant modes of oscillations are the direct effect of small-amplitude variations about the equilibrium state. The conservation laws that govern the evolution of the fluids constituting the star are:

|                                                                                                                                                                                                                                                                                                                  |
|------------------------------------------------------------------------------------------------------------------------------------------------------------------------------------------------------------------------------------------------------------------------------------------------------------------|
| <b>The equation of mass continuity:</b> $\frac{dp}{dt} = -\rho \nabla \cdot \mathbf{v}$ _____ (I. B. 1. a)                                                                                                                                                                                                       |
| <b>Newton's 2<sup>nd</sup> law of motion:</b> $\rho \frac{d\mathbf{v}}{dt} = -\nabla p + \rho \mathbf{g} + \mathbf{f}_{\text{other}}$ _____ (I. B. 1. b)                                                                                                                                                         |
| <b>1<sup>st</sup> Law of Thermodynamics:</b> $\frac{dq}{dt} = \frac{du}{dt} + p \frac{d(1/\rho)}{dt} = \frac{1}{\rho(\Gamma_3-1)} \left( \frac{dp}{dt} - \frac{\Gamma_1 p}{\rho} \frac{d\rho}{dt} \right) = \frac{1}{\rho(\Gamma_3-1)} \left( \frac{dp}{dt} - c_s^2 \frac{d\rho}{dt} \right)$ _____ (I. B. 1. c) |
| <b>Poisson Equation for Gravitational potential:</b> $\nabla^2 \Phi = 4\pi G \rho$ _____ (I. B. 1. d)                                                                                                                                                                                                            |

where  $\rho$  =fluid mass density,  $p$  =fluid pressure,  $q$ =heat supplied per unit mass,  $u$ =internal energy per unit mass,  $\mathbf{v}$ =velocity of fluid,  $\mathbf{g}$ =gravitational acceleration= $-\nabla\Phi$ ,  $\mathbf{f}_{\text{other}}$ =other forces acting per unit volume of the fluid,  $\Gamma_1 = \left( \frac{\partial \ln p}{\partial \ln \rho} \right)_{ad}$ ,  $\Gamma_3 - 1 = \left( \frac{\partial \ln T}{\partial \ln \rho} \right)_{ad}$ ,  $T$  = temperature of the fluid,  $c_s$ =adiabatic sound speed.

Considering a non-rotating spherically symmetric star in hydrostatic and thermodynamic equilibrium with  $\mathbf{f}_{\text{oth}} = 0$ , we have:  $\nabla p_0 = -\rho_0 g_0 \hat{\mathbf{r}}$ , where subscript '0' indicates equilibrium quantities. Now we introduce small, linear, adiabatic ( $dq = 0$ ) perturbations to all quantities about equilibrium. If  $y(r, \theta, \phi, t)$  be a scalar property of the gas, we introduce the linear perturbations  $y'$  and  $\delta y$  where  $y = y_0 + y'$  and  $\delta y = y' + \xi \cdot \nabla y_0$  where  $\xi$ =displacement vector. Thus velocity of fluid element is  $= \frac{d\xi}{dt} \approx \frac{\partial \xi}{\partial t}$ .

The aforementioned set of equations now becomes:

$$\begin{aligned}
 \rho' &= -\nabla \cdot (\rho_0 \xi) && \text{_____ (I. B. 2. a)} \\
 \rho_0 \frac{\partial^2 \xi}{\partial t^2} &= -\nabla p' - \rho_0 \nabla \Phi' - \rho' \nabla \Phi_0 && \text{_____ (I. B. 2. b)} \\
 p' + \xi \cdot \nabla p_0 &= \frac{\Gamma_{1,0} p_0}{\rho_0} (\rho' + \xi \cdot \nabla \rho_0) && \text{_____ (I. B. 2. c)} \\
 \nabla^2 \Phi' &= 4\pi G \rho' && \text{_____ (I. B. 2. d)}
 \end{aligned}$$



Here, we have 4 equations with 4 variables (provided the equilibrium conditions are known) which are:  $\rho', p', \Phi', \xi$ . With appropriate boundary conditions, these equations can be solved. Considering  $f' = \{\rho', p', \Phi'\}$ , we can show by substituting that the general solutions as can be of the form:

$$f'(r, \theta, \phi, t) = \text{Re}\{f'(r)Y_l^m(\theta, \phi)e^{i\omega t}\} \quad \text{---(I.B.3.a)}$$

$$\xi(r, \theta, \phi, t) = \text{Re}\left\{\left[\xi_r(r)Y_l^m(\theta, \phi)\hat{r} + \xi_h(r)\left(\frac{\partial Y_l^m(\theta, \phi)}{\partial \theta}\hat{\theta} + \frac{1}{\sin \theta}\frac{\partial Y_l^m(\theta, \phi)}{\partial \phi}\hat{\phi}\right)\right]e^{-i\omega t}\right\} \quad \text{---(I.B.3.b)}$$

where  $\xi_r$  indicates the depth-dependent part of radial displacement,  $\xi_h$  indicates depth-dependent part of non-radial displacement,  $Y_l^m(\theta, \phi)$  are the spherical harmonics,  $\omega$  is the frequency of oscillation.

We then eliminate  $\xi_h$  using continuity equation and  $\rho'(r)$  using adiabatic equation. Hence, we obtain:

$$\frac{1}{r^2}\frac{d}{dr}(r^2\xi_r) - \frac{g_0}{c_0^2}\xi_r - \left(\frac{S_l^2}{\omega^2} - 1\right)\frac{1}{c_0^2\rho_0}p' = \frac{l(l+1)}{r^2\omega^2}\Phi' \quad \text{---(I.B.4.a)}$$

$$\frac{dp'}{dr} + \frac{g_0}{c_0^2}p' - \rho_0(\omega^2 - N_0^2)\xi_r = -\rho_0\frac{d\Phi'}{dr} \quad \text{---(I.B.4.b)}$$

$$\frac{1}{r^2}\frac{d}{dr}\left(r^2\frac{d\Phi'}{dr}\right) - \frac{l(l+1)}{r^2}\Phi' = 4\pi G\left(\frac{p'}{c_0^2} + \frac{\rho_0 N_0^2}{g_0}\xi_r\right) \quad \text{---(I.B.4.c)}$$

**Cowling approximation** of the radial perturbation gives us:

$$\frac{d^2\xi_r}{dr^2} = -\frac{\omega^2}{c^2}\left(1 - \frac{N_0^2}{\omega^2}\right)\left(1 - \frac{S_l^2}{\omega^2}\right)\xi_r \quad \text{---(I.B.5)}$$

where  $\xi_r$  is a dimensionless variable indicating radial displacement,  $\omega$  is the angular frequency of the oscillation that satisfies the equation.,  $N_0^2 = -g_0\left[\frac{1}{\Gamma_1}\frac{d \ln \rho_0}{dr} - \frac{d \ln \rho_0}{dr}\right]$ : the **Brunt – Väisälä frequency**,  $S_l^2 = \frac{l(l+1)}{r^2}c^2$ : the **Lamb frequency**. The oscillatory eigenfunctions of this equation are trapped in regions where:

i.)  $\omega^2 > N_0^2$  and  $\omega^2 > S_l^2$ : p-modes

ii.)  $0 < \omega^2 < N_0^2$  and  $\omega^2 < S_l^2$ : g-modes (are absent in convectively unstable zones as  $N_0^2 < 0$ )

There exist values for  $\omega$  where trapping regions of p-mode and g-mode are very close by, breaking the uniformity in the mode spacing.

The eigenvalues of  $\nu = \frac{\omega}{2\pi}$  are given by boundary conditions and are computed numerically. We shall get back to them in section I.E. The net oscillation of the star includes all the possible modes.

Thus the Solar-like oscillations visible on the disk of the star may be described in terms of **spherical harmonic functions**  $Y_l^m$  of co-latitude  $\theta$  and longitude  $\phi$  defined at each radial eigen-mode  $n$ .

The **spherical harmonic functions** are given by:

$$Y_l^m(\theta, \phi) = (-1)^m c_{lm} P_l^m(\cos \theta) e^{im\phi} \quad \text{---(I.B.6)}$$

where  $P_l^m$  is a **Legendre function (polynomial)**; and normalization factor:  $c_{lm}$  is determined by:

$$c_{lm}^2 = \frac{(2l+1)(l-m)!}{4\pi(l+m)!} \quad \text{---(I.B.7)}$$

## I.C: SPATIAL RESPONSE OF OBSERVATIONS:

The integration inherent in the disc-averaged signal applies a strong spatial filter, making observation sensitive to modes in *low* angular degree  $l$  (due to averaging of values corresponding to *high* values of  $l$  to extremely small values), which measures the **total horizontal wave number**  $k_h$  on the surface by:

$$k_h = \frac{\sqrt{l(l+1)}}{R}, \text{ where } R = \text{Radius of the star.}$$

This  $k_h$  is the square root of eigenvalue obtained on operating the Laplacian in spherical coordinates over the  $Y_l^m(\theta, \phi)$  on the surface of the star (i.e., at  $r = R$ ).

$$\text{Equivalently the wavelength is: } \lambda = \frac{2\pi}{k_h}.$$

$$\text{Thus: } \sqrt{l(l+1)} = \frac{2\pi R}{\lambda} \text{ ----- (I. C. 1) .}$$

Let the position and time dependent **intensity perturbation due to oscillations** be:  $I(t; \theta, \phi)$ . Then the **integrated signal**  $\bar{I}(t)$  given by integration over the area of visible disc  $A$  is:

$$\bar{I}(t) = \int_A I(t; \theta, \phi) W(\cos \theta) dA, \text{----- (I. C. 2)}$$

Where  $W(\cos \theta)$  is a **weighting factor** that is assumed to depend only on the angular distance from rotation axis of the star. For **photometric observations**, the **dominant contribution that describes the change in intensity is of limb darkening which is generally of the form:**

$$W(\cos \theta) = 1 - \sum_{k=1}^N c_k [1 - \cos \theta]^k \text{ ----- (I. C. 3)}$$

where  $c_k$  are the limb-darkening co-efficients.

The intensity perturbation (*real* part of eigenfunction at the surface) of a mode of given  $l, m$  and radial order  $n$  having amplitude  $A_{nlm}$ , angular (eigen-) frequency  $\omega_{nlm}$ , and an initial phase  $\delta_{nlm}$  is then given as:

$$I_{nlm}(t; \theta, \phi) = \sqrt{4\pi} (-1)^m c_{lm} P_l^m(\cos \theta) A_{nlm} \cos(m\phi - \omega_{nlm}t + \delta_{nlm}). \text{----- (I. C. 4)}$$

Considering the rotation axis of the star to be pointing along the line-of-sight ( $\angle i_s \neq 0^\circ$ ), there is a net cancellation of terms wherever  $m \neq 0$ , leaving behind terms containing  $m = 0$ . We, thereby, rewrite equation I.C.2 as:

$$\bar{I}_{nl}(t) = S_l A_{nl} \cos(\omega_{nl}t - \delta_{nl}), \text{----- (I. C. 5)}$$

where we have composed a **visibility function**  $S_l$  independent of  $n$  for high-order modes (good assumption for solar-like oscillators):

$$S_l = \begin{cases} 2\pi\sqrt{2l+1} \int_0^{\pi/2} P_l(\cos \theta) W(\cos \theta) \cos \theta \sin \theta d\theta & \text{--- (I. C. 6. a)} \\ 2\pi\sqrt{2l+1} \int_0^{\pi/2} P_l(\cos \theta) W(\cos \theta) \cos^2 \theta \sin \theta d\theta & \text{--- (I. C. 6. b)} \end{cases}$$

Equation I.C.6.a is used whenever scalar quantities (like photon flux) are measured, whereas I.C.6.b is used whenever projection of vectors (like Doppler velocity) along line-of-sight are measured (an extra  $\cos \theta$  term in the integrand for the sake of projection along L.o.S.).

Estimated squared, normalized sensitivities with a quadratic limb-darkening law

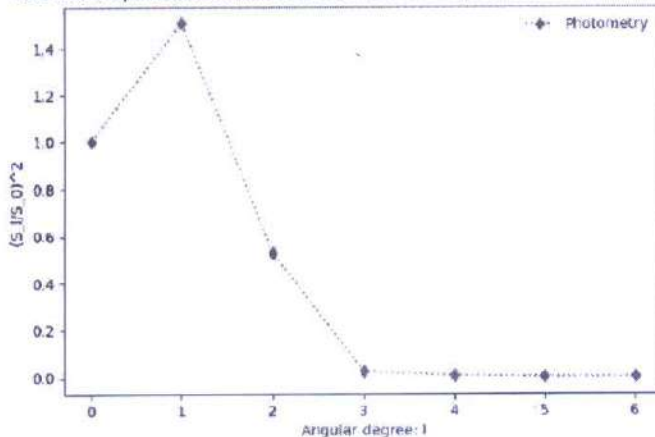


Fig. 1: Shown aside are the estimated squared, normalised sensitivities  $\left(\frac{S_l}{S_0}\right)^2$  against angular degrees  $l$  for photometric observations with a limb-darkening law having  $c_1 = 0.44$ ,  $c_2 = 0.23$ , and  $c_k = 0$  for  $k \geq 3$ .



Therefore, we see from Fig. 1 that the modes of oscillations belonging to  $l \geq 3$  are extremely small compared to the rest and are thus not always prominent enough to be identified. They are usually lost in the noise.

The response corresponding to a different choice of polar axis can be obtained by integration of the spherical harmonics (acted upon by *rotation operator* in spherical polar coordinates) over the visible stellar disc. An important special case arises when the polar axis lies in the plane of the sky. The effective visibility function for the signal then turns out to be:

$$S_{l,m} = \sqrt{\varepsilon_{l,m} \left(\frac{\pi}{2}\right)} S_l \quad \text{--- (I.C.7)}$$

where  $\varepsilon_{l,m} \left(\frac{\pi}{2}\right)$  can be found for different values of  $l$  and  $m$  on substituting  $i_s = \frac{\pi}{2}$  in the formula:

$$\varepsilon_{l,m}(i_s) = \frac{(l - |m|)!}{(l + |m|)!} [P_l^{|m|}(\cos i_s)]^2 \quad \text{--- (I.C.8)}$$

It is quite evident from equation I.C.8 that  $\varepsilon_{l,-m}(i_s) = \varepsilon_{l,m}(i_s)$ .

For odd values of  $l - m$ , there exist odd number of latitudes (since, number of latitudes =  $l - |m|$ ) and thereby one of the latitudes is the equator (equal number of latitudes being present on either sides of the equator). Since  $P_l^m(\cos \theta)$  is anti-symmetric around the equator, therefore there will be a net cancellation of intensities. Also as evident from equation I.10, since  $P_l^{|m|}(0) = 0$  [We know,  $P_l^{|m|}(-x) = (-1)^{l+|m|} P_l^{|m|}(x)$ ; for  $x = 0$ ,  $P_l^{|m|}(0) = (-1)^{l+|m|} P_l^{|m|}(0)$ ; for odd values of  $l + |m|$ ,  $P_l^{|m|}(0) = -P_l^{|m|}(0) \Rightarrow P_l^{|m|}(0) = 0$ ] therefore  $\varepsilon_{l,m} \left(\frac{\pi}{2}\right) = 0$  for the same.

## LD: FOURIER ANALYSIS OF THE TIME SERIES DATA:

The pulsations of stars like the Sun can be approximated to a number of superposed linear harmonic oscillating signals (S.H.O.s.) of small-amplitudes. The data corresponding to the signals are collected and their time series is constructed. Fourier analysis of this time string lends us important information about the star's oscillations, and thereby its interiors.

Let us start off with 1 S.H.O.:  $\tilde{I}(t) = A_0 \cos(\omega_0 t - \delta_0)$  whose data has been collected over a time interval  $T$ . It's Fourier transform (in **positive** angular frequency domain) is:

$$\widetilde{I}_*(\omega) = \frac{T A_0}{2} \left\{ e^{i \left[ \frac{T(\omega - \omega_0)}{2} + \delta_0 \right]} \text{sinc} \left[ \frac{T(\omega - \omega_0)}{2} \right] \right\} \quad \text{--- (I.D.1)}$$

The power spectrum  $P(\omega)$  is given by:

$$P(\omega) = ||\widetilde{I}_*(\omega)||^2 \simeq \frac{1}{4} T^2 A_0^2 \text{sinc}^2 \left[ \frac{T}{2} (\omega - \omega_0) \right] \quad \text{--- (I.D.2)}$$

**Simultaneous scillations** are richer in information as they give us an interference pattern when they are closely spaced.

Let us consider a periodic wave which is a superposition of 2 S.H.O.s:

$\tilde{I}(t) = a_1 \cos(\omega_1 t - \delta_1) + a_2 \cos(\omega_2 t - \delta_2)$  whose data has been collected over time interval 0 to  $T$ . It's Fourier transform (in **positive** angular frequency domain) is:

$$\widetilde{I}_*(\omega) = \frac{T}{2} \left\{ a_1 e^{i \left[ \frac{T(\omega - \omega_1)}{2} + \delta_1 \right]} \text{sinc} \left[ \frac{T(\omega - \omega_1)}{2} \right] + a_2 e^{i \left[ \frac{T(\omega - \omega_2)}{2} + \delta_2 \right]} \text{sinc} \left[ \frac{T(\omega - \omega_2)}{2} \right] \right\} \quad \text{--- (I.D.3)}$$

The power spectrum  $P(\omega)$  is given by:

$$P(\omega) = ||\widetilde{I}_*(\omega)||^2$$



$$= \frac{T^2}{4} \left\{ a_1^2 \text{sinc}^2 \left[ \frac{T(\omega - \omega_1)}{2} \right] + a_2^2 \text{sinc}^2 \left[ \frac{T(\omega - \omega_2)}{2} \right] + 2a_1 a_2 \text{sinc} \left[ \frac{T(\omega - \omega_1)}{2} \right] \text{sinc} \left[ \frac{T(\omega - \omega_2)}{2} \right] \cos \left[ \frac{T(\omega_2 - \omega_1)}{2} - (\delta_2 - \delta_1) \right] \right\} \quad \text{---(I.D.4)}$$

The last term in equation I.D.4 corresponds to the interference pattern formed in the plot of the power spectrum. The two major peaks give us information about the frequency of the individual oscillating signals whereas the interference pattern (provided the peaks are considerably close to each other) gives us information regarding the phase differences between the S.H.O.s.

There arise cases where the time series' **data contains gaps**, as if a mathematical *window function* operates over the signal, due to periodic rising and setting of the object of interest or due to temporary shutdown of C.C.D.s for downloading the collected data. Its Fourier transform can be easily deduced using the convolution theorem of Fourier analysis. Thereby, its corresponding power spectrum is deduced. Let us consider a single S.H.O.:

The data for  $\tilde{I}(t) = a_0 \cos(\omega t - \delta_0)$  has been collected in time intervals 0 to T and  $\tau$  to T +  $\tau$ . Therefore, we consider the window function as:

$$W(t) = \begin{cases} 1, & \text{for } 0 < t < T \text{ and } \tau < t < \tau + T \\ 0, & \text{for } T < t < \tau \text{ and } t > T + \tau \end{cases}$$

Our power spectrum now is:

$$P(\omega) = \left| \widetilde{W}_*(\omega) * \widetilde{I}_*(\omega) \right|^2 = \left| \int_{\text{all } \omega'} \widetilde{W}_*(\omega - \omega') \widetilde{I}_*(\omega') d\omega' \right|^2 \quad \text{---(I.D.5)}$$

If the **oscillation signals are damped** and their data are collected over a very large interval ( $T \rightarrow \infty$ ) then we obtain a power spectrum which is a **Lorentzian profile**. This profile has a half-width at half-maximum of the *damping co-efficient*. The mode profile centred on  $\nu = \nu_0$  with amplitude  $a$  and half-width-half-maximum (HWHM)  $\sigma$  is:  $P(\nu) = \frac{a}{1 + \frac{(\nu - \nu_0)^2}{\sigma^2}}$

The starlight contains not one but numerous damped oscillation signals which is received as the time-series data, commonly known as the light-curve. The power spectrum of this light-curve now contains Lorentzians centred at their corresponding frequency with a particular amplitude and mode width. Moreover when the star is rotating, modes with angular degrees  $l$  are split into  $2l + 1$  azimuthal orders each of which is  $\epsilon_{lm}(i_s)$  times the total amplitude of the mode.

Now the effective power spectrum containing all the modes of oscillations will be of the form:

$$P_{n,l,m}(\nu) = \sum_{n,l} \sum_{m=-l}^l \frac{\bar{A}_{nl} \epsilon_{lm}(i_s)}{1 + \frac{[\nu - (\nu_{nl} + m\Omega_s)]^2}{[\Gamma_{nlm}]^2}} \quad \text{---(I.D.6)}$$

where:  $\bar{A}_{nl}$  = net amplitude of the  $(n,l)$  mode  
 $\nu_{nl}$  = central frequency of the  $(n,l)$  mode  
 $\Gamma_{nlm}$  = half-width of the  $(n,l,m)$  mode  
 $i_s$  = angle of inclination of the star's rotational axis with the line of sight  
 $\Omega_s$  = rotational splitting of the  $(n,l)$  mode due to rotation  
 $\epsilon_{lm}(i_s)$  is the relative amplitude of mode inside a multiplet; defined in equation (I.C.8)

## 1.E: NATURE OF THE FREQUENCIES IN THE POWER SPECTRUM

Detailed analysis of the power spectrum helps draw out various conclusions regarding the periodic motions on the star. Filtering out the "noise" (in asteroseismology's perspective), e.g., data due to stellar activities, granulations, transits, eclipses, star-spots, shot-noise, etc. are done with the help of rigorous mathematics and statistics.

Once the different noises are filtered out and the region containing oscillation modes are isolated, they are minutely analysed so as to precisely determine the stellar interiors.

High overtone p-modes (where  $\frac{l}{n} \rightarrow 0$ ) are analysed using conclusions drawn mathematically [Tassoul—1980] from asymptotic theory ( $\omega^2 \gg N^2$ ):

$$v_{nlm} \simeq \Delta v \left( n + \frac{l}{2} + \epsilon \right) - \Delta v^2 \left\{ \frac{Al(l+1) - B}{v_{nl0}} \right\} + \frac{m}{2\pi} \int_0^R \int_0^\pi K_{nlm}(r, \theta) \Omega_{\text{rot}}(r, \theta) r dr d\theta \quad \text{---(I.E.1)}$$

where  $n$ =radial overtone number,  $l$ =degree of oscillation,  $m$ = azimuthal order,  $K_{nlm}$  is the weighting kernel,  $\Omega_{\text{rot}}(r, \theta)$  is the position dependent internal angular velocity,  $\epsilon$  depends on the cavity boundary conditions,  $B$  is a correction dependent on the surface boundary conditions,  $c$  is the sound speed and:

$$\Delta v = \left( 2 \int_0^R \frac{dr}{c} \right)^{-1} \quad \text{and} \quad A = \frac{1}{4\pi^2 \Delta v} \left( \frac{c(R)}{R} - \int_0^R \frac{dc}{dr} \frac{dr}{r} \right)$$

Thus, we find that,  $\Delta v_{nl} = v_{nl0} - v_{n-1, l0} \simeq \Delta v$ ,  $v_{n, l+10} - v_{n, l0} \simeq \Delta v/2$ .  $\Delta v_{nl}$  is known as the large frequency separation.  $\langle \Delta v_{nl} \rangle \propto \langle \rho \rangle^{\frac{1}{2}}$ . The  $v_{nl}$  defined in equa<sup>n</sup> (I.16) is equal to  $v_{nl0}$  in equa<sup>n</sup> (I.17).

$$\delta v_{l, l+2}(n) = v_{n, l0} - v_{n-1, l+20} \simeq -\frac{(4l+6)\Delta v}{4\pi^2 v_{nl0}} \int_0^R \frac{dc}{dr} \frac{dr}{r} \quad \text{---(I.E.2)}$$

$\delta v_{l, l+2}(n)$  is known as the small frequency separation which depends on the velocity gradient inside the star. We see that  $\delta v_{1,3}(n) \simeq \frac{5}{3} \delta v_{0,2}(n)$ . The inner turning point exists at  $r_t$  where  $\frac{c(r_t)}{r_t} = \frac{\omega}{\sqrt{l(l+1)}}$ .

$\Delta v = \langle \Delta v_{nl} \rangle \propto \sqrt{\bar{\rho}} \propto \left( \frac{M}{R^3} \right)^{0.5}$  and  $v_{\text{max}} \propto v_{\text{ac}} \propto \frac{M}{R^2 \sqrt{T_{\text{eff}}}}$ , where  $v_{\text{max}} \equiv$  frequency with maximum power. The frequencies corresponding to higher values of angular order are hard to detect, usually from  $l \geq 4$ , due to low visibilities and geometric cancellation.

High-order g-modes are analysed using conclusions drawn mathematically from asymptotic theory:

$$\Pi_{nl} = \frac{2\pi^2}{\sqrt{l(l+1)}} \left( \int_{r_1}^{r_2} N \frac{dr}{r} \right)^{-1} \left( n + \frac{l}{2} + \epsilon_g \right) \quad \text{---(I.E.3)}$$

where  $\Pi_{nl}$  are the periods and  $\Delta \Pi_l = \Pi_{nl} - \Pi_{n-1, l} = \Pi_{nl} \left( n + \frac{l}{2} + \epsilon_g \right)^{-1}$  is known as the period separation,  $r_1$  and  $r_2$  are the inner and outer turning points of g-mode respectively (where  $\omega^2 \approx N^2$ ).

Plotting the frequency echelle diagram for p-modes and the period echelle diagram for g-modes help study the trends better. Let  $q$  be the required quantity such that  $q = k\Delta q + q'$ , where  $k \in \mathbb{Z}$ ,  $0 \leq q' < \Delta q$ . Then the echelle diagram for  $q$  is the plot of  $q$  against  $q \bmod \Delta q$ , i.e.,  $q$  against  $q'$ .  $q$  is the frequency for p-modes and period for g-modes.



## II: DETERMINATION OF MODE PARAMETERS FROM ASTEROSEISMIC ANALYSIS

### II.A: GENERATING THE POWER SPECTRUM TO BE USED FOR ANALYSIS:

In this project, we have developed a python code to fit the model of the power spectrum to the power spectrum of the star which can be retrieved by constructing the Lomb-Scargle periodogram (ref. [VanderPlas 2017, Arxiv e-prints, arXiv:1703.09824](#)) [which is similar to discrete/fast Fourier Transform, except that it enables us to compute the Fourier Transform of non-uniformly sampled data] of the light-curve containing normalized flux (with NaNs removed) or by directly acquiring the complete raw Power Spectral Density (henceforth will be referred to as "PSD") profile available from the [Kepler Asteroseismic Science Operations Centre](#) or [TESS Asteroseismic Science Operations Centre](#). The light-curve data obtained from *Kepler* are available in 2 cadences:  $\Delta t = 29.43$  minutes (long cadences) and  $\Delta t = 58.85$  seconds (short cadences). We use short cadence data for better resolution and higher nyquist frequency  $\left[ = \frac{1}{2\Delta t} \right]$ .

Once we have in hand our power spectrum, we recognise the peaks in the PSD that we will be using for parameter estimation. Then we set the limit for frequencies over which we will be fitting our model--- The range of frequencies is defined as: [min-freq, max-freq]. This is identical to performing point-wise product of raw PSD and the window function  $(v) = \begin{cases} 1, & v \in [\text{min\_freq}, \text{max\_freq}] \\ 0, & \text{elsewhere} \end{cases}$ .

Now, the PSD we have with us has a multiplicative noise that is distributed as  $\chi^2$  with 2 degrees of freedom with respect to the limit spectrum (the model obtained on optimization).

We can also perform smoothing of the power spectrum by convolving it a few times (say, twice or thrice) with the 1D box filter of a desired width. The prominent modes of oscillations are aptly visible in this smoothed PSD and by observing this spectrum we provide the initial guess to the model parameters.

### II.B: CREATING THE MODEL TO BE FITTED:

The model to be fitted to the data contains not only the various modes of oscillations, but also contains some background components. Now, we will define the different components of the model:

- i.) **White/Shot noise:** This is a constant noise which is independent of the frequency and arises mostly due to photon shot noise on the CCDs of the telescopes. Therefore the component of model contributing to the shot noise is:

$$M_{\text{shot}}(v_i) = e^{a_0}$$

where  $a_0$  is the natural logarithm of the constant shot noise.

[Note: We will use the notation  $v_i$  because our dataset is discrete where the resolution=

$$v_{i+1} - v_i = \frac{1}{\text{Total duration of observation of the star (in seconds)}}].$$

- ii.) **Stellar activities, granulation and other stellar phenomenon having very low frequencies:** Contribution of convective granulation, stellar activity and instrumental noise lies mostly in the low-frequency regime. The contribution of these phenomena, known as the **red noise**, to the background are often estimated to be a semi-Lorentzian centred at  $v_i = 0$ :

$$M_{\text{granulation}}(v_i) = \frac{e^{a_1}}{1 + \frac{v_i^2}{e^\Gamma}}$$

where  $a_1$  = natural logarithm of the amplitude of the semi-lorentzian

$\Gamma$  = natural logarithm of the square of its HWHM.

- iii.) **The modes of stellar oscillations:**

As we have discussed earlier in Part I, Solar-Like Oscillators oscillate with certain specific frequencies which depend on the structure and composition of the star.



The effective contribution to the power spectrum due to seismic activities is:

$$M_{seismic}(v_i) = \sum_{n,l} \sum_{m=-l}^l \frac{e^{a_{nl}} \varepsilon_{lm}(i_s)}{1 + \frac{[v_i - (v_{nl} + m\Omega_s)]^2}{\left[\frac{e^{\Gamma_{nl} + w_0}}{2l+1}\right]^2}}$$

where  $a_{nl}$  = natural logarithm of the total amplitude of the mode  $(n, l)$

$v_{nl}$  = centre of the oscillation mode  $(n, l)$

$\frac{e^{\Gamma_{nl} + w_0}}{2l+1}$  = The HWHM of the mode  $(n, l, m)$

$\Omega_s$  = Splitting due to rotation of the star

$i_s$  = angle of inclination of the star's rotation axis with respect to the line of sight

$w_0$  = A constant of the order of resolution

$\varepsilon_{lm}(i_s)$  = the relative amplitude of mode inside a multiplet of the angular degree

$$= \frac{(l-|m|)!}{(l+|m|)!} [P_l^{|m|}(\cos i_s)]^2$$

We have discussed earlier that all modes of oscillations of higher angular degree ( $l \geq 3$ ) are not very prominent (Fig. 1). Thus we have considered only the prominent peaks corresponding to  $l = 0, 1, 2$  and a few  $l = 3$  for estimation of parameters.

Therefore, the complete model whose parameters are to be estimated and fitted to the raw power spectrum is:

$$M(v_i; \mathbf{p}) = e^{a_0} + \frac{e^{a_1}}{1 + \frac{v_i^2}{e^{\Gamma}}} + \sum_n \sum_{l=0}^{2 \text{ or } 3} \sum_{m=-l}^l \frac{e^{a_{nl}} \varepsilon_{lm}(i_s)}{1 + \frac{[v_i - (v_{nl} + m\Omega_s)]^2}{\left[\frac{e^{\Gamma_{nl} + w_0}}{2l+1}\right]^2}} \quad \text{---(II.B.1)}$$

Here, we assume that for a particular angular degree of a mode all multiplets have equal widths. Also we keep  $w_0 = 0.03$  (of the order of resolution) here because the resolution does not allow a half-width of less than itself to be identified.

The  $3n + 5$  parameters whose values are to be estimated are:  $a_0, a_1, \Gamma, a_{nl}, v_{nl}, \Gamma_{nl}, i_s, \Omega_s$ . Here,

$$\mathbf{p} = (a_{n0} \ v_{n0} \ \Gamma_{n0} \ a_{n1} \ v_{n1} \ \Gamma_{n1} \ a_{n2} \ v_{n2} \ \Gamma_{n2} \ a_{(n+1)0} \ v_{(n+1)0} \ \Gamma_{(n+1)0} \dots a_0 \ a_1 \ \Gamma \ i_s \ \Omega_s) \quad \text{---(II.B.2)}$$

## II.C: MAXIMUM LIKELIHOOD FUNCTION:

We are supposed to find the most likely values for the parameters such that the model described in equation II.1 fits the unsmoothed PSD. The time-series data (light-curve) contains random processes. These processes, abiding by the central limit theorem, produce noises which are distributed about the limit spectrum in the form of the Gaussian individually in the real and imaginary parts of the Fourier transform. Thus the Fourier transform, and thereby the PSD (the norm-squared of the Fourier transform) abide by  $\chi^2$  statistics with 2 degrees of freedom.

Since the PSD is known to be distributed around the limit spectrum, i.e., here our  $M(v_i; \mathbf{p})$  with  $\chi^2$  2 degrees of freedom statistics, the likelihood function  $L$  is:

$$L(P; \mathbf{p}) = \prod_i \frac{1}{M(v_i; \mathbf{p})} e^{-\frac{P(v_i)}{M(v_i; \mathbf{p})}} \quad \text{---(II.C.1)}$$

where  $P$  = Raw power spectral density profile.

Owing to the available optimization techniques available, instead of maximizing the likelihood we minimize the negative logarithm of the likelihood which is:

$$F(\mathbf{p}) = -\ln L = \sum_i \ln M(v_i; \mathbf{p}) + \sum_i \frac{P(v_i)}{M(v_i; \mathbf{p})} \quad \text{---(II.C.2)}$$

Now that we have the model  $M(v_i; \mathbf{p})$ , the unsmoothed power spectral density  $P(v_i)$ , we proceed to minimize the function  $F(\mathbf{p})$  using a non-linear minimization technique known as the **Broyden-Fletcher-Goldfarb-Shanno Algorithm (B.F.G.S. Algorithm)** [Shanno--1970].

## II.D: BROYDEN-FLETCHER-GOLDFARB-SHANNO (B.F.G.S.) ALGORITHM:

This algorithm is a quasi-Newton method which estimates the values of parameters  $\mathbf{p} = (p_0 \ p_1 \ p_2 \ \dots \ p_n)$  to find the minimum value of the function  $F(\mathbf{p})$  which is preferably differentiable twice. It starts with an initial guess to the parameters such that it proceeds iteratively to get a better estimate of the parameters by using the **gradient** of the function  $\nabla F(\mathbf{p})$  where the  $k^{th}$  element of the element is  $\frac{\partial F}{\partial p_k}$ . BFGS uses a matrix known as the **Hessian matrix** which is defined as:

$$H = \begin{bmatrix} \frac{\partial^2 F}{\partial p_0^2} & \frac{\partial^2 F}{\partial p_0 \partial p_1} & \dots & \frac{\partial^2 F}{\partial p_0 \partial p_n} \\ \frac{\partial^2 F}{\partial p_1 \partial p_0} & \frac{\partial^2 F}{\partial p_1^2} & \dots & \frac{\partial^2 F}{\partial p_1 \partial p_n} \\ \vdots & \vdots & \ddots & \vdots \\ \frac{\partial^2 F}{\partial p_n \partial p_0} & \frac{\partial^2 F}{\partial p_n \partial p_1} & \dots & \frac{\partial^2 F}{\partial p_n^2} \end{bmatrix}$$

This approximate Hessian matrix, initialized as the identity matrix  $I_{n \times n}$ , checks the concavity of the  $F$  when the parameters have the value  $\mathbf{p}$ . It is used along with the gradient of the function to determine the direction in which it will proceed in the parameter space so as to minimize  $F$  and gets itself updated each time. The **inverse of the Hessian matrix**  $H^{-1}$  is more important in this context as it contains the co-variance of the parameters (random variables with a Gaussian distribution), i.e.,  $(H^{-1})_{ij} = \sigma_i \sigma_j$ . The elements on the principal diagonal of the  $H^{-1}$  matrix contain information about the errors in the obtained values of the parameters. The error in the estimation of the element  $p_k$  of  $\mathbf{p}$  is given as:

$$\Delta p_k = \sigma_k = \sqrt{(H^{-1})_{kk}}$$

Ideally, this algorithm is supposed to terminate when  $||\nabla F(\mathbf{p})|| = 0$ . But since the precision of the machine might not allow the partial derivatives to reach an exact 0, we set a limit  $\rho$  which has a very small value such that the code exits when  $||\nabla F(\mathbf{p})|| < \rho$  and returns to us the final estimate of  $\mathbf{p}_k$ .

In general, the **B.F.G.S. algorithm** we have used requires 4 inputs:

- i.) The peaks taken into consideration are visually assigned their corresponding values of angular degree  $l$ .
- ii.) The function to be minimized. In our case, the function to be minimized is  $F(\mathbf{p})$  as defined in equation(II.C.2).
- iii.) The initial guess to the parameters  $\mathbf{p}$  which is given by observing the smoothed PSD.
- iv.) The gradient vector  $\nabla F(\mathbf{p})$  of the function  $F(\mathbf{p})$  where:

$$\nabla F(\mathbf{p}) = \left( \frac{\partial F}{\partial a_{n0}}, \frac{\partial F}{\partial v_{n0}}, \frac{\partial F}{\partial \Gamma_{n0}}, \frac{\partial F}{\partial a_{n1}}, \frac{\partial F}{\partial v_{n1}}, \frac{\partial F}{\partial \Gamma_{n1}}, \frac{\partial F}{\partial a_{n2}}, \frac{\partial F}{\partial v_{n2}}, \frac{\partial F}{\partial \Gamma_{n2}}, \right. \\ \left. \frac{\partial F}{\partial a_{(n+1)0}}, \frac{\partial F}{\partial v_{(n+1)0}}, \frac{\partial F}{\partial \Gamma_{(n+1)0}}, \dots, \frac{\partial F}{\partial a_0}, \frac{\partial F}{\partial a_1}, \frac{\partial F}{\partial \Gamma}, \frac{\partial F}{\partial i_s}, \frac{\partial F}{\partial \Omega_s} \right) \quad \text{---(II.D.1)}$$



Using  $F(\mathbf{p})$  as defined in equation (II. C. 2), we can write:

$$\frac{\partial F}{\partial p_k} = \sum_i \left[ \left( \frac{1}{M(v_i; \mathbf{p})} - \frac{P(v_i)}{(M(v_i; \mathbf{p}))^2} \right) * \frac{\partial M(v_i; \mathbf{p})}{\partial p_k} \right] \text{---(II. D. 2)}$$

We hereby calculate the  $\frac{\partial M(v_i; \mathbf{p})}{\partial p_k}$  for the different parameters and feed them into the gradient using equation II. D. 2:

$$\frac{\partial M(v_i; \mathbf{p})}{\partial a_{nl}} = \sum_{m=-l}^l \frac{e^{a_{nl}} \varepsilon_{lm}(i_s)}{1 + \frac{[v_i - (v_{nl} + m\Omega_s)]^2}{\left[ \frac{e^{\Gamma_{nl}} + w_0}{2l+1} \right]^2}}$$

$$\frac{\partial M(v_i; \mathbf{p})}{\partial v_{nl}} = \frac{2}{\left[ \frac{e^{\Gamma_{nl}} + w_0}{2l+1} \right]^2} \sum_{m=-l}^l \left( \frac{e^{a_{nl}} \varepsilon_{lm}(i_s)}{\left\{ 1 + \frac{[v_i - (v_{nl} + m\Omega_s)]^2}{\left[ \frac{e^{\Gamma_{nl}} + w_0}{2l+1} \right]^2} \right\}^2} * \{v_i - (v_{nl} + m\Omega_s)\} \right)$$

$$\frac{\partial M(v_i; \mathbf{p})}{\partial \Gamma_{nl}} = \frac{2e^{\Gamma_{nl}}(2l+1)^2}{[e^{\Gamma_{nl}} + w_0]^3} \sum_{m=-l}^l \left( \frac{e^{a_{nl}} \varepsilon_{lm}(i_s)}{\left\{ 1 + \frac{[v_i - (v_{nl} + m\Omega_s)]^2}{\left[ \frac{e^{\Gamma_{nl}} + w_0}{2l+1} \right]^2} \right\}^2} * \{v_i - (v_{nl} + m\Omega_s)\}^2 \right)$$

$$\frac{\partial M(v_i; \mathbf{p})}{\partial a_0} = e^{a_0}$$

$$\frac{\partial M(v_i; \mathbf{p})}{\partial a_1} = \frac{e^{a_1}}{1 + \frac{v_i^2}{e^{\Gamma}}}$$

$$\frac{\partial M(v_i; \mathbf{p})}{\partial \Gamma} = \frac{e^{a_1}}{\left(1 + \frac{v_i^2}{e^{\Gamma}}\right)^2} \frac{v_i^2}{e^{\Gamma}}$$

$$\frac{\partial M(v_i; \mathbf{p})}{\partial i_s} = \sum_{all\ l} \sum_{m=-l}^l \frac{e^{a_{nl}} * \frac{(l-|m|)!}{(l+|m|)!} P_l^{|m|}(\cos i_s) * [P_l^{|m|+1}(\cos i_s) - (l+|m|)(l-|m|+1)P_l^{|m|-1}(\cos i_s)]}{1 + \frac{[v_i - (v_{nl} + m\Omega_s)]^2}{\left[ \frac{e^{\Gamma_{nl}} + w_0}{2l+1} \right]^2}}$$

$$\frac{\partial M(v_i; \mathbf{p})}{\partial \Omega_s} = \sum_{all\ l} \sum_{m=-l}^l \left( \frac{e^{a_{nl}} \varepsilon_{lm}(i_s)}{\left\{ 1 + \frac{[v_i - (v_{nl} + m\Omega_s)]^2}{\left[ \frac{e^{\Gamma_{nl}} + w_0}{2l+1} \right]^2} \right\}^2} * 2m * \frac{\{v_i - (v_{nl} + m\Omega_s)\}}{\left[ \frac{e^{\Gamma} + w_0}{2l+1} \right]^2} \right)$$

The algorithm returns us the parameters that give us a local minimum of the likelihood function.



## II.E: THE OUTPUT:

The BFGS Algorithm gives us the values of each of the parameters after optimisation. We estimate the large separation corresponding to angular degree  $l = 0$ . We plot the curve of  $\nu_{n0}$  against  $n$ . The slope of the best fit straight line  $[\nu_0(n; \langle \Delta \nu_0 \rangle, c) = n \langle \Delta \nu_0 \rangle + c]$  to this curve is plotted by minimizing the function :

$$F = \sum_i \left( \frac{\nu_{n0} - \nu(n; \langle \Delta \nu_0 \rangle, c)}{\sigma_{n0}} \right)^2$$

By fitting the straight line, we find the slope  $\langle \Delta \nu_0 \rangle$  and the standard deviation in its measurement. We consider  $\langle \Delta \nu \rangle \simeq \langle \Delta \nu_0 \rangle$ . Subsequently, we plot the **frequency échelle diagram** for the corresponding star. As we have discussed earlier in Section I.E, this diagram is a plot of  $\nu_{nl}$  against  $\nu \bmod \langle \Delta \nu \rangle$ .

## II.F: RESULTS OBTAINED:

### a.) 16 Cyg A (KIC 12069424):

16 Cyg A is a G-Type main sequence star which has been observed by NASA's *Kepler* telescope in short cadence from Quarters 6.1 to 17.2. We have obtained the unweighted PSD profile from the Kepler Asteroseismic Science Consortium generated using the corrected and concatenated time-series.

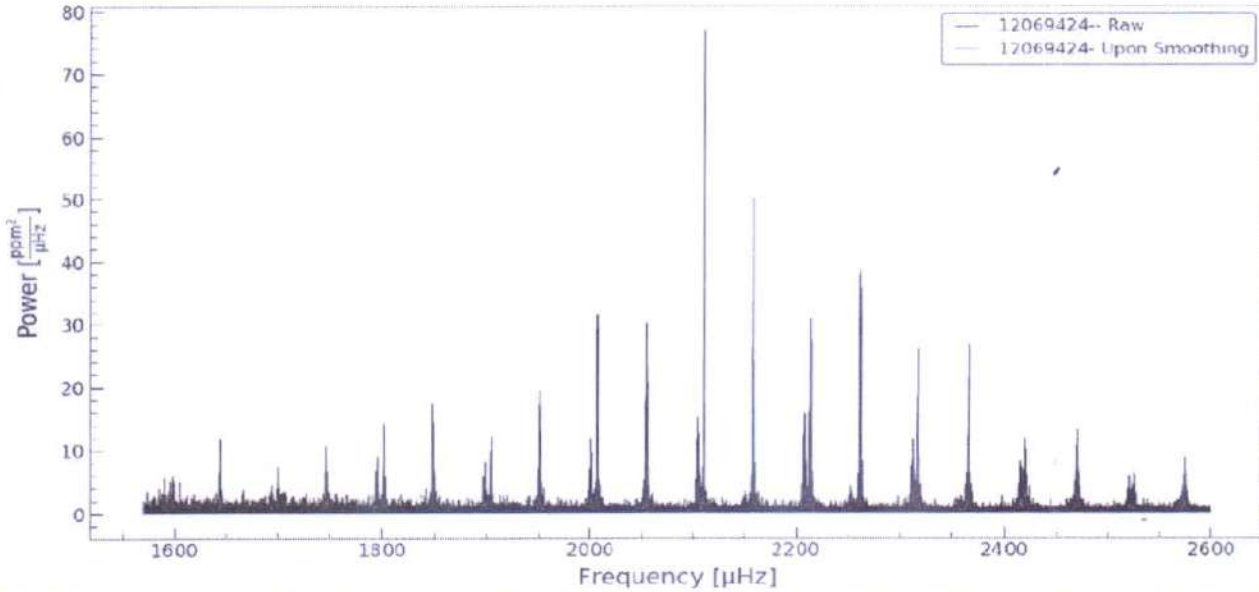


**Fig.2:** The raw unweighted power spectral density of 16 Cyg A containing the most prominent peaks [1570  $\mu\text{Hz}$  – 2600  $\mu\text{Hz}$ ] has been plotted in black. The plot in red indicates the spectrum on performing boxkernel smoothing of width 0.2  $\mu\text{Hz}$  thrice on the raw spectrum. The PSD profile was retrieved from the Kepler Asteroseismic Science Consortium.

Frequencies of the modes received as output are:

| Angular degree | Mean value of frequencies, $\nu$ (in $\mu\text{Hz}$ ) | Error $\sigma$ (in $\mu\text{Hz}$ ) |
|----------------|-------------------------------------------------------|-------------------------------------|
| $l = 0$        | 1598.697                                              | 0.060                               |
| $l = 0$        | 1700.926                                              | 0.094                               |
| $l = 0$        | 1802.320                                              | 0.073                               |
| $l = 0$        | 1904.591                                              | 0.050                               |
| $l = 0$        | 2007.564                                              | 0.045                               |
| $l = 0$        | 2110.899                                              | 0.042                               |
| $l = 0$        | 2214.273                                              | 0.050                               |
| $l = 0$        | 2317.327                                              | 0.055                               |
| $l = 0$        | 2420.981                                              | 0.087                               |
| $l = 0$        | 2525.311                                              | 0.140                               |
| $l = 1$        | 1644.982                                              | 0.093                               |
| $l = 1$        | 1747.182                                              | 0.079                               |
| $l = 1$        | 1849.015                                              | 0.056                               |
| $l = 1$        | 1952.030                                              | 0.053                               |

|         |          |       |
|---------|----------|-------|
| $l = 1$ | 2055.495 | 0.047 |
| $l = 1$ | 2159.158 | 0.048 |
| $l = 1$ | 2262.562 | 0.050 |
| $l = 1$ | 2366.225 | 0.062 |
| $l = 1$ | 2470.379 | 0.080 |
| $l = 1$ | 2574.626 | 0.137 |
| $l = 2$ | 1591.191 | 0.084 |
| $l = 2$ | 1694.026 | 0.172 |
| $l = 2$ | 1795.821 | 0.114 |
| $l = 2$ | 1898.343 | 0.093 |
| $l = 2$ | 2001.712 | 0.077 |
| $l = 2$ | 2105.328 | 0.048 |
| $l = 2$ | 2208.946 | 0.071 |
| $l = 2$ | 2312.548 | 0.095 |
| $l = 2$ | 2416.391 | 0.131 |
| $l = 2$ | 2521.161 | 0.338 |
| $l = 3$ | 1941.096 | 0.292 |
| $l = 3$ | 2045.807 | 0.196 |
| $l = 3$ | 2149.924 | 0.150 |
| $l = 3$ | 2253.433 | 0.194 |
| $l = 3$ | 2357.173 | 0.180 |
| $l = 3$ | 2461.791 | 0.315 |

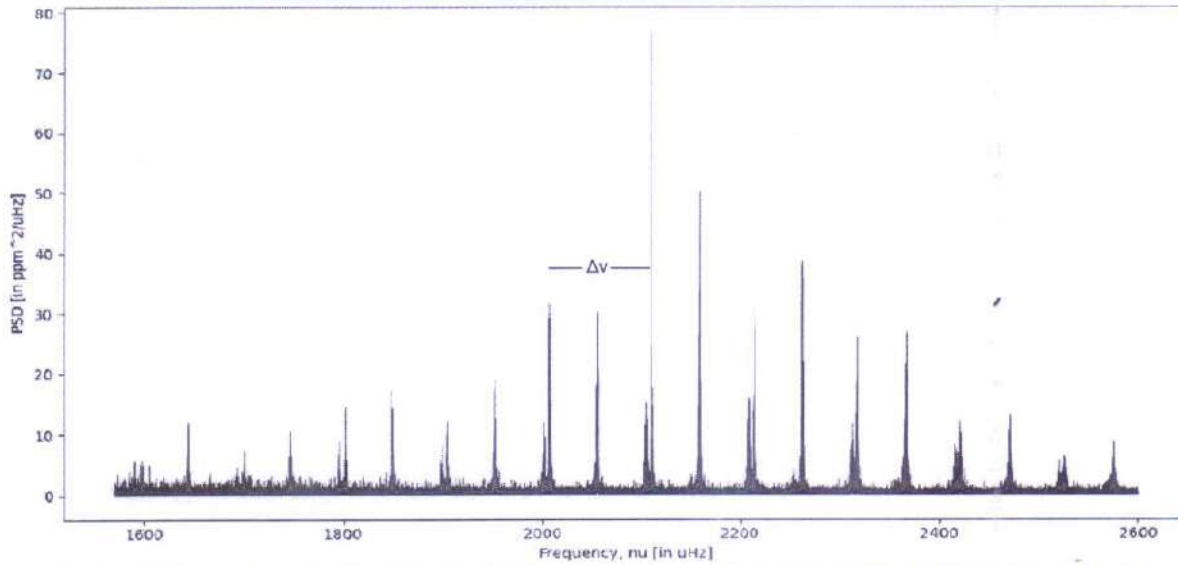


**Fig. 3:** The plot in blue indicates the unsmoothed power spectral density profile and one in red is the model that fits the PSD profile. The fitted model is the one for which we received the least value of  $F$  after altering the guess to the parameters slightly a few times.

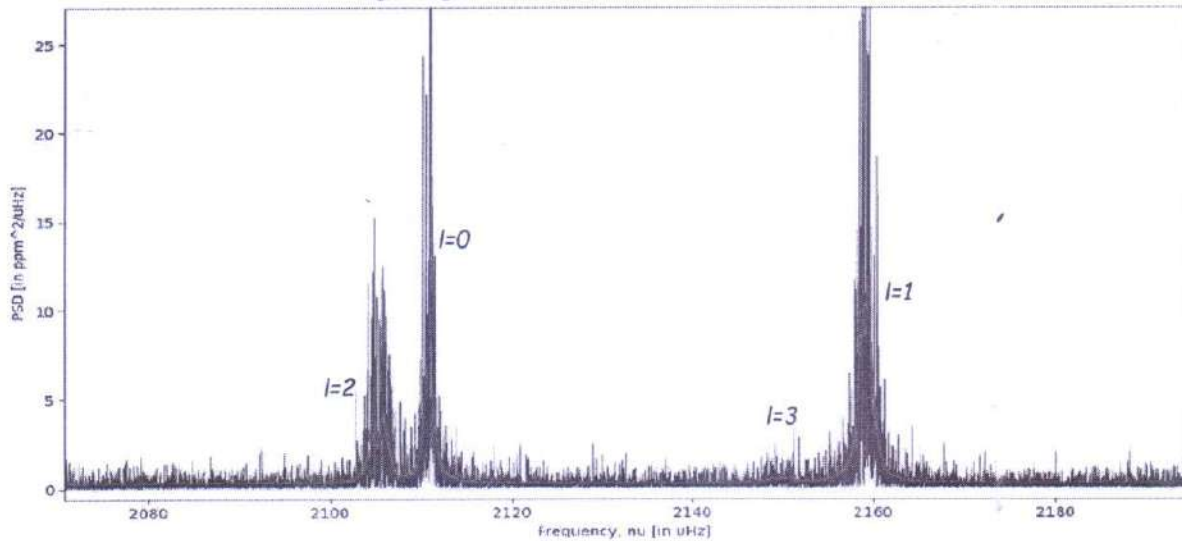


**Fig. 4:** On zooming into the plot as shown in Fig 3, we find that the splitting in the various modes and angular degrees are prominent.



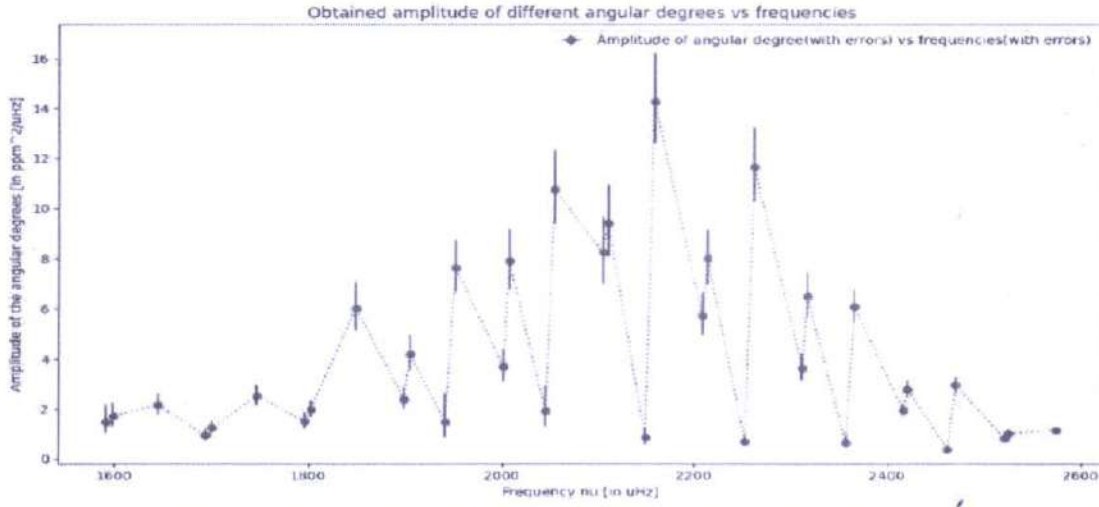


Fig. 5: Plot of the amplitude  $e^{a_{nl}}$  vs central frequency of each mode  $\nu_{nl}$  with their corresponding errors (the error in the frequencies are too small to be identified in the plot)

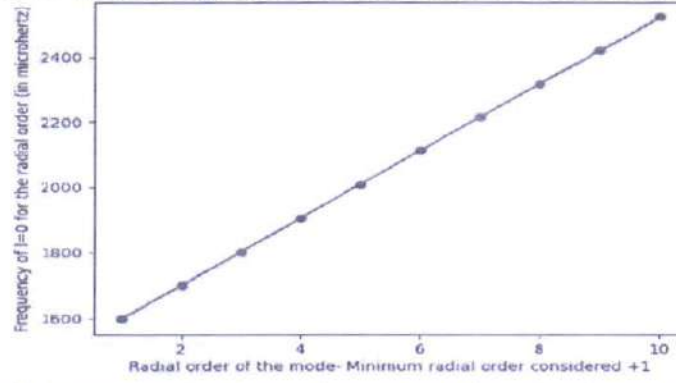


Fig. 6: The slope of the best fit line to the plot of eigenfrequencies of angular degree  $l=0$  with respect to the proxy of the radial orders gives us the value of the large separation.

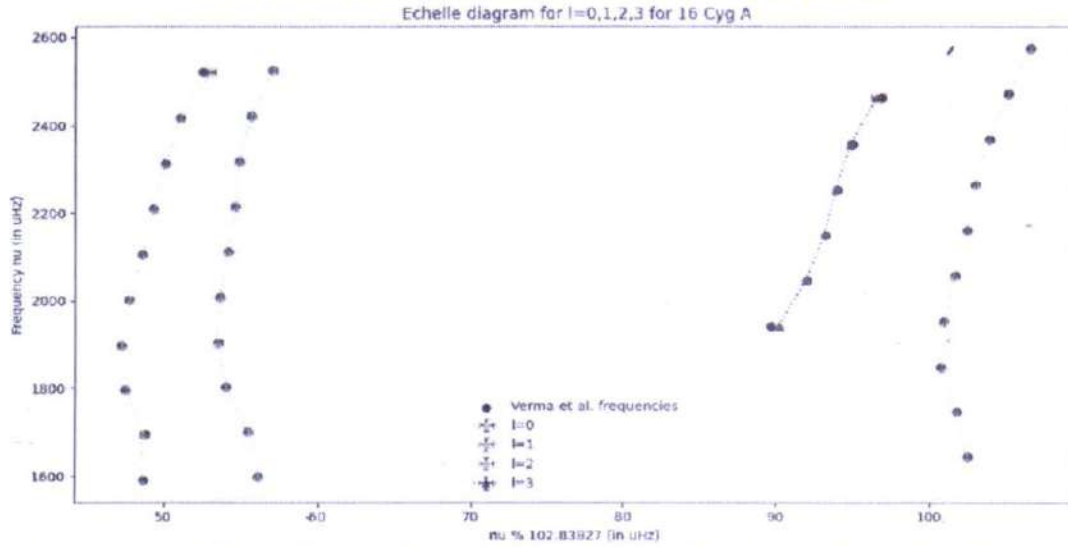


Fig. 7: The frequency échelle diagram of the obtained frequencies for  $l = 0, 1, 2, 3$  with  $\langle \Delta \nu \rangle = \langle \Delta \nu_0 \rangle = 102.838 \mu\text{Hz}$ . Also, we have plotted the observed frequencies of the considered modes as given in [Verma et. al \(2014\)](#) and we find that these are in good agreement with the ones we have calculated.

| Observable/Quantity                                           | Values obtained/calculated       |
|---------------------------------------------------------------|----------------------------------|
| Angle of inclination with respect to line-of-sight, $i_s$     | $50.331^\circ \pm 1.877^\circ$   |
| Rotational Splitting, $\Omega_s$                              | $0.513 \pm 0.012 \mu\text{Hz}$   |
| Mean Large frequency separation, $\langle \Delta \nu \rangle$ | $102.838 \pm 0.140 \mu\text{Hz}$ |

### III: PYTHON PACKAGES USED:

We have made use of several python packages to develop this code:

- a. Numpy
- b. Scipy
- c. Matplotlib
- d. Astropy
- e. Lightkurve
- f. Pandas
- g. Numba
- h. Time

### IV: CONCLUSION:

In this project, we started off by introducing ourselves to the underlying concepts and basic theory of solar-like oscillations. We have made use of various statistical concepts and rigorous numerical techniques to find out the frequencies of various modes so as to deduce important values which enable us to study the orientation and the internal structure of a Solar-Like Oscillator. The python code we have developed has been successful to a considerable extent, mostly where the angular degrees  $l$  of the eigenmodes could be visually identified. In order to figure out the best possible model, the minimum value of the negative logarithm of the likelihood function was considered by using different initial guesses and the best one was reported. Here, we have only reported the result obtained on performing model fitting of the power spectrum of the very popular 16 Cyg A star.

Using the output obtained, we can also find out other physically important measurables which help us study the stellar interiors in greater detail. The limitation of using this technique lies in the fact that this technique works well for Solar-like oscillators with modes whose angular degree can be identified. But for stars where the values of angular degrees cannot be clearly identified, hypothesis testing and Bayesian analysis provide help.

Despite its limitations, this technique has proven efficient in obtaining the modes frequencies of the Solar-like oscillators with prominent oscillation modes and hence can be used to perform asteroseismic analysis. To take this code to the next level, we will try to incorporate peak bagging and analysis of Solar-like oscillators with mixed modes.

### V: ACKNOWLEDGEMENTS:

I would like to thank my project supervisor Dr. Anwesh Mazumdar of Homi Bhabha Centre for Science Education-TIFR, Mumbai and Prof. H.M. Antia of Tata Institute of Fundamental Research for guiding me through the project by giving me valuable suggestions and helping me out with necessary resources. I would like to acknowledge support from the NIUS Programme of HBCSE-TIFR and the staff of HBCSE-TIFR which enabled me to carry this project out efficiently. I would also like to thank NASA's *Kepler* team and KASOC team for making the pre-processed data available to us. I am grateful to the faculty and staff of my parent institution Ramakrishna Mission Residential College (Autonomous) for providing me help in many ways including access to computational resources for the sake of my project. Finally, I thank my family members who have given me immense support and motivation for these past months.

### VI: BIBLIOGRAPHY:

Stellar Interiors--1994: Hansen, Kawaler, Trimble,  
Asteroseismic Data Analysis--2017: S. Basu, W. Chaplin  
Lecture notes on Stellar Oscillations--2003: Christensen-Dalsgaard,  
Asteroseismology--2010: C. Aerts, J.C.D, D. Kurtz

|                                     |                             |                              |                          |
|-------------------------------------|-----------------------------|------------------------------|--------------------------|
| <u>Chaplin &amp; Migilio-- 2013</u> | <u>Garcia, Ballot--2019</u> | <u>Anderson et al.--1990</u> | <u>Appourchaux--2003</u> |
| <u>Kamiyaka et al.--2017</u>        | <u>Verma et al.--2014</u>   | <u>VanderPlas--2017</u>      | <u>Tassoul--1980</u>     |
| <u>Cunha--2017</u>                  | <u>Shanno--1970</u>         |                              |                          |



## **Smart Water Tap monitoring system**

*Project Report submitted to the Department of Physics, Ramakrishna Mission Residential College (Autonomous), Narendrapur, Kolkata for the partial fulfilment of the requirements of the degree of*

### **Bachelor of Science (Hons.) in Physics**

Submitted by:

Arghya Jana [Roll No.: PHUG/092/17]  
Pritam Pal [Roll No.: PHUG/110/17]

Semester VI, B.Sc. Physics (Hons.)

University of Calcutta, Kolkata  
2020



**Ramakrishna Mission Residential College (Autonomous)**

**Vivekananda Centre for Research**

**Ramakrishna Mission Ashrama**

(A Branch Centre of Ramakrishna Mission, Belur Math, Howrah-711202)

**Narendrapur, Kolkata - 700 103, West Bengal, India**

A Scientific Industrial Research Organisation, Recognised by DST, Govt. of India

College with Potential for Excellence (CPE), Re-accredited by NAAC - 'A' (CGPA 3.56 out of 4)

---

## **DEPARTMENT OF PHYSICS**

### **Certificate**

This is to certify that Pritam Pal, a student of B. Sc has successfully completed the project of UG curriculum entitled "Smart Water Tap monitoring system" in the period from January to May, 2020.

*Malay Purkait*  
.....  
30.06.2020

**Signature Of HOD**

**Dept. of Physics**

**Dr. Malay Purkait**

Associate Prof. & Head

Department of Physics

Ramakrishna Mission Residential College

(Autonomous)

Narendrapur, Kolkata-700 103, (W.B.)



Mr. Tanmay Biswas

Assistant Professor

Ramakrishna Mission Residential  
College (Autonomous)  
Narendrapur, Kolkata-700103

## CERTIFICATE OF APPROVAL

Date: 1 July, 2020

This is to certify that the project report entitled "Smart Water Tap Monitoring System" has been done under my supervision at the Department of Physics, Ramakrishna Mission Residential College (Autonomous). I also endorse that this work submitted by **Pritam Pal** (Reg. No: A03-1112-0110-17) is original and has not been submitted to any other University for the award of any Degree or Diploma. I therefore, recommend the project work for the award of **Bachelor of Science (Honours) in Physics**.

  
(Mr. Tanmay Biswas)

## Acknowledgement

I would like to express my deep sense of gratitude to my respected and learned guide Mr. Tanmay Biswas (Assistant Professor, Department of Electronics) for his valuable guidance in completing this project.

I am also grateful to my respected principal, vice principal and respected Prof. Malay Purkait, (HOD, Department of physics) for permitting me all the necessary facilities of the institution. I am also thankful to all other faculty and staff members of our department of their kind cooperation.

Lastly I would like to thank my parents and friends to help me a lot in finishing this project in time.

Pritam Pal .

01-07-20

(Signature of student)



### **Abstract**

In the design we have constructed a sensor water tap monitoring system using the components viz arduino board, solenoid valve, SPDT relay, IR sensor etc. The main purpose of this project is to stop wastage of water. We have used the IR Sensor which is connected to a SPDT relay which controls the solenoid valve to control the water flow to the tap. As a result sensor tap is automatically shut off after use.

## **Introduction:**

Water is most precious. Living bodies depend on it. Our responsibility is to conserve it. Nowadays we are interested to be automated. The project titled "sensor Water Tap monitoring system" is the modern version of the traditional hand operated tap. The water taps that we use in our daily life are mechanically operated. Water flows through the tap when we turn on the tap and the flow stops when we turn off the tap. This hand operated tap system causes water loss.

Sensor water taps save water significantly. Sensor water tap is automatically shut off after hand washing and as a result water shortage is reduced. Sensor tap is hygienic, that is very important for us. This tap is more energy efficient than traditional hand operated water tap. In the automatic water tap we use a IR sensor which is connected to a SPDT relay which controls the solenoid valve to control the water flow to the tap [4]. This tap reduced the wastage of water as it is automatically closed after hand washing.

Some related works are:

- Water Quality Monitoring System Based on IOT [1] : In this paper the authors have presented a design and development of a low cost system for real time monitoring of the water quality in IOT. They have measured the physical and chemical properties of water such as temperature, PH,turbidity, flow sensor etc. using sensors and arduino model.
- Design a Smart Faucet for reducing the water wastage using IOT [2] : In this paper the authors have designed a smart water faucet using the components Node MCU,relay,solenoidvalve,DC motor,temperature sensor, servo motor for reducing the wastage of water.



### **Proposed Design:**

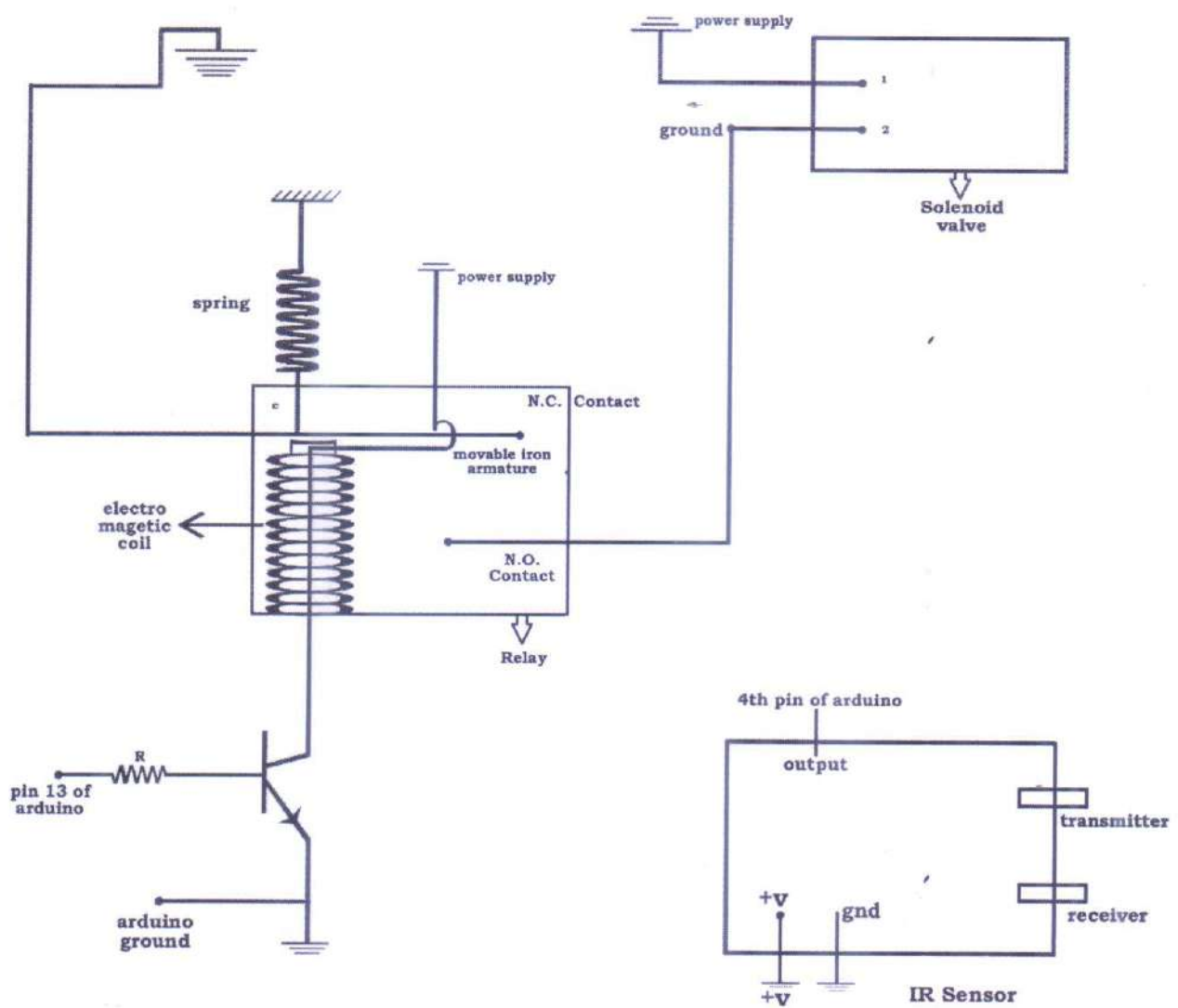
We have designed a sensor water tap monitoring system .Here we have used an infrared sensor in the tap that has a light emitting diode. This LED emits light continuously. When an object or human hand enters into the range of LED, the solenoid valve will be opened, which allows the water to flow through the tap. When the object is removed from the range of LED, the valve will be closed and it stops water running.

### **Implementation:-**

The Components that are required for constructing the sensor water tap monitoring system are

- i) Solenoid Valve
- ii) Single Pole Double Throw (SPDT) relay
- iii) Infra-red sensor
- iv) Arduino board
- v) Power Supply
- vi) Spring
- vii) Resistance
- viii) Electromagnetic coil

Solenoid Valve is an electrically Controlled automatic device. It's basic working Principle is just like as a relay. There are two types of Solenoid Valves i) normally open type and ii) normally closed type. By applying the voltage the state of the solenoid can be changed from open to close or from close to open. Here the normally closed type solenoid valve has two ends. One end is connected to a power supply and the other end is connected to normally open contact of a relay. Relay's common end is connected to the ground. Its common end, attached with a spring system, is connected with the normally closed



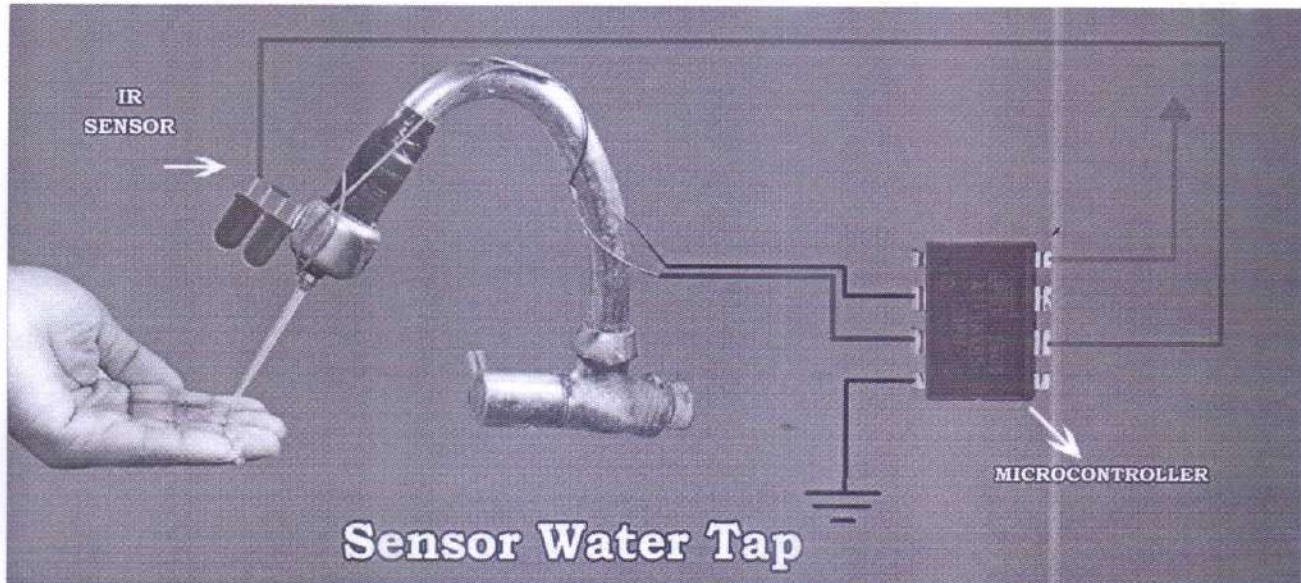
**Block diagram of Sensor water tap Monitoring System**



contact through a movable iron armature. There is an electromagnetic coil; a coil of wire is wound on a soft iron core. One end of this coil is connected to some voltage and the other end of this coil is connected to the ground through a n-p-n transistor. The base of the transistor is connected to a pin of arduino board via some resistance.

Here we used a IR Sensor that has a light emitting diode-IR transmitter continuously emits the light. When some object enters into the range of the LED, the infra-red light signal is reflected by the object and the receiver of the IR sensor receives that light. That's why some voltage will be showed across the receiver. This voltage is automatically supplied by the sensor to that pin of arduino, which is connected to the base of the transistor via some resistance, such that current will flow through the electromagnetic coil and the coil generates a magnetic field through the soft iron core. Due to this the movable iron armature is attracted towards the electromagnetic core and the armature will move to open condition by breaking the normally closed contact condition. Normally open contacts get to closed condition. Then a complete circuit will be formed and the solenoid valve will remain in "on" state. The valve is opened and it allows the water to flow through the tap.

Again, when the object is removed from the range of LED, the receiver of the sensor will not show any voltage and the current flowing through the electromagnetic coil will be switched off, the relay coil gets de-energized then the armature is returned to its original position by the spring system. The armature will move to N.C. contact condition by breaking the N.O. contact condition. Hence the solenoid valve will remain in "off" state. The valve is closed and it stops the water running.



When some object or human hand enters into the range of LED of the IR sensor as shown in fig, which emits the light continuously, the solenoid valve will be opened and that allows the water to flow through the tap. Again when the object is removed from the range of LED, the valve will be closed and it stops water running.



## **Result:**

The sensor water tap monitoring system plays important role in the following fields:

- Significant water saving:

Electronic taps are generally constructed to get much lower stream rate than the traditional hand operated taps. Hand operated taps can use up to 10-15 liters of water per minute whereas the sensor tap offers flow rates of water as little as 2 liters per minute. Sensor tap is automatically shut off after hand washing and hence water wastage is reduced.

- Hygienic:

Sensor tap doesn't require to touch - it is hygienic.

- Cleaner and more efficient:

In case of sensor taps the flow rate is predetermined whereas for hand operated taps the user can choose their preferred flow rate every time. This is very inefficient. Prefixing the flow rate helps to reduce splashing.

- More energy efficient:

Sensor taps need electricity for their operation while the traditional hand operated taps don't require any electricity in order to work. Every time a traditional hand tap expends a great deal of energy by choosing the user's preferred water flow and temperature. But in case of sensor taps water always remain at a constant temperature, so energy is not expended by changing the water temperature. So sensor taps are more energy efficient than hand taps.

### **Application:**

Sensor water tap monitoring system is extremely valuable in home, old age home, hotel, school, office, shop, nursing home, hospital, industrial application, eatery etc.

### **Conclusion:**

Due to this sensor water tap monitoring system our life style has been quite automated. Due to significant progress in science and technology, we are approaching an era of artificial intelligence and consequently the interaction between man and machines gets reduced. The sensor water tap is such a machine that has reduced the human labor mostly. We can implement this method in the public water podium stands which eliminates the usage of water taps, which are extremely inefficient. This automated system is very helpful in everyday life specially for physically handicapped, patients and elderly people. It gives them a safe and independent living by providing the tap automation. It is also very helpful in conservation of water which can be efficiently implemented in garden, park etc.



## Reference

1. Vaishnavi V. Daigavane and Dr. M.A. Gaikwad.
2. LalithMohon S, Kavinprabhu L, Jayaseelan T, Naveen Kumar V, Suresh babu Y, (International Journal of Recent Technology and Engineering). Volume - 8 Issue - 6, March 2020.
3. Automatic tap control system in the smart home using android and arduino-Vani K.S. and Shrinidhi P.C. International Journal of computer application - volume 127-No-8, October 2015.
4. Programmingdigest.com

# An Introduction to GTR and GPS

July 4, 2020

A project report on

"An Introduction to GTR and GPS systems"

Submitted by,  
SOUNAK PAL  
Dept. of Physics  
RKMRC,NARENDRAPUR  
Roll no. -PHUG/179/17

Project Guide  
Dr. SOUMYA SADHUKHAN  
Assistant Professor  
Dept. of Physics  
RKMRC,NARENDRAPUR





**Ramakrishna Mission Residential College (Autonomous)**

**Vivekananda Centre for Research**

**Ramakrishna Mission Ashrama**

(A Branch Centre of Ramakrishna Mission, Belur Math, Howrah-711202)

**Narendrapur, Kolkata - 700 103, West Bengal, India**

A Scientific Industrial Research Organisation, Recognised by DST, Govt. of India

College with Potential for Excellence (CPE), Re-accredited by NAAC - 'A' (CGPA 3.56 out of 4)

---

## **DEPARTMENT OF PHYSICS**

### **Certificate**

This is to certify that Sounak Pal, a student of B. Sc has successfully completed the project of UG curriculum entitled "An Introduction to GTR and GPS systems" in the period from January to May, 2020.

*Malay Purkait*  
.....  
30.06.2020.

**Signature Of HOD**

**Dept. of Physics**

**Dr. Malay Purkait**

**Associate Prof. & Head**

**Department of Physics**

**Ramakrishna Mission Residential College**

**(Autonomous)**

**Narendrapur, Kolkata-700 103. (W.B.)**



# To Whom It May Concern

## Certificate of Completion of the project

This is to certify that Sounak Pal (Roll-PHUG/179/17) bearing the CU registration no. "A03-1112-0179-17", a student of Bsc final year (2020) has successfully completed his Bsc physics project on "Introduction to GTR and GPS systems" under the guidance of Dr. Soumya Sadhukhan. He is a bonafide student of RKMRC physics dept. of the 2017-2020 batch.

Date: 20.06.2020.

S. Sadhukhan

Sign of the guide





## ACKNOWLEDGEMENT

*I(sounak pal) would like to express my special thanks of gratitude to my guide Dr. Soumya Sadhukhan as well as our principal ,who gave me the golden opportunity to do this wonderful project on the topic “Introduction to GTR and GPS systems”, which also helped me in doing a lot of Research and i came to know about so many new things. I am really thankful to them.*

*Secondly, I would also like to thank my parents and friends who helped me a lot in finalizing this project within the limited time frame.*

*Sounak Pal*

Sign of the student

## Contents

|                                           |           |
|-------------------------------------------|-----------|
| <b>1.Introduction to GTR .....</b>        | <b>3</b>  |
| Graviy as geometry.....                   | 5         |
| Curvature .....                           | 6         |
| Twin paradox.....                         | 8         |
| Gravity makes time lazy.....              | 10        |
| <b>2.Introduction to GPS systems.....</b> | <b>11</b> |
| Qualitative study.....                    | 12        |
| GPS mechanism.....                        | 12        |
| Time offset .....                         | 13        |
| <b>3.Application.....</b>                 | <b>13</b> |
| Orbital frequency shifts.....             | 14        |



## 1 Introduction to GTR

Inertial frames means frames with no acceleration, where no objects are around to provide or create any type of force for acceleration. Special theory of Relativity (STR) deals with this perspective of inertial frame in detail. The underlying geometry of STR is very simple and it is the normal euclidean geometry. Let us think of two close points in space denoted by  $(x^1, x^2, x^3)$  and  $(x^1 + dx^1, x^2 + dx^2, x^3 + dx^3)$ . The distance between them can be written as

$$ds = \sqrt{(dx^1)^2 + (dx^2)^2 + (dx^3)^2}.$$

In general it can be written for N-dimension as

$$ds^2 = \sum_{i=1}^N (dx^i)^2.$$

This concept of co-ordinate distance was very famous before the invention of General Theory of Relativity (GTR). Then almost all problems were treated by Newton's equations in Minkowskian flat space time, where time is considered to be absolute. Towards the ending decades of eighteenth century there was a problem which needed to be addressed was about maintaining the speed of causality in which informations were traveled. But Newton came up with his famous formula of gravitation as i.e

$$\vec{F} = \frac{GMm}{r^2} \hat{r}$$

Now if we change one of the masses adiabatically i.e

$$\vec{F} = \frac{GMm(t)}{r^2} \hat{r}$$

in space, the force between them must be changed simultaneously. This demands the information to travel at speeds greater than  $c$  (speed of light) for instantaneous action. So Einstein came up with his great idea of gravity here. Though there are many fallacies like superluminal motion, twin paradox etc. that supports Einstein's work later, was remained to be addressed still. We would discuss some of them in greater detail in further sections. Einstein's thought was to see the 'Gravity' as a consequence of the geometry of spacetime. Mass helps to bend the spacetime fabric and then the concept of curvature pokes in, instead of Newton's concept of flat spacetime.

## Gravity as geometry

As we had written in euclidean geometry, the concept of distance is not same in curved spaces. A straight line is not a straight line in curved spaces, as that will leave the surface of that curved surface. A simple model of a curved space is  $S^2$ . The geometry we need to consider for curved surfaces is a very famous geometry named as **Riemannian geometry for curved manifolds**. The line element here is written as:

$$ds^2 = g_{\mu\nu} dx^\mu dx^\nu.$$

It is a general form of notion that incorporates metric tensor  $g_{\mu\nu}$  into consideration. Now a simple question comes to the mind that why do we need such a complex thing to consider?? Here in lies the concept of curvature. The motivation is, when we had written for euclidean space-

$$ds^2 = \sum_{i=1}^N (dx^i)^2$$

This can also be written as :

$$ds^2 = \begin{pmatrix} dx^1 & dx^2 & dx^3 & \dots & dx^N \end{pmatrix} \begin{pmatrix} 1 & 0 & 0 & 0 & \dots & 0 \\ 0 & 1 & 0 & 0 & \dots & 0 \\ 0 & 0 & 1 & 0 & \dots & 0 \\ 0 & 0 & 0 & 1 & \dots & 0 \\ \vdots & \vdots & \vdots & \vdots & \ddots & \vdots \\ 0 & 0 & 0 & 0 & \dots & 1 \end{pmatrix} \begin{pmatrix} dx^1 \\ dx^2 \\ dx^3 \\ \vdots \\ dx^N \end{pmatrix} \quad (1)$$

The matrix  $g_{\mu\nu}$  is something, which tells something about the nature of the space. Diagonal representation guarantees its orthogonality of co-ordinates. We also have to think that the basis of vector spaces are not same from point to point in a curved space. So they are the function of co-ordinates. Hence the diagonal positive elements of the metric tensor  $g_{\mu\nu}$  is not always constant but is a function of co-ordinates. Let us think of an example:

$$X = \mu\nu$$

$$Y = \frac{1}{2}(\mu^2 - \nu^2)$$



now,

$$ds = \sqrt{dX^2 + dY^2}$$

$$ds = dX \sqrt{1 + \frac{dY^2}{dX^2}}$$

we can write;

$$dX = \frac{\partial X}{\partial \mu} d\mu + \frac{\partial X}{\partial \nu} d\nu = \nu d\mu + \mu d\nu$$

$$dY = \frac{\partial Y}{\partial \mu} d\mu + \frac{\partial Y}{\partial \nu} d\nu = \mu d\mu - \nu d\nu$$

$$ds = (\nu d\mu + \mu d\nu) \sqrt{1 + \frac{(\mu d\mu - \nu d\nu)^2}{(\nu d\mu + \mu d\nu)^2}}$$

$$ds^2 = (\mu^2 + \nu^2)(d\mu^2 + d\nu^2)$$

$$g_{\mu\nu} = \begin{pmatrix} (\mu^2 + \nu^2) & 0 \\ 0 & (\mu^2 + \nu^2) \end{pmatrix} \quad (2)$$

so it is a function of coordinates  $\mu$  and  $\nu$ . The equation of a circle in euclidean space can be written as

$$x^2 + y^2 = r^2$$

$$\mu^2 \nu^2 + \frac{1}{4}(\mu^2 - \nu^2)^2 = (2r)^2$$

$$\mu^2 + \nu^2 = 2r$$

These set of coordinates are called **parabolic coordinates**.

## curvature

There are basically three types of curvatures: if  $c$  is the circumference and  $r$  is the radii, we would talk about an arbitrary curved surface.

$$\frac{c}{r} > 2\pi$$

(it is called the surface of negative curvature)

$$\frac{c}{r} = 2\pi$$

(it is called the surface of zero curvature)

$$\frac{c}{r} < 2\pi$$

(it is called the surface of positive curvature) we would provide an example here before proceeding to the another feature of curved spaces.

$$c = \int_0^{2\pi} a \sin(\theta) d\phi$$

say for a fixed  $\theta = \psi$

$$= 2\pi a \sin(\psi)$$

Now,  $r = a\psi$  gives

$$\frac{C}{r} = \frac{2\pi a \sin(\psi)}{a\psi} = 2\pi \frac{\sin(\psi)}{\psi}$$

$$= 2\pi \frac{\sin(\frac{r}{a})}{\frac{r}{a}}$$

and it is only defined for  $r < a$ . Hence  $\frac{c}{r} = 2\pi$ . So, for large radii spheres and near the poles it seems that there is almost no curvature at all. Another glorifying property of this curvature is that the sum of internal angles of a triangle is not  $\pi$ , it could be more than that. We would not prove it here, it requires a little bit of geometry and actually very easy to prove.

Non-holonomic basis is a very important part of our discussion in the field of curvatures. We would come to this topic later.



## Twin paradox

Now, let's shift our attention to the discussion of twin paradox and its solution as we proposed previously. The Velocity fourvector is:

$$u^\mu = \frac{dx^\mu}{d\tau} = (c \frac{dt}{d\tau}, \frac{dx}{d\tau}, \frac{dy}{d\tau}, \frac{dz}{d\tau})$$

$$u^\mu u_\mu = -c^2$$

$$\partial_t(u^\mu u_\mu) = 0$$

$$\Rightarrow 2 \frac{d}{dt}(u^\mu) u_\mu = 0$$

$$\eta_{\mu\nu} u^\mu u^\nu = -c^2$$

$$\eta_{\mu\nu} a^\mu u^\nu = 0$$

so

$$-(u^0)^2 + (u^1)^2 = -c^2$$

$$-(a^0 u^0) + (a^1 u^1) = 0$$

now

$$-(a^0)^2 + (a^1)^2 = g^2$$

$$-(u^0)^2 + (u^1)^2 = -c^2$$

therefore

$$a^1 u^1 = a^0 u^0$$

$$\Rightarrow a^1 = \frac{a^0 u^0}{u^1}$$

$$= \left(\frac{a^0 u^0}{u^1}\right)^2 - (a^0)^2 = g^2$$

$$\Rightarrow a^0 = \frac{g u^1}{c}$$

$$a^1 = \frac{g u^0}{c}$$

now

$$\frac{da^0}{d\tau} = \frac{g}{c} \frac{du^1}{d\tau} = \frac{g^2}{c^2} u^0$$

so

$$\frac{d^2 u^0}{d(\tau)^2} = \frac{g^2}{c^2} u^0$$

similarly

$$\frac{d^2 u^1}{d\tau^2} = \frac{g^2}{c^2} u^1$$

so it gives

$$u^1 = A e^{\frac{g\tau}{c}} + B e^{-\frac{g\tau}{c}}$$

$$\frac{du^1}{d\tau} = \frac{g}{c} (A e^{\frac{g\tau}{c}} - B e^{-\frac{g\tau}{c}})$$

now suitable boundary condition gives  $A = -B = \frac{c}{2}$  hence

$$u^1 = \frac{dx}{d\tau} = c \sinh\left(\frac{g\tau}{c}\right)$$

$$a^0 = g \sinh\frac{g\tau}{c}$$

similarly

$$u^0 = c \frac{dt}{d\tau} = c * \cosh\frac{g\tau}{c}$$

so the final solution comes out to be

and

$$x = \frac{c^2}{g} \cosh\left(\frac{g\tau}{c}\right)$$

$$ct = \frac{c^2}{g} \sinh\left(\frac{g\tau}{c}\right)$$

Now let's think about Amit who is sitting on earth and measures the time needed to travel to another planet by Sumit. They are twins to each other. Sumit moves in a spaceship at a velocity  $\frac{4c}{5}$  towards a distant star 20 light years away. Now the time needed as measured by Sumit is 25 years. In Amit's frame the time needed is dilated by a factor of

$$\frac{1}{\gamma} = \left(1 - \frac{v^2}{c^2}\right)^{\frac{1}{2}}$$

So

$$t = (25) / \frac{3}{5}$$

= 41.6 years almost. So according to this, Amit is now older than Sumit. He is older by almost  $2 * (41.6 - 25) = 33.2$  years (considering return to



earth also). But here we have neglected the time needed for retardation and acceleration. Now from our previously achieved equations we get that

$$\frac{dx}{d\tau} = c \sinh\left(\frac{a\tau}{c}\right)$$

so,

$$c * \sinh\left(\frac{a\tau}{c}\right) = 4 \frac{c}{5}$$

so this comes out to be

$$\tau = \frac{c}{a} \sinh^{-1}\left(\frac{4}{5}\right)$$

=

$$\tau = \frac{c}{a} \sinh^{-1}(0.8)$$

=21960000s=9 months almost, assuming  $g = 10m/s^2$ . So here we haven't consider that time can be slowed down by gravity itself. So we need to take consideration of that also. How gravity affects time, will be considered in the next section.

## Gravity makes time lazy

The fact that gravity slows down time is of immense importance. Suppose Rohit stands in front of a spaceship which is moving with an acceleration  $9.8m/s^2$  and Amit is at the tail end. This frame is same as a spaceship standing still in earth's surface by 'equivalence principle'. Now let's go back to the moving frame at constant acceleration. If at  $t=0$  Amit releases a signal or em wave towards Rohit then as the frame is accelerating the signal will require different time intervals to reach Rohit in different time instants. As the spaceship is accelerating, so Rohit would say Amit's clock is slow and Amit will say Rohit's clock is going faster. This discrepancy is well described by gravitational time dilation. At the event horizon of the black holes time is almost frozen. As we all know that a black hole is a point of larger curvature or a singularity to be better from Einstein's field equations. Rotations are of great importance also. Because if a disc is rotating at very high angular velocity then the clock ticking rate at the centre of the disc and at the perimeter would be different. This is called **the Sagnac effect**.

## 2 Introduction to GPS systems

The **sagnac effect** is very important in case of making a coordination with rotation and relativity. Now, generally assuming spherical symmetry of our planet we can write for a rotating coordinate frame at some angular vel.  $\omega$ , now for primed frame  $r=r', \theta = \frac{\pi}{2}, \phi = \phi' - \omega t, t = t'$  Now  $ds^2 = -(1 - \frac{2GM}{Rc^2})(cdt)^2 + (r^2 d\phi^2) = c^2 d\tau^2$ . Now putting

$$r = R, \frac{d\phi}{dt} = \omega,$$

we can say that  $d\tau^2 = [(1 - \frac{2GM}{Rc^2}) - \frac{R^2\omega^2}{c^2}]dt^2$  Now using suitable approximation method we can write that

$$d\tau = [1 - \frac{GM}{Rc^2} - \frac{R^2\omega^2}{2c^2}]dt \dots \dots \dots (1)$$

Now for a satellite moving at height  $h$  from the surface of the earth, the proper time and usual time relation can be written by

$$d\tau' = [1 - \frac{GM}{(R+h)C^2} - \frac{[(R+h)\omega + v]^2}{2c^2}]dt$$

Now we will try to compute the difference between two proper times ..so i.e

$$|d\tau - d\tau'| = [\frac{-GMh}{R^2C^2} + \frac{(2R\omega + v)}{2c^2}v]dt$$

case - 1 :

Checking the formula we can say easily that a planet rotating faster than planet earth will have more difference between these time measurements. So its a challenge for the technical procedures how to set a gps system for a planet rotating very fast. What should we do? It is wise to use a rover that is loaded with a atomic clock and the rotating satellite should use another atomic clock, for minute calculations and getting actual coordinates of the rover in that planet.

case : 2

One set of effects that has been "rediscovered" many times are the red-shifts due to other solar system bodies. The Principle of Equivalence implies that sufficiently near the earth, there can be no linear terms in the effective gravitational potential due to other solar system bodies, because the earth



and its satellites are in free fall in the fields of all these other bodies. The net effect locally can only come from tidal potentials, the third terms in the Taylor expansions of such potentials about the origin of the local freely falling frame of reference. Such tidal potentials from the sun, at a distance  $r$  from earth, are of order  $\frac{GM_\odot r^2}{R^3}$  where  $R$  is the earth-sun distance. The gravitational frequency shift of GPS satellite clocks from such potentials is a few parts in 10<sup>16</sup> and is currently neglected in the GPS.

## Qualitative study

In the upper portion calculations we neglected the effect of earth's mass curvature. If we consider earth's mass is that much heavier to make a curvature in the spacetime fabric, then there is a resolution to the equation of Einstein's field equation. GPS systems are used to measure precisely the position and coordinate of a object by satellite signals and gravitomagnetic clock effects. Seperate coordinate systems are used such that ECEF, TAI etc. usually many satellites are situated in orbits around earth, but for precise measurement we need at least three satellites. The fourth one is used for more precise measurement. It was a most innovative discovery of modern era. GPS systems are now in frequent usage in car's navigation systems and they have revolutionized the way, modern communication systems work.

## GPS mechanism

GPS mechanisms are very interesting. A man standing at the surface of the earth is in connection of at least three satellites for tracing his location. The process is called **Trilateration**. We know from our fundamental geometry that when two circles intersect we get two points. The possibility of one point is excluded by using the reality that this intersection point should be on the surface of the earth. In 2-d trilateration process two satellites are supposed to be at distances  $r_1$  and  $r_2$ . We make circles of respective  $(r_1, r_2)$  radius. Now they intersect and we generally get the location. But two satellites is very poor for precision and invoking the concept of 3d space we use 3d trilateration process rather than 2d. So we construct spheres and the intersection of two spheres will be a circle. This circle is intersected by another sphere two get a point on the surface of the earth. Now fourth satellite is needed for precision. There are in total 26 satellites orbiting the planet earth in different orbits and orbital velocities.

## Time offset

Time offset is a very important thing in gps systems. Time offsets are measured by the time difference between the clocks set at the satellite and in the mobile GPS receiver. Atomic clocks have precision of order  $10^{-15}$  seconds. But the mobile GPS receiver's time is not so accurate. Now the fact is, the signals travel at very high speeds. A small fractional change in time can create a distance gap of almost 10 to 12 kms. per day, making the gps system unsuccessful to use. Time offsets are used to measure the time gap between the satellite's time and GPS receiver's time.

## 3 Application

The number of applications of GPS have been astonishing. It would take several paragraphs just to list them. Accurate positioning and timing, other than for military navigation, include synchronization of power line nodes for fault detection, communications, VLBI, navigation in deep space, tests of fundamental physics, measurements on pulsars, tests of gravity theories, vehicle tracking, search and rescue, surveying, mapping, and navigation of commercial aircraft, to name a few. These are too numerous to go into in much detail here, but some applications are worth mentioning. The Nobel-prizewinning work of Joseph Taylor and his collaborators on the measurement of the rate of increase of the binary pulsar period depended on GPS receivers at the Arecibo observatory, for transferring UTC from the U.S. Naval Observatory and NIST to the local clock. Time standards around the world are compared using GPS in common-view; Precise position information can assist in careful husbandry of natural resources, and animal and vehicle fleet tracking can result in improved efficiency. Precision agriculture makes use of GPS receivers in real-time application of pesticides or fertilizers, minimizing waste. Sunken vessels or underwater ruins with historically significant artifacts can be located using the GPS and archeologists can return again and again with precision to the same location. Monster ore trucks or earth-moving machines can be fitted with receivers and controlled remotely with minimal risk of collision or interference with other equipment. Disposable GPS receivers dropped through tropical storms transmit higher resolution measurements of temperature, humidity, pressure, and wind speed than can be obtained by any other method; these have led to improved understanding of how tropical storms intensify. Slight movements of bridges or buildings, in response to various loads, can be monitored in real time. Relative movements of remote parts of earth's crust can be accurately measured in a short time,



contributing to better understanding of tectonic processes within the earth and, possibly, to future predictions of earthquakes. With the press of a button, a lost hiker can send a distress signal that includes the hikers' location. These and many other creative applications of precise positioning and timing are leading to a rapid economic expansion of GPS products and services. Manufacturers produce hundreds of different GPS products for commercial, private, and military use and the number and variety of products is increasing. The number of receivers manufactured each year is in excess of two million, and different applications are continually being invented.

## Orbital frequency shifts

When satellites move in a orbit which is circular, there may be some gravitational frequency shift in the rate of beating of the clocks. Using the relation (from eq. 1)

$$d\tau^2 = \left[ \left(1 - \frac{2GM}{Rc^2}\right) - \frac{R^2\omega^2}{c^2} \right] dt^2$$

and integrating we can write..

$$\int_{path} d\tau = \int_{path} dt \left[ 1 - V/c^2 + \phi(0)/c^2 + v^2/2c^2 \right]$$

here V is the potential term,  $\phi(0)$  is constant. It comes from time change i.e  $t'' = (1 + \frac{\phi(0)}{c^2})t'$ , and v defines the velocity. now from energy coservation,

$$\frac{v^2}{2} - \frac{GM}{r} = -\frac{GM}{2a}$$

where a is the length of the semimajor axis. Now from here,

$$v^2 = 2GM \left( \frac{1}{r} - \frac{1}{2a} \right)$$

Now it leads to,

$$\int_{path} dt \left[ 1 - 3GM/2ac^2 + \phi(0)/c^2 - 2GM(1/a - 1/r)/c^2 \right]$$

The last two rate correction values lead to the correction term of order  $4.4 * 10^{-7}$ . So, for setting beat rate of the clock to some 10.4 mhz arbitrary we need to shift the frequency of the atomic clock to 10.3399 mhz, which is a slightly lower frequency. **Rough estimation:** Considering the effects of

second-order Doppler shifts of clocks fixed on earth's surface due to earth rotation and Gravitational frequency shifts of clocks in GPS satellites due to earth's mass, earth's oblateness causes a periodic fractional frequency shift with period of almost 6 hours and amplitude  $0.695 \times 10^{-14}$ s. Considering GTR effects its more precise.

## 4 Conclusion and summary

1. We have learnt that how the STR and GTR effects are of immense importance for precise measurements on gps systems. Different perturbaton anomalies and crazy potentials (angle dependent perturbations i.e cosidering the quadropole moment of earth) make this theory more complicated.

2.New GTR aspects from STR convention has been acheived in this project. For flat spacetimes we get that the schwarzschild's metric is stationary (time independent). The first term (coeff. of  $dt^2$ ) contains only a constant term  $-c^2$  but in switching to GTR we get that term is dependent on potential i.e the space around the mass considered.

3.Cesium and Quartz atomic clocks are very famous atomic clocks boarded in satellites. GPS systems are developing day by day for security and navigation purposes. Automated car controls or air force automatic pilot control is completely determined by using the gps systems in daily basis.

## 5 Reference

- [1] Ashby, N., and Weiss, M., Global Positioning System Receivers and Relativity, NIST Technical Note, TN 1385, (National Institute of Standards and Technology, Boulder, CO, 1999).
2. Buisson, J.A., Easton. R.L., andMcCaskill. T.B., "InitialResultsoftheNAVS-TARGPSNTS2 Satellite", in Rueger, L.J. et al., ed., 9th Annual Precise Time and Time Interval (PTTI) Applications and Planning Meeting, Proceedings of the meeting, held at NASA Goddard Space Flight Center, November 29-December 1, 1977, pp. 177-200, (Technical Information and Administrative Support Division, Goddard Space Flight Center, Greenbelt, MD, 1978).



3. Epstein, M., Stoll, E., and Fine, J., "Observable Relativistic Frequency Steps Induced by GPS Orbit Changes", in Breakiron, L.A., ed., 33rd Annual Precise Time and Time Interval.
4. Fitzpatrick, P., The Principles of Celestial Mechanics, (Academic Press, New York, 1970). 5, 9, 9, 9, 9.
5. Malys, S., and Slater, J., "Maintenance and Enhancement of the World Geodetic System 1984", in Proceedings of the 7th International Technical Meeting of The Satellite Division of The Institute of Navigation (ION GPS-94), September 20-23, 1994,
6. Salt Palace Convention Center - Salt Lake City, UT, pp. 17-24, (Institute of Navigation, Fairfax, VA, 1994). 2
7. Taylor, J.H., "Binary Pulsars and Relativistic Gravity", Rev. Mod. Phys., 66, 711-719, (1994)
8. Mashhoon, B., "On the Coupling of Intrinsic Spin with the Rotation of the Earth", Phys. Lett. A, 198, 9-13, (1995).

### Acknowledgement

Presentation inspiration and motivation have always played a key role in the success of any venture. I express my sincere thanks to our principal maharaj sw. **Sastrajnanandaji**.

I pay my deep sense of gratitude and special thanks to **Dr. Soumya Jana** for providing me the proper way of writing the project and correcting the project. I am immensely obliged to our H.O.D **Dr. Malay Purkait** for providing me the opportunity to prepare the project.

I am immensely obliged to my friends for their elevating inspiration, encouraging guidance and kind supervision in the completion of my project. I feel to acknowledge my indebtedness and deep sense of gratitude to my guide **Dr. Soumya Sadhukhan**, whose valuable guidance and kind supervision given to me throughout the course which shaped the present work as its show.

Last, but not the least, my parents are also an important inspiration for me. So with due regards, I express my gratitudes to them.

Although, this report has been prepared with utmost care and deep routed

interest. Even then i accept respondent and imperfection. Also take this oppurtunity to express a deep sense of gratitude to all the professors of our department for prsenting to us a way to express our knowledge and hard work which we have devoted to this project.



Name: Suman Debnath

Roll: PHUG/23817

Year: 3rd Year

Project on: Time Independent Perturbation Theory

Project Guide: Dr. Debrarayan Jara.

Date: 04/07/20





**Ramakrishna Mission Residential College (Autonomous)**

**Vivekananda Centre for Research**

**Ramakrishna Mission Ashrama**

(A Branch Centre of Ramakrishna Mission, Belur Math, Howrah-711202)

**Narendrapur, Kolkata - 700 103, West Bengal, India**

A Scientific Industrial Research Organisation, Recognised by DST, Govt. of India

College with Potential for Excellence (CPE), Re-accredited by NAAC - 'A' (CGPA 3.56 out of 4)

---

## **DEPARTMENT OF PHYSICS**

### **Certificate**

This is to certify that Suman Debnath, a student of B.Sc has successfully completed the project of UG curriculum entitled "Time Independent Perturbation Theory" in the period from January to May, 2020.

Malay Purkait  
.....  
30.06.2020.

**Signature Of HOD**

**Dept. of Physics**

**Dr Malay Purkait**

Associate Prof. & Head

Department of Physics

Ramakrishna Mission Residential College

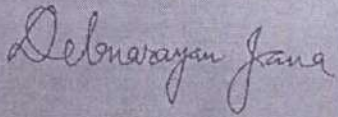
(Autonomous)

Narendrapur, Kolkata - 700 103, W.B.

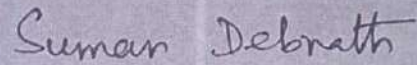


### Certificate

This is to certify that "Suman Debnath" of final year of B.Sc. Physics, roll no- PHUG/238/17 in Ramakrishna Mission Residential College (Autonomous) Narendrapur has successfully completed his project work entitled "Application of Time Independent Perturbation Theory on Vander Waals Force and three Dimensional Harmonic Oscillator Problem" under the guidance of "Dr. Debnarayan Jana" during the academic year 2020-2021. It has been found satisfactory and hereby approved for the submission.



Dr. Debnarayan jana



Suman Debnath



content: Q (i) Question no 1 on Vander Waals

Interaction

(ii) Question no 2 on Isotropic

Harmonic oscillator.



① ~~context~~ Question no-1

consider two atoms a distance  $R$  apart. Because they are electrically neutral you might suppose there would be no force between them, but if they are ~~polarised~~ polarizable there is in fact a weak attraction. To model this system picture each atom as an electron attached by a spring to the nucleus as in figure. We will assume the nuclei are heavy and essentially motionless. The unperturbed Hamiltonian

$$H^0 = \frac{1}{2m} P_1^2 + \frac{1}{2} \kappa x_1^2 + \frac{1}{2m} P_2^2 + \frac{1}{2} \kappa x_2^2$$



The Coulomb interaction between the atoms is

$$H' = \frac{1}{4\pi\epsilon_0} \left( \frac{e^2}{R} - \frac{e^2}{R+x_1} - \frac{e^2}{R+x_2} + \frac{e^2}{4\pi\epsilon_0(R+x_1-x_2)} \right)$$

(a) Explain the perturbation term. Show that

$$H' = -\frac{e^2 x_1 x_2}{4\pi\epsilon_0 R^3} \quad |x_1| \text{ and } |x_2| \ll R$$

(b) Show that the total Hamiltonian separates into two harmonic oscillator Hamiltonians

$$H = \left[ \frac{1}{2m} P_1^2 + \frac{1}{2} \left( \kappa - \frac{e^2}{4\pi\epsilon_0 R^3} \right) x_1^2 \right] + \left[ \frac{1}{2m} P_2^2 + \frac{1}{2} \left( \kappa + \frac{e^2}{4\pi\epsilon_0 R^3} \right) x_2^2 \right]$$

under the change of variable  $x_{\pm} = \frac{1}{\sqrt{2}}(x_1 \pm x_2)$



(c) The ground state energy

$$E = \frac{1}{2} \hbar (\omega_+ + \omega_-) \text{ where}$$

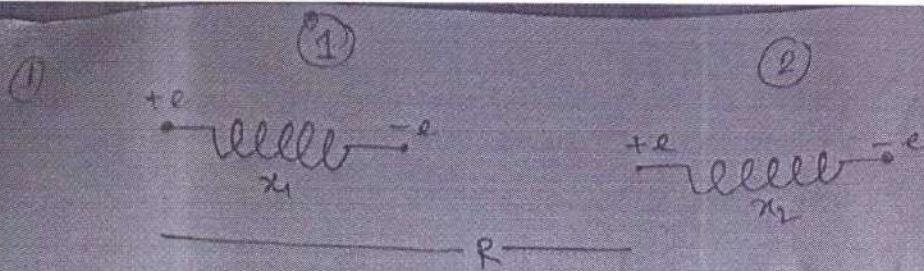
$$\omega_{\pm} = \sqrt{\frac{\kappa \pm e\sqrt{4\alpha\hbar\omega_0^3}}{m}}$$

Show that

$$\Delta V \equiv E - E_0 = -\frac{\hbar}{2m^2\omega_0^3} \left( \frac{e\sqrt{\hbar}}{4\alpha\hbar} \right)^2 \frac{1}{2\epsilon}$$

(d) Now do the same calculation using second order perturbation theory.





Unperturbed potential Hamiltonian

$$H^0 = \frac{1}{2m} p_1^2 + \frac{1}{2} k x_1^2 + \frac{1}{2m} p_2^2 + \frac{1}{2} k x_2^2$$

② If we put the nucleus of ① hydrogen in vacuum and then put the electron at a distance  $x_1$ , Coulomb energy  $-\frac{1}{4\pi\epsilon_0} \frac{e^2}{x_1}$ . A 2nd nucleus will act with 1st nucleus and 1st electron. Interaction energy  $\frac{e^2}{4\pi\epsilon_0 R}$  and  $-\frac{e^2}{4\pi\epsilon_0 (R-x_1)}$ . A 2nd electron will interact with all three charges. Energy  $-\frac{1}{4\pi\epsilon_0} \frac{e^2}{R+x_2}$ ,  $\frac{e^2}{4\pi\epsilon_0 (R+x_2-x_1)}$ ,  $-\frac{e^2}{4\pi\epsilon_0 x_2}$ .

Total energy

$$H = -\frac{1}{4\pi\epsilon_0} \frac{e^2}{x_1} + \frac{e^2}{4\pi\epsilon_0 R} - \frac{e^2}{4\pi\epsilon_0 (R-x_1)} - \frac{1}{4\pi\epsilon_0} \frac{e^2}{R+x_2} + \frac{e^2}{4\pi\epsilon_0 (R+x_2-x_1)} - \frac{e^2}{4\pi\epsilon_0 x_2}$$

1st and last term will contribute to the potential energy part of the unperturbed Hamiltonian. Rest will be regarded as perturbation Hamiltonian.

$$H' = + \frac{e^2}{4\pi\epsilon_0} \left[ \frac{1}{R} - \frac{1}{R-x_1} - \frac{1}{R+x_2} + \frac{1}{R+x_2-x_1} \right]$$

$$= \frac{e^2}{4\pi\epsilon_0} \left[ \frac{R-x_1-R}{R(R-x_1)} - \frac{R+x_2-x_1-R-x_2}{(R+x_2)(R+x_2-x_1)} \right]$$



$$= \frac{e^2}{4\pi\epsilon_0} \left[ -\frac{x_1}{R(R-x_1)} + \frac{x_1}{(R+x_2)(R+x_2-x_1)} \right]$$

$$= \frac{e^2 x_1}{4\pi\epsilon_0} \left[ -\frac{1}{R(R-x_1)} + \frac{1}{(R+x_2)(R+x_2-x_1)} \right]$$

$$= \frac{e^2 x_1}{4\pi\epsilon_0} \left[ \frac{-(R+x_2)(R+x_2-x_1) + R(R-x_1)}{R(R-x_1)(R+x_2)(R+x_2-x_1)} \right]$$

$$= \frac{e^2 x_1}{4\pi\epsilon_0} \left[ \frac{-R^2 - Rx_2 + Rx_1 - Rx_2 - x_2^2 + x_2 x_1 + R^2 - Rx_1}{R(R-x_1)(R+x_2)(R+x_2-x_1)} \right]$$

$$= \frac{e^2 x_1}{4\pi\epsilon_0} \left[ \frac{(2R+x_2-x_1)(-x_2)}{R^4 \left(1-\frac{x_1}{R}\right) \left(1+\frac{x_2}{R}\right) \left(1+\frac{x_2-x_1}{R}\right)} \right]$$

$$= -\frac{e^2 x_1 x_2}{4\pi\epsilon_0 R^3} \left[ \frac{2 + \frac{x_2}{R} - \frac{x_1}{R}}{\left(1-\frac{x_1}{R}\right) \left(1+\frac{x_2}{R}\right) \left(1+\frac{x_2-x_1}{R}\right)} \right]$$

$$\therefore H' = -\frac{e^2 x_1 x_2}{4\pi\epsilon_0 R^3}$$

[If we assume  
the ~~inter~~ distance  
between nucleus and electron  
cloud centre is very small  
than the two ~~big~~ that of  
the two H-atoms.]

i.e.  $x_1, x_2 \ll R$

⑥ ~~the~~ <sup>①</sup> The total ~~hamiltonian~~ hamiltonian of the system

$$H = H^0 + H' = \frac{p_1^2}{2m} + \frac{1}{2} k x_1^2 + \frac{p_2^2}{2m} + \frac{1}{2} k x_2^2 - \frac{e^2 x_1 x_2}{4\pi\epsilon_0 R^3}$$

$$\text{Let } p_1 = \frac{1}{\sqrt{2}} (p_+ + p_-)$$

$$p_2 = \frac{1}{\sqrt{2}} (p_+ - p_-)$$

$$x_1 = \frac{1}{\sqrt{2}} (x_+ + x_-)$$

$$x_2 = \frac{1}{\sqrt{2}} (x_+ - x_-)$$

Replacing,



$$\begin{aligned}
H &= \frac{1}{2m} \left[ \frac{1}{2} (\vec{p}_+ + \vec{p}_-)^2 + \frac{1}{2} (\vec{p}_+ - \vec{p}_-)^2 \right] \\
&\quad + \frac{1}{2} k \left[ \frac{1}{2} (\vec{x}_+ + \vec{x}_-)^2 + \frac{1}{2} (\vec{x}_+ - \vec{x}_-)^2 \right] \\
&\quad - \frac{e^2}{4\pi\epsilon_0 R^3} \cdot \frac{1}{2} (\vec{x}_+ + \vec{x}_-) \cdot (\vec{x}_+ - \vec{x}_-) \\
&= \frac{1}{2m} \cdot \frac{1}{2} \cdot 2 \cdot [\vec{p}_+^2 + \vec{p}_-^2] + \frac{1}{2} k \cdot \frac{1}{2} \cdot 2 (\vec{x}_+^2 + \vec{x}_-^2) \\
&\quad - \frac{e^2}{4\pi\epsilon_0 R^3} \cdot (\vec{x}_+ - \vec{x}_-) \cdot (\vec{x}_+ + \vec{x}_-) \\
(1) \quad &= \frac{\vec{p}_+^2}{2m} + \frac{\vec{p}_-^2}{2m} + \frac{1}{2} \left[ k - \frac{e^2}{2\pi\epsilon_0 R^3} \right] \vec{x}_+^2 \\
&\quad + \frac{1}{2} \left[ k + \frac{e^2}{2\pi\epsilon_0 R^3} \right] \vec{x}_-^2
\end{aligned}$$

This is a two independent SHM system on the coordinate  $\vec{p}_+, \vec{x}_+, \vec{p}_-, \vec{x}_-$ .

Total energy in ground state

$$\begin{aligned}
&= \frac{1}{2} \hbar \omega_+ + \frac{1}{2} \hbar \omega_- \\
&= \frac{1}{2} \hbar \sqrt{\frac{k - \frac{e^2}{2\pi\epsilon_0 R^3}}{m}} + \frac{1}{2} \hbar \sqrt{\frac{k + \frac{e^2}{2\pi\epsilon_0 R^3}}{m}} \\
&= \frac{1}{2} \hbar \sqrt{\frac{k}{m}} \left( 1 - \frac{e^2}{2\pi\epsilon_0 R^3 k} \right)^{\frac{1}{2}} \\
&\quad + \frac{1}{2} \hbar \sqrt{\frac{k}{m}} \left( 1 + \frac{e^2}{2\pi\epsilon_0 R^3 k} \right)^{\frac{1}{2}} \\
&= \frac{1}{2} \hbar \sqrt{\frac{k}{m}} \left[ 1 - \frac{e^2}{4\pi\epsilon_0 R^3 k} - \frac{1}{8} \left( \frac{e^2}{2\pi\epsilon_0 R^3 k} \right)^2 + \dots \right] \\
&\quad + \frac{1}{2} \hbar \sqrt{\frac{k}{m}} \left[ 1 + \frac{e^2}{4\pi\epsilon_0 R^3 k} - \frac{1}{8} \left( \frac{e^2}{2\pi\epsilon_0 R^3 k} \right)^2 + \dots \right] \\
&= \frac{1}{2} \hbar \sqrt{\frac{k}{m}} \left[ 2 - \frac{2}{8} \left( \frac{e^2}{2\pi\epsilon_0 R^3 k} \right)^2 \right] \\
&= \hbar \sqrt{\frac{k}{m}} \left[ 1 - \frac{1}{8} \left( \frac{e^2}{2\pi\epsilon_0 R^3 k} \right)^2 \right]
\end{aligned}$$



Total

Unperturbed

$$\text{energy} = \frac{1}{2} \hbar \omega_0 + \frac{1}{2} \hbar \omega_1$$

$$= \hbar \omega_0$$

$$2 \hbar \sqrt{\frac{\kappa}{m}}$$

contribute to

Energy ~~due to~~ perturbation term

$$= \hbar \sqrt{\frac{\kappa}{m}} \left[ 1 - \frac{1}{8} \left( \frac{e^2}{2\pi\epsilon_0 \hbar^3 \kappa} \right)^2 \right] - \hbar \sqrt{\frac{\kappa}{m}}$$

$$2 \hbar \sqrt{\frac{\kappa}{m}} - \frac{\hbar \sqrt{\frac{\kappa}{m}}}{8} \left( \frac{e^2}{2\pi\epsilon_0 \hbar^3 \kappa} \right)^2 \frac{1}{\hbar^6} \frac{1}{\omega_0^2}$$

$$= - \frac{\hbar}{8} \omega_0^2 \left( \frac{e^2}{2\pi\epsilon_0 \hbar^3 \kappa} \right)^2 \frac{1}{\hbar^6} \frac{1}{\omega_0^4 m^2}$$

$$\Delta E = 2 - \frac{\hbar}{8 m^2 \omega_0^3} \left( \frac{e^2}{2\pi\epsilon_0 \hbar^3 \kappa} \right)^2 \frac{1}{\hbar^6}$$



(d)  
(pb)

6.35(d)

$$E_0^2 \rightarrow \sum_{n=1}^{\infty}$$

$$\frac{|\langle \psi_n^0 | H' | \psi_{00}^0 \rangle|^2}{E_0^0 - E_n^0}$$

(Assumed)  
 $\psi_n^0 = \psi_{nm}^0$

$$= \frac{|\langle \psi_{10}^0 | H' | \psi_{00}^0 \rangle|^2}{E_{00}^0 - E_{10}^0} + \frac{|\langle \psi_{01}^0 | H' | \psi_{00}^0 \rangle|^2}{E_{00}^0 - E_{01}^0} + \frac{|\langle \psi_{20}^0 | H' | \psi_{00}^0 \rangle|^2}{E_{00}^0 - E_{20}^0} + \frac{|\langle \psi_{01}^0 | H' | \psi_{00}^0 \rangle|^2}{E_{00}^0 - E_{11}^0} + \dots$$

Now

~~Q. 6.35~~ Evaluating  $\langle \psi_{10}^0 | H' | \psi_{00}^0 \rangle$

$$\psi_{10} = \frac{A_1}{\sqrt{2m}} A_1(a_1) e^{-\frac{m\omega x_1^2}{2\hbar}} A_0 e^{-\frac{m\omega x_2^2}{2\hbar}}$$

$$= \frac{A_1}{\sqrt{2m}} [2im\omega x_1] e^{-\frac{m\omega x_1^2}{2\hbar}} A_0 e^{-\frac{m\omega x_2^2}{2\hbar}}$$

$$\psi_{00}^0 = A_0 e^{-\frac{m\omega x_1^2}{2\hbar}} e^{-\frac{m\omega x_2^2}{2\hbar}}$$

$$\therefore \langle \psi_{10}^0 | H' | \psi_{00}^0 \rangle = H' = -\frac{\partial^2 \psi_{10}}{2m(a_1 a_2)}$$

$$\langle \psi_{10}^0 | H' | \psi_{00}^0 \rangle = \int_{-\infty}^{\infty} \int_{-\infty}^{\infty} \frac{A_1^*}{\sqrt{2m}} [2im\omega x_1] e^{-\frac{m\omega x_1^2}{2\hbar}} A_0 e^{-\frac{m\omega x_2^2}{2\hbar}} \left( -\frac{\partial^2 \psi_{10}}{2m(a_1 a_2)} \right) A_0 e^{-\frac{m\omega (x_1^2 + x_2^2)}{2\hbar}} dx_1 dx_2$$

$$= (2im\omega) \frac{A_1^* A_0^* A_0^2}{\sqrt{2m}} \left( -\frac{\partial^2}{2m(a_1 a_2)} \right) \int_{-\infty}^{\infty} \int_{-\infty}^{\infty} x_1^2 e^{-\frac{m\omega x_1^2}{\hbar}} x_2^2 e^{-\frac{m\omega x_2^2}{\hbar}} dx_1 dx_2$$

$$= (2im\omega) \frac{A_1^* A_0^* A_0^2}{\sqrt{2m}} \left( -\frac{\partial^2}{2m(a_1 a_2)} \right) \int_{-\infty}^{\infty} x_1^2 e^{-\frac{m\omega x_1^2}{\hbar}} dx_1 \times 0$$

$\geq 0$

Similarly  $\langle \psi_{01}^0 | H' | \psi_{00}^0 \rangle \geq 0$



We can see the integral won't be zero if the individual wave functions of the composite wave function  $\Psi_{n_1 n_2}$  be antisymmetric.

And  $\Psi_{n_1}$  and  $\Psi_{n_2}$  will be odd, antisymmetric iff  $n_1, n_2$  odd.

∴ Evaluating  $\langle \Psi_{11}^0 | H' | \Psi_{00}^0 \rangle$

$$\Psi_{11}^0 = A_1(x_1) e^{-\frac{m\omega x_1^2}{2\hbar}} \cdot A_1(x_2) e^{-\frac{m\omega x_2^2}{2\hbar}}$$

$$= \left(\frac{A_1}{\sqrt{2\pi}}\right)^2 (2i m \omega)^2 x_1 x_2 e^{-\frac{m\omega}{2\hbar} (x_1^2 + x_2^2)}$$

$$\therefore \langle \Psi_{11}^0 | H' | \Psi_{00}^0 \rangle = \int_{-\infty}^{\infty} \int_{-\infty}^{\infty} \left(\frac{A_1}{\sqrt{2\pi}}\right)^2 (-2i m \omega)^2 x_1 x_2 e^{-\frac{m\omega}{2\hbar} (x_1^2 + x_2^2)} \cdot \frac{e^{\frac{eV}{2\hbar\omega R^3}} A_0^2 e^{-\frac{m\omega}{2\hbar} (x_1^2 + x_2^2)}}{2\pi\hbar\omega R^3} dx_1 dx_2$$

$$= A_0^2 \left(\frac{A_1}{\sqrt{2\pi}}\right)^2 (2i m \omega)^2 \left(-\frac{e^V}{2\pi\hbar\omega R^3}\right) \int_{-\infty}^{\infty} \int_{-\infty}^{\infty} x_1^2 x_2^2 e^{-\frac{m\omega}{\hbar} (x_1^2 + x_2^2)} dx_1 dx_2$$

$$= A_0^2 \left(\frac{A_1}{\sqrt{2\pi}}\right)^2 (2i m \omega)^2 \left(-\frac{e^V}{2\pi\hbar\omega R^3}\right) \cdot \frac{1}{2} \frac{\sqrt{\frac{1+\sqrt{2}}{2}}}{\left(\frac{m\omega}{\hbar}\right)^{3/4}} \cdot \frac{1}{2} \frac{\sqrt{\frac{1+\sqrt{2}}{2}}}{\left(\frac{m\omega}{\hbar}\right)^{3/4}}$$

$$= A_0^2 \left(\frac{A_1}{\sqrt{2\pi}}\right)^2 (2i m \omega)^2 \left(-\frac{e^V}{2\pi\hbar\omega R^3}\right) \left(\frac{1}{2} \sqrt{\pi}\right)^2 \left(\frac{\hbar}{m\omega}\right)^3$$

$$= \left(\frac{m\omega}{\pi\hbar}\right)^{1/2} \cdot \frac{1}{2m} \left[\left(\frac{m\omega}{\pi\hbar}\right)^{1/4} \frac{i}{\sqrt{\hbar m\omega}}\right]^2 (2i m \omega)^2 \left(-\frac{e^V}{2\pi\hbar\omega R^3}\right) \frac{R^4}{4} \left(\frac{\hbar}{m\omega}\right)^3$$

$$= -\frac{\cancel{m\omega}}{\pi\hbar} \cdot \frac{1}{2\hbar} \cdot \frac{1}{\hbar m\omega} A_0^2 m^2 \omega^2 \frac{e^V}{2\pi\hbar\omega R^3} \cdot \frac{R^4}{4} \left(\frac{\hbar}{m\omega}\right)^3$$

$$= -\frac{1}{2\hbar^2} m^2 \omega^2 \left(\frac{e^V}{2\pi\hbar\omega R^3}\right) \left(\frac{\hbar}{m\omega}\right)^3$$

$$= -\frac{1}{2} \left(\frac{e^V}{2\pi\hbar\omega R^3}\right) \frac{\hbar}{m\omega}$$



$$\frac{|\langle \psi_{10}^0 | H' | \psi_{00}^0 \rangle|^2}{E_{00}^0 - E_{11}^0} = \frac{\frac{1}{4} \left( \frac{e^2}{4\pi\epsilon_0 r^3} \right)^2 \frac{\hbar^2}{m^2 \omega^2}}{\hbar\omega - 3\hbar\omega}$$

$$= -\frac{1}{8} \frac{\hbar}{m^2 \omega^3} \left( \frac{e^2}{4\pi\epsilon_0 r^3} \right)^2$$

$$\therefore E_0^2 = 0 + 0 + \dots + \frac{|\langle \psi_{11}^0 | H' | \psi_{00}^0 \rangle|^2}{E_{00}^0 - E_{11}^0} + \frac{|\langle \psi_{33}^0 | H' | \psi_{00}^0 \rangle|^2}{E_{00}^0 - E_{33}^0} + \frac{|\langle \psi_{55}^0 | H' | \psi_{00}^0 \rangle|^2}{E_{00}^0 - E_{55}^0} + \dots$$

$$= \frac{|\langle \psi_{11}^0 | H' | \psi_{00}^0 \rangle|^2}{E_{00}^0 - E_{11}^0}$$

[Neglecting other small terms]

$$= -\frac{\hbar}{8m^2 \omega^3} \left( \frac{e^2}{4\pi\epsilon_0 r^3} \right)^2$$



~~Problem 10.20~~

2. Consider isotropic three-dimensional harmonic oscillator. Discuss the effect (in first order) of the perturbation,  $V = \lambda x y z$

(a) The ground state.

(b) The (triple degenerate) first excited state.

- Hamiltonian unperturbed

$$H = -\frac{\hbar^2}{2m} \nabla^2 + \frac{1}{2} m \omega^2 x^2 + \frac{1}{2} m \omega^2 y^2 + \frac{1}{2} m \omega^2 z^2$$

Unperturbed stationary states are

$$\psi_{n_x n_y n_z} = \psi_{n_x}(x) \psi_{n_y}(y) \psi_{n_z}(z)$$

where  $\psi_{n_x}(x), \psi_{n_y}(y), \psi_{n_z}(z)$  are one-dimensional harmonic oscillator wave functions.

Unperturbed Energy

$$E_{n_x n_y n_z} = \left( n_x + n_y + n_z + \frac{3}{2} \right) \hbar \omega$$

Now

a given perturbation is  $H' = \lambda x y z$

(a) As the ground state is non degenerate

1st order ~~energy~~ correction

Total Hamiltonian

$$H = H^0 + H'$$

Now 1st order energy correction is

$$E' = \langle \psi | H' | \psi \rangle$$

$$\psi(x,y,z) = \left( \frac{m\omega}{\pi\hbar} \right)^{3/4} e^{-\frac{m\omega}{2\hbar}(x^2+y^2+z^2)} \cdot e^{-\frac{i E_0 t}{\hbar}}$$



~~Work~~

$$B^1 = \iiint_{-\infty}^{\infty} \psi^* H^1 \psi \, dx \, dy \, dz$$

$$= \iiint_{-\infty}^{\infty} \left( \frac{m\omega}{\pi\hbar} \right)^{3/4} e^{-\frac{m\omega}{2\hbar}(x^2+y^2+z^2)} \lambda \, x \, y \, z \, dx \, dy \, dz$$

$$\left( \frac{m\omega}{\pi\hbar} \right)^{3/4} e^{-\frac{m\omega}{2\hbar}(x^2+y^2+z^2)} \, dx \, dy \, dz$$

$$= \lambda \left( \frac{m\omega}{\pi\hbar} \right)^{3/4} \iiint_{-\infty}^{\infty} x \, y \, z \, e^{-\frac{m\omega}{2\hbar}(x^2+y^2+z^2)} \, dx \, dy \, dz$$

$$= \lambda \left( \frac{m\omega}{\pi\hbar} \right)^{3/4} \int_{-\infty}^{\infty} x \, e^{-\frac{m\omega}{2\hbar}x^2} \, dx \int_{-\infty}^{\infty} y \, e^{-\frac{m\omega}{2\hbar}y^2} \, dy \int_{-\infty}^{\infty} z \, e^{-\frac{m\omega}{2\hbar}z^2} \, dz$$

$$= \int_{-\infty}^{\infty} z \, e^{-\frac{m\omega}{2\hbar}z^2} \, dz$$

$$= 0$$

$$\left[ \text{as } \int y \, e^{-\frac{m\omega}{2\hbar}y^2} \, dy \text{ odd function} \right]$$

So first order correction to ground state is zero.

$\therefore$  ground state energy (upto 1st-order corrected term)  $= E^0 = \frac{3}{2}\hbar\omega$

(b) First excited state is triply degenerate. so we will use degenerate perturbation theory. By giving perturbation the three degenerate states may be non degenerate but it will depend on particular perturbation.

let

$$H^0 |\psi_a\rangle = E_1^0 |\psi_a\rangle$$

$$H^0 |\psi_b\rangle = E_1^0 |\psi_b\rangle$$

$$H^0 |\psi_c\rangle = E_1^0 |\psi_c\rangle$$

$$\frac{-i\hbar \partial}{\partial t}$$

Analysis



Then

$$H^0|\psi\rangle = E_1^0 (\alpha|\psi_a\rangle + \beta|\psi_b\rangle + \gamma|\psi_c\rangle)$$

We will find the Matrix Eigenvalue equation.

$$\begin{pmatrix} W_{aa} & W_{ab} & W_{ac} \\ W_{ba} & W_{bb} & W_{bc} \\ W_{ca} & W_{cb} & W_{cc} \end{pmatrix} \begin{pmatrix} \alpha \\ \beta \\ \gamma \end{pmatrix} = E_1^0 \begin{pmatrix} \alpha \\ \beta \\ \gamma \end{pmatrix}$$

The three obtained values of  $E_1^0$  is the three 1st order corrected term.

$$W_{aa} = \langle \psi_a | H^1 | \psi_a \rangle$$

Unperturbed 1st excited states

are

$$\psi_a = \psi_1(x) \psi_0(y) \psi_0(z)$$

$$\psi_b =$$

$$\psi_b = \psi_0(x) \psi_1(y) \psi_0(z)$$

$$\psi_c = \psi_0(x) \psi_0(y) \psi_1(z)$$

Now,

$$W_{aa} = \iiint_{-\infty}^{\infty} \lambda x y z |\psi_a|^2 dx dy dz$$

$$= 0 \quad \text{as } |\psi_a|^2 \text{ is an even function}$$

$$\text{and } \int_{-\infty}^{\infty} y |\psi_a|^2 dy = 0$$

$$W_{bb} = 0$$

$$W_{cc} = 0$$



$$W_{ab} = \langle \psi_a | H | \psi_b \rangle$$

$$= \lambda \int_{-\infty}^{\infty} x^2 y z^2 \psi_a \psi_b dx$$

$$(\psi_a \neq \psi_b)$$

$$= 0$$

$$W_{ba} = 0$$

$$W_{ac} = 0 = W_{ca}$$

$$W_{bc} = \lambda \int_{-\infty}^{\infty} x^2 y z^2 \psi_0(x) \psi_1(y) \psi_0(z) \psi_0(x) \psi_0(y) \psi_1(z) dx dy dz$$

$$= \lambda \int_{-\infty}^{\infty} x^2 y z^2 (\psi_0(x))^2 \psi_1(y) \psi_0(y) \psi_0(z) \psi_1(z) dx dy dz$$

$$= \lambda \int_{-\infty}^{\infty} x^2 y z^2 A_0^2 e^{-\frac{m\omega x^2}{\hbar}} \cdot A_1 y e^{-\frac{m\omega y^2}{2\hbar}} \cdot A_0 e^{-\frac{m\omega z^2}{2\hbar}} \cdot A_1 y z e^{-\frac{m\omega z^2}{2\hbar}} A_0 e^{-\frac{m\omega y^2}{2\hbar}} A_0 e^{-\frac{m\omega x^2}{2\hbar}} dx dy dz$$

$$= \lambda \cdot A_0^4 A_1^2 \int_{-\infty}^{\infty} x^2 e^{-\frac{m\omega x^2}{\hbar}} dx \int_{-\infty}^{\infty} y^2 e^{-\frac{m\omega y^2}{\hbar}} dy \int_{-\infty}^{\infty} z^2 e^{-\frac{m\omega z^2}{\hbar}} dz$$

$$= \lambda \cdot A_0^4 A_1^2 \left[ 2 \cdot \frac{1}{2} \cdot \frac{\sqrt{\frac{1+\sqrt{2}}{2}}}{\left(\frac{m\omega}{\hbar}\right)^{1/4}} \right]^3$$

$$= \lambda \cdot A_0^4 A_1^2 \left[ \frac{\frac{1}{2} \sqrt{\pi}}{\left(\frac{m\omega}{\hbar}\right)^{3/4}} \right]^3$$

$$= \lambda \cdot A_0^4 A_1^2 \left[ \frac{1}{2} \sqrt{\pi} \cdot \left(\frac{\hbar}{m\omega}\right)^{3/4} \right]^3$$

$$= \lambda \cdot A_0^4 A_1^2 \left[ \frac{1}{8} \cdot \pi^{3/2} \cdot \left(\frac{\hbar}{m\omega}\right)^{9/4} \right]$$

$$\approx 0.000000$$



Q2

$$= \lambda \left( \frac{m\omega}{\hbar} \right) \left( \frac{m\omega}{\hbar} \right)^{1/2} \frac{2m\omega}{\hbar} \frac{1}{8} \hbar^{3/2} \left( \frac{\hbar}{m\omega} \right)^{3/2}$$

$$= \lambda \left( \frac{m\omega}{\hbar} \right) \frac{1}{\sqrt{\pi}} \cdot \frac{2m\omega}{\hbar} \frac{1}{8} \hbar^{3/2} \cdot \left( \frac{\hbar}{m\omega} \right)^{3/2}$$

$$= \lambda \frac{m\omega}{\hbar} \cdot \frac{2m\omega}{\hbar} \cdot \frac{1}{8} \cdot \left( \frac{\hbar}{m\omega} \right)^4$$

$$= \lambda \cdot \frac{2m^2\omega^2}{\hbar^2} \cdot \frac{1}{8} \cdot \left( \frac{\hbar}{m\omega} \right)^4$$

$$= \lambda \cdot \frac{m^2\omega^2}{4\hbar^2} \cdot \left( \frac{\hbar}{m\omega} \right)^4 = \frac{\lambda}{4} \cdot \frac{\hbar^2}{m\omega} = m \text{ (let)}$$

Wcb > ~~2m~~ m

$$\therefore \begin{pmatrix} 0 & 0 & 0 \\ 0 & 0 & m \\ 0 & m & 0 \end{pmatrix} \begin{pmatrix} x \\ y \\ z \end{pmatrix} = E_0' \begin{pmatrix} x \\ y \\ z \end{pmatrix}$$

or, det  $\begin{pmatrix} -E_0' & 0 & 0 \\ 0 & -E_0' & \frac{\lambda m^2\omega^2}{4\hbar^2} \\ 0 & \frac{\lambda m^2\omega^2}{4\hbar^2} & -E_0' \end{pmatrix} = 0$

or,  $\begin{pmatrix} -E_0' \\ 0 \\ 0 \end{pmatrix} \begin{pmatrix} E_0' \\ -\frac{\lambda m^2\omega^2}{4\hbar^2} \\ \frac{\lambda m^2\omega^2}{4\hbar^2} \end{pmatrix} = 0$   $E_0' = 0$   
 $E_0' = \pm \frac{\lambda m^2\omega^2}{4\hbar^2}$   $E_0' = \pm m$

$\therefore$  The perturbed energies are

$$E_1' = E_1^0 + E_0' = \frac{\phi}{2} \pm m$$



and  $E_2' = E_1^0 + E_2^1 = \frac{5}{2} \hbar \omega + \frac{\hbar \omega}{4} m$   
 $= \frac{5}{2} \hbar \omega + \frac{1}{4} \frac{\hbar \omega}{m \omega}$

$E_3' = \frac{5}{2} \hbar \omega - \frac{\hbar \omega}{4} \frac{1}{m \omega}$  Ans.

So the three degenerated states will be separated and will turn out to be non degenerate states.

# PROJECT WORK

6th Semester 2020

Department of Physics

Ramkrishna Mission Residential college

*Narendrapur (Autonomous)*

Kolkata 103

**NILANJAN NAG**

ROLL NO : PHUG/194/17

Regd No : A03 1142 0194 17





**Ramakrishna Mission Residential College (Autonomous)**

**Vivekananda Centre for Research**

**Ramakrishna Mission Ashrama**

(A Branch Centre of Ramakrishna Mission, Belur Math, Howrah-711202)

**Narendrapur, Kolkata - 700 103, West Bengal, India**

A Scientific Industrial Research Organisation, Recognised by DST, Govt. of India

College with Potential for Excellence (CPE), Re-accredited by NAAC - 'A' (CGPA 3.56 out of 4)

---

**DEPARTMENT OF PHYSICS**

**Certificate**

This is to certify that Nilanjan Nag, a student of B.Sc has successfully completed the project of UG curriculum entitled "Dirac Equation and its consequences" in the period from January to May, 2020.

Malay Purkait  
.....  
30.06.2020

**Signature Of HOD**

**Dept. of Physics**

**Dr. Malay Purkait**

Associate Prof. & Head

Department of Physics

Ramakrishna Mission Residential College

(Autonomous)

Narendrapur, Kolkata-700 103, (W.B.)

## CERTIFICATE

This is to certify that "Milanjam Nag", student of B.Sc in Physics Honours, has successfully completed his project on "Dirac Equation and its consequences" under the guidance of "Dr. Rajeshwar Chatterjee".

Rajeshwar Chatterjee

Signature of Project guide

Milanjam Nag

Signature of student



## Acknowledgement

I would like to express my special thanks of gratitude my teacher Dr. Rajsekhar Bhattacharyya as well as our Head of the Physics Department Dr. Malay Purkait who gave me the golden opportunity to do this wonderful project on the topic Dirac Equation and its consequences which also helped me in doing a lot of Research and I came to know about so many things.

Secondly I would also like to thank my parents and friends who helped me a lot in finishing this project within the limited time.

Thanks again to all who helped me.

Rajsekhar Bhattacharyya

Signature of the project guide

Nilanjan Nag

B.Sc (3rd year)

Roll no: PHUG/194/17

### Contents:

1. Introduction to Dirac Equation
2. Establishment of Pauli Equation
3. Covariance
4. Charge Conjugation

## 1. Introduction to Dirac Equation

The four momentum vector  $p^\mu = i\hbar \frac{\partial}{\partial x_\mu} = i\hbar \left\{ \frac{\partial}{\partial(ct)}, -\frac{\partial}{\partial x}, -\frac{\partial}{\partial y}, -\frac{\partial}{\partial z} \right\}$

$$p^\mu = i\hbar \left\{ \frac{\partial}{\partial(ct)}, -\nabla \right\}$$

$$p^\mu p_\mu = \frac{E^2}{c^2} - (\vec{p} \cdot \vec{p}) = m_0^2 c^2$$

Thus we obtain the *Klein Gordon* equation for free particles ,

$$p^\mu p_\mu \psi = m_0^2 c^2 \psi \quad \text{which results in } E = \pm \sqrt{p^2 + m_0^2 c^2}$$

There exists solutions for both positive and negative energy solutions

The non relativistic Schrodinger Equation,

$$i\hbar \frac{\partial}{\partial t} \psi = -\frac{\hbar^2 \nabla^2}{2m} \psi + V(x) \psi$$

Now we take the relativistic Hamiltonian  $H = (p^2 c^2 + m^2 c^4)^{1/2}$

Using the fact  $[A, B] = 0$  and  $A \psi = B \psi$  implies  $A^2 \psi = B^2 \psi$  then we get,

$$-\hbar^2 \frac{\partial^2}{\partial t^2} \psi = [-\hbar^2 \nabla^2 c^2 + m^2 c^4] \psi$$

$$\text{implies } [\square + \left(\frac{mc}{\hbar}\right)^2] \psi = 0 \dots (1) \quad \text{where } \square = \nabla_\mu \nabla^\mu$$

$$\text{and } \nabla^\mu \nabla_\mu = \frac{\partial}{\partial x^\mu} \frac{\partial}{\partial x_\mu} = \frac{1}{c^2} \frac{\partial^2}{\partial t^2} - \left( \frac{\partial^2}{\partial x^2} + \frac{\partial^2}{\partial y^2} + \frac{\partial^2}{\partial z^2} \right)$$

Multiplying  $\psi$  from the left of (1) and  $\psi^*$  from the left of conjugate of (1), then we get,

$$\psi^* \left[ \square + \frac{m^2 c^4}{\hbar^2} \right] \psi - \psi \left[ \square + \frac{m^2 c^4}{\hbar^2} \right] \psi^* = 0$$

$$\nabla^\mu (\psi^* \nabla_\mu \psi - \psi \nabla_\mu \psi^*) = 0$$



$$\text{Or, } \frac{\partial}{\partial t} \left[ \frac{i\hbar}{2mc} (\psi^* \frac{\partial \psi}{\partial t} - \psi \frac{\partial \psi^*}{\partial t}) \right] + \text{div} \frac{\hbar}{2mi} (\psi^* \nabla \psi - \psi \nabla \psi^*) = 0$$

We can interpret,  $\frac{\partial \rho}{\partial t} + \text{div} \vec{J} = 0$

The probability density  $\rho$  is not a positive definite expression. The deeper reason is that *Klein Gordon equation* is  $2^{nd}$  order in time so we must know  $\psi(x, t)$  and  $\frac{\partial \psi}{\partial t}$

If we expand the relativistic Hamiltonian, an equation containing all powers of derivative operator, such calculations are very difficult to handle and present an unattractive version of Schrodinger equation in which space and time co ordinates appear in an unsymmetrical form.

For the drawback of these situations, Dirac introduced the linearization of relativistic Hamiltonian  $H = c(\vec{\alpha} \cdot \vec{p}) + \beta mc^2$

$\alpha = \sum_{i=1}^3 \alpha_i \mathbf{n}_i$  and  $p = \sum_{i=1}^3 p_i \mathbf{n}_i$  where  $p_i = -i\hbar \frac{\partial}{\partial x_i}$  and  $\mathbf{n}_i$ 's are the unit vector in 4 dimensional space.

$$c \sum_{i=1}^3 \alpha_i p_i + \beta mc^2 = (p^2 c^2 + m^2 c^4)^{1/2} \dots$$

Equating the coefficients,  $\alpha_i \alpha_k + \alpha_k \alpha_i = 2\delta_{ik}$  ;  $\alpha_i \beta + \beta \alpha_i = 0$  ;

$$\alpha_i^2 = \beta^2 = 1$$

**Properties of  $\alpha_i$  and  $\beta$  :**

1. The  $\alpha_i$  and  $\beta$  must be traceless.

The anti commutation relation imply that,  $\beta \alpha_i \beta = -\alpha_i$  and by the cyclic process of trace  $\text{Tr} AB = \text{Tr} BA$

$$\text{Tr} \alpha_i = \text{Tr} \beta^2 \alpha_i = \text{Tr} \beta \alpha_i \beta = -\text{Tr} \alpha_i$$

$$\text{Tr} \alpha_i = 0$$

similar argument for  $\text{Tr} \beta = 0$

2.  $\alpha_i$  and  $\beta$  are Hermitian as the Hamiltonian operator is Hermitian. It can be satisfied from Quantum mechanical postulates.

3. Since  $\alpha_i$  and  $\beta$  are Hermitian, they can be diagonalised because  $\alpha_i^2 = \beta^2 = 1$ .

So, the diagonal elements (eigen values) can only take  $\pm 1$ .

4. In diagonal form, the diagonal elements of  $\alpha_i$  and  $\beta$  can take only  $\pm 1$  and because of traceless, all of these matrices must have same no of  $+1$ 's and  $-1$ 's.

Hence the dimension can only be even.

5. In two dimension, there exist only three anti commuting matrices namely  $\sigma_1, \sigma_2, \sigma_3$ ; the Pauli Matrices which are linearly independent.

We need four anti commuting matrices in 2 dimension. We assume the matrices exist in 2 dimension.

To prove this, We choose a matrix  $A$  with the help of the bases

$$A = a_0 \mathbb{I} + a_1 \sigma_1 + a_2 \sigma_2 + a_3 \sigma_3$$

where  $a_i$  are all complex coefficients.

Now we assume  $\{A, \sigma_i\} = 0$  where  $i = 1, 2, 3$

Recall that  $\sigma_i^2 = \mathbb{I}$  and  $\{\sigma_i, \sigma_j\} = 2\delta_{ij}$

If  $\{A, \sigma_1\} = 0$

then  $\{a_0 \mathbb{I} + a_1 \sigma_1 + a_2 \sigma_2 + a_3 \sigma_3, \sigma_1\} = 0$

$$\text{or, } a_0 2\sigma_1 + a_1 2\mathbb{I} = 0 \quad [\because \{\sigma_1, \mathbb{I}\} = 2\sigma_1]$$

$$\text{or, } \sigma_1 = -\frac{a_0}{a_1} \mathbb{I}$$

It can not be possible that  $\sigma_1$  is identity matrix multiplied with some number. So, this is the contradiction.



We can not get four simultaneously anti commuting matrix in two dimension.

To get the requirements, we need higher dimension .

As the dimensions of the vector space must be even, then Dirac matrices are constructed in Four dimension .

In a particular explicit representation ,the matrices are

$$\alpha_i = \begin{pmatrix} 0 & \sigma_i \\ \sigma_i & 0 \end{pmatrix} \quad \text{and} \quad \beta = \begin{pmatrix} 1 & 0 \\ 0 & -1 \end{pmatrix}$$

where the  $\sigma_i$  are the  $2 \times 2$  Pauli matrices and the unit entries in  $\beta$  stand for  $2 \times 2$  unit matrices.

#### Calculation of Probability Density:

To construct the differential law of current conservation, we introduce a complex wave function  $\psi$

Now we take relativistic Hamiltonian in Schrodinger equation and multiply  $\psi^\dagger$  from the left ,

$$i\hbar\psi^\dagger \frac{\partial\psi}{\partial t} = \frac{\hbar c}{i} \sum_{k=1}^3 \psi^\dagger \alpha_k \frac{\partial\psi}{\partial x^k} + mc^2 \psi^\dagger \beta \psi \quad (1)$$

Taking complex conjugate of schrodinger Equation and multiply by  $\psi$  from the right

$$-i\hbar \frac{\partial\psi^\dagger}{\partial t} \psi = -\frac{\hbar c}{i} \sum_{k=1}^3 \frac{\partial\psi^\dagger}{\partial x^k} \alpha_k \psi + mc^2 \psi \beta \psi^\dagger \dots (2)$$

Subtracting from (1) to (2),

$$i\hbar \frac{\partial}{\partial t} \psi \psi^\dagger = \sum_{k=1}^3 \frac{\hbar c}{i} \frac{\partial}{\partial x^k} (\psi^\dagger \alpha_k \psi)$$

We can interpret ,  $\frac{\partial \rho}{\partial t} + \nabla \cdot \vec{J} = 0$  Here the probability density  $\rho (= \psi^* \psi)$  is a positive definite expression .

*This is the Success of Dirac Equation.*



## 2. Establishment of Pauli Equation

We consider the Hamiltonian for a free particle  $H = \beta mc^2$  and its corresponding Schrodinger equation,

$$i\hbar \frac{\partial \psi}{\partial t} = \beta mc^2 \psi \dots\dots(1)$$

Since the De Broglie wavelength is infinitely large and wave function is uniform all over the space.

We can get four independent solutions for  $\beta$  when the electron is at rest as  $\beta$  is in four dimension.

The positive energy solutions have a sensible non relativistic reduction to the two component Pauli Spin Theory. We introduce an interaction with an external electromagnetic field described by a four potential  $A^\mu : (\phi, \vec{A})$ ,

The coupling is introduced by means of the gauge invariant substitution

$p^\mu \rightarrow p^\mu - \frac{e}{c} A^\mu$  made in classical relativistic mechanics to describe the interaction of a point charge "e" with an applied field.

The Hamiltonian becomes

$(c\vec{\alpha} \cdot (\vec{p} - \frac{e}{c} \vec{A}) + \beta mc^2 + e\phi)$  and its corresponding Schrodinger Equation becomes

$$i\hbar \frac{\partial \psi}{\partial t} = (c\vec{\alpha} \cdot (\vec{p} - \frac{e}{c} \vec{A}) + \beta mc^2 + e\phi) \psi \dots\dots(2)$$

This equation expresses the minimal interaction of a Dirac particle, considered to be a point charge, with an applied electro magnetic field.

$H = H_0 + H'$  where  $H' = -e(\vec{\alpha} \cdot \vec{p}) + \beta mc^2$

The matrix  $c\alpha$  appears here as the velocity operator in the classical expression for the interaction energy of a point charge "e",  $v_{op} = c\alpha$

The relativistic expression of the Ehrenfest relations ,

$$\frac{dr}{dt} = \frac{i}{\hbar} [H, r] = c\alpha \equiv v_{op}$$

$$\text{Here, } \frac{d\pi}{dt} = \frac{i}{\hbar} [H, \pi] - \frac{e}{c} \frac{\partial}{\partial t} A \dots (3)$$

$$\text{With } \pi \equiv p - \frac{e}{c} A$$

The above equation(2) is the operator equation of motion of a point charge "e".

The wave function  $\psi$  in terms of two component column matrix

$$\psi = \begin{pmatrix} \check{\phi} \\ \check{\chi} \end{pmatrix} \quad \text{We then obtain from equation (2),}$$

$$i\hbar \frac{\partial}{\partial t} \begin{pmatrix} \check{\phi} \\ \check{\chi} \end{pmatrix} = c\beta \cdot \pi \begin{pmatrix} \check{\chi} \\ \check{\phi} \end{pmatrix} + e\phi \begin{pmatrix} \check{\phi} \\ \check{\chi} \end{pmatrix} + mc^2 \begin{pmatrix} \check{\phi} \\ -\check{\chi} \end{pmatrix} \dots (4)$$

In the non relativistic limit the rest energy is  $mc^2$  the largest energy. We can write,

$$\begin{pmatrix} \check{\phi} \\ \check{\chi} \end{pmatrix} = e^{-\frac{imc^2 t}{\hbar}} \begin{pmatrix} \phi \\ \chi \end{pmatrix}$$

$$\frac{\partial \check{\phi}}{\partial t} = \left\{ \frac{-imc^2}{\hbar} \phi + \frac{\partial \phi}{\partial t} \right\} e^{-\frac{imc^2 t}{\hbar}} \quad \text{and} \quad \frac{\partial \check{\chi}}{\partial t} = \left\{ \frac{-imc^2}{\hbar} \chi + \frac{\partial \chi}{\partial t} \right\} e^{-\frac{imc^2 t}{\hbar}}$$

We put these in the coupled differential equation (4) ,

$$i\hbar \frac{\partial}{\partial t} \begin{pmatrix} \phi \\ \chi \end{pmatrix} = c\beta \cdot \pi \begin{pmatrix} \chi \\ \phi \end{pmatrix} + e\phi \begin{pmatrix} \phi \\ \chi \end{pmatrix} - 2mc^2 \begin{pmatrix} 0 \\ \chi \end{pmatrix}$$

$\chi$  is defined by  $\frac{6\pi}{2mc} \phi$  as it is the "small" components of the wave function  $\psi$  in comparison with the "large" components  $\phi$ . Relative to  $(\phi, \chi)$  is reduced by



$\frac{v}{c} \ll 1$  in the non relativistic approximation.

We obtain the two component spinor equation

$$i\hbar \frac{\partial \varphi}{\partial t} = \left( \frac{\vec{\sigma} \cdot \vec{\pi} \vec{\sigma} \cdot \vec{\pi}}{2m} + e\phi \right) \varphi$$

This is further reduced by the identity of Pauli spin matrices,

$$\vec{\sigma} \cdot \vec{a} \vec{\sigma} \cdot \vec{b} = \vec{a} \cdot \vec{b} + i \vec{\sigma} \cdot \vec{a} \times \vec{b}$$

$$\vec{\sigma} \cdot \vec{\pi} \vec{\sigma} \cdot \vec{\pi} = \pi^2 + i \vec{\sigma} \cdot \vec{\pi} \times \vec{\pi}$$

$$= \pi^2 - \frac{e\hbar}{c} \vec{\sigma} \cdot \vec{B}$$

Then we have

$$i\hbar \frac{\partial \varphi}{\partial t} = \left[ \frac{p^2 - \frac{e}{c} A^2}{2m} - \frac{e\hbar}{2mc} \vec{\sigma} \cdot \vec{B} + e\phi \right] \varphi \quad \dots(5)$$

*which is recognized as Pauli equation.*

### 3. CO VARIANCE

In discussing covariance it is desirable to express the Dirac equation in a four dimensional notation which preserves the symmetry between  $ct$  and  $x^i$ . Multiplying Dirac equation by  $\beta/c$  and we get,

$$i\hbar(\gamma^0 \frac{\partial}{\partial x^0} + \gamma^1 \frac{\partial}{\partial x^1} + \gamma^2 \frac{\partial}{\partial x^2} + \gamma^3 \frac{\partial}{\partial x^3})\psi - mc\psi = 0 \dots\dots(1) \text{ where } \gamma^0 = \beta \text{ and } \gamma^i = \beta\alpha_i \text{ where } i=1,2,3, \dots \text{ and so on}$$

The  $\gamma^i$  matrices hold anti commutation relation  $\gamma^\mu \gamma^\nu + \gamma^\nu \gamma^\mu = 2g^{\mu\nu}$  II

Where  $g^{\mu\nu}$  is the rank 4 matrix tensor. In matrix form

$$\gamma^0 = \begin{pmatrix} 1 & 0 \\ 0 & -1 \end{pmatrix} \text{ and } \gamma^i = \begin{pmatrix} 0 & \sigma^i \\ \sigma^i & 0 \end{pmatrix}$$

In order to establish Lorentz covariance of Dirac equation we must satisfy two requirements. The first thing is that there must be an explicit prescription which allows observer  $O'$  given the  $\psi(x)$  of observer  $O$ , to compute  $\psi'(x')$  which describes to  $O'$  the same physical state.

The transformation between  $\psi$  and  $\psi'$  be linear, since both the Dirac equation and the Lorentz transformation and Lorentz transformation of coordinates are themselves linear. We introduce them in the form

$$\psi'(x') = \psi'(ax) = S(a)\psi(x) = S(a)\psi(a^{-1}x') \dots\dots(1)$$

where  $S(a)$  is a  $4 \times 4$  matrix which operates on the four component of the column vector  $\psi(x)$ . It depends upon the relative velocities and spatial orientation of  $O$  and  $O'$ .  $S$  must have an inverse, so that if  $O$  knows  $\psi'(x')$  which  $O'$  uses to describe his observation of a given physical state, he may construct his own physical state  $\psi(x)$

$$\psi(x) = S^{-1}(a)\psi'(x') = S^{-1}(a)\psi'(ax) \dots\dots(2)$$

we could equally write using (1),

$$\psi(x) = S(a^{-1})\psi'(ax)$$



which provides the identification ,  $S(a^{-1}) = S^{-1}(a)$

It is convenient to introduce,  $A = A^\mu \gamma_\mu g_{\mu\nu} A^\nu = \gamma^0 A^0 - \gamma \cdot \nabla$

$$\nabla = \gamma^0 \frac{\partial}{\partial x^\mu} = \frac{\gamma^0}{c} \frac{\partial}{\partial t} + \gamma \cdot \nabla$$

From equation (1),  $(i\hbar\nabla - mc)\psi = 0 \dots(2)$

With the electromagnetic interaction  $p \rightarrow p - \frac{e}{c}\vec{A}$

Then  $(p - \frac{e}{c} - mc) = 0 \dots\dots(3)$

Secondly, Dirac equation is invariant in the primed co ordinate.

It is clear from the definition that  $\gamma^i$  is anti hermitian and  $(\gamma^i)^2 = -1$ ,

$\gamma^0$  is hermitian and  $(\gamma^0)^2 = 1$

For any unitary transformation,  $U^\dagger = U^{-1}$

$\gamma \rightarrow \gamma' = U^\dagger \gamma U$  and  $\psi \rightarrow \psi'$

$$(\gamma' \frac{\partial}{\partial x'} - mc) \psi' = 0$$

$$U^\dagger (\gamma U \frac{\partial}{\partial x'} - mc) \psi' = 0$$

$$U^\dagger \gamma \frac{\partial}{\partial x'} (U \psi') - mc U^\dagger U \psi' = 0$$

$$U^\dagger (\gamma \frac{\partial}{\partial x'} - mc) (U \psi') = 0$$

$$(\gamma \frac{\partial}{\partial x'} - mc) \psi' = 0$$

The co variant form of **Dirac Equation** with  $\gamma^\mu$  matrices ,

$$(\gamma^\mu [p_\mu - eA_\mu(x)] - m)\psi(x) = 0$$

Then for any Lorentz transformation  $\Lambda$  which transforms the co ordinates and

four vector potential from an unprimed frame to primed frame,

$$x' = \Lambda x \quad \text{and} \quad A'(x') = \Lambda A(x)$$

We seek a representation  $S(\Lambda)$  which transforms the **Dirac wave function** from the unprimed to primed co ordinate system

$$\psi'(x') = S(\Lambda)\psi(x)$$

*Covariance is the requirement that the transformation leave **Dirac Equation** invariant in form .*

So that in the primed frame ,

$$(\gamma^\mu [p'_\mu - eA'_\mu(x')] - m)\psi'(x') = 0$$

This requirement determines  $S(\Lambda)$

The four momentum vector in primed frame transforms as

$$p^{\mu'} = \frac{\partial}{\partial x_{\mu'}} = \frac{\partial x^\nu}{\partial x_{\mu'}} \frac{\partial}{\partial x^\nu} = \Lambda^\mu_{\nu} p^\nu \quad \text{implies that} \quad p'_\mu = (\Lambda^{-1})^\mu_{\nu} p_\nu$$

The magnetic vector potential in primed frame for a uniform magnetic field

$$\mathbf{B} = B_0 \hat{n} ;$$

$$\begin{aligned} A^{\mu'} &= \frac{1}{2} (\mathbf{B} \times \mathbf{x}^{\mu'}) \\ &= \frac{1}{2} (\mathbf{B} \times \Lambda^\mu_{\nu} x^\nu) \\ &= \Lambda^\mu_{\nu} \frac{1}{2} (\mathbf{B} \times \mathbf{x}^\nu) \end{aligned}$$

$$A^{\mu'} = \Lambda^\mu_{\nu} A^\nu \quad \text{implies that} \quad A'_\mu = (\Lambda^{-1})^\mu_{\nu} A_\nu$$

Multiply the above equation by  $S^{-1}(\Lambda)$  and we get,

$$S^{-1}(\Lambda) \left\{ \gamma^\mu (\Lambda^{-1})^\mu_{\nu} (p_\mu - eA_\mu(x)) - m \right\} S(\Lambda) \psi(x) = 0$$

This equation is invariant in form if

$$(\Lambda^{-1})^\mu_{\nu} S^{-1}(\Lambda) \gamma^\mu S(\Lambda) = \gamma^\nu \quad \text{Implies that} \quad S^{-1}(\Lambda) \gamma^\mu S(\Lambda) = \Lambda^\mu_{\nu} \gamma^\nu$$



#### 4. Charge conjugation

From the hole theory we came to know that there is an anti particle for each particle. The existence of electrons implies the existence of positrons.

We use to form directly the wave function of a positrons from the missing negative energy electron .

A hole in the negative energy sea recording the absence of an energy  $-E$  ( $E > 0$ ), and the absence of a charge " $e$ " for an electron ( $e < 0$ ) is equivalent to the presence of a positron of positive energy  $+E$  and charge  $-e$

We have one to one correspondence between the negative energy solutions to the **Dirac Equation**

$$(i\nabla - eA - m)\psi = 0 \quad \dots(1)$$

And the positron eigenfunctions. Since positrons are positively charged electrons,

The positron wave function  $\psi_c$  will be the positive energy solution of the equation,

$$(i\nabla + eA - m)\psi_c = 0 \quad \dots(2)$$

Electrons will then emerge from reinterpretation of the hole theory as the absence of negative energy solutions.

It is necessary to change the relative sign between  $i\nabla$  and  $A$  in transforming from (1) to (2) .We take the complex conjugate :

$$i \frac{\partial}{\partial x^\mu} = -(i \frac{\partial}{\partial x^\mu})^* \quad \text{and} \quad A_\mu = +A_\mu$$

Upon doing this, we find (1) becomes,

$$\left[ \left( i \frac{\partial}{\partial x^\mu} + eA_\mu \right) \gamma^{\mu*} + m \right] \psi^* = 0$$

If we find a non singular matrix , denoted by  $C\gamma^0$  ,with the algebra

$$(C\gamma^0)\gamma^\mu(C\gamma^0)^{-1} = -\gamma^\mu \dots(3)$$

We get,  $(i\nabla + eA - m)(C\gamma^0\psi^*) = 0$

With  $\gamma^0\psi^* = C\psi^T = \psi_c$  ; the positive wave function.

From the representation of  $\gamma$  matrices by JAMES D BJORKEN,

$\gamma^0\gamma^\mu\gamma^0 = \gamma^{\mu T}$  so that equation (3) becomes

$$C\gamma^{\mu T}C^{-1} = -\gamma^\mu \text{ Or, } C^{-1}\gamma^\mu C = -\gamma^{\mu T}$$

$C$  must commute with  $\gamma^1$  and  $\gamma^3$  and anti commute with  $\gamma^0$  and  $\gamma^2$

Suitable choice for  $C$  is  $C = i\gamma^2\gamma^0 = -C^{-1} = -C^\dagger = -C^T$

**This is the construction of  $C$  .**

When an unitary transformation is applied on  $C$  ,it will give a matrix in new representation.  $U^\dagger C U = C^{-1}$

The transformation  $\psi_c = C\psi^T = i\gamma^2\psi^*$  does a negative energy free particle eigenfunction.

For a negative energy electron at rest with spin down,the wave function

$$\psi^* = N \begin{bmatrix} 0 \\ 0 \\ 0 \\ 1 \end{bmatrix} e^{imt} \text{ where } N \text{ is normalization constant}$$

The corresponding positron solution is,



$$i\gamma^2\psi^* = i \begin{bmatrix} 0 & 0 & 0 & -i \\ 0 & 0 & i & 0 \\ 0 & i & 0 & 0 \\ -i & 0 & 0 & 0 \end{bmatrix} \begin{bmatrix} 0 \\ 0 \\ 0 \\ 1 \end{bmatrix} N e^{-imt} = N \begin{bmatrix} 1 \\ 0 \\ 0 \\ 0 \end{bmatrix} e^{-imt}$$

$$i\gamma^2\psi^* = \psi$$

That is the absence of a spin down negative energy electron at rest is equivalent to the presence of a spin up positive energy positron at rest. In the field case ,there is no difference between electron and positron.

Negative energy solution is described by four momentum  $p_\mu$  and polarization  $s_\mu$  ;the positive energy solution described by same  $p_\mu$  and  $s_\mu$ .

In terms of free particle spinors ,

$$e^{i\phi(p,s)} v(p,s) = C u^T(p,s)$$

$$e^{i\phi(p,s)} u(p,s) = C v^T(p,s)$$

Showing that  $u(p,s)$  and  $v(p,s)$  are conjugate spinors within a phase factor  $\phi(p,s)$ .

We may develop an invariance operation for the **Dirac equation** by defining the additional operator which changes the sign of the electromagnetic field.

Taking the complex conjugate of equation (1) and replacing  $A_\mu$  by  $-A_\mu$  is a symmetry operation of the **Dirac theory**.

The transformation from (1) to (2) for the electron [positron] into the same equation for the positron [electron] and is called "**Charge conjugation transformation**" denoted by  $C$ .

The physically realizable state contains an electron in a potential  $A_\mu(x)$  there correspondence a physically realizable state of a positron in a potential  $-A_\mu(x)$ . The  $C$  changes the spin up electrons of positive energy to spin up positrons of positive energy solution of (1) to a negative energy solution of the same equation, that is ,to a positron according to the hole theory.



# PROJECT WORK

6th Semester 2020

Department of Physics

Ramkrishna Mission Residential college

*Narendrapur (Autonomous)*

Kolkata 103

**NILANJAN NAG**

ROLL NO : PHUG/194/17

Regd No : A03 1142 0194 17



**Ramakrishna Mission Residential College (Autonomous)**

**Vivekananda Centre for Research**

**Ramakrishna Mission Ashrama**

(A Branch Centre of Ramakrishna Mission, Belur Math, Howrah-711202)

**Narendrapur, Kolkata - 700 103, West Bengal, India**

A Scientific Industrial Research Organisation, Recognised by DST, Govt. of India

College with Potential for Excellence (CPE), Re-accredited by NAAC - 'A' (CGPA 3.56 out of 4)

---

**DEPARTMENT OF PHYSICS**

**Certificate**

This is to certify that Nilanjan Nag, a student of B.Sc has successfully completed the project of UG curriculum entitled "Dirac Equation and its consequences" in the period from January to May, 2020.

Malay Purkait  
.....  
30.06.2020

**Signature Of HOD**

**Dept. of Physics**

**Dr. Malay Purkait**

Associate Prof. & Head

Department of Physics

Ramakrishna Mission Residential College

(Autonomous)

Narendrapur, Kolkata-700 103, (W.B.)



## CERTIFICATE

This is to certify that "Milanjam Nag", student of B.Sc in Physics Honours, has successfully completed his project on "Dirac Equation and its consequences" under the guidance of "Dr. Rajeshwar Chatterjee".

Rajeshwar Chatterjee

Signature of Project guide

Milanjam Nag

Signature of student



## Acknowledgement

I would like to express my special thanks of gratitude my teacher Dr. Rajsekhar Bhattacharyya as well as our Head of the Physics Department Dr. Malay Purkait who gave me the golden opportunity to do this wonderful project on the topic Dirac Equation and its consequences which also helped me in doing a lot of Research and I came to know about so many things.

Secondly I would also like to thank my parents and friends who helped me a lot in finishing this project within the limited time.

Thanks again to all who helped me.

Rajsekhar Bhattacharyya

*Signature of the project guide*

Nilanjan Nag

B.Sc (3rd year)

Roll no: PHUG/194/17

### Contents:

1. Introduction to Dirac Equation
2. Establishment of Pauli Equation
3. Covariance
4. Charge Conjugation



## 1. Introduction to Dirac Equation

The four momentum vector  $p^\mu = i\hbar \frac{\partial}{\partial x_\mu} = i\hbar \left\{ \frac{\partial}{\partial(ct)}, -\frac{\partial}{\partial x}, -\frac{\partial}{\partial y}, -\frac{\partial}{\partial z} \right\}$

$$p^\mu = i\hbar \left\{ \frac{\partial}{\partial(ct)}, -\nabla \right\}$$

$$p^\mu p_\mu = \frac{E^2}{c^2} - (\vec{p} \cdot \vec{p}) = m_0^2 c^2$$

Thus we obtain the *Klein Gordon* equation for free particles ,

$$p^\mu p_\mu \psi = m_0^2 c^2 \psi \quad \text{which results in } E = \pm \sqrt{p^2 + m_0^2 c^2}$$

There exists solutions for both positive and negative energy solutions

The non relativistic Schrodinger Equation,

$$i\hbar \frac{\partial}{\partial t} \psi = -\frac{\hbar^2 \nabla^2}{2m} \psi + V(x) \psi$$

Now we take the relativistic Hamiltonian  $H = (p^2 c^2 + m^2 c^4)^{1/2}$

Using the fact  $[A, B] = 0$  and  $A \psi = B \psi$  implies  $A^2 \psi = B^2 \psi$  then we get,

$$-\hbar^2 \frac{\partial^2}{\partial t^2} \psi = [-\hbar^2 \nabla^2 c^2 + m^2 c^4] \psi$$

implies  $[\square + (\frac{mc}{\hbar})^2] \psi = 0 \dots (1) \quad \text{where } \square = \nabla_\mu \nabla^\mu$

$$\text{and } \nabla^\mu \nabla_\mu = \frac{\partial}{\partial x^\mu} \frac{\partial}{\partial x_\mu} = \frac{1}{c^2} \frac{\partial^2}{\partial t^2} - \left( \frac{\partial^2}{\partial x^2} + \frac{\partial^2}{\partial y^2} + \frac{\partial^2}{\partial z^2} \right)$$

Multiplying  $\psi$  from the left of (1) and  $\psi^*$  from the left of conjugate of (1), then we get,

$$\psi^* \left[ \square + \frac{m^2 c^4}{\hbar^2} \right] \psi - \psi \left[ \square + \frac{m^2 c^4}{\hbar^2} \right] \psi^* = 0$$

$$\nabla^\mu (\psi^* \nabla_\mu \psi - \psi \nabla_\mu \psi^*) = 0$$

$$\text{Or, } \frac{\partial}{\partial t} \left[ \frac{i\hbar}{2mc} (\psi^* \frac{\partial \psi}{\partial t} - \psi \frac{\partial \psi^*}{\partial t}) \right] + \text{div} \frac{\hbar}{2mi} (\psi^* \nabla \psi - \psi \nabla \psi^*) = 0$$

We can interpret,  $\frac{\partial \rho}{\partial t} + \text{div } \vec{J} = 0$

The probability density  $\rho$  is not a positive definite expression. The deeper reason is that *Klein Gordon equation* is 2<sup>nd</sup> order in time so we must know  $\psi(x, t)$  and  $\frac{\partial \psi}{\partial t}$

If we expand the relativistic Hamiltonian, an equation containing all powers of derivative operator, such calculations are very difficult to handle and present an unattractive version of Schrodinger equation in which space and time co ordinates appear in an unsymmetrical form.

For the drawback of these situations, Dirac introduced the linearization of relativistic Hamiltonian  $H = c(\vec{\alpha} \cdot \vec{p}) + \beta mc^2$

$\alpha = \sum_{i=1}^3 \alpha_i \mathbf{n}_i$  and  $p = \sum_{i=1}^3 p_i \mathbf{n}_i$  where  $p_i = -i\hbar \frac{\partial}{\partial x_i}$  and  $\mathbf{n}_i$ 's are the unit vector in 4 dimensional space.

$$c \sum_{i=1}^3 \alpha_i p_i + \beta mc^2 = (p^2 c^2 + m^2 c^4)^{1/2} \dots$$

Equating the coefficients,  $\alpha_i \alpha_k + \alpha_k \alpha_i = 2\delta_{ik}$  ;  $\alpha_i \beta + \beta \alpha_i = 0$  ;

$$\alpha_i^2 = \beta^2 = 1$$

**Properties of  $\alpha_i$  and  $\beta$  :**

1. The  $\alpha_i$  and  $\beta$  must be traceless.

The anti commutation relation imply that,  $\beta \alpha_i \beta = -\alpha_i$  and by the cyclic process of trace  $\text{Tr} AB = \text{Tr} BA$

$$\text{Tr} \alpha_i = \text{Tr} \beta^2 \alpha_i = \text{Tr} \beta \alpha_i \beta = -\text{Tr} \alpha_i$$

$$\text{Tr} \alpha_i = 0$$

similar argument for  $\text{Tr} \beta = 0$



2.  $\alpha_i$  and  $\beta$  are Hermitian as the Hamiltonian operator is Hermitian. It can be satisfied from Quantum mechanical postulates.

3. Since  $\alpha_i$  and  $\beta$  are Hermitian, they can be diagonalised because  $\alpha_i^2 = \beta^2 = 1$ .

So, the diagonal elements (eigen values) can only take  $\pm 1$ .

4. In diagonal form, the diagonal elements of  $\alpha_i$  and  $\beta$  can take only  $\pm 1$  and because of traceless, all of these matrices must have same no of  $+1$ 's and  $-1$ 's.

Hence the dimension can only be even.

5. In two dimension, there exist only three anti commuting matrices namely  $\sigma_1, \sigma_2, \sigma_3$ ; the Pauli Matrices which are linearly independent.

We need four anti commuting matrices in 2 dimension. We assume the matrices exist in 2 dimension.

To prove this, We choose a matrix  $A$  with the help of the bases

$$A = a_0 \mathbb{I} + a_1 \sigma_1 + a_2 \sigma_2 + a_3 \sigma_3$$

where  $a_i$  are all complex coefficients.

Now we assume  $\{A, \sigma_i\} = 0$  where  $i = 1, 2, 3$

Recall that  $\sigma_i^2 = \mathbb{I}$  and  $\{\sigma_i, \sigma_j\} = 2\delta_{ij}$

If  $\{A, \sigma_1\} = 0$

then  $\{a_0 \mathbb{I} + a_1 \sigma_1 + a_2 \sigma_2 + a_3 \sigma_3, \sigma_1\} = 0$

$$\text{or, } a_0 2\sigma_1 + a_1 2\mathbb{I} = 0 \quad [\because \{\sigma_1, \mathbb{I}\} = 2\sigma_1]$$

$$\text{or, } \sigma_1 = -\frac{a_0}{a_1} \mathbb{I}$$

It can not be possible that  $\sigma_1$  is identity matrix multiplied with some number. So, this is the contradiction.

We can not get four simultaneously anti commuting matrix in two dimension.

To get the requirements, we need higher dimension .

As the dimensions of the vector space must be even, then Dirac matrices are constructed in Four dimension .

In a particular explicit representation ,the matrices are

$$\alpha_i = \begin{pmatrix} 0 & \sigma_i \\ \sigma_i & 0 \end{pmatrix} \quad \text{and} \quad \beta = \begin{pmatrix} 1 & 0 \\ 0 & -1 \end{pmatrix}$$

where the  $\sigma_i$  are the  $2 \times 2$  Pauli matrices and the unit entries in  $\beta$  stand for  $2 \times 2$  unit matrices.

#### Calculation of Probability Density:

To construct the differential law of current conservation, we introduce a complex wave function  $\psi$

Now we take relativistic Hamiltonian in Schrodinger equation and multiply  $\psi^\dagger$  from the left ,

$$i\hbar\psi^\dagger \frac{\partial\psi}{\partial t} = \frac{\hbar c}{i} \sum_{k=1}^3 \psi^\dagger \alpha_k \frac{\partial\psi}{\partial x^k} + mc^2 \psi^\dagger \beta \psi \quad (1)$$

Taking complex conjugate of schrodinger Equation and multiply by  $\psi$  from the right

$$-i\hbar \frac{\partial\psi^\dagger}{\partial t} \psi = -\frac{\hbar c}{i} \sum_{k=1}^3 \frac{\partial\psi^\dagger}{\partial x^k} \alpha_k \psi + mc^2 \psi \beta \psi^\dagger \dots (2)$$

Subtracting from (1) to (2),

$$i\hbar \frac{\partial}{\partial t} \psi \psi^\dagger = \sum_{k=1}^3 \frac{\hbar c}{i} \frac{\partial}{\partial x^k} (\psi^\dagger \alpha_k \psi)$$



We can interpret ,  $\frac{\partial \rho}{\partial t} + \nabla \cdot \vec{J} = 0$  Here the probability density  $\rho (= \psi^* \psi)$  is a positive definite expression .

*This is the Success of Dirac Equation.*

## 2. Establishment of Pauli Equation

We consider the Hamiltonian for a free particle  $H = \beta mc^2$  and its corresponding Schrodinger equation,

$$i\hbar \frac{\partial \psi}{\partial t} = \beta mc^2 \psi \dots\dots(1)$$

Since the De Broglie wavelength is infinitely large and wave function is uniform all over the space.

We can get four independent solutions for  $\beta$  when the electron is at rest as  $\beta$  is in four dimension.

The positive energy solutions have a sensible non relativistic reduction to the two component Pauli Spin Theory. We introduce an interaction with an external electromagnetic field described by a four potential  $A^\mu : (\phi, \vec{A})$ ,

The coupling is introduced by means of the gauge invariant substitution

$p^\mu \rightarrow p^\mu - \frac{e}{c} A^\mu$  made in classical relativistic mechanics to describe the interaction of a point charge "e" with an applied field.

The Hamiltonian becomes

$(c\vec{\alpha} \cdot (\vec{p} - \frac{e}{c} \vec{A}) + \beta mc^2 + e\phi)$  and its corresponding Schrodinger Equation becomes

$$i\hbar \frac{\partial \psi}{\partial t} = (c\vec{\alpha} \cdot (\vec{p} - \frac{e}{c} \vec{A}) + \beta mc^2 + e\phi) \psi \dots\dots(2)$$

This equation expresses the minimal interaction of a Dirac particle, considered to be a point charge, with an applied electro magnetic field.

$H = H_0 + H'$  where  $H' = -e(\vec{\alpha} \cdot \vec{p}) + \beta mc^2$



The matrix  $c\alpha$  appears here as the velocity operator in the classical expression for the interaction energy of a point charge "e",  $v_{op} = c\alpha$

The relativistic expression of the Ehrenfest relations ,

$$\frac{dr}{dt} = \frac{i}{\hbar} [H, r] = c\alpha \equiv v_{op}$$

$$\text{Here, } \frac{d\pi}{dt} = \frac{i}{\hbar} [H, \pi] - \frac{e}{c} \frac{\partial}{\partial t} A \dots (3)$$

$$\text{With } \pi \equiv p - \frac{e}{c} A$$

The above equation(2) is the operator equation of motion of a point charge "e".

The wave function  $\psi$  in terms of two component column matrix

$$\psi = \begin{pmatrix} \check{\phi} \\ \check{\chi} \end{pmatrix} \quad \text{We then obtain from equation (2),}$$

$$i\hbar \frac{\partial}{\partial t} \begin{pmatrix} \check{\phi} \\ \check{\chi} \end{pmatrix} = c\beta \cdot \pi \begin{pmatrix} \check{\chi} \\ \check{\phi} \end{pmatrix} + e\phi \begin{pmatrix} \check{\phi} \\ \check{\chi} \end{pmatrix} + mc^2 \begin{pmatrix} \check{\phi} \\ -\check{\chi} \end{pmatrix} \dots (4)$$

In the non relativistic limit the rest energy is  $mc^2$  the largest energy. We can write,

$$\begin{pmatrix} \check{\phi} \\ \check{\chi} \end{pmatrix} = e^{-\frac{imc^2 t}{\hbar}} \begin{pmatrix} \phi \\ \chi \end{pmatrix}$$

$$\frac{\partial \check{\phi}}{\partial t} = \left\{ \frac{-imc^2}{\hbar} \phi + \frac{\partial \phi}{\partial t} \right\} e^{-\frac{imc^2 t}{\hbar}} \quad \text{and} \quad \frac{\partial \check{\chi}}{\partial t} = \left\{ \frac{-imc^2}{\hbar} \chi + \frac{\partial \chi}{\partial t} \right\} e^{-\frac{imc^2 t}{\hbar}}$$

We put these in the coupled differential equation (4) ,

$$i\hbar \frac{\partial}{\partial t} \begin{pmatrix} \phi \\ \chi \end{pmatrix} = c\beta \cdot \pi \begin{pmatrix} \chi \\ \phi \end{pmatrix} + e\phi \begin{pmatrix} \phi \\ \chi \end{pmatrix} - 2mc^2 \begin{pmatrix} 0 \\ \chi \end{pmatrix}$$

$\chi$  is defined by  $\frac{6\pi}{2mc} \phi$  as it is the "small" components of the wave function  $\psi$  in comparison with the "large" components  $\phi$ . Relative to  $(\phi, \chi)$  is reduced by

$\frac{v}{c} \ll 1$  in the non relativistic approximation.

We obtain the two component spinor equation

$$i\hbar \frac{\partial \varphi}{\partial t} = \left( \frac{\vec{\sigma} \cdot \vec{\pi} \vec{\sigma} \cdot \vec{\pi}}{2m} + e\phi \right) \varphi$$

This is further reduced by the identity of Pauli spin matrices,

$$\vec{\sigma} \cdot \vec{a} \vec{\sigma} \cdot \vec{b} = \vec{a} \cdot \vec{b} + i \vec{\sigma} \cdot \vec{a} \times \vec{b}$$

$$\vec{\sigma} \cdot \vec{\pi} \vec{\sigma} \cdot \vec{\pi} = \pi^2 + i \vec{\sigma} \cdot \vec{\pi} \times \vec{\pi}$$

$$= \pi^2 - \frac{e\hbar}{c} \vec{\sigma} \cdot \vec{B}$$

Then we have

$$i\hbar \frac{\partial \varphi}{\partial t} = \left[ \frac{p^2 - \frac{e^2 A^2}{c}}{2m} - \frac{e\hbar}{2mc} \vec{\sigma} \cdot \vec{B} + e\phi \right] \varphi \quad \dots(5)$$

*which is recognized as Pauli equation.*



### 3. CO VARIANCE

In discussing covariance it is desirable to express to express the Dirac equation in a four dimensional notation which preserves the symmetry between  $ct$  and  $x^i$ . Multiplying Dirac equation by  $\beta/c$  and we get,

$$i\hbar(\gamma^0 \frac{\partial}{\partial x^0} + \gamma^1 \frac{\partial}{\partial x^1} + \gamma^2 \frac{\partial}{\partial x^2} + \gamma^3 \frac{\partial}{\partial x^3})\psi - mc\psi = 0 \dots\dots(1) \sim \text{ where } \gamma^0 = \beta \text{ and } \gamma^i = \beta\alpha_i \\ \text{where } i=1,2,3, \dots\dots \text{ and so on}$$

The  $\gamma^i$  matrices hold anti commutation relation  $\gamma^\mu \gamma^\nu + \gamma^\nu \gamma^\mu = 2g^{\mu\nu}$  II

Where  $g^{\mu\nu}$  is the rank 4 matrix tensor. In matrix form

$$\gamma^0 = \begin{pmatrix} 1 & 0 \\ 0 & -1 \end{pmatrix} \text{ and } \gamma^i = \begin{pmatrix} 0 & \sigma^i \\ \sigma^i & 0 \end{pmatrix}$$

In order to establish Lorentz covariance of Dirac equation we must satisfy two requirements. The first thing is that there must be an explicit prescription which allows observer  $O'$  given the  $\psi(x)$  of observer  $O$ , to compute  $\psi'(x')$  which describes to  $O'$  the same physical state.

The transformation between  $\psi$  and  $\psi'$  be linear, since both the Dirac equation and the Lorentz transformation and Lorentz transformation of co ordinates are themselves linear. We introduce them in the form

$$\psi'(x') = \psi'(ax) = S(a)\psi(x) = S(a)\psi(a^{-1}x') \dots\dots(1)$$

where  $S(a)$  is a  $4 \times 4$  matrix which operates on the four component of the column vector  $\psi(x)$ . It depends upon the relative velocities and spatial orientation of  $O$  and  $O'$ .  $S$  must have an inverse, so that if  $O$  knows  $\psi'(x')$  which  $O'$  uses to describe his observation of a given physical state, he may construct his own physical state  $\psi(x)$

$$\psi(x) = S^{-1}(a)\psi'(x') = S^{-1}(a)\psi'(ax) \dots\dots(2)$$

we could equally write using (1),

$$\psi(x) = S(a^{-1})\psi'(ax)$$

which provides the identification ,  $S(a^{-1}) = S^{-1}(a)$

It is convenient to introduce,  $A = A^\mu \gamma_\mu g_{\mu\nu} A^\nu = \gamma^0 A^0 - \gamma \cdot \nabla$

$$\nabla = \gamma^0 \frac{\partial}{\partial x^\mu} = \frac{\gamma^0}{c} \frac{\partial}{\partial t} + \gamma \cdot \nabla$$

From equation (1),  $(i\hbar\nabla - mc)\psi = 0 \dots(2)$

With the electromagnetic interaction  $p \rightarrow p - \frac{e}{c}\vec{A}$

Then  $(p - \frac{e}{c} - mc) = 0 \dots\dots(3)$

Secondly, Dirac equation is invariant in the primed co ordinate.

It is clear from the definition that  $\gamma^i$  is anti hermitian and  $(\gamma^i)^2 = -1$ ,

$\gamma^0$  is hermitian and  $(\gamma^0)^2 = 1$

For any unitary transformation,  $U^\dagger = U^{-1}$

$\gamma \rightarrow \gamma' = U^\dagger \gamma U$  and  $\psi \rightarrow \psi'$

$$(\gamma' \frac{\partial}{\partial x'} - mc) \psi' = 0$$

$$U^\dagger (\gamma U \frac{\partial}{\partial x'} - mc) \psi' = 0$$

$$U^\dagger \gamma \frac{\partial}{\partial x'} (U \psi') - mc U^\dagger U \psi' = 0$$

$$U^\dagger (\gamma \frac{\partial}{\partial x'} - mc) (U \psi') = 0$$

$$(\gamma \frac{\partial}{\partial x'} - mc) \psi' = 0$$

The co variant form of **Dirac Equation** with  $\gamma^\mu$  matrices ,

$$(\gamma^\mu [p_\mu - eA_\mu(x)] - m)\psi(x) = 0$$

Then for any Lorentz transformation  $\Lambda$  which transforms the co ordinates and

four vector potential from an unprimed frame to primed frame,



$$x' = \Lambda x \quad \text{and} \quad A'(x') = \Lambda A(x)$$

We seek a representation  $S(\Lambda)$  which transforms the **Dirac wave function** from the unprimed to primed co ordinate system

$$\psi'(x') = S(\Lambda)\psi(x)$$

*Covariance is the requirement that the transformation leave **Dirac Equation** invariant in form .*

So that in the primed frame ,

$$(\gamma^\mu [p'_\mu - eA'_\mu(x')] - m)\psi'(x') = 0$$

This requirement determines  $S(\Lambda)$

The four momentum vector in primed frame transforms as

$$p^{\mu'} = \frac{\partial}{\partial x_{\mu'}} = \frac{\partial x^\nu}{\partial x_{\mu'}} \frac{\partial}{\partial x^\nu} = \Lambda^\mu_{\nu} p^\nu \quad \text{implies that} \quad p'_\mu = (\Lambda^{-1})^\mu_{\nu} p_\nu$$

The magnetic vector potential in primed frame for a uniform magnetic field

$$\mathbf{B} = B_0 \hat{n} ;$$

$$\begin{aligned} A^{\mu'} &= \frac{1}{2} (\mathbf{B} \times \mathbf{x}^{\mu'}) \\ &= \frac{1}{2} (\mathbf{B} \times \Lambda^\mu_{\nu} x^\nu) \\ &= \Lambda^\mu_{\nu} \frac{1}{2} (\mathbf{B} \times \mathbf{x}^\nu) \end{aligned}$$

$$A^{\mu'} = \Lambda^\mu_{\nu} A^\nu \quad \text{implies that} \quad A'_\mu = (\Lambda^{-1})^\mu_{\nu} A_\nu$$

Multiply the above equation by  $S^{-1}(\Lambda)$  and we get,

$$S^{-1}(\Lambda) \left\{ \gamma^\mu (\Lambda^{-1})^\mu_{\nu} (p_\mu - eA_\mu(x)) - m \right\} S(\Lambda) \psi(x) = 0$$

This equation is invariant in form if

$$(\Lambda^{-1})^\mu_{\nu} S^{-1}(\Lambda) \gamma^\mu S(\Lambda) = \gamma^\nu \quad \text{Implies that} \quad S^{-1}(\Lambda) \gamma^\mu S(\Lambda) = \Lambda^\mu_{\nu} \gamma^\nu$$

#### 4. Charge conjugation

From the hole theory we came to know that there is an anti particle for each particle. The existence of electrons implies the existence of positrons.

We use to form directly the wave function of a positrons from the missing negative energy electron .

A hole in the negative energy sea recording the absence of an energy  $-E$  ( $E > 0$ ), and the absence of a charge " $e$ " for an electron ( $e < 0$ ) is equivalent to the presence of a positron of positive energy  $+E$  and charge  $-e$

We have one to one correspondence between the negative energy solutions to the **Dirac Equation**

$$(i\nabla - eA - m)\psi = 0 \quad \dots(1)$$

And the positron eigenfunctions. Since positrons are positively charged electrons,

The positron wave function  $\psi_c$  will be the positive energy solution of the equation,

$$(i\nabla + eA - m)\psi_c = 0 \quad \dots(2)$$

Electrons will then emerge from reinterpretation of the hole theory as the absence of negative energy solutions.

It is necessary to change the relative sign between  $i\nabla$  and  $A$  in transforming from (1) to (2) .We take the complex conjugate :

$$i \frac{\partial}{\partial x^\mu} = -(i \frac{\partial}{\partial x^\mu})^* \quad \text{and} \quad A_\mu = +A_\mu$$

Upon doing this, we find (1) becomes,

$$\left[ \left( i \frac{\partial}{\partial x^\mu} + eA_\mu \right) \gamma^{\mu*} + m \right] \psi^* = 0$$



If we find a non singular matrix , denoted by  $C\gamma^0$  ,with the algebra

$$(C\gamma^0)\gamma^\mu(C\gamma^0)^{-1} = -\gamma^\mu \dots(3)$$

We get,  $(i\nabla + eA - m)(C\gamma^0\psi^*) = 0$

With  $\gamma^0\psi^* = C\psi^T = \psi_c$  ; the positive wave function.

From the representation of  $\gamma$  matrices by JAMES D BJORKEN,

$\gamma^0\gamma^\mu\gamma^0 = \gamma^{\mu T}$  so that equation (3) becomes

$$C\gamma^{\mu T}C^{-1} = -\gamma^\mu \text{ Or, } C^{-1}\gamma^\mu C = -\gamma^{\mu T}$$

$C$  must commute with  $\gamma^1$  and  $\gamma^3$  and anti commute with  $\gamma^0$  and  $\gamma^2$

Suitable choice for  $C$  is  $C = i\gamma^2\gamma^0 = -C^{-1} = -C^\dagger = -C^T$

**This is the construction of  $C$  .**

When an unitary transformation is applied on  $C$  ,it will give a matrix in new representation.  $U^\dagger C U = C^{-1}$

The transformation  $\psi_c = C\psi^T = i\gamma^2\psi^*$  does a negative energy free particle eigenfunction.

For a negative energy electron at rest with spin down,the wave function

$$\psi^* = N \begin{bmatrix} 0 \\ 0 \\ 0 \\ 1 \end{bmatrix} e^{imt} \text{ where } N \text{ is normalization constant}$$

The corresponding positron solution is,

$$i\gamma^2\psi^* = i \begin{bmatrix} 0 & 0 & 0 & -i \\ 0 & 0 & i & 0 \\ 0 & i & 0 & 0 \\ -i & 0 & 0 & 0 \end{bmatrix} \begin{bmatrix} 0 \\ 0 \\ 0 \\ 1 \end{bmatrix} N e^{-imt} = N \begin{bmatrix} 1 \\ 0 \\ 0 \\ 0 \end{bmatrix} e^{-imt}$$

$$i\gamma^2\psi^* = \psi$$

That is the absence of a spin down negative energy electron at rest is equivalent to the presence of a spin up positive energy positron at rest. In the field case ,there is no difference between electron and positron.

Negative energy solution is described by four momentum  $p_\mu$  and polarization  $s_\mu$  ;the positive energy solution described by same  $p_\mu$  and  $s_\mu$ .

In terms of free particle spinors ,

$$e^{i\phi(p,s)} v(p,s) = C u^T(p,s)$$

$$e^{i\phi(p,s)} u(p,s) = C v^T(p,s)$$

Showing that  $u(p,s)$  and  $v(p,s)$  are conjugate spinors within a phase factor  $\phi(p,s)$ .

We may develop an invariance operation for the **Dirac equation** by defining the additional operator which changes the sign of the electromagnetic field.

Taking the complex conjugate of equation (1) and replacing  $A_\mu$  by  $-A_\mu$  is a symmetry operation of the **Dirac theory**.

The transformation from (1) to (2) for the electron [positron] into the same equation for the positron [electron] and is called "**Charge conjugation transformation**" denoted by  $C$ .



The physically realizable state contains an electron in a potential  $A_\mu(x)$  there correspondence a physically realizable state of a positron in a potential  $-A_\mu(x)$ . The  $C$  changes the spin up electrons of positive energy to spin up positrons of positive energy solution of (1) to a negative energy solution of the same equation, that is ,to a positron according to the hole theory.



UNDERGRADUATE

PROJECT

ON

**“METAL ELECTRODE THIN FILM  
DEPOSITION BY THERMAL EVAPORATION  
METHOD ON GLASS SUBSTRATE”**

— SUBMITTED BY,  
**SOUVIK KUMAR NASKAR**

Roll No. (PHUG/200/17)

Reg No. : A03-1122-0200-17

On behalf of RAMAKRISHNA MISSION RESIDENTIAL COLLEGE, NARENDRAPUR,  
KOLKATA: 700103

Submission date of the project: 30<sup>th</sup> JUNE 2020

As a B.sc. project (experimental) under the supervision of,

**DR. DEBAMALYA BANERJEE**

ASSISTANT PROFESSOR

DEPARTMENT OF PHYSICS

**INDIAN INSTITUTE OF TECHNOLOGY, KHARAGPUR**

SIGNATURE

**KHARAGPUR-721302**





**Ramakrishna Mission Residential College (Autonomous)**

**Vivekananda Centre for Research**

**Ramakrishna Mission Ashrama**

(A Branch Centre of Ramakrishna Mission, Belur Math, Howrah-711202)

**Narendrapur, Kolkata - 700 103, West Bengal, India**

A Scientific Industrial Research Organisation, Recognised by DST, Govt. of India

College with Potential for Excellence (CPE), Re-accredited by NAAC - 'A' (CGPA 3.56 out of 4)

---

## **DEPARTMENT OF PHYSICS**

### **Certificate**

This is to certify that Souvik Kumar Naskar, a student of B. Sc has successfully completed the project of UG curriculum entitled "METAL ELECTRODE thin film DEPOSITION BY THERMAL EVAPORATION METHOD ON GLASS SUBSTRATE" in the period from January to May, 2020.

*Malay Purkait*  
.....30.06.2020

**Signature Of HOD**

**Dept. of Physics**

**Dr. Malay Purkait**

Associate Prof. & Head

Department of Physics

Ramakrishna Mission Residential College

(Autonomous)

Narendrapur, Kolkata-700 103, (W.B.)

### ACKNOWLEDGEMENTS:

Foremost, I would like to express my sincere gratitude to my advisor Dr. Debamalya Banerjee for his continuous support to this project, for his patience, motivation, enthusiasm and immense knowledge. His guidance helped me in all the time of research and writing of this paper. Beside of my advisor, I would like to thank the rest of DB Electrical Characterization research group, his phd students named Sudipta Khamrui, Abdullah Bin Rahaman, Atri Sarkar for their encouragement and helping me to learn the experimental techniques in a insightful manner. They helped me and supported me all the time to work. I would not forget to remember their name for their encouragement and moreover for the timely support and guidance till the completion of my project work. I am thankful to and fortunate enough to get constant support from the whole DB research group in the Dept. of Physics in IIT Kharagpur.

I would also pay my gratitude to our H.O.D. Dr. Malay Purkait for giving me the permission to go to IIT-KGP and constantly helping me to access the project work. I am also grateful to our respected professor Dr. Debabrata Das for giving me his kind advice for how I can spend time to do my project work within my current B.Sc. course. Thanks also have to be given to Dr. Sourav Chatterjee, Dr. Amal Sarkar without whom I can't express how to represent any project/ internship report in front of viewers'.

I am also thankful my parents for their all time economic as well as mental support during the whole time when I have to stay in IIT-KGP accommodation block. I am also thankful to my friends for all time encouragement.

Sounik kr. Naskar

---

Signature



## INDEX

| <u>TOPIC</u>                                                                                                                                         | <u>PAGE NO.</u> |
|------------------------------------------------------------------------------------------------------------------------------------------------------|-----------------|
| Motivation                                                                                                                                           | 03              |
| Vacuum Techniques                                                                                                                                    | 03-04           |
| High Pumping Technology                                                                                                                              | 04-05           |
| Thin Film Deposition                                                                                                                                 | 05              |
| Application of Thin Film                                                                                                                             | 05-06           |
| Vacuuming and Deposition procedure                                                                                                                   | 06-07           |
| Experimental section                                                                                                                                 | 07-08           |
| Dependence of resistance with the variation of separation between two electrodes using Drop Casting Method along with Thermal Evaporation Technology | 08-12           |
| Determination of Schottky effect in the metal-semiconductor junction in top to bottom configuration by J-V graph using spin coating                  | 12-15           |
| Acknowledgement                                                                                                                                      | 15-16           |
| References                                                                                                                                           | 16              |

## **MOTIVATION:**

The aim of this project is to provide a concise reference and description of the processes, methods, and equipment for depositing technologically important materials. Emphasis is placed on the most recently developed process and technique of film deposition for applications in high technology. The discussions of the principles of operation of deposition technique and its suitability, performance, control, capabilities, and limitations for production applications are intended to provide with a basic understanding with this whole system. Thin film deposition is the technical base of the entire device fabrication industry, and is probably the most economically important manufacturing technologies today. The properties of thin films can be governed by the deposition method. Almost all thin film deposition and characterization methods require either a vacuum or some sort of reduced-pressure ambient. Direct techniques like evaporation is widely used for thin film fabrication. In this project, mainly thermal evaporation technique and some of its relatable experiments have been performed to have a clear view of what actually thin film is and where the importance of thermal evaporation lies.

## **VACUUM TECHNIQUES:**

One of the common methods of Vapor Deposition is Thermal Evaporation. This is a form of Thin Film Deposition, which is a vacuum technology for applying coatings of pure materials to the surface of various objects. The coatings, also called films, are usually in the thickness range of angstroms to microns. Here the object to be coated is referred to as the substrate, and can be any of a wide variety of things like glass plate, silicon, quartz etc. Thermal Evaporation involves heating a solid material inside a high vacuum chamber. Inside the vacuum, even a relatively low vapor pressure is sufficient to raise a vapor cloud inside the chamber. This evaporated material now constitutes a vapor stream, which traverses the chamber and hits the substrate, sticking to it as a coating or film. Since, in most instances of thermal evaporation processes the material is heated to its melting point, it is usually located in the bottom of the chamber. The vapor then rises above this bottom source, and the substrates are held inverted in appropriate fixtures at the top of the chamber.



Figure 1. Diffusion pump



The surfaces intended to be coated are thus facing down toward the heated source material to receive their coating. The main procedure of heating the source material is Filament Evaporation, is a simple electrical resistive heat element of filament: Here we use Tungsten filament (The filament source offers the safety of low voltage, although very high current is required, usually several hundred amps). Here the evaporation rate is determined by the vapor pressure of the source material and the evaporation temperature. We take that elements for evaporation whose melting point is less than 1400 degree Celsius (as we pass 0.400A current through Tungsten filament); Here we take Al and Ag for evaporating material. A deposition chamber under high vacuum ( $\sim 10^{-6}$  m.bar) is necessary in order to avoid the oxidation of source material. We use two Gauges here named Pirani Gauge and Penning Gauge which are used for measuring the pressure in vacuum system. Penning gauge is usually used for measuring the pressure below  $10^{-3}$  Torr and it is very sensitive due to random pressure fluctuation.

### **HIGH PUMPING TECHNOLOGY:**

To vacuum the evaporation chamber highly, here two pumps are used named as Rotary Pump or Roughing Pump and Diffusion Pump. Pumps that operates in high vacuum range typically don't operate at atmospheric pressure, whereas pumps that work efficiently at atmospheric pressure usually can't produce a vacuum lower than  $10^{-3}$  Torr. Here roughing pump vacuums near about  $10^{-3}$  m.bar order. In this time Pirani Gauge plays the role to display the vapor pressure. In this Rotary Pump, gas enters to a suction pump and is compressed by the "rotor" which has two blades and expelled to the atmosphere through the discharge valve.

Now it becomes suitable for starting the high vacuum pump so named as Diffusion Pump. Diffusion Pump is actually a vapor jet pump where motive fluid is used like Mercury, Hydrocarbon oil. Here oil is heated in oil bath and consequently it is vaporized flowing up through the chimney and then flows out through the nozzles which are situated throughout the wall of pump jacket. These nozzles direct the vapor stream downward towards the cooled outer wall which is made cooled by a chiller and cooled by liquid nitrogen. (This cooling system is so arranged that the coolest region is where the vapor stream strikes the pump wall and get cooled and condensed to get its oil form again.) These vapors are made to flow in supersonic jet motion and collide with the gas particles. The gas particles are given a downward momentum and by this momentum transfer they are ejected to higher pressure. Often Baffles are used in DP to avoid so called Back streaming and Back migration also.

However, this pump can't eject the particles itself to the atmosphere. The gas must be "backed" by another pump called "Backing Pump". Here Rotary vane is used as backing pump.

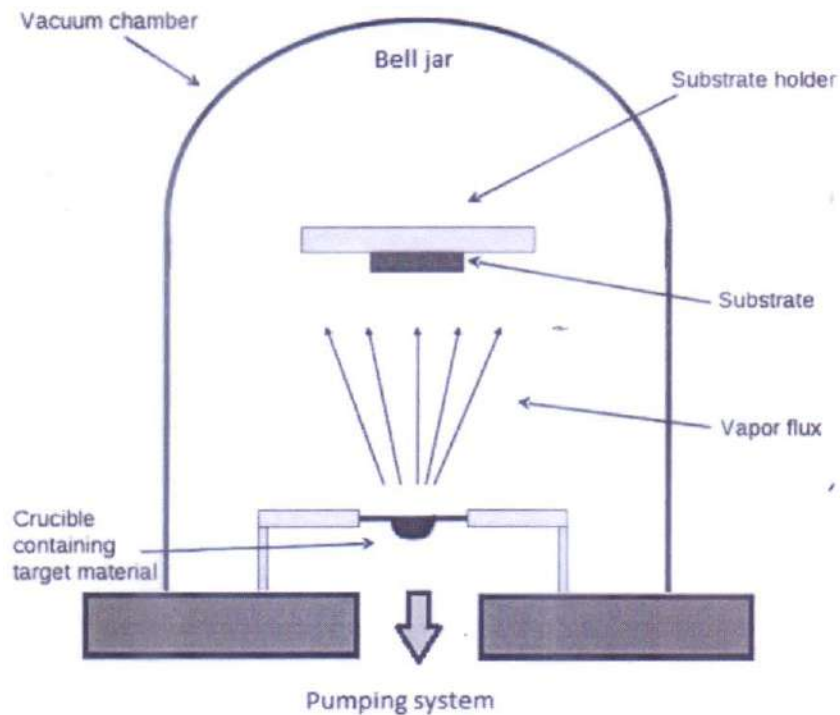


Figure 2 .Schematic diagram for vapor deposition.

### THIN FILM DEPOSITION:

Thin film deposition is one of the most required techniques in vacuum technology that is required for a variety of application in mainly material science. "Thin" is a relative term, but most deposition techniques control layer thickness within a few tens of nanometers. Thin film can be produced by drop casting and then oil bathing subsequently, can be produced through spin coating. Spin coating or spin casting, uses a liquid precursor, or sol-gel precursor deposited onto a smooth, flat substrate which is subsequently spun at a high velocity to centrifugally spread the solution over the substrate with a certain r.p.m. The speed at which the solution is spun and the viscosity of the sol determine the ultimate thickness of the deposited film. Repeated depositions can be carried out to increase the thickness of films as desired.

### APPLICATION OF THIN FILM:

Our society overlooks the importance of vacuum coatings in products they use. The semiconductor industry relies heavily on thin film technology to produce flash memory and computer chips. Companies developing optical products often use optical polarizers and beam splitters in their designs. Other industries also use thin film technology most of which is for cosmetic purposes, such as mirrors and toys. It is useful in the manufacture of optics (for reflective, anti-reflective coatings or self-cleaning glass, for instance), electronics (layers of insulators, semiconductors, and conductors form integrated circuits). Thin-film technologies are also being developed as a means of substantially reducing the cost of solar cells. The rationale



for this is thin-film solar cells are cheaper to manufacture owing to their reduced material costs, energy costs, handling costs and capital costs.

### **VACUUMING AND DEPOSITION PROCEDURE:**

- Pumping to Low Vacuum:

1. Pull the source shutter and take the air admittance valve right handed. Take on the main switch as well as of chiller also.
2. Switching on the vacuum pump and then GH2 (digital pirani gauge) now take on roughing valve and wait approx. 20 minutes till the pressure comes to  $10^{-2}$  milibar.
3. Now switch off the roughing valve and on the backing valve. ( this order should be maintained properly).
4. Switch on GH2 and turn on the diffusion pump and wait for 15 minutes approx.

- Pumping to High Vacuum:

1. Turn on High vacuum valve. Check the penning gauge to take the pressure  $10^{-6}$  milibar.
2. Wait approx. 30 to 40 minutes till penning gauge shows required pressure.

- Deposition Procedure:

The deposition process is still under development. It is best to clean the slides with methanol or isopropyl alcohol and then let cleaning agent evaporate fully prior to placement in the chamber. Recording more data will help us to better tune this process and improve control over film characteristics.

1. Weigh the glass slide after cleaning and prior to placing it in the chamber.
2. While the chamber is open place a few Al/Ag pellets in the crucible.
5. After reaching a high vacuum connect the power supply .
6. Turn on the power supply and turn the voltage control all the way up so the power output is dependent on the current control knob.
7. Slowly increase the current output (LT 1). This is done by increasing the output by 0. 400 amps and then waiting a 20 sec. for the crucible to reach a thermal equilibrium, then push the shutter.
8. During deposition record the time elapsed ( I take here 1 minute), power supply settings, and the chamber pressure before and during the deposition process.
9. When done, decrease the current output in the same manner that was increased it (one can decrement the current in larger amounts) and eventually turn off the power supply.

10. After waiting for 5 minutes, will close high vacuum valve and then same also for the pirani gauge.

11. After then turn off diffusion pump and wait upto 20 minutes

12. now this is the time for closing the backing valve, next vacuum pump and at the last of all the switch is turned off for both the chiller and from the mains.

## **EXPERIMENTAL SECTION:**

### **Material used:**

rGO - ZnSe composition (given sample) , Aluminum (Al) , Silver (Ag) , ITO glass plate , Normal glass plate , Tungsten (filament) , 2-Propanol , Acetone , liquid nitrogen , Nitric acid, Hydrochloric acid, de ionized water.

### **Equipment used:**

Source meter Unit (SMU), Thermal evaporation unit( includes- High vacuum pump, Rotary pump, Digital Pirani gauge, Digital Penning Gauge, Chiller, Backing valve ,Roughing valve) Digital Vernier Caliper, Tweezers, Crocodile clip, Digital multimeter, ultrasonic bath, silicon oil hot bath, spin coater, drop casting dropper.



Figure 3: silicon oil bath



Figure 4: spin coat unit



Figure 5. drop cast dropper

**INTRODUCTORY THEORY:** We all know that Graphene is not attractive in optoelectronic device applications as graphene is a zero band gap semiconductor. So, to increase the level of band gap, oxidized functional groups are imposed on Graphene layer. Here GO is synthesized from Graphite powder by some method (Hummers method) . But now the separation of band gap is so much extended that electrical conducting phenomenon is prohibited to occur. So it is now needed to reduce the band gap but not too much as it was. Now this becomes rGO, i.e. reduced graphene oxide, which is not well conducting. So now it is the time to dope zinc selenide ( ZnSe)



upon it as acceptor. Now the composite rGO-ZnSe becomes eligible for showing opto-electronic behavior.

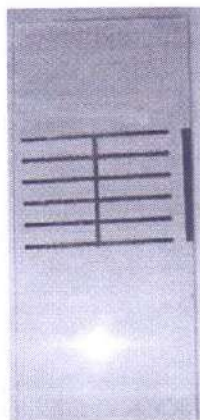


Figure 6. Ag deposition using shadow mask on glass plate.



Figure 7. rGO – ZnSe sample

- ***Dependence of resistance with the variation of separation between two electrodes using Drop Casting Method along with Thermal Evaporation Technology***

**Experimental Procedure:** Here we have taken six glass plates, cleaned by acetone, as the substrate of evaporation. Silver pieces are taken as source material for thermal evaporation. First of all, celotapes of various breadths are attached in the upper surface of six glass plates. Finally, Ag is deposited onto the celotape attached surface by thermal evaporation under vacuum pressure of  $5 \times 10^{-6}$  mbar. After that, deposited glass plates are taken out from thermal

evaporation unit and celotapes are removed from the surfaces. Now these become like two silver deposited electrodes separated by certain bare distance from each other and here we have taken active area to be equal. Here I have taken the separation between two electrodes as 1mm, 1.49mm, 2.02mm, 2.51mm, 3.50mm, 5.23mm which are measured by HITSAN INCORPORATION 100mm LCD Digital Electronic Carbon Fiber Vernier Caliper. Now ultrasonic vibration is given to rGO-ZnSe composite for 30 minutes and now this composition is ready for drop casting between the electrodes. We have given two drops of composite sample between the electrodes to make a junction between them and the glass plates are made to bake for 10 minutes in 120 degree Celsius.

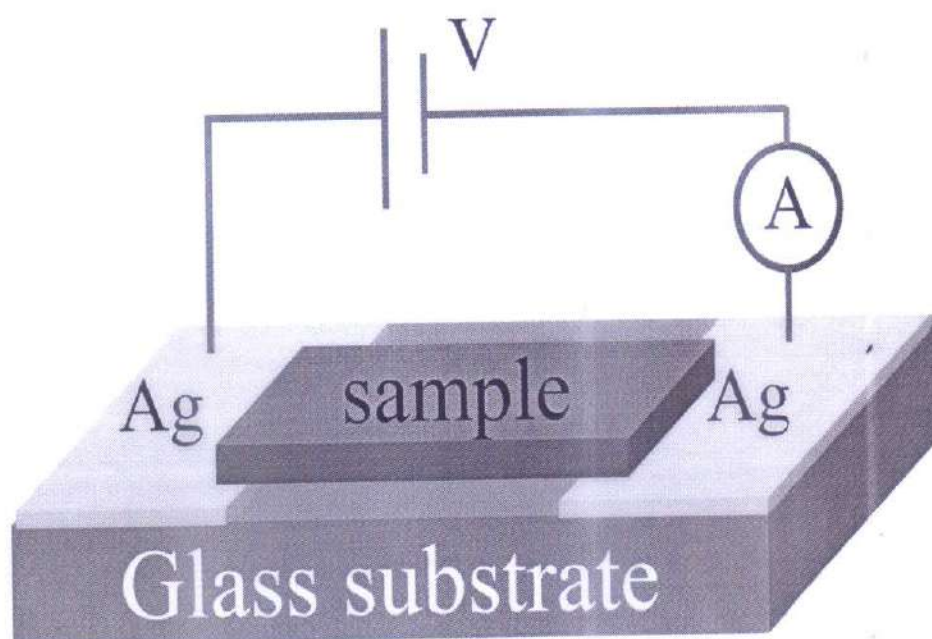


Figure 8. Glass substrate with sample diagram.

#### OBSERVATION:

Now we have measured  $I$  vs  $V$  characteristics through these electrodes one by one in Source measure unit (SMU). We have given bias voltage to be -10 to +10 volt and have taken 101 data each time. Now we have decided to measure the slope for those 7 samples in between same voltage range 2.4 to 7.5 volt and have some slope for each and then have plotted  $I$  vs  $V$  characteristics in log-log scale. We also have plotted Distance vs Resistance Graph, where distance refers to the separation between two electrodes for each sample. The observed graphs are shown below:



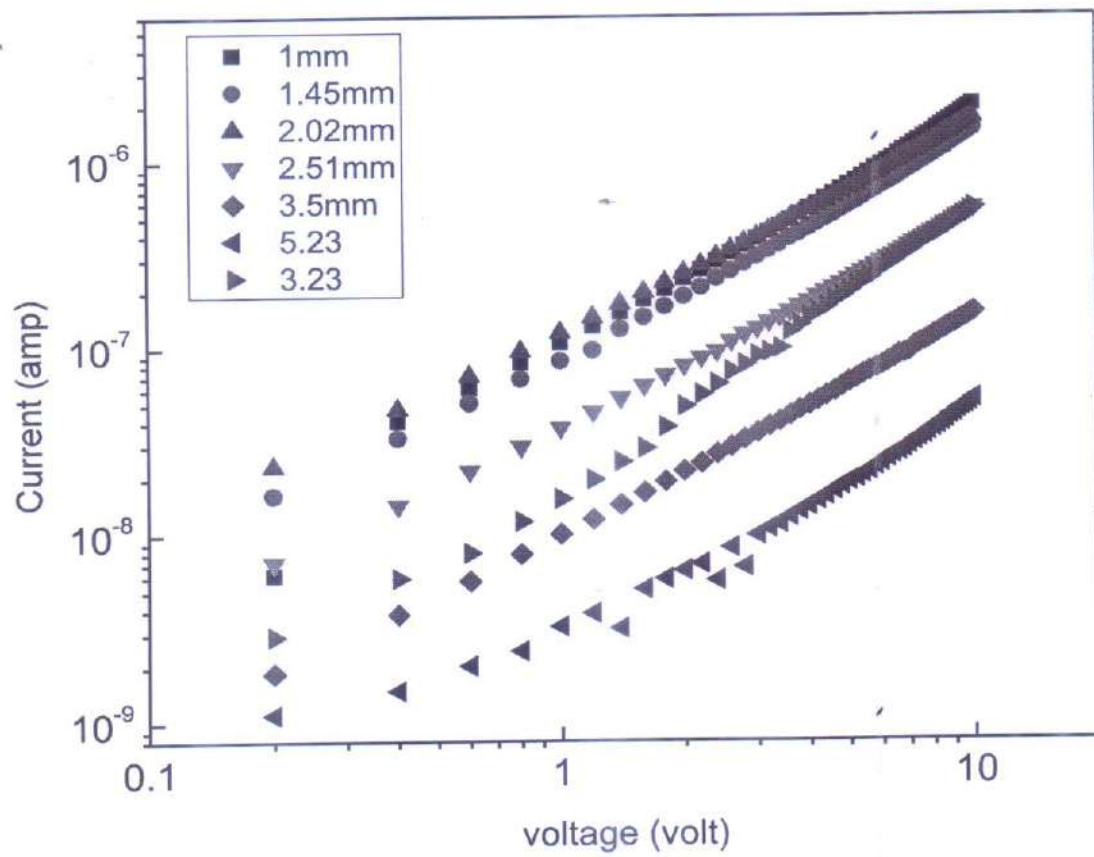


Figure 9. I vs V plot for varying electrode distances.



Figure 10. Thermal evaporation unit

Here we have seen I vs V graph for various separation between electrodes. Now we have shown the actual plotting of distance vs slope (which is basically resistance) graph. As we take I vs V graph, the actual slopes are just inverse of the slopes which are calculated from the graph. Here is the table of the data chart for Distance – Resistance plotting.

| Distance(in mm) | Resistance (in ohm) |
|-----------------|---------------------|
| 1               | $4.95 \times 10^6$  |
| 1.45            | $6.8 \times 10^6$   |
| 2.02            | $5.8 \times 10^6$   |
| 2.51            | $1.8 \times 10^7$   |
| 3.23            | $1.68 \times 10^7$  |
| 3.5             | $6.5 \times 10^7$   |
| 5.23            | $1.968 \times 10^8$ |

If we plot the corresponding I vs V graph in log-log scale then we have the following graph :



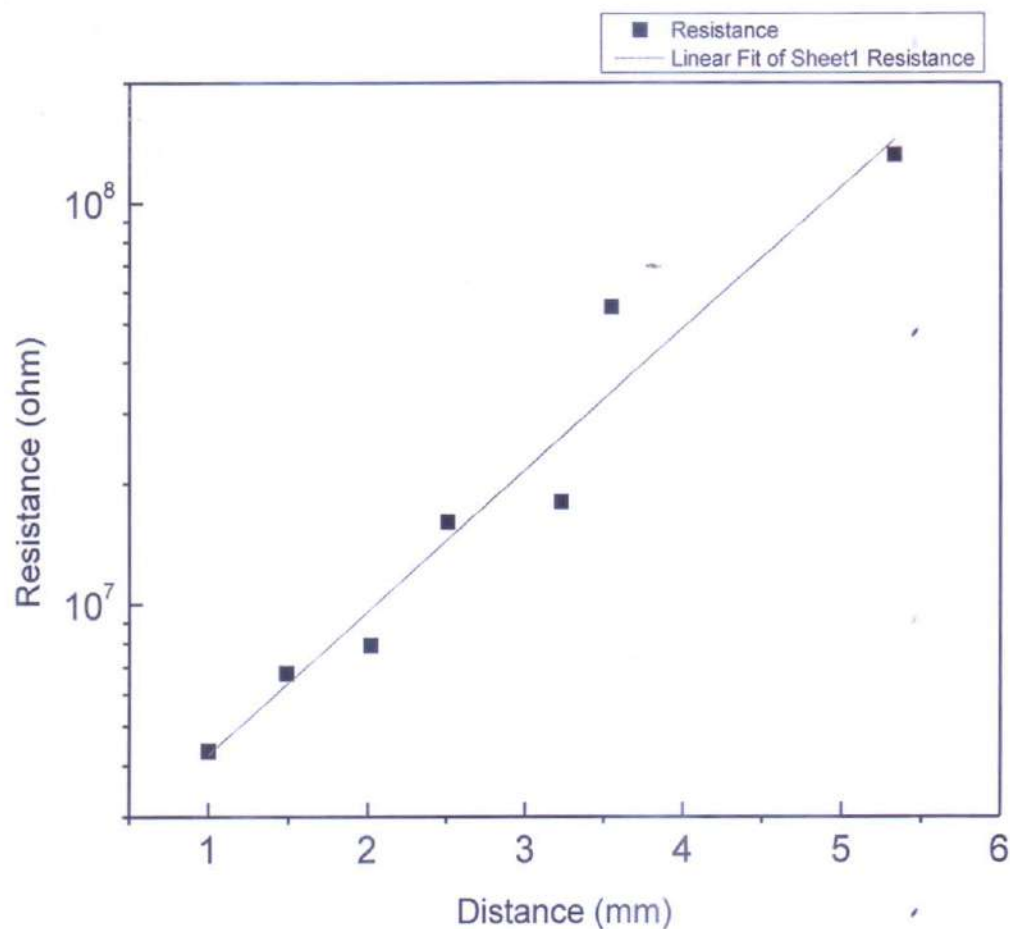


Figure 11. Graph for distances vs resistance plotting.

**RESULT AND DISCUSSION:** we know that resistance is proportional to length (for active area is constant and resistivity is also same for each sample here). Our experiment also verifies that! So, we can say that the composite system acts as a conductor and obeys the Ohm's law in this separation. However we have noticed a malfunction in the I-V plotting for separation 3.23mm. The reason is that, there is a little bit more ZnSe component ratio in rGO-ZnSe composite sample; And ZnSe is actually semiconductor in nature. So we get a diodic effect in the junction for that particular.

- ***Determination of Schottky effect in the metal-semiconductor junction in top to bottom configuration by J-V graph using spin coating***

**EXPERIMENTAL PROCEDURE:** Here we have taken a Indium tin oxide (ITO) coated glass substrate which was coated with 2.5mm celotape film and then was cleaned through ultrasonic treatment sequentially in de-ionized water, acetone and 2-propanol for 15 min each. Now we make a composition of 15% Nitric acid and Hydrochloric acid in molar ratio 1:3 .then the substrate is deeped in this 15% Aqua regia for 20 minutes to clean the ITO coating from the surface of glass plate, though there is still the coating of ITO in the beneath of celotape. Now we have removed the celotape and again have cleaned the whole substrate with acetone, 2-propanol and distilled water. Taking a digital multimeter we have also checked to be assured whether there is still remaining the layer of ITO where the celotape film was coated. Now it is ready for spin coating of rGO-ZnSe onto the substrate for 30 seconds with 1500 rpm in a spin coater. The fabricated active layer was annealed at 150 °C for 10 min in a silicone oil bath. Finally, an Al electrode was deposited onto the active layer by thermal evaporation through a shadow mask under vacuum pressure of  $5 \times 10^{-6}$  mbar. The substrate must be taken inside of a vacuum flask to avoid oxidization. Thus we have made a top to bottom electrode configuration.

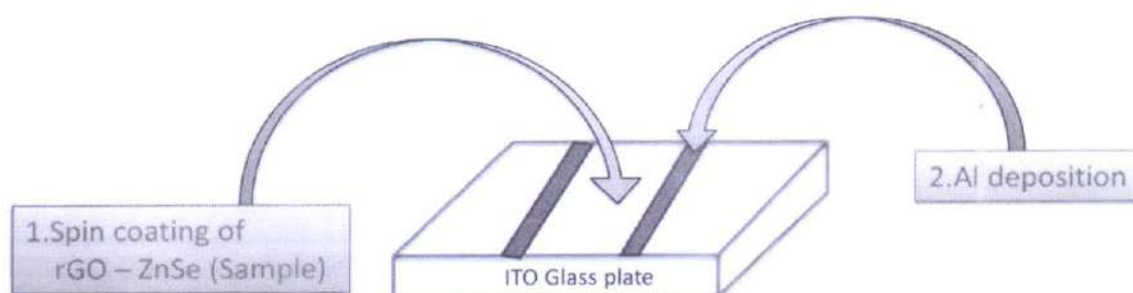


Figure 12. Diagram of spin coating on ITO glass plate

**OBSERVATION:** We have measured the I-V characteristics of this composite substrate in Source meter unit (SMU) with bias voltage -1 to +1 v. WE have attached the negative end of crocodile clip with Al and the positive end with ITO layer to complete the circuit. The corresponding graph will be discussed later.

**RESULT AND DISCUSSION:** I-V measurements are mainly used to check the charge transport behavior in organic semiconductor thin film. The above graph is shown in double log scale and shows two different slope which indicates different charge transport phenomena. The I-V plot shows two different slopes, indicating different charge transport mechanisms at different bias voltages. We could fit individual regions by  $I \propto V^m$  power law. In the region I where the applied bias is low, the slope is nearly 1, implying that it is followed by Ohm's law. In this region, charge transport is due to thermally generated carriers.



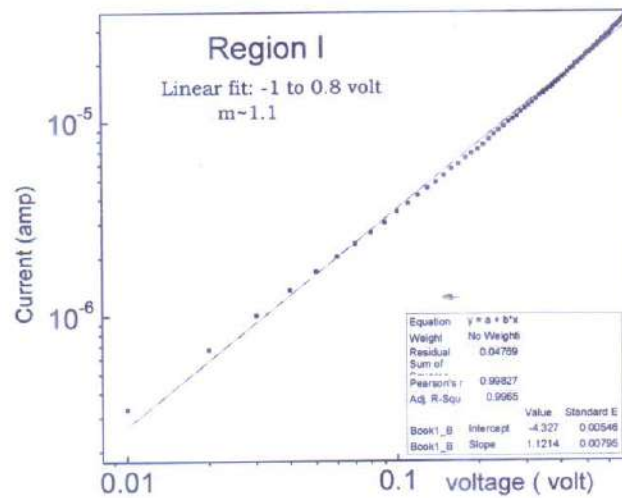


Figure 13. I vs V plotting for Region I.

Whereas in region II, i.e. for high voltage the slope is near about 3, implying there is more injected charge carriers than thermally generated carriers. i.e., we have observed Schottky effect in this region for top to bottom metal semiconductor junction configuration. This region is called space charge limited current conduction (SCLC region).

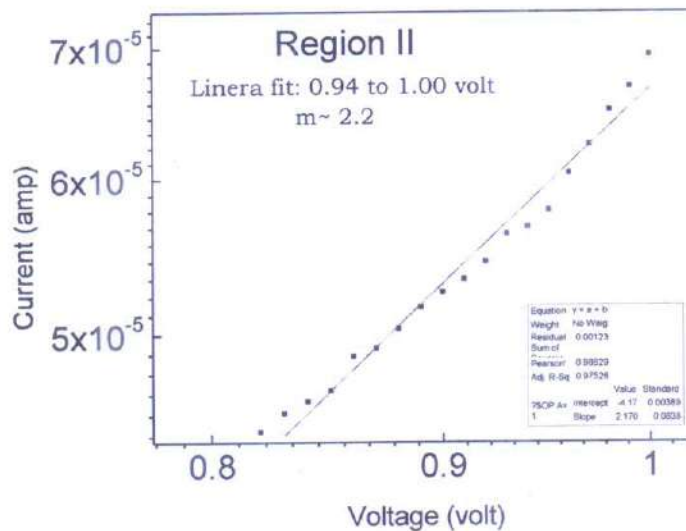


Figure 14. I vs V plotting for Region II.

If I inset both the two region in one graph and show the actual graph from where I zoomed out two region then it will be as given below.

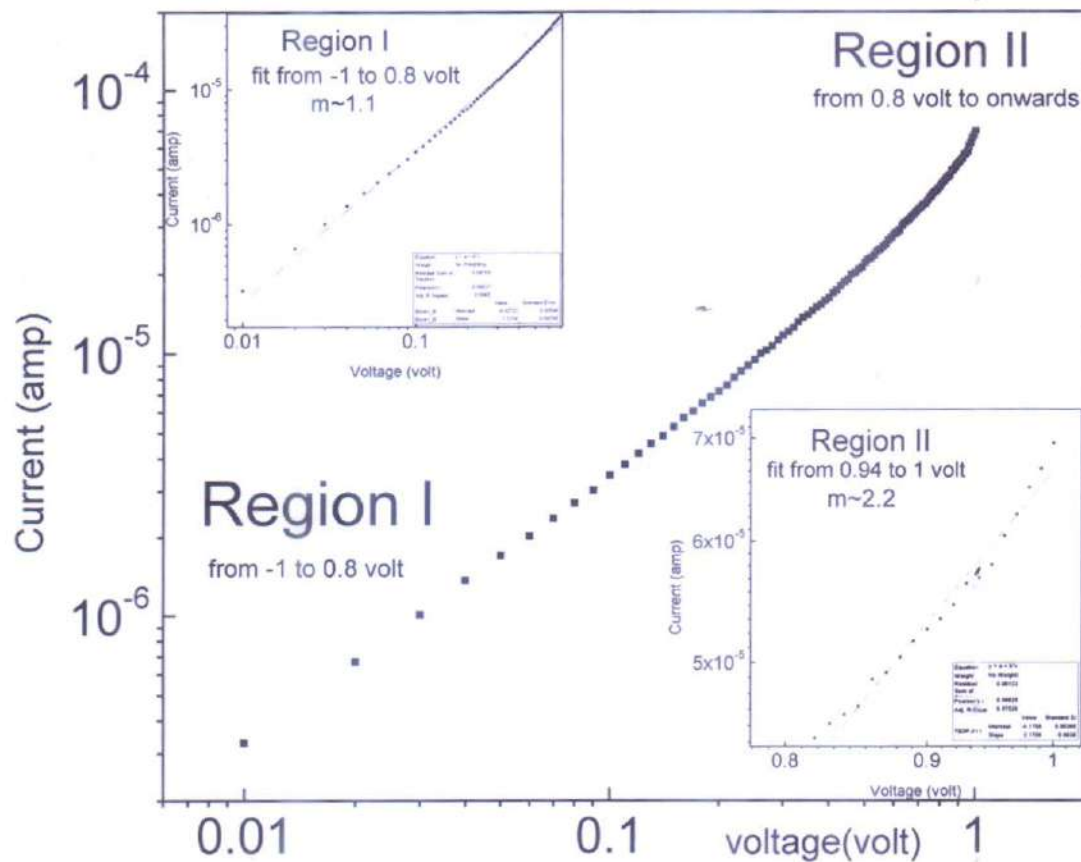


Figure 15. Current – voltage relationship for both regions in one diagram.

Actually, if I give more bias voltage which would be more than 1 volt, say approx. 2 volt, then it will be more and more prominent to show the schottky behavior in the second region where ohmic condition is not satisfied (i.e., slope is not equal to 1 throughout the second region). The transition between ohmic and non-ohmic region is called trap-filled limited conduction (TFL) and after that, SCLC region is observed (In this time conduction is followed by Child's law where current is proportional to the square of the applied bias).

#### ACKNOWLEDGEMENTS:

Foremost, I would like to express my sincere gratitude to my advisor Dr. Debamalya Banerjee for his continuous support to this project, for his patience, motivation, enthusiasm and immense knowledge. His guidance helped me in all the time of research and writing of this paper.

Beside of my advisor, I would like to thank the rest of DB Electrical Characterization research group, his phd students named Sudipta Khamrui, Abdullah Bin Rahaman, Atri Sarkar for their encouragement and helping me to learn the experimental techniques in a insightful manner. They helped me and supported me all the time to work. I would not forget to remember their name for their encouragement and moreover for the timely support and guidance till the completion of my



project work. I am thankful to and fortunate enough to get constant support from the whole DB research group in the Dept. of Physics in IIT Kharagpur.

I would also pay my gratitude to our H.O.D. Dr. Malay Purkait for giving me the permission to go to IIT-KGP and constantly helping me to access the project work. I am also grateful to our respected professor Dr. Debabrata Das for giving me his kind advice for how I can spend time to do my project work within my current B.Sc. course. Thanks also have to be given to Dr. Sourav Chatterjee, Dr. Amal Sarkar without whom I can't express how to represent any project/ internship report in front of viewers'.

I am also thankful my parents for their all time economic as well as mental support during the whole time when I have to stay in IIT-KGP accommodation block. I am also thankful to my friends for all time encouragement.

## REFERENCES:

- [1] Atri Sarkar et al 2018 Temperature dependent charge transport studies across thermodynamic glass transition in P3HT:PCBM bulk heterojunction: insight from  $J - V$  and impedance spectroscopy, *J. Phys. D: Appl. Phys.* 51 095602
- [2] Abdullah bin rahman; Sarkar, A.; Pal, T.; et al 2019 Observation of different charge transport processes and origin of magnetism in rGO and rGO-ZnSe composite, *J. Phys. Chem. C* 2019, 123, 15441-15450
- [3] Thin film, evaporation, Gauges, Thermal evaporation Google Wikipedia
- [4] Advanced Deposition Techniques for Thin Film and Coating ;chapter 8, intechopen.com
- [5] Stefan Cannon Lofgran, *Brigham Young University*—Idaho April 2013: Thin film deposition & Vacuum Technology, Vacuum procedure 26-28
- [6] John F. O'Hanlon. A User's Guide to Vacuum Technology. John Wiley & Sons, Inc., 3rd edition. Rotary vane pump and rotary piston pump 183-187, Pumping mechanism 217, Diffusion pump 366-369.
- [7] D.M. Mattox., Handbook of Physical Vapor Deposition (PVD) processing .William Andrew Publishing/Noyes, 1st edition, 1998.
- [8] Dr. Walter Umrath. Fundamentals of vacuum technology. Technical report, Oerlikon Leybold Vacuum, 2007.
- [9] Thermal evaporation- an overview | ScienceDirect Topics
- [10] Monica Katiyar, TEQIP IIT Kanpur, Thin film deposition lec.

***Android Based Smart Body-Temperature Monitoring and Recording System***

*A project report submitted to Ramakrishna Mission Residential College  
(Autonomous) for the partial fulfilment of award of the degree of*

**Bachelor of Science (Honours)**

Submitted by

**Arunabha Mondal**

**Subrata Maiti**

Roll- PHUG/113/17

and

Roll- PHUG/218/17

(Reg. No.: A03-1112-0113-17)

(Reg. No.: A03-1112-0218-17)



**Department of Physics**

**Ramakrishna Mission Residential College (Autonomous)**

**University of Calcutta**





**Ramakrishna Mission Residential College (Autonomous)**

**Vivekananda Centre for Research**

**Ramakrishna Mission Ashrama**

(A Branch Centre of Ramakrishna Mission, Belur Math, Howrah-711202)

**Narendrapur, Kolkata - 700 103, West Bengal, India**

A Scientific Industrial Research Organisation, Recognised by DST, Govt. of India

College with Potential for Excellence (CPE), Re-accredited by NAAC - 'A' (CGPA 3.56 out of 4)

---

## **DEPARTMENT OF PHYSICS**

### **Certificate**

This is to certify that Subrata Maiti, a student of B.Sc has successfully completed the project of UG curriculum entitled "Android Based Smart Body-Temperature Monitoring and Recording System" in the period from January to May, 2020.

*Malay Purkait*

.....  
30.06.2020.

**Signature Of HOD**

**Dept. of Physics**

**Dr. Malay Purkait**

Associate Prof. & Head

Department of Physics

Ramakrishna Mission Residential College

(Autonomous)

Narendrapur, Kolkata-700 103. (W.B.)

---

PHONES : 24772201(3lines), 24772205 FAX : 033-24773597 EMAIL : rkmcnpur@vsnl.com

WEBSITE : [www.rkmcnarendrapur.org](http://www.rkmcnarendrapur.org)

Mr. Tanmay Biswas

Assistant Professor

Ramakrishna Mission Residential  
College (Autonomous)  
Narendrapur, Kolkata-700103

## CERTIFICATE OF APPROVAL

Date: 1 July, 2020

This is to certify that the project report entitled "Android Based Smart Body-Temperature Monitoring and Recording System" has been done under my supervision at the Department of Physics, Ramakrishna Mission Residential College (Autonomous). I also endorse that this work submitted by Subrata Maiti (Reg. No: A03-1112-0218-17) is original and has not been submitted to any other University for the award of any Degree or Diploma. I therefore, recommend the project work for the award of **Bachelor of Science (Honours) in Physics**.



(Mr.

Tanmay

Biswas)



## ACKNOWLEDGEMENT

*The successful completion of the project would not be possible without the help and support of the following people.*

*We would like to take the opportunity to thank and express our gratitude to our project supervisor Mr. Tanmay Biswas (Assistant Professor, Department of Electronics). He did support us at every stage of the project. Every time we would come up with a new idea or modification to the existing project, he would patiently listen and correct our approach and most importantly support our idea.*

*We would also like to thank The Department of Physics, Ramakrishna Mission Residential College (Autonomous) in particular and the college in general for providing us the platform to create and present a project.*

*We would like to thank all the teachers of The Department of Physics whose simplified explanation and continued support in academics made it possible for us to understand the subjects properly and focus on the applicability of the subjects.*

*Last but not the least, we would take the privilege to thank our parents and both our sisters and all our friends for their valuable inputs.*

*We hope that we can build upon the experience and knowledge gathered during the development of this project and make a valuable contribution towards our College.*

*Arunabha Mondal*

Arunabha Mondal

*Subrata Maiti*

Subrata Maiti

## ABSTRACT

*The spirit behind this project was to address the challenges posed to educational institution reopening after lifting of lockdown situation imposed due to the CoVID-19 pandemic. Such institutions can be opened only after assurance of regular and thorough check-up of CoVID symptoms like high body-temperature. But the facilities available nowadays mostly involve human participation like use of hand-held temperature guns, etc. In this era of automation, our aim was to build a device with requisite sensors installed on an Arduino platform, whose working can be controlled by an Android. Thus refraining human contact, this device will measure the body temperature of the student and record it.*

*Keywords- Arduino Uno, sensors, actuators, Bluetooth module, microcontroller, MLX90614 sensor, HCSR04 sensor, mobile app.*



## ACKNOWLEDGEMENT

*The successful completion of the project would not be possible without the help and support of the following people.*

*We would like to take the opportunity to thank and express our gratitude to our project supervisor Mr. Tanmay Biswas (Assistant Professor, Department of Electronics). He did support us at every stage of the project. Every time we would come up with a new idea or modification to the existing project, he would patiently listen and correct our approach and most importantly support our idea.*

*We would also like to thank The Department of Physics, Ramakrishna Mission Residential College (Autonomous) in particular and the college in general for providing us the platform to create and present a project.*

*We would like to thank all the teachers of The Department of Physics whose simplified explanation and continued support in academics made it possible for us to understand the subjects properly and focus on the applicability of the subjects.*

*Last but not the least, we would take the privilege to thank our parents and both our sisters and all our friends for their valuable inputs.*

*We hope that we can build upon the experience and knowledge gathered during the development of this project and make a valuable contribution towards our College.*

# CONTENTS

|                                                              | Page No. |
|--------------------------------------------------------------|----------|
| 1. Introduction                                              | 1        |
| 1.1 Using Arduino Uno as the Programmable Automaton          | 1        |
| 1.1.1 Architecture of the Uno board                          | 2        |
| 1.2 Prototype Requirements                                   | 3        |
| 1.3 Components                                               | 3        |
| 1.3.1 Sensors and Actuators                                  | 3        |
| 1.3.2 Streaming real-time data                               | 4        |
| 1.3.3 Communication                                          | 5        |
| 1.3.4 Mobile Application                                     | 6        |
| 2. Objectives                                                | 6        |
| 2.1 Flowchart Diagram representation of the Objective        | 7        |
| 3. Model Classroom for the Project                           | 8        |
| 4. Methodology                                               | 8        |
| 4.1 Electronic Design                                        | 8        |
| 4.2 Programming on Arduino IDE                               | 9        |
| 4.3 Receiving and recording the data from Arduino into Excel | 9        |
| 4.4 Creating the Mobile App to control from our mobiles      | 10       |
| 5. Budget                                                    | 11       |
| 6. Expected Result                                           | 11       |
| 7. Applications                                              | 12       |
| 8. Conclusion                                                | 13       |
| 9. Reference                                                 | 14       |



## 1. INTRODUCTION

The year 2020 had been sadly shadowed by the CoVID-19 pandemic. Till now no vaccine has been discovered. Hence Governments and health organizations are coming together to find alternative solutions. Throughout the world, all countries are mostly abiding by the standard regulations set by the World Health Organization to fight this pandemic. The most common precautions used are Social Distancing, testing, hand-sanitizing and increased awareness among individuals.

Even after the Lockdown, which is prevalent in our country, is lifted, regular monitoring of symptoms (eg. Body-temperature) is to be carried out. Say for example, automatic monitoring and registering of body temperature of students attending an educational institute, automatic measurement of temperature of guests visiting relatives, automatic monitoring of customers visiting banks, malls, boarding public transport, etc.

In our project, we have developed a device of *Automated Monitoring and Registering Body-Temperature of Individuals* attending any public infrastructure through a *Unique ID* using an Arduino board and sensors and a Mobile App.

### 1.1 Using Arduino Uno as the Programmable Automaton

The boost in DIY stuff among people of various professions, who know little or nothing about electronics or coding, be it engineers, artists, hobbyists, students, etc. lead to the birth of Arduino, an open-source software and hardware company [1]. Several Arduino boards, with microcontroller chips installed on them, are available which can be used to create DIY projects, home-automation and large scale automatic control systems [2],[3]. Among the several Arduino boards available, Arduino Uno is the most popular because of its easy availability, low cost, sufficiently varied availability of Digital I/O pins and Analog Input pins, sufficient Flash Memory, SRAM and EEPROM for general to high-end purposes [4].

Hence, keeping in mind all these facilities, we will be using an Arduino Uno board as the local controller of our Project.

### 1.1.1 Architecture of the Arduino Uno board

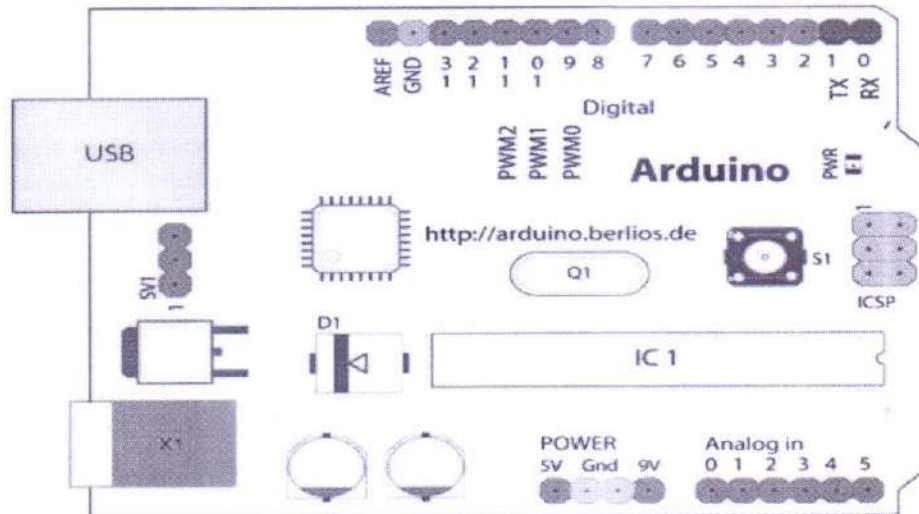


**Fig 1.1: Diagram of the Arduino Uno board [5].**

The basic components and features of the Arduino Uno board are discussed as follows:

- **Microcontroller ATmega328P**- This is a single-chip microcontroller created by Atmel. It combines 23 general purpose I/O lines, 32 general purpose working registers, three flexible timer/counters with compare modes, internal and external interrupts, serial programmable USART, a byte-oriented 2-wire serial interface, SPI serial port, 6-channel 10-bit A/D converter (8-channels in TQFP and QFN/MLF packages), programmable watchdog timer with internal oscillator, and five software selectable power saving modes. It is the brain of the Uno development platform [6]. It is designated as IC 1 in Fig 1.1.
- **Pins**- There are 14 Digital I/O pins (of which 6 provide PWM output). They are labelled from 0-13 designated by green coloured pins on the top of Fig 1.1.  
There are 6 Analog Input pins marked from 0-5 in blue-colour in the bottom-right of Fig 1.1.
- **Flash Memory**- 32 KB-ISP flash memory (ATmega328P) with read-while-write capabilities, of which 0.5 kb is used by the bootloader.
- **SRAM**- 2 kb (ATmega328P).
- **EEPROM**- 1 kb (ATmega328P).
- **Operating Voltage**- 5V
- **Input Voltage (recommended)**- 7-12V
- **Input Voltage (limit)**- 6-20V
- **DC Current per I/O Pin**- 20 milliAmperes



- DC Current for 3.3V Pin- 50 milliAmperes
- Clock Speed- 16 MHz.
- Length- 68.6 mm
- Width- 53.4 mm
- Weight- 25g.

## 1.2 Prototype Requirements

The main soul of our Prototype is the *Arduino Uno board* which will act as the local controller of our automation system. Two sensors are required namely *MLX90614* and *HCSR04* which are non-contact IR temperature sensor and ultrasonic distance sensor respectively. A *Bluetooth module HC-05* is used for communication between the mobile phone and the Arduino Uno board. A *16X2 LCD Display* is used as an actuator to interact with the user along with a *potentiometer* to control the contrast of the display of the LCD.

## 1.3 Components

### 1.3.1 Sensors and Actuators

- *MLX90614*- This is an infrared thermometer for non-contact temperature measurements built by Melexis Corporation [7].

#### Features-

- Temperature Range: -40 to 125°C for sensor temperature and -70 to 380°C for object temperature.
- Accuracy: 0.5°C accuracy over a wide range of temperature.
- SMBus compatible digital interface for fast temperature readings and building sensor networks.
- Customizable PWM output for continuous reading.

- *HCSR04*- This is a non-contact ultrasonic distance measurement sensor [8].

#### Features-

- Working voltage: 5V
- Working current: 15 milliAmperes
- Working frequency: 40 Hz

- Measurement Range: 2cm to 4m
- Measurement accuracy: 3mm
- Trigger Input Signal: 10Us TTL pulse
- Echo Output Signal: Input TTL lever signal and the range in proportion.

➤ 16X2 LCD Display Module- This is an Actuator. LCD stands for Liquid Crystal Display. It has 16 columns and 2 rows and can display a total of 32 characters [9].

#### Features-

- Pins: A total of 16 Pins
- Operating voltage: 4.7V to 5.3V
- Current Consumption: 1 milliAmpere without backlight

### 1.3.2 Streaming real-time data

Several microcontrollers are available that give various data as output. This output can be recorded and visualized in an Excel workbook. To do so, software like PLX-DAQ by Parallax Inc [10], add-ins like Data Streamer Add-In for MS Excel is available. These help to import data from the connected device to an Excel workbook. We will be using MS Data Streamer Add-In since Microsoft is the most popular OS in India.

Steps to be followed to install MS Data Streamer: [11]

- We can download Microsoft Data Streamer from the link below-  
<https://www.microsoft.com/en-us/download/details.aspx?id=56976>
- It is installed by following standard installation process for Windows.
- Next we open MS Excel.
- We go to File Menu and then click on "Excel Options".
- On the left, there will be an option called "Add-Ins". We click on it.
- Under Manage, we click on the drop-down button and select "COM Add-Ins". We click on "Go".
- The COM Add-Ins dialog box will appear with the list of available Add-Ins installed on our PC. We select the "Microsoft Data Streamer for Excel" and then finally click on "OK".

A physical connection has been set up between the MS Excel and Arduino Uno. MS Excel is now ready to store data obtained from the board.



### 1.3.3 Communication

#### ➤ Bluetooth Communication

Bluetooth enables the transmission of data and voice between different devices through a radiofrequency link in the 2.4 GHz ISM band [12]. All Bluetooth devices have a unique address of 48 bits and a device name that allows the identification of each other. Devices that incorporate this protocol can communicate with one another when within its reach. The communications are by radiofrequency so that the devices do not have to be aligned and can even be in separate rooms if the transmission power is sufficient. These devices are classified as Class 1, Class 2 and Class 3 depending on the transmission power. There are two types of Bluetooth modules compatible with Arduino: HC-05 and HC-06. Both are of Class 2 type and hence their range is 10 metres [13]. For several governing factors we will be using the HC-05 module.

#### ➤ HC-05 Bluetooth Module [14]-

##### Main Features-

- Configurable as Slave and as Master
- Radio Chip: CSR BC417143
- Frequency: 2.4 GHz ISM band
- Modulation: GFSK (Gaussian Frequency Shift Keying)
- Built-in PCB antenna
- Emission Power:  $\leq 4\text{dBm}$  (Class 2)
- Range: 10 metres
- Speed: Asynchronous- 2.1 Mbps/160 kbps; Synchronous- 1Mbps/1 Mbps
- Security: Authentication and Encryption
- Profiles: Serial port Bluetooth
- Current consumption: 50 milliAmperes
- Supply voltage: 3.6V-6V
- Operation temperature: 20°C-75°C

### **1.3.4 Mobile Application**

Mobile phones have become an existential need of today's society. Every pocket has a mobile phone and every mobile phone has several apps to perform various tasks. Our project is based on automation where we need some medium to receive the input from the user that will trigger the process. What could be better than a mobile app as mobile apps are available to almost everyone? Earlier creating mobile apps was upon Software developers who knew how to code. But with the increase in demand of creating more and more apps, several software have been developed that allow users to create Mobile-based applications without knowing to code.

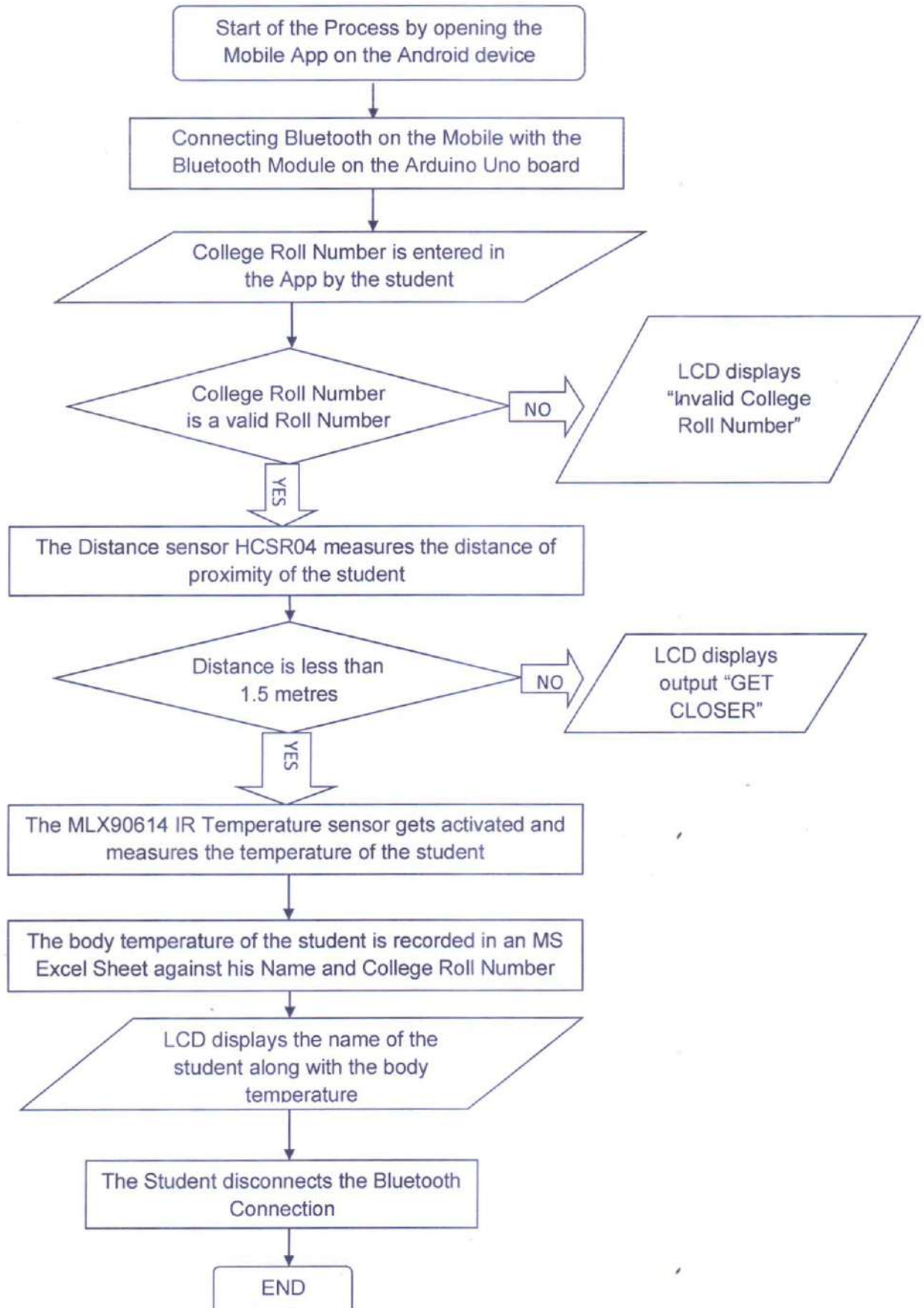
For our purpose too, we will be using such software that allows us to create an app. We will be using the Web application MIT App Inventor, originally provided by Google and now maintained by the Massachusetts Institute of Technology (MIT). It is free and open-source and allows creation of apps for Android and IOS.

## **2. OBJECTIVE**

Our objective while building this prototype was to build a device which will be installed at the door of our classroom. All students will have to install an official application for Android (to be created) on their Mobile phones (available at Google Play Store). They will then have to connect their phone with the device through Bluetooth. During an ongoing academic semester, the College Roll Number of each student is unique. The student then enters his unique Roll Number in the app and it automatically triggers the device to measure the body-temperature of the student and records this data on a Computer in MS Excel. In doing so, the attendance of the student too is recorded and hence teachers need not devote time in Roll-calling. Thus we will be able to upgrade our smart-class to fight CoVID-19.



### 2.1 Flowchart Diagram representation of the Objective:



### 3. MODEL CLASSROOM FOR THE PROJECT

As our model classroom, we will take our class- 3<sup>rd</sup> year Physics Honours classroom in the Department of Physics (Room Number- 2.2) on the 1<sup>st</sup> floor of Ramakrishna Mission Residential College (Autonomous) Main College Building. Our class consists of 26 students, each with a unique College Roll Number.

### 4. METHODOLOGY

#### 4.1 Electronic Design

The Schematic Design of our automation device is given below:

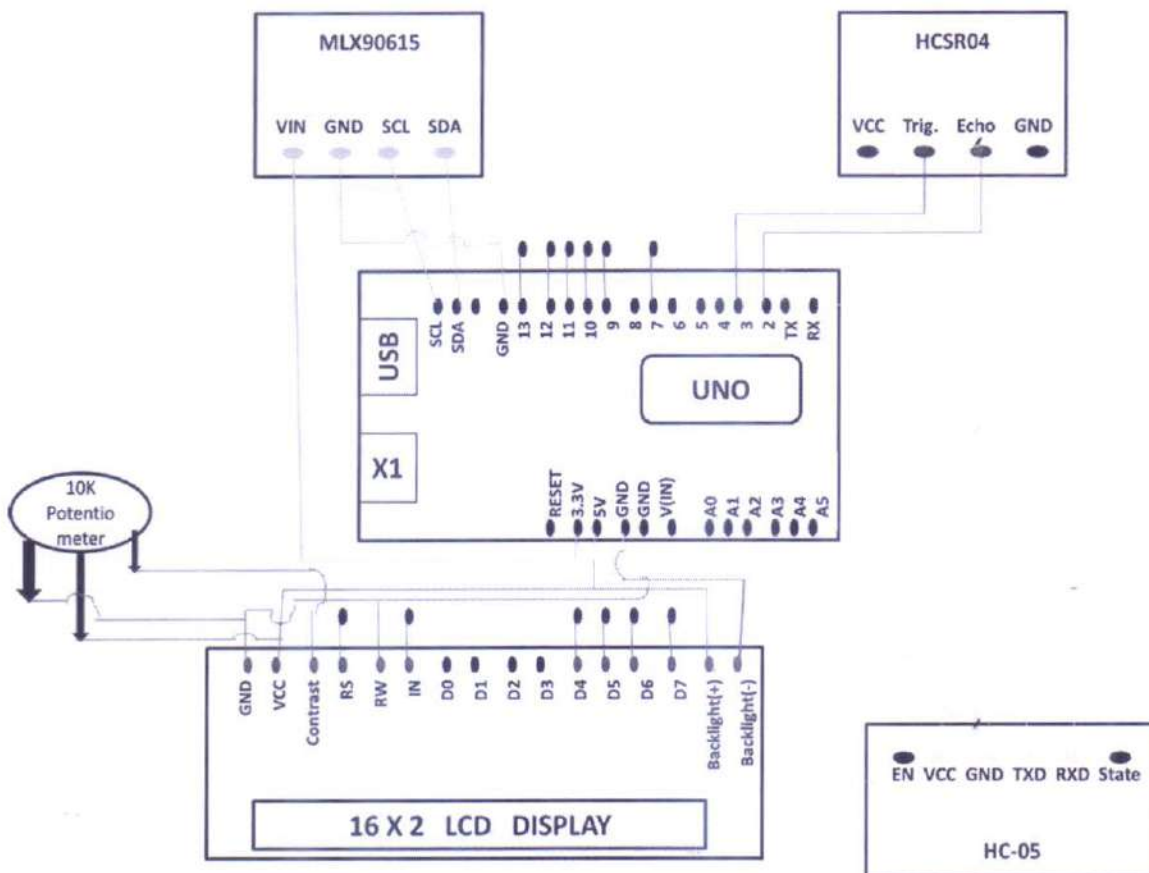


**Fig. 4.1:** Schematic Diagram of the proposed device. Orange lines represent wires connecting MLX90614 to Arduino Uno. Blue lines represent wires connecting HCSR04 to Arduino Uno. Yellow lines represent wires connecting HC-05 module to Arduino Uno. Green lines represent wires connecting LCD to Arduino Uno and potentiometer to LCD display.



## 4.2 Programming in Arduino IDE

The Arduino Integrated Development Environment (IDE) is a cross-platform application (for Windows, macOS, Linux) and is open-source that is written in functions from C and C++. It will be used by us to write and upload the program onto the Arduino Uno board. The uploaded program, called sketch, will instruct the ATmega328P microcontroller chip to perform the task desired by us.

## 4.3 Receiving and recording the data obtained from Arduino into Excel [15]

The sensor installed on the device will record the temperature of the student. Now the data needs to be stored on MS Excel. Note that the following steps are in accordance with Microsoft 365.

If Data Streamer has been installed, the Excel ribbon will contain a new "Data-Streamer" Tab.

- Step 1:- We first click on the "Data-Streamer". This contains all the primary controls for the add-in.
- Step 2:- We connect a Data Source (in our case the Data Source is the Arduino Uno). We then click on "Connect a Device" and select Arduino Uno in the sub-ribbon that appears.
- Step 3:- We go to the "Advanced" option. In the prompt that appears, we go to "Settings".
- Step 4:- Under Settings, we change the 'Number of Data Rows' from the 'default 15' to 'the total number of students in the Class i.e., 26 in our sample classroom'.
- Step 5:- We then change the 'Number of data channels' from the 'default 20' to the number of different types of data columns we will be requiring.
- Step 6:- We then give value to the 'Data delay (ms)' as 60000 ms (i.e., 1 min) so that each student registers only 1 data on the Excel sheet and then has sufficient time to disconnect the Bluetooth connection with the Bluetooth module.
- Step 7:- We select 'Newest last' option for 'Data orientation'. With this, all setting up has been done and now it's time to stream data from the data source.
- Step 8:- Once we are ready to receive data, we click on "Start Data" option under the Excel ribbon. The data received will be visible in the below format-

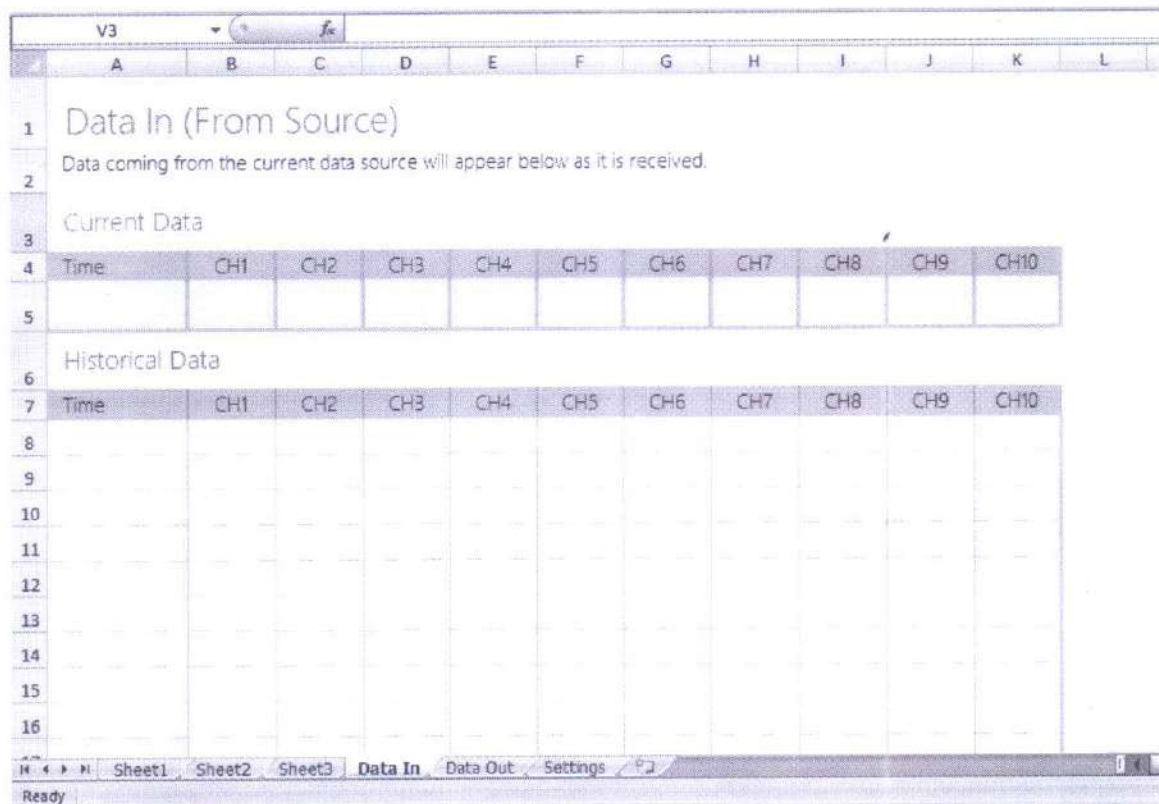


**Fig. 4.2: Screen view of an Excel workbook ready to record data [16].**

#### 4.4 Creation of the Mobile Application [17]

The app is needed to relay the input trigger from the student. The app will have a field where the student needs to enter his College Roll Number. On entering this data, the app will recognize the student, measure his temperature and store it against his name in MS Excel.

- To create the app, first we go to <http://beta.appinventor.mit.edu/>. We will see a blank projects page (if visiting for the first time) or the created projects list (if already some projects have been created).
- We then click on “New” on the top-left and in the dialog box, enter the name of the project. Finally clicking “OK”.
- The “Designer” page opens where we will have to design the look of our App by using the default elements available.
- Next we go to the “Blocks Editor”, where we have to specify the flow of control of the app.
- In this way, the app will be created. After all this is done, we can publish the app on Google Play Store.



## 5. BUDGET

The following is the budget overview for building this prototype:

| COMPONENT                   | PRICE | NUMBER OF UNITS  | ABOUT VENDOR        |
|-----------------------------|-------|------------------|---------------------|
| Arduino Uno                 | ₹380  | 1                | Shop in Kolkata     |
| MLX90614 Sensor             | ₹3800 | 1                | Robokits.co.in      |
| HCSR04 Sensor               | ₹99   | 1                | Robu.in             |
| HC-05 Bluetooth Module      | ₹510  | 1                | Amazon.in           |
| 16X2 LCD Display            | ₹105  | 1                | ElectronicsComp.com |
| Potentiometer               | ₹9    | 1                | ElectronicsComp.com |
| Jumper Wires                | ₹50   | 25 (₹2 per unit) | Shop in Kolkata     |
| Total Hardware Cost= ₹ 4953 |       |                  |                     |

Time engaged to write the code on Arduino IDE (approximately) = 8-10 hours

Time engaged to create the Mobile App (approximately) = 18-20 hours

Now, depending on working hour price for developing the software and the Mobile App, the Total Prototype cost will increase.

## 6. EXPECTED RESULTS

The datasheet to be obtained on MS Excel can be expected to be something like the figure below:

|        |                                                                               |        |        |         |          |          |     |     |     |     |      |   |
|--------|-------------------------------------------------------------------------------|--------|--------|---------|----------|----------|-----|-----|-----|-----|------|---|
| R3     |                                                                               | fx     |        |         |          |          |     |     |     |     |      |   |
|        | A                                                                             | B      | C      | D       | E        | F        | G   | H   | I   | J   | K    | L |
| 1      | Data In (From Source)                                                         |        |        |         |          |          |     |     |     |     |      |   |
| 2      | Data coming from the current data source will appear below as it is received. |        |        |         |          |          |     |     |     |     |      |   |
| 3      | Current Data                                                                  |        |        |         |          |          |     |     |     |     |      |   |
| 4      | Time                                                                          | CH1    | CH2    | CH3     | CH4      | CH5      | CH6 | CH7 | CH8 | CH9 | CH10 |   |
| 5      | 10:31:12:57                                                                   | 98.7   |        |         |          |          |     |     |     |     |      |   |
| 6      | Historical Data                                                               |        |        |         |          |          |     |     |     |     |      |   |
| 7      | Time                                                                          | CH1    | CH2    | CH3     | CH4      | CH5      | CH6 | CH7 | CH8 | CH9 | CH10 |   |
| 8      | 10:29:44:24                                                                   | 97.8   |        |         |          |          |     |     |     |     |      |   |
| 9      | 10:30:10:15                                                                   | 98.9   |        |         |          |          |     |     |     |     |      |   |
| 10     | 10:31:12:57                                                                   | 98.7   |        |         |          |          |     |     |     |     |      |   |
| 11     |                                                                               |        |        |         |          |          |     |     |     |     |      |   |
| 12     |                                                                               |        |        |         |          |          |     |     |     |     |      |   |
| 13     |                                                                               |        |        |         |          |          |     |     |     |     |      |   |
| 14     |                                                                               |        |        |         |          |          |     |     |     |     |      |   |
| 15     |                                                                               |        |        |         |          |          |     |     |     |     |      |   |
| 16     |                                                                               |        |        |         |          |          |     |     |     |     |      |   |
| Sheet1 |                                                                               | Sheet2 | Sheet3 | Data In | Data Out | Settings |     |     |     |     |      |   |

**Fig. 6.1:** An Excel worksheet in 'Data In' mode showing that it has recorded 3 data received from the data source.

## 7. APPLICATIONS

The device has so much potential that it can be used in several sectors:

- With slight modifications in the Arduino sketch, it can be used at banks, malls, hospitals, private companies, etc., to keep a regular record of symptoms of the employees.
- The device can be installed at the entrance of our homes to know the body-temperature of guests.



## **8. CONCLUSION**

As aimed for in the objectives, we have been able to come up with the electronic design of our device. We have also explained the step-by-step process of installing the MS Excel Add-In. We have also given the synopsis of the program to be uploaded on the Arduino Uno board and the process of developing the Mobile application. Thus we have been able to present an overview of the idea and how to implement it in an actual environment, our objectives have been sufficed.

## 9. REFERENCE

- [1] Kaswan K.S., Singh S.P., Sagar S., "Role of Arduino in real world applications," International Journal of Scientific and Technology Research Volume 9, ISSN 2277-8616, 2020.
- [2] Mallick B. And Patro A.K., "Heart rate monitoring system using fingertip through Arduino and processing software," International Journal of Science, Engineering and Technology Research, vol. 5, no. 1, pp. 82-89, 2016.
- [3] Rubio H., Soriano E. And Barber R., "A low cost lab monitoring system based on Arduino microcontroller and Android," Proceedings of ICEI 2015 Conference, pp. 8014-8022, 2015.
- [4] Louis L., "Working principle of Arduino and using it as a tool for study and research," International Journal of Control, Automation, Communication and Systems, vol. 1, no. 2, pp. 21-29, 2016.
- [5] <https://www.arduino.cc/en/Guide/Board?from=Tutorial.ArduinoBoard> [Accessed 22<sup>nd</sup> Jun, 2020]
- [6] <https://en.m.wikipedia.org/wiki/ATmega328> [Accessed 23<sup>rd</sup> Jun, 2020]
- [7] <https://www.melexis.com/en/product/MLX90614/Digital-Plug-Play-Infrared-Thermometer-TO-Can> [Accessed 25<sup>th</sup> Jun, 2020]
- [8] Zhmud V A, Kondratiev N O, Kuznetsov K A, Trubin V G and Dimitrov L V, "Application of ultrasonic sensor for measuring distances in Robotics," International Conference Information Technologies in Business and Industry, doi: 10.1088/1742-6596/1015/3/032189 (2018).
- [9] <https://components101.com/16x2-lcd-pinout-datasheet> [Accessed 25<sup>th</sup> Jun, 2020].
- [10] [www.parallax.com](http://www.parallax.com) [Accessed 1<sup>st</sup> Jul, 2020].
- [11] <https://support.microsoft.com/en-us/office/enable-the-data-streamer-add-in-70052b28-3b00-41e7-8ab6-8a9f142dffe8> [Accessed 25<sup>th</sup> Jun, 2020].
- [12] Jeong H J, Lim J, Hyun W S and Lee W J, "A remote lock system using Bluetooth communication," Innovative Mobile and Internet Services in Ubiquitous Computing, doi: 10.1109/IMIS.2014.63 (2014).
- [13] Herreros A.M., Sin S.T., "Home automation application based on Arduino controllable from mobile," 2017.



[14] <https://www.arduino.cc> [Accessed 25<sup>th</sup> Jun, 2020].

[15] <https://support.microsoft.com/en-us/office/navigating-the-ribbon-in-data-streamer-9c4cae5-5504-40e2-8015-8c9be5567476> [Accessed 1st Jul, 2020].

[16] A “Data In” workbook sheet of Microsoft Office Excel 2007.

[17] <https://appinventor.mit.edu/explore/start-first-time> [Accessed 28th Jun, 2020].

**A PROJECT REPORT ON  
"STUDY OF QUARKONIUM USING  
TWO DIFFERENT POTENTIAL  
MODELS"**

**Submitted by,  
ADITYA KUMAR MANDAL  
Dept. of Physics  
RKMRC, Narendrapur  
PHUG/117/17**

**Project Guide  
Dr. SOUMYA SADHUKHAN  
Assistant Professor  
RKMRC, Narendrapur**





**Ramakrishna Mission Residential College (Autonomous)**

**Vivekananda Centre for Research**

**Ramakrishna Mission Ashrama**

(A Branch Centre of Ramakrishna Mission, Belur Math, Howrah-711202)

**Narendrapur, Kolkata - 700 103, West Bengal, India**

A Scientific Industrial Research Organisation, Recognised by DST, Govt. of India

College with Potential for Excellence (CPE), Re-accredited by NAAC - 'A' (CGPA 3.56 out of 4)

---

## **DEPARTMENT OF PHYSICS**

### **Certificate**

This is to certify that Aditya Kumar Mandal, a student of B. Sc has successfully completed the project of UG curriculum entitled **"STUDY OF QUARKONIUM USING TWO DIFFERENT POTENTIAL MODELS"** in the period from January to May, 2020.

*Malay Purkait*  
.....  
30.06.2020

**Signature Of HOD**

**Dept. of Physics**

**Dr. Malay Purkait**

Associate Prof. & Head

Department of Physics

Ramakrishna Mission Residential College

(Autonomous)

Narendrapur, Kolkata-700 103, (W.B.)

# To Whom It May Concern,

## Certificate of Completion of the project

This is to certify that Aditya Kumar Mandal (Roll-PHUG/117/17) bearing the CU registration no. "A03-1122-0117-17", a student of Bsc final year (2020) has successfully completed his Bsc physics project on "Study Of Quarkonium Using Two Different Potential Models" under the guidance of Dr. Soumya Sadhukhan. He is a bonafide student of RKMRC physics dept. of the 2017-2020 batch.

Date: 20.06.2020

S. Sadhukhan

Sign of the guide



## ACKNOWLEDGEMENT

Successfully completion of any type of project requires help from a number of persons. I have also taken help from different people for the preparation of the report. I show my deep gratitude to all those helpful persons.

First of all, I convey my sincere gratitude to my project guide **Dr. Soumy Sadhukhan, Assistant Professor, RKMRC, Narendrapur**. Without his kind direction and proper guidance this study would have little success. In every phase of the project his supervision and guidance shaped this report to be completed perfectly.

I would like to thank **Dr. Malay Purkait, Head of Department of Physics, RKMRC, Narendrapur** as well as my college **RKMRC, Narendrapur** for giving me the opportunity.

Last but not least, I give my heart full thank to all of my friends who have helped me a lot to complete this project.

*Aditya Kumar Mandal*  
Signature of the student



## INDEX

|                                                                     |       |
|---------------------------------------------------------------------|-------|
| 1. INTRODUCTION                                                     | 1     |
| 2. AN ANALOGY BETWEEN HYDROGEN ATOM<br>POSITRONIUM AND QUARKONIUM   | 2-3   |
| 3. QUARK-ANTIQUARK POTENTIALS                                       | 4-5   |
| 4a. GENERAL THEORY OF SUPER SYMMETRY<br>QUANTUM MECHANICS (SUSY QM) | 5-8   |
| 4b. SUSY QM TREATMENT OF CORNELL<br>POTENTIAL                       | 8-10  |
| 5. SOLUTION OF ENERGY DEPENDENT<br>POTENTIAL MODEL                  | 10-12 |
| 6. CONCLUSION                                                       | 13    |
| 7. ACKNOWLEDGEMENT                                                  | 14    |
| 8. REFERENCES                                                       | 15    |



# **STUDY OF QUARKONIUM USING TWO DIFFERENT POTENTIAL MODELS**

## **1. INTRODUCTION:**

In particle physics, quarkonium is a flavorless particle whose constituents are a heavy quark and its own antiquark. Now quark and anti-quark have same amount of charge but of opposite type, which makes the quarkonium a neutral particle. Quarkonium is its own anti-particle, which is quite interesting. As the quarks are quite heavy, one can assume the motion of quarks in quarkonium to be non-relativistic, much like non-relativistic hydrogen atom. So in order to get the various properties of a quarkonium what we have to do is to model the quarkonium as a two particle system, namely the quark and its anti-quark, set up the corresponding non-relativistic Schrödinger equation and then solve it. An effective way to calculate energies, mass, is to formulate different potential models. In this technique, the potentials are chosen to be static. Various potential models were able to fit the data of energies of various excitation states of quarkonium with good accuracy. But still problems remain to justify the splitting of energy levels due to spin-spin interaction, decay rate from one quarkonium state to other state. Which makes the topic quite interesting, and still developing.

Here we are going to study two different potential model and their solution. At first we are going to study an analogy between quarkonium, positronium and hydrogen atom; and then we will discuss about the potentials; at the last two section we are going to solve the non-relativistic Schrödinger equation regarding these potentials.

## 2. ANALOGY BETWEEN HYDROGEN ATOM, POSITRONIUM, AND QUARKONIUM:

The simplest atomic bound-state is hydrogen atom, which is composed of a proton and an electron. The Time Independent Schrödinger Equation (TISE) in three dimension is given by,

$$\left(-\frac{\hbar^2}{2m}\nabla^2 - \frac{1}{4\pi\epsilon_0}\frac{e^2}{r}\right)\Psi(r) = E\Psi(r)$$

The eigenstates are characterized by the by the number of nodes  $N$  in the radial wave functions and the orbital angular momentum  $\ell$ . The principle quantum number is given by  $n = N + \ell + 1$ . The allowed energy levels are found to be

$$E_n = -\frac{\alpha^2 mc^2}{2n^2}.$$

Where  $\alpha$  is the electromagnetic coupling constant and  $m$  is the reduced mass of the system:  $m = \frac{M_p m_e}{M_p + m_e} \simeq m_e$ . The spin-orbit interaction and the spin-spin interaction split the degeneracy of the principle energy levels.

The energy states of positronium, the  $e^+e^-$  system, can be found in an analogous way to the above. The main differences are the reduced mass ( $m = m_e/2$ ) is only half the value of the hydrogen case and the spin-spin coupling is much larger than before. The stronger spin-spin coupling means that the positronium spectrum does not display the clear hierarchy of fine and hyperfine structure that we know from hydrogen atom. Thus for positronium the total spin  $\mathbf{S}$  and the total angular momentum  $\mathbf{J}$  as well as the principle quantum number  $n$  and the orbital angular momentum  $\mathbf{L}$  are the useful quantum number.  $\mathbf{S}$  can take on value 0 (singlet) and 1 (triplet), and  $\mathbf{J}$  obeys,  $|\mathbf{L} - \mathbf{S}| \leq \mathbf{J} \leq \mathbf{L} + \mathbf{S}$ . The notation  $n^{2S+1}L_J$  is commonly used.

Quarkonium, which is a system built up of strongly interacting quark-antiquark pairs (such as  $c\bar{c}$ ,  $b\bar{b}$ ) can be investigated in an analogous manner. Here the main difference is that the interaction between



electron and positron is purely Coulombic interaction (relatively long range), on the other hand the interaction between the quark and anti-quark is short range interaction (strong interaction).

- **Charmonium :**

Bound state of  $c$  and  $\bar{c}$ -quarks are called charmonium.  $c\bar{c}$  pairs are most easily produced in the decay of virtual photon generated in  $e^+e^-$  collisions

$$e^+ + e^- \rightarrow \gamma \rightarrow c\bar{c}.$$

Because of this intermediate virtual photon, only  $c\bar{c}$  states of similar quantum number to this virtual photon ( $J^P=1^-$ ) can be created in this way. The lowest state with such quantum number is the  $1^3S_1$ , which is called the  $J/\psi$  meson. It has spin 1 and mass  $3.097 \text{ GeV}/c^2$ .

Charmonium states have finite life time. Excited charmonium states, by the emission of photon, can decay into a lower energy states, just as in atomic physics. If one generates the excited charmonium state  $\psi$  ( $2^3S_1$ ), it primarily decays into the  $1^3P_J$  charmonium triplet system, which then further decay into the  $J/\psi$  state.

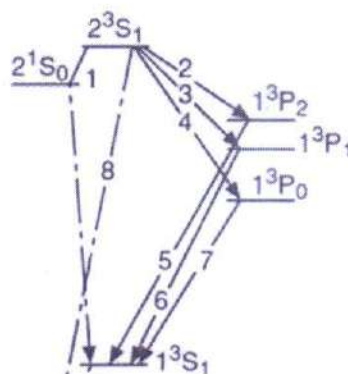


Fig 2.1: The photon spectrum in the decay of  $\psi$  ( $2^3S_1$ ).

### 3. QUARK-ANTIQUARK POTENTIALS:

If we compare the spectra of charmonium and positronium, we find that the states with  $n=1$  and  $n=2$  are very similarly arranged, if an overall scaling of about  $10^8$  eV is taken into account for charmonium.

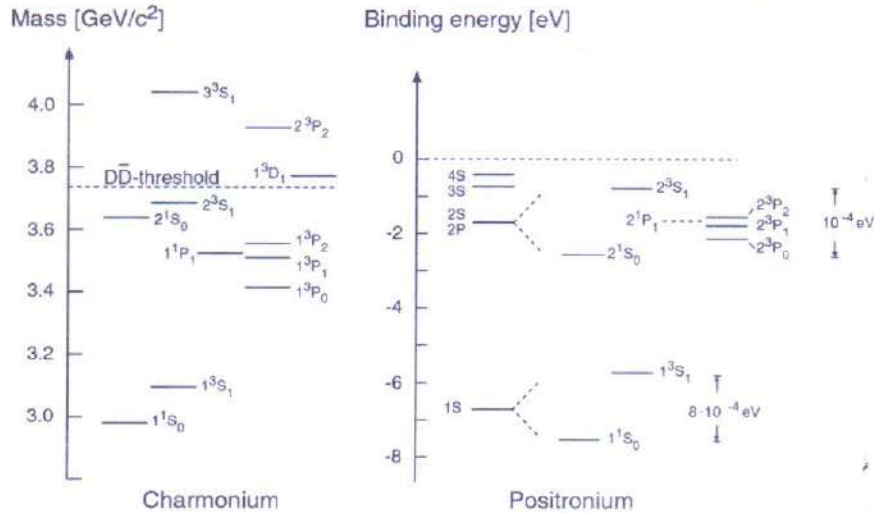


Fig 3.1: Comparison of energy levels between charmonium and positronium. (Source: B. Povh et al., Particles and Nuclei)

Since the potential determines the relative positions of different energy levels, it is clear that the potential of the strong interaction must be of Coulomb type (at least at very short distances, for  $n=1,2$ ), similar to the electromagnetic one. On the other hand since the quarks have not been experimentally observed, suggest that the potential cant not be of pure Coulomb form. It is plausible to postulate a potential which is of Coulomb type at short distance and grows linearly at greater separation thus leading to the confinement of quarks in hadrons. So the potential is given by,

$$V(r) = -\frac{B}{r} + Ar$$

Where  $A$  and  $B$  are parameters, whose values are determined from experimental results. This potential is called Cornell potential.



The Coulomb potential describes forces that decreases with distance. The integral of this force gives the ionization energy. At relatively large separation, Cornell potential describes a force between quark and anti-quark which remains constant. This means, to remove a quark from a hadron we need an infinite amount of energy. This explains the non-existence of free quark.

Another different kind of potential, which is energy dependent have been known for a long time in physics. At present it is not possible to obtain exact potential for entire range of distance for a quarkonium. Moreover most of proposed potentials have not been able to account for the observed saturation pattern in the experimental mass spectra of quarkonium. The advantage of this energy dependent potential is that it saturate the mass spectra. In view of this the potential is of the form harmonic plus Inverse square, with a small linear energy dependence on the confining harmonic oscillator potential term. One great advantage of this potential is that this potential admits exact analytical solution for the radial part of Schrodinger equation. The potential is given by,

$$V(r, E_{n,l}) = \frac{1}{2} m \omega^2 r^2 (1 + \gamma E_{n,l}) + \frac{g}{r^2}$$

Where  $\omega$ ,  $g$  and  $\gamma$  are constants.

#### **4a. GENERAL THEORY OF SUPER SYMMETRY QUANTUM MECHANICS (SUSY QM):**

In this section we are going to summarized main features of SUSY QM, which is used to study the energy states and energy eigenfunctions of Cornell potential.

We consider the Schrödinger equation for the ground state with an energy eigenvalue equal to zero (this can be done without loss of generality). Thus the ground state wave function  $\psi_0$  obeys,

$$H_1 \psi_0(x) = -\frac{\hbar^2}{2m} \frac{d^2 \psi_0(x)}{dx^2} + V_1(x) \psi_0(x) = 0. \quad (1)$$

Then,

$$V_1(X) = \frac{\hbar^2}{2m} \frac{\psi_0''(x)}{\psi_0(x)}. \quad (2)$$

The Hamiltonian  $H_1$  can be factorized as

$$H_1 = A^\dagger A, \quad (3)$$

Where,

$$A = \frac{\hbar}{\sqrt{2m}} \frac{d}{dx} + W(x) \text{ and } A^\dagger = -\frac{\hbar}{\sqrt{2m}} \frac{d}{dx} + W(x) \quad (4)$$

With this we observe,

$$V_1(x) = -\frac{\hbar}{\sqrt{2m}} \frac{dW(x)}{dx} + W^2(x) \quad (5)$$

Now once we satisfy  $A\psi_0 = 0$ , we automatically have a solution to  $H_1\psi_0 = A^\dagger A\psi_0 = 0$ . Which gives,

$$W(x) = -\frac{\hbar}{\sqrt{2m}} \frac{\psi_0'(x)}{\psi_0(x)} \quad (6)$$

The next step is to define a new operator  $H_2 = AA^\dagger$ . From (4) we can see  $H_2$  is in fact a Hamiltonian corresponding to a new potential  $V_2(x)$  given by,

$$V_2(x) = \frac{\hbar}{\sqrt{2m}} \frac{dW(x)}{dx} + W^2(x) \quad (7)$$

The potentials  $V_1(x)$  and  $V_2(x)$  are known as supersymmetric partner potential, and the  $W(x)$  is known as "super potential".

Now we shall see the energy eigenvalues and the wave functions of  $H_1$  and  $H_2$  are related as following,

$$H_1\psi_n^{(1)} = A^\dagger A\psi_n^{(1)} = E_n^{(1)}\psi_n^{(1)} \quad (8)$$

Implies



$$H_2(A\psi_n^{(1)}) = AA^\dagger A\psi_n^{(1)} = E_n^{(1)}(A\psi_n^{(1)}) \quad (9)$$

Similarly for  $H_2$  we have,

$$H_2\psi_n^{(2)} = AA^\dagger\psi_n^{(2)} = E_n^{(2)}\psi_n^{(2)} \quad (10)$$

Implies,

$$H_1(A^\dagger\psi_n^{(2)}) = A^\dagger AA^\dagger\psi_n^{(2)} = E_n^{(2)}(A^\dagger\psi_n^{(2)}) \quad (11)$$

Now from eq. (8) and (11) we can write,

$\psi_{n+1}^{(1)} = cA^\dagger\psi_n^{(2)}$ , where  $c$  is a normalization constant, which is easily found to be equal to  $\frac{1}{\sqrt{E_n^{(2)}}}$ , hence we have

$$\psi_{n+1}^{(1)} = \frac{1}{\sqrt{E_n^{(2)}}}A^\dagger\psi_n^{(2)} \quad (12)$$

Similarly from eq. (9) and (10) we have,

$$\psi_n^{(2)} = \frac{1}{\sqrt{E_{n+1}^{(1)}}}A\psi_{n+1}^{(1)} \quad (13)$$

$$\text{And } E_n^{(2)} = E_{n+1}^{(1)}, E_0^{(1)} = 0 \quad (14)$$

Now carefully observing eq. (12)-(14) we see, except the ground state of  $H_1$ , additional levels are same in both the Hamilton  $H_1$  and  $H_2$ , i.e., potentials  $V_1$  and  $V_2$  are isospectrals except  $E_0^{(1)}$ .

Therefore the ground state of  $H_2$  corresponding to the first excited state of  $V_1$ . This fact is very important because we know that the variational method in quantum mechanics is a good tool to get an approximate values of ground state in the Schrödinger equation. Therefore this method can be used to obtain the ground states of different supersymmetry partner potential of Cornell potential obtained

using SUSY QM method. That's why I believe that SUSY QM method will be a good way to estimate the various state of Cornell potential.

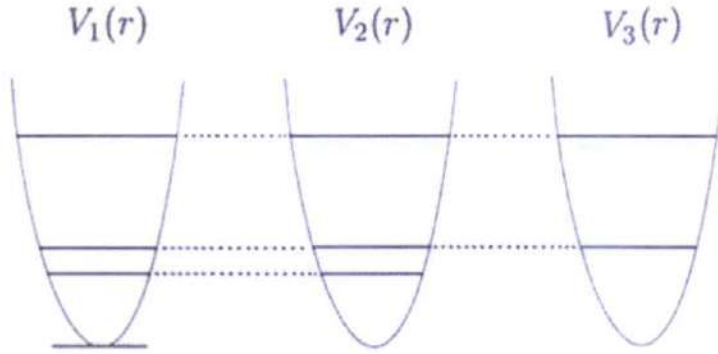


Fig 4.1: Schematic presentation of potential  $V_1$  and its supersymmetric partner potentials  $V_2$  and  $V_3$  (the shape of each potential will be different ofcourse). The ground state of  $V_1$  is not present in  $V_2$ , ground state of  $V_2$  is not present in  $V_3$ .

#### 4b. SUSY QM TREATMENT OF CORNELL POTENTIAL:

Here we will use the potential of the form  $V(r) = -\frac{B}{r} + Ar$ , here  $A$  and  $B$  are parameters. The three dimensional Schrödinger equation is,

$$\left[-\frac{\hbar^2}{2\mu} \nabla^2 + V(r, E_{n,l})\right] \psi_{n,l}(r, \theta, \phi) = E_{n,l} \psi_{n,l}(r, \theta, \phi)$$

The wave function can be written as,  $\psi_{n,l,m} = \frac{u_{n,l}(r)}{r} Y_{l,m}(\theta, \phi)$

The radial equation is,  $-\frac{1}{2\mu} \frac{d^2 U_{nl}(r)}{dr^2} + V_{eff}(r) U_{nl}(r) = E_{n,l} U_{nl}(r)$  (15)

Where  $\hbar=1$ , and  $\mu$  is the reduced mass of quark-antiquark system, and

$$V_{eff}(r) = V(r) + \frac{l(l+1)}{2mr^2}$$

For simplicity in calculation we first take  $l = 0$  (S state). Thus the effective potential is the Cornell potential,

$$V_{eff}(r) = V(r) = -\frac{B}{r} + Ar$$



Unfortunately the equation (15) with  $V_{eff}(r) = V(r) = -\frac{B}{r} + Ar$ , cannot be solved exactly! So it's good to use the variational method to obtain the ground states (approximate) of different partner potential. Now for the variational method we consider the trial wave function to be

$$U(r) = Nr^\gamma e^{-ar^b}. \quad (16)$$

Here a, b are variational parameters, and N is normalization constant.

This trial wave function can be used to obtain the ground state of the Cornell potential and its super symmetric partners.  $\gamma$  takes the value 1, 2, 3... depending on the calculation of the ground state of potentials  $V_1, V_2, \dots$ . In order to gain finite value of the ground state wave function of different partner potential at the origin, changing the value of  $\gamma$  in this way is important.

Now to calculate the ground state for the Cornell potential we use (15) with  $\gamma=1$  in (16). Thus the expectation value of energy is

$$E = -\frac{1}{2\mu} \int_0^\infty U(r) \frac{d^2 U(r)}{dr^2} dr + \int_0^\infty \left( Ar - \frac{B}{r} \right) U^2(r) dr$$

Using  $U(r)$  from (16) with  $\gamma=1$ , we get

$$E(a, b) = \frac{1}{ab(2a)^{\frac{1}{b}}} \left[ \frac{A}{(2a)^{\frac{3}{b}}} \Gamma\left(\frac{4}{b}\right) - \frac{B}{(2a)^{\frac{1}{b}}} \Gamma\left(\frac{2}{b}\right) \right] - \frac{(b+1)}{4b(2a)^{\frac{1}{b}}} \Gamma\left(\frac{1}{b}\right)$$

By minimizing this, an approximate value for the energy and the parameters a, b are obtained. Let's call the parameters associated with the ground state  $a_0$  and  $b_0$ . Therefore the ground state wave function is  $U(r) = Nre^{-a_0 r^{b_0}}$ .

Now from (6) we obtain the super potential  $W = -\frac{1}{\sqrt{2\mu}} \frac{U'(r)}{U(r)} = \frac{-1 + a_0 b_0 r^{b_0}}{\sqrt{2\mu} r}$ .

From this we can build the potential  $V_2$  which is a partner potential of the Cornell potential,

$$V_2 = W^2(r) + \frac{1}{\sqrt{2\mu}} \frac{dW}{dr} = \frac{2 + a_0 b_0 r^{b_0} (-3 + a_0 b_0 + a_0 b_0 r^{b_0})}{2\mu r^2}$$

Now the variational method is used to find the ground state of this potential and its energy value. Let  $a_0^1$  and  $b_0^1$  be the parameter associated with this state. This state will be the first excited state of Cornell potential. By repeating the procedure for other partner potentials we obtain different excited states of Cornell potential. It is important to note that the ground state energy is to be zero in our discussion for SUSY QM. If the ground state energy of the partner potential  $V_1$  is  $E_1$ , and of  $V_2$  is  $E_2$ , then the energy for the first excited state is  $E = E_1 + E_2$ . Similarly for other excited states also.

From (12) we have  $\psi_1^{(1)} \sim A^\dagger \psi_0^{(2)} = \left( -\frac{1}{\sqrt{2\mu}} \frac{\partial}{\partial r} + \frac{-1 + a_0 b_0 r^{b_0}}{\sqrt{2\mu} r} \right) \psi_0^{(2)}$ .

Using  $\psi_0^{(2)} = N r^2 e^{-a_0^1 r^{b_0^1}}$ , we can find  $\psi_1^{(1)}$ , i.e., the first excited state of Cornell potential system. Other excited states can also be found in the same way.

## 5. SOLUTION OF ENERGY DEPENDENT POTENTIAL MODEL:

The potential is of the form spin independent harmonic oscillator with a small linear energy dependent term plus an inverse square term,

$$V(r, E_{n,l}) = \frac{1}{2} m \omega^2 r^2 (1 + \gamma E_{n,l}) + \frac{g}{r^2}, \quad (17)$$

Here  $\omega$ ,  $g$  and  $\gamma$  are constants.

The three dimensional Schrödinger equation is,



$$\left[-\frac{\hbar^2}{2\mu} \nabla^2 + V(r, E_{n,l})\right] \psi_{n,l}(r, \theta, \phi) = E_{n,l} \psi_{n,l}(r, \theta, \phi)$$

The wave function can be written as,  $\psi_{n,l,m} = \frac{u_{n,l}(r)}{r} Y_{l,m}(\theta, \phi)$

The radial equation is,  $-\frac{1}{2\mu} \frac{d^2 U_{nl}(r)}{dr^2} + V_{eff}(r) U_{nl}(r) = E_{n,l} U_{nl}(r)$  (18)

Where  $V_{eff}(r) = \frac{1}{2} m \omega^2 r^2 (1 + \gamma E_{n,l}) + \frac{g}{r^2} + \frac{l(l+1)}{2\mu r^2}$ .

Now putting  $\omega'^2 = \omega^2 (1 + \gamma E)$ ,  $t = m \omega' r^2$ ,  $\alpha = \frac{2E}{\omega'}$ , and  $\beta = l(l+1) + 2\mu g$ , equation (18) reduces to

$$t u'' + \frac{u'(t)}{2} + \frac{1}{4} \left[ \alpha - \frac{\beta}{t} - t \right] u(t) = 0 \quad (19)$$

Now the solution of the radial equation has to be bound to infinity and zero at the origin. So as  $t$  tends to infinity we must have,

$u''(t) + \frac{u(t)}{4} = 0$ , which has a physically acceptable solution  $u(t) = \exp(-\frac{t}{2})$ , therefore we seek the solution of the form,

$$u(t) = t^\eta \exp(-\frac{t}{2}) R_l(t), \eta > 0. \quad (20)$$

Substituting (20) into (19) we have

$$t R_l''(t) + \left[ 2\eta + \frac{1}{2} - t \right] R_l'(t) - \left[ \eta + \frac{1}{4} - \frac{\alpha}{4} \right] R_l(t) = 0 \quad (21)$$

Where we have taken  $\eta = \frac{1}{4} (1 + \sqrt{(2l+1)^2 + 8\mu g})$

Now (21) is of the form

$$z y'' + (c - z) y' - a y = 0, \text{ with } c = 2\eta + \frac{1}{2} \text{ and } a = \eta + \frac{1}{4} - \frac{\alpha}{4}. \quad (22)$$

Which is the well-known Kummer's Equation. The non-singular solution of this equation is the Degenerate Hypergeometric series, which is given by,

$$F(a, c; z) = \sum_{k=0}^{\infty} \frac{(a)_k}{(c)_k} \frac{z^k}{k!} = 1 + \left(\frac{a}{c}\right)z + \frac{a(a+1)}{c(c+1)} \frac{z^2}{2!} + \dots, c \neq 0, -1, -2, \dots \quad (23)$$

Therefore the solution of (21) is,

$$R_l(t) = F\left[\eta + \frac{1}{4} - \frac{\alpha}{4}, 2\eta + \frac{1}{2}; t\right] \quad (24)$$

From (22) we see  $u(t)$  increases without bound as  $t \rightarrow \infty$  unless the series (24) reduces to polynomial. From (23) we see this happens when  $a$  is some negative integer, so let,

$$\eta + \frac{1}{4} - \frac{\alpha}{4} = -n; n = 0, 1, 2.. \quad (25)$$

Now putting the values of  $\alpha, \eta$  in (25) and simplifying we get,

$$E_{n,l} = -\frac{1}{8}a^2\omega^2\gamma + \frac{a\omega}{8}\sqrt{a^2\omega^2\gamma^2 + 16} \quad (26)$$

Where  $a = 4n - 2 + \sqrt{(2l + 1)^2 + 8\mu g}$ .

The parameter  $\omega, \gamma$  and  $g$  are obtained from fit to the experimental Data.

Here is the plot of radial wave functions  $U_1(r)$  ( $n=1, l=0$ ) and  $U_2(r)$  ( $n=2, l=0$ ). Here  $c=1, \mu = 1.50 \text{ GeV}, \gamma = 0 \text{ GeV}^{-1}, \omega = 0.174 \text{ GeV}, g = -0.073 \text{ GeV}^{-1}$ . [3]

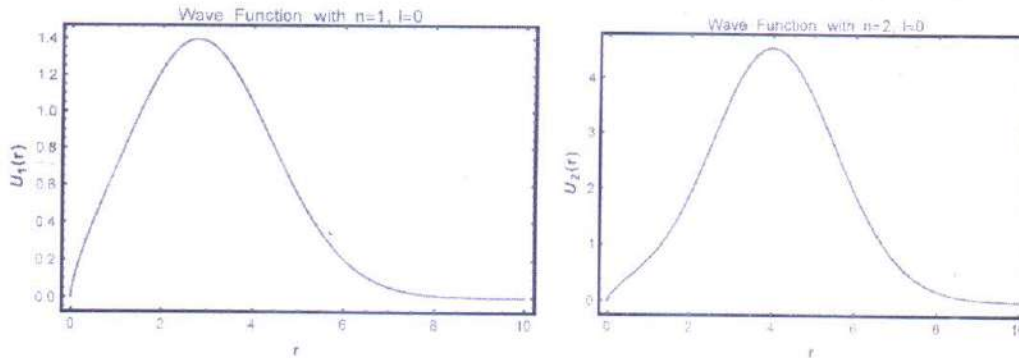


Fig. 5.1: left: radial wave function  $U_1(r)$  with  $n=1, l=0$  right: radial wave function  $U_2(r)$  with  $n=2, l=0$ .



## 6. CONCLUSION:

So here we have used the SUSY QM methods to solve the approximate eigenstates and energy eigenvalues for the Cornell potential model. For lower states this approach provides good result. If we use the trial wave function with several more variable, undoubtedly more accurate result can be obtained. Moreover this method to obtain the excited states can be used as an alternative of using WKB method.

In the second part we use the energy dependent potential model, which luckily possess exact solution of Schrödinger equation. Saturation pattern is observed in the experimental mass spectra of quarkonium. Using this potential model such saturation pattern in mass spectra of quarkonium can be explained.

## 7. ACKNOWLEDGEMENT:

Successfully completion of any type of project requires help from a number of persons. I have also taken help from different people for the preparation of this report. I show my deep gratitude to all those helpful persons.

First of all, I convey my sincere gratitude to my project guide **Dr. Soumya Sadhukhan, Assistant Professor, RKMRC, Narendrapur**. Without his kind direction and proper guidance this study would have little success. In every phase of the project his supervision and guidance shaped this report to be completed perfectly.

I would like to thank **Dr. Malay Purkait, Head of Department of Physics, RKMRC, Narendrapur** as well as my college **RKMRC, Narendrapur** for giving me this opportunity.

Last but not least, I give my heart full thank to all of my friends who have helped me a lot to complete this project.



## REFERENCES

- [1]. Heavy quarkonium properties from Cornell potential using variational method and supersymmetric quantum mechanics; ALFREDO VEGA and JORGE FLORE; *Pramana – J. Phys.* (2016); DOI 10.1007/s12043-016-1278-7.
- [2]. Supersymmetry and Quantum Mechanics; Fred Cooper, Avinash Khare, Uday Sukhatme; arxiv:hep-th/9405029v2.
- [3]. Study of Heavy Quarkonium with Energy Dependent Potential; Pramila Gupta, Indira Mehrotra; *Journal of Modern Physics*, 2012, 3.
- [4]. Particles and Nuclei; Bogdan Povh, Klaus Rith, Christoph Scholz, Frank Zetsche, Werner Rodejohann.
- [5]. Selected Special Functions for Fundamental Physics; Valeriya Akhmedova, Emil T. Akhmedov.

RAMAKRISHNA MISSION RESEDENTIAL COLLEGE

(AUTONOMOUS)

NARENDRAPUR, KOLKATA – 700103



“BRIEF INTRODUCTION TO SHORT CHANNEL  
EFFECTS AND DETAILED CALCULATION OF NATURAL  
LENGTHS OF DIFFERENT MULTIGATE TRANSISTORS”

Supervised by: Dr. SOURAV CHATTOPADHYAY

(Assistant Professor, Department of Physics, RKMRC Narendrapur)

Project done by: Akash Sinha

Roll No: PHUG/109/17

B.Sc. 6th semester





**Ramakrishna Mission Residential College (Autonomous)**

**Vivekananda Centre for Research**

**Ramakrishna Mission Ashrama**

(A Branch Centre of Ramakrishna Mission, Belur Math, Howrah-711202)

**Narendrapur, Kolkata - 700 103, West Bengal, India**

A Scientific Industrial Research Organisation, Recognised by DST, Govt. of India

College with Potential for Excellence (CPE), Re-accredited by NAAC - 'A' (CGPA 3.56 out of 4)

---

## **DEPARTMENT OF PHYSICS**

### **Certificate**

This is to certify that Akash Sinha, a student of B.Sc has successfully completed the project of UG curriculum entitled "**BRIEF INTRODUCTION TO SHORT CHANNEL EFFECTS AND DETAILED CALCULATION OF NATURAL LENGTHS OF DIFFERENT MULTIGATE TRANSISTORS**" in the period from January to May, 2020.

*Malay Purkait*  
.....  
30.06.2020.

**Signature Of HOD**

**Dept. of Physics**

**Dr. Malay Purkait**  
Associate Prof. & Head  
Department of Physics  
Ramakrishna Mission Residential College  
(Autonomous)  
Narendrapur, Kolkata-700 103, (W.B.)

---

PHONES : 24772201(3lines), 24772205 FAX : 033-24773597 EMAIL : rkmcnpur@vsnl.com

WEBSITE : [www.rkmcnarendrapur.org](http://www.rkmcnarendrapur.org)

TO WHOM IT MAY CONCERN

This to certify that Mr. Akash Sinha (Roll Number: PHUG/109/17) of B.Sc. 6th semester student is known to me for three years in the Department of Physics, Ramakrishna Mission Residential College (Autonomous), Narendrapur. He had done this project as a part of B.Sc. 6thSemester Course Curriculum.

*Sourav Chattopadhyay*  
20/6/20  
Dr. SOURAV CHATTOPADHYAY

Assistant Professor

Department of Physics, Ramakrishna Mission Residential College (Autonomous)

Narendrapur, Kolkata-103



## ACKNOWLEDGEMENT

I acknowledge with pleasure the support of Dr. Sourav Chattopadhyay, Assistant Professor of Department of Physics, Ramakrishna Mission Residential College Narendrapur. Under his supervision, I have completed my project report. I thank Dr. Malay Purkait, H.O.D. of Department of Physics of RKMRC Narendrapur, for supporting me at every step. This project has been very insightful and I consider myself lucky to be a part of it.

*Akash Sinha*

**Akash Sinha**

PH IG/109/17

Department of Physics

R K M R C Narendrapur

## CONTENTS

|                                                         |    |
|---------------------------------------------------------|----|
| 1. Introduction to MOSFET.....                          | 4  |
| 2. Short-Channel-effects.....                           | 6  |
| 3. A brief history of multiple gate MOSFETs.....        | 7  |
| 4. Basic geometric structures of multigate MOSFETs..... | 8  |
| 5. Natural Length.....                                  | 9  |
| 6. Detailed calculation of Natural Length.....          | 10 |
| 7. Conclusion.....                                      | 19 |
| 8. Acknowledgement.....                                 | 21 |
| 9. Reference .....                                      | 22 |



## □ Introduction to MOSFET:

An p-channel metal-oxide-semiconductor field effect transistor (MOSFET) consists of a lightly doped n-type substrate (referred as body) into which two highly doped p regions (referred one as source and one as drain) are diffused. A thin layer (1000 to 2000 Å) of insulating silicon dioxide is grown over the surface of the structure and holes are cut into the oxide layer allowing contact with the source and drain. If we ground the substrate and apply a negative voltage at the gate, an electric field will be directed perpendicular through the oxide. This field will end on inducing positive charges on the semiconductor site. The positive charges which are minority carriers in the n-type substrate, form an

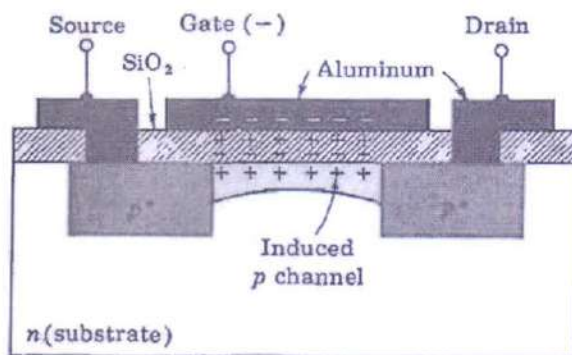


Fig. 10-9 Enhancement in a p-channel MOSFET. (Courtesy of Motorola Semiconductor Products, Inc.)

'Inversion layer'. As the magnitude of the negative voltage on the gate increases the induction increases. The region beneath the oxide now has p-type carriers, the conductivity increases and current flows from source to drain through induced channel. This kind of MOSFET is called "Enhancement type MOSFET".

A second type of MOSFET can be made if, to the basic structure a channel is diffused between the source and drain, with the same type of

impurity as used for the source and drain diffusion. Let us consider such an n-channel structure. With this device an appreciable drain current  $I_{DSS}$  flows for zero gate to source voltage. If the gate voltage is made negative, positive charges are induced in the channel. Since the current in this MOSFET is due to majority carriers, the induced positive charges make the channel less conductive and the drain current drops as  $V_{GS}$  is made more negative. The redistribution of charges in the channel causes an effective depletion of majority carriers, which accounts for the

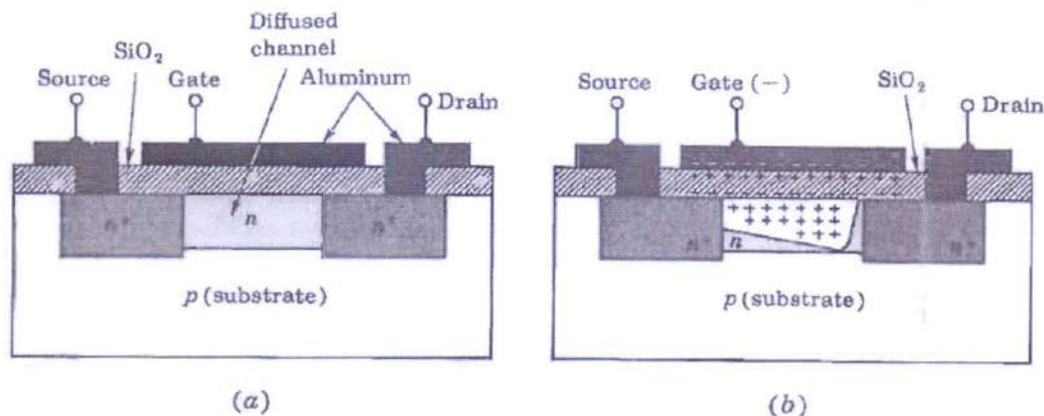


Fig. 10-12 (a) An n-channel depletion-type MOSFET. (b) Channel depletion with the application of a negative gate voltage. (Courtesy of Motorola Semiconductor Products, Inc.)

designation 'Depletion MOSFET'. Because of the voltage drop due to drain current, the channel region near to drain is more depleted than is the volume near the source. If we apply a positive voltage so that negative charges are induced into the n-channel. In this manner the conductivity of the channel increases. In this manner a MOSFET of depletion type may also be operated in an enhancement mode.

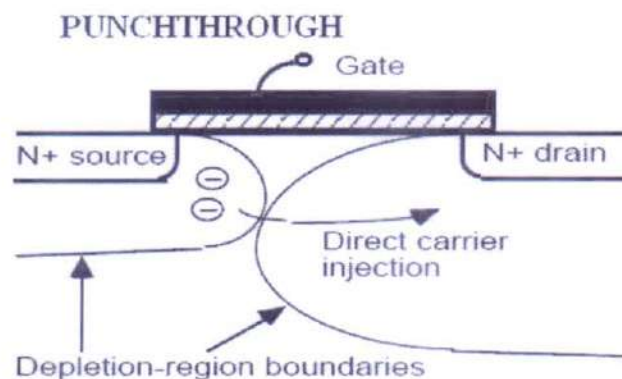


## Short channel effects:

As the dimensions of MOSFET are shrunk, the close proximity between the source and drain reduces the ability of the gate electrode to control the potential distribution and the flow of current in the channel region, and undesirable effects called 'Short Channel Effects'(SCE) arise. A MOSFET is considered to be short when the channel length( $L$ ) is the same order of magnitude as the depletion layer widths ( $X_{dD}, X_{dS}$ ) of the drain and source junctions. When,

$$L = X_{dD} + X_{dS}$$

so that two depletion layers merge, 'punchthrough' occurs.



### :Types of SCEs:

1. The limitation imposed on the electron drift characteristic in the channel.
2. The modification of threshold voltage due to the shortening channel length.
3. Drain induced barrier lowering and punchthrough.
4. Surface scattering.
5. Velocity scattering.
6. Impact ionization.
7. Hot electron.

## A brief history of Multiple-Gate MOSFETs:

In a continuous effort to increase current drive and better control over short channel effects, silicon-on-insulator MOSFETs have evolved from classical, planar, single gate devices into three dimensional devices with a multigate structures (double, triple, quadruple-gate-devices). It is worth noting that in most cases the term ‘double gate’ refers to a single gate electrode that is present on two opposite sides of the device. Similarly the term ‘triple gate’ used for a single gate electrode that is folded over three sides of the device. One remarkable exception is the MIGFET (Multiple Independent Gate FET) where two separate gate electrode can be biased with different potentials.

The diagram bellow shows the “Family Tree” of SOI and multigate MOSFETs.

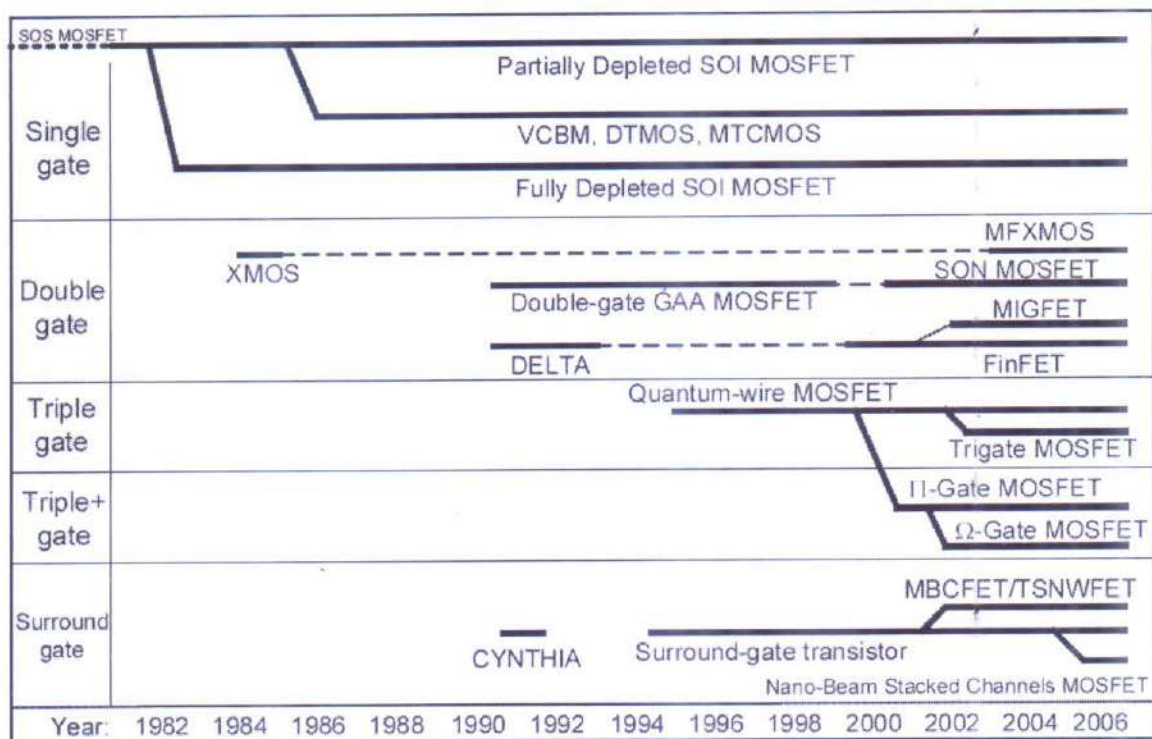
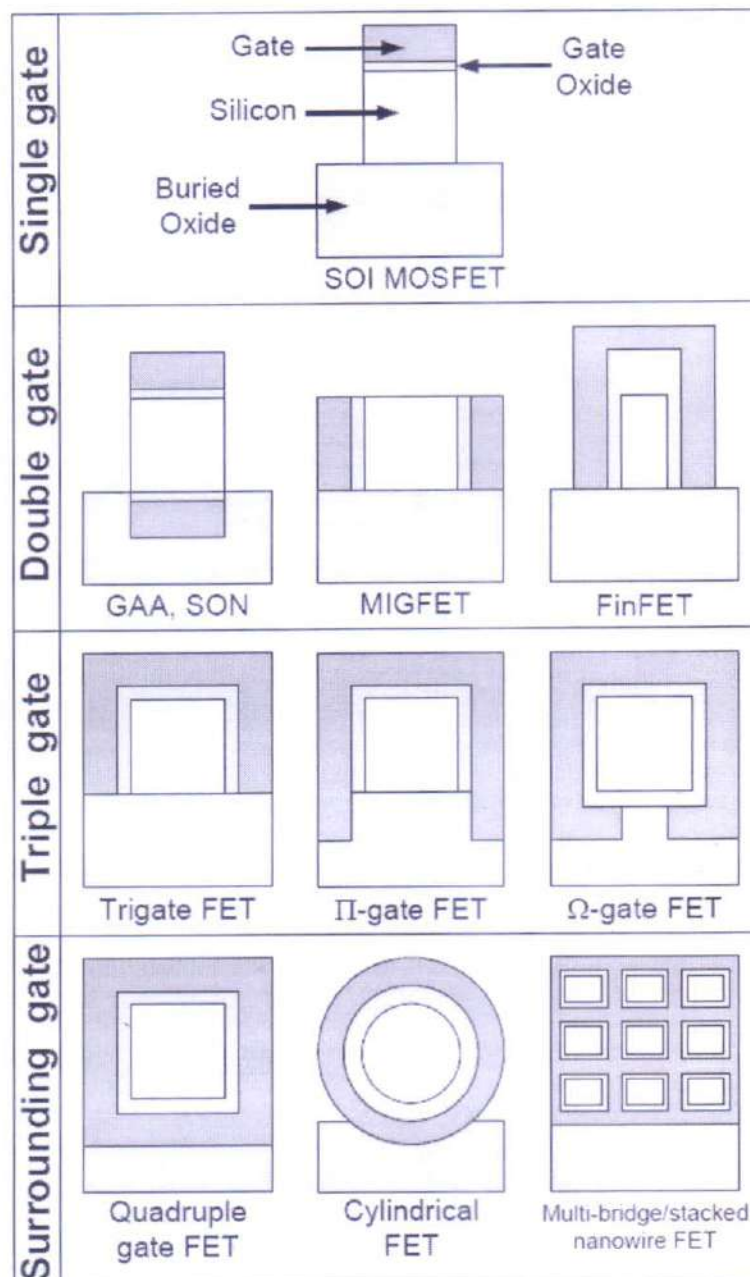


Fig. “Family tree” of SOI and multigate MOSFETs.



## Basic geometric structures of multigate MOSFETs:

Basically the multigate MOSFETs differ from each other by how the gate and gate oxide layer wraps around the channel. The geometric structures of these multigate MOSFETs are shown in the diagram given below.



## □ Natural length:

Starting from Poisson's equation, Yan and coworkers and Lee and coworkers introduced a powerful concept, the "Natural Length" ( $\lambda$ ) which is a measure of SCE in multigate MOSFETs. It represents the distance of penetration of the drain electric field into the channel. A device will be free of SCEs if the channel length is atleast six times the natural length. The natural length depends on the gate oxide thickness, the silicon film thickness and the geometry of the gate, number of gates. The table shown below summarizes the expression of  $\lambda$ , for different device geometries.

Table

|                                                      |                                                                                                                                          |
|------------------------------------------------------|------------------------------------------------------------------------------------------------------------------------------------------|
| Single gate                                          | $\lambda_1 = \sqrt{\frac{\epsilon_{si}}{\epsilon_{ox}}} t_{si} t_{ox}$                                                                   |
| Double gate                                          | $\lambda_2 = \sqrt{\frac{\epsilon_{si}}{2\epsilon_{ox}}} t_{si} t_{ox}$                                                                  |
| Quadruple gate<br>(square channel cross section)     | $\lambda_4 \cong \sqrt{\frac{\epsilon_{si}}{4\epsilon_{ox}}} t_{si} t_{ox}$                                                              |
| Surrounding gate<br>(circular channel cross section) | $\lambda_o = \sqrt{\frac{2\epsilon_{si} t_{si}^2 \ln\left(1 + \frac{2t_{ox}}{t_{si}}\right) + \epsilon_{ox} t_{si}^2}{16\epsilon_{ox}}}$ |



## □ Detailed calculation of Natural Lengths:

The potential distribution in the channel of a fully depleted multigate MOSFET can be obtained by solving Poisson's equation using the depletion approximation:

$$\frac{d^2\Phi(x, y, z)}{dx^2} + \frac{d^2\Phi(x, y, z)}{dy^2} + \frac{d^2\Phi(x, y, z)}{dz^2} = \frac{qN_a}{\epsilon_{si}}$$

Where  $N_a$  is the number density of charge carriers and  $\epsilon_{si}$  is the electrical permittivity of the silicon channel.

Let us first understand the meaning of this equation. It can be rewritten in the form:

$$\frac{dE_x(x, y, z)}{dx} + \frac{dE_y(x, y, z)}{dy} + \frac{dE_z(x, y, z)}{dz} = C$$

This relationship means that, at any point (x,y,z) in the channel, the sum of the variations of the electric field components in the x, y and z directions is equal to a constant. Thus, if one of the components increases, the other ones (or, to be more precise, their sum) must decrease. The x-component of the electric field,  $E_x$ , represents the encroachment of the drain electric field on the channel region, and, therefore, short-channel effects. The influence of  $E_x$  on a small

element of the channel region located at coordinates  $(x,y,z)$  can be reduced by either increasing the channel length,  $L$ , or by increasing the control exerted by the top/bottom gates,  $\frac{dE_y(x,y,z)}{dy}$ , or the lateral gates,  $\frac{dE_z(x,y,z)}{dz}$ , on this channel. This can be achieved by reducing the silicon fin thickness  $t_{si}$ , and/or the fin width,  $W_{si}$ . In addition, an increase of  $\frac{dE_y(x,y,z)}{dy} + \frac{dE_z(x,y,z)}{dz}$ , and, hence, in a better control of the channel by the gates and less short-channel effects, can also be obtained by increasing the number of gates:  $\frac{dE_y(x,y,z)}{dy}$  can be increased by having two gates (top and bottom gates) instead of a single gate, and  $\frac{dE_z(x,y,z)}{dz}$  is increased by the presence of lateral gates. Figure below illustrates how the electric field from the gates and from the drain compete for the control of the channel.

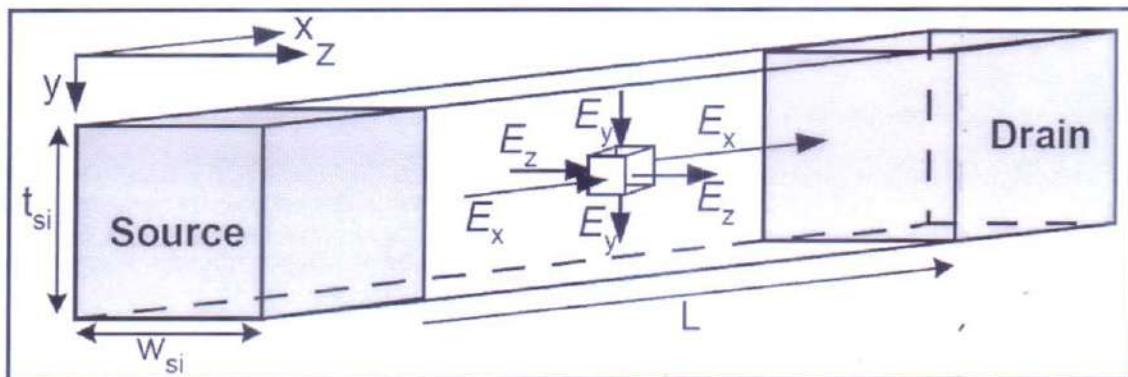


Fig. Coordinate system and electric field components in a multiple-gate device.

In the case of a wide single- or double-gate device, we have  $\frac{d\Phi}{dz} = 0$ , and Poisson's equation becomes

$$\frac{d^2\Phi(x,y)}{dx^2} + \frac{d^2\Phi(x,y)}{dy^2} = \frac{qN_a}{\epsilon_{si}}$$



(1.0)

Simplified one-dimensional analysis of a fully depleted device yields a parabolic potential distribution in the silicon film in the  $y$  (vertical) direction. Assuming a similar distribution in the  $y$ -direction for a two-dimensional analysis Poisson's equation becomes

$$\Phi(x, y) = c_0(x) + c_1(x)y + c_2(x)y^2 \quad (1.1)$$

### :Single gate SOI MOSFET:

In the case of a single-gate SOI device the boundary conditions to equation 1.1 are:

1.  $\Phi(x, 0) = \Phi_f(x) = c_0(x)$  where  $\Phi_f(x)$  is the front surface potential;

$$2. \left. \frac{d\Phi(x, y)}{dy} \right|_{y=0} = \frac{\epsilon_{ox}}{\epsilon_{si}} \frac{\Phi_f(x) - \Phi_{gs}}{t_{ox}} = c_1(x)$$

where  $\Phi_{gs} = V_{gs} - V_{FBF}$  is the front gate voltage,  $V_{gs}$ , minus the front-gate flat-band voltage,  $V_{FBF}$ .

3. If we assume that the buried oxide is very thick the potential difference across any finite distance in the BOX is negligible in the  $y$  direction we can write  $\frac{d\Phi(x, y)}{dy} \cong 0$  in the BOX. Therefore,

$$\text{we have: } \left. \frac{d\Phi(x, y)}{dy} \right|_{y=t_{si}} = c_1(x) + 2t_{si}c_2(x) \cong 0 \text{ and thus } c_2(x) \cong -\frac{c_1(x)}{2t_{si}}.$$

Introducing these three boundary conditions in equation 1.1 we obtain:

$$\Phi(x, y) = \Phi_f(x) + \frac{\epsilon_{ox}}{\epsilon_{si}} \frac{\Phi_f(x) - \Phi_{gs}}{t_{ox}} y - \frac{1}{2t_{si}} \frac{\epsilon_{ox}}{\epsilon_{si}} \frac{\Phi_f(x) - \Phi_{gs}}{t_{ox}} y^2 \quad (1.2)$$

Substituting equation 1.2 into equation 1.0, and setting  $y=0$ , at which depth  $\Phi(x, y) = \Phi_f(x)$ , we obtain:

$$\frac{d^2\Phi_f(x)}{dx^2} - \frac{\epsilon_{ox}}{\epsilon_{si}} \frac{\Phi_f(x) - \Phi_{gs}}{t_{si}t_{ox}} = \frac{qN_a}{\epsilon_{si}} \quad (1.3)$$

Now if we define:

$$\lambda_1 = \sqrt{\frac{\epsilon_{si}}{\epsilon_{ox}} t_{ox} t_{si}}$$

and

$$\varphi(x) = \Phi_f(x) - \Phi_{gs} + \frac{qN_a}{\epsilon_{si}} \lambda_1^2$$

Then equation 1.3 becomes

$$\frac{d^2\varphi(x)}{dx^2} - \frac{\varphi(x)}{\lambda_1^2} = 0$$

This equation has a solution in the form  $\varphi(x) = \varphi_0 \exp\left(\pm \frac{x}{\lambda_1}\right)$  where  $\lambda_1$  is a parameter that represents the spread of the electric potential in the  $x$ -direction. Note that  $\varphi(x)$  differs from  $\Phi_f(x)$  only by an  $x$ -independent term. Parameter  $\lambda_1$  is called the “*natural length*” of the device. It depends on the gate oxide thickness and the silicon film thickness. The thinner the gate oxide and/or the silicon film, the smaller the natural length and, hence, the influence of the drain electric field on the channel region. Numerical simulations show that the effective gate length of a MOS device must be larger than 5 to 10 times the natural length to avoid short-channel effects.



## :Double-gate SOI MOSFET:

In the case of double-gate SOI MOSFET the boundary conditions are:

1.  $\Phi(x, 0) = \Phi(x, t_{si}) = \Phi_f(x) = c_o(x)$  where  $\Phi_f(x)$  is the front surface potential;
2.  $\left. \frac{d\Phi(x, y)}{dy} \right|_{y=0} = \frac{\epsilon_{ox}}{\epsilon_{si}} \frac{\Phi_f(x) - \Phi_{gs}}{t_{ox}} = c_1(x)$  where  $\Phi_{gs} = V_{gs} - V_{FBF}$  is the front gate voltage,  $V_{gs}$ , minus the front gate flat-band voltage,  $V_{FBF}$ .
3.  $\left. \frac{d\Phi(x, y)}{dy} \right|_{y=t_{si}} = -\frac{\epsilon_{ox}}{\epsilon_{si}} \frac{\Phi_f(x) - \Phi_{gs}}{t_{ox}} = c_1(x) + 2t_{si} c_2(x) = -c_1(x)$  and thus  $c_2(x) = \frac{-c_1(x)}{t_{si}}$ .

Substituting these boundary conditions in equation 1.1 we get:

$$\Phi(x, y) = \Phi_f(x) + \frac{\epsilon_{ox}}{\epsilon_{si}} \frac{\Phi_f(x) - \Phi_{gs}}{t_{ox}} y - \frac{1}{t_{si}} \frac{\epsilon_{ox}}{\epsilon_{si}} \frac{\Phi_f(x) - \Phi_{gs}}{t_{ox}} y^2$$

The key difference between this expression and equation 1.2 is that the term  $1/2t_{si}$  has now been replaced by  $1/t_{si}$ . In other words it looks as if the double-gate device was twice as thin as the single-gate transistor. The natural length of the double-gate device can be derived the same way it was done for the single-gate case, which yields:

$$\lambda_2 = \sqrt{\frac{\epsilon_{si}}{2\epsilon_{ox}} t_{ox} t_{si}}$$

If we consider punchthrough and assuming that the punchthrough occurs at the center of the channel we can define a new  $\lambda$ . The new  $\lambda$  has the same meaning as before but it can better explain some of the experimental results. Starting with Poisson's equation

$$\frac{d^2\Phi(x, y, z)}{dx^2} + \frac{d^2\Phi(x, y, z)}{dy^2} + \frac{d^2\Phi(x, y, z)}{dz^2} = \frac{qN_a}{\epsilon_{si}} \quad (2.0)$$

For single-gate or double-gate devices  $\frac{d\phi}{dz} = 0$ , such that Equation reduced to:

$$\frac{d^2\Phi(x, y)}{dx^2} + \frac{d^2\Phi(x, y)}{dy^2} = \frac{qN_{sub}}{\epsilon_{si}}$$

Assuming a parabolic potential distribution in the y-direction, we can write:

$$\Phi(x, y) \approx c_0(x) + c_1(x)y + c_2(x)y^2 \quad (2.1)$$

We now apply the boundary condition  $\left. \frac{d\Phi(x, y)}{dy} \right|_{y=0} = 0$  at  $y = \frac{t_{si}}{2}$ ,

which yields:

$$\Phi(x, y) = \Phi_f(x) + \frac{\epsilon_{ox}}{\epsilon_{si}} \frac{\Phi_s(x) - \Phi_{gs}}{t_{ox}} y - \frac{1}{t_{si}} \frac{\epsilon_{ox}}{\epsilon_{si}} \frac{\Phi_s(x) - \Phi_{gs}}{t_{ox}} y^2 \quad (2.2)$$

where  $\Phi_s(x)$  is the front- and back-surface potential and  $\Phi_{gs} = V_{gs} - V_{FBF}$  is the front gate voltage  $V_{gs}$  minus the flat-band voltage,  $V_{FB}$ . Since the potential at the center of the fin,  $\Phi_c(x)$ , is the most relevant to SCE, we extract a relationship between  $\Phi_c(x)$  and  $\Phi_s(x)$  from

substituting  $y = \frac{t_{si}}{2}$  as follows:



(2.2)

$$\Phi_s(x) = \frac{1}{1 + \frac{\epsilon_{ox}}{4\epsilon_{si}} \frac{t_{si}}{t_{ox}}} \left( \Phi_c(x) + \frac{\epsilon_{ox}}{4\epsilon_{si}} \frac{t_{si}}{t_{ox}} \Phi_{gs} \right)$$

Expressing  $\Phi(x, y)$  as a function of  $\Phi_c(x)$  we obtain:

$$\Phi(x, y) = \left( 1 + \frac{\epsilon_{ox}}{\epsilon_{si}} \frac{y}{t_{ox}} - \frac{\epsilon_{ox}}{\epsilon_{si}} \frac{y^2}{t_{ox} t_{si}} \right) \left( \frac{\Phi_c(x) + \frac{\epsilon_{ox}}{4\epsilon_{si}} \frac{t_{si}}{t_{ox}} \Phi_{gs}}{1 + \frac{\epsilon_{ox}}{4\epsilon_{si}} \frac{t_{si}}{t_{ox}}} \right) - \left( \frac{\epsilon_{ox}}{\epsilon_{si}} \frac{y}{t_{ox}} \Phi_{gs} - \frac{\epsilon_{ox}}{\epsilon_{si}} \frac{y^2}{t_{ox} t_{si}} \Phi_{gs} \right)$$

Substituting 2.7 back in 2.3 we get:

$$\frac{d^2 \Phi_c(x)}{dx^2} + \frac{\Phi_{gs} - \Phi_c(x)}{\lambda^2} = \frac{qN_A}{\epsilon_{si}}$$

where natural length  $\lambda$  is now written:

$$\lambda = \sqrt{\frac{\epsilon_{si}}{2\epsilon_{ox}} \left( 1 + \frac{\epsilon_{ox}}{4\epsilon_{si}} \frac{t_{si}}{t_{ox}} \right) t_{si} t_{ox}}$$

## :Quadruple-gate SOI MOSFET:

The original publication on the natural length concept analyzes single- and double-gate structures only. The concept can, however, be extended to quadruple-gate devices with a square cross section by noting that  $\frac{d^2\Phi}{dy^2} = \frac{d^2\Phi}{dz^2}$  in the center of the device, where the influence of the electric field lines from the drain on the device body is the strongest. In that case the Poisson equation becomes:

$$\frac{d^2\Phi(x, y, z)}{dx^2} + 2\frac{d^2\Phi(x, y, z)}{dy^2} = \frac{qN_a}{\epsilon_{si}}$$

and the natural length is equal to:

$$\lambda_4 = \sqrt{\frac{\epsilon_{si}}{4\epsilon_{ox}}} t_{ox} t_{si}$$

In the case cylindrical surrounding gate device similar kind of calculation using the laplacian operator in cylindrical coordinate system with the help of the fact that the potential must be cylindrically symmetric with respect to the axis of the cylindrical channel can be found to be

$$\lambda_o = \sqrt{\frac{2\epsilon_{si} t_{si}^2 \ln\left(1 + \frac{2t_{ox}}{t_{si}}\right) + \epsilon_{ox} t_{si}^2}{16\epsilon_{ox}}}$$



The following observations can be made: the natural length (and hence short-channel effects) can be reduced by decreasing the gate oxide thickness, the silicon film thickness and by using a high-k gate dielectric instead of  $\text{SiO}_2$ . In addition, the natural length is reduced when the number of gates is increased. In very small devices, the reduction of oxide thickness below 1.5 nm causes gate tunneling current problems. Using multi-gate devices, it is possible to trade a thin gate oxide for thin silicon film/fin thinning since  $\lambda$  is proportional to the product  $t_{\text{si}} \times t_{\text{ox}}$ .

The concept of an “equivalent number of gates” ( $ENG$ ) can be introduced at this stage. It is basically equal to the number of gates (a square cross section is assumed) but is also equal to the number that divides  $\frac{\epsilon_{\text{si}}}{\epsilon_{\text{ox}}} t_{\text{si}} t_{\text{ox}}$  in the equations defining the natural length,  $\lambda$ . Thus we have  $ENG=1$  for a single-gate FDSOI MOSFET,  $ENG=2$  for a double-gate device and  $ENG=4$  for a quadruple-gate MOSFET.  $ENG=3$  for a triple-gate device and, by some strange twist of fate,  $ENG$  is close to  $\pi$  in a  $\Pi$ -gate device. In the  $\Omega$ -gate device the value of  $ENG$  ranges between 3 and 4 depending on the extension of the gate under the fin.

## Conclusion:

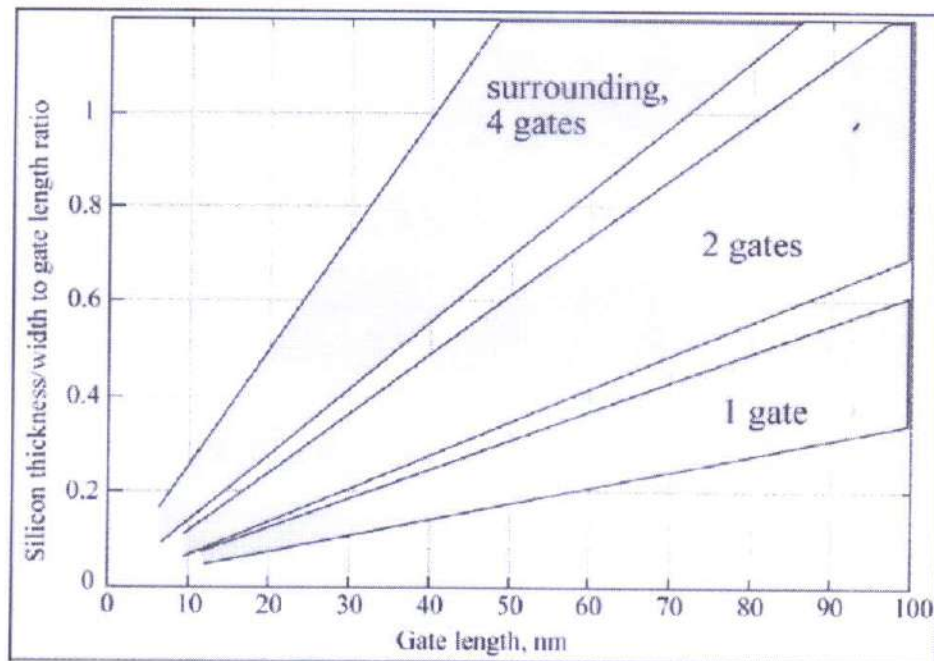


Fig. Maximum allowed silicon film thickness and device width vs. gate length to avoid short channel effects

The natural length can be used to estimate the maximum silicon film thickness and device width that can be used in order to avoid short-channel effects. Figure above shows the maximum allowed silicon film thickness (and device width in a triple-gate device with a square cross section) to avoid short-channel effects. The calculation assumes a gate oxide thickness of 1.5 nm. It reveals that for a gate length of 50 nm, for instance, the thickness of the silicon film in a single-gate, fully depleted



device needs to be 3 to 5 times smaller than the gate length. If a double-gate structure is used, the requirements on silicon film thickness are more relaxed and the film needs to be thinned to only half the gate length. Further relaxation is obtained using a surrounding-gate structure, where the silicon film thickness/width/diameter can be as large as the gate length. The film thickness requirements for triple-gate,  $\Pi$ -gate and  $\Omega$ -gate devices are located between those for double-gate and surrounding-gate devices.

## ACKNOWLEDGEMENT

I acknowledge with pleasure the support of Dr. Sourav Chattopadhyay, Assistant Professor of Department of Physics, Ramakrishna Mission Residential College Narendrapur. Under his supervision, I have completed my project report. I thank Dr. Malay Purkait, H.O.D. of Department of Physics of RKMRC Narendrapur, for supporting me at every step. This project has been very insightful and I consider myself lucky to be a part of it.





## References:

1. FinFETs and Other Multi-Gate Transistors, J.P.Colinge (Springer Publication).
2. Integrated Electronics, Millman.Halkias.
3. Short –Channel Effects in MOSFETs, Fabio D'Agostino.Daniele Quercia(December 11<sup>th</sup>,2000)
4. Wikipedia



RAMAKRISHNA MISSION  
RESIDENTIAL COLLEGE

(AUTONOMOUS)

PHASE TRANSITION  
AND  
LOSCHMIDT ECHO

(UNDER THE GUIDANCE OF DR. ATANU RAJAK)

QUANTUM PHYSICS

ALIPRIYO HOORY

ROLL NO. - PHUG/116/17





**Ramakrishna Mission Residential College (Autonomous)**

**Vivekananda Centre for Research**

**Ramakrishna Mission Ashrama**

(A Branch Centre of Ramakrishna Mission, Belur Math, Howrah-711202)

**Narendrapur, Kolkata - 700 103, West Bengal, India**

A Scientific Industrial Research Organisation, Recognised by DST, Govt. of India

College with Potential for Excellence (CPE), Re-accredited by NAAC - 'A' (CGPA 3.56 out of 4)

---

## **DEPARTMENT OF PHYSICS**

### **Certificate**

This is to certify that Alipriyo Hoory, a student of B.Sc has successfully completed the project of UG curriculum entitled "Phase Transition and Loschmidt Echo" in the period from January to May, 2020.

*Malay Purkait*  
.....  
30.06.2020.

**Signature Of HOD**

**Dept. of Physics**

Dr. Malay Purkait  
Associate Prof. & Head  
Department of Physics  
Ramakrishna Mission Residential College  
(Autonomous)  
Narendrapur, Kolkata-700 103 (W.B.)

## Acknowledgement Letter

To  
The Head of the Department  
Physics Department  
Ramakrishna Mission Residential College  
Narendrapur, Kolkata-700103

Dear Colleague,

This is to inform you that your student Mr. Alipriyo Hoory has done his UG project under my supervision. He has worked with me from September, 2019 to June, 2020. His project title was "Phase transition and Loschmidt Echo". Alipriyo did his project work sincerely. I wish him every success in his future career.

Date: 10/10/2020

Thanking you,  
Alipriyo Hoory  
ALIPRIYO HOORY  
PHUG/116/17

Regards  
Yours sincerely

*Atanu Rajak*

Dr. Atanu Rajak  
Assistant Professor  
Department of Physics  
Presidency University  
86/1 College Street  
Kolkata-700073



## ABSTRACT

We first review the exact solution of the transverse field Ising model in one-dimension. We then study the transition of a qubit from a pure state to a mixed one when it is coupled with an environment modeled as a transverse field Ising model. In this context, we have calculated Loschmidt echo and have shown that the environment affects the system maximally at the quantum critical point.

## CONTENTS :

|                                       |    |
|---------------------------------------|----|
| • <u>INTRODUCTION</u> .....           | 1  |
| • <u>TRANSVERSE ISING MODEL</u> ..... | 2  |
| • <u>LOSCHMIDT ECHO</u> .....         | 5  |
| • <u>CONCLUSION</u> .....             | 10 |
| • <u>REFERENCES</u> .....             | 11 |

## 1. INTRODUCTION :

A quantum phase transition is zero temperature transition of a quantum many body system. It is quantum fluctuations which causes transitions at zero temperature. This fluctuation arises from a non-commutating term of quantum Hamiltonian. By tuning a non-thermal parameter attached to the non-commutating part of the Hamiltonian, the different phases of the system can be traversed. These phases are separated by the phase boundaries.

A few physical quantities show drastic changes in their behavior when a critical point is crossed. The singularities of these quantities at the critical points are dictated by the critical exponents. These exponents characterize a quantum critical point. At a quantum critical point the Hamiltonian of the system  $H(\lambda) = H_0 + \lambda H_1$  where  $H_0$  and  $H_1$  do not commute. Now the energy gap  $\Delta_\lambda$  between ground state and first excited state at second order phase transition point vanishes for an infinite size system. The energy gap  $\Delta_\lambda$  vanishes with the parameter  $\lambda$  as it approaches critical point is  $\lambda_c$ .  $\Delta_\lambda \propto |\lambda - \lambda_c|^{\nu z}$ , Where  $\nu, z$  are the correlation length and dynamical exponents respectively. In a continuous phase transition there is two length scales i.e length of the system and the correlation length  $\xi$ . Correlation length determine a length scale which the system is spatially correlated. The correlation length diverges with the critical exponent  $\nu$  as the system tends to the critical point

$$\xi \propto |\lambda - \lambda_c|^\nu$$

Up to now we describe the behavior of the phase transition at zero temperature only, but for the general we now discuss the effect of finite temperature on quantum phase transitions. There are two type of fluctuations which causes the phase transition (i) classical (ii) Quantum. The larger strength of the fluctuations which are determined by critical exponents plays the role to determine the characterization of the phase transition. Below the graph describes behaviour of the system near quantum critical point.



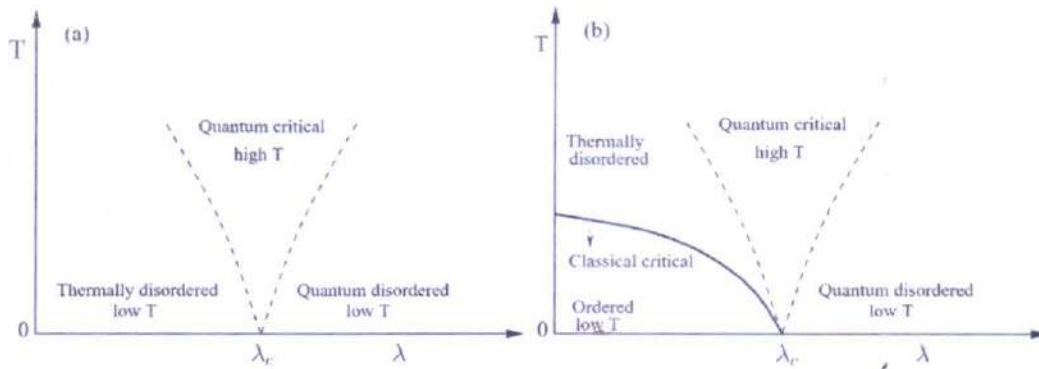


**Figure 1.1: Schematic of two possible phase diagrams close to a quantum critical point. Fig. (a) represents the case where a non-vanishing order parameter exists only at  $T = 0$ , for example, the one-dimensional transverse field Ising model (TFIM) with  $\lambda$  defining as the transverse field. The other case is shown in Fig. (b) representing that order can exist even at finite temperature, for example, the two-dimensional TFIM. The solid curve in Fig. (b) corresponds to the phase boundary. The above graph is taken from Atanu Rajak, Dynamics and quantum information studies of quantum many body systems, Res. Develop 2015**

In this project, we first solve one-dimensional quantum Ising model exactly and then discuss the behavior of the Loschmidt echo for this system. The concept of the Loschmidt echo has been proposed in connection to this quantum-classical transition in quantum chaos to describe the hypersensitivity of the time evolution of a system to the perturbation experienced by its surrounding. we shall introduce the notion of the Loschmidt echo connecting it to the decoherence in the vicinity of a quantum critical point . In this context, the central spin model where a central spin or a qubit is coupled globally to all the spins of an environment will be introduced. In the real world, a physical system can never be isolated; the interaction between the quantum system and its environment leads to decoherence. The decoherence is a process through which the quantum-classical transition occurs by a reduction from a pure state to a mixed state i.e become a entangled state. Entanglement is one of the most fascinating features of quantum mechanics and plays a central role in quantum information processing .

## **2. TRANSVERSE ISING MODEL :**

The Ising model features a lattice with nearest neighbour interaction determined by the alignment and anti-alignment of spin projections along z axis and as well as an external magnetic field perpendicular to the z axis ( without loss of generality here is in x axis) which creates an energetic bias for one x axis spin direction over the other. The two spin of x and z axis are non-commuting observable quantities.

For one dimension has phase transition only at  $T_c = 0$  with  $\lambda = \lambda_c$ . Therefore this is clear that it can't be observabed at any real experiment as because attend of  $T=0$  k till now not possible. Although for two dimensional ising model there exist such system which has ordered state at finite temperature. But in this transition it is dominated by thermal fluctuations. Thus proves that quantum phase transition is only possible at 0 k. Now we will briefly discuss the zero temperature phase diagram of a one dimension on transverse ising model in presence of three spin interaction. The Hamiltonian of the Transverse ising model

$$H = -\frac{1}{2} \sum_{n=1}^N [\sigma_n^z (h(n)) + J_x(n) \sigma_n^x \sigma_{n+1}^x] \quad (1)$$

Where  $\sigma_n^x$  and  $\sigma_n^z$  are the usual Pauli spin matrices at each site  $n$ ,  $J_x(n)$  is the site dependent coupling constant of the nearest neighbor ferromagnetic interaction in  $x$  direction. We impose periodic boundary condition is  $\sigma_{n+N}^x = \sigma_n^x$  this model. This transformation reduces all the quatric terms of the Hamiltonian into quadratic in terms of the spinless fermions.

We now introduce two operators  $\sigma_n^+ = (\sigma_n^x + i\sigma_n^y)/2$  and  $\sigma_n^- = (\sigma_n^x - i\sigma_n^y)/2$  which are called spin raising and lowering operators respectively. They act on the spin states as  $\sigma^+ |\downarrow\rangle = |\uparrow\rangle$  and  $\sigma^- |\uparrow\rangle = |\downarrow\rangle$  Using these operators the Hamiltonian (1) takes the form

$$H = -\frac{1}{2} \sum_{n=1}^N [h(n) \sigma_n^z + J_x(n) (\sigma_n^+ \sigma_{n+1}^+ + \sigma_n^+ \sigma_{n+1}^- + \sigma_n^- \sigma_{n+1}^+ + \sigma_n^- \sigma_{n+1}^-)] \quad (2)$$

It is important to note that the spin raising and lowering operators satisfy a complicated commutation relations, i.e., commute on different sites and follow anti-commutation relations on same site :

$$\begin{aligned} [\sigma_m^+, \sigma_n^-] &= [\sigma_m^+, \sigma_n^+] = [\sigma_m^-, \sigma_n^-] = 0 \text{ for } m \neq n \\ \{\sigma_m^+, \sigma_n^-\} &= 1, \{\sigma_m^-, \sigma_n^-\} = \{\sigma_n^+, \sigma_n^+\} = 0, \end{aligned} \quad (3)$$

These operators  $\sigma_m^+$  are not ordinary bosonic operator. This are hard-core constraint  $(\sigma_m^+)^2 |0\rangle = 0$ , i.e., at most one boson is allowed in each site. The hard-core constraint seems to be ideally representable in terms of spinless fermions  $C_n^+$ , where the absence of double occupancy is automatically enforced by the Pauli exclusion principle, and the anticommutation on the same site comes for free.

$$\begin{aligned} \sigma_n^- &= e^{[i\pi \sum_{j=1}^{n-1} c_j^\dagger c_j]} c_n = \prod_{j=1}^{n-1} (-\sigma_j^z) c_n \\ \sigma_n^+ &= e^{[-i\pi \sum_{j=1}^{n-1} c_j^\dagger c_j]} c_n^\dagger = \prod_{j=1}^{n-1} (-\sigma_j^z) c_n^\dagger \\ \sigma_n^z &= 2C_n^+ C_n - 1 \end{aligned} \quad (4)$$

We can observe from Eq. (4) that the spin operators are related with the fermionic operators by a phase term, can be called a "Jordan-Wigner string". This string actually takes care the fermionic nature of the  $c$ -particles for different sites. In terms of the JW fermions the Hamiltonian in Eq. (2) can be expressed as



$$\begin{aligned}
H = & -\frac{1}{2} \sum_{n=1}^N h(n) (2C_n^\dagger C_n - 1) \\
& - \sum_{n=1}^{N-1} J_x(n) (C_n^\dagger C_{n+1} + C_n^\dagger C_{n+1}^\dagger + H.c.) + J_x(N) (C_N^\dagger C_1 + C_N^\dagger C_1^\dagger + \\
& H.c.) e^{[i\pi \sum_{n=1}^N C_n^\dagger C_n]}
\end{aligned} \tag{5}$$

The only tricky point has to do with the boundary conditions. If one uses periodic boundary conditions, both the sum runs over  $n=1, \dots, N$  and there is a term involving site  $N+1=1$ . All the boundary terms contain an exponential factor which is nothing but parity of the system. Parity of the system is defined as

$$P = \exp [i\pi \sum_{n=1}^N C_n^\dagger C_n] = \prod_{n=1}^N (-\sigma_n^z) \tag{6}$$

Now the parity operator commutes with the Hamiltonian.  $[H, P] = 0$ . Now putting the boundary condition to the spinless fermions for both the sectors: for periodic boundary conditions ( $C_{n+N} = C_n$ ),  $P = -1$  and anti-periodic boundary conditions ( $C_{n+N} = -C_n$ ),  $P = 1$ . Finally both the Hamiltonians in Eq. (6) can be written in the compact form

$$H^\pm = -\frac{1}{2} \sum_{n=1}^N [h(n) (2C_n^\dagger C_n - 1) - J_x(n) (C_n^\dagger C_{n+1} + C_n^\dagger C_{n+1}^\dagger + H.c.)] \tag{7}$$

For the homogeneous case ( $h(n) = h$  and  $J_x(n) = J_x$ ) the model in Eq. (7) is translationally invariant and so, momentum is a good quantum number here. Then we can define Fourier transform of the fermion operators as

$$C_n = 1/\sqrt{N} \sum_k c_k e^{ink} \quad \text{and} \quad c_n^\dagger = 1/\sqrt{N} \sum_k c_k^\dagger e^{-ink} \tag{8}$$

Using Eq. (8) both the Hamiltonians (7) can be simplified as

$$\begin{aligned}
H = & -\frac{1}{2} \sum_{k>0} [2(h + J_x \cos k) (C_k^\dagger c_k + \\
& C_{-k}^\dagger c_k) + 2i(J_x \sin k) (C_k^\dagger C_{-k}^\dagger + \\
& c_k c_{-k}) - h]
\end{aligned} \tag{9}$$

The Hamiltonian in Eq. (9) decouples as a direct sum of independent terms for each  $k$ , thus gets reduced to the direct product of decoupled  $2 \times 2$  Hamiltonians for each momentum  $k$ , which in the basis  $|0\rangle$  (vacuum state) and  $|k, -k\rangle$  (two JW fermion state) can be written as,

$$H_k(h) = \begin{pmatrix} h + \cos k & J_x \sin k \\ J_x \sin k & -h - \cos k \end{pmatrix}$$

Since the Hamiltonian (9) is quadratic in terms of  $c$  fermions, one can diagonalize it using Bogoliubov transformation defined as

$$\begin{aligned}
c_k &= \cos(\theta_k/2) b_k + i \sin(\theta_k/2) b_{-k}^\dagger \\
c_{-k} &= \cos(\theta_k/2) b_{-k} - i \sin(\theta_k/2) b_k^\dagger
\end{aligned} \tag{10}$$

where  $b_k$ 's are Bogoliubov fermionic operators and  $\theta_k$  is defined as

$$\tan \theta_k = \frac{J_x \sin k}{h + J_x \cos k} \tag{11}$$

After Bogoliubov transformation, the diagonalized Hamiltonian can now be written as with the corresponding eigen energy for the  $k$ -th mode as

$$H = \sum_k \epsilon_k (b_k^\dagger b_k - 1/2) \tag{12}$$

$$\epsilon_k = (h^2 + J_x^2 + 2hJ_x \cos k)^{1/2} \tag{13}$$

The Hamiltonian in Eq. (12) represents a system of non-interacting fermions  $b_k$  which are called quasiparticles. To excite a quasiparticle mode  $b_k$ , the system requires  $\epsilon_k$  amount of energy. The ground state  $|\psi\rangle$  of the model is one without any quasiparticles, i.e., the vacuum

state of  $b_k$  fermions. It is now convenient to express  $|\psi\rangle$  in terms of the  $c$ -fermions. In this form  $|\psi\rangle$  is given by

$$|\psi_0\rangle = \prod_{k>0} b_k b_{-k} |0\rangle \tag{14}$$

Where  $|0\rangle$  is the vacuum state of  $c$ -fermions satisfying  $C_k|0\rangle = 0$  for each  $k$ . Eq. (14) actually represents the ground state of the system since application of annihilation operator  $b_k$  on it gives in fact zero. Now considering the inverse transformations of Eq. (10) and imposing the normalization condition  $\langle \psi | \psi \rangle = 1$  we obtain

$$|\psi_0\rangle = \prod_{k>0} \cos(\theta_k/2) + i \sin(\theta_k/2) c_k^\dagger c_{-k}^\dagger |0\rangle \tag{15}$$

### 3. LOSCHMIDT ECHO:

The notion of the Loschmidt echo dates back to J. Loschmidt (1876) in the context of the microscopic theory of the second law of thermodynamics. This is in contrast to the Boltzmann's proposal for the impossibility of a perfect time-reversal experiment which leads to an "arrow of time"; therefore, for a macroscopic system entropy should always increase. The Loschmidt echo can also be interpreted from the perspective of a time reversal scenario. In this viewpoint, we evolve the initial wave function  $|\psi_0\rangle$  with the Hamiltonian  $H_1$  forward in time up to  $t$ . For simplicity, we shall again choose  $|\psi_0(t)\rangle$  to be an eigenstate of the Hamiltonian  $H_1$ . One then arrives at the wave function:  $|\tilde{\psi}(t)\rangle = e^{-iH_1 t} |\psi_0(t)\rangle$ . Thereafter, we



consider a time reversed process with a modified Hamiltonian<sup>1</sup>  $H_2$ . Setting  $t \rightarrow -t$ , one gets (the time reversed) the final state:  $|\psi_f(t)\rangle = e^{iH_2 t} e^{-iH_1 t} |\psi_0(t)\rangle$ . One can therefore define the Loschmidt echo as the overlap

$$\mathcal{L}(t) = |\langle \psi_0 | e^{-iHt} | \psi_0 \rangle|^2 \quad (16)$$

since,  $|\psi_0(t)\rangle$  is an eigenstate of  $H_1$ . Clearly, the overlap measures the probability of the survival of the initial state in the final time reversed state. The quantification of the Loschmidt echo requires a Hamiltonian  $H$  that makes the evolution of the ground state  $|\psi_0\rangle$  non-trivial. This Hamiltonian  $H$  can be generated considering a central spin model in which a central spin  $S$  is coupled globally to an environmental spin model  $E$ . In this regard, we will study here the transition of the central spin  $S$  from a pure state to a mixed one induced by the criticality of the environmental spin system and show that the decay of the LE is best enhanced by the Quantum phase transition of the surrounding environment and (described earlier). We will provide here a general formalism for calculating the LE considering a three-spin interacting Transverse field ising model defined in Eq. (1) as an environment ( $E$ ) that is coupled to a central spin-1/2 (qubit)  $S$ . We shall denote the ground state and excited state of the central spin  $S$  by  $|g\rangle$  and  $|e\rangle$  respectively.

Now the Hamiltonian can be written in the form,

$$H_T(h, \delta) = -\frac{1}{2} \sum_{n=1}^N [\sigma_n^z (h(n)) + \delta \sigma_n^z \sigma_S^z + J_x(n) \sigma_n^x \sigma_{n+1}^x] \quad (17)$$

where  $\sigma_S^z$  denotes the Pauli matrix of the qubit and  $\delta$  is the coupling strength of  $S$  to  $E$ . Here we ignored  $J_3$  term from eq (1) for simplicity. As all the operator commutes only in his site so we can prove  $[\sigma_S^z, H_T] = 0$  which signifies that  $\sigma_S^z$  is constant in motion. So there is no exchange of energy between system and the bath. The above condition ensures that in this case the qubit evolution is purely decoherent.

Now we can simplify as a  $H_T = H + H_1$  where  $H$  is a Hamiltonian of the environment as described in eq (1), excluded  $J_3$  term and  $H_1$  is the perturbing term. The global coupling between the CS and the  $E$  is represented by the Hamiltonian:  $H_{SE} = \delta |e\rangle\langle e| H_1$ , such that whenever the central spin is in the  $|e\rangle$  state the environmental spin chain's Hamiltonian gets modified to  $H'_E = H_0 + (h + \delta) H_0$ . Similarly we can get evolved Hamiltonian for ground state. Hence, depending on the state of the CS, the  $E$  evolves with two different Hamiltonians,  $H_E(h) = H_g$  and  $H'_E(h + \delta) = H_e$ . we shall work in the weak coupling limit,  $\delta \rightarrow 0$ . Owing to this, the evolution of the  $E$  initially prepared in the ground state  $|\phi(0)\rangle$  gets divided into two channels, (a)  $|\phi_g(t)\rangle = e^{-iH_g t} |\phi(0)\rangle$ , and (b)  $|\phi_e(t)\rangle = e^{-iH_e t} |\phi(0)\rangle$ . We can now explore the evolution the total wave function (i.e., CS plus the  $E$ ) influenced by the state of the CS. At  $t = 0$ , the CS and the  $E$  are un-entangled and hence the initial state is a direct product state at  $t = 0$ , given by:  $|\psi(0)\rangle = (C_g |g\rangle + C_e |e\rangle) \otimes |\phi_g(t)\rangle$ . However, the evolution of the state  $|\psi(0)\rangle$  of the  $E$  is dictated by two Hamiltonians due to the coupling with the CS; hence, the total wave function of the composite system at time  $t$  becomes:  $|\psi(t)\rangle = (C_g |g\rangle \otimes |\phi_g(t)\rangle) + (C_e |e\rangle \otimes |\phi_e(t)\rangle)$ . One can now obtain the density matrix  $\rho(t)$  for the total wave function at time  $t$  as

$$\begin{aligned}
\rho(t) &= |\psi(t)\rangle\langle\psi(t)| \\
&= |C_g|^2 |g\rangle\langle g| \langle\phi_g(t)|\phi_g(t)\rangle + C_g C_e^* |g\rangle\langle g| \langle\phi_g(t)|\phi_e(t)\rangle \\
&\quad + C_e C_g^* |e\rangle\langle e| \langle\phi_e(t)|\phi_g(t)\rangle + |C_e|^2 |e\rangle\langle e| \langle\phi_e(t)|\phi_e(t)\rangle
\end{aligned} \tag{18}$$

Once we have obtained the final state density matrix at time  $t$ , as shown in Eq. (18), we can trace out the  $E$  to extract the information about the state of the CS at the final time  $t$ . Therefore, we obtain the reduced density matrix by taking the partial trace over the  $E$  states as:

$$\begin{aligned}
\rho_S = \text{Tr}_E \rho(t) &= \begin{pmatrix} |C_g|^2 & C_g C_e^* D(t) \\ C_e C_g^* D^*(t) & |C_e|^2 \end{pmatrix}
\end{aligned} \tag{19}$$

In the above equation,  $D(t) = \langle\phi_g(t)|\phi_e(t)\rangle$  is the 'decoherence factor'

One therefore finds the decay of the Loschmidt echo given by

$$\begin{aligned}
\mathcal{L}(t) &= |\langle\phi_g(t)|\phi_e(t)\rangle|^2 \\
&= |\langle\phi(0)|e^{-iH_g t} e^{-iH_e t}|\phi(0)\rangle|^2 \\
&= |\langle\phi(0)|e^{-iH_E(h+\delta)t}|\phi(0)\rangle|^2
\end{aligned} \tag{20}$$

we have used the fact that the  $|\phi(0)\rangle$  is an eigenstate of the Hamiltonian (17) with anisotropy parameter  $\lambda$ .

As mentioned already, the Hamiltonian (1) can be solved by using the JW transformation followed by the Bogoliubov transformations and can be written in the form

$$\begin{aligned}
H_E(h) &= \sum_k \epsilon_k(h) (b_{k,g}^\dagger b_{k,g} - 1/2) \\
H_E(h+\delta) &= \sum_k \epsilon_k(h+\delta) (a_{k,e}^\dagger a_{k,e} - 1/2)
\end{aligned} \tag{21}$$

Where  $b_{k,g}$  and  $a_{k,e}$  are Bogoliubov fermionic operators

And the energy spectrum of excited state are given by

$$\epsilon_k(h(n) + \delta) = (h(n) + \delta)^2 + J_x^2 + 2hJ_x \cos k \tag{22}$$

clearly,  $\epsilon_k(h+\delta) = \epsilon_k(h)$  with  $\delta = 0$ . In fact, under the JW transformation the Hamiltonian (17) gets reduced to the direct product of decoupled  $2 \times 2$  Hamiltonians for each momentum  $k$ , which in the basis  $|0\rangle$  (vacuum state) and  $|k, -k\rangle$  (two JW fermion state) can be written as

$$H_k(h) = \begin{pmatrix} h + \cos k & J_x \sin k \\ J_x \sin k & -h - \cos k \end{pmatrix}$$



The Bogoliubov operators are related to the JW operators through the relation

$$a_{k,e} = \cos\theta_k(h + \delta)c_k - i \sin\theta_k(h + \delta)c_{-k}^\dagger \quad (24)$$

$$b_{k,g} = \cos\theta_k(h)c_k - i \sin\theta_k(h)c_{-k}^\dagger$$

where,  $c_k$  are the Fourier transform of the JW operators as derived through the JW transformations of spins. Using Eq. (23), one can further arrive at a relation connecting the Bogoliubov operators of the two Hamiltonians as:

$$b_{k,g} = \cos\gamma_k a_{k,e} - i \sin\gamma_k a_{-k,e}^\dagger$$

$$\text{Where } \gamma_k = \frac{\theta_k(h) - \theta_k(h + \delta)}{2}$$

Now the ground state of both the Hamiltonians can be solved by putting the Bogoliubov operators in  $b_{k,g}|\phi(0, h)\rangle = 0$  and  $a_{k,e}|\phi(0, h + \delta)\rangle = 0$  and by normalize it we can get

$$|\phi(0, h)\rangle = \prod_{k>0} \cos\gamma_k + i \sin\gamma_k a_{k,e}^\dagger a_{-k,e}^\dagger |\phi(0, h + \delta)\rangle \quad (25)$$

Now putting eq (25) in eq (20) we get

$$\begin{aligned} \mathcal{L}(t) &= |\langle \phi(0, h) | e^{-iH_e t} | \phi(0, h) \rangle|^2 \\ &= |\langle \phi(0, h + \delta) | \prod_{k>0} (\cos\gamma_k - i \sin\gamma_k a_{k,e} a_{-k,e}) e^{-iH_e t} \prod_{k>0} (\cos\gamma_k + i \sin\gamma_k a_{k,e}^\dagger a_{-k,e}^\dagger) | \phi(0, h + \delta) \rangle|^2 \\ &= \prod_{k>0} |\cos^2\gamma_k + \sin^2(\gamma_k) e^{-2i\epsilon_k(h+\delta)t}|^2 \\ &= \prod_k [1 - \sin^2(2\gamma_k) \sin^2(\epsilon_k(h + \delta)t)] \end{aligned} \quad (26)$$

Since each factor  $\mathcal{L}(t)$  in Eq (26) has a norm less than unity, we may well expect  $\mathcal{L}(t)$  to decrease to zero in the large N limit under some reasonable conditions. Now we study in detail the critical behavior of the surrounding system near the critical point  $\lambda_c = 1$  and its relation to the sensitive evolution of the Loschmidt Echo perturbed by the central system even for a finite N. This turns out to reveal a novel mechanism responsible for the enhanced decay of Loschmidt Echo. Let us first make a heuristic analysis of the features of the Loschmidt Echo. For a cut-off frequency  $k_c$  we define the partial product for the Loschmidt Echo.  $\mathcal{L}_c(t) \geq \mathcal{L}(t)$ .

Now putting anisotropic parameter  $\lambda$  in equation (17) we can write  $(h(n) + \delta) = J(\lambda + \delta)$  so eq (22)

$$\epsilon_k = 2J[(\lambda + \delta)^2 + 1 - 2(\lambda + \delta) \cos(ka)]^{\frac{1}{2}} \quad (27)$$

Let us define,  $\mathcal{L}_c(\lambda, t) = \prod_{k>0}^{k_c} F_k \geq \mathcal{L}(\lambda, t)$  and corresponding partial sum  $S(\lambda, t) = \ln \mathcal{L}_c(t)$

$$= -\prod_{k>0}^{k_c} \frac{|\ln F_k|}{(\delta k a)^2} . \text{ Now , for small } k \text{ wave vector } \epsilon_k(h + \delta) \approx 2J|1 - \lambda - \delta| \text{ and } \sin^2(2\gamma_k) \approx \frac{(1-\lambda)^2(1-\lambda-\delta)^2}{(1-\lambda)^2(1-\lambda-\delta)^2} .$$

Now putting this values in the partial sum we get

$$S(\lambda, t) \approx \frac{\delta^2 \sin^2(2J|1 - \lambda - \delta|t) E(k_c)}{(1 - \lambda)^2(1 - \lambda - \delta)^2}$$

Where  $E(k_c) = \prod_{k>0}^{k_c} (ka)^2$  Now using the bloch wave vector , i.e  $k = \frac{2n\pi}{Na}$

$$= \prod_{n>0}^{N_c} \frac{4n^2\pi^2}{N^2 a^2} a^2 = \frac{4\pi^2 N_c(N_c+1)(N_c+2)}{6N^2}$$

Where  $N_c$  is the nearest integer to  $\frac{NK_c a}{2\pi}$ . Now this follows can be approximated to  $\mathcal{L}_c(\lambda, t) \approx \exp(-\Omega t^2)$  when  $\lambda \rightarrow \lambda_c = 1$ , where  $\Omega = \frac{\delta^2 E(k_c) 4J^2}{(1-\lambda)^2}$

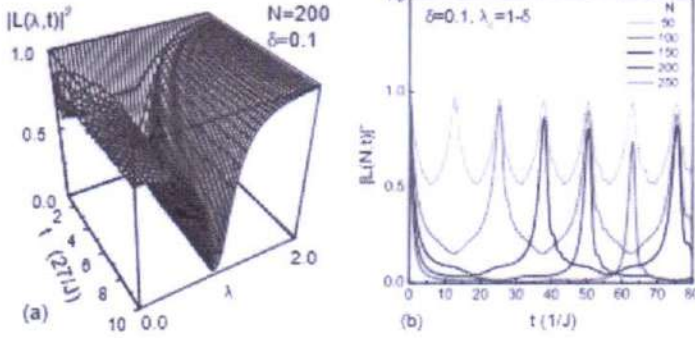


FIG. 2: (Color online) (a) Three dimensional (3-D) diagram of the LE  $|L(\lambda, t)|^2$  as the function of  $\lambda$  and  $t$  for the system with  $N = 200$ . The valley around the critical point  $\lambda_c=1$  indicates that the decay of LE is enhanced by the QPT. The profile at  $\lambda = 1$  is in agreement with the analytical analysis. (b) The cross sections of the 3-D surface for the systems of  $N = 50, 100, 150, 200$ , and  $250$  at  $\lambda = \lambda_c - \delta = 0.9$ . It shows that the quasi-period of the LE is proportional to the size of the surrounding system.

So from the above heuristic analysis we may expect that, when  $N$  is large enough and  $\lambda$  is adjusted to the vicinity of the critical point  $\lambda_c = 1$ , the LE will exceptionally vanish with time. On the other hand, we observe that  $\gamma$  seems to approach zero in the thermodynamic limit  $N \rightarrow \infty$  for  $Na$  keeps as a constant in the process of taking this limit and  $E(k_c) \propto 1/N^2$ . Since a true QPT can occur just in the thermodynamic limit, it is natural to doubt whether the QPT, and thus the induced decay of the LE, can happen at the critical point. In fact, due to the vanishing denominator  $(1 - \lambda)^2$  of  $\Omega$  at the critical point of the QPT, the decay of the LE is still possible even for  $\Omega$  having a vanishing numerator. For a practical system used to demonstrate the QPT induced decay of the LE, the particle



number  $N$  is large, but finite, and then the practical  $\Omega$  does not vanish. Now we resort to numerical calculation to test the heuristic analysis. For  $N = 50 \sim 250$ ,  $\delta = 0.1$ , the LE are calculated numerically from the exact expression (8) with the parameters within the ranges  $\lambda \in [0, 2]$ ,  $t \in [0, 27/J]$ , and plot it in the graph. The results are demonstrated in fig 2. The graph was taken from the H.T. Quan, Z. Song, X.F. Liu, P. Zanardi and C.P. Sun, Decay of Loschmidt Echo Enhanced by Quantum Criticality, Res. Develop 2006.

## **4.CONCLUSION:**

In this project we have discussed about transverse ising model and by using exact model we solve the one dimensional spin interaction in presence of transverse field described by the Hamiltonian in eq (1). First we solve the exact solution of the Hamiltonian with the help of Jordan wigner transformation (This transformation reduces all the terms of the Hamiltonian into quadratic in terms of the spinless fermions) and bogoliubov transformation (This transformation used to diagonalize Hamiltonians, which yields the stationary solutions of the corresponding Schrodinger equation).

We have obtained the exact expression of the transverse field and analyzed the possible relation between the quantum-classical transition of the central system, characterized by the Loschmidt echo of the surrounding system, and the occurrence of a Quantum phase transition in its surrounding system Environment Hamiltonian. The time evolution of two qubits immersed in thermal environments. The necessary calculations we performed reveal a novel mechanism of the decay of the LE. We have investigated the effects of system-environment coupling strength. Then we calculate the decoherence between the two states  $\mathcal{L}(t)$  which will tell us how much the states are entangled. It is clear that  $\mathcal{L}(t)$  value is smaller than 1 and it can be tend to 1 for smaller interaction between environment and spin. If the value is 0 the. The effective interaction between environment and spin qubit is maximum. Therefore near quantum critical point the central spin pure state become mixed state due to its maximum Entanglement with the environment, and the decay  $\mathcal{L}(t)$  has minimal value. The novel phenomenon of the synchronization between the QPT and the enhanced decay of the LE mentioned above and its physical implication deserves further exploring. Generally, the two terms in He represent two competitive physical effects with different order tendencies: in the weak coupling case  $\lambda \ll 1$  the ground state is either all spins up or all spins down, while in the strong coupling case  $\lambda \gg 1$  the ground state tends to the saturated ferromagnetic state with all the spins pointing right. When  $\lambda$  takes the value of the order unity, the qualitative properties of the ground states for  $\lambda > 1$  and  $\lambda < 1$  are similar to those for  $\lambda \gg 1$  and  $\lambda \ll 1$  respectively. Only the critical point  $\lambda = 1$  has genuinely different properties. That means the central spin state transforms to pure state to mixed state when a quantum phase transition of E takes place in one of the two evolution branches. This result suggests and unexplored and rather intriguing relationship among engagement Loschmidt echo, decoherence and criticality.

#### **4.REFERENCES:**

H.T. Quan, Z. Song, X.F. Liu , P. Zanardi and C.P. Sun, Decay of Loschmidt Echo Enhanced by Quantum Criticality, Res. Develop 2006

Mean Field Theory Solution of the Ising Model, Franz Utermohlen

Atanu Rajak, Dynamics and quantum information studies of quantum many body systems, Res. Develop 2015

Some notes on the Quantum Ising chain by Giuseppe E. Santoro, SISSA, Trieste, 2013

Subir Sachdev, Quantum phase transition, 2011

R.J Baxter, Exactly Solved Models in Statistical Mechanics, 1989

Fidelity susceptibility and Loschmidt echo for generic paths in a threespin interacting transverse Ising model, A. Rajak and U. Divakaran, J. Stat. Mech., P04023 (2014).



## **Smart Water Tap monitoring system**

*Project Report submitted to the Department of Physics, Ramakrishna Mission Residential College (Autonomous), Narendrapur, Kolkata for the partial fulfilment of the requirements of the degree of*

## **Bachelor of Science (Hons.) in Physics**

Submitted by:

Arghya Jana [Roll No.: PHUG/092/17]  
Pritam Pal [Roll No.: PHUG/110/17]

Semester VI, B.Sc. Physics (Hons.)

University of Calcutta, Kolkata  
2020



**Ramakrishna Mission Residential College (Autonomous)**

**Vivekananda Centre for Research**

**Ramakrishna Mission Ashrama**

(A Branch Centre of Ramakrishna Mission, Belur Math, Howrah-711202)

**Narendrapur, Kolkata - 700 103, West Bengal, India**

A Scientific Industrial Research Organisation, Recognised by DST, Govt. of India

College with Potential for Excellence (CPE), Re-accredited by NAAC - 'A' (CGPA 3.56 out of 4)

---

## **DEPARTMENT OF PHYSICS**

### **Certificate**

This is to certify that Arghya Jana, a student of B.Sc has successfully completed the project of UG curriculum entitled "Smart Water Tap monitoring system" in the period from January to May, 2020.

Malay Purkait  
.....  
30.06.2020

**Signature Of HOD**

**Dept. of Physics**

**Dr. Malay Purkait**  
Associate Prof. & Head  
Department of Physics  
Ramakrishna Mission Residential College  
(Autonomous)  
Narendrapur, Kolkata-700 103, (W.B.)



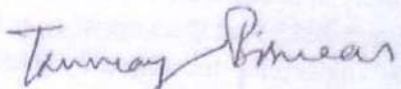
## CERTIFICATE

---

This is to certify that Arghya Jana, student of BSc. 3<sup>rd</sup> year Physics(Hons.) of Ramakrishna Mission Residential College (Autonomous), Narendrapur, Kolkata has successfully completed the project work titled "Smart Water Tap Monitoring System" for the partial fulfilment of the requirements of the degree of Bachelor of Science (Hons.) in Physics.

He has worked under my guidance.

TANMAY BISWAS  
Name of Project Guide

  
Signature of Project Guide



### Acknowledgement

I would like to express my deep sense of gratitude to my respected and learned guide Mr. Tanmay Biswas (Assistant Professor, Department of Electronics) for his valuable guidance in completing this project.

I am also grateful to my respected principal, vice principal and respected Prof. Malay Purkait, (HOD, Department of physics) for permitting me all the necessary facilities of the institution. I am also thankful to all other faculty and staff members of our department of their kind cooperation.

Lastly I would like to thank my parents and friends to help me a lot in finishing this project in time.

*Arghya Jana*



### **Abstract**

In the design we have constructed a sensor water tap monitoring system using the components viz arduino board, solenoid valve, SPDT relay, IR sensor etc. The main purpose of this project is to stop wastage of water. We have used the IR Sensor which is connected to a SPDT relay which controls the solenoid valve to control the water flow to the tap. As a result sensor tap is automatically shut off after use.

## **Introduction:**

Water is most precious. Living bodies depend on it. Our responsibility is to conserve it. Nowadays we are interested to be automated. The project titled "sensor Water Tap monitoring system" is the modern version of the traditional hand operated tap. The water taps that we use in our daily life are mechanically operated. Water flows through the tap when we turn on the tap and the flow stops when we turn off the tap. This hand operated tap system causes water loss.

Sensor water taps save water significantly. Sensor water tap is automatically shut off after hand washing and as a result water shortage is reduced. Sensor tap is hygienic, that is very important for us. This tap is more energy efficient than traditional hand operated water tap. In the automatic water tap we use a IR sensor which is connected to a SPDT relay which controls the solenoid valve to control the water flow to the tap [4]. This tap reduced the wastage of water as it is automatically closed after hand washing.

Some related works are:

- Water Quality Monitoring System Based on IOT [1] : In this paper the authors have presented a design and development of a low cost system for real time monitoring of the water quality in IOT. They have measured the physical and chemical properties of water such as temperature, PH, turbidity, flow sensor etc. using sensors and arduino model.
- Design a Smart Faucet for reducing the water wastage using IOT [2] : In this paper the authors have designed a smart water faucet using the components Node MCU, relay, solenoid valve, DC motor, temperature sensor, servo motor for reducing the wastage of water.



## **Proposed Design:**

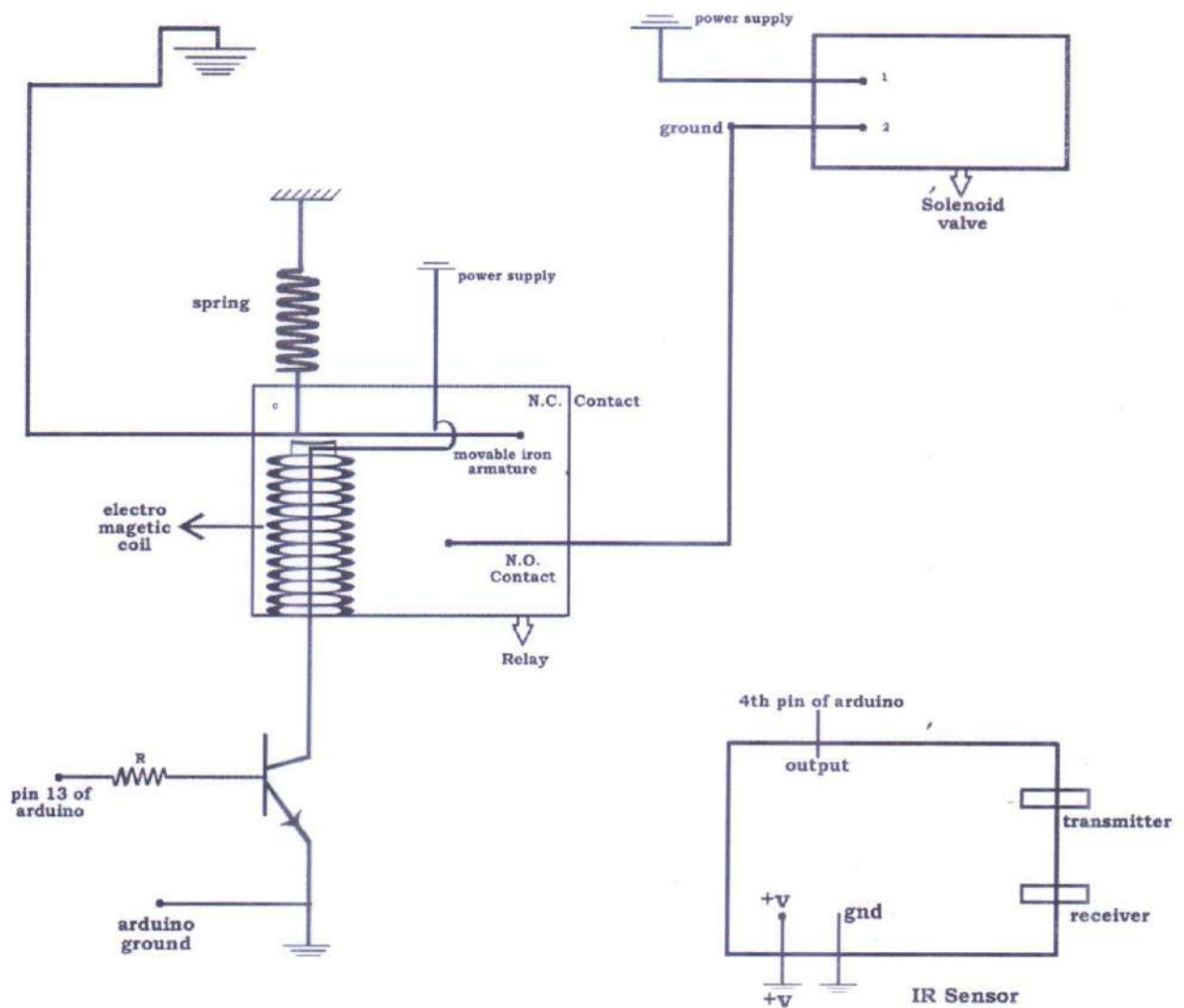
We have designed a sensor water tap monitoring system. Here we have used an infrared sensor in the tap that has a light emitting diode. This LED emits light continuously. When an object or human hand enters into the range of LED, the solenoid valve will be opened, which allows the water to flow through the tap. When the object is removed from the range of LED, the valve will be closed and it stops water running.

## **Implementation:-**

The Components that are required for constructing the sensor water tap monitoring system are

- i) Solenoid Valve
- ii) Single Pole Double Throw (SPDT) relay
- iii) Infra-red sensor
- iv) Arduino board
- v) Power Supply
- vi) Spring
- vii) Resistance
- viii) Electromagnetic coil

Solenoid Valve is an electrically Controlled automatic device. Its basic working Principle is just like as a relay. There are two types of Solenoid Valves i) normally open type and ii) normally closed type. By applying the voltage the state of the solenoid can be changed from open to close or from close to open. Here the normally closed type solenoid valve has two ends. One end is connected to a power supply and the other end is connected to normally open contact, of a relay. Relay's common end is connected to the ground. Its common end, attached with a spring system, is connected with the normally closed



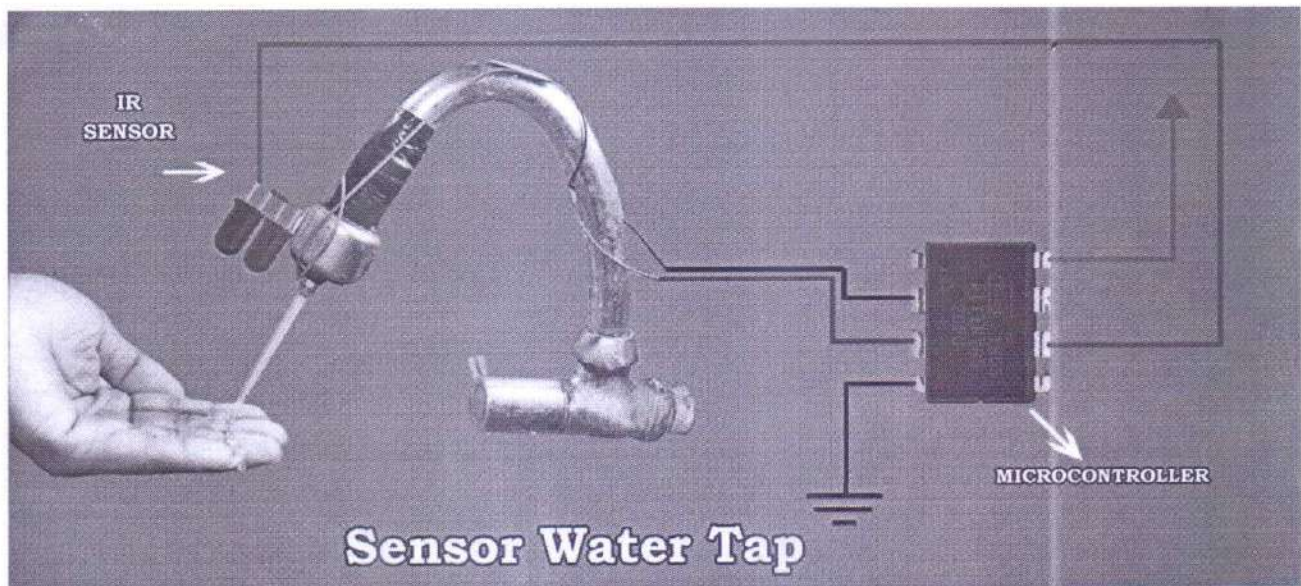
**Block diagram of Sensor water tap Monitoring System**



contact through a movable iron armature. There is an electromagnetic coil; a coil of wire is wound on a soft iron core. One end of this coil is connected to some voltage and the other end of this coil is connected to the ground through a n-p-n transistor. The base of the transistor is connected to a pin of arduino board via some resistance.

Here we used a IR Sensor that has a light emitting diode-IR transmitter continuously emits the light. When some object enters into the range of the LED, the infra-red light signal is reflected by the object and the receiver of the IR sensor receives that light. That's why some voltage will be showed across the receiver. This voltage is automatically supplied by the sensor to that pin of arduino, which is connected to the base of the transistor via some resistance, such that current will flow through the electromagnetic coil and the coil generates a magnetic field through the soft iron core. Due to this the movable iron armature is attracted towards the electromagnetic core and the armature will move to open condition by breaking the normally closed contact condition. Normally open contacts get to closed condition. Then a complete circuit will be formed and the solenoid valve will remain in "on" state. The valve is opened and it allows the water to flow through the tap.

Again, when the object is removed from the range of LED, the receiver of the sensor will not show any voltage and the current flowing through the electromagnetic coil will be switched off, the relay coil gets de-energized then the armature is returned to its original position by the spring system. The armature will move to N.C. contact condition by breaking the N.O. contact condition. Hence the solenoid valve will remain in "off" state. The valve is closed and it stops the water running.



When some object or human hand enters into the range of LED of the IR sensor as shown in fig, which emits the light continuously, the solenoid valve will be opened and that allows the water to flow through the tap. Again when the object is removed from the range of LED, the valve will be closed and it stops water running.



## **Result:**

The sensor water tap monitoring system plays important role in the following fields:

- Significant water saving:

Electronic taps are generally constructed to get much lower stream rate than the traditional hand operated taps. Hand operated taps can use up to 10-15 liters of water per minute whereas the sensor tap offers flow rates of water as little as 2 liters per minute. Sensor tap is automatically shut off after hand washing and hence water wastage is reduced.

- Hygienic:

Sensor tap doesn't require to touch - it is hygienic.

- Cleaner and more efficient:

In case of sensor taps the flow rate is predetermined whereas for hand operated taps the user can choose their preferred flow rate every time. This is very inefficient. Prefixing the flow rate helps to reduce splashing.

- More energy efficient:

Sensor taps need electricity for their operation while the traditional hand operated taps don't require any electricity in order to work. Every time a traditional hand tap expends a great deal of energy by choosing the user's preferred water flow and temperature. But in case of sensor taps water always remain at a constant temperature, so energy is not expended by changing the water temperature. So sensor taps are more energy efficient than hand taps.

### **Application:**

Sensor water tap monitoring system is extremely valuable in home, old age home, hotel, school, office, shop, nursing home, hospital, industrial application, eatery etc.

### **Conclusion:**

Due to this sensor water tap monitoring system our life style has been quite automated. Due to significant progress in science and technology, we are approaching an era of artificial intelligence and consequently the interaction between man and machines gets reduced. The sensor water tap is such a machine that has reduced the human labor mostly. We can implement this method in the public water podium stands which eliminates the usage of water taps, which are extremely inefficient. This automated system is very helpful in everyday life specially for physically handicapped, patients and elderly people. It gives them a safe and independent living by providing the tap automation. It is also very helpful in conservation of water which can be efficiently implemented in garden, park etc.



## Reference

1. Vaishnavi V. Daigavane and Dr. M.A. Gaikwad.
2. LalithMohon S, Kavinprabhu L, Jayaseelan T, Naveen Kumar V, Suresh babu Y, (International Journal of Recent Technology and Engineering). Volume - 8 Issue - 6, March 2020.
3. Automatic tap control system in the smart home using android and arduino-Vani K.S. and Shrinidhi P.C. International Journal of computer application - volume 127-No-8, October 2015.
4. Programmingdigest.com

***Android Based Smart Body-Temperature Monitoring and Recording System***

*A project report submitted to Ramakrishna Mission Residential College  
(Autonomous) for the partial fulfilment of award of the degree of*

**Bachelor of Science (Honours)**

Submitted by

**Arunabha Mondal**

**Subrata Maiti**

Roll- PHUG/113/17

and

Roll- PHUG/218/17

(Reg. No.: A03-1112-0113-17)

(Reg. No.: A03-1112-0218-17)



**Department of Physics**

**Ramakrishna Mission Residential College (Autonomous)**

**University of Calcutta**





**Ramakrishna Mission Residential College (Autonomous)**

**Vivekananda Centre for Research**

**Ramakrishna Mission Ashrama**

(A Branch Centre of Ramakrishna Mission, Belur Math, Howrah-711202)

**Narendrapur, Kolkata - 700 103, West Bengal, India**

A Scientific Industrial Research Organisation, Recognised by DST, Govt. of India

College with Potential for Excellence (CPE), Re-accredited by NAAC - 'A' (CGPA 3.56 out of 4)

---

## **DEPARTMENT OF PHYSICS**

### **Certificate**

This is to certify that Arunabha Mondal, a student of B.Sc has successfully completed the project of UG curriculum entitled "Android Based Smart Body-Temperature Monitoring and Recording System" in the period from January to May, 2020.

*Malay Purkait*  
.....  
30.06.2020

**Signature Of HOD**

**Dept. of Physics**

**Dr. Malay Purkait**

Associate Prof. & Head

Department of Physics

Ramakrishna Mission Residential College

(Autonomous)

Narendrapur, Kolkata-700 103, (W.B.)

Mr. Tanmay Biswas


Assistant Professor

Ramakrishna Mission Residential  
College (Autonomous)  
Narendrapur, Kolkata-700103

## CERTIFICATE OF APPROVAL

Date: 1 July, 2020

This is to certify that the project report entitled "**Android Based Smart Body-Temperature Monitoring and Recording System**" has been done under my supervision at the Department of Physics, Ramakrishna Mission Residential College (Autonomous). I also endorse that this work submitted by **Arunabha Mondal** (Reg. No: A03-1112-0113-17) is original and has not been submitted to any other University for the award of any Degree or Diploma. I therefore, recommend the project work for the award of **Bachelor of Science (Honours) in Physics**.

  
(Mr. Tanmay Biswas)



## ACKNOWLEDGEMENT

*The successful completion of the project would not be possible without the help and support of the following people.*

*We would like to take the opportunity to thank and express our gratitude to our project supervisor Mr. Tanmay Biswas (Assistant Professor, Department of Electronics). He did support us at every stage of the project. Every time we would come up with a new idea or modification to the existing project, he would patiently listen and correct our approach and most importantly support our idea.*

*We would also like to thank The Department of Physics, Ramakrishna Mission Residential College (Autonomous) in particular and the college in general for providing us the platform to create and present a project.*

*We would like to thank all the teachers of The Department of Physics whose simplified explanation and continued support in academics made it possible for us to understand the subjects properly and focus on the applicability of the subjects.*

*Last but not the least, we would take the privilege to thank our parents and both our sisters and all our friends for their valuable inputs.*

*We hope that we can build upon the experience and knowledge gathered during the development of this project and make a valuable contribution towards our College.*

*Arunabha Mondal*

Arunabha Mondal

*Subrata Maiti*

Subrata Maiti

## ABSTRACT

*The spirit behind this project was to address the challenges posed to educational institution reopening after lifting of lockdown situation imposed due to the CoVID-19 pandemic. Such institutions can be opened only after assurance of regular and thorough check-up of CoVID symptoms like high body-temperature. But the facilities available nowadays mostly involve human participation like use of hand-held temperature guns, etc. In this era of automation, our aim was to build a device with requisite sensors installed on an Arduino platform, whose working can be controlled by an Android. Thus refraining human contact, this device will measure the body temperature of the student and record it.*

*Keywords- Arduino Uno, sensors, actuators, Bluetooth module, microcontroller, MLX90614 sensor, HCSR04 sensor, mobile app.*



## ACKNOWLEDGEMENT

*The successful completion of the project would not be possible without the help and support of the following people.*

*We would like to take the opportunity to thank and express our gratitude to our project supervisor Mr. Tanmay Biswas (Assistant Professor, Department of Electronics). He did support us at every stage of the project. Every time we would come up with a new idea or modification to the existing project, he would patiently listen and correct our approach and most importantly support our idea.*

*We would also like to thank The Department of Physics, Ramakrishna Mission Residential College (Autonomous) in particular and the college in general for providing us the platform to create and present a project.*

*We would like to thank all the teachers of The Department of Physics whose simplified explanation and continued support in academics made it possible for us to understand the subjects properly and focus on the applicability of the subjects.*

*Last but not the least, we would take the privilege to thank our parents and both our sisters and all our friends for their valuable inputs.*

*We hope that we can build upon the experience and knowledge gathered during the development of this project and make a valuable contribution towards our College.*

# CONTENTS

|                                                              | Page No. |
|--------------------------------------------------------------|----------|
| 1. Introduction                                              | 1        |
| 1.1 Using Arduino Uno as the Programmable Automaton          | 1        |
| 1.1.1 Architecture of the Uno board                          | 2        |
| 1.2 Prototype Requirements                                   | 3        |
| 1.3 Components                                               | 3        |
| 1.3.1 Sensors and Actuators                                  | 3        |
| 1.3.2 Streaming real-time data                               | 4        |
| 1.3.3 Communication                                          | 5        |
| 1.3.4 Mobile Application                                     | 6        |
| 2. Objectives                                                | 6        |
| 2.1 Flowchart Diagram representation of the Objective        | 7        |
| 3. Model Classroom for the Project                           | 8        |
| 4. Methodology                                               | 8        |
| 4.1 Electronic Design                                        | 8        |
| 4.2 Programming on Arduino IDE                               | 9        |
| 4.3 Receiving and recording the data from Arduino into Excel | 9        |
| 4.4 Creating the Mobile App to control from our mobiles      | 10       |
| 5. Budget                                                    | 11       |
| 6. Expected Result                                           | 11       |
| 7. Applications                                              | 12       |
| 8. Conclusion                                                | 13       |
| 9. Reference                                                 | 14       |



## 1. INTRODUCTION

The year 2020 had been sadly shadowed by the CoVID-19 pandemic. Till now no vaccine has been discovered. Hence Governments and health organizations are coming together to find alternative solutions. Throughout the world, all countries are mostly abiding by the standard regulations set by the World Health Organization to fight this pandemic. The most common precautions used are Social Distancing, testing, hand-sanitizing and increased awareness among individuals.

Even after the Lockdown, which is prevalent in our country, is lifted, regular monitoring of symptoms (eg. Body-temperature) is to be carried out. Say for example, automatic monitoring and registering of body temperature of students attending an educational institute, automatic measurement of temperature of guests visiting relatives, automatic monitoring of customers visiting banks, malls, boarding public transport, etc.

In our project, we have developed a device of *Automated Monitoring and Registering Body-Temperature of Individuals* attending any public infrastructure through *a Unique ID* using an Arduino board and sensors and a Mobile App.

### 1.1 Using Arduino Uno as the Programmable Automaton

The boost in DIY stuff among people of various professions, who know little or nothing about electronics or coding, be it engineers, artists, hobbyists, students, etc. lead to the birth of Arduino, an open-source software and hardware company [1]. Several Arduino boards, with microcontroller chips installed on them, are available which can be used to create DIY projects, home-automation and large scale automatic control systems [2],[3]. Among the several Arduino boards available, Arduino Uno is the most popular because of its easy availability, low cost, sufficiently varied availability of Digital I/O pins and Analog Input pins, sufficient Flash Memory, SRAM and EEPROM for general to high-end purposes [4].

Hence, keeping in mind all these facilities, we will be using an Arduino Uno board as the local controller of our Project.

### 1.1.1 Architecture of the Arduino Uno board

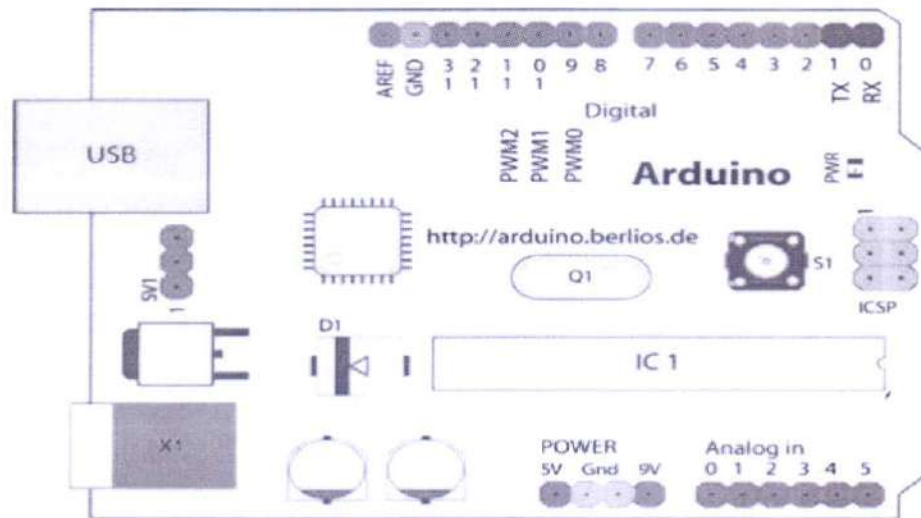


Fig 1.1: Diagram of the Arduino Uno board [5].

The basic components and features of the Arduino Uno board are discussed as follows:

- **Microcontroller ATmega328P**- This is a single-chip microcontroller created by Atmel. It combines 23 general purpose I/O lines, 32 general purpose working registers, three flexible timer/counters with compare modes, internal and external interrupts, serial programmable USART, a byte-oriented 2-wire serial interface, SPI serial port, 6-channel 10-bit A/D converter (8-channels in TQFP and QFN/MLF packages), programmable watchdog timer with internal oscillator, and five software selectable power saving modes. It is the brain of the Uno development platform [6]. It is designated as IC 1 in Fig 1.1.
- **Pins**- There are 14 Digital I/O pins (of which 6 provide PWM output). They are labelled from 0-13 designated by green coloured pins on the top of Fig 1.1.  
There are 6 Analog Input pins marked from 0-5 in blue-colour in the bottom-right of Fig 1.1.
- **Flash Memory**- 32 KB ISP flash memory (ATmega328P) with read-while-write capabilities, of which 0.5 kb is used by the bootloader.
- **SRAM**- 2 kb (ATmega328P).
- **EEPROM**- 1 kb (ATmega328P).
- **Operating Voltage**- 5V
- **Input Voltage (recommended)**- 7-12V
- **Input Voltage (limit)**- 6-20V
- **DC Current per I/O Pin**- 20 milliAmperes



- DC Current for 3.3V Pin- 50 milliAmperes
- Clock Speed- 16 MHz.
- Length- 68.6 mm
- Width- 53.4 mm
- Weight- 25g.

## 1.2 Prototype Requirements

The main soul of our Prototype is the *Arduino Uno board* which will act as the local controller of our automation system. Two sensors are required namely *MLX90614* and *HCSR04* which are non-contact IR temperature sensor and ultrasonic distance sensor respectively. A *Bluetooth module HC-05* is used for communication between the mobile phone and the Arduino Uno board. A *16X2 LCD Display* is used as an actuator to interact with the user along with a *potentiometer* to control the contrast of the display of the LCD.

## 1.3 Components

### 1.3.1 Sensors and Actuators

- *MLX90614*- This is an infrared thermometer for non-contact temperature measurements built by Melexis Corporation [7].

Features-

- Temperature Range: -40 to 125°C for sensor temperature and -70 to 380°C for object temperature.
- Accuracy: 0.5°C accuracy over a wide range of temperature.
- SMBus compatible digital interface for fast temperature readings and building sensor networks.
- Customizable PWM output for continuous reading.

- *HCSR04*- This is a non-contact ultrasonic distance measurement sensor [8].

Features-

- Working voltage: 5V
- Working current: 15 milliAmperes
- Working frequency: 40 Hz

- Measurement Range: 2cm to 4m
- Measurement accuracy: 3mm
- Trigger Input Signal: 10Us TTL pulse
- Echo Output Signal: Input TTL lever signal and the range in proportion.

➤ 16X2 LCD Display Module- This is an Actuator. LCD stands for Liquid Crystal Display. It has 16 columns and 2 rows and can display a total of 32 characters [9].

#### Features-

- Pins: A total of 16 Pins
- Operating voltage: 4.7V to 5.3V
- Current Consumption: 1 milliAmpere without backlight

### 1.3.2 Streaming real-time data

Several microcontrollers are available that give various data as output. This output can be recorded and visualized in an Excel workbook. To do so, software like PLX-DAQ by Parallax Inc [10], add-ins like Data Streamer Add-In for MS Excel is available. These help to import data from the connected device to an Excel workbook. We will be using MS Data Streamer Add-In since Microsoft is the most popular OS in India.

Steps to be followed to install MS Data Streamer: [11]

- We can download Microsoft Data Streamer from the link below-  
<https://www.microsoft.com/en-us/download/details.aspx?id=56976>
- It is installed by following standard installation process for Windows.
- Next we open MS Excel.
- We go to File Menu and then click on "Excel Options".
- On the left, there will be an option called "Add-Ins". We click on it.
- Under Manage, we click on the drop-down button and select "COM Add-Ins". We click on "Go".
- The COM Add-Ins dialog box will appear with the list of available Add-Ins installed on our PC. We select the "Microsoft Data Streamer for Excel" and then finally click on "OK".

A physical connection has been set up between the MS Excel and Arduino Uno. MS Excel is now ready to store data obtained from the board.



### 1.3.3 Communication

#### ➤ Bluetooth Communication

Bluetooth enables the transmission of data and voice between different devices through a radiofrequency link in the 2.4 GHz ISM band [12]. All Bluetooth devices have a unique address of 48 bits and a device name that allows the identification of each other. Devices that incorporate this protocol can communicate with one another when within its reach. The communications are by radiofrequency so that the devices do not have to be aligned and can even be in separate rooms if the transmission power is sufficient. These devices are classified as Class 1, Class 2 and Class 3 depending on the transmission power. There are two types of Bluetooth modules compatible with Arduino: HC-05 and HC-06. Both are of Class 2 type and hence their range is 10 metres [13]. For several governing factors we will be using the HC-05 module.

#### ➤ HC-05 Bluetooth Module [14]-

##### Main Features-

- Configurable as Slave and as Master
- Radio Chip: CSR BC417143
- Frequency: 2.4 GHz ISM band
- Modulation: GFSK (Gaussian Frequency Shift Keying)
- Built-in PCB antenna
- Emission Power:  $\leq 4\text{dBm}$  (Class 2)
- Range: 10 metres
- Speed: Asynchronous- 2.1 Mbps/160 kbps; Synchronous- 1Mbps/1 Mbps
- Security: Authentication and Encryption
- Profiles: Serial port Bluetooth
- Current consumption: 50 milliAmperes
- Supply voltage: 3.6V-6V
- Operation temperature: 20°C-75°C

#### **1.3.4 Mobile Application**

Mobile phones have become an existential need of today's society. Every pocket has a mobile phone and every mobile phone has several apps to perform various tasks. Our project is based on automation where we need some medium to receive the input from the user that will trigger the process. What could be better than a mobile app as mobile apps are available to almost everyone? Earlier creating mobile apps was upon Software developers who knew how to code. But with the increase in demand of creating more and more apps, several software have been developed that allow users to create Mobile-based applications without knowing to code.

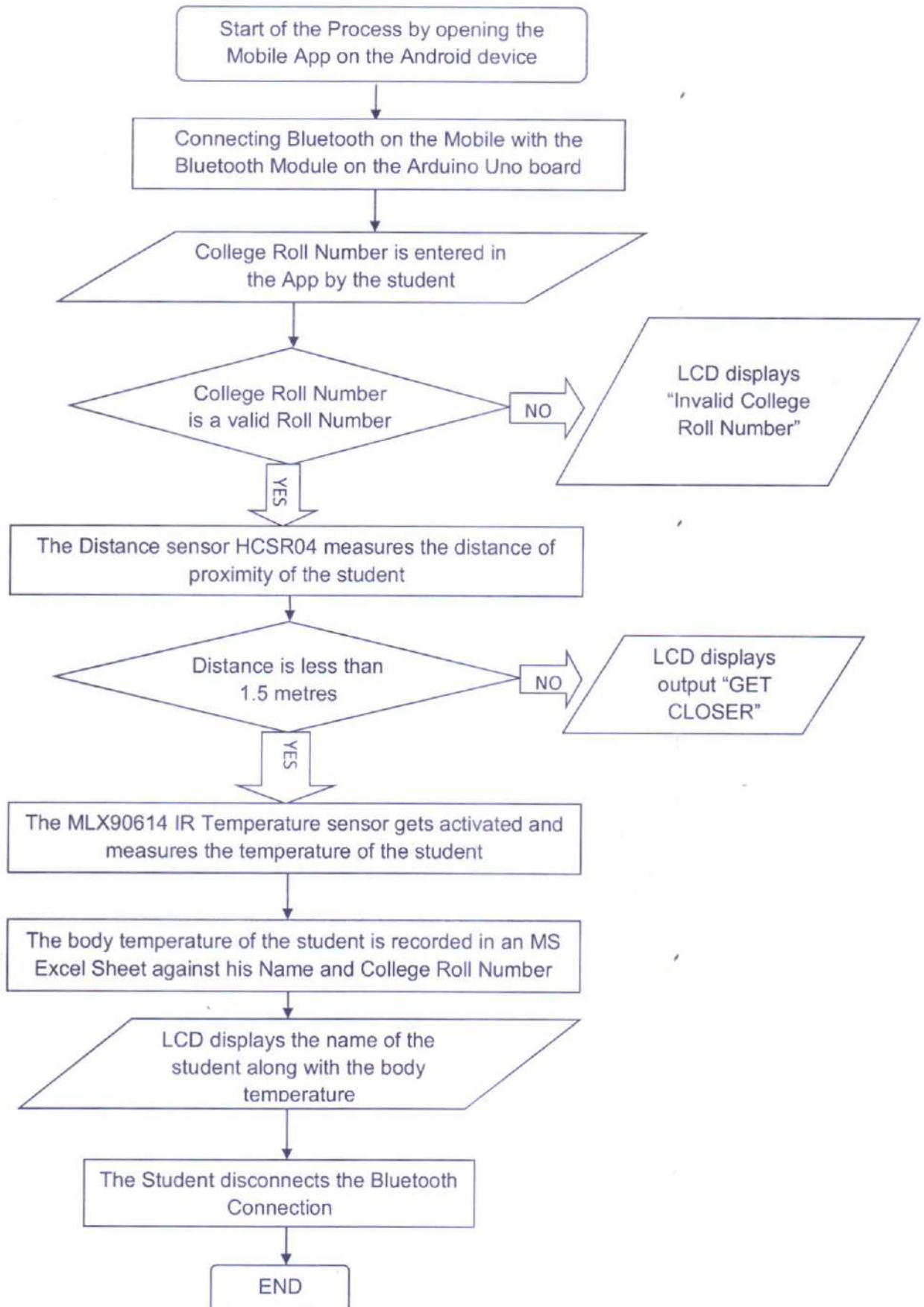
For our purpose too, we will be using such software that allows us to create an app. We will be using the Web application MIT App Inventor, originally provided by Google and now maintained by the Massachusetts Institute of Technology (MIT). It is free and open-source and allows creation of apps for Android and IOS.

## **2. OBJECTIVE**

Our objective while building this prototype was to build a device which will be installed at the door of our classroom. All students will have to install an official application for Android (to be created) on their Mobile phones (available at Google Play Store). They will then have to connect their phone with the device through Bluetooth. During an ongoing academic semester, the College Roll Number of each student is unique. The student then enters his unique Roll Number in the app and it automatically triggers the device to measure the body-temperature of the student and records this data on a Computer in MS Excel. In doing so, the attendance of the student too is recorded and hence teachers need not devote time in Roll-calling. Thus we will be able to upgrade our smart-class to fight CoVID-19.



### 2.1 Flowchart Diagram representation of the Objective:



### 3. MODEL CLASSROOM FOR THE PROJECT

As our model classroom, we will take our class- 3<sup>rd</sup> year Physics Honours classroom in the Department of Physics (Room Number- 2.2) on the 1<sup>st</sup> floor of Ramakrishna Mission Residential College (Autonomous) Main College Building. Our class consists of 26 students, each with a unique College Roll Number.

### 4. METHODOLOGY

#### 4.1 Electronic Design

The Schematic Design of our automation device is given below:

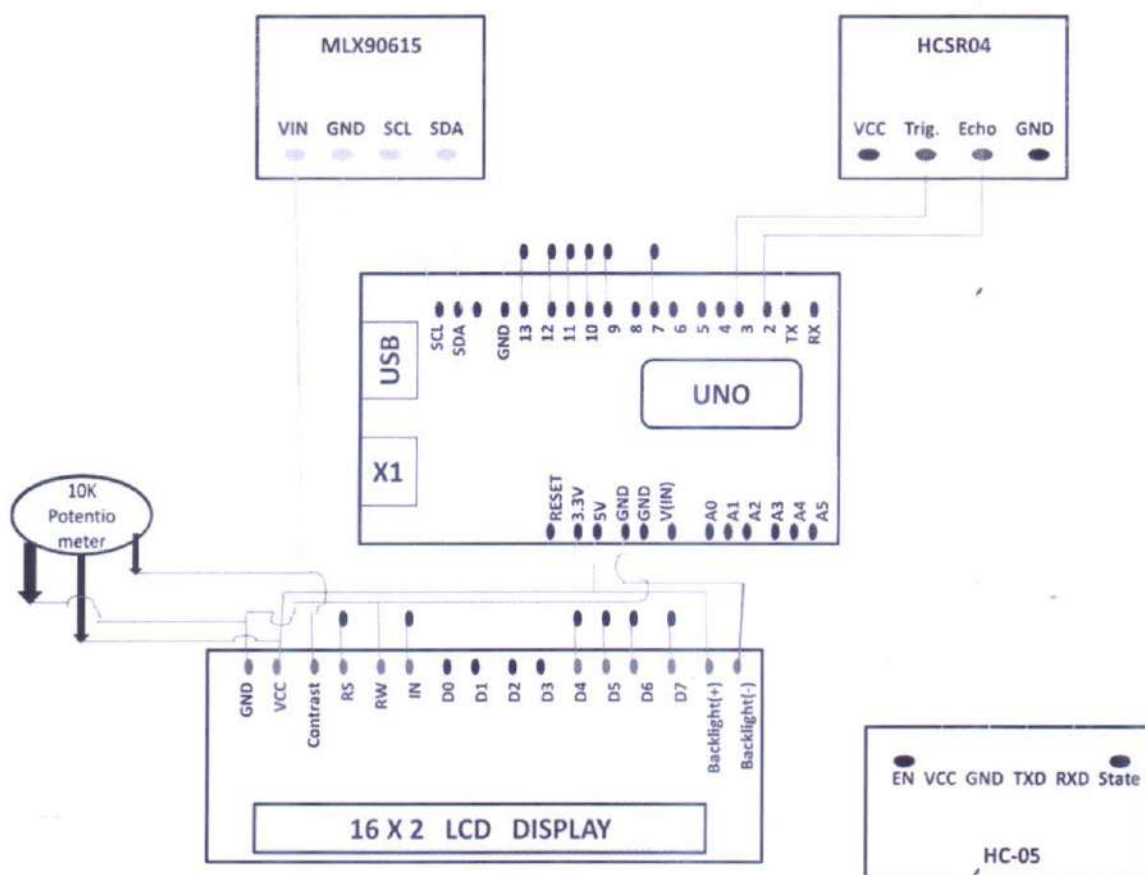


**Fig. 4.1:** Schematic Diagram of the proposed device. Orange lines represent wires connecting MLX90614 to Arduino Uno. Blue lines represent wires connecting HCSR04 to Arduino Uno. Yellow lines represent wires connecting HC-05 module to Arduino Uno. Green lines represent wires connecting LCD to Arduino Uno and potentiometer to LCD display.



## 4.2 Programming in Arduino IDE

The Arduino Integrated Development Environment (IDE) is a cross-platform application (for Windows, macOS, Linux) and is open-source that is written in functions from C and C++. It will be used by us to write and upload the program onto the Arduino Uno board. The uploaded program, called sketch, will instruct the ATmega328P microcontroller chip to perform the task desired by us.

## 4.3 Receiving and recording the data obtained from Arduino into Excel [15]

The sensor installed on the device will record the temperature of the student. Now the data needs to be stored on MS Excel. Note that the following steps are in accordance with Microsoft 365.

If Data Streamer has been installed, the Excel ribbon will contain a new "Data-Streamer" Tab.

- Step 1:- We first click on the "Data-Streamer". This contains all the primary controls for the add-in.
- Step 2:- We connect a Data Source (in our case the Data Source is the Arduino Uno). We then click on "Connect a Device" and select Arduino Uno in the sub-ribbon that appears.
- Step 3:- We go to the "Advanced" option. In the prompt that appears, we go to "Settings".
- Step 4:- Under Settings, we change the 'Number of Data Rows' from the 'default 15' to 'the total number of students in the Class i.e., 26 in our sample classroom'.
- Step 5:- We then change the 'Number of data channels' from the 'default 20' to the number of different types of data columns we will be requiring.
- Step 6:- We then give value to the 'Data delay (ms)' as 60000 ms (i.e., 1 min) so that each student registers only 1 data on the Excel sheet and then has sufficient time to disconnect the Bluetooth connection with the Bluetooth module.
- Step 7:- We select 'Newest last' option for 'Data orientation'. With this, all setting up has been done and now it's time to stream data from the data source.
- Step 8:- Once we are ready to receive data, we click on "Start Data" option under the Excel ribbon. The data received will be visible in the below format-

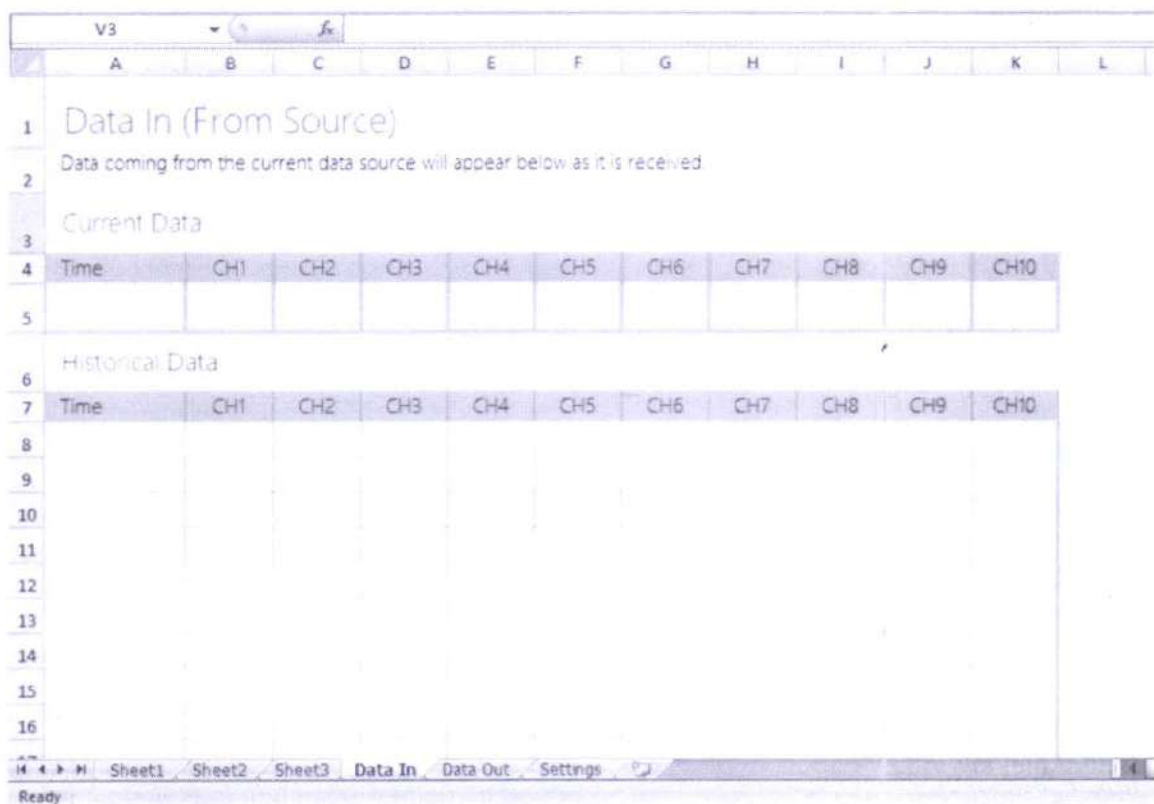


**Fig. 4.2: Screen view of an Excel workbook ready to record data [16].**

#### 4.4 Creation of the Mobile Application [17]

The app is needed to relay the input trigger from the student. The app will have a field where the student needs to enter his College Roll Number. On entering this data, the app will recognize the student, measure his temperature and store it against his name in MS Excel.

- To create the app, first we go to <http://beta.appinventor.mit.edu/>. We will see a blank projects page (if visiting for the first time) or the created projects list (if already some projects have been created).
- We then click on "New" on the top-left and in the dialog box, enter the name of the project. Finally clicking "OK".
- The "Designer" page opens where we will have to design the look of our App by using the default elements available.
- Next we go to the "Blocks Editor", where we have to specify the flow of control of the app.
- In this way, the app will be created. After all this is done, we can publish the app on Google Play Store.



## 5. BUDGET

The following is the budget overview for building this prototype:

| COMPONENT                   | PRICE | NUMBER OF UNITS  | ABOUT VENDOR        |
|-----------------------------|-------|------------------|---------------------|
| Arduino Uno                 | ₹380  | 1                | Shop in Kolkata     |
| MLX90614 Sensor             | ₹3800 | 1                | Robokits.co.in      |
| HCSR04 Sensor               | ₹99   | 1                | Robu.in             |
| HC-05 Bluetooth Module      | ₹510  | 1                | Amazon.in           |
| 16X2 LCD Display            | ₹105  | 1                | ElectronicsComp.com |
| Potentiometer               | ₹9    | 1                | ElectronicsComp.com |
| Jumper Wires                | ₹50   | 25 (₹2 per unit) | Shop in Kolkata     |
| Total Hardware Cost= ₹ 4953 |       |                  |                     |

Time engaged to write the code on Arduino IDE (approximately) = 8-10 hours

Time engaged to create the Mobile App (approximately) = 18-20 hours

Now, depending on working hour price for developing the software and the Mobile App, the Total Prototype cost will increase.

## 6. EXPECTED RESULTS

The datasheet to be obtained on MS Excel can be expected to be something like the figure below:





## **8. CONCLUSION**

As aimed for in the objectives, we have been able to come up with the electronic design of our device. We have also explained the step-by-step process of installing the MS Excel Add-In. We have also given the synopsis of the program to be uploaded on the Arduino Uno board and the process of developing the Mobile application. Thus we have been able to present an overview of the idea and how to implement it in an actual environment, our objectives have been sufficed.

## 9. REFERENCE

- [1] Kaswan K.S., Singh S.P., Sagar S., "Role of Arduino in real world applications," International Journal of Scientific and Technology Research Volume 9, ISSN 2277-8616, 2020.
- [2] Mallick B. And Patro A.K., "Heart rate monitoring system using fingertip through Arduino and processing software," International Journal of Science, Engineering and Technology Research, vol. 5, no. 1, pp. 82-89, 2016.
- [3] Rubio H., Soriano E. And Barber R., "A low cost lab monitoring system based on Arduino microcontroller and Android," Proceedings of ICEI 2015 Conference, pp. 8014-8022, 2015.
- [4] Louis L., "Working principle of Arduino and using it as a tool for study and research," International Journal of Control, Automation, Communication and Systems, vol. 1, no. 2, pp. 21-29, 2016.
- [5] <https://www.arduino.cc/en/Guide/Board?from=Tutorial.ArduinoBoard> [Accessed 22<sup>nd</sup> Jun, 2020]
- [6] <https://en.m.wikipedia.org/wiki/ATmega328> [Accessed 23<sup>rd</sup> Jun, 2020]
- [7] <https://www.melexis.com/en/product/MLX90614/Digital-Plug-Play-Infrared-Thermometer-TO-Can> [Accessed 25<sup>th</sup> Jun, 2020]
- [8] Zhmud V A, Kondratiev N O, Kuznetsov K A, Trubin V G and Dimitrov L V, "Application of ultrasonic sensor for measuring distances in Robotics," International Conference Information Technologies in Business and Industry, doi: 10.1088/1742-6596/1015/3/032189 (2018).
- [9] <https://components101.com/16x2-lcd-pinout-datasheet> [Accessed 25<sup>th</sup> Jun, 2020].
- [10] [www.parallax.com](http://www.parallax.com) [Accessed 1<sup>st</sup> Jul, 2020].
- [11] <https://support.microsoft.com/en-us/office/enable-the-data-streamer-add-in-70052b28-3b00-41e7-8ab6-8a9f142dffe8> [Accessed 25<sup>th</sup> Jun, 2020].
- [12] Jeong H J, Lim J, Hyun W S and Lee W J, "A remote lock system using Bluetooth communication," Innovative Mobile and Internet Services in Ubiquitous Computing, doi: 10.1109/IMIS.2014.63 (2014).
- [13] Herreros A.M., Sin S.T., "Home automation application based on Arduino controllable from mobile," 2017.



# Review of Higher Moments of Net Proton Multiplicity Distribution Measurement in STAR Experiment at the Relativistic Heavy Ion Collider

B.Sc. 3rd Year Project

By

**Bappaditya Mondal**

College Roll No: PHUG/111/17

REG. No : AO3-1112-0111-17

Supervisor

**Prof. Amal Sarkar**

Department of Physics



Ramakrishna Mission Residential College (autonomous)  
Narendrapur, Kolkata, West Bengal, India- 70013



**Ramakrishna Mission Residential College (Autonomous)**

**Vivekananda Centre for Research**

**Ramakrishna Mission Ashrama**

(A Branch Centre of Ramakrishna Mission, Belur Math, Howrah-711202)

**Narendrapur, Kolkata - 700 103, West Bengal, India**

A Scientific Industrial Research Organisation, Recognised by DST, Govt. of India

College with Potential for Excellence (CPE), Re-accredited by NAAC - 'A' (CGPA 3.56 out of 4)

---

## **DEPARTMENT OF PHYSICS**

### **Certificate**

This is to certify that Bappaditya Mondal, a student of B.Sc has successfully completed the project of UG curriculum entitled "Review of Higher Moments of Net Proton Multiplicity Distribution Measurement in STAR Experiment at the Relativistic Heavy Ion Collider" in the period from January to May, 2020.

*Malay Purkait*  
.....  
30.06.2020

**Signature Of HOD**

**Dept. of Physics**

**Dr. Malay Purkait**

Associate Prof. & Head

Department of Physics

Ramakrishna Mission Residential College

(Autonomous)

Narendrapur, Kolkata-700 103, (W.B.)



## Certification

This is to certify that the project entitled "Review of Higher Moments of Net Proton Multiplicity Distribution Measurement in STAR Experiment at the Relativistic Heavy Ion Collider" by Bappaditya Mandal, a final year B.Sc student of the Department of Physics, RKMRC, Narendrapur Kolkata, completed his project work under my supervision. I wish him every success in his future.

Supervisor Amal Sarkar.

Dr. Amal Sarkar  
Assistant Professor  
Department of Physics  
RKMRC, Narendrapur  
Kolkata, India - 700103

Date: 26/06/2020

Place: Kolkata

## Declaration

I hereby declare that I have not copied anything from any book or any other resources to complete my project work. I have not used any unauthorized data in this work. I have mentioned the references from where the required information have been taken.

Date.....04/07/2020

Sign.....Bappaditya Mondal

(Bappaditya Mondal)



# CONTENTS

|                                                                        |    |
|------------------------------------------------------------------------|----|
| 1. Introduction.....                                                   | 1  |
| 2. Higher Order Moments.....                                           | 4  |
| 2.1 Moment.....                                                        | 4  |
| 2.1.a Skewness.....                                                    | 4  |
| 2.1.b Kurtosis.....                                                    | 4  |
| 2.2 Cumulants.....                                                     | 4  |
| 2.3 Moments and Cumulants in Heavy Ion Collisions.....                 | 5  |
| 2.4 Why Moments and Cumulants Matter.....                              | 5  |
| 2.4.a Baryon Number Susceptibility ( $\chi_B$ ).....                   | 5  |
| 2.4.b Dependence of Cumulants on $\chi_B$ .....                        | 5  |
| 2.4.c Baryon Number Susceptibility ( $\chi_B$ ) at Critical Point..... | 6  |
| 2.5 Relation Between Correlation length ( $\xi$ ) and Cumulants.....   | 6  |
| 2.6 Moments and Cumulants at Critical Point.....                       | 7  |
| 3. Experimental Setup.....                                             | 8  |
| 3.1 Intduction.....                                                    | 8  |
| 3.2 RHIC.....                                                          | 8  |
| 3.3.a Room Temperature Solenoidal Magnet.....                          | 9  |
| 3.3.b Silicon Vertex Tracker (SVT).....                                | 10 |
| 3.3.C Time Projection Chamber.....                                     | 10 |
| 3.3.d Photon Multiplicity Detector (PMD).....                          | 10 |
| 3.3.e Muon Telescope Detector (MTD).....                               | 11 |
| 3.3.f Electromagnetic Calorimeter (EMC).....                           | 11 |
| 3.3.g Time of Flight Detector (TOF).....                               | 11 |
| 4. Result and Analysis.....                                            | 12 |
| 5. Summary and Conclusion.....                                         | 15 |

## Chapter 1

### Introduction

One of the important physics goals of high energy physics is to examine the properties of quark gluon plasma (QGP) and to scan the QCD phase diagram in order to search **critical point**. First, it will be good to discuss what is QCD, why it is important and what about the QCD phase diagram.

All the visible matter (which is almost 4% of the whole universe) around us is made of protons and neutrons. These nucleons are also made of tiny quarks and gluons (basic building blocks of matter). At low temperature quarks and gluons are in confined state and together they form proton (uud) and neutron (udd). Strong force (one of the four fundamental forces) comes to play an important role to bind quarks and gluons to form hadrons (baryon and meson). The dynamics that deals with strong force and its properties is called **Quantum Chromo Dynamics (QCD)**. When the temperature is too high (more than billion times the temperature of the sun) the quarks and gluons can't stay in a confined (in hadrons) state. The value of coupling constant decreasing with increasing energy (this behavior is known as **asymptotic freedom of QGP**) indicates that at higher energy quarks and gluons become deconfined (free) creating a plasma like (ideal liquid) state with quarks and gluons degrees of freedom. This state of matter is called **QCD matter**.

Just after the **Big Bang** there had been no proton and neutron, only free quark and gluon (QCD matter) was there for a for a very short period of time (less than a billionth of a second). As the temperature cools down freely moving quarks and gluons were getting confined to form protons, neutrons and other subatomic particles. And till now (13 billion year after the Big Bang) they (quarks and gluons) still remain inseparable around us.

In **RHIC** (Relativistic heavy ion collider) Au ions collide at very high energy to smash the nucleons to create QGP. As a result of this, scientists are able to go back in time to recreate QGP (the state of matter that was believed to exist 13 billion years ago).

Here in this paper, we will discuss about the properties of QCD matter, more specifically about the possible signature of critical point. A possible QCD phase diagram is given in Fig. 1.

QCD phase diagram depends on two parameters – temperature (**T**) and baryonic chemical potential ( **$\mu_B$** ). Theory suggests that at  **$\mu_B=0$**  there occurs a crossover transition from hadronic matter to deconfined state of quarks and gluons [1]. Also, at **T=0** there is a first order phase transition between these two states [2]. If this is the case, then we can also claim that there must exist a critical point between these two transitions (cross over transition and first order phase transition). To find the critical point, scientists scan the phase diagram (that means to change  **$\mu_B$**  and **T**)

- Baryonic chemical potential ( **$\mu_B$** ) changes with  $\sqrt{s_{NN}}$  energy [3] (center of mass energy) as 
$$\mu_B = \frac{N_B}{E}.$$



- Temperature changes with the size of ions participate in the collision. But Scanning in  $\sqrt{s_{NN}}$  is easier than changing the size of ions.

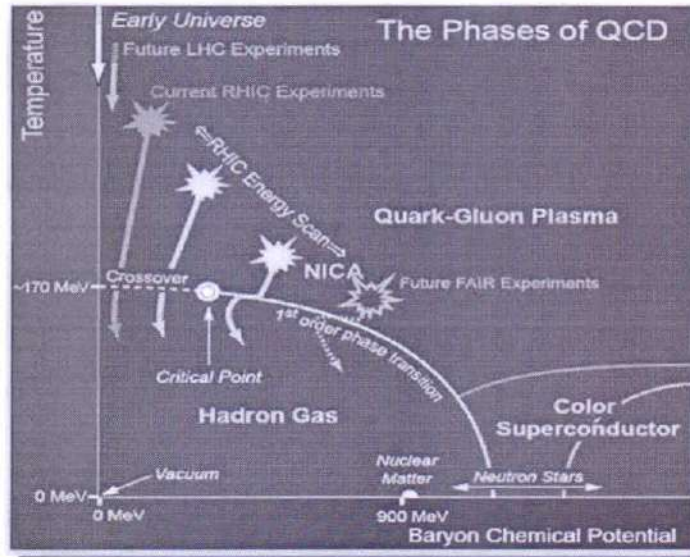


Figure. 1: QCD phase diagram.

The moments of conserved quantities such as **net baryon**, **net kaon**, **net strangeness** are important to find the critical point. They are suggested to be sensitive to the critical point [4]. They (moments of conserved quantities) are related to the **baryon number susceptibility** ( $\chi_B$ ) as well as the **correlation length** ( $\xi$ ) of the system. As correlation length diverges near the critical point due to the fluctuation of **order parameter** (it is a measure of the degree of order that can distinguish two different phases across a phase boundary), the moments are predicted to have non monotonous variation with  $\sqrt{s_{NN}}$  energy. We collide Au ions beam (running nearly at the speed of light) to create quark gluon plasma state. As the system (QGP) cools down a huge number of subatomic particles are made from these QGP state. Here in this project **Time Projection Chamber (TPC)** of the **STAR detector (RHIC, BNL)** is used to measure only proton and anti proton out of this huge amount of subatomic particles. We use proton as a proxy of baryon (as it is very difficult to measure neutrons and also the number of protons are maximum among all the produced baryons). Theoretical calculation predicts that net proton instead of net baryon also shows a good signature near the critical point.

The project report is organized as follows. In chapter 2 we moments and their importance in order to find the critical point are discussed. In chapter 3 we discuss about experimental setup, collider and detectors. In chapter 4 the result of the experiment has presented. In chapter 5 a summary and conclusion are given.

## Chapter 2

### Higher Order Moments

Physics is quite unique at the critical point. A lot of properties (such as susceptibility, specific heat, correlation length) behave in a unique manner at that point. So, if we get some observables which have direct relation with these above said properties then we can easily detect the signature of critical point by measuring these observables only. Moments are the one of such observables that can help us to locate the critical point.

#### 2.1 Moments

To define something, some parameters are desperately needed because they can provide a complete information about that thing. Similarly, in statistics moments can provide us a clear and complete information about probability distribution. Now there are another parameter which is nothing but the **Central moments**. Central moments are the moments about the mean of the distribution. nth order central moments of a distribution divided by nth power of standard deviation of that particular distribution is called **normalized central moment or standardized moments**. For example, if  $f(x)$  is a real valued continuous function then the nth order moment of that function about a point  $c$  is

$$\mu_n = \int_{-\infty}^{\infty} (x - c)^n f(x) dx \quad (2.1)$$

we define moments with  $c = 0$  and we define central moments with  $c$  as the mean ( $\mu$ ) of the function. A generalized expression of central moments is

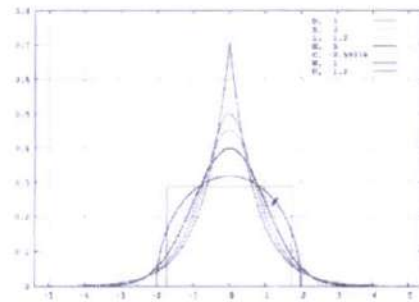
$$\mu_n = E(x - \mu)^n = \int_{-\infty}^{\infty} (x - \mu)^n f(x) d(x) \quad (2.2)$$

nth order normalized central moments is defined as :  $M_n = \frac{E(x - \mu)^n}{\sigma^n}$

The first moment is mean, first central moment is zero (as it is taken about mean), 2<sup>nd</sup> central moment is variance,  $\sigma^2$  (measure the width of a distribution), 3<sup>rd</sup> and 4<sup>th</sup> normalized central moment is respectively skewness ( $s$ ) and kurtosis ( $k$ ). Now we will discuss a little about the skewness and kurtosis.



Skewness (3<sup>rd</sup> normalized central moment) of a distribution is defined as  $s = M_3 = \frac{\mu_3}{\mu_2^{3/2}}$ . It measures the horizontal deviation from a symmetric or Gaussian distribution. There are two types of skewness, **positive skewness** (indicates a distribution with longer tail on the right side than that of the left side of the distribution) shown in Fig. 2 and **negative skewness** (indicates a distribution with longer tail on the left side than that of the right side) shown in Fig. 2. Skew value is zero for a gaussian distribution.



### 2.1.b Kurtosis

## 2.2 Cumulant

$$C_2=\mu_2; C_3=\mu_3; C_4=\mu_4-3\mu_2^2 \quad (2.4)$$

The various moments can be written as  $M = c_1; \sigma^2 = c_2; S = \frac{c_3}{c_2^{3/2}}; \kappa = \frac{c_4}{c_2^2}$

And the product of moments are  $S\sigma = \frac{c_3}{c_2}, \kappa\sigma^2 = \frac{c_4}{c_2}$ . Later we will discuss elaborately why we take product of moment.

## 2.3 Moments and Cumulants in Heavy Ion Collisions

In high energy experiment we measure particle multiplicities for each event. In this paper we define  $N_p$  as the proton multiplicity in one event and  $\Delta N_p$  ( $N_{\text{proton}} - N_{\text{antiproton}}$ ) is defined as net proton number. We define  $\langle N \rangle$  as the average value of  $N$  over the entire event ensemble. The various order cumulants of  $N$  of event by event distribution is given below

$$\begin{aligned} c_1 &= \langle N \rangle; \\ c_2 &= \langle (\Delta N)^2 \rangle; \\ c_3 &= \langle (\Delta N)^3 \rangle; \\ c_4 &= \langle (\Delta N)^4 \rangle - 3 \langle (\Delta N)^2 \rangle^2. \end{aligned} \tag{2.5}$$

Here we use  $\Delta N = N - \langle N \rangle$ .

## 2.4 Why Moments and Cumulants Matter

The very first question that comes to our mind is why we are so much interested to study moments/cumulants in order to find QGP (1<sup>st</sup> order phase transition and signature of critical point). Is it helpful to locate the critical point? The answer is simple yes. There are basically two reasons why for choosing cumulants to find critical point. These are

- Cumulants have stronger dependence on baryon number susceptibility [5,6]
- Baryon number susceptibility diverges at critical point [5].

If this is the case then we have to discuss three major points first, what is baryon number susceptibility, second, dependence of cumulants on baryon number susceptibility, third, why does baryon number susceptibility diverge near critical point. The discussions are given below.

### 2.4.a Baryon Number Susceptibility ( $\chi_B$ )

It is the measure of the rate of the density ( $\rho$ ) fluctuation in the system with respect to quark chemical potential ( $\mu$ ). It is defined as:  $\chi_B(T, \mu) = [\sum_{i=1}^{N_f} \frac{\partial}{\partial \mu_i}] (\sum_{i=1}^{N_f} \rho_i)$ .

### 2.4.b Dependence of Cumulants on $\chi_B$



In a grand canonical ensemble framework, the  $n$ th order cumulants of net baryon number distribution and the  $\chi_B$  are related by  $c_n = VT^3 \chi_B^{(n)}(T, \mu_B)$ . Where  $V$  is the volume of the system. we can define mean, variance, skewness, kurtosis of net baryon number distribution as follows

$$M = VT^3 \chi_B^{(1)}; \quad (2.6)$$

$$\sigma^2 = VT^3 \chi_B^{(2)}; \quad (2.7)$$

$$S = \frac{VT^3 \chi_B^{(3)}}{\sigma^3}; \quad (2.8)$$

$$\kappa = \frac{VT^3 \chi_B^{(4)}}{\sigma^4}. \quad (2.9)$$

One important information needs to be discussed here. Here we see that all the cumulants and moments are volume dependent. But the measurement of volume is very difficult in heavy ion collision experiment. To cancel out these volume dependency, we take ratio of cumulants/moment as follows

$$S\sigma = \frac{c_3}{c_2} = \frac{\chi_B^{(3)}}{\chi_B^{(2)}}; \quad (2.10)$$

$$\kappa\sigma^2 = \frac{c_4}{c_2} = \frac{\chi_B^{(4)}}{\chi_B^{(2)}}. \quad (2.11)$$

## 2.4.c Baryon Number Susceptibility( $\chi_B$ ) at Critical Point

As we discuss above  $\chi_B$  is the rate of change of density fluctuation. At the critical point, density fluctuation is very high compare to its normal phase point. This is because near the critical point correlation length ( $\xi$ ) of fluctuation diverges. For example, in a water vapour system at the critical point, we see the phenomenon so called **critical opalescence**. The reason behind this is nothing but the fluctuation of density at critical point. A large scale water molecules can easily convert (because at the critical point latent heat require for a phase transition is zero) into gas molecules and also gas molecules can convert easily into water. So the fluctuation of density is very high causing correlation length of fluctuation and susceptibility to diverge at critical point.

## 2.5 Relation Between Correlation length ( $\xi$ ) and Cumulants

we already know that moments depend on susceptibility ( $\chi_B$ ) and  $\chi_B$  depends on  $\xi$ . Then there must be a direct relation between moments and correlation length  $\xi$  [7]. These are given below  $\sigma^2 \propto \xi^2$ ;  $S\sigma \propto \xi^{4.5}$ ;  $S\sigma \propto \xi^{2.5}$ ;  $\kappa\sigma^2 \propto \xi^5$

As near the critical point  $\xi$  shows an unique behaviour, so does moment. Near the critical point moments and cumulants show an abrupt deviation from their natural values with the change of collision energy. It must be noted that although  $\xi$  diverges at critical point, but in the high energy experiment due to **finite size, higher cooling rate, critical slowing down** the maximum value of  $\xi$  lies between 2-3fm as compared to its natural value 0.5fm [8].

## 2.6 Moments and Cumulants at Critical Point

At the critical point QCD based calculation suggests that net baryon number distribution would be non-gaussian causing  $S\sigma$  and  $\kappa\sigma^2$  to follow a non monotonic variation with collision energy.  $S\sigma$  and  $\kappa\sigma^2$  ratio are expected to deviate from unity [9].



## Chapter 3

# Experimental setup

### 3.1 Introduction

In order to find the existence of quark gluon plasma and to search the critical point of QCD matter we have to collide high energetic nucleons to get the quarks and gluons out of the nucleons. The **Relativistic Heavy Ion collider (RHIC)** is one of the leading collider in the world that can provide us an suitable environment to execute our high energy collision experiment to find the QGP ,a state of matter believed to be exist earlier in the universe just after the **Big Bang**.

### 3.2. RHIC

Relativistic heavy ion collider at BNL, New York is the first machine that is capable of colliding beams of ions. Here two ion beams running opposite to each other at the speed of light (0.9995c) collide. In the RHIC machine we create a little Big Bang like environment to find quark gluon plasma and its properties. There are four detectors in four junctions of RHIC machine. These are **STAR, PHENIX, PHOBOS** and **BRAHMS**. This machine can collide heavy ions up to a center of mass energy  $\sqrt{s_{NN}} = 200\text{Gev}$  per nucleon for Au +Au collisions. Each collision produces both primary and secondary particles.

- Primary particles are produced from the direct collision of two high energetic ion beams running opposite to each other. For example a Au+Au collision (central collision) can create more than 1000 primary particles (each having transverse momentum 500 MeV/c ) per unit pseudo rapidity.
- Particles are produced from the collision of primary particles with material in the detector and also from the decay of primary particles that have very short half life. RHIC detectors are well built to suppress the contamination from secondary particles by detecting (tracking and identifying) both the primary and secondary particles.

### 3.3. STAR Detector

RHIC uses various detectors to accomplish its task in order to find the physics goals of the experiment. **STAR** is a huge detector specializes for basically particles path tracking with high special and temporal resolution, particles momentum analysis and particle identification. It has large uniform acceptance  $|\eta| < 1$  with excellent purity of particles identification and full azimuthal angle coverage ( $\phi=2\pi$ ) [10]. STAR physics program can be divided into three main categories

- First, finding the evidence of strongly interacting matter (i.e. QGP) and study of the behavior of that matter at high energy density.
- Second, properties of QGP phase (first order phase transition line and critical point).
- Third, to understand the evolution of collision process with space and time in relativistic heavy ion collision.

Various parts of the STAR detector that are used to identify thousands of particles produced by each ion collision at RHIC will be discussed here. A perspective view of the STAR detector is shown in Fig.4.

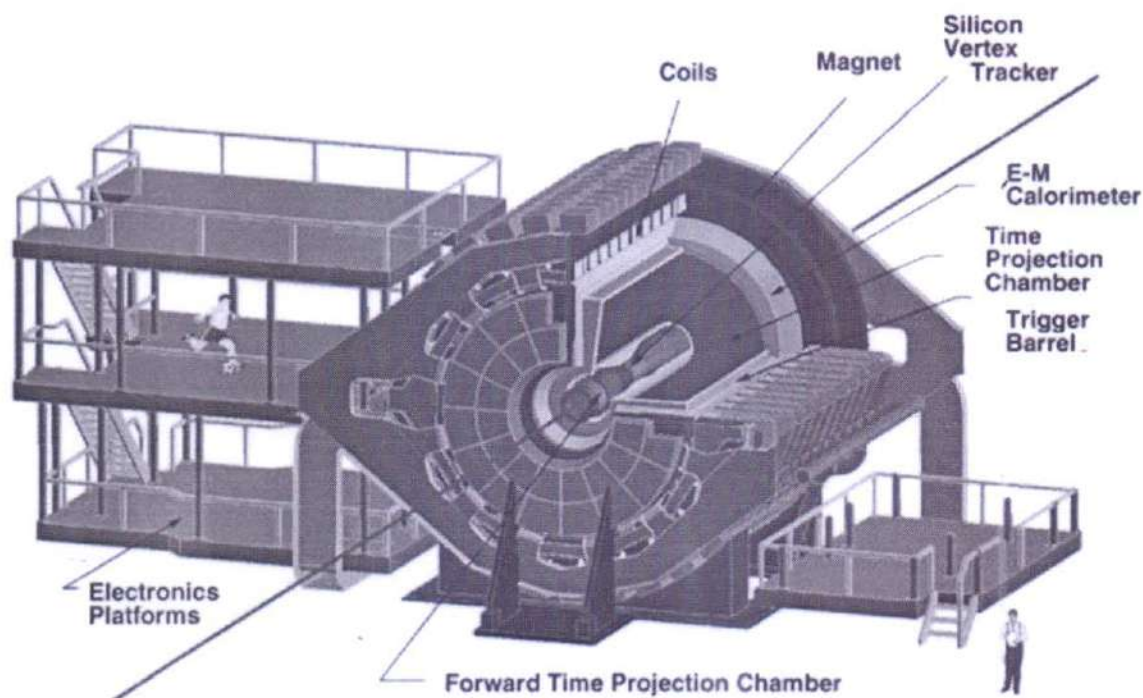


Figure. 4: Perspective view of STAR detector.

#### 3.3.a Room Temperature Solenoidal Magnet



STAR uses a room temperature solenoidal magnet that can produce a uniform magnetic field of 0.5 T. It is used for momentum analysis of charged particles.

### 3.3.b Silicon Vertex Tracker (SVT)

It is used to track charged particles and identify them near the interaction region. A cut view perpendicular to the beam axis is shown in Fig. 5. SVT contains 216 silicon drift detectors (equivalent to a total 13 millions pixels) that are arranged in consecutive three cylindrical layers (barrels). The barrels are positioned radially at 5.97 cm, 10.16 cm, 14.91 cm respectively. The maximum length of SVT is 44.1 cm [11]. It has almost a pseudo rapidity range  $|\eta| < 1$  and full azimuthal angle coverage  $\phi = 2\pi$ . Later a fourth layer **silicon drift detector** was installed in STAR for better performance.

### 3.3.c Time Projection Chamber

It is a primary tracking device that is capable of tracking the particles, measuring their momentum (over a range of 100 MeV/c to 30 GeV/c) and identifying particles (over a range of 100 MeV/c to greater than 1 GeV/c) by measuring their ionization energy loss ( $dE/dx$ ). It has an almost pseudo rapidity range  $|\eta|$  pseudo rapidity range  $|\eta| < 1.8$  and full azimuthal angle coverage  $\phi = 2\pi$ . **STAR TPC** is shown schematically in Fig. 6. TPC is 4.2m long and 4m in diameter, located at a distance radially from 50 to 200 cm from beam axis. TPC is filled with P10 gas (10% methane, 90% argon above atmospheric pressure) which is used to track the particles by reconstructing the paths of primary ionization particles passing through the gas volume [12]. Also a uniform electric field is used in reconstruction purpose. Besides there are cathode, field cage, endcaps with anodes and pad planes in TPC.

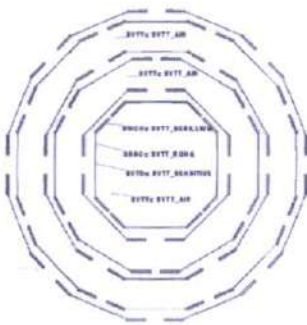


Figure. 5: Cut view of SVT.

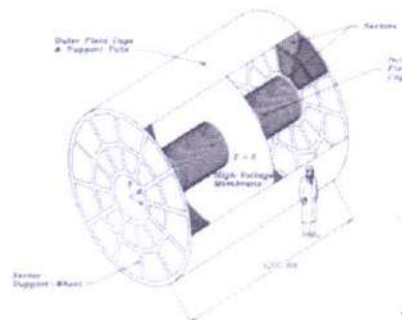


Figure. 6: Schematic diagram of TPC

### 3.3.d Photon Multiplicity Detector (PMD)

Photon Multiplicity Detector measures photon multiplicity and their distribution event by event basis [13]. It is basically particle shower detector. PMD has been provided by a group of Indian institute.

### **3.3.e Muon Telescope Detector (MTD)**

Muon Telescope Detector is also installed in the STAR detector. It is used to measure and identity cosmic ray muon.

### **3.3.f Electro magnetic calorimeter (EMC)**

Electro Magnetic Calorimeter is installed in STAR experiment to increase pseudo rapidity range of experimental measurement. EMC measures transverse energy of events, transverse momentum of photons, electrons, electromagnetically decaying hadrons [14].

### **3.3.g Time of Flight Detector (TOF)**

It is a cylindrical detector covering pseudo rapidity range  $|\eta| < 0.9$  with full azimuthal angle coverage. It measures mass of the particles by measuring their time of flight and momentum. TOF is capable of differentiate between lighter and heavier particles having same momentum. Here in this paper the measured event by event multiplicities is not obtained by TOF, rather we use TPC and other detector for measurement.



## Chapter 4

### Result and analysis

Here in this experiment we deal with data obtained by TPC of STAR (RHIC,BNL). Two ion beams of Au ion running opposite to each other (nearly at the speed of light) collide at various collision energy. We measure the multiplicity of proton ( $N_p$ ) and anti proton ( $N_{\bar{p}}$ ) for each event. The range of collision center of mass energy  $\sqrt{s_{NN}}$  is from 7.7 GeV to 200 GeV. This range of  $\sqrt{s_{NN}}$  energy covers the  $\mu_B$  range from 420 MeV to 20 MeV.

The measurement of event by event  $N_{\bar{p}}$  and  $N_p$  multiplicities carried out at  $\sqrt{s_{NN}} = 7.7, 11.5, 14.5, 19.6, 27, 39, 62.4$  and 200 GeV. 14.5 GeV data was taken in the year 2014. 19.6 GeV and 27 GeV were taken in the year 2011 and all the remaining data were collected in the year 2010. The measured number of events for 7.7, 11.5, 14.5, 19.6, 27, 39, 62.4, 200 GeV are respectively 3M, 7M, 13M, 15M, 30M, 86M, 47M, 238M.

The data was taken for  $|z| = 50$ cm for 7.7 GeV, 60 cm for 14.5 GeV and 30 cm for other collision energy (Here  $z$  is the distance along the beam axis from the TPC center). The measured multiplicities of  $N_{\bar{p}}$  and  $N_p$  were taken by TPC over full azimuthal angle and within pseudo rapidity range  $|\eta| < 1$  in mid rapidity  $|y| < 0.5$  for various collision energy. To get a good measurement of proton sample (approximately 80% purity) and also to avoid the contamination from secondary particles (produced by the collision of primary particles with beam pipe) we take the  $p_t$  range  $0.4 < p_t < 0.8$  GeV/c and only choose the events within radial vertex position 2 cm from the center of TPC in the transverse plane of beam axis.  $\Delta N_p$  multiplicity distribution for 0-5% centrality for various  $\sqrt{s_{NN}}$  energy is shown in Fig. 7.

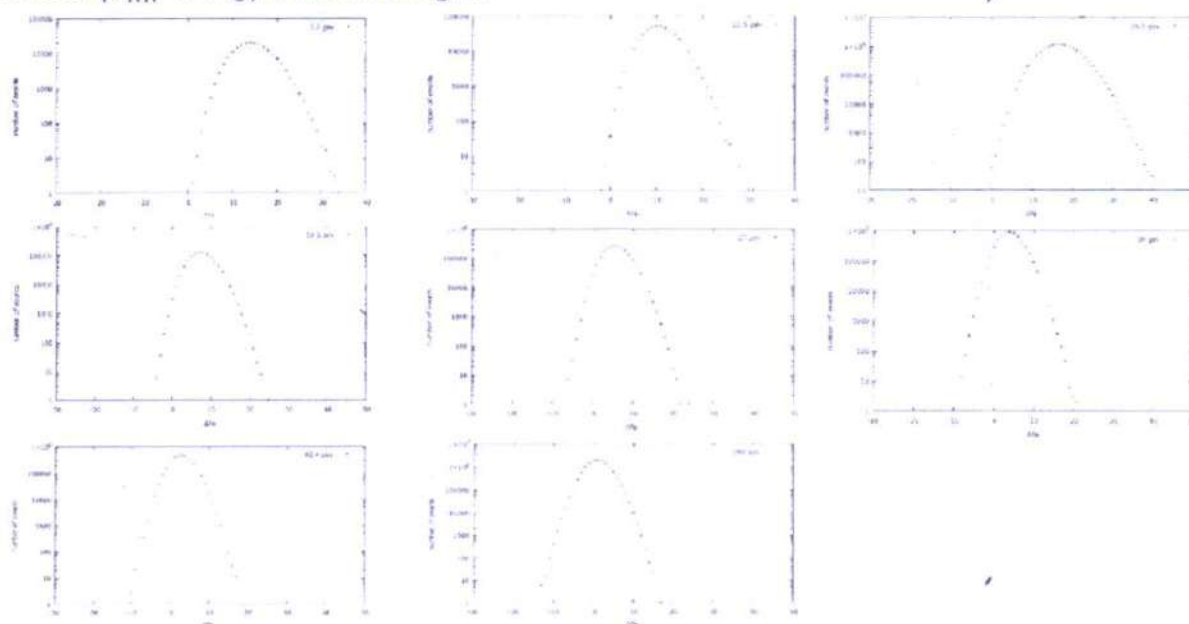


Figure. 7: Net proton multiplicity distribution for various collision energy.

The one thing that we can easily observe is that, as the collision energy increases the peak of the  $\Delta N_p$  multiplicity distribution goes towards the point zero. This is because at higher energy pair production is much higher than that of the lower energy. As we know at the critical point  $\Delta N_p$  distribution would deviate from Gaussian shape, so we can say by simply observing Fig.7 that critical point may exist at lower energy [15] but definitely not at the higher energy. This is because at the higher energies the distributions look like more bell shaped (gaussian) than that of the lower energies.

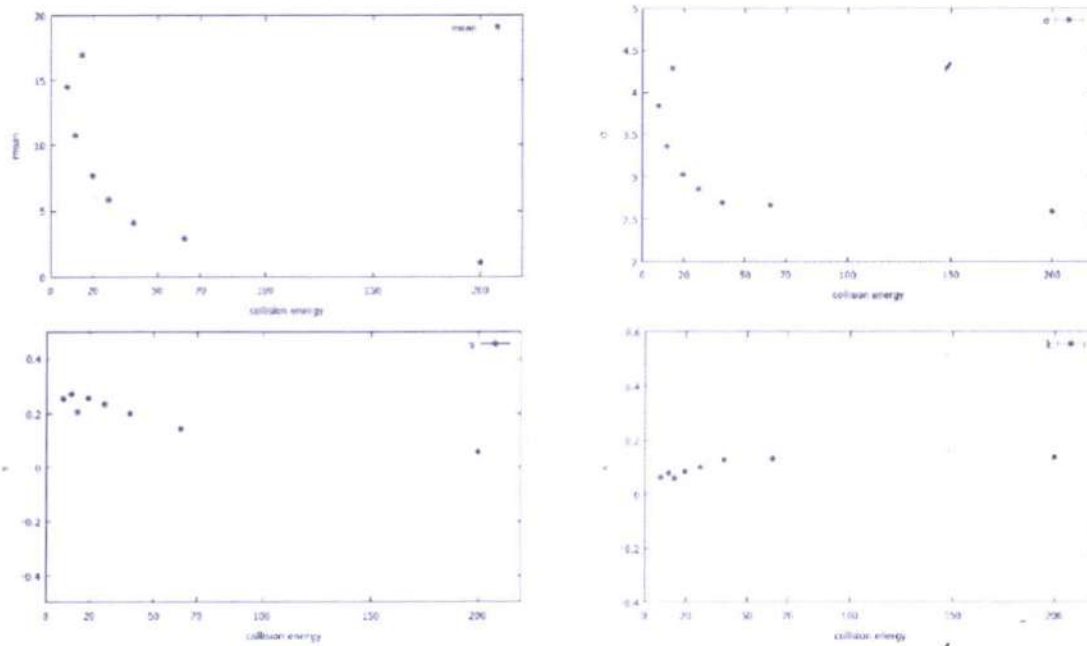


Figure. 8: Energy dependence of moments of net proton multiplicity distribution.

In Fig. 8 energy dependence of various moments ( $M, \sigma, S, \kappa$ ) of net proton multiplicity distribution are shown. They are decreasing with increasing collision energy. Decreasing of skew value with increasing collision energy indicates that the higher energy distributions are more bell shaped i.e. they are almost look like gaussian distribution. We also observe that fluctuations of moments are more detectable as the order of moments increases. Higher order moments ( $S$  and  $\kappa$ ) show a fluctuation (non monotonic variation) at lower energies, but lower order moments ( $M, \sigma$ ) don't show any such fluctuation with collision energy. This is because dependency of moments on correlation length ( $\xi$ ) of the system. Higher order moments have larger dependence on correlation length ( $S \propto \xi^{4.5}; \kappa \propto \xi^5$ ) than that of the lower order moments ( $\sigma^2 \propto \xi^2; S \propto$



$\xi^{2.5}$ ). More dependence on  $\xi$  implies easier to detect the fluctuation in order to search the signature of critical point.

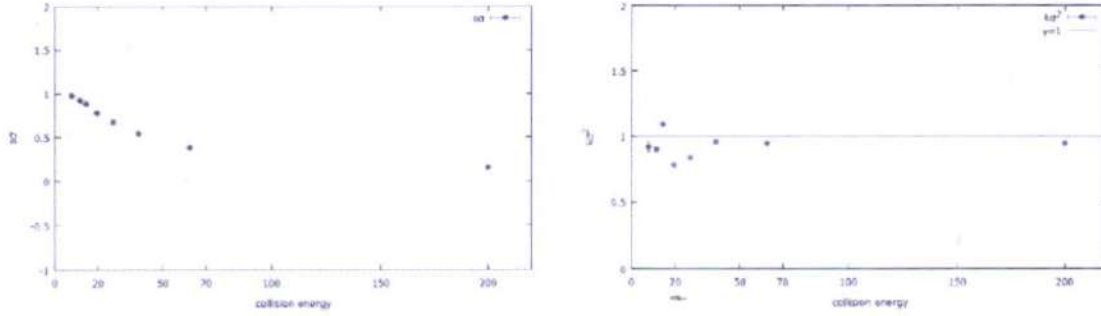


Figure. 9: Energy dependence of  $S\sigma$  and  $\kappa\sigma^2$

Collision energy dependence of  $\kappa\sigma^2$  and  $S\sigma$  of  $\Delta N_p$  multiplicity distribution is given in Fig. 9. For both  $\kappa\sigma^2$  and  $S\sigma$  we observe that there is a non-monotonic variation from nearly 11.5 GeV to 62.4 GeV energy range. If we look at the  $\kappa\sigma^2$  we can observe that at 19.6 GeV 27 GeV there is a significant deviation from unity which may be a very good signature of critical point. Any deviation from QCD based model (a theoretical model that include critical point) suggests the possible existence of critical point. From this  $\kappa\sigma^2$  graph, we see a very significant sign (deviation unity) of existence of the critical point any where in the energy range from 7.7 GeV to 62.4 GeV.

## Chapter 5

### Summary and conclusion

In summary, we have presented here the measurement of higher order moments of net proton multiplicity distribution over a large  $\sqrt{s_{NN}}$  energy range (7.7 – 200 GeV) and baryonic chemical potential ( $\mu_B$ ) (20-420 MeV) for Au + Au central collision (0-5% centrality) at midrapidity ( $|y| < 0.5$ ) within transverse momentum  $p_t$  range (0.4-0.8 GeV/c). Our aim is to search for the signature of critical point and properties of phase transition of the QCD matter. We discussed the reasons why we choose higher order moments/cumulants in order to search for the signature of critical point and also we defined the relations between moments/cumulants and correlation length ( $\xi$ ). Here we have also presented the possible discussion about the experimental setup, detectors that were used in the experiment. We have completed the calculation of product of moments  $S\sigma$  and  $K\sigma^2$  from net proton multiplicity distribution for various  $\sqrt{s_{NN}}$  energy. We clearly observe their ( $S\sigma$ ,  $K\sigma^2$ ) non monotonic variation with  $\sqrt{s_{NN}}$  energy. This indicates the possible signature of critical point. We end up by saying that critical point may exist in lower energy region (higher  $\mu_B$  region) but the particular point where it (critical point) may be located is still unknown to us. Maybe we need more data sets (statistics).

Though it is clear that signature of critical point may exist in lower energy region, but the problem is that, at the low energy region there is a lack of sufficient data. To claim some thing new about critical point, scientists need more and more statistical data. Particles identification is another issue that contribute an important role in order to find critical point. In this experiment proton efficiency must be increased to get more information about critical point.



**Ramakrishna Mission Residential College (Autonomous)**

**Vivekananda Centre for Research**

**Ramakrishna Mission Ashrama**

(A Branch Centre of Ramakrishna Mission, Belur Math, Howrah-711202)

**Narendrapur, Kolkata - 700 103, West Bengal, India**

A Scientific Industrial Research Organisation, Recognised by DST, Govt. of India

College with Potential for Excellence (CPE), Re-accredited by NAAC - 'A' (CGPA 3.56 out of 4)

---

## **DEPARTMENT OF PHYSICS**

### **Certificate**

This is to certify that Indranil Dey, a student of B.Sc has successfully completed the project of UG curriculum entitled "Bose-Einstein Condensation in Anisotropic Harmonic Oscillator Potential" in the period from January to May, 2020.

*Malay Purkait*

.....  
30.06.2020.

**Signature Of HOD**

**Dept. of Physics**

**Dr. Malay Purkait**

Associate Prof. & Head

Department of Physics

Ramakrishna Mission Residential College

(Autonomous)

Narendrapur, Kolkata-700 103, (W.B.)

---

PHONES : 24772201(3lines), 24772205 FAX : 033-24773597 EMAIL : rkmcnpur@vsnl.com

WEBSITE : [www.rkmcnarendrapur.org](http://www.rkmcnarendrapur.org)



# Ramakrishna Mission Residential College

## DEPARTMENT OF PHYSICS

### Certificate

This is to certify that Indranil Dey, a BSc third year student of Ramakrishna Mission Residential College, Narendrapur (Autonomous) has successfully completed a project on Bose-Einstein Condensation in Anisotropic Harmonic Oscillator Potential with Finite Number Boson Correction under the guidance of Dr. Debnarayan Jana, professor of University of Calcutta.

Name of mentor  
Dr. Debnarayan Jana

Signature

*Debnarayan Jana*

08/10/2020

## ACKNOWLEDGEMENT

I have completed the project under the guidance of respected professor Debnarayan Jana of Calcutta University. He was always there to help me whenever I had doubts. I convey my heartiest gratitude to him. I would also like to convey my respect and gratitude to all the faculties and staffs of Department of Physics RKMRC Narendrapur and our Principal Maharaj Sw. Sastragganandaji.

Indranil Dey

# BOSE-EINSTEIN CONDENSATION IN ANISOTROPIC HARMONIC OSCILLATOR POTENTIAL

Indranil Dey

PHUG/115/17

RKMRC Nazendrapur

Guide: Prof. Debnatayan Jana

Calcutta University

djphy@caluniv.ac.in

(6th Sem: Papers: XIV: Unit-II)

## Introduction

All particles in nature can be divided into bosons and fermions according to their statistics. The particles having integer spin angular momentum (in units of  $\hbar$ ) are known as bosons while the particles having odd half integer spin are termed as fermions. Electrons, protons and neutrons are all fermions. An atom, which contains all three can also be treated as a single (composite) particle. Whether this composite particle is bosonic or fermionic depends on the total number of its constituents. For example,  $\text{He}^4$  contains two electrons, two protons and two neutrons and thus it is



a boson. But the isotope  $\text{He}^3$  is a fermion. Fermions obey the Pauli exclusion principle while there is no such restriction on bosons. This means that the electrons effectively repel each other. However, in the case of bosons we can put as many of them as we want as we want in the same state. Hence, effectively bosons attract each other. It was Einstein who actually showed how the quantum nature of Bose particles (incidentally, the particles are named after Prof. S.N. Bose who formulated the statistics of the particles) can enforce them into same state without having interaction between them. This is the phenomenon of Bose-Einstein Condensation (BEC). It is a surprising fact that its occurrence has been conjectured rather than directly observed until recently. This condensation occurs in momentum space unlike other condensation phenomena and it happens due to the quantum nature of the particles and their statistics.

in ordinary condensation process which actually happens in coordinate space (e.g. freezing of water) ; but for bosons, at certain temperature called critical temperature, particles started to transfer to  $p = p_c$  or 0 state in a huge amount (though this depends on the potential and dimension of space). So, it is called the BEC happens in momentum space.

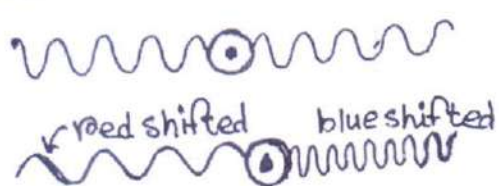
The BEC phenomenon has been invoked to explain certain features associated with superconductivity. It is argued that superconductivity can be understood as the condensation of Cooper pairs (composite bosons comprising of up and down spin electrons). The condensation phenomenon has also found its application in the phase transition of the early universe.



## Experimental Observation of BEC

To produce low-temperature, earlier approach is by evaporative cooling. In this method, the hydrogen atoms are first refrigerated and then trapped in a magnetic field. Then, the atoms which are hotter enough can come out of the trap leaving behind the colder atoms.

Another method is via laser cooling which works best for alkali atoms. The laser cooling works by bombarding atoms with photons. The laser is tuned to a frequency slightly low than the resonant frequency for the atoms to absorb when they are still. When an atom moves in any direction, one laser is red shifted and other is blue shifted (laser along which the direction of motion is is blue shifted). So, the atom absorbs the photons and loses momentum. Thus cooling is produced. Laser cooling can chill atoms to less than a millionth of a degree within absolute zero degree. But for BEC to occur, many fold colder temperature is required. This is done by first laser cooling Rubidium required. This is done by first laser cooling Rubidium (A.No: 87) and then evaporatively cooling them. To hold the laser cooled atoms and to increase the density of the atoms, magnetic field as well as the optical field produced by the laser is used.



[laser cooling in 1D]



## BEC for free Bosons

If we perform BEC for free bosons, whether we find a critical temperature for a system depends on the dimensionality of space.

Using BE statistics, we find for d-dimension, the particle density,

$$n = \frac{g}{\lambda^d} f_{d/2}^+(z) \left[ f_m^+(z) = \frac{1}{\Gamma(m)} \int_0^\infty \frac{x^{m-1} dx}{z^{-1}e^x - 1} \right]$$

$$\Rightarrow \frac{n\lambda^d}{g} = f_{d/2}^+(z) \quad (*) \quad = z + \frac{z^2}{2^m} + \frac{z^3}{3^m} + \dots$$

$f_m^+(z)$  has the property:  $\lim_{z \rightarrow 1} f_m^+(z) = \zeta(m)$  for  $m > 1$ .

equation (\*) forms a transcendental equation,

For 3 dim. ( $d=3$ ):  $f_{3/2}^+(1) = \zeta(3/2)$

So, as  $T$  decreases, the value of  $\frac{n\lambda^3}{g}$  increases till it hits  $\zeta_{3/2}$ ,

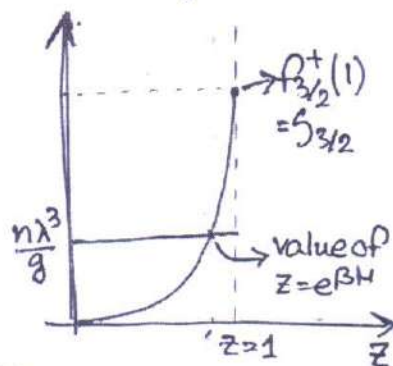
the corresponding temperature is called critical temperature,

$$\frac{n\lambda_c^3}{g} = \zeta(3/2) \Rightarrow T_c = \frac{h^2}{2\pi m k_B} \left( \frac{n}{g \zeta_{3/2}} \right)^{2/3}, \text{ after } T_c, \text{ as}$$

$T < T_c$ ,  $z$  get fixed at 1, and particles start to accumulate in ground state, and condensation occurs, in 3dim, for  $T < T_c$ ;

$$N_{\text{ground}}(T) \propto 1 - \left( \frac{T}{T_c} \right)^{3/2}$$

for  $d=1$ dim,  $d=2$ dim, condensation does not occur for free boson as  $f_{d/2}^+(z)$  diverges at  $z=1$ , and hence  $z$  can't get fixed at 1 for a finite temperature, so we don't get critical temperature. in  $d < 3$  dim.



From BE statistics, we also find, in 3dim, for ideal free Bose gas,

pressure of BEC  $p = k_B T \frac{g}{\lambda^3} \zeta_{5/2}$  (for  $T < T_c$ )  
 $\sim T^{5/2}$

at very high T,

$$p = nk_B T$$

At  $T = T_c$ , as the transition occurs, there's a jump in entropy between the Bose gas (excited) and the condensate, which can lead to the existence of latent heat, from Clausius-Clapeyron eq,

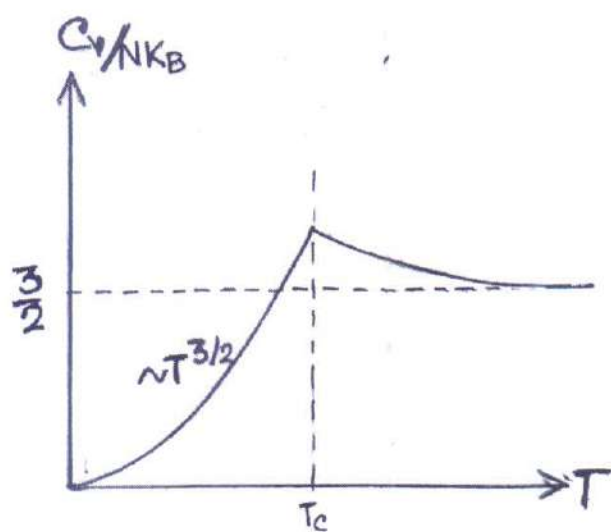
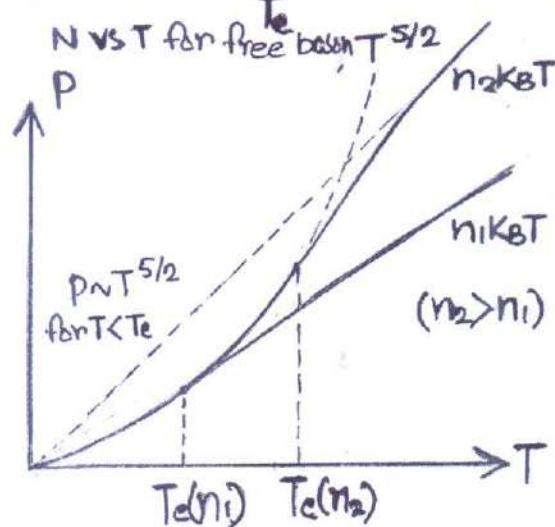
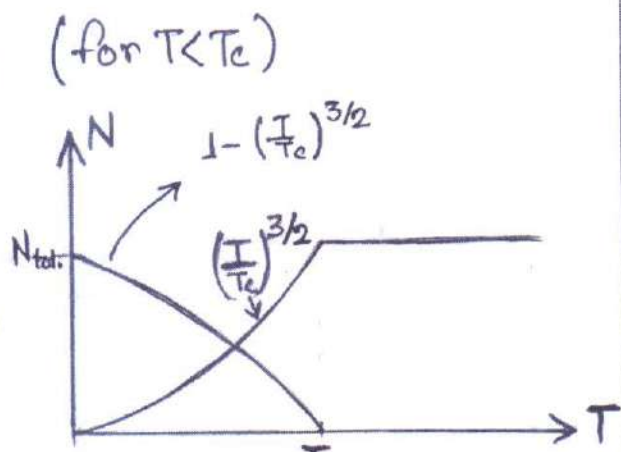
$$L = \frac{5}{2} \frac{\zeta_{5/2}}{\zeta_{3/2}} k_B T_c$$

Heat Capacity ( $C_v$ ): From BE stat for free bosons, we also see,  $C_v$  has a discontinuity in the derivative  $C_v$  w.r.to  $T$  at  $T = T_c$ , but it is continuous at  $T = T_c$ .

$$\left. \frac{C_v}{N k_B} \right|_{T=T_c} = \frac{3}{2} \frac{g}{\lambda^3} \left[ \frac{5}{2} \frac{\rho^+}{\zeta_{5/2}^2} - \frac{3}{2} \frac{\rho_{3/2}^+}{\zeta_{3/2}^2} \right]$$

$$\left. \frac{C_v}{N k_B} \right|_{T < T_c} = \frac{15}{4} \frac{\zeta_{5/2}}{\zeta_{3/2}} \left( \frac{T}{T_c} \right)^{3/2}$$

For large T,  $C_v \simeq \frac{3}{2} N k_B$



$\frac{C_v}{N k_B}$  vs T for free boson



$$\text{So, } V(\langle B \rangle_t) = V_0 - \mu(B_1) \frac{B_0^2}{4B_1} (x^2 + y^2 + 8z^2)$$

So, we can see, an anisotropic harmonic potential has been created whose,

$$\left. \begin{aligned} \omega_x^2 = \omega_y^2 &= - \frac{\mu(B_1) B_0^2}{2mB_1} \\ \omega_z^2 &= - \frac{8\mu(B_1) B_0^2}{2mB_1} \end{aligned} \right\}$$

Here, though the expression has -ve sign,  $\omega_x^2, \omega_y^2, \omega_z^2$  will be positive.

This type of trap is usually called the "TOP Trap".



## Construction of Anisotropic Harmonic Trap

We will be describing how would be the nature of BEC if the bosons are trapped in anisotropic harmonic potential. Now, to make such potential in lab to trap uncharged bosons we need the following theory.

We need to have a non-uniform rapidly varying (with time) magnetic field to trap the boson in harmonic potential.

Suppose, we have a  $\vec{B}$  field such that,

$$\vec{B} = (B_0 x + B_1 \cos \omega t) \hat{i} + (B_0 y + B_1 \sin \omega t) \hat{j} - (2B_0 z) \hat{k}$$

such that  $\vec{\nabla} \cdot \vec{B} = 0$ .

Now, after some calculation, we get,

$$\begin{aligned} |\vec{B}| &= [B_1^2 + 2B_0 B_1 \{(\cos \omega t)x + (\sin \omega t)y\} + B_0^2 (x^2 + y^2 + 4z^2)]^{1/2} \\ &= B_1 \left\{ 1 + \frac{2B_0}{B_1} (x \cos \omega t + y \sin \omega t) + \frac{B_0^2}{B_1^2} (x^2 + y^2 + 4z^2) \right\}^{1/2} \end{aligned}$$

For  $|\vec{B}|$  sufficiently small,  $x, y, z \rightarrow \epsilon$  ( $\epsilon > 0^+$ )

Time averaging it, we get,

$$\begin{aligned} \langle |\vec{B}| \rangle_t &= B_1 + \frac{B_0^2}{2B_1} (x^2 + y^2 + 4z^2) - \frac{B_0^2}{4B_1} (x^2 + y^2) \\ &= B_1 + \frac{B_0^2}{4B_1} (x^2 + y^2 + 8z^2) \quad [x, y, z \text{ small}] \end{aligned}$$

Now, potential energy of a particle in a magnetic field depends on the magnitude of the magnetic field.

$$V(B) = -\vec{\mu} \cdot \vec{B} = -\mu B$$

where  $\mu$  is the magnetic moment of the particle along the magnetic field. An uncharged particle can still acquire magnetic potential energy because of its intrinsic magnetic moment (such as, neutron, ~~it~~ has non-zero  $\mu$ ). So, the bosons can also be trapped in such potential.

$$\text{Now, } V(\langle B \rangle_t) = V(B_1 + \frac{B_0^2}{4B_1} (x^2 + y^2 + 8z^2))$$

$$= V(B_1) + \frac{\partial V}{\partial \langle B \rangle_t} \bigg|_{\langle B \rangle_t = B_1} \left( \frac{B_0^2}{4B_1} \right) (x^2 + y^2 + 8z^2)$$

$$V(\langle B \rangle_t) = V(B_1) - \mu(B_1) \frac{B_0^2}{4B_1} (x^2 + y^2 + 8z^2)$$

$V(B_1) = \text{const. potential energy due to constant } B_1 \text{ field.}$

$\mu(B_1) = \text{magnetic moment in the direction of } \langle B \rangle_t \text{ field.}$

So, it is an anisotropic harmonic oscillator potential with,

$$\omega_x^2 = \omega_y^2 = - \frac{\mu(B_1) B_0^2}{2mB_1};$$

$$\omega_z^2 = - \frac{8\mu(B_1) B_0^2}{2mB_1}$$

here, though  $\omega_x^2, \omega_y^2, \omega_z^2$  has -ve sign in their expression, they will be positive.



## Density of States for Quantum Harmonic Oscillator Potential

Very large N case:

If the total number of trapped bosons is infinite, energy of the system will be very large, so  $E \gg \hbar\omega$  and hence we can neglect the contribution of zero point energy, to the energy of the system.

For a single particle energy level, the expression of energy levels,

$$\begin{aligned} E_{n_x, n_y, n_z} &= n_x \hbar \omega_x + n_y \hbar \omega_y + n_z \hbar \omega_z \\ &\quad \text{(neglecting zero point energy)} \\ &= \hbar (n_x \omega_x + n_y \omega_y + n_z \omega_z) \\ &= E \end{aligned}$$

Now, we can think this 3dim. anisotropic harmonic oscillator as three independent 1 dim. harmonic oscillator with different frequency of oscillation,



For convenience, we'll denote  $x, y, z$  component of  $E$  rather than  $E_1, E_2, E_3$ .

$$E_x = n_x \hbar \omega_x$$

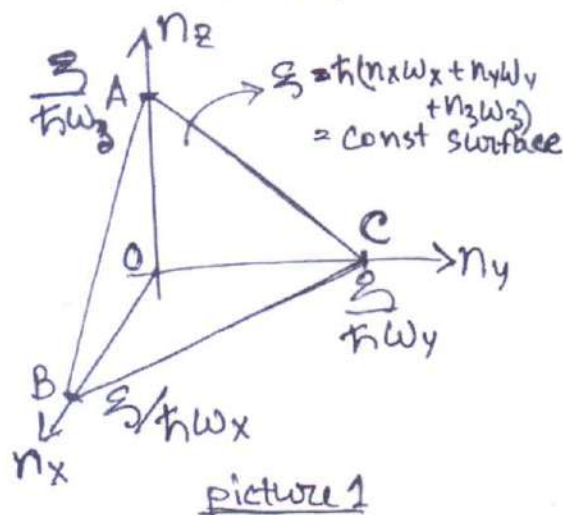
$$E_y = n_y \hbar \omega_y$$

$$E_z = n_z \hbar \omega_z$$

$$\Rightarrow n_x = \frac{E_x}{\hbar \omega_x} \quad (n_x = 0, 1, 2, \dots)$$

$$n_y = \frac{E_y}{\hbar \omega_y} \quad (n_y = 0, 1, 2, \dots)$$

$$n_z = \frac{E_z}{\hbar \omega_z} \quad (n_z = 0, 1, 2, \dots)$$



Now, in picture one, we see a surface in  $(n_x, n_y, n_z)$  coordinate space. The equation of the hypersurface,

$$n_x \hbar \omega_x + n_y \hbar \omega_y + n_z \hbar \omega_z = E \text{ (const.)}$$

Now,  $n_x, n_y, n_z$  can take any integer value, such that the above equation satisfies.

now, every different combination of  $(n_x, n_y, n_z)$  that satisfies the above equation will be considered as different states with energy  $E$ , subject to the condition  $(n_x, n_y, n_z \in \mathbb{Z}^+)$

Now, we also have,  $\Delta n_x = \Delta n_y = \Delta n_z = 1$ .  
(comes from quantum mechanical calculation)

So, the volume of a particular quantum state in  $(n_x, n_y, n_z)$  space =  $(1)^3 = 1$

So, the number of states with energy  $\leq \xi$

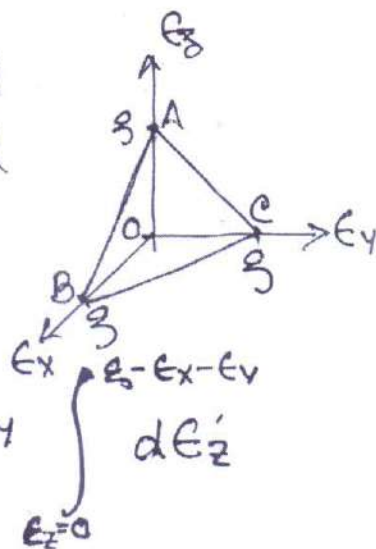
$$G(\xi) = \frac{\text{Volume of the simplex OABC}}{\text{Volume of each state}}$$

$$G(\xi) = \frac{1}{(1)^3} \iiint_V dn_x dn_y dn_z$$

$$= \frac{1}{h^3 \omega_x \omega_y \omega_z} \oint_{V_{OABC}} d\epsilon_x d\epsilon_y d\epsilon_z$$

where the volume integral is over the simplex formed in  $(\epsilon_x, \epsilon_y, \epsilon_z)$  space.

$$G(\xi) = \frac{1}{h^3 \omega_x \omega_y \omega_z} \int_{\epsilon_x=0}^{\xi} d\epsilon_x \int_{\epsilon_y=0}^{\xi-\epsilon_x} d\epsilon_y \int_{\epsilon_z=0}^{\xi-\epsilon_x-\epsilon_y} d\epsilon_z$$



$$G(\mathcal{E}) = \frac{1}{h^3 \bar{\omega}^3} \frac{\mathcal{E}^3}{6} \quad [\omega_x \omega_y \omega_z = \bar{\omega}^3]$$

Hence, the number of quantum states having energy in between  $\mathcal{E}$  to  $\mathcal{E} + d\mathcal{E}$  is,

$$\frac{dG(\mathcal{E})}{d\mathcal{E}} d\mathcal{E} = g(\mathcal{E}) d\mathcal{E} = \frac{\mathcal{E}^2}{2(h\bar{\omega})^3} d\mathcal{E}$$

$\Rightarrow g(\mathcal{E}) = \frac{\mathcal{E}^2}{2(h\bar{\omega})^3}$  is the density of states

for SHD potential is considering  $\mathcal{E}$  to be large ( $N$  being sufficiently huge).

For finite particle system, we need correction terms in the density of states calculation.

### DOS calculation for isotropic SHD system

There's another way to find exact density of states for isotropic 3dim. harmonic oscillator,  $\omega_x = \omega_y = \omega_z = \omega$

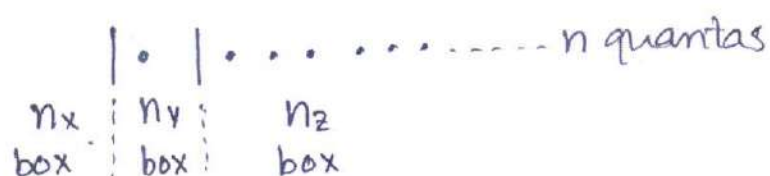
$$E_n = \left(n + \frac{3}{2}\right) h\omega$$



where  $n = n_x + n_y + n_z$ .

Degeneracy in  $n$ th energy level:  
to find it, we are supposed to assume,  
there are  $n$  quantas and they are  
partitioned into 3 boxes named ' $n_x$ ',  
' $n_y$ ', ' $n_z$ ' in all possible ways.

3 boxes = 2 partitions,



So, degeneracy  $g(n) = \frac{(n+2)!}{n! 2!} = \frac{(n+1)(n+2)}{2}$

For  $d$ -dimensional harmonic oscillator,

$$E = (n_1 + n_2 + \dots + n_d + \frac{d}{2}) \hbar \omega$$

Then, the number of partitions =  $(d-1)$

$$\text{degeneracy} = \frac{(n+d-1)!}{(d-1)! n!} = {}^{n+d-1}C_{d-1}$$

So, whatever, for 3 dim. isotropic harmonic potential,

$$g(n) = \frac{(n+1)(n+2)}{2} = \frac{n^2}{2} + \frac{3}{2}n + 1$$

$$E_n = (n + \frac{3}{2}) \hbar \omega = n \hbar \omega + \mathcal{E}_0 \quad (\mathcal{E}_0 = \text{zero point energy})$$

$$E_n = \mathcal{E} + \mathcal{E}_0 \quad (\mathcal{E} = n \hbar \omega)$$

So, we have,  $n = \left( \frac{\mathcal{E}}{\hbar \omega} \right)$

⇒ The number of states between  $n$  and  $n+dn$ ,

$$g(n)dn = \left( \frac{n^2}{2} + \frac{3}{2}n + 1 \right) dn$$

$$g(\mathcal{E})_{\text{iso}} d\mathcal{E} = \left( \frac{1}{2} \frac{\mathcal{E}^2}{(\hbar \omega)^3} + \frac{3}{2} \frac{\mathcal{E}}{(\hbar \omega)^2} + \frac{1}{\hbar \omega} \right) d\mathcal{E}$$

$$\text{So, } g(\mathcal{E})_{\text{isotropic}} = \frac{1}{2} \frac{\mathcal{E}^2}{(\hbar \omega)^3} + \frac{3}{2} \frac{\mathcal{E}}{(\hbar \omega)^2} + \frac{1}{\hbar \omega}$$

For anisotropic case, we saw upto an approximation,

$$g(\mathcal{E}) \Big|_{\substack{N \rightarrow \infty \\ \text{anisotropic}}} \approx \frac{1}{2} \frac{\mathcal{E}^2}{(\hbar \omega)^3} \quad \text{which matches}$$

with the above expression for  $\mathcal{E}$  being very large so that  $\mathcal{E}^2$  dominates over  $\mathcal{E}$  term.

For finite  $N$  system,  $g(\mathcal{E}) = \frac{1}{2} \frac{\mathcal{E}^2}{(\hbar \omega)^3}$  approximation will not be enough and we need corrections to  $g(\mathcal{E})$ .

We assume, for anisotropic case,

$$g(\xi)|_{\text{aniso}} = \frac{1}{2} \frac{\xi^2}{(\hbar\bar{\omega})^3} + \gamma \frac{\xi}{(\hbar\bar{\omega})^2} + \delta$$

$$\text{where } \xi = \hbar(n_x\omega_x + n_y\omega_y + n_z\omega_z)$$

and  $E_{n_x, n_y, n_z} = \xi + \xi_0$ ,  $\xi_0$   
being zero point energy.

Here,  $\gamma, \delta$  are constant and depends on  $\omega_x, \omega_y, \omega_z$  and converges to  $\frac{3}{2}$  and 1 respectively for isotropic case ( $\bar{\omega} = \omega$ )

Upto a first order correction due to finite numbers of Bosons in the system, we take,

$$g(\xi)d\xi = \left\{ \frac{1}{2} \frac{\xi^2}{(\hbar\bar{\omega})^3} + \gamma \frac{\xi}{(\hbar\bar{\omega})^2} \right\} d\xi$$

Now, we will try to find what the value or expression of  $\gamma$  is in the following way,



Calculation of DOS considering zero point correction in order to use it to finite number of Boson system

$$E = E_{n_x, n_y, n_z} = (n_x + \frac{1}{2})\hbar\omega_x + (n_y + \frac{1}{2})\hbar\omega_y + (n_z + \frac{1}{2})\hbar\omega_z$$

$$\xi + \xi_0 = \epsilon'_x + \epsilon'_y + \epsilon'_z \quad \left[ \begin{array}{l} \epsilon'_x = (n_x + \frac{1}{2})\hbar\omega_x \\ \epsilon'_y = (n_y + \frac{1}{2})\hbar\omega_y \\ \epsilon'_z = (n_z + \frac{1}{2})\hbar\omega_z \end{array} \right]$$

Now, energy less than  $\xi_0$  is not accessible quantum mechanically,

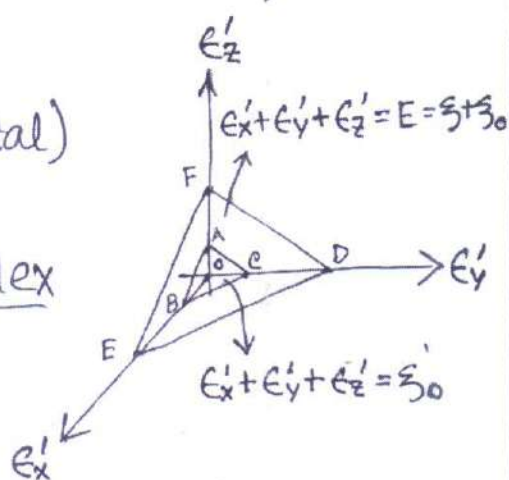
So, the number of states (total) less having energy  $\leq E$

$$= \frac{\text{Volume of the truncated simplex}}{(\hbar\omega_x)(\hbar\omega_y)(\hbar\omega_z)}$$

$$= \frac{\frac{E^3}{6} - \frac{\xi_0^3}{6}}{\hbar^3 \bar{\omega}^3}$$

$$G(\xi) = \frac{(\xi + \xi_0)^3 - \xi_0^3}{6(\hbar\bar{\omega})^3}$$

$$\Rightarrow g(\xi)d\xi = \frac{dG(\xi)}{d\xi}d\xi = \frac{1}{2(\hbar\bar{\omega})^3}(\xi + \xi_0)^2 d\xi$$



$$g(\xi) d\xi = \frac{1}{2(\hbar\bar{\omega})^3} (\xi^2 + 2\xi_0\xi + \xi_0^2) d\xi$$

$$g(\xi) d\xi = \frac{\xi^2 d\xi}{2(\hbar\bar{\omega})^3} + \left(\frac{\xi_0}{\hbar\bar{\omega}}\right) \frac{\xi d\xi}{(\hbar\bar{\omega})^2} + \left(\frac{\xi_0}{\hbar\bar{\omega}}\right)^2 \frac{d\xi}{\hbar\bar{\omega}}$$

$$\text{Here } \xi_0 = \frac{1}{2} \hbar(\omega_x + \omega_y + \omega_z) = \frac{3}{2} \hbar \omega_m$$

$$(\omega_m = \frac{\omega_x + \omega_y + \omega_z}{3})$$

$$\Rightarrow g(\xi) \Big|_{\text{finite-N case}} = \frac{1}{2} \frac{\xi^2}{(\hbar\bar{\omega})^3} + \left(\frac{3}{2} \frac{\omega_m}{\bar{\omega}}\right) \frac{\xi}{(\hbar\bar{\omega})^2} + \left(\frac{3}{2\sqrt{2}} \frac{\omega_m}{\bar{\omega}}\right)^2 \frac{1}{\hbar\bar{\omega}}$$

We see, in the limit  $\bar{\omega} = \omega_m$  (isotropic case)

$$\frac{3}{2} \frac{\omega_m}{\bar{\omega}} = \frac{3}{2}$$

$$\left(\frac{3}{2\sqrt{2}} \frac{\omega_m}{\bar{\omega}}\right)^2 = \left(\frac{3}{2\sqrt{2}}\right)^2 = 1.125 \approx 1$$

So, the density of states almost converges in the isotropic limit ( $\omega_m = \bar{\omega}$ ).

So,

$$g(\xi) \approx \frac{1}{2} \frac{\xi^2}{(\hbar\bar{\omega})^3} + \left(\frac{3}{2} \frac{\omega_m}{\bar{\omega}}\right) \frac{\xi}{(\hbar\bar{\omega})^2} \text{ upto}$$

$$\text{first order correction } \left[ \gamma = \frac{3}{2} \frac{\omega_m}{\bar{\omega}} \right]$$

$$\xi = \hbar(n_x \omega_x + n_y \omega_y + n_z \omega_z)$$

So, now, total no. of particles in the excited states,

$$\begin{aligned}
 N_{ex} &= \int_{\epsilon=0}^{\infty} g(\epsilon) f(\epsilon) d\epsilon \\
 &= \int_0^{\infty} \frac{1}{2} \frac{\epsilon^2}{(\hbar\bar{\omega})^3} \frac{d\epsilon}{e^{\beta(\epsilon+\epsilon_0-\mu)} - 1} \\
 &\quad + \gamma \int_0^{\infty} \frac{\epsilon}{(\hbar\bar{\omega})^2} \frac{d\epsilon}{e^{\beta(\epsilon+\epsilon_0-\mu)} - 1}
 \end{aligned}$$

Now, here it is important to notice, that this integral corresponds to  $N_{ex}$ . because this integration does not contribute to ground state occupation as for  $\epsilon=0$ , the integrand vanishes. We need to consider ground state occupancy separately.

$$\begin{aligned}
 N_{ex} &= \frac{1}{2} \left( \frac{k_B T}{\hbar\bar{\omega}} \right)^3 \int_0^{\infty} \frac{(\beta\epsilon)^2 d(\beta\epsilon)}{e^{-\beta(\mu-\epsilon_0)} e^{\beta\epsilon} - 1} \\
 &\quad + \gamma \left( \frac{k_B T}{\hbar\bar{\omega}} \right)^2 \int_0^{\infty} \frac{(\beta\epsilon) d(\beta\epsilon)}{e^{-\beta(\mu-\epsilon_0)} e^{\beta\epsilon} - 1}
 \end{aligned}$$

We define  $z = e^{\beta(\mu-\epsilon_0)}$   
then, we get,

$$N_{ex} = \frac{1}{2} \left( \frac{k_B T}{\hbar\bar{\omega}} \right)^3 \Gamma(3) f_3(z) + \gamma \left( \frac{k_B T}{\hbar\bar{\omega}} \right)^2 \Gamma(2) f_2(z)$$



Total number of particles of the system

$$N = N_0 + \frac{1}{2} \left( \frac{k_B T}{\hbar \bar{\omega}} \right)^3 \Gamma(3) f_3(z) + \gamma \left( \frac{k_B T}{\hbar \bar{\omega}} \right)^2 \Gamma(2) f_2(z)$$

$$N \approx N_0 + \left( \frac{k_B T}{\hbar \bar{\omega}} \right)^3 f_3(z) + \gamma \left( \frac{k_B T}{\hbar \bar{\omega}} \right)^2 f_2(z)$$

↑  
ground state occupancy

Now, for  $T > T_c$ ;  $N_0 \approx 0$  ; so,  $N \approx N_{ex}$ .

but for  $T < T_c$ ;  $N_0$  is not negligible.

From the definition of critical temperature  
we know  $\mu = \epsilon_0 \Rightarrow z = 0$  and  $N_0 = 0$ .

$$\text{Then } N = \left( \frac{k_B T_c}{\hbar \bar{\omega}} \right)^3 g(3) + \gamma \left( \frac{k_B T_c}{\hbar \bar{\omega}} \right)^2 g(2) \text{ at } T = T_c$$

where  $f_3(z=1) = g(3)$  and  $f_2(z=1) = g(2)$ .

We have,

$$N = \left( \frac{k_B T_c}{\hbar \bar{\omega}} \right)^3 g(3) + \gamma \left( \frac{k_B T_c}{\hbar \bar{\omega}} \right)^2 g(2)$$

$$\left( \frac{k_B T_c}{\hbar \bar{\omega}} \right)^3 g(3) = N - \gamma \left( \frac{k_B T_c}{\hbar \bar{\omega}} \right)^2 g(2)$$

$$\Rightarrow \left( \frac{k_B T_c}{\hbar \bar{\omega}} \right)^3 = \frac{N}{g(3)} - \gamma \left( \frac{k_B T_c}{\hbar \bar{\omega}} \right)^2 \frac{g(2)}{g(3)}$$

$$\Rightarrow T_c = \frac{\hbar \bar{\omega}}{k_B} \left( \frac{N}{g(3)} \right)^{1/3} \left[ 1 - \gamma \frac{g(2)}{g(3)} \frac{g(3)}{N} \left( \frac{k_B T_c}{\hbar \bar{\omega}} \right)^2 \right]^{1/3}$$

$$T_c = \frac{\hbar \bar{\omega}}{k_B} \left( \frac{N}{g(3)} \right)^{1/3} \left[ 1 - \frac{\gamma}{3} \frac{g(2)}{(g(3))^{2/3}} \frac{1}{N^{1/3}} \right]$$

$$\left[ \begin{array}{l} \text{Putting } T_c = \left( \frac{\hbar \bar{\omega}}{k_B} \right) \left( \frac{N}{g(3)} \right)^{1/3} \\ \text{to get the expression upto first} \\ \text{order correction} \end{array} \right]$$

We see, that for finite  $N$ -system, the critical temperature is less than the critical temperature for infinite- $N$  case,

for  $N$ -being infinite or extremely large

$$T_c|_{N \rightarrow \infty} = T_0 = \frac{\hbar \bar{\omega}}{k_B} \left( \frac{N}{g(3)} \right)^{1/3}$$

$$\Rightarrow T_c = T_0 \left[ 1 - \frac{\gamma}{3} \frac{g(2)}{(g(3))^{2/3}} \frac{1}{N^{1/3}} \right]$$

[ $T_0$  = critical temperature for infinite  $N$ -case]



So, we get so far,

$$N = \left(\frac{K_B T_c}{\hbar \bar{\omega}}\right)^3 \zeta(3) + \gamma \left(\frac{K_B T_c}{\hbar \bar{\omega}}\right)^2 \zeta(2)$$

as  $N$  goes to very large value ( $N \rightarrow \infty$ )

$$N^\infty = \left(\frac{K_B T_0}{\hbar \bar{\omega}}\right)^3 \zeta(3)$$

This clearly shows as  $N^\infty \gg N$  ;  $T_0 > T_c$  ; a small change in critical temperature would correspond to a large change in  $N$ .

Now, for  $T < T_c$  ; (finite-  $N$ -system),

$$N_{ex}(T) = \left(\frac{K_B T}{\hbar \bar{\omega}}\right)^3 \zeta(3) + \gamma \left(\frac{K_B T}{\hbar \bar{\omega}}\right)^2 \zeta(2)$$

$\Rightarrow$  Ground state occupancy for  $T < T_c$ ,

$$N_0(T) = N - N_{ex}(T)$$

$$\Rightarrow \frac{N_0(T)}{N} = 1 - \frac{1}{N} \left\{ \left(\frac{K_B T}{\hbar \bar{\omega}}\right)^3 \zeta(3) + \gamma \left(\frac{K_B T}{\hbar \bar{\omega}}\right)^2 \zeta(2) \right\}$$

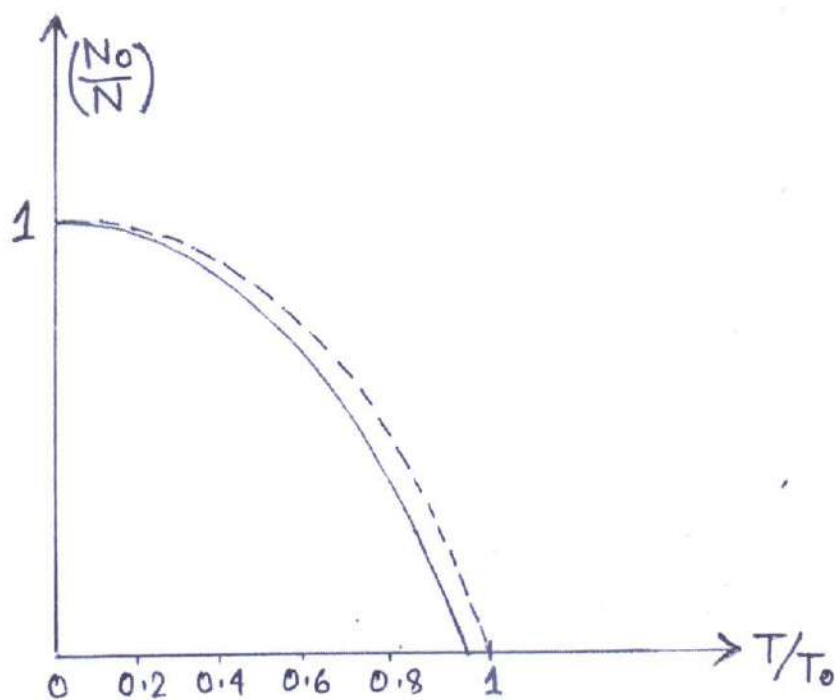
$$\Rightarrow \frac{N_0(T)}{N} = 1 - \left(\frac{T}{T_0}\right)^3 - \gamma \left(\frac{T}{T_0}\right)^2 \frac{\zeta(2)}{(K_B T_0)} \frac{(\hbar \bar{\omega})}{\zeta(3)}$$

$$\Rightarrow \frac{N_0(T)}{T} = 1 - \left(\frac{T}{T_0}\right)^3 - \gamma \left(\frac{T}{T_0}\right)^2 \frac{\zeta(2)}{\zeta(3)^{2/3}} \frac{1}{N^{1/3}}$$

$$\left[ \text{as } T_0 = \frac{\hbar \bar{\omega}}{K_B} \left( \frac{N}{\zeta(3)} \right)^{1/3} \right]$$

So, as  $N$  is very large, the third term is very small, so we can neglect it, and hence, we get,

$$\left. \frac{N_0(T)}{N} \right|_{N \rightarrow \infty} = 1 - \left( \frac{T}{T_0} \right)^3$$



Condensate fraction  $N_0/N$  as a function of  $T/T_0$

Dashed Line :  $N$  very large (thermodynamic limit)

Solid Line : Finite  $N$  bosonic system

Now, we know, if  $Q$  be grand canonical partition function, then,

$$\ln Q = - \sum_i \ln [1 - e^{\beta(\mu - \epsilon_i)}]$$

$$= - \int_{\epsilon=0}^{\infty} g(\epsilon) \ln(1 - e^{\beta(\mu - \epsilon_0)} e^{-\beta \epsilon}) d\epsilon$$

where  $g(\epsilon) = \frac{1}{2(\hbar\omega)^3} \epsilon^2 + \gamma \frac{\epsilon}{(\hbar\omega)^2} = A\epsilon^2 + B\epsilon$

$$\left[ A = \frac{1}{2(\hbar\omega)^3} ; B = \frac{\gamma}{(\hbar\omega)^2} \right]$$

$$\ln Q = - \int_0^{\infty} (A\epsilon^2 + B\epsilon) \ln(1 - ze^{-\beta\epsilon}) d\epsilon$$

$$= -A \int_0^{\infty} \epsilon^2 \ln(1 - ze^{-\beta\epsilon}) d\epsilon - B \int_0^{\infty} \epsilon \ln(1 - ze^{-\beta\epsilon}) d\epsilon$$

$$= -A \ln(1 - ze^{-\beta\epsilon}) \frac{\epsilon^3}{3} \Big|_0^{\infty} + A \int_0^{\infty} \frac{ze^{-\beta\epsilon} \beta \epsilon^3}{1 - ze^{-\beta\epsilon}} \frac{1}{3} d\epsilon$$

$$- B \ln(1 - ze^{-\beta\epsilon}) \frac{\epsilon^2}{2} \Big|_0^{\infty} + B \int_0^{\infty} \frac{ze^{-\beta\epsilon} \beta \epsilon^2}{1 - ze^{-\beta\epsilon}} \frac{1}{2} d\epsilon$$

$$\ln Q = \frac{A}{3} \int_0^{\infty} \frac{\beta \epsilon^3 d\epsilon}{ze^{-\beta\epsilon} - 1} + \frac{B}{2} \int_0^{\infty} \frac{\beta \epsilon^2 d\epsilon}{ze^{-\beta\epsilon} - 1}$$

$$= \frac{A}{3\beta^3} \int_0^{\infty} \frac{x^3 dx}{z^{-1}e^x - 1} + \frac{B}{2} \frac{1}{\beta^2} \int_0^{\infty} \frac{x^2 dx}{z^{-1}e^x - 1}$$

$$\Rightarrow \ln Q = \frac{A}{3\beta^3} \Gamma(4) f_4^+(z) + \frac{B}{2} \frac{1}{\beta^2} \Gamma(3) f_3^+(z).$$



$$\ln Q = \left( \frac{k_B T}{\hbar \bar{\omega}} \right)^3 \rho_4^+(z) + \gamma \left( \frac{k_B T}{\hbar \bar{\omega}} \right)^2 \rho_3^+(z)$$

Now, for potential,

$$V(x, y, z) = \frac{1}{2} m \omega_x^2 x^2 + \frac{1}{2} m \omega_y^2 y^2 + \frac{1}{2} m \omega_z^2 z^2$$

For a particle with energy  $E$ , it will classically have a spatial ellipsoid accessible to move.

the equation of ellipsoid,

$$\frac{x^2}{\left( \sqrt{2E/m\omega_x^2} \right)^2} + \frac{y^2}{\left( \sqrt{2E/m\omega_y^2} \right)^2} + \frac{z^2}{\left( \sqrt{2E/m\omega_z^2} \right)^2} = 1$$

$$a = \sqrt{\frac{2E}{m\omega_x^2}} \quad ; \quad b = \sqrt{\frac{2E}{m\omega_y^2}} \quad ; \quad c = \sqrt{\frac{2E}{m\omega_z^2}}$$

The volume of the ellipsoid  $= \frac{4}{3} \pi abc$

$$= \frac{4}{3} \pi \left( \frac{2E}{m\omega_x^2} \right)^{1/2} \left( \frac{2E}{m\omega_y^2} \right)^{1/2} \left( \frac{2E}{m\omega_z^2} \right)^{1/2}$$

$$V(E) = \frac{4}{3} \pi \left( \frac{2E}{m} \right)^{3/2} \frac{1}{\bar{\omega}^3}$$

So, the volume accessible to a boson with energy  $E$  is roughly  $V(E)$  depending on its energy.

Now, we define a volume which depends only on the structure of the potential, but not on  $E$ , we call it "canonical volume" ( $\mathcal{V}$ ).

$$\mathcal{V} = \frac{1}{\bar{\omega}^3} \quad [ \bar{\omega}^3 = \omega_x \omega_y \omega_z ]$$

We already have,  $\ln Q = \left(\frac{k_B T}{\hbar \omega}\right)^3 f_4^+(\beta) + \gamma \left(\frac{k_B T}{\hbar \omega}\right)^2 f_3^+(\beta)$

We know,  $P = \frac{\partial \ln Q}{\partial V}$

So, we define a canonical pressure  $\phi$ ; such that,

$$\phi = \frac{\partial \ln Q}{\partial V} = \frac{\partial}{\partial V} \left( \left(\frac{k_B T}{\hbar}\right)^3 V f_4^+(\beta) + \gamma \left(\frac{k_B T}{\hbar}\right)^2 V^{2/3} f_3^+(\beta) \right)$$

$$\phi = \left(\frac{k_B T}{\hbar}\right)^3 f_4^+(\beta) + \frac{2}{3} \gamma \left(\frac{k_B T}{\hbar}\right)^2 \frac{f_3^+(\beta)}{V^{1/3}}$$

$$\phi V = \left(\frac{k_B T}{\hbar \omega}\right)^3 f_4^+(\beta) + \frac{2}{3} \gamma k_B T \left(\frac{k_B T}{\hbar \omega}\right)^2 f_3^+(\beta)$$

$$\Rightarrow 3\phi V = 3 \left(\frac{k_B T}{\hbar \omega}\right)^3 f_4^+(\beta) + 2\gamma k_B T \left(\frac{k_B T}{\hbar \omega}\right)^2 f_3^+(\beta)$$

$$3\phi V = \langle E \rangle_{\text{tot.}} - \xi_0 N$$

$$\Rightarrow 3\phi V + \xi_0 N = \langle E \rangle_{\text{tot.}}$$

$$\Rightarrow 3 \left( \phi + \frac{\xi_0 N}{3V} \right) V = \langle E \rangle_{\text{tot.}}$$

$$\Rightarrow 3P V = \langle E \rangle_{\text{tot.}} \quad \left[ \text{We define, } P = \phi + \frac{\xi_0 N}{3V} \right]$$

$$\Rightarrow P = \frac{\langle E \rangle_{\text{tot.}} / V}{3} = \frac{\langle u \rangle_{\text{tot.}}}{3}$$



So, we have,

$$P = k_B T \left( \frac{k_B T}{\hbar} \right)^3 \zeta_4^+(z) + \frac{2\gamma}{3} k_B T \left( \frac{k_B T}{\hbar} \right)^2 \frac{\zeta_3^+(z)}{V^{1/3}} + \frac{\epsilon_0 N}{3V}$$

for  $T < T_c$ ,

$$P = k_B T \left( \frac{k_B T}{\hbar} \right)^3 \zeta_4(1) + \frac{2\gamma}{3} k_B T \left( \frac{k_B T}{\hbar} \right)^2 \frac{\zeta_3(z)}{V^{1/3}} + \frac{\epsilon_0}{3V} \left( N_{\text{ex}}(T)_{T < T_c} + N_{\text{ground}}(T)_{T < T_c} \right)$$

So, if we put,  $T=0$ , we get, due to

$$N_{\text{ex}}(0) = 0,$$

$$N_{\text{ground}}(0) = N$$

$$P_0 = \frac{\epsilon_0 N}{3V} = \text{zero point pressure}$$

as temperature decreases, the bosons jump from excited states to the ground state at  $T < T_c$ , and ground state has a finite non-zero energy, the condensate will have a zero point pressure ( $P_0$ ) and at  $T=0$ ; as all bosons are condensed to  $E = \epsilon_0$  states, so, total particle in ground state is  $N$  and

$$P_0 = \frac{\epsilon_0 N}{3V} = \frac{1}{3} \frac{\epsilon_0}{V} N = \frac{1}{2} \hbar \omega_m \bar{\omega} N$$

It's important to note that this pressure may not have the dimension of pressure, because it comes from canonical pressure ( $\phi = 1/\omega^3$  and  $P = \phi + \frac{\epsilon_0 N}{3V}$ ).



we can also do,

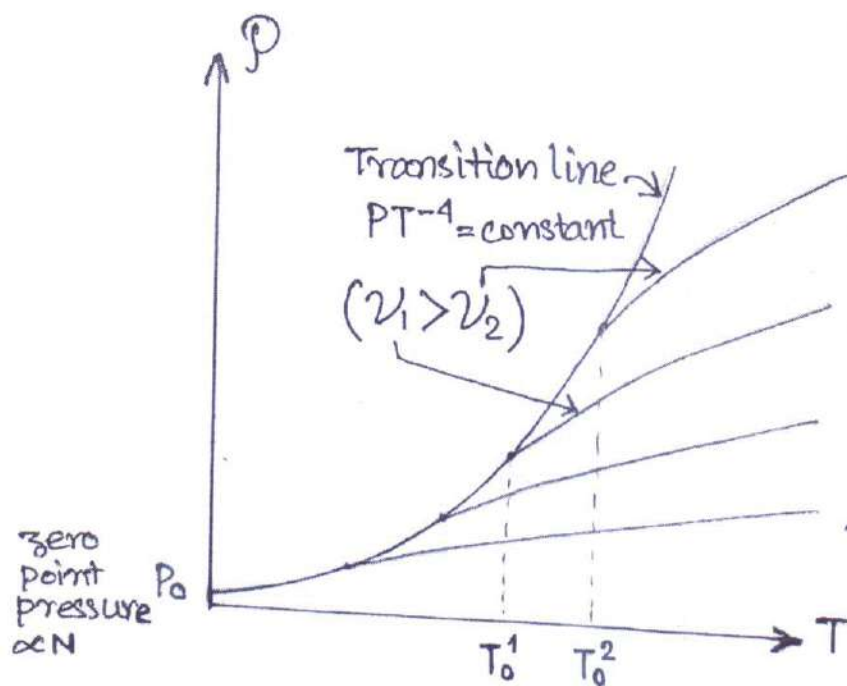
$$P_{T < T_c} = k_B T \left( \frac{k_B T}{\hbar} \right)^3 g(4) + \frac{2\gamma}{3} k_B T \left( \frac{k_B T}{\hbar} \right)^2 \frac{g(3)}{V^{1/3}} \\ + \frac{\xi_0}{3V} \left\{ \left( \frac{k_B T_c}{\hbar \bar{\omega}} \right)^3 g(3) + \gamma \left( \frac{k_B T_c}{\hbar \bar{\omega}} \right)^2 g(2) \right\}$$

In the thermodynamic limit, as  $N \rightarrow \infty$ ,

$$P = k_B T \left( \frac{k_B T}{\hbar} \right)^3 g(4) + \frac{\xi_0}{3V} \left( \frac{k_B T_0}{\hbar \bar{\omega}} \right)^3 g(3) \quad (\text{for } T < T_0)$$

[because for large  $N$  ( $N \rightarrow \infty$ ), we don't have  $\gamma$  term as it's enough to take  $g(3) = \frac{1}{2} \frac{\xi^2}{(\hbar \bar{\omega})^3}$ , and  $T_c|_{N \rightarrow \infty} = T_0$ ]

So, we see,  $P \propto T^4$  (for  $T < T_0$ )



Pressure vs Temperature as  $N \rightarrow \infty$   
 thermodynamic limit

Since, there exists a change of entropy between the gas phase and condensed phase, hence, there should be a latent heat associated with the transition. Thus BEC can be regarded as a first order phase transition.

Using Clausius-Clapeyron's equation, we find the latent heat associated with the transition.

$$\begin{aligned} \left. \frac{dP}{dT} \right|_{\text{transition}} &= \frac{L}{T_c (v)} \quad [v = \text{specific volume of gas phase}] \\ &= \frac{L N}{T_c V} \left[ \because v = \frac{1}{n} = \left( \frac{N_{\text{ex}}(T_c)}{V} \right)^{-1} \right. \\ &\quad \left. = \frac{V}{N_{\text{ex}}(T_c)} = \frac{V}{N} \right] \\ \Rightarrow \left. \frac{dP}{dT} \right|_{\text{transition}} &= \frac{L N \bar{v}^3}{T_c} \quad (\text{because at transition temperature, the particles being in gas phase} = \text{total number of particles of system}) \end{aligned}$$

$$\begin{aligned} \left. \frac{dP}{dT} \right|_{T=T_c} &= \frac{d}{dT} \left\{ k_B T \left( \frac{k_B T}{h} \right)^3 g(4) + \frac{2\gamma}{3} k_B T \left( \frac{k_B T}{h} \right)^2 \frac{g(3)}{V^{1/3}} + \frac{z_0 N}{3V} \right\} \\ &= 4k_B \left( \frac{k_B}{h} \right)^3 T_c^3 g(4) + \frac{2\gamma}{3} k_B \left( \frac{k_B}{h} \right)^2 T_c^2 \frac{g(3)}{V^{1/3}} \left[ \because \left. \frac{dN}{dT} \right|_{T=T_c} = 0 \right] \end{aligned}$$

$$\Rightarrow \frac{LN\bar{\omega}^3}{T_c} = 4K_B \left(\frac{K_B}{\hbar}\right)^3 T_c^3 \zeta(4) + 2\gamma K_B \left(\frac{K_B}{\hbar}\right)^2 T_c^2 \frac{\zeta(3)}{2^{1/3}}$$

$$L = \frac{4K_B \left(\frac{K_B}{\hbar}\right)^3 T_c^4 \zeta(4) + 2\gamma K_B \left(\frac{K_B}{\hbar}\right)^2 T_c^3 \bar{\omega} \frac{\zeta(3)}{1}}{N\bar{\omega}^3}$$

$$L = \frac{4K_B \left(\frac{K_B T_c}{\hbar \bar{\omega}}\right)^3 T_c \zeta(4) + 2\gamma K_B \left(\frac{K_B T_c}{\hbar \bar{\omega}}\right)^2 T_c \zeta(3)}{\left(\frac{K_B T_c}{\hbar \bar{\omega}}\right)^3 \zeta(3) + \gamma \left(\frac{K_B T_c}{\hbar \bar{\omega}}\right)^2 \zeta(2)}$$

In the thermodynamic limit ( $N \rightarrow \infty$ ) : we will ignore terms involving  $\gamma$ ,

$$\Rightarrow L = \frac{4K_B \left(\frac{K_B T_0}{\hbar \bar{\omega}}\right)^3 T_0 \zeta(4)}{\left(\frac{K_B T_0}{\hbar \bar{\omega}}\right)^3 \zeta(3)}$$

$$\Rightarrow L_{N \rightarrow \infty} = 4K_B \frac{\zeta(4)}{\zeta(3)} T_0$$

$L_{N \rightarrow \infty}$  is the latent heat of transition in the thermodynamic limit.



Total average energy due to excited states,

$$\begin{aligned}\langle E \rangle_{\text{ex.}} &= \int_{\xi=0}^{\infty} E g(\xi) f(\xi) d\xi \\ &= \int_0^{\infty} (\xi + \xi_0) \left( \frac{1}{2} \frac{\xi^2}{(\hbar\omega)^3} + \gamma \frac{\xi}{(\hbar\omega)^2} \right) \frac{d\xi}{z^{-1}e^{\beta\xi} - 1} \\ &\quad [z = e^{\beta(\mu - \xi_0)}]\end{aligned}$$

Here,  $\xi=0$  or  $E=\xi_0$  contribution into total average energy is not taken into account because for  $\xi=0$ ; we see the integrand is zero.

$$\begin{aligned}\Rightarrow \langle E \rangle_{\text{total}} &= \int_0^{\infty} \frac{1}{2(\hbar\omega)^3} \frac{\xi^3 d\xi}{z^{-1}e^{\beta\xi} - 1} + \frac{\gamma}{(\hbar\omega)^2} \int_0^{\infty} \frac{\xi^2 d\xi}{z^{-1}e^{\beta\xi} - 1} \\ &\quad + \xi_0 \int_0^{\infty} \left\{ \frac{1}{2} \frac{\xi^2}{(\hbar\omega)^3} + \gamma \frac{\xi}{(\hbar\omega)^2} \right\} \frac{d\xi}{z^{-1}e^{\beta\xi} - 1} + \xi_0 N_0 \\ &\quad [ \xi_0 = \text{ground state energy} ] \\ &\quad [ N_0 = \text{ground state occupancy} ]\end{aligned}$$

$$\langle E \rangle_{\text{tot.}} = \frac{(k_B T)^4}{2(\hbar\omega)^3} \rho_4^+(z) \Gamma(4) + \gamma \frac{(k_B T)^3}{(\hbar\omega)^2} \Gamma(3) \rho_3^+(z) + \xi_0 N$$

$$\Rightarrow U - \xi_0 N = 3k_B T \left( \frac{k_B T}{\hbar \bar{\omega}} \right)^3 \zeta_4^+(2) + 2\gamma k_B T \left( \frac{k_B T}{\hbar \bar{\omega}} \right)^2 \zeta_3^+(2)$$

[for  $T > T_c$ ]

$$= 3k_B T_c \left( \frac{k_B T_c}{\hbar \bar{\omega}} \right)^3 \zeta(4) + 2\gamma k_B T_c \left( \frac{k_B T_c}{\hbar \bar{\omega}} \right)^2 \zeta(3)$$

[at  $T = T_c$ ]

$$= 3k_B T \left( \frac{k_B T}{\hbar \bar{\omega}} \right)^3 \zeta(4) + 2\gamma k_B T \left( \frac{k_B T}{\hbar \bar{\omega}} \right)^2 \zeta(3)$$

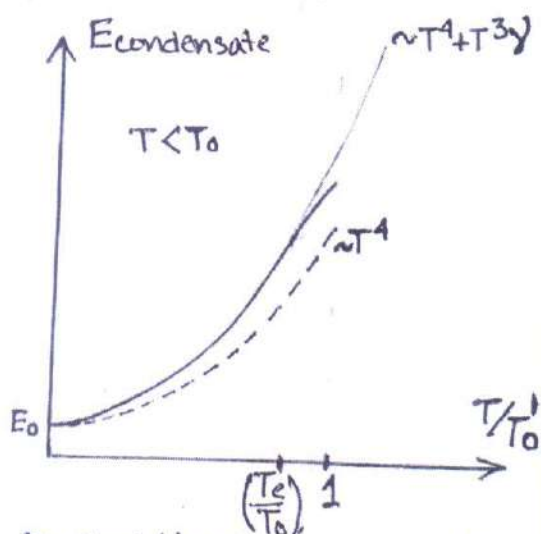
[for  $T < T_c$  ;  $\zeta$  is fixed to 1,  
as  $\mu$  fixed at  $\xi_0$ ]

If we put  $T=0$ , at absolute zero, all the boson are condensed in the ground state ( $E = \xi_0$ ) so, at  $T=0$ ,  $U$  should be  $\xi_0 N$  which matches with the value  $U|_{T=0}$  for  $T < T_c$  expression.

$$U|_{T=0} = \xi_0 N$$

( $T < T_c$ )

After some calculation,  
For large temperature,



Dashed Line:  $\langle E \rangle_{\infty}$  vs  $T/T_0$  as  $N \rightarrow \infty$   
Solid Line:  $\langle E \rangle_{\text{col}}$  vs  $T/T_0$  for  $N$  finite

## Heat Capacity

We already have, for  $T < T_c$ ,

$$U = 3k_B T \left( \frac{k_B T}{\hbar \omega} \right)^3 \zeta(4) + 2 \gamma k_B T \left( \frac{k_B T}{\hbar \omega} \right)^2 \zeta(3) + \zeta_0 N$$

Heat capacity for  $T < T_c$ ;  $C_- = \left( \frac{\partial U}{\partial T} \right)_{T < T_c, N}$

$$\frac{\partial U}{\partial T} = 12 k_B \left( \frac{k_B T}{\hbar \omega} \right)^3 \zeta(4) + 6 \gamma k_B \left( \frac{k_B T}{\hbar \omega} \right)^2 \zeta(3)$$

$$\frac{C_-}{N} = 12 k_B \left( \frac{T}{T_0} \right)^3 \frac{\zeta(4)}{\zeta(3)} + 6 \gamma k_B \left( \frac{T}{T_0} \right)^2 \frac{\zeta(3)^{1/3}}{N^{1/3}}$$

$$\Rightarrow \frac{C_-}{N k_B} = 12 \left( \frac{\zeta(4)}{\zeta(3)} \right) \left( \frac{T}{T_0} \right)^3 + 6 \gamma \frac{\zeta(3)^{1/3}}{N^{1/3}} \left( \frac{T}{T_0} \right)^2$$

In the thermodynamic limit,  $N \rightarrow$  very large and second term becomes negligible,

$$\left. \frac{C_-}{N k_B} \right|_{N \rightarrow \infty} \simeq 12 \frac{\zeta(4)}{\zeta(3)} \left( \frac{T}{T_0} \right)^3$$

for  $T > T_c$ ,  $C_+ = \left( \frac{\partial U}{\partial T} \right)_{T > T_c, N}$

$$U|_{T > T_c} = 3k_B T \left( \frac{k_B T}{\hbar \omega} \right)^3 \rho_4^+(z) + 2 \gamma k_B T \left( \frac{k_B T}{\hbar \omega} \right)^2 \rho_3^+(z) + \zeta_0 N$$

$$C_+ = \left( \frac{\partial U}{\partial T} \right)_N = 12 k_B \left( \frac{k_B T}{\hbar \omega} \right)^3 \rho_4^+(z) + 6 \gamma k_B \left( \frac{k_B T}{\hbar \omega} \right)^2 \rho_3^+(z) + 3 k_B T \left( \frac{k_B T}{\hbar \omega} \right)^3 \frac{\rho_3^+(z)}{z} \frac{dz}{dT} + 2 \gamma k_B \left( \frac{k_B T}{\hbar \omega} \right)^2 \frac{\rho_2^+(z)}{z} \frac{dz}{dT}$$



Now, we need to find  $\frac{1}{z} \frac{dz}{dT} \Big|_N$

We have,

$$N = \left( \frac{k_B T}{\hbar \omega} \right)^3 f_3^+(z) + \gamma \left( \frac{k_B T}{\hbar \omega} \right)^2 f_2^+(z) + N_0$$

[ $N_0$  = # particles occupied the ground state, negligible at  $T > T_c$ ]

Here,  $N$  should be constant but not depend on temperature, the  $T$  dependence of  $f_3^+(z)$  cancels with the powers of  $(k_B T)$  to make  $N$ ,  $T$  independent, for  $T > T_c$ .

$$\Rightarrow \frac{dN}{dT} = 3 \left( \frac{k_B}{\hbar \omega} \right)^3 T^2 f_3^+(z) + 2\gamma \left( \frac{k_B}{\hbar \omega} \right)^2 T f_2^+(z) + \left( \frac{k_B T}{\hbar \omega} \right)^3 \frac{f_2^+(z) dz}{z} \frac{dz}{dT} \Big|_N + \gamma \left( \frac{k_B T}{\hbar \omega} \right)^2 \frac{f_1^+(z) dz}{z} \frac{dz}{dT} \Big|_N = 0$$

$$\Rightarrow \frac{1}{z} \frac{dz}{dT} \Big|_N \left\{ \left( \frac{k_B T}{\hbar \omega} \right)^3 f_2^+(z) + \gamma \left( \frac{k_B T}{\hbar \omega} \right)^2 f_1^+(z) \right\} = - \frac{3}{T} \left( \frac{k_B T}{\hbar \omega} \right)^3 f_3^+(z) - \frac{2\gamma}{T} \left( \frac{k_B T}{\hbar \omega} \right)^2 f_2^+(z)$$

$$\Rightarrow \frac{T}{z} \frac{dz}{dT} \Big|_N = - \frac{3 \left( \frac{k_B T}{\hbar \omega} \right)^3 f_3^+(z) + 2\gamma \left( \frac{k_B T}{\hbar \omega} \right)^2 f_2^+(z)}{\left( \frac{k_B T}{\hbar \omega} \right)^3 f_2^+(z) + \gamma \left( \frac{k_B T}{\hbar \omega} \right)^2 f_1^+(z)}$$

$$\Rightarrow \frac{T}{z} \frac{dz}{dT} \Big|_N = -3 \left[ \frac{f_3^+(z) + \frac{2\gamma \hbar \bar{\omega}}{3k_B T} f_2^+(z)}{f_2^+(z) + \frac{\gamma \hbar \bar{\omega}}{k_B T} f_1^+(z)} \right]$$

Putting the value of  $\frac{T}{z} \frac{dz}{dT} \Big|_N$  in the expression of  $C_+$  we get,

$$C_+ = 12k_B \left( \frac{k_B T}{\hbar \bar{\omega}} \right)^3 f_4^+(z) + 6\gamma k_B \left( \frac{k_B T}{\hbar \bar{\omega}} \right)^2 f_3^+(z) - \left\{ 3k_B \left( \frac{k_B T}{\hbar \bar{\omega}} \right)^3 f_3^+(z) + 2\gamma \left( \frac{k_B T}{\hbar \bar{\omega}} \right)^2 f_2^+(z) \right\} \times \left\{ \frac{3 \left\{ f_3^+(z) + \frac{2\gamma \hbar \bar{\omega}}{3k_B T} f_2^+(z) \right\}}{f_2^+(z) + \frac{\gamma \hbar \bar{\omega}}{k_B T} f_1^+(z)} \right\}$$

Now, we know,

$$f_m^+(z) = \frac{1}{\Gamma(m)} \int_0^\infty \frac{dx x^{m-1}}{z^{-1} e^x - 1} = \sum_{\alpha=1}^\infty \frac{z^\alpha}{\alpha^m} = z + \frac{z^2}{2^m} + \frac{z^3}{3^m} + \dots$$

For high temperature,  $z$  is small, so, at very high temperature,  $f_m^+(z) \approx z$ , now, we are ignoring  $\gamma$  terms in  $\frac{1}{z} \frac{dz}{dT} \Big|_N$  because they goes like  $1/T$ , so they are close to zero.

$$\text{So, } \left( \frac{T}{z} \frac{dz}{dT} \right)_N \Big|_{T \rightarrow \infty} \simeq -3 \frac{f_3^+(z)}{f_2^+(z)} = -3$$

$$\text{So, } \left. \frac{C_+}{N} \right|_{\text{large } T} \simeq 12K_B \left( \frac{f_4^+(z)}{f_3^+(z)} \right) + 6\gamma K_B \left( \frac{\hbar\omega}{K_B T} \right) - 3 \left\{ 3K_B + 2\gamma K_B \left( \frac{\hbar\omega}{K_B T} \right) \frac{f_2^+(z)}{f_3^+(z)} \right\}$$

$$\left[ \because \text{for } T > T_c, \text{ approximately } N \simeq \left( \frac{K_B T}{\hbar\omega} \right)^3 f_3^+(z) \right]$$

$$\Rightarrow \left. \frac{C_+}{N} \right|_{\text{large } T} \simeq 12K_B \left( \frac{f_4^+(z)}{f_3^+(z)} \right) + 6\gamma K_B \left( \frac{\{f_3^+(z)\}^{1/3}}{N^{1/3}} \right) - 3 \left\{ 3K_B + 2\gamma K_B \frac{f_2^+(z)}{\{f_3^+(z)\}^{2/3} N^{1/3}} \right\}$$

$$\left[ \because T \simeq \frac{\hbar\omega}{K_B} \left( \frac{N}{f_3^+(z)} \right) \text{ for large } T; (T > T_c); N_0 \text{ being negligible} \right]$$

$$= 12K_B \cdot \frac{z}{z} + 6\gamma K_B \frac{z^{1/3}}{N^{1/3}} - 3 \left\{ 3K_B + 2\gamma K_B \frac{z^{1/3}}{N^{1/3}} \right\}$$

$$\left. \frac{C_+}{N} \right|_{\text{large } T} = 12K_B + 6\gamma K_B \frac{z^{1/3}}{N^{1/3}} - 9K_B - 6\gamma K_B \frac{z^{1/3}}{N^{1/3}}$$



$$\Rightarrow \frac{C_+}{N} \Big|_{\text{target}} \simeq 3K_B$$

$$\Rightarrow C_{+\text{target}} \simeq 3NK_B$$

$$U_{+\text{target}} \simeq 3NK_B T$$

Now, near critical temperature,  $T \rightarrow T_c$ ;  $z \simeq 1$ ,  
 but  $f_1(z=1) = g(1) = \infty$ ;  $\Rightarrow \frac{T}{z} \frac{dz}{dT} \Big|_{N, T \rightarrow T_c} \simeq 0$

$$\frac{C_+}{N} \Big|_{T \rightarrow T_c^+} = 12K_B \frac{g(4)}{g(3)} + 6\gamma K_B \frac{g(3)^{1/3}}{N^{1/3}} \left\{ 3K_B + 2\gamma K_B \frac{g(2)}{g(3)^{2/3} N^{1/3}} \right\}$$

$$\frac{C_+}{N} \Big|_{T \rightarrow T_c^+} = 12K_B \frac{g(4)}{g(3)} + 6\gamma K_B \frac{g(3)^{1/3}}{N^{1/3}}$$

$$\Rightarrow \frac{C_+}{NK_B} \Big|_{T \rightarrow T_c^+} \simeq 12 \frac{g(4)}{g(3)} + 6\gamma \frac{g(3)^{1/3}}{N^{1/3}} \quad [\text{for finite } N]$$

Now, we already had,

$$\frac{C_-}{NK_B} = 12 \frac{g(4)}{g(3)} \left( \frac{T}{T_0} \right)^3 + 6\gamma \frac{g(3)^{1/3}}{N^{1/3}} \left( \frac{T}{T_0} \right)^2$$

$$\left[ T_0 = \left( \frac{\hbar \bar{\omega}}{K_B} \right) \left( \frac{N}{g(3)} \right)^{1/3} \right]$$

$$\text{So, } \frac{C_-}{NK_B} \Big|_{T \rightarrow T_c^-} = 12 \frac{g(4)}{g(3)} \left( \frac{T_c}{T_0} \right)^3 + 6\gamma \frac{g(3)^{1/3}}{N^{1/3}} \left( \frac{T_c}{T_0} \right)^2$$

Now, for a large variation in  $N$ , critical temperature changes by very small amount, so, roughly we can take  $T_c \approx T_0$  though ( $T_c < T_0$ ).

$$\Rightarrow \frac{C_-}{Nk_B} \Big|_{T \rightarrow T_c^-} = 12 \frac{\zeta(4)}{\zeta(3)} + 6\gamma \left( \frac{\zeta(3)^{1/3}}{N^{1/3}} \right)$$

[for finite  $N$ ]

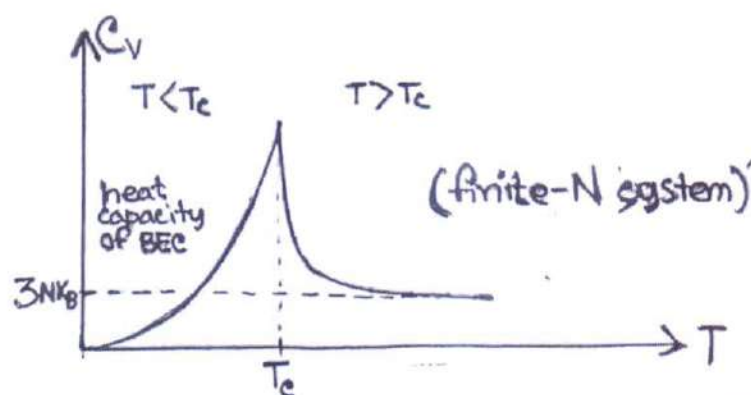
So, we see,

$$\frac{C_+}{Nk_B} \Big|_{T \rightarrow T_c^+} \approx \frac{C_-}{Nk_B} \Big|_{T \rightarrow T_c^-} \quad \text{for finite boson system}$$

$\Rightarrow$  Heat capacity is more or less continuous at  $T = T_c$  neighbourhood for finite boson

though  $\frac{dC_+}{dT} \Big|_{T \rightarrow T_c^+} \neq \frac{dC_-}{dT} \Big|_{T \rightarrow T_c^-}$ , so, that means

in  $C$  vs  $T$  graph for finite boson system, there's a cusp at  $T = T_c$ .



heat capacity in the thermodynamic limit ( $N \rightarrow \infty$ )

We had, for finite boson system, trapped in anisotropic harmonic potential,

$$\frac{C}{Nk_B} \Big|_{T < T_c} = 12 \frac{\zeta(4)}{\zeta(3)} \left( \frac{T}{T_0} \right)^3 + 6\gamma \frac{\zeta(3)^{1/3}}{N^{1/3}} \left( \frac{T}{T_0} \right)^2$$

$$\frac{C}{Nk_B} \Big|_{T > T_c} = 12 \frac{f_4^+(z)}{f_3^+(z)} + 6\gamma \frac{f_3^+(z)}{N^{1/3}} + \left\{ 3 + \frac{2\gamma f_2^+(z)}{f_3^+(z)^{2/3} N^{1/3}} \right\} \frac{T}{z} \frac{dz}{dT} \Big|_N$$

$$\text{where } \frac{T}{z} \frac{dz}{dT} \Big|_N = -3 \left[ \frac{f_3^+(z) + \frac{2\gamma}{3} \frac{f_3^+(z)^{1/3}}{N^{1/3}} f_2^+(z)}{f_2^+(z) + \gamma \frac{f_3^+(z)^{1/3}}{N^{1/3}} f_1^+(z)} \right]$$

$$\left[ \because \text{putting } T = \frac{\hbar \bar{\omega}}{k_B} \left( \frac{N}{f_3^+(z)} \right)^{1/3} \text{ in the previous expression of } \frac{T}{z} \frac{dz}{dT} \Big|_N \right]$$

We can see, the  $\gamma$  terms are involving  $\frac{1}{N^{1/3}}$ ,

so, as  $N \rightarrow \infty$ , we can neglect those terms,

(for large  $N$  case, we can neglect  $\gamma$  term in

$g(z)$  ; so, there should not be any  $\gamma$  sitting in any expression for infinite  $N$  or large  $N$  bosonic system)

$$\Rightarrow \frac{C}{Nk_B} \Big|_{T < T_0}^{N \text{ very large}} = 12 \frac{\zeta(4)}{\zeta(3)} \left( \frac{T}{T_0} \right)^3 \quad \Big| \quad \frac{C}{Nk_B} \Big|_{T > T_0}^{N \text{ very large}} = 12 \frac{f_4^+(z)}{f_3^+(z)} - 9 \frac{f_3^+(z)}{f_2^+(z)}$$



$$\text{So, } \left. \frac{C}{Nk_B} \right|_{T \rightarrow T_0^-} = 12 \frac{g(4)}{g(3)} \left( \frac{T_0}{T_0} \right)^3 = 12 \frac{g(4)}{g(3)}$$

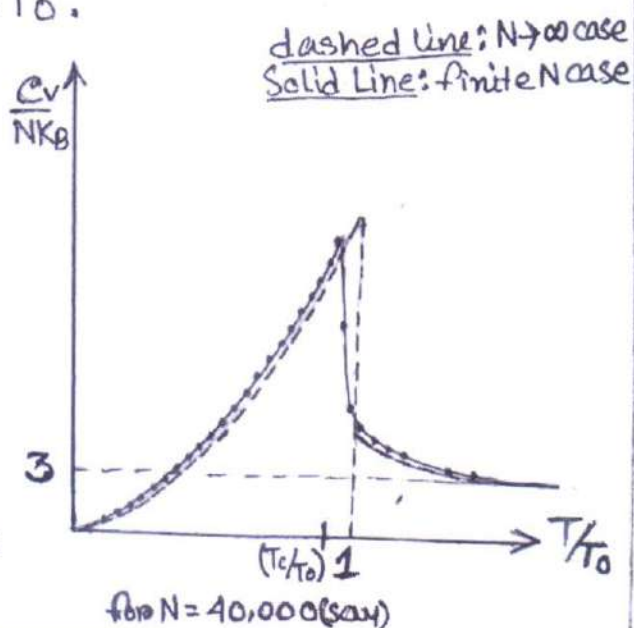
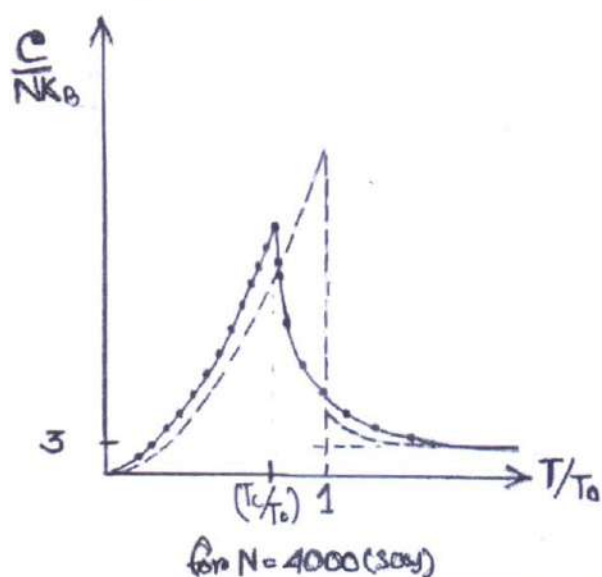
$$\text{and, } \left. \frac{C}{Nk_B} \right|_{T \rightarrow T_0^+} = 12 \frac{g(4)}{g(3)} - 9 \frac{g(3)}{g(2)} \left[ f_m^+(1) = g(m) \right]$$

$$= \left. \frac{C}{Nk_B} \right|_{T \rightarrow T_0^-} - 9 \frac{g(3)}{g(2)}$$

$$\Rightarrow \left. \frac{C}{Nk_B} \right|_{T \rightarrow T_0^+} - \left. \frac{C}{Nk_B} \right|_{T \rightarrow T_0^-} = -9 \frac{g(3)}{g(2)}$$

$$\Rightarrow \left. \frac{\Delta C}{Nk_B} \right|_{T \rightarrow T_0} = -9 \frac{g(3)}{g(2)} \quad \text{for } N \text{ being very large, tends to infinite}$$

So, in the thermodynamic limit,  $C$  is discontinuous at  $T = T_0$ .



The two  $\frac{C}{Nk}$  vs  $T$  graph for  $N = 4000$  and  $N = 40,000$  shows how as the number of bosons in the system increases, the graph converges with the thermodynamic limit ( $N \rightarrow \infty$ ). As  $N$  increases, the graph tends to be discontinuous at  $T \rightarrow T_c$  and  $T_c$  tends to  $T_0$ .

## References

1. Statistical Physics : Kerson Huang
2. Statistical Physics of particles : Mehran Kardar
3. Pethick Smith ; Bose-Einstein Condensation in Dilute gases
4. Trapping Ultracold atoms in time averaged adiabatic potential : Marcus Gildermeisters
5. Thermodynamics of an ideal Gas of bosons Harmonically Trapped : Equation of states and susceptibilities : Rochin and Bagnato
6.  $\lambda$ -transition to Bose-Einstein Condensate : Grossmann and Holthaus
7. Bose Einstein Condensation : Debnarayan Jana
8. Statistical Physics : Landau Lifshitz



# **Two-Dimensional p-n Junctions and 2D-Bipolar Junction Transistors**

Ramakrishna Mission  
Residential College (Autonomous),  
Narendrapur

## **Physics Project**

Name : Koushtav Sarkar  
Roll No.: PHUG/212/17  
Class : BSc.(H) 3<sup>rd</sup> year  
Examination : BSc. Semester 6 (2020)  
Paper : XIV(B)



**Ramakrishna Mission Residential College (Autonomous)**

**Vivekananda Centre for Research**

**Ramakrishna Mission Ashrama**

(A Branch Centre of Ramakrishna Mission, Belur Math, Howrah-711202)

**Narendrapur, Kolkata - 700 103, West Bengal, India**

A Scientific Industrial Research Organisation, Recognised by DST, Govt. of India

College with Potential for Excellence (CPE), Re-accredited by NAAC - 'A' (CGPA 3.56 out of 4)

---

## **DEPARTMENT OF PHYSICS**

### **Certificate**

This is to certify that Koushtav Sarkar, a student of B.Sc has successfully completed the project of UG curriculum entitled "Two-Dimensional p-n Junctions and 2D-Bipolar Junction Transistors" in the period from January to May, 2020.

Malay Purkait  
.....  
30.06.2020

**Signature Of HOD**

**Dept. of Physics**

**Dr. Malay Purkait**

Associate Prof. & Head

Department of Physics

Ramakrishna Mission Residential College

(Autonomous)

Narendrapur, Kolkata-700 103, (W.B.)

## Certificate

To whomsoever it may concern,

It is to certify that Koushtav Sarkar (Roll No.: PHUG/212/17), student of BSc.(Honours) in 3<sup>rd</sup> year, has successfully completed the project on the topic "**Two-Dimensional p-n Junctions and 2D-Bipolar Junction Transistors**", under the guidance of Dr. Sourav Chattopadhyay.

Sourav Chattopadhyay  
26.6.2020.



## **Acknowledgement**

I would like to express my special thanks of gratitude to my teacher Dr. Sourav Chattopadhyay who gave me the golden opportunity to do this wonderful project on topic "Two-Dimensional p-n Junctions and 2D-Bipolar Junction Transistors", which also helped me in doing a lot of Research and I came to know about so many new things I am really thankful to them.

Secondly, I would also like to thank my parents and friends who helped me a lot in finalizing this project within the limited time-frame.

Koushik Sarkar

---

**Signature**

# CONTENTS

| <u>S.No.</u> | <u>Topics</u>                                                                                                                                                                                                                                                                                  | <u>Page No.</u> |
|--------------|------------------------------------------------------------------------------------------------------------------------------------------------------------------------------------------------------------------------------------------------------------------------------------------------|-----------------|
| <u>1</u>     | Abstract                                                                                                                                                                                                                                                                                       | 1               |
| <u>2</u>     | Introduction                                                                                                                                                                                                                                                                                   | 2               |
| <u>3</u>     | Physical Parameters                                                                                                                                                                                                                                                                            | 3               |
| <u>4</u>     | 2D P-N Junction <ul style="list-style-type: none"><li>• <i>Built-in Potential and Depletion Layer</i></li><li>• <i>Current-Voltage Characteristics</i></li><li>• <i>The Continuity Equation in Logarithmic Form</i></li><li>• <i>Approximate Solution to the Continuity Equation</i></li></ul> | 4-8             |
| <u>5</u>     | n-p-n Bipolar Transistor <ul style="list-style-type: none"><li>• <i>Current Gain</i></li><li>• <i>Small-Signal Model</i></li><li>• <i>Large-Signal Model</i></li></ul>                                                                                                                         | 9-12            |
| <u>6</u>     | Approximate Formulae for an n-p-n 2D-BJT                                                                                                                                                                                                                                                       | 13              |
| <u>7</u>     | Conclusion                                                                                                                                                                                                                                                                                     | 15              |
| <u>8</u>     | Reference                                                                                                                                                                                                                                                                                      | 16              |

## Abstract

Recent development in fabrication technology of planar two-dimensional (2D) materials has brought up possibilities of numerous novel applications. Our recent analysis has revealed that by definition of p-n junctions through appropriate patterned doping of 2D semiconductors, ideal exponential I-V characteristics may be expected. However, the theory of 2D junctions turns out to be very much different to that of the standard bulk junctions. Based on this theory of 2D diodes, here we construct a model to describe the 2D Bipolar Junction Transistors (2D-BJTs). We derive the small-signal equivalent model, and estimate the performance of a 2D-BJT device based on Graphene as the example material. A current gain of about 138 and maximum threshold frequency of 77 GHz, together with a power-delay product of only 4 fJ per 1  $\mu\text{m}$  lateral width is expected at an operating voltage of 5 V. Also, we derive necessary formulae and a new approximate solution for continuity equation in the 2D configuration, which have been verified against numerical solutions.



# Introduction

Graphene was discovered in 2004, leading to interest in 2-D materials. The common feature of 2D materials is that they are all only one monatomic layer thick. In general, basic properties of 2D materials can be routinely engineered by doping, functionalisation, and chemical modification, such as hydrogenation or oxidization. The fully-hydrogenated Graphene, or Graphane, should be obtainable as a stable 2D hydrocarbon. Since then, a great deal of research has been focused on its properties, investigating its electronic, optical, nanotube allotropes, and even superconductive properties. Although perfectly-ordered Graphane may be difficult to obtain, however, it has been shown, the influence of substrate material on the quality of 2D crystal domains cannot be neglected.

Recently, a similar material with identical chemical configuration has been created by hydrogenation of Germanene, named as Germanane [14]. These monolayer hydrogenated dielectrics are very much similar and are expected to be described by identical theories. Single-sided hydrogenation of Graphene is however much better suited for most of our applications, commonly referred to as Graphone. It has been shown that stacks of 2D materials could also lead to unprecedented applications in everyday's science and technology. With the advent of insulating 2D-Boron Nitride, further properties of such layered 2D sandwiches have been proposed. Using tight binding calculations Graphane has been shown to have potential advantages over Graphene with regard to having a controllable bandgap which makes it highly desirable for integrated electronic applications. Many articles are concerned with simulations of material properties only, whereas studying the operation of the proposed class of 2D structures would need a significantly different theory. The formulation discussed in this article is based on the theory of 2D p-n rectifying junction diodes. Evidently, a pair of similar 2D junctions may provide a fairly good basis for operation of a 2D Bipolar Junction Transistors (2D-BJTs). This article discusses the design of a 2D-BJT with abrupt doping profile, and Graphone is used as the host 2D material. An electrostatic analysis of the transistor is done together with Shockley's law. The small-signal equivalent circuit of the 2D-BJT in its active region is obtained, and it is shown that extremely large output resistances together with vanishingly small power-delay products are possible at once, thus bringing the ultralow power circuits one step closer to the reality.

This article derives the necessary formulae for description of 2D-BJTs, study the 2D continuity equations, and suggests useful approximate analytical solutions. Accuracy of approximate analytical solutions is established by comparing to the exact numerical solutions. It is anticipated that 2D-BJTs based on Graphane, Germanane, and similar 2D materials, would also share similar theories.

## Physical Parameters

Some of the required physical parameters are already reported in literature, and the remaining data are derived from band structure and/or available relations. These include the effect of dopant type & concentration of carrier mobility, effective dielectric constant, effective mass & the 2D density of states. There exist experiments which have probed the influence of chemical dopants on the carrier mobility in Graphene. Hall measurements revealed that NO and H<sub>2</sub>O adsorption act as acceptors whereas NH<sub>3</sub> and CO are donors. It is reported that when Graphene is treated with atomic hydrogen, it starts exhibiting an insulating behavior because of increasing band gap. This is while the electron mobility of Graphene has been also measured in experiment, and it is found that by annealing, the mobility of Graphene is recovered to the Graphene mobility 3,500 cm<sup>2</sup> V<sup>-1</sup>s<sup>-1</sup>. Also, it has been reported that the influence of chemical dopants on the carrier mobility in Graphene. It is observed that even for surface chemical dopant concentrations in excess of 10<sup>12</sup> cm<sup>-2</sup> there is no observable change in the carrier mobility. It has been found the effective mass and 2D density of states from Graphene band structure. For this purpose, the tight-binding method has been used to obtain band structure, leading to the effective masses  $m_c^* = 1.03$ ,  $m_v^* = 0.63$ . Based on these data, the total planar density of states was obtained to be

$$N_{c(v)}^{2D} = \frac{m_{c(v)} k_B T}{\pi \hbar^2}$$

The relative dielectric constant of Graphene is also about 2.5. But there is no available measurement on the dielectric constant of Graphene. Here, the dielectric image method has been used to take on a value of 2.7 for the relative dielectric constant of Graphene layer on SiO<sub>2</sub> substrate. Using the electrostatic image method, we see that the effective permittivity seen by charges lying on an interface between two dielectrics is simply

$$\epsilon_{\text{eff}} = (\epsilon_2 + \epsilon_1) / 2\epsilon_1$$

Hence, if the substrate is SiO<sub>2</sub> with the relative permittivity 4.4 and the covering layer on the Graphene is vacuum or air, then the effective permittivity of the layer will be given by

$$\epsilon_{\text{eff}} = (4.4 + 1) / 2 = 2.7$$

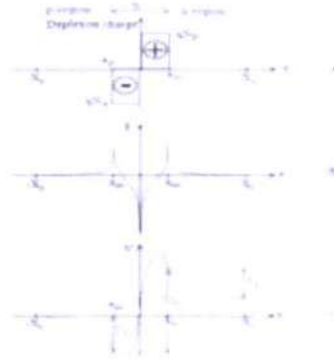


Figure 1. Abrupt p-n junction in the thermal equilibrium: (a) Space charge distribution; (b) Electric field distribution; (c) Potential distribution.



## 2D P-N Junction

We design an abrupt p-n junction with submicron dimensions. This requirement will be needed to obtain high gain and bandwidth. For this purpose, we resolve the continuity equation for a limited length junction. Also we will drive the necessary theoretical formulae and compare them with numerical calculation

### • Built-in Potential and Depletion Layer

In a bulk 3D p-n junction we deal with space charge within the depletion region. But for a 2D junction, there is a surface charge. So we have introduced a new charge model to illustrate this 2D system. This charge sheet is divided into infinitely many thin line charges with differential line charge densities  $A$  and  $D$  in p and n depletion regions, respectively. Figure 2 shows this idea schematically. The electric field due to each line charge is  $E(r) = \lambda/r$  where  $r$  is measured with respect to the symmetry axis of the line charge. The total electric field had been reported for the four regions over the surface of the junction in, which may be now combined into one unified equation in the following manner.

1) For a single infinite line charge lying along the y-axis and positioned at  $(x=x_0, z=0)$ , x-axis directed electric field along the  $z=0$  plane is given by

$$E_x(x, x_0)|_{line} = \frac{qN_{1D}}{2\pi\epsilon_{eff}(x-x_0)}$$

If we divide a block of sheet charge representing the space charge region of a 2D lateral p-n junction that extends from  $x_1$  to  $x_2$  into infinitely many line charges the line charge density for a single line is given by

$$qN_{1D} = \lim_{x \rightarrow \infty} qN_{2D} \frac{(x_2 - x_1)}{n} = qN_{2D} dx_0, \text{ where } qN_{2D} \text{ is the sheet charge density of the block (in C/area).}$$

The x-directed electric field due to one of these infinitely many line charges is given by

$$dE_x(x, x_0) = \frac{qN_{2D} dx_0}{2\pi\epsilon_{eff}(x-x_0)}$$

such that the x-directed electric field for the entire block of charge is equal to

$$E_x(x, x_0)|_{block} = \int_{x_1}^{x_2} dE_x(x, x_0) = \int_{x_1}^{x_2} \frac{qN_{2D} dx_0}{2\pi\epsilon_{eff}(x-x_0)} = \lambda \ln \left| \frac{x-x_1}{x-x_2} \right|, \text{ whereas } \lambda = \frac{qN_{2D}}{2\pi\epsilon_{eff}}$$

For the 2D lateral p-n junction shown in Fig.2(a), the combined electric field due to the p and n block of depletion charge is given by

$$E_x(x)|_{depletion\ charge} = -\lambda_A \left| \frac{x+x_{p0}}{x} \right| + \lambda_D \left| \frac{x}{x-x_{n0}} \right| = \lambda_A \left| \frac{x}{x+x_{p0}} \right| - \lambda_D \left| \frac{x-x_{n0}}{x} \right|$$

where  $\lambda_A = \frac{qN_{A,2D}}{2\pi\epsilon_{eff}}$  and  $\lambda_D = \frac{qN_{D,2D}}{2\pi\epsilon_{eff}}$ ;  $N_{A,2D}$  and  $N_{D,2D}$  are the charge densities of ionized acceptors and donors of the p and n regions, respectively, and the negative sign in front of the  $\lambda_A$  term accounts for the negative charge of ionized acceptors.  $x_p$  and  $x_n$  are depletion widths for the p and n sides of the junction. Figure 1 shows this abrupt p-n junction under the thermal equilibrium. It may be noticed that since  $\frac{\partial E(x, z=0)}{\partial x} \cdot \hat{z} \neq 0$ , the derivative  $\frac{\partial E(x)}{\partial x}$  does not reproduce the initial charge distribution, unlike the regular step junctions. This is simply because  $\frac{\partial E(x)}{\partial x} \neq \nabla \cdot E(x, z=0)$ .

Now, from the Poisson equation, the potential distribution is obtained. The potential across the depletion region, gives the built-in potential. The electric field in the p-region  $E_1$  and the n-region  $E_2$  are respectively,

$$E_1 = \lambda_A \left| \frac{x}{x+x_{p0}} \right| \text{ and } E_2 = -\lambda_D \left| \frac{x-x_{n0}}{x} \right|$$

To calculate the built-in potential,

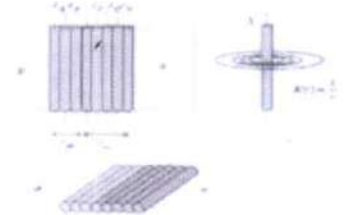


Figure 2. New charge model to illustrate surface charge.



$$\begin{aligned}
V_{bi} &= - \int_{x_{p0}}^{x_{n0}} E dx = - \int_0^{x_{n0}} E_1 dx - \int_{-x_{p0}}^0 E_2 dx = - \int_0^{x_{n0}} \lambda_A \left| \frac{x}{x+x_{p0}} \right| dx - \int_{-x_{p0}}^0 -\lambda_D \left| \frac{x-x_{n0}}{x} \right| dx \\
&= -\lambda_A \left[ x \ln \left| \frac{x}{x+x_{p0}} \right|_0^{x_{n0}} + - \int_0^{x_{n0}} \frac{x_{p0} dx}{x+x_{p0}} \right] + \lambda_D \left[ x \ln \left| \frac{x_{n0}-x}{x} \right|_{-x_{p0}}^0 - \int_{-x_{p0}}^0 \frac{-x_{n0} dx}{x_{n0}-x} \right] \\
&= -\lambda_A \left[ x \ln \left| \frac{x}{x+x_{p0}} \right|_0^{x_{n0}} - x_{p0} \ln |x+x_{p0}|_0^{x_{n0}} \right] + \lambda_D \left[ x \ln \left| \frac{x_{n0}-x}{x} \right|_{-x_{p0}}^0 - x_{n0} \ln |x_{n0}-x|_{-x_{p0}}^0 \right] \\
&= \lambda_A \left[ x_{n0} \ln \left| \frac{x_{n0}+x_{p0}}{x_{n0}} \right| + x_{p0} \ln \left| \frac{x_{n0}+x_{p0}}{x_{p0}} \right| \right] + \lambda_D \left[ x_{p0} \ln \left| \frac{x_{n0}+x_{p0}}{x_{p0}} \right| + x_{n0} \ln \left| \frac{x_{n0}+x_{p0}}{x_{n0}} \right| \right] \\
&= (\lambda_A + \lambda_D) \left[ x_{n0} \ln \left| \frac{x_{n0}+x_{p0}}{x_{n0}} \right| + x_{p0} \ln \left| \frac{x_{n0}+x_{p0}}{x_{p0}} \right| \right]
\end{aligned}$$

$$\therefore V_{bi} = (\lambda_A + \lambda_D) \left[ x_{n0} \ln \left| \frac{W}{x_{n0}} \right| + x_{p0} \ln \left| \frac{W}{x_{p0}} \right| \right] \quad \dots\dots\dots(2)$$

where  $W = x_{n0} + x_{p0}$ . For a symmetric abrupt junction,  $x_{n0}=x_{p0}=W/2$ ,  $\lambda_D=\lambda_A = \lambda$ .

Hence (2) is reduced to

$$\therefore V_{bi} = \lambda W \ln 2 \quad \dots\dots\dots(3)$$

The built in potential is proportional to  $W$  while for a conventional bulk p-n junction it is proportional to  $W$ . Now since the electric field is non-zero inside the p and n neutral regions, the potential drops across these regions are found as

$$V_p = -(\lambda_A + \lambda_D)[x_{p0} \ln x_{p0} + x_p \ln x_p] + \lambda_A(x_p - x_{p0}) \ln(x_p - x_{p0}) - \lambda_D W \ln W + \lambda_A(x_p + x_{n0}) \ln(x_p + x_{n0}) \quad \dots\dots\dots(4)$$

$$V_n = (\lambda_A + \lambda_D)[x_{n0} \ln x_{n0} - x_n \ln x_n] + \lambda_A(x_n + x_{p0}) \ln(x_n + x_{p0}) - \lambda_A W \ln W + \lambda_D(x_n - x_{n0}) \ln(x_n - x_{n0}) \quad \dots\dots\dots(5)$$

To simplify the analysis, the depletion approximation is here used. Hence, under the thermal equilibrium, the total negative charge per unit width in the p-side must be equal to the total negative

$$\begin{array}{ccccccc}
\text{charge} & & \text{per} & & \text{unit} & & \text{width} & & \text{in} & & \text{the} & & \text{n-side} \\
N_A x_{p0} = N_D x_{n0} & & & & & & & & & & & & \dots\dots\dots(6)
\end{array}$$

For an abrupt junction the built-in potential is equal to

$$V_{bi} = E_{Fn0} - E_{Fp0} = E_i + \frac{kT}{q} \ln \frac{N_D}{n_i} - \left( E_i - \frac{kT}{q} \ln \frac{N_A}{n_i} \right) = \frac{kT}{q} \ln \left( \frac{N_D N_A}{n_i^2} \right) = V_T \ln \left( \frac{N_D N_A}{n_i^2} \right) \quad \dots\dots\dots(7)$$

From (2), (6) and (7), the depletion width is calculated to be

$$W = \frac{2\pi\epsilon}{q} \times \frac{V_T \ln \frac{N_A N_D}{n_i^2}}{N_D \ln \left( 1 + \frac{N_A}{N_D} \right) + N_A \ln \left( 1 + \frac{N_D}{N_A} \right)} \quad \dots\dots\dots(8)$$

## • Current-Voltage Characteristics

The injected minority-carriers distribution in the n-side is governed by the continuity conditions at the two edges, subject to the Shockley's boundary conditions

In the n-side,

$$-\frac{p_n(x) - p_{n0}}{\tau_p} - \mu_p(E(x) \frac{dp_n(x)}{dx} + V_T \frac{d^2 p_n(x)}{dx^2}) = 0 \quad \dots\dots\dots(9)$$

$$p_n(x = x_{n0}) = p_{n0} \exp\left(\frac{V}{V_T}\right) \quad \text{and} \quad p_n(x = x_n) = p_{n0}$$

and similarly in the p-side,

$$-\frac{n_p(x) - n_{p0}}{\tau_n} + \mu_n(E(x) \frac{dn_p(x)}{dx} + V_T \frac{d^2 n_p(x)}{dx^2}) = 0 \quad \dots\dots\dots(10)$$

$$n_p(x = -x_{p0}) = n_{p0} \exp\left(\frac{V}{V_T}\right) \quad \text{and} \quad n_p(x = -X_p) = n_{p0}$$

As mentioned before, in the neutral region the electric field is non-zero and  $E(x)$  represents the local electric field of each point in this region. To solve these equations numerically, besides using these equations directly, we can also use the logarithmic form discussed in the next subsection.

### The Continuity Equation in Logarithmic

Form A useful and stable method for solving this equation is to transform the equation into Logarithmic form. We start from (11) and first define

$$n_p = n_{p0} \exp(N(x)).$$

Then we have by differentiating both sides

$$n_p'(x) = n_{p0} \exp(N(x)) \times N'(x) = n_p N' \Rightarrow \frac{n_p'(x)}{n_p} = N' \quad \dots\dots\dots(11)$$

Differentiating both sides again,

$$\frac{n_p n_p'' - n_p'^2}{n_p^2} = N''(x) \Rightarrow \frac{n_p''}{n_p} - \left(\frac{n_p'}{n_p}\right)^2 = N''(x) \Rightarrow \frac{n_p''}{n_p} = N'' + N'^2 \quad \dots\dots\dots(12)$$

Multiplying by  $\tau_n$  and dividing by  $n_p$  on both sides of equation (10), we get,

$$\begin{aligned} -\frac{n_p(x) - n_{p0}}{n_p} + \frac{\mu_n \tau_n}{n_p} (E(x) \frac{dn_p(x)}{dx} + V_T \frac{d^2 n_p(x)}{dx^2}) &= 0 \\ \Rightarrow -\left(1 - \frac{n_{p0}}{n_p}\right) + \mu_n \tau_n \left(E \frac{n_p'}{n_p} + V_T \frac{n_p''}{n_p}\right) &= 0 \Rightarrow -(1 - \exp(-N)) + \mu_n \tau_n V_T \left(\frac{E}{V_T} \frac{n_p'}{n_p} + \frac{n_p''}{n_p}\right) = 0 \\ \Rightarrow -(1 - \exp(-N)) + L_n^2 \left(\frac{E(x)}{V_T} N'(x) + (N'' + N'^2)\right) &= 0 \quad \dots\dots\dots(13), \end{aligned}$$

where  $L_n = \sqrt{\tau_n \mu_n V_T}$ . Hence, we may rewrite equation (10) as the second-order non-linear equation,

$$\exp(-N) - 1 + L_n^2 \left[ \frac{E}{V_T} N' + (N'' + N'^2) \right] = 0 \quad \dots\dots\dots(14)$$

$$N(x=0) = \frac{V}{V_T} \quad \text{and} \quad N(x=W) = 0$$

We now define two parameters  $M = N'$  and  $f = \frac{E}{V_T}$ . Using these parameters and from equation (13), we obtain the nonlinear first-order system of equations, So, from equation, we get,

$$\begin{aligned} \therefore \exp(-N) - 1 + L_n^2 \left[ \frac{E}{V_T} N' + (N'' + N'^2) \right] &= 0 \\ \Rightarrow \exp(-N) - 1 + L_n^2 [f.M + (M)' + (M)^2] &= 0 \Rightarrow L_n^2 [f.M + (M)' + (M)^2] = 1 - \exp(-N) \\ \Rightarrow M' = -(M^2 + fM) + \frac{1 - \exp(-N)}{L_n^2} \end{aligned}$$

$$\begin{bmatrix} N \\ M \end{bmatrix}' = \begin{bmatrix} M \\ M^2 + fM + \frac{1 - \exp(-N)}{L_n^2} \end{bmatrix} \quad \dots\dots\dots(15)$$

which can be solved by the well-known Runge-Kutta method. The solutions in both exponential and logarithmic forms agree, but the logarithmic form is far more stable.

### Approximate Solution to the Continuity Equation

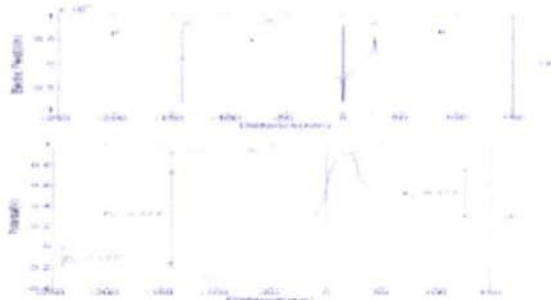


Figure 3. (a) Electric field distribution; (b) Electric potential distribution

Here, we suggest an analytical approximation to (9,10). First, we suppose that the electric field at each point located in the neutral region is a constant parameter. Then we solve the equation just if as the electric field would have zero derivatives. Once the expression is found, the position-dependent electric field is plugged in. Obviously, this method is sufficiently accurate for slowly varying electric fields. Thus, this approximation gives,

$$p_n(x) - p_{n0} \approx p_{n0} \left[ \exp\left(\frac{V}{V_T}\right) - 1 \right] \times \frac{\exp\left[\frac{x}{L_{p2}(x)}\right] \exp\left[\frac{x_n}{L_{p1}(x)}\right] - \exp\left[\frac{x}{L_{p1}(x)}\right] \exp\left[\frac{x_n}{L_{p2}(x)}\right]}{\exp\left[\frac{x_{n0}}{L_{p2}(x)}\right] \exp\left[\frac{x_n}{L_{p1}(x)}\right] - \exp\left[\frac{x_{n0}}{L_{p1}(x)}\right] \exp\left[\frac{x_n}{L_{p2}(x)}\right]} \quad \dots\dots(16)$$

$$\text{where } L_{pi}(x) = 2\tau_p V_T \left[ \tau_p E(x) - (-1)^i \sqrt{\tau^2 E^2(x) + \frac{4\tau_p V_T}{\mu_p}} \right]^{-1}$$

Similarly, we obtain the injected holes distribution in the p-side theoretically as

$$n_p(x) - n_{p0} \approx n_{p0} \left[ \exp\left(\frac{V}{V_T}\right) - 1 \right] \times \frac{\exp\left[\frac{-x}{L_{n1}(x)}\right] \exp\left[\frac{x_p}{L_{n2}(x)}\right] - \exp\left[\frac{-x}{L_{n2}(x)}\right] \exp\left[\frac{x_p}{L_{n1}(x)}\right]}{\exp\left[\frac{x_{p0}}{L_{n2}(x)}\right] \exp\left[\frac{x_p}{L_{n1}(x)}\right] - \exp\left[\frac{x_{p0}}{L_{n1}(x)}\right] \exp\left[\frac{x_p}{L_{n2}(x)}\right]} \quad \dots\dots(17)$$

$$\text{where } L_{ni}(x) = 2\tau_n V_T \left[ \tau_n E(x) - (-1)^i \sqrt{\tau^2 E^2(x) + \frac{4\tau_n V_T}{\mu_n}} \right]^{-1}$$

In practice, these approximations have been verified against numerical solutions of the exponential and logarithmic nonlinear differential equations, yielding surprisingly good agreements, as discussed later below. Now, we proceed to design of the step 2D p-n junction. The overall device length is taken to be about 370nm

and the surface dopant concentrations are  $N_D = 1 \times 10^{12} \text{ cm}^{-2}$  and  $N_A = 5 \times 10^{11} \text{ cm}^{-2}$  as depicted in figure 2. All calculations are here done per unit-width of the device.

The results prove the acceptable accuracy of the formulas. Now, we continue to derive the current densities. At,  $x = x_{n0}$ , the hole current density is

$$J_p = q\mu_p \left( E p_n - V_T \frac{dp_n}{dx} \right) \Big|_{x=x_{n0}} = J_{p0} \left[ \exp\left(\frac{V}{V_T}\right) - 1 \right] \quad \dots\dots(18)$$

$$J_{p0} = \frac{q\mu_p p_{n0} E(x_{n0}) - \frac{q\mu_p p_{n0} V_T}{A(x_{n0})} \left[ \frac{\exp\left[\frac{x_{n0}}{L_{p1}(x_{n0})}\right] \exp\left[\frac{x_n}{L_{p2}(x_{n0})}\right]}{L_{p1}(x_{n0})} - \frac{\exp\left[\frac{x_{n0}}{L_{p2}(x_{n0})}\right] \exp\left[\frac{x_n}{L_{p1}(x_{n0})}\right]}{L_{p2}(x_{n0})} \right]}{1}$$

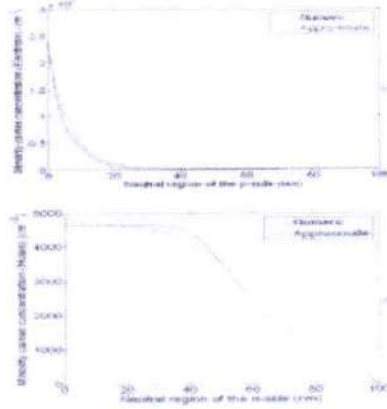


**Figure 4.** Minority carrier distributions under forward bias: (a) Hole concentration in the n-region; (b) Electron concentration in the p-region.

$$A(x_{n0}) = \exp\left[\frac{x_{n0}}{L_{p1}(x_{n0})}\right] \exp\left[\frac{x_n}{L_{p2}(x_{n0})}\right] - \exp\left[\frac{x_{n0}}{L_{p2}(x_{n0})}\right] \exp\left[\frac{x_n}{L_{p1}(x_{n0})}\right]$$

Similarly, we obtain the electron current in the p-side at  $x = -x_{p0}$  as

$$J_n = q\mu_n \left( E n_p - V_T \frac{dn_p}{dx} \right) \Big|_{x=-x_{p0}} = J_{n0} \left[ \exp\left(\frac{V}{V_T}\right) - 1 \right] \quad \dots\dots(19)$$

$$J_{n0} = q\mu_p n_{p0} E(-x_{p0}) - \frac{q\mu_p n_{p0} V_T}{A(x_{p0})} \left[ \frac{\exp\left[\frac{x_{p0}}{L_{n1}(-x_{p0})}\right] \exp\left[\frac{x_p}{L_{n2}(-x_{p0})}\right]}{L_{p1}(x_{n0})} - \frac{\exp\left[\frac{x_{p0}}{L_{n2}(-x_{p0})}\right] \exp\left[\frac{x_p}{L_{n1}(-x_{p0})}\right]}{L_{p2}(x_{n0})} \right]$$

$$A(x_{p0}) = \exp\left[\frac{x_{p0}}{L_{n1}(-x_{p0})}\right] \exp\left[\frac{x_p}{L_{n2}(-x_{p0})}\right] - \exp\left[\frac{x_{p0}}{L_{n2}(-x_{p0})}\right] \exp\left[\frac{x_p}{L_{n1}(-x_{p0})}\right]$$



**Table-1**

Numerical values of hole and electron current densities

| $J_{p0}$ (pA/cm) | $J_{n0}$ (pA/cm) |
|------------------|------------------|
| 0.332            | 0.310            |

Table 1 shows the numerical values of the hole and electron current densities expected for this p-n junction. The total current density is given by the sum of the (18) and (19) as

$$J = J_p + J_n = b + a \left[ \exp \left( \frac{V}{V_T} \right) - 1 \right] = (J_{p0} + J_{n0}) \left[ \exp \left( \frac{V}{V_T} \right) - 1 \right]$$

.....(20)

# The n-p-n Bipolar Transistor

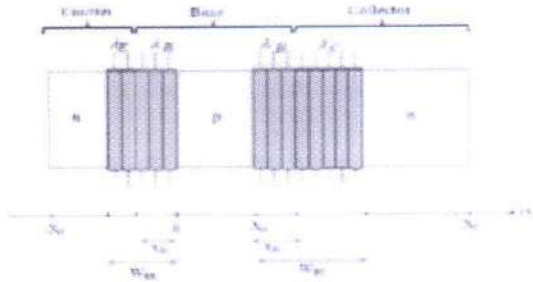


Figure 5. Electrostatic model for n-p-n transistor to approximate planar charge distribution using line charges.

In this section, we design and analyze an n-p-n 2D-BJT with abrupt charge doping profile and finite width. Figure 5 shows the electrostatic model to approximate planar charge distribution using line charges with infinitesimal width and charge density. Based on this charge model the unified equation for the total electric field over the surface of the device is given by

$$E(x) = -\lambda_E \ln \left| \frac{x+x_{B1}}{x+W_{BE}} \right| + \lambda_B \ln \left| \frac{x-(x_B+x_{B2})}{(x+x_{B1})(x-x_B)} \right| - \lambda_C \ln \left| \frac{x-(x_B+W_{BC})}{x-(x_B+x_{B2})} \right| \quad \dots\dots (21)$$

where  $\lambda_\mu = \frac{N_\mu}{2\pi\epsilon}$ ,  $\mu = E, B, C$ . Figure 6 illustrates the electric field and potential distributions over the surface of our designed 2D-BJT with a total width of about  $7.7 \mu\text{m}$ . Here, the dopant concentrations are  $N_E=1 \times 10^{12} \text{ cm}^{-2}$ ,  $N_B=1 \times 10^{11} \text{ cm}^{-2}$  and  $N_C=1 \times 10^{10} \text{ cm}^{-2}$ . The lengths of terminals are supposed to be  $124 \text{ nm}$ ,  $464 \text{ nm}$  and  $7.1 \mu\text{m}$  for emitter, base and collector respectively. Based on (8), the depletion widths are found to be  $x_{B1}=242.5 \text{ nm}$ ,  $W_{BE}=266.75 \text{ nm}$ ,  $x_{B2}=211.58 \text{ nm}$ ,  $W_{BC}=2.33 \mu\text{m}$  as shown in Figure 6. Now, we may proceed to obtain the basic parameters introduced for a planar 2D bipolar transistor.

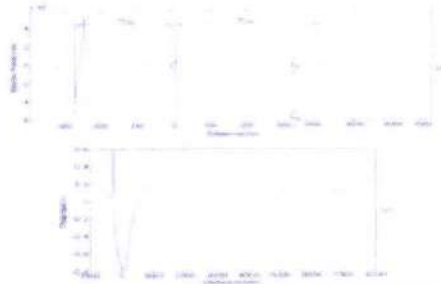


Figure 6. (a) Electric field distribution, (b) Electric potential distribution for the mentioned n-p-n transistor

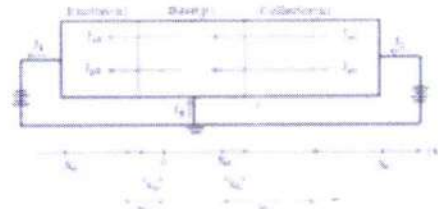


Figure 7. An n-p-n transistor under the normal forward operating conditions

## • Current Gain

Figure 7 presents a schematic of an n-type 2D-BJT, connected in an external bias circuit. We here assume a common base configuration and normal (active) mode of operation to find the corresponding current gain. Calculation of current gain would obviously need a thorough analysis of carrier transport across the width of structure. All the terminal currents are partitioned into hole and electron components, and then from the continuity equation we obtain the steady-state currents. The transport in the neutral base region of the device is non-trivial and contains both diffusion and drift terms. Hence, the distribution of injected minority-carriers (electrons) in the base region is governed by the continuity conditions at the two edges, subject to the Shockley's boundary conditions

$$-\frac{n_p(x)-n_{p0}}{\tau_n} + \mu_n(E(x)) \frac{dn_p(x)}{dx} + V_T \frac{d^2 n_p(x)}{dx^2} = 0 \quad \dots\dots (22)$$

$$n_p(x = -x_{p0}) = n_{p0} \exp\left(\frac{V}{V_T}\right) \quad \text{and} \quad n_p(x = -x_p) = n_{p0}$$

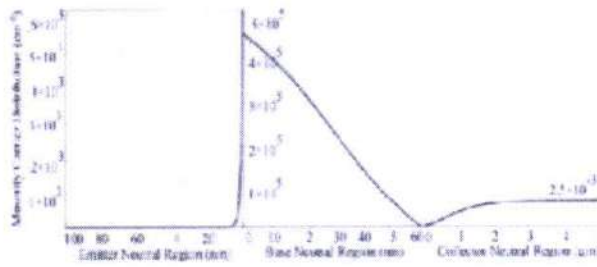


Figure 8. Minority carries distributions in neutral regions of the emitter, base and collector.

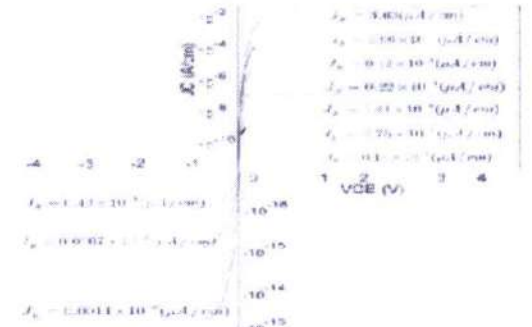


Figure 9. Output characteristics common emitter configuration

Figure 8 shows the electron distribution in the neutral base region based on numerical solution of this equation. The electron surface current densities at the emitter edge  $J_{nE}$  and the collector edge  $J_{nC}$  are given by

$$J_{nE} = q\mu_n \left( E n_p - V_T \frac{dn_p}{dx} \right) \Big|_{x=0} = a_{nE} \left[ \exp \left( \frac{V_{BE}}{V_T} \right) - 1 \right] - b_{nE} \left[ \exp \left( \frac{V_{BC}}{V_T} \right) - 1 \right] \quad \dots\dots(23)$$

$$J_{nC} = q\mu_n \left( E n_p - V_T \frac{dn_p}{dx} \right) \Big|_{x=x_B} = a_{nC} \left[ \exp \left( \frac{V_{BE}}{V_T} \right) - 1 \right] - b_{nC} \left[ \exp \left( \frac{V_{BC}}{V_T} \right) - 1 \right] \quad \dots\dots(24)$$

Similarly, in the pseudo-neutral emitter and collector regions, the equations for minority-carriers  $p_n$  are

$$-\frac{p_{nE(C)} - p_{n0}}{\tau_p} - \mu_p \left( E(x) \frac{dp_{nE(C)}}{dx} + V_T \frac{d^2 p_{nE(C)}}{dx^2} \right) = 0 \quad \dots\dots(25)$$

$$p_{nE(C)}(x = x_{0E(C)}) = p_{n0E(C)} \exp \left( \frac{V_{BE(BC)}}{V_T} \right) \quad \text{and} \quad p_{nE(C)}(x = x_{endE(C)}) = p_{n0E(C)}$$

with  $x_{0E} = -W_{BE}$ ,  $x_{0C} = X_B + W_{BC}$ ,  $x_{endE} = -X_E$  and  $x_{endC} = X_C$  as illustrated in figure 7 Numerical solutions of these equations are shown in figure 8. The hole surface current densities at the emitter edge  $J_{pE}$  and the collector edge  $J_{pC}$  are given by

$$J_{pE(C)} = q\mu_{pE(C)} \left( p_{nE(C)} E - V_T \frac{dp_{nE(C)}}{dx} \right) \Big|_{x=x_{0E(C)}} = a_{pE(C)} \left[ \exp \left( \frac{V_{BE(BC)}}{V_T} \right) - 1 \right] \quad \dots\dots(26)$$

Numerical parameter values for the constant parameters in the above sets of equations (23,24,25) are enlisted in Table 2. Now, the terminal surface current densities & be summed over respective electron and hole currents as

$$J_E = J_{nE} + J_{pE}, \quad J_C = J_{nC} + J_{pC}, \quad \text{and} \quad J_B = J_E - J_C.$$

Hence, the common-base and common-emitter current gains are found to be

$$\alpha = \frac{J_C}{J_E} = \frac{J_{nC}}{J_E} \cdot \frac{J_{nE}}{J_{nE}} \cdot \frac{J_C}{J_{nC}} = 0.993 \quad \dots\dots(27)$$

$$\beta = \frac{\alpha}{1-\alpha} = 138 \quad \dots\dots(28)$$

Figure 9 shows  $J_C$  versus  $V_{CE}$  for the common-emitter configuration under normal and inverted bias configuration. The saturation region is here defined as  $V_{CE} < V_{CE,sat} = 0.1V$  and the current gain in inverted mode is found to be  $\beta_i = 0.9$ . In contrast, standard bulk BJTs start to enter the saturation at  $V_{CE} < 0.2V$ , and therefore 2D-BJTs may operate at smaller voltages comparing to their bulk counterparts.



**Table-2**

Numerical values of constants for the hole and electron current densities

| $J_{nE}$ (pA/cm) |                      | $J_{nC}$ (pA/cm) |                       | $J_{pE}$ (pA/cm)     | $J_{pC}$ (pA/cm)      |
|------------------|----------------------|------------------|-----------------------|----------------------|-----------------------|
| $a_{nE}$         | $b_{nE}$             | $a_{nC}$         | $b_{nC}$              | $a_{pE}$             | $a_{pC}$              |
| 2.04             | $3.9 \times 10^{-2}$ | 2.03             | $3.91 \times 10^{-2}$ | $1.4 \times 10^{-2}$ | $9.16 \times 10^{-3}$ |

- Small-Signal Model**

The equivalent circuit for the behavior of this planar BJT is identical to that of a bulk BJT. Small-signal model parameters are here defined as transconductance  $g_m = \frac{\partial i_C}{\partial v_{BE}}$  output resistance  $r_o$ , and input resistance  $r_\pi = \frac{\partial i_B}{\partial v_{BE}} = \frac{\beta}{g_m}$ . Based on the flatness of the  $I_C$  curves, the Early voltage  $V_A$  is obtained to be infinity, and hence the output resistance expressed as  $r_o \equiv \left( \frac{\partial i_C}{\partial v_{CE}} \right)^{-1} = \frac{V_A}{I_C}$  was obtained as virtually unlimited.

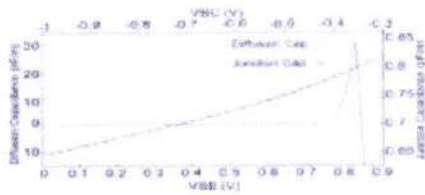


Figure 10. Diffusion and junction capacitance versus voltage

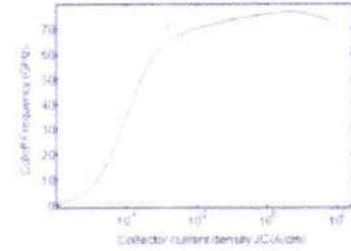


Figure 11. Cutoff frequency versus current density

This is particularly important for obtaining very large voltage gains at low operating voltages and power consumptions using properly designed p-n-p 2D-BJT as active loads, and also for designing near-ideal current-sources. The diffusion capacitance represents the injected electron concentration versus distance in the neutral base given as

$$C_\pi = q \int \frac{\partial n(x,V)}{\partial V} dx \quad \dots\dots\dots(29)$$

Variation of  $C_\pi$  as a function of applied voltage is shown in Figure 10. The general trend is that it attains a maximum value of roughly  $C_{\pi,max} = 32 \left( \frac{nF}{cm} \right)$  at a bias of about  $V_{BE} = 0.82$  (V), and starts to fall afterwards.

This behavior is quite typical and also seen in bulk BJTs as well. Also, the uncompensated dopants in the transition regions of a p-n junction cause dipoles, causing the junction capacitance Figure 9. Output

$$C_s = \left| \frac{dQ}{dV} \right| \quad \dots\dots\dots(30)$$

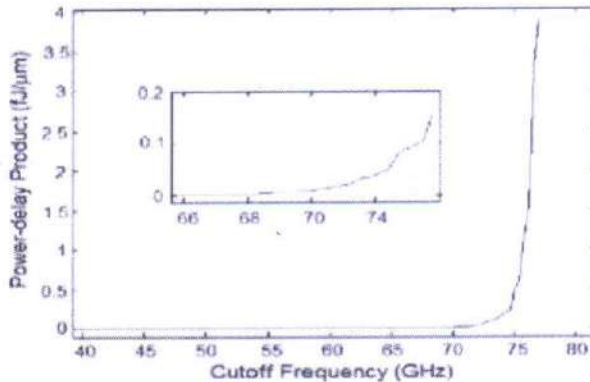


Figure 12. Power-delay versus cutoff frequency; the inset shows a magnification of the knee

Figure 11 also depicts the junction capacitance of the reverse-biased B-C junction versus  $V_{BC}$ . Now we assume that an AC signal is fed into the device by a current source  $I_b$  connected to the base. The cutoff frequency  $f_T$  is the frequency at which the AC current gain  $\beta_{ac} = \frac{i_c}{i_b}$  falls to unity. Figure 11 shows the variation of  $f_T$  as a function of collector surface current density  $J_C$ . The maximum value of this frequency is about 77 GHz at a fairly surface current density of 0.38 mA/μm. The typical consumed power is very small. A comparison to an existing design of bulk BJTs may be made by taking an identical base width of 1 μm. Then at the maximum

operating frequency which corresponds to a transit time of  $\tau_t = \frac{1}{2\pi f_T} = 2.1 \text{ ps}$ , and taking a collector bias voltage of 5V, then operating power (per  $1 \mu\text{m}$  width) would be around 1.9 mW. Hence, the estimated power-delay product will be around 4 fJ, far less than the typical record values which are of the order of tens of femto-Joules. It has to be mentioned that this power-delay product has been derived when the 2D-BJT is such biased to allow the maximum operation speed. As it has been shown in Figure 12, much smaller power-delay products can be expected if lower bias current and therefore the threshold frequency is chosen. Actually, the power-delay product blows up at large bias currents, and for instance if one limits the cutoff frequency to 70 GHz, the resulting power-delay product will be strictly limited to the record value of  $0.01 \text{ fJ}/\mu\text{m}$ .

- **Large-Signal Model**

The DC emitter and collector currents in active mode are well modeled by an approximation to the Ebers-Moll model. We have thus the relationships

$$J_E = J_{ED} \left[ \exp\left(\frac{V_{BE}}{V_T}\right) - 1 \right] - \alpha_I J_{CD} \left[ \exp\left(\frac{V_{BC}}{V_T}\right) - 1 \right] \quad \dots\dots\dots(31)$$

$$J_C = \alpha_N J_{ED} \left[ \exp\left(\frac{V_{BE}}{V_T}\right) - 1 \right] - J_{CD} \left[ \exp\left(\frac{V_{BC}}{V_T}\right) - 1 \right] \quad \dots\dots\dots(32)$$

Numerical parameter values for these set of equations are enlisted in Table 3.

**Table-3**  
Numerical value of Ebers-Moll parameters

| $J_{ED} \text{ (pA/cm)}$ | $J_{CD} \text{ (pA/cm)}$ | $\alpha_N$ | $\alpha_I$ |
|--------------------------|--------------------------|------------|------------|
| 2.04                     | 2.03                     | 0.995      | 0.98       |

## Approximate Formulae for an n-p-n 2D-BJT

Here we will derive parameters of n-type 2D-BJT's based on the theory derived for p-n junction in section 3. A dual analysis will be evidently applicable to p-type 2D-BJT's by changing the carrier types and voltage and current polarities. For calculation of transistor parameters, the injected minority-carriers distributions are necessary, and here we present the approximation solutions following the equations calculated in the above sections. Starting with the minority-carriers in the base, we have to solve (23). The approximate solution to this equation is Figure 10. Diffusion and junction capacitance versus voltage. Figure 11. Cutoff frequency versus current density. Figure 12. Power-delay versus cutoff frequency; the inset shows a magnification of the knee.

$$n_{pB}(x) - n_{p0B} \approx \frac{\left(\exp\left[-\frac{x}{L_{B2}(x)}\right] - \exp\left[-\frac{x}{L_{B1}(x)}\right]\right)}{\exp\left[-\frac{X_B}{L_{B2}(x)}\right] - \exp\left[-\frac{X_B}{L_{B1}(x)}\right]} n_{p0} \left[ \exp\left(\frac{V_{BC}}{V_T}\right) - 1 \right] + \frac{\exp\left[-\frac{x}{L_{B1}(x)}\right] \exp\left[-\frac{X_B}{L_{B2}(x)}\right] - \exp\left[-\frac{x}{L_{B2}(x)}\right] \exp\left[-\frac{X_B}{L_{B1}(x)}\right]}{\exp\left[-\frac{X_B}{L_{B2}(x)}\right] - \exp\left[-\frac{X_B}{L_{B1}(x)}\right]} \times n_{p0} \left[ \exp\left(\frac{V_{BE}}{V_T}\right) - 1 \right] \quad \text{.....(33)}$$

$$\text{where } L_{nBi}(x) = 2\tau_n V_T \left[ \tau_n E(x) - (-1)^i \sqrt{\tau_n^2 E^2(x) + \frac{4\tau_n V_T}{\mu_n}} \right]^{-1}$$

The electron surface current density of the emitter is similarly given by

$$J_{nE} = a_{nE} \left[ \exp\left(\frac{V_{BC}}{V_T}\right) - 1 \right] + b_{nE} \left[ \exp\left(\frac{V_{BE}}{V_T}\right) - 1 \right] \quad \text{.....(34)}$$

$$a_{nE} = q\mu_n n_{p0} E(0) - \frac{q\mu_n n_{p0} V_T}{\exp\left[-\frac{X_B}{L_{B2}(0)}\right] - \exp\left[-\frac{X_B}{L_{B1}(0)}\right]} \times \left[ \frac{1}{L_{B1}(0)} \exp\left[-\frac{X_B}{L_{B2}(0)}\right] - \frac{1}{L_{B2}(0)} \exp\left[-\frac{X_B}{L_{B1}(0)}\right] \right]$$

$$b_{nE} = \frac{q\mu_n n_{p0} V_T}{\exp\left[-\frac{X_B}{L_{B2}(0)}\right] - \exp\left[-\frac{X_B}{L_{B1}(0)}\right]} \left( \frac{1}{L_{B1}(0)} - \frac{1}{L_{B2}(0)} \right)$$

The electron surface current density of the collector will be

$$J_{nC} = a_{nC} \left[ \exp\left(\frac{V_{BE}}{V_T}\right) - 1 \right] + b_{nC} \left[ \exp\left(\frac{V_{BC}}{V_T}\right) - 1 \right] \quad \text{.....(35)}$$

$$a_{nC} = q\mu_n n_{p0} V_T \frac{\exp\left[-\frac{X_B}{L_{B2}(X_B)}\right] \exp\left[-\frac{X_B}{L_{B1}(X_B)}\right]}{\exp\left[-\frac{X_B}{L_{B2}(X_B)}\right] - \exp\left[-\frac{X_B}{L_{B1}(X_B)}\right]} \times \left[ \frac{1}{L_{B2}(X_B)} - \frac{1}{L_{B1}(X_B)} \right]$$

$$b_{nC} = q\mu_n n_{p0} E(X_B) + \frac{q\mu_n n_{p0} V_T}{\exp\left[-\frac{X_B}{L_{B2}(X_B)}\right] - \exp\left[-\frac{X_B}{L_{B1}(X_B)}\right]} \times \left[ \frac{1}{L_{B1}(X_B)} \exp\left[-\frac{X_B}{L_{B2}(X_B)}\right] - \frac{1}{L_{B2}(X_B)} \exp\left[-\frac{X_B}{L_{B1}(X_B)}\right] \right]$$

The hole distributions in the emitter and collector are obtainable using (25). The solutions are like those obtained junction, given by

$$p_{nE(C)}(x) - p_{n0E(C)} \approx \frac{p_{n0E(C)}}{A(x)} \left[ \exp\left(\frac{V_{BE(BC)}}{V_T}\right) - 1 \right] \times \left[ \exp\left[\frac{x}{L_{pE(C)2}(x)}\right] \exp\left[\frac{x_{endE(C)}}{L_{pE(C)1}(x)}\right] - \exp\left[\frac{x}{L_{pE(C)1}(x)}\right] \exp\left[\frac{x_{endE(C)}}{L_{pE(C)2}(x)}\right] \right] \quad \text{.....(36)}$$

$$A(x) = \exp\left[\frac{x_{0E(C)}}{L_{pE(C)2}(x)}\right] \exp\left[\frac{x_{endE(C)}}{L_{pE(C)1}(x)}\right] - \exp\left[\frac{x_{0E(C)}}{L_{pE(C)1}(x)}\right] \exp\left[\frac{x_{endE(C)}}{L_{pE(C)2}(x)}\right]$$

$$\text{with } L_{pE(C)i}(x) = 2\tau_p V_T \left[ \tau_p E(x) - (-1)^i \sqrt{\tau_p^2 E^2(x) + \frac{4\tau_p V_T}{\mu_p}} \right]^{-1}$$

Also, we have  $x_{0E} = -W_{BC}$ ,  $x_{0C} = X_B + W_{BC}$ ,  $x_{endE} = -X_E$  and  $x_{endC} = X_C$ , as illustrated in Figure 7. The hole surface current densities in the emitter and collector are obtained as



$$J_{pE(C)} = a_{pE(C)} \left[ \exp \left( \frac{V_{BE(BC)}}{V_T} \right) - 1 \right] \dots\dots\dots(37)$$

$$a_{pE(C)} = q\mu_p p_{n0E(C)} E - \frac{q\mu_p p_{n0(C)} V_T}{A(x_{0E(C)})} B(x_{0E(C)})$$

$$B(x_{0E(C)}) = \frac{1}{L_{E(C)1}(x_{0E(C)})} \exp \left[ \frac{x_{0E(C)}}{L_{E(C)1}(x_{0E(C)})} \right] \exp \left[ \frac{x_{endE(C)}}{L_{E2}(x_{0E(C)})} \right] - \frac{1}{L_{E(C)2}(x_{0E(C)})} \exp \left[ \frac{x_{0E(C)}}{L_{E(C)2}(x_{0E(C)})} \right] \exp \left[ \frac{x_{endE(C)}}{L_{E(C)1}(x_{0E(C)})} \right]$$

## Conclusion

We derived necessary formulae in studying 2D step p-n junctions and suggested an approximate analytical solution for continuity equations, which exhibited good agreement with exact numerical solutions. Then, we proceeded to develop the theory of 2D BJTs, and used the one-sided hydrogenated Graphene, or Graphone, as the example 2D material. Distributions of electric field and potential were calculated, and the small signal hybrid- $\pi$  model of the transistor was obtained. The results showed that this 2D-BJT would operate somewhat similar to bulk BJTs in DC and AC circuits, however, with very different performance parameters. The maximum frequency and current gain were found to be respectively as 77 GHz and 138, at a maximum power-delay product of  $4\text{fJ}/\mu\text{m}$ . This is while much smaller power-delay products would be possible at the expense of less threshold frequency. This preliminary analysis demonstrates the usefulness of such 2D-BJTs, in several aspects. As we have shown, a 2D-BJT would allow appreciable current gain, large operating frequencies, yet very small power-delay products which may be ultimately attributed to the associated ultrathin 2D materials. Furthermore, when used as active loads in a properly designed circuit, 2D-BJTs may be able to outperform their CMOS counterparts with regard to the large voltage gains at exceedingly small power consumption.

## Reference

The following are the resources that I have alluded to while doing this project :-

- *"Two-Dimensional Bipolar Junction Transistors"* by Behnaz Gharekhanlou, Sina Khorasani, Reza Sarvari
- *"The 2D pn Junction Driven Out-of-Equilibrium"* by Ferney A. Chavez, Pedro C. Feijoo, David Jimenez
- *"Electrostatics of lateral p-n junctions in atomically thin materials"* by Ankur Nipane, Sirisha Jayanti, Abhinandan Borah, James T. Teherani



A PROJECT REPORT ON  
"A STUDY OF QUARKONIUM BOUND STATES WITH  
ASYMPTOTIC ITERATION  
METHOD"

Submitted by,  
MRINAL KANTI SARKAR  
Dept. of Physics  
RKMRC, Narendrapur  
PHUG/121/17

Project Guide  
Dr. SOUMYA SADHUKHAN  
Assistant Professor  
RKMRC, Narendrapur



**Ramakrishna Mission Residential College (Autonomous)**

**Vivekananda Centre for Research**

**Ramakrishna Mission Ashrama**

(A Branch Centre of Ramakrishna Mission, Belur Math, Howrah-711202)

**Narendrapur, Kolkata - 700 103, West Bengal, India**

A Scientific Industrial Research Organisation, Recognised by DST, Govt. of India

College with Potential for Excellence (CPE), Re-accredited by NAAC - 'A' (CGPA 3.56 out of 4)

---

## **DEPARTMENT OF PHYSICS**

### **Certificate**

This is to certify that Mrinal Kanti Sarkar, a student of B.Sc has successfully completed the project of UG curriculum entitled "A study of Quarkonium bound states with asymptotic iteration method" in the period from January to May, 2020.

*Malay Purkait*  
.....  
30.06.2020.

**Signature Of HOD**

**Dept. of Physics**

**Dr. Malay Purkait**

**Associate Prof. & Head**

**Department of Physics**

**Ramakrishna Mission Residential College**  
**(Autonomous)**

**Narendrapur, Kolkata-700 103, (W.B.)**

---

PHONES : 24772201(3lines), 24772205 FAX : 033-24773597 EMAIL : rkmcpur@vsnl.com

WEBSITE : [www.rkmcnarendrapur.org](http://www.rkmcnarendrapur.org)



## To Whom It May Concern

### Certificate of Completion of the project

This is to certify that Mrinal Kanti Sarkar (Roll-PHUG/121/17) bearing the CU registration no. "A03-1122-0121-17", a student of Bsc final year (2020) has successfully completed his Bsc physics project on "A Study Of Quarkonium Bound States With Asymptotic Iteration Method" under the guidance of Dr. Soumya Sadhukhan. He is a bonafide student of RKMRC physics dept. of the 2017-2020 batch.

Date : 21.06.2020

S. Sadhukhan  
Sign of the guide



## ACKNOWLEDGEMENT

In the accomplishment of this project successfully, many people have best owned upon me their blessings and hard pledged support, This time I am utilizing to thank all the people who have been concerned with this project.

Foremost I would like to express my sincere thanks to our honorable principal maharaj sw. Shastrajnananda.

Next I pay my deep sense of gratitude to our departmental HOD Dr. Malay Purkait for providing me the opportunity to prepare the project.

Then I would like to express my special thanks of gratitude to my project guide Dr. Soumya Sadhukhan, who gave me the golden opportunity to do this wonderful project on "A study of Quarkonium Bound states with Asymptotic Iteration method", which also helped me in doing a lot of research and I came to know about so many new things. His suggestions and instructions have served as the major contributor towards the completion of the project.

After that I would like to thank my parents and friends who have helped me with their valuable suggestions and guidance has been Very helpful in various phases of the completion of the project.

Last but not the least I would like to thank my classmates who have helped me a lot.

Mrinal Kanti Sarker

Signature of the Student.



# A STUDY OF QUARKONIUM BOUND STATES, WITH ASYMPTOTIC ITERATION METHOD

04.07.2020

## 1. INTRODUCTION:

The study of bound states has been important throughout the history of particle physics. In the beginning of 20th century, the need to understand the atomic structure was one of the challenges that led to the development of quantum mechanics. When physicists started to probe the structure of matter at even smaller scales, they found out that atomic and subatomic particles were bound states as well. In order to explain the system where the constituents are bounded by a potential function, investigations are carried out to achieve mass and energy spectrum of the system. In the quantum mechanics formulation the solutions always involve solving the Schrödinger equations for bound states. To investigate the properties of bound state where the potential function is given several mathematical methods can be put to use. One of the powerful method that can be employed to solve the Schrödinger equation is 'Asymptotic Iteration Method' (AIM). It can be used for obtaining the perturbative energy eigenvalues of a system without any help of unperturbative eigen states. Using AIM one can solve a Schrödinger equation analytically as well as numerically.

Quarks are the fundamental components of particle physics. The bound states those are composed of pairs of quark and antiquark are called 'Quarkonium'. Since the first half of 1970 there are several studies on these quarkonium states.

obtained perturbatively comes from the quark antiquark interaction in the approximation of one gluon exchange ( $O(\alpha_s)$ ). It can be related to elastic scattering inside the bound states and can be computed from the theory of gluon propagator. The second one is a linearly-rising confining potential inspired by lattice calculations. The resulting potential is of the form —

$$V(r) = -\frac{4}{3} \frac{\alpha_s \hbar c}{r} + F_0 r \quad \text{----- (1)}$$

where  $\alpha_s$  is the chromodynamic analog to fine structure constant and  $\frac{4}{3}$  is the appropriate color factor. Experimentally  $F_0$  is measured to be 16 tons approximately, which is to say quark antiquark attract one another by a force of at least 16 tons regardless how far they are. That is why no one has ever managed to pull a quark out of hadron.

### 3. THE 'ASYMPTOTIC ITERATION METHOD (AIM)':

The method AIM is generally used to solve 2nd order homogeneous linear differential equations of the form —

$$y''(x) = \lambda_0(x)y'(x) + s_0(x)y(x) \quad \text{----- (2)}$$

where  $\lambda_0(x)$  &  $s_0(x)$  are functions in  $C_0(a,b)$ . If there is an asymptotic condition:  $\frac{\lambda_n}{\lambda_{n-1}} = \frac{s_n}{s_{n-1}} = \alpha$ ; where  $\lambda_k = \lambda_{k-1}' + s_{k-1} + \lambda_0 \lambda_{k-1}$  and  $s_k = s_{k-1}' + s_0 \lambda_{k-1}$  for  $k=1, 2, \dots, n$



then equation (2) has a solution of the form —

$$y(x) = \exp\left(-\int_0^x \alpha dt\right) \left[ C_2 + C_1 \int_0^x dt \exp\left(\int_0^t (\lambda_0(\tau) + 2\alpha(\tau)) d\tau\right) \right] \dots \dots (3)$$

The AIM can be used to solve Schrödinger equation for energy eigenvalue problem. The eigen energies can be obtained through the following quantization condition:

$$S_n(x, E) = S_n(x, E) \lambda_{n-1}(x, E) - \lambda_n(x, E) S_{n-1}(x, E) = 0 \dots \dots (4)$$

The problem is exactly solvable if the energy eigenvalue obtained from (4) is independent of 'x'. In this case the eigenvalue and the eigen functions of the nth energy levels can be derived explicitly algebraic form via nth iteration. But there are some limited number of forms with this category.

For numerically solvable problem  $S_n$  depends on both  $x$  and  $E$ .

In this case an approximate value  $x = x_0$  should be determined to solve  $S_n(x, E) = 0$  w.r.t 'E'. The energy eigen state of nth level is obtained through qth iterations where  $q \geq n$ .

#### 4. FORMULATION OF THE PROBLEM:

Consider the following 'Cornell potential' —

$$V(r) = -\frac{A}{r} + B^2 r \dots \dots \dots (5)$$

Where A, B are real positive constants and  $r \in (0, \infty)$ . If we substitute  $V(r)$  into Schrödinger equation in three dimensions we have —

$$\left\{ \frac{d^2}{dr^2} + E - \left[ -\frac{\alpha}{r} + pr + \frac{\ell(\ell+1)}{r^2} \right] \right\} \psi(r) = 0 \dots \dots \dots (6)$$

where  $E = 2\mu E_n$ ,  $\alpha = 2\mu A$  and  $p = 2\mu B^2$ .  $E_n$  and  $\mu = \frac{m_1 m_2}{m_1 + m_2}$  are eigenvalue of nth level and reduced mass respectively ( $m_1, m_2$  are quark masses). Besides we study natural units (i.e.  $\hbar = 1, c = 1$ ) for the system.

After choosing the variable as  $r = u^2$ , then substituting  $\psi(u) = u^{\frac{\ell+1}{2}} g(u)$ , we get,  $g''(u) + \left[ 4Eu^2 + 4\alpha - 4pu^4 - \frac{4\ell(\ell+1) + 3}{u^2} \right] g(u) = 0 \dots \dots \dots (7)$

Now we are going to change the variable 'u' to 'z', where 'u' and 'z' are connected by  $z = (4P)^{1/6} u$ . Then equation (7) leads to —

$$g''(z) + \left[ \omega + \sigma z^2 - z^4 - \frac{\gamma(\gamma+1)}{z^2} \right] g(z) = 0 \quad \text{--- (8)}$$

where  $\frac{4E}{(4P)^{1/3}} = \sigma$ ,  $\frac{4\alpha}{(4P)^{1/3}} = \omega$ ,  $\gamma = 2l + \frac{1}{2}$

Next we examine the asymptotic form of the solution of (8)

Case-I: For small  $z$  i.e.  $z \rightarrow 0$  eqn (8) leads to —

$$g''(z) - \frac{\gamma(\gamma+1)}{z^2} g(z) = 0, \text{ solving this we get } g(z) = A z^{\frac{\gamma+1}{2}} + \frac{B}{z^{\frac{\gamma+1}{2}}}$$

For physically acceptable solution  $B=0$ , otherwise it will blow up at  $z=0$ .

Case-II: For large  $z$  i.e.  $z \rightarrow \infty$  to take into account  $z^4$  term we need to consider  $e^{-z^{3/3}}$  term in the solution.

So, finally we will take —

$$g(z) = z^{\gamma+1} e^{-z^{3/3}} f(z) \quad \text{--- (9)}$$

Where the function  $f(z)$  will take care the solution in between

$z \rightarrow 0$  &  $z \rightarrow \infty$ . After putting equation (9) into (8) we get,

$$f''(z) = 2 \left[ z^2 - \frac{\gamma+1}{z} \right] f'(z) + [2(\gamma+1)z - \sigma z^2 - \omega] f(z) \quad \text{--- (10)}$$

Finally this equation is suitable for applying AIM. After this point we can apply AIM to this problem in two different ways — one is direct application to get the numerical results and another is AIM in scope of perturbation theory to obtain perturbative energy eigenvalues

## 5. RESULTS & DISCUSSION:

In this section we will directly apply AIM to equation (10). It is easily seen that  $\lambda_0(z) = 2 \left[ z^2 - \frac{\gamma+1}{z} \right]$ ,  $S_0(z) = 2(\gamma+1)z - \omega$  according to (2). For simplicity in calculation the reduced mass  $\mu$  has been considered as  $\mu = \frac{1}{2}$  and the potential parameters have been chosen as  $A=1$ ,  $B=1$  (eV



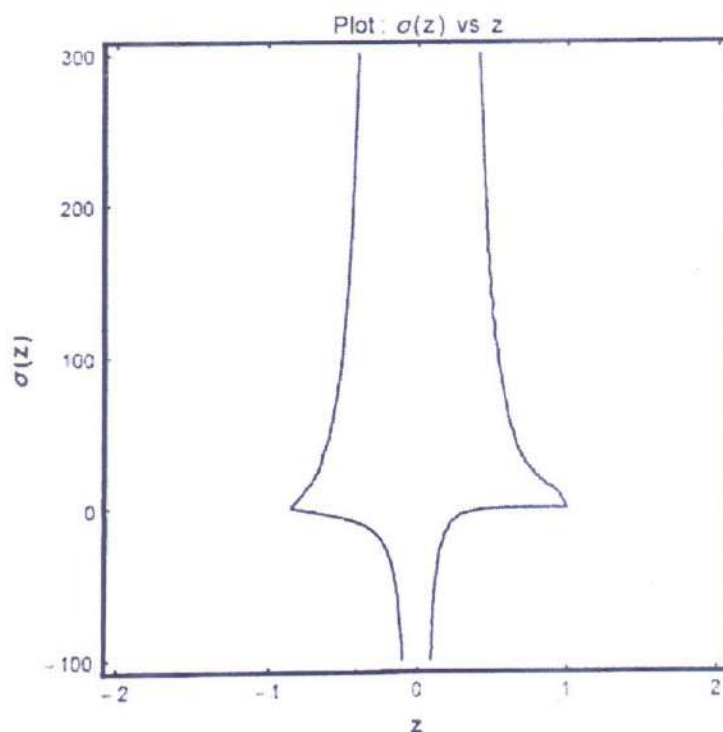
Here I am going to elaborate the calculation for  $n=1$ ,  $l=0$ ; which inturn gives —

$$\delta_n(x, E) = 0 ; \frac{s_0}{\lambda_0} = \frac{s_1}{\lambda_1} \Rightarrow s_0 \lambda_1 - s_1 \lambda_0 = 0 \quad \text{--- (11)}$$

Calculating  $\lambda_1$  &  $s_1$  and putting it into (11) we get —

$$z^4 \sigma^2 + \sigma (-6z^3 + 2\omega z^2 - 9) + (15z^2 - 10\omega z + \frac{18}{z} - \frac{3\omega}{z^2}) = 0 \quad \text{--- (12)}$$

As  $z$  is related to  $\sqrt{r}$ ,  $z$  can be positive or negative. If we plot  $\sigma$  vs  $z$  using equation (12), we will get a schematic diagram as given below



According to the diagram one thing can be understood that  $z=z_0$  can't be chosen arbitrarily. It can't be zero anymore. As  $z \propto \sqrt{r}$  for  $z=0$ ,  $r=0$  and in this case  $\sigma(z)$  which is related to energy eigenvalue will blow up.



We have to choose wisely  $z=z_0$  in the range where  $\sigma$  takes finite values. So there will be a physically forbidden region at  $z=0$  and to some extent around  $z=0$ . From this analogy one can get an idea about charge radius of quarks. The two charge centers of quarks and antiquarks can't be superimposed anymore. The minimum distance between the quark centers will be the sum of their radii or it can be more than that. And the plot we present clearly elaborates this idea.

The choice of  $z_0$  can be critical to the speed of convergence to the eigen values as well as the stability of the process. Although we don't have at the moment a specific method to determine the best initial value  $z_0$ , we may suggest the following approaches.

(a) One choice of  $z=z_0$  can be the value of  $z_0$  that minimizes the potential.

(b) Another possible choice will be setting  $s_0=0$

## 6. PERTURBATION TECHNIQUE IN CONTEXT OF AIM:

Now here I am going to give an idea about perturbation technique in frame of AIM. Assuming that the potential of a system is written as —

$$V(x) = V_0(x) + \eta V_p(x) \text{ ----- (13)}$$

where  $V_0(x)$  is exactly solvable potential,  $V_p(x)$  and  $\eta$  are perturbed hamiltonian and expansion parameter respectively.

Expanding energy eigen value  $E_n$  as a series expansion of  $j$ th order correction we get,  $\therefore$

$$\begin{aligned} E_n &= E_n^0 + \eta E_n^1 + \eta^2 E_n^2 + \dots \\ &= \sum_{j=0}^{\infty} \eta^j E_n^j \end{aligned}$$

After substituting  $\psi(x) = \psi_0(x)f(x)$  &  $V(x) = V_0(x) + \eta V_p(x)$  into the Schrödinger equation one can obtain the following equation for  $f(x)$ :

$$f''(x) = \lambda_0(x, \eta, E) f'(x) + S_0(x, \eta, E) f(x)$$

the termination condition will be —

$$\delta_n(x, \eta, E) = \delta_n(x, \eta, E) \lambda_{n-1}(x, \eta, E) - \lambda_n(x, \eta, E) \delta_{n-1}(x, \eta, E)$$

Expanding  $\delta_n(x, \eta, E)$  w.r.t  $\eta=0$  we obtain,

$$\begin{aligned} \delta_n(x, \eta, E) &= \delta_n(x, 0, E) + \frac{\eta}{1!} \frac{\partial \delta_n(x, \eta, E)}{\partial \eta} \bigg|_{\eta=0} + \dots \\ &= \sum_{k=0}^{\infty} \eta^k \delta_n^k(x, E) = 0 \end{aligned}$$

$$\text{Where } \delta_n^K(x, E) = \frac{1}{K!} \left. \frac{\partial^K \delta_n(x, \eta, E)}{\partial \eta^K} \right|_{\eta=0} \dots \dots \dots (14)$$

According to perturbation method in the framework of AIM, solving the equation  $\delta_n(x, 0, E) = 0$  with respect to unknown  $E$  gives  $E_n^0$  (eigen values of the unperturbative hamiltonian), equation  $\delta_n^1(x, E) = 0$  gives  $E_n^1$  (first order corrections to  $E_n$ ),  $\delta_n^2(x, E) = 0$  gives  $E_n^2$  (second order correction to  $E_n$ , and so on. Besides, the perturbative eigen functions can be achieved in the same way with the eigenvalues. This is an alluring feature of AIM, usage in perturbation theory for obtaining the eigenfunctions  $f_n(x)$  given as follows —

$$f_n(x) = \exp\left(-\int^x \alpha_n(t, \eta) dt\right) \dots \dots \dots (15)$$

where  $\alpha_n(t, \eta) \equiv S_n(t, \eta) / \lambda_n(t, \eta)$ . It is expanded about  $\eta=0$  in a similar manner, done for obtaining the eigenvalues so,

$$\alpha_n(t, \eta) = \sum_{K=0}^{\infty} \eta^K \alpha_n^{(K)}(t) \dots \dots \dots (16)$$

where  $\alpha_n^{(K)} = \frac{1}{K!} \left. \frac{\partial^K \alpha_n(x, \eta)}{\partial \eta^K} \right|_{\eta=0}$ . Thus perturbation expression of  $f_n(x)$  is written as follows:

$$\begin{aligned} f_n(x) &= \exp\left[\sum_{K=0}^{\infty} \eta^K \left(-\int \alpha_n^{(K)}(t) dt\right)\right] \\ &= \prod_{K=0}^{\infty} f_n^K(x) \dots \dots \dots (17) \end{aligned}$$

where  $K$ th order correction  $f_n^K(x)$  to  $f_n(x)$  is

$$f_n^K(x) = \exp\left[\eta^K \left(-\int \alpha_n^K dt\right)\right]$$



As the procedure of the perturbation theory expanding  $\sigma(n, l)$  w.r.t  $w$  for equation (10) we get —

$$\sigma(n, l) = \sigma_0(n, l) + \sigma_1(n, l)w + w^2 \sigma_2(n, l) + \dots \quad (18)$$

where  $w$  is the expansion parameter. So the energy eigenvalue of the system will be —

$$E_{nl} = \frac{(4P)^{2/3}}{8\mu} \sigma(n, l)$$

$$\Rightarrow E_{nl} = \frac{(4P)^{2/3}}{8\mu} \sigma_0(n, l) + \frac{(4P)^{1/3}}{2\mu} \sigma_1(n, l) + \frac{2\alpha^2}{\mu} \sigma_2(n, l) + \dots \quad (19)$$

The zeroth order correction  $\sigma_0$  can be obtained from  $\delta^0(z, 0, \sigma_0) = 0$ . Similarly, first order and 2nd order corrections can be obtained by solving  $\delta^1(z, 0, \sigma_1)$  &  $\delta^2(z, 0, \sigma_2)$  respectively, and so on.

So, the mass-energy relation in the form of A, B is —

$$E_{nl} = (8\mu)^{-1/3} B^{1/3} A^{-1} \sigma_0(n, l) + 8\mu^{5/3} B^{4/3} A \sigma_1(n, l) + \dots \quad (20)$$

Now one thing we have to keep in mind that the more correction term we add to the perturbative expansion, the more compatible results we get.

## CONCLUSION:

In this work I have applied AIM to 'Cornell potential' for getting the energy eigenvalues and masses for general  $l$  states. Finally we achieved a semi-analytical formula for constructing the energy spectrum and obtaining the masses of the Quarkonium using the method AIM in the scope of perturbation theory. Furthermore, AIM gives polynomial solutions for asymptotic forms of the wave functions of the system. Again I can say that equation (20) can be used as an eigenvalue formula for Schrödinger equation in case of 'Cornell potential' for practical purposes. Besides, it can be fit to mass formula of experimental values for determining the potential parameters  $A$  &  $B$ . The main advantage of equation (20) is that the coefficients  $\sigma_0, \sigma_1, \sigma_2$  are independent of potential parameters.

## REFERENCES :

- [1] Asymptotic iteration method for eigen value problems  
article in journal of physics A general physics - 2003  
DOI: 10.1088/0305-4470/36/47/008. Source: arXiv. Authors: Hakan Ciftci, Nasser Saad, Richard L. Hall.
- [2] O. ÖZER<sup>1</sup>, G. LEVAI<sup>2</sup>; "Asymptotic iteration method applied to bound states problems with unbroken and broken Supersymmetry"
- [3] A J sous and AD Alhaidari, J. Appl. Math. Physics. 4, 79 (2016)
- [4] I A Assi, A J Sous, and A N Ikot, Eur. Phys. J. plus 132(12), 525 (2017)
- [5] E. Eichten, K. Gottfried, T. Kinoshita, K. D. Lane, and T. M. Yan, "Charmonium: The model," Physical Review D: Particles, Fields, Gravitation and Cosmology, vol 17, no 11, pp. 3090-3117, 1978
- [6] R. L. Hall, "Simple eigenvalue formula for coulomb plus linear potential," Physical Review D, vol. 30, P. 433, 1984
- [7] F. Cooper, A. Khare, and U. Sukhatme, "Supersymmetry and quantum mechanics," Physics Reports, vol. 251, no. 5-6, pp. 267-385, 1995.
- [8] 'Heavy - Quarkonium Potential with input from Lattice Gauge Theory' by William Mitioli Serenone.
- [9] Chris Quigg<sup>1</sup>, "Realizing the potential of Quarkonium" Fermi National Accelerator Laboratory<sup>2</sup>.



**RAMAKRISHNA MISSION RESIDENTIAL COLLEGE**  
**(AUTONOMOUS)**

**NARENDRAPUR, KOLKATA - 700103**



**ELECTROSTATICS OF PN JUNCTION DIODE IN A NEW**  
**APPROACH FOR 3D, 2D AND 1D**

Supervised by : Dr. SOURAV CHATTOPADHYAY

(Assistant Professor, Department of Physics, RKMRC Narendrapur)

Project done by : NILADRI GHORUI

Roll Number : PHUG/112/17

B.Sc. 6th Semester



**Ramakrishna Mission Residential College (Autonomous)**

**Vivekananda Centre for Research**

**Ramakrishna Mission Ashrama**

(A Branch Centre of Ramakrishna Mission, Belur Math, Howrah-711202)

**Narendrapur, Kolkata - 700 103, West Bengal, India**

A Scientific Industrial Research Organisation, Recognised by DST, Govt. of India

College with Potential for Excellence (CPE), Re-accredited by NAAC - 'A' (CGPA 3.56 out of 4)

---

## **DEPARTMENT OF PHYSICS**

### **Certificate**

This is to certify that Niladri Ghorui, a student of B.Sc has successfully completed the project of UG curriculum entitled "ELECTROSTATICS OF PN JUNCTION DIODE IN A NEW APPROACH FOR 3D, 2D AND 1D" in the period from January to May, 2020.

*Dr. Malay Purkait*  
.....  
30.06.2020

**Signature Of HOD**

**Dept. of Physics**

**Dr. Malay Purkait**

Associate Prof. & Head

Department of Physics

Ramakrishna Mission Residential College  
(Autonomous)

Narendrapur, Kolkata-700 103. (W.B.)

## TO WHOM IT MAY CONCERN

This is to certify that Mr. NILADRI GHORUI (Roll Number : PHUG/112/17) of B.Sc. 6th Semester student is known to me for three years in the Département of Physics, Ramakrishna Mission Residential College (Autonomous), Narendrapur. He had done this project as a part of B.Sc. 6th Semester Course Curriculum. During the tenure of this project, he has made "electrostatics of PN Junction diode in a new approach for 3d, 2d and 1d" and studied it's performance.

*Sourav Chattopadhyay*  
20/6/20  
Dr. SOURAV CHATTOPADHYAY

Assistant professor

Department of Physics Ramakrishna Mission Residential College (Autonomous)

Narendrapur, Kolkata-103



## ACKNOWLEDGEMENT

I acknowledge with pleasure the support of Dr. Sourav Chattopadhyay, Assistant Professor of Department of Physics, Ramakrishna Mission Residential College Narendrapur. Under his supervision, I have completed my project report. I thank Dr. Malay Purkait, H.O.D. of Department of Physics of RKMRC Narendrapur, for supporting me at every step. This project has been very insightful and I consider myself lucky to being a part of it.

Signature of project guide

*Niladri Ghosai*

Student's Signature  
ROLL-PHUG/112/17

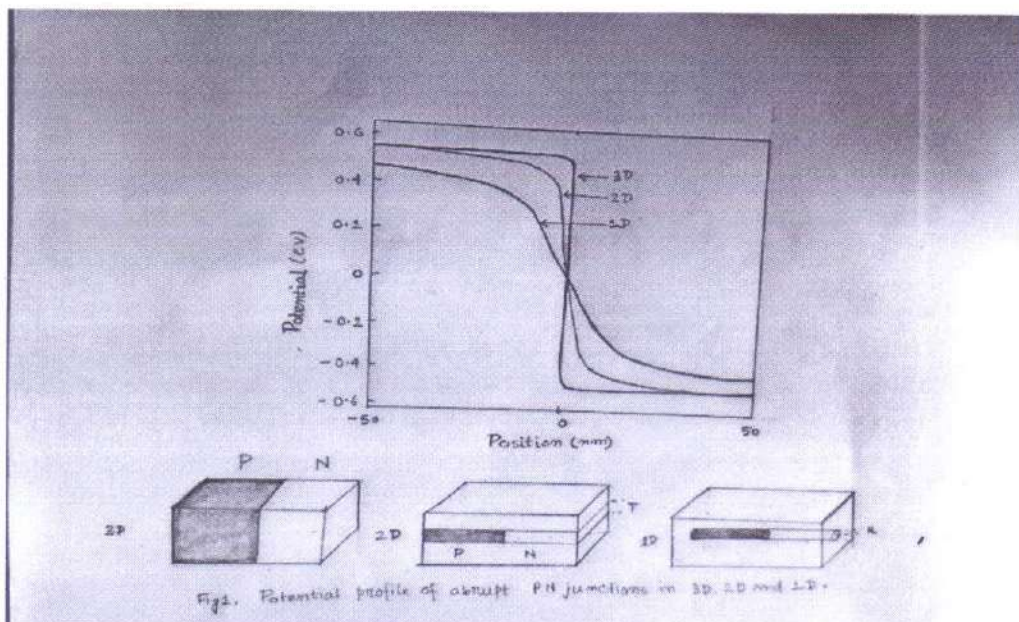
## **CONTENTS**

|                                        |      |
|----------------------------------------|------|
| 1. INTRODUCTION.....                   | 4    |
| 2. NUMERICAL SIMULATION.....           | 5    |
| 3. ANALYTICAL MODEL.....               | 6-9  |
| 4. THE ANALYSIS OF 1D PN JUNCTION..... | 9-11 |
| 5. APPROXIMATE EQUATIONS.....          | 11   |
| 6. CONCLUSION.....                     | 12   |
| 7. ACKNOWLEDGEMENT.....                | 12   |
| 8. REFERENCES.....                     | 13   |

**IN BIRD'S EYE** : Low dimensional material systems provide a unique set of properties useful for solid state devices. We know the PN Junction diodes are the building block of solid state electronics. In this discussion I shall present a dramatic difference in the analysis of the electrostatics of PN Junction in several dimension i.e. 3D, 2D and 1D. The analytical method of calculation different electrostatic parameters is unique. From this novel method the parameters like electric field, potential difference and depletion width have maximum matching with experimental result. In this way, we found some new relations of the parameters that helps us to get a new perspective in electronics nanotechnology.

**1.INTRODUCTION** : Low dimensional materials have become too much famous in nanotechnology, thermoelectric and optoelectronic applications like the high mobility graphene, carbon nanotube and III-V nanowires for transistors, transition metal, dichalcogenides and phosphorene for tunnel transistors, high ZT nanoribbon and nanowire thermoelectrics and 2D photodetectors. Almost all electronic and optical devices are based on PN Junctions. Hence the knowledge of the electrostatics of PN Junction is crucial in predictive device design. For example, the tunnelling current in tunnel diodes and tunnel FETs depends exponentially on the depletion width. Low dimensional material systems, however, present significant differences compared to their 3D counterparts.

Although the impact of the dimensionality of PN junctions on their electrostatics has usually been ignored in literature, there exist experiments supporting this claim. In the case of 2D materials, Reuter et al. have measured depletion widths (WD) of a 2D PN junction as a function of reverse bias using optical techniques and have shown the difference in behavior of WD of 2D junctions as against their 3D counterparts. More recently, Zheng et al. have used Kelvin Probe Force Microscopy (KPFM) technique to show that the potential profile itself changes significantly in low dimensions.





Several theoretical models have been developed to explain some of these anomalous behaviour in electrostatics of low dimensional systems. For 1D systems, Leonard and Tersoff at IBM noticed the new length scales in nanotubes and provided approximate analytic equations for depletion width. In 2D, Achoyan et al. have derived equations for a 2D PN junction with zero thickness. Later on, Gharekhanlou et al. and Yu et al. have used different methods to model 2D junctions. However, in all of the above models, the thickness of the PN junction has been ignored and there is no validation against numerical simulations. These issues have been addressed in this paper.

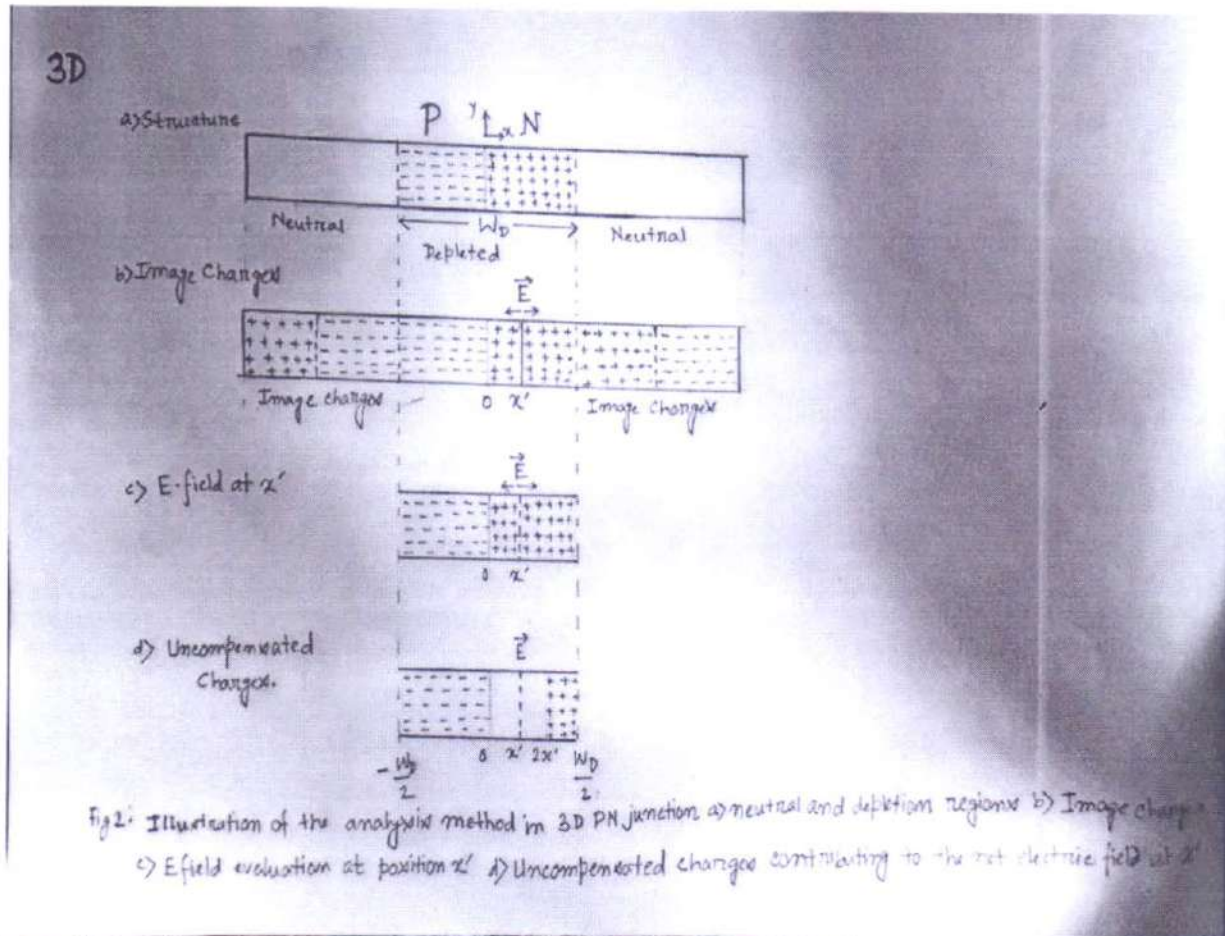
In this work, a novel approach is proposed for analytic modelling of PN junctions. The equations governing the potential profiles and depletion width of 3D, 2D and 1D systems are presented. Experiments on PN junctions demonstrate an enormous impact of dimensionality on the electrostatics. The rapid progress in doping thin flakes of 2D materials and 1D nanowires over the last two decades and its role in low dimensional MOSFETs and tunnel transistors call for a thorough analytical understanding of the low dimensional PN junctions, well validated against numerical simulations. In the following sections, the numerical simulation method is discussed first. A novel approach to obtain the analytic equations, including the impact of neutral regions, is introduced next. The results of the analytical model are then compared with experimental measurements and numerical simulations. Finally, the approximate equations for depletion width of PN junctions in different dimensions are presented.

**2. NUMERICAL SIMULATION METHOD :** The potential profile in 2D and 1D PN junctions, as shown in Fig. 1, are obtained by self-consistently solving Poisson equation with the drift-diffusion equation using the finite element method in NEMO5. The carrier densities are obtained from Fermi integrals based on the difference between Fermi level and band edges. It is important to consider a large enough dielectric environment in the simulations (i.e. dielectric thickness larger than depletion width) since a zero electric field boundary condition is used at the dielectric boundaries of the simulation domain. If these boundaries are close to the junction, they can artificially impact the fringing field pattern and the potential profile within semiconductor. Therefore, it is critical to make the simulation domain large enough so that boundaries do not affect the results.

For the sake of simplicity, it is assumed here that the P and N doping levels are both equal to  $N$  and the dielectric constants of channel and surrounding dielectric equal.  $\Delta V$  is the potential drop across the PN junction which equals  $V_{bi} - V_a$  where  $V_{bi}$  is the built-in potential and  $V_a$  is the applied bias.

Fig. 1 shows the simulated potential profile of PN junctions, in different dimensions, with the same doping of  $5 \times 10^{19} \text{ cm}^{-3}$  using finite-element method. It is clear that the well known 3D electrostatics does not apply to low dimensional junctions and dimensionality of material has a significant impact on the depletion width and potential profile.

### 3. ANALYTICAL MODEL :



In this section, the analytic method to obtain exact analytical equations for 3D, 2D and 1D PN junctions is introduced. The depletion and neutral regions are shown in Fig1. Free carriers in the neutral regions play an important role in screening the electric field. In the conventional depletion approximation, the electric field in neutral regions is zero. This zero field boundary condition, at the interface of neutral and depletion regions, can be captured by introducing image charges. Ignoring these image charges and considering only the E-field due to the charges in the depletion region leads to wrong results such as large electric fields at the boundaries of depletion region and non-monotonic potential profile in 2D and 1D. The steps involved in determining the analytic equation for potential are presented in Figs2.) Place image charges to enforce the zero E-field boundary condition at the interfaces of neutral and depletion regions. 2) Find the E-field at position  $x_0$ . 3) Integrate E-field to obtain the potential. The 2nd step for evaluation of E-field involves the following: a) Removing charges whose E-fields cancel out. After these cancellations, a negative block of charge and a positive block of charge remain. b) E-field evaluation at position  $x_0$  due two remaining blocks of charge. For a symmetric case, it is sufficient to evaluate E-field due to one block and multiply it by 2.



To demonstrate the new approach, we start with the well known 3D case. The potential in 3D case can be easily obtained by solving 1D differential equation but our purpose here is to introduce the method in the simplest case. Fig. 2b shows the equivalent structure where neutral regions are replaced by image charges to enforce zero E-field at the boundaries of the depletion region. Now that all charges are in place, the E-field at position  $x_0$  should be evaluated. First, the contribution of image charges to E-field is shown in Fig. 2b.

The image charges inducing positive E-field at  $X_0$  due to an infinite plane of charge is independent of the distance from the plane, the positive and negative E-fields due to the image charges in 3D cancel each other out. Moreover, as shown in Fig. 2c, the field due to charges from 0 to  $X_0$  compensates the ones from  $X_0$  to  $2X_0$ . Fig. 2d shows all the charges which contribute to  $E_{net}$ , the net electric field at position  $X_0$ .

\* The field from the block of negative charges is proportional to their net charge and equals  $-\frac{\rho w_D}{4\epsilon}$  — (i)

$\rho \rightarrow$  charge density (here we consider it uniform)

whereas the field due to positive block equals

$$-\frac{\rho}{2\epsilon} (w_D - 2x') \quad \text{--- (ii)}$$

Hence the net electric field equals to:

$$\begin{aligned} E_{net}^{3D}(x') &= -\frac{\rho}{4\epsilon} (w_D + w_D - 4x') \\ &= \frac{\rho}{\epsilon} (x' - \frac{w_D}{2}) = \frac{qN}{\epsilon} (x' - \frac{w_D}{2}) \quad [N = \text{number density}] \end{aligned}$$

Integrating electric field gives the potential. Considering the reference potential to be the value at  $x=0$  results in:

$$\begin{aligned} V^{3D}(x) &= -\int_0^x E_{net}^{3D}(x') dx' \\ &= -\frac{qN}{2\epsilon} x (w_D - x) \quad \text{--- (iii)} \end{aligned}$$

As expected, the potential profile has a parabolic form in the depleted region. From (iii)  $w_D$  can be derived

$$\begin{aligned} V(-\frac{w_D}{2}) &= -\frac{qN}{2\epsilon} (-\frac{w_D}{2}) (w_D + \frac{w_D}{2}) \\ &= -\frac{qN}{2\epsilon} (\frac{3w_D^2}{4}) \end{aligned}$$

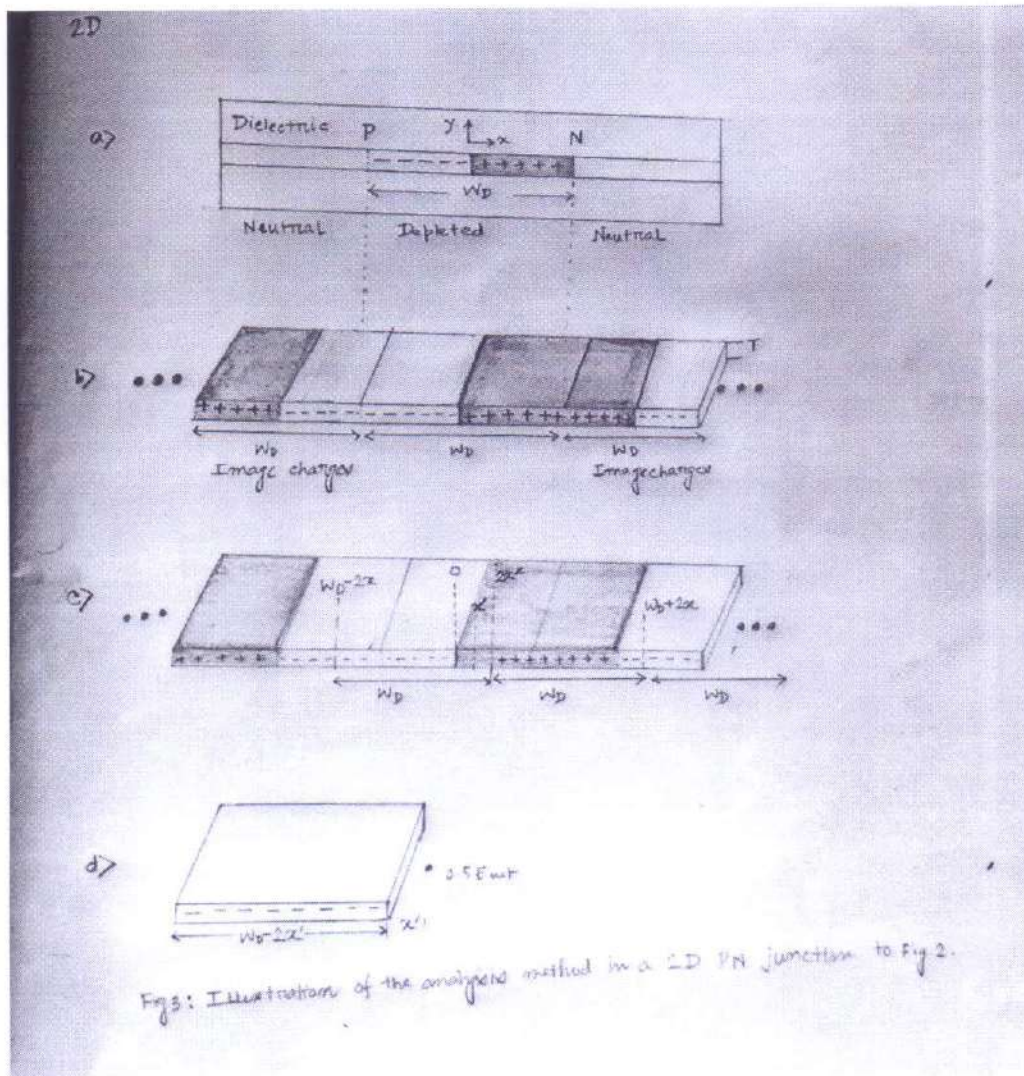
$$\begin{aligned} V(\frac{w_D}{2}) &= \frac{qN}{2\epsilon} \frac{w_D}{2} \times \frac{w_D}{2} \\ &= \frac{qN}{2\epsilon} \frac{w_D^2}{4} \end{aligned}$$

$$\therefore \Delta V = \frac{qN}{2\epsilon} \left[ \frac{3w_D^2}{4} - \frac{w_D^2}{4} \right]$$

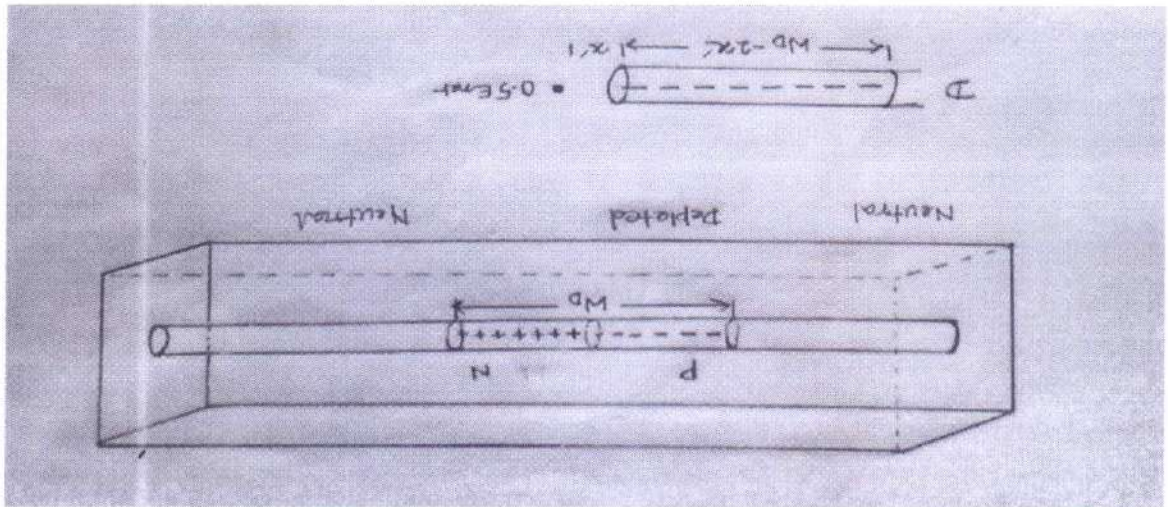
$$\Rightarrow w_D^{3D} = 2 \sqrt{\frac{\Delta V \epsilon}{qN}} \quad \text{--- (iv)}$$



Hence, we recover the well known electrostatics of bulk PN junctions. The same procedure can be followed for 2D junctions to find the potential profile as shown in Fig. 3. However, it is important to note that the net electric field due to image charges in 2D and 1D junctions is not zero, unlike in 3D, since the field from a finite block of charge now depends on the distance. The regions of image charges with positive and negative blocks of charge behave similar to electric dipoles with a finite net field. To the first order, the nearest neighbour block of image charges are considered first. The impact of charges further away are discussed later. Fig. 3c shows the uncompensated charges for a 2D junction. Finally, the net electric field at a distance  $X_0$  is obtained from a 2D block of charge with length  $W_D - 2X_0$  and thickness  $T$  and multiplied with a factor of 2 as shown in Fig. 3d:



We can calculate the net electric field by calculating for the one side of the 2D diode and then the expression is multiplied by 2. To calculate it analytically we can consider the 2D charged region as an assembly of continuous line charges. For a small strip of charge we calculate the electric field at  $X'$  and then integrate the expression for some suitable limit.



#### 4. THE ANALYSIS OF 1D PN JUNCTION IS SIMILAR TO THAT OF 2D :

Unlike in 3D,  $W_D$  has a linear dependence on  $\Delta V$  and is inversely proportional to  $N$ . To validate this significant difference from conventional PN junction behaviour, the analytical results are compared with the experimental measurements of a PN junction made from 2DEGs (2 Dimensional Electron Gases). Figure 4 shows a good match between the analytical calculations and optical measurements of  $W_D$  in 2D.



To calculate net electric field in 1D diode we consider the charged region as a solid cylindrical charged region. And for a small element of the cylinder we calculate the electric field. Then integrate it to get net electric field.

For one side

$$\begin{aligned}
 E_{\text{net}}(x') &= \frac{\rho_0}{2\epsilon} \int_0^R r \left[ \frac{1}{[r^2 + (x' - W_D)^2]^{3/2}} - \frac{1}{[r^2 + (x' + W_D)^2]^{3/2}} \right] dr \\
 &= \frac{\rho_0}{2\epsilon} \left\{ [r^2 + (x' - W_D)^2]^{-1/2} - [r^2 + (x' + W_D)^2]^{-1/2} \right\} \Big|_0^R \\
 &= \frac{\rho_0}{2\epsilon} \left\{ [R^2 + (x' - W_D)^2]^{-1/2} - |x' - L| - [R^2 + (x' + W_D)^2]^{-1/2} + |x' + W_D| \right\}
 \end{aligned}$$

to get total electric field

$$2E_{\text{net}}(x') = \frac{\rho_0}{\epsilon} \left\{ [R^2 + (x' - W_D)^2]^{-1/2} - |x' - L| - [R^2 + (x' + W_D)^2]^{-1/2} + |x' + W_D| \right\}$$

$\rho_0 \Rightarrow$  uniform charge density

$$\therefore E_{\text{net}}^{1D}(x) = -\frac{qN}{\epsilon} \left\{ [R^2 + (x' - W_D)^2]^{-1/2} - |x' - L| - [R^2 + (x' + W_D)^2]^{-1/2} + |x' + W_D| \right\}$$

$[R \Rightarrow \text{radius of nanowire}]$

To calculate  $V^{1D}(x)$  we have to integrate this expression.

From the electric field the potential is obtained to be:

$$\begin{aligned}
 \frac{V^{1D}(x)}{V_0^{1D}} &= \sinh^{-1}\left(\frac{x}{R}\right) + \sinh^{-1}\left(\frac{W_D - x}{R}\right) - \sinh^{-1}\left(\frac{W_D}{R}\right) \\
 &+ \frac{x\sqrt{R^2 + x^2} + (W_D - x)\sqrt{R^2 + (W_D - x)^2} - 2x(W_D - x)}{R^2}
 \end{aligned}$$

Where  $V_0^{1D}$  is defined as  $\frac{qN}{2\epsilon} R^2$ . The depletion widths of 1D PN Junctions exhibit an exponential dependence on  $\frac{\Delta V_E}{N}$

$$W_s^{1D} \approx R \exp\left(\frac{2G\Delta V}{qNR^2} - \frac{1}{2}\right)$$

↓



To make the analytic model work for all thicknesses even beyond  $W_D$ , the simplifications used to approximate the depletion width equations should be avoided. These simplifications are: a) Semiconductor thickness is much smaller than depletion width ( $T \ll W_D$  and  $R \ll W_D$ ), and b) Ignoring the E-field of distant charges (farther than  $W_D$ ). The exact analytic equations for potential profile in 2D and 1D are listed in table I. It is noteworthy that the potential attains an additional factor  $\beta$  for large thicknesses due to the impact of distant charges as shown in table I.  $\beta$  equals 2 for thicknesses close to 0, whereas it decreases to 1 for infinitely thick junctions (equivalent to 3D). Figure 6 shows the depletion width as a function of junction thickness in different dimensions. For a thickness beyond depletion width, the fringing field gets screened at the surface and  $W_D$  gets close to the corresponding value in 3D. However, for smaller thicknesses,  $W_D$  deviates from 3D case. Especially, 1D case shows a significantly higher  $W_D$  values and increased sensitivity to the diameter.  $W_D$  has a similar response to variations in  $N$ . The increased sensitivity of  $W_D$  with respect to junction parameters in low dimensions enables the possibility of new sensors.

## 5. APPROXIMATE EQUATIONS :

The approximate equations for depletion widths ( $W_D$ ) of PN junctions in different dimensions as obtained in this work. The approximate  $W_D$  equations in 1D and 2D are valid when the thickness of the semiconductor is much smaller than  $W_D$  ( $R \ll W_D$  and  $T \ll W_D$ ). An error less than 10% can be achieved using these approximations if  $T < W_D/7$  in 2D or  $R < W_D$  in 1D. Interestingly, the square root dependence of  $W_D$  on  $e/N$  in 3D, changes to a linear and exponential dependence for 2D and 1D, respectively. Such an exponential dependence leads to high sensitivity of 1D PN junction to its control parameters, which can be used towards new sensors. For example, a small change in the biasing of 1D PN junction affects  $W_D$  significantly through  $\Delta V$ . Such a junction under illumination can result in a large output current response.

## **6. CONCLUSION**

In summary, using a new analysis, the electrostatics of PN junctions in low dimensional material systems have been shown to differ significantly from the 3D junctions. Reducing the dimensionality increases the depletion width and its sensitivity to doping and thickness of PN junction, attractive towards sensing applications. The analytic results match closely with experimental measurements and numerical simulations.

## **7. ACKNOWLEDGEMENT**

I acknowledge with pleasure the support of Dr. Sourav Chattopadhyay, Assistant Professor of Department of Physics, Ramakrishna Mission Residential College Narendrapur. Under his supervision, I have completed my project report. I thank Dr. Malay Purkait, H.O.D. of Department of Physics of RKMRC Narendrapur, for supporting me at every step. This project has been very insightful and I consider myself lucky to being a part of it.

## **8. References:**

1. D. Chattopadhyay, P. C. Rakshit, Electronics Fundamentals And Applications, (New Age International Publishers, 12th edition)
2. [www.elctroschematics.com](http://www.elctroschematics.com)
3. [www.electrnicshub.org](http://www.electrnicshub.org)
4. Wikipedia



## **Smart Water Tap monitoring system**

*Project Report submitted to the Department of Physics, Ramakrishna Mission Residential College (Autonomous), Narendrapur, Kolkata for the partial fulfilment of the requirements of the degree of*

## **Bachelor of Science (Hons.) in Physics**

Submitted by:

Arghya Jana [Roll No.: PHUG/092/17]  
Pritam Pal [Roll No.: PHUG/110/17]

Semester VI, B.Sc. Physics (Hons.)

University of Calcutta, Kolkata  
2020



**Ramakrishna Mission Residential College (Autonomous)**

**Vivekananda Centre for Research**

**Ramakrishna Mission Ashrama**

(A Branch Centre of Ramakrishna Mission, Belur Math, Howrah-711202)

**Narendrapur, Kolkata - 700 103, West Bengal, India**

A Scientific Industrial Research Organisation, Recognised by DST, Govt. of India

College with Potential for Excellence (CPE), Re-accredited by NAAC - 'A' (CGPA 3.56 out of 4)

---

## **DEPARTMENT OF PHYSICS**

### **Certificate**

This is to certify that Pritam Pal, a student of B. Sc has successfully completed the project of UG curriculum entitled "Smart Water Tap monitoring system" in the period from January to May, 2020.

*Malay Purkait*  
.....  
30.06.2020

**Signature Of HOD**

**Dept. of Physics**

**Dr. Malay Purkait**

Associate Prof. & Head

Department of Physics

Ramakrishna Mission Residential College

(Autonomous)

Narendrapur, Kolkata-700 103, (W.B.)

Mr. Tanmay Biswas

Assistant Professor

Ramakrishna Mission Residential  
College (Autonomous)  
Narendrapur, Kolkata-700103

## CERTIFICATE OF APPROVAL

Date: 1 July, 2020

This is to certify that the project report entitled "Smart Water Tap Monitoring System" has been done under my supervision at the Department of Physics, Ramakrishna Mission Residential College (Autonomous). I also endorse that this work submitted by **Pritam Pal** (Reg. No: A03-1112-0110-17) is original and has not been submitted to any other University for the award of any Degree or Diploma. I therefore, recommend the project work for the award of **Bachelor of Science (Honours) in Physics**.

  
(Mr. Tanmay Biswas)



## Acknowledgement

I would like to express my deep sense of gratitude to my respected and learned guide Mr. Tanmay Biswas (Assistant Professor, Department of Electronics) for his valuable guidance in completing this project.

I am also grateful to my respected principal, vice principal and respected Prof. Malay Purkait, (HOD, Department of physics) for permitting me all the necessary facilities of the institution. I am also thankful to all other faculty and staff members of our department of their kind cooperation.

Lastly I would like to thank my parents and friends to help me a lot in finishing this project in time.

Pritam Pal .

01-07-20

(Signature of student)

### **Abstract**

In the design we have constructed a sensor water tap monitoring system using the components viz arduino board, solenoid valve, SPDT relay, IR sensor etc. The main purpose of this project is to stop wastage of water. We have used the IR Sensor which is connected to a SPDT relay which controls the solenoid valve to control the water flow to the tap. As a result sensor tap is automatically shut off after use.

## **Introduction:**

Water is most precious. Living bodies depend on it. Our responsibility is to conserve it. Nowadays we are interested to be automated. The project titled "sensor Water Tap monitoring system" is the modern version of the traditional hand operated tap. The water taps that we use in our daily life are mechanically operated. Water flows through the tap when we turn on the tap and the flow stops when we turn off the tap. This hand operated tap system causes water loss.

Sensor water taps save water significantly. Sensor water tap is automatically shut off after hand washing and as a result water shortage is reduced. Sensor tap is hygienic, that is very important for us. This tap is more energy efficient than traditional hand operated water tap. In the automatic water tap we use a IR sensor which is connected to a SPDT relay which controls the solenoid valve to control the water flow to the tap [4]. This tap reduced the wastage of water as it is automatically closed after hand washing.

Some related works are:

- Water Quality Monitoring System Based on IOT [1] : In this paper the authors have presented a design and development of a low cost system for real time monitoring of the water quality in IOT. They have measured the physical and chemical properties of water such as temperature, PH,turbidity, flow sensor etc. using sensors and arduino model.
- Design a Smart Faucet for reducing the water wastage using IOT [2] : In this paper the authors have designed a smart water faucet using the components Node MCU,relay,solenoidvalve,DC motor,temperature sensor, servo motor for reducing the wastage of water.



### **Proposed Design:**

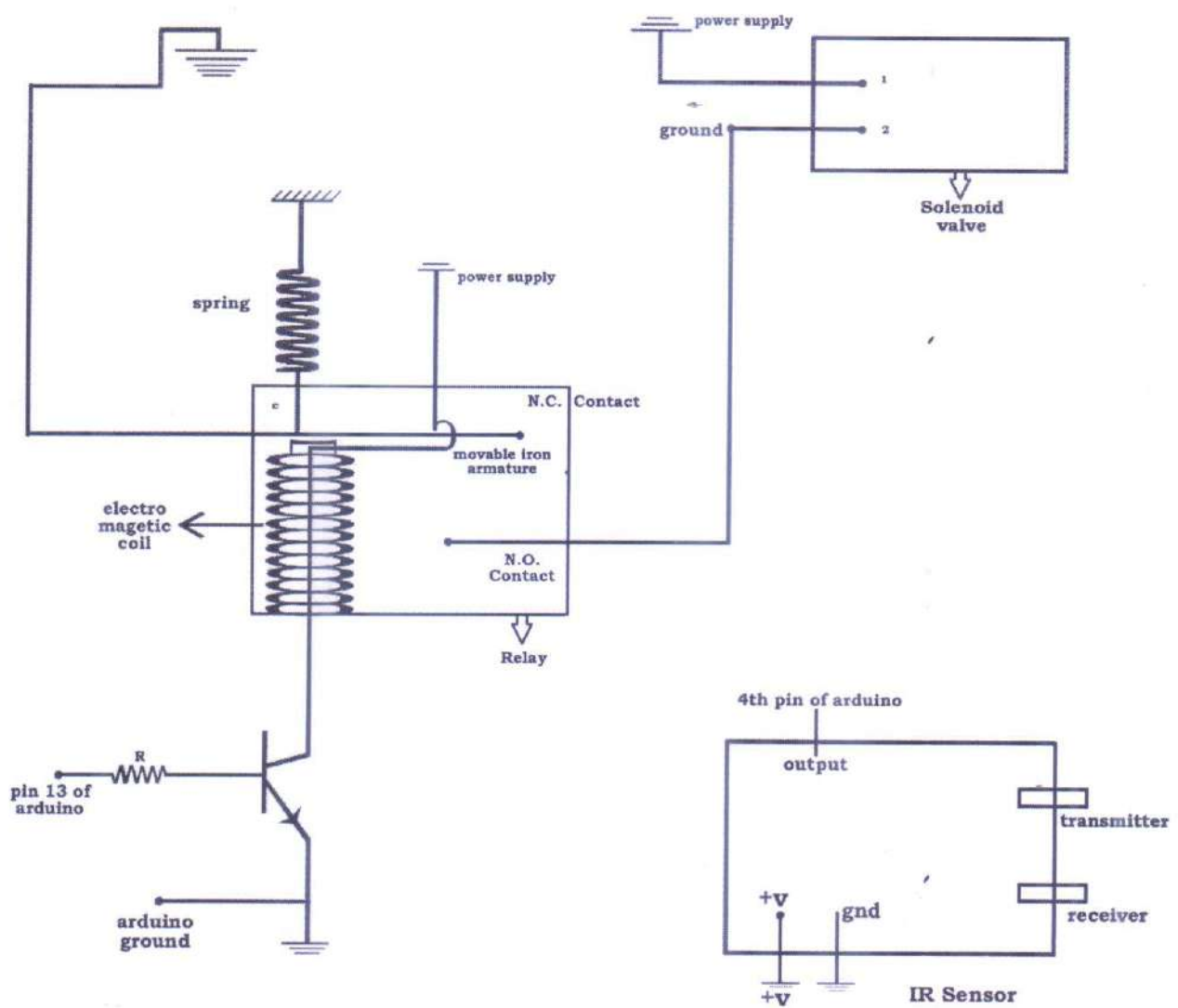
We have designed a sensor water tap monitoring system .Here we have used an infrared sensor in the tap that has a light emitting diode. This LED emits light continuously. When an object or human hand enters into the range of LED, the solenoid valve will be opened, which allows the water to flow through the tap. When the object is removed from the range of LED, the valve will be closed and it stops water running.

### **Implementation:-**

The Components that are required for constructing the sensor water tap monitoring system are

- i) Solenoid Valve
- ii) Single Pole Double Throw (SPDT) relay
- iii) Infra-red sensor
- iv) Arduino board
- v) Power Supply
- vi) Spring
- vii) Resistance
- viii) Electromagnetic coil

Solenoid Valve is an electrically Controlled automatic device. It's basic working Principle is just like as a relay. There are two types of Solenoid Valves i) normally open type and ii) normally closed type. By applying the voltage the state of the solenoid can be changed from open to close or from close to open. Here the normally closed type solenoid valve has two ends. One end is connected to a power supply and the other end is connected to normally open contact of a relay. Relay's common end is connected to the ground. Its common end, attached with a spring system, is connected with the normally closed



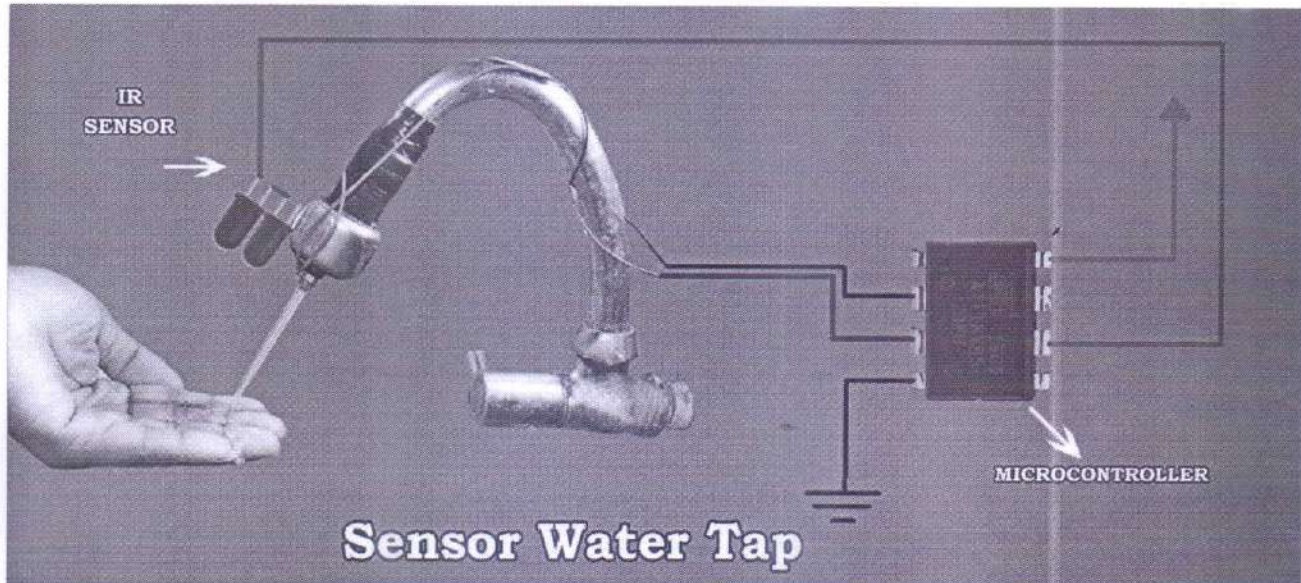
**Block diagram of Sensor water tap Monitoring System**

contact through a movable iron armature. There is an electromagnetic coil; a coil of wire is wound on a soft iron core. One end of this coil is connected to some voltage and the other end of this coil is connected to the ground through a n-p-n transistor. The base of the transistor is connected to a pin of arduino board via some resistance.

Here we used a IR Sensor that has a light emitting diode-IR transmitter continuously emits the light. When some object enters into the range of the LED, the infra-red light signal is reflected by the object and the receiver of the IR sensor receives that light. That's why some voltage will be showed across the receiver. This voltage is automatically supplied by the sensor to that pin of arduino, which is connected to the base of the transistor via some resistance, such that current will flow through the electromagnetic coil and the coil generates a magnetic field through the soft iron core. Due to this the movable iron armature is attracted towards the electromagnetic core and the armature will move to open condition by breaking the normally closed contact condition. Normally open contacts get to closed condition. Then a complete circuit will be formed and the solenoid valve will remain in "on" state. The valve is opened and it allows the water to flow through the tap.

Again, when the object is removed from the range of LED, the receiver of the sensor will not show any voltage and the current flowing through the electromagnetic coil will be switched off, the relay coil gets de-energized then the armature is returned to its original position by the spring system. The armature will move to N.C. contact condition by breaking the N.O. contact condition. Hence the solenoid valve will remain in "off" state. The valve is closed and it stops the water running.





When some object or human hand enters into the range of LED of the IR sensor as shown in fig, which emits the light continuously, the solenoid valve will be opened and that allows the water to flow through the tap. Again when the object is removed from the range of LED, the valve will be closed and it stops water running.

## **Result:**

The sensor water tap monitoring system plays important role in the following fields:

- Significant water saving:

Electronic taps are generally constructed to get much lower stream rate than the traditional hand operated taps. Hand operated taps can use up to 10-15 liters of water per minute whereas the sensor tap offers flow rates of water as little as 2 liters per minute. Sensor tap is automatically shut off after hand washing and hence water wastage is reduced.

- Hygienic:

Sensor tap doesn't require to touch - it is hygienic.

- Cleaner and more efficient:

In case of sensor taps the flow rate is predetermined whereas for hand operated taps the user can choose their preferred flow rate every time. This is very inefficient. Prefixing the flow rate helps to reduce splashing.

- More energy efficient:

Sensor taps need electricity for their operation while the traditional hand operated taps don't require any electricity in order to work. Every time a traditional hand tap expends a great deal of energy by choosing the user's preferred water flow and temperature. But in case of sensor taps water always remain at a constant temperature, so energy is not expended by changing the water temperature. So sensor taps are more energy efficient than hand taps.

### **Application:**

Sensor water tap monitoring system is extremely valuable in home, old age home, hotel, school, office, shop, nursing home, hospital, industrial application, eatery etc.

### **Conclusion:**

Due to this sensor water tap monitoring system our life style has been quite automated. Due to significant progress in science and technology, we are approaching an era of artificial intelligence and consequently the interaction between man and machines gets reduced. The sensor water tap is such a machine that has reduced the human labor mostly. We can implement this method in the public water podium stands which eliminates the usage of water taps, which are extremely inefficient. This automated system is very helpful in everyday life specially for physically handicapped, patients and elderly people. It gives them a safe and independent living by providing the tap automation. It is also very helpful in conservation of water which can be efficiently implemented in garden, park etc.



## Reference

1. Vaishnavi V. Daigavane and Dr. M.A. Gaikwad.
2. LalithMohon S, Kavinprabhu L, Jayaseelan T, Naveen Kumar V, Suresh babu Y, (International Journal of Recent Technology and Engineering). Volume - 8 Issue - 6, March 2020.
3. Automatic tap control system in the smart home using android and arduino-Vani K.S. and Shrinidhi P.C. International Journal of computer application - volume 127-No-8, October 2015.
4. Programmingdigest.com

# **Anderson Localization for One Dimensional Disordered System**

Project Report Submitted  
for

6<sup>th</sup> Semester Examination of  
**Bachelor of Science (Honours)**  
Degree in Physics

Submitted by

**Mr. Rupak Majumder**  
Roll No.: PHUG/231/17  
Registration No.: A03-1112-0231-17

June, 2020



**Ramakrishna Mission Residential College (Autonomous)**  
**Narendrapur**

Supervised by

**Dr. Atanu Rajak**  
Department of Physics,  
**Presidency University**



**Ramakrishna Mission Residential College (Autonomous)**

**Vivekananda Centre for Research**

**Ramakrishna Mission Ashrama**

(A Branch Centre of Ramakrishna Mission, Belur Math, Howrah-711202)

**Narendrapur, Kolkata - 700 103, West Bengal, India**

A Scientific Industrial Research Organisation, Recognised by DST, Govt. of India

College with Potential for Excellence (CPE), Re-accredited by NAAC - 'A' (CGPA 3.56 out of 4)

---

## **DEPARTMENT OF PHYSICS**

### **Certificate**

This is to certify that Rupak Majumder, a student of B. Sc has successfully completed the project of UG curriculum entitled "Anderson Localization for One Dimensional Disordered System" in the period from January to May, 2020.

*Malay Purkait*  
.....  
30.06.2020.

**Signature Of HOD**

**Dept. of Physics**

**Dr. Malay Purkait**

Associate Prof. & Head

Department of Physics

Ramakrishna Mission Residential College

(Autonomous)

Narendrapur, Kolkata-700 103, (W.B.)



## Acknowledgement Letter

To  
The Head of the Department  
Physics Department  
Ramakrishna Mission Residential College  
Narendrapur, Kolkata-700103

Dear Colleague,

This is to inform you that your student Mr. Rupak Majumder has done his UG project under my supervision. He has worked with me from September, 2019 to June, 2020. His project title was "Anderson Localization for One Dimensional Disordered System". Rupak did his project work sincerely. I wish him every success in his future career.

Date: 12/10/2020

Regards  
Yours sincerely

*Atanu Rajak*

Dr. Atanu Rajak  
Assistant Professor  
Department of Physics  
Presidency University  
86/1 College Street  
Kolkata-700073

## Declaration

I declare here that the report included in this project entitled "Anderson Localization for One Dimensional Disordered System" is my undergraduate project carried out by me in the department of Physics, Presidency University, Kolkata under the supervision of Dr. Atanu Rajak, from September, 2019 to June, 2020.

In keeping the general practice of scientific observation, due acknowledgements have been made whenever the work described is based on the findings of other investigators.

15/10/2020

Date

Kharidaha

Place

Rupak Majumder

RUPAK MAJUMDER

Student's signature



## CONTENTS:

|   |                           |       |    |
|---|---------------------------|-------|----|
| ▪ | Abstract                  | ----- | 2  |
| ▪ | Introduction              | ----- | 3  |
| ▪ | Goal and Work Flow        | ----- | 4  |
| ▪ | Expression of Resistance: | ----- | 4  |
|   | Landauer's Formula        |       |    |
| ▪ | Basic Formalism:          | ----- | 9  |
|   | Tight Binding Model       |       |    |
| ▪ | Incorporating Disorder    | ----- | 10 |
| ▪ | Resistivity Calculation   | ----- | 12 |
| ▪ | Numerical Calculations    | ----- | 16 |
| ▪ | Summery                   | ----- | 19 |
| ▪ | Acknowledgement           | ----- | 19 |
| ▪ | Appendix                  | ----- | 20 |
| ▪ | References                | ----- | 22 |

### Abstract

In this project we review Anderson Localization for one-dimensional disordered system. We shall first deal the problem analytically and then visualize it through numerical computation.



## I. Introduction

Anderson localization is a well-studied problem. This was first introduced theoretically in 1958 by P. W. Anderson in an analytical paper in the context of low temperature conduction in disordered metal. In 2006 using time resolved measurements of light diffusion in highly scattering materials Störzer et al. provided clear experimental evidence for the existence of a transition to Anderson localization of visible light [6].

In standard description of electrical conduction, metals have partially filled energy band. Electrons in this band effectively form an electron gas. Applying semi-classical argument of scattering of electron, the conductivity of this gas becomes  $\sigma = ne^2\tau/m$ . As  $T \rightarrow 0K$ ,  $\sigma$  increases monotonically to a finite, non-zero value  $\sigma_0$ .

But this description does not hold for a wide class of metallic solids. It is found that many “disordered” metals becomes insulator at  $T=0K$ . Under very general condition, the eigenstates of the random potential are peaked at a particular point and decays exponentially away from that point. This means electron described by that associated wave function gets localized. This phenomenon is known as Anderson Localization.

For **1D** and **2D systems** localization happens no matter how small the disorder is. But for **3D systems**, when the disorder is weak delocalization happens and the system behaves as a conductor. But if the strength of this disorder is greater than a critical value, electrons become localized. The system then behaves as an insulator. This critical strength depends on the energy of the eigenstate. The qualitative character of the eigenstates changes as a function of the degree of disorder in the system. This transition from extended to localized states is now known as an Anderson transition. Depending upon disorder strength, **3D systems** undergoes a phase transition from Metallic to Insulator phase. But no phase transition occurs in **1D** and **2D systems**. Here we want to study the exact calculation of Anderson Localization for 1D disordered system.

- **Physical Idea:** Disorder in metal gives rise to a random potential in 1D. The wave function of electron suffers multiple reflections at each barrier. After superposition, the random relative phase cause them to cancel on average. The only remaining contribution after  $N$  barriers is from waves which are unscattered, decays exponentially.



## II. Goal and work flow

We are interested here to study the effect of disorder in one-dimensional non-interacting system. Here we to review the Anderson localization problem in 1D using both analytical and numerical calculations. For analytical calculations, we investigate resistivity of the system which is given by Landauer's formula. For numerical calculations, we have diagonalized the Hamiltonian for non-interacting system in presence of disorder.

We have organized this work in following way. In Sec. III, we will reproduce Landauer's formula for resistivity. In Sec. IV, we will review 1D tight-binding problem that will be used in the next section. In Sec. V, we will consider a one-dimensional non-interacting system in presence of disorder and investigate its localization properties using Landauer's formula. In Sec. VI, we have shown some numerical results for this problem. Finally, in Sec. VII, we conclude our work.

## III. Expression of Resistance: Landauer's Formula

Landauer's Formula gives the DC electrical resistance of a 1D chain of non-interacting chain of electrons (i.e. spinless electrons). Here we derive LF from an experimental point of view. Let through our 1D system, ' $I$ ' current is flowing through it. A potential drop of ' $\delta V$ ' is maintained across the sample by two reservoir. By definition, electrical resistance of this system is  $R = \frac{\delta V}{I}$ . Now in equilibrium,  $= e\delta V$ . So resistivity,

$$\rho = \frac{\delta V}{J} = \frac{\delta \mu}{ej}. \quad (1)$$

Here our goal is to define resistance in terms of chemical potential ( $\mu$ ) difference of the two reservoir rather than their voltage difference. But chemical difference. But  $\mu$  is not well defined when current is flowing through a

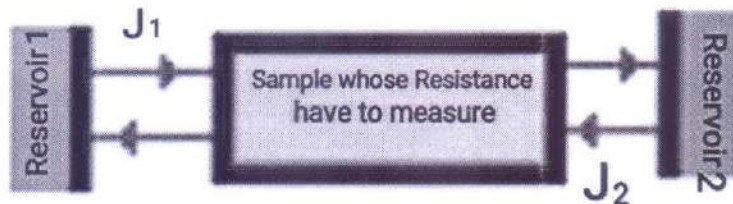


Fig. 1

reservoir. To avoid this, we introduce an ideal potentiometer. This potentiometer parameters are defined in such a way that it re-distributes the incoming currents (shown in red lines in Fig. 2) into the three outgoing channels (shown in blue lines in Fig. 2) such that **the net in-going and out-going currents for each reservoirs becomes equal**. This enables us to define each reservoirs with a well-defined Chemical potential ( $\mu$ ).

- The Potentiometer is defined by the matrix  $S$  which relates in-going current amplitudes (red lines) with the outgoing current amplitudes (blue lines) as:

$$\begin{pmatrix} b_1 \\ b_2 \\ b_3 \end{pmatrix} = \begin{pmatrix} r_1 & t_{12} & t_{13} \\ t_{21} & r_2 & t_{23} \\ t_{31} & t_{32} & r_3 \end{pmatrix} \begin{pmatrix} a_1 \\ a_2 \\ a_3 \end{pmatrix}$$

$$\rightarrow B = SA, \quad (2)$$

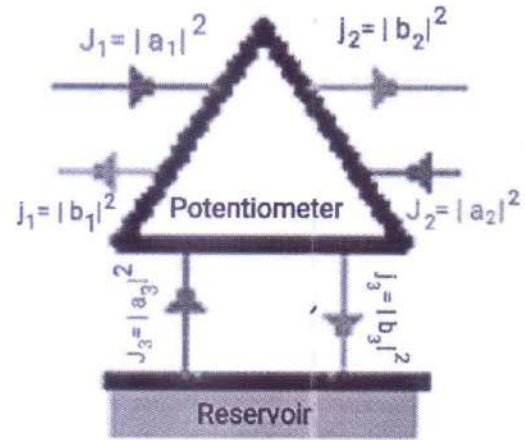


Fig. 2: Potentiometer Work

$A$  is in-going current amplitudes and  $B$  is outgoing current amplitudes. Matrix element  $t_{ij}$  is the fraction of in-coming current amplitude in channel 'j' which is transmitted to the outgoing current in channel 'i'.

Now *net in-coming current must be equal to net outgoing current*, where current density is defined by  $J = |a|^2$ . This gives:  $A^\dagger A = B^\dagger B \rightarrow S^\dagger S = S S^\dagger = I$

So  $S$  is Unitary. This gives:  $|t_{13}|^2 + |t_{23}|^2 + |r_3|^2 = 1$ .

So we can take  $|t_{31}| = |t_{32}| = \sqrt{\varepsilon}$ ,  $|r_3| = 1 - \varepsilon$ ,  $\varepsilon \ll 1$  (transmission coeff. of the sample). Also  $|t_{21}| = 1 + O(\varepsilon)$ ,  $|r_1| = |r_2| = O(\varepsilon^n)$   $n \geq 1/2$

Since the reservoir has finite width, the current to and from is determined by the phase averaged reflection and transmission coefficient. The difference of the outgoing current ( $J_3$ ) from the reservoir with chemical potential  $\mu$  and the current density at equilibrium is:



$$J_3 = \frac{e}{2} \int_{-\infty}^{+\infty} [f(E - \mu) - f(E)] v(E) N(E) dE, \quad (3)$$

Where  $v(E)$  is the velocity of electron,  $f(E)$  is the fermi distribution function and  $N(E)$  is the density of state. The energy is measured relative to the chemical potential of the sample at equilibrium. Now for 1D system, we know  $v = \frac{\partial E}{\partial p}$  and  $N(E) = (1/\pi\hbar) \times \left(\frac{\partial p}{\partial E}\right)$  (Appendix I). Upon Taylor expansion of eq. 3 we get:

$$J_3 = \frac{e}{2} \int_{-\infty}^{+\infty} [f(E - \mu) - f(E)] dE \approx \frac{e}{h} \mu \quad \rightarrow \quad J_3 = \frac{e}{h} \mu \quad (4)$$

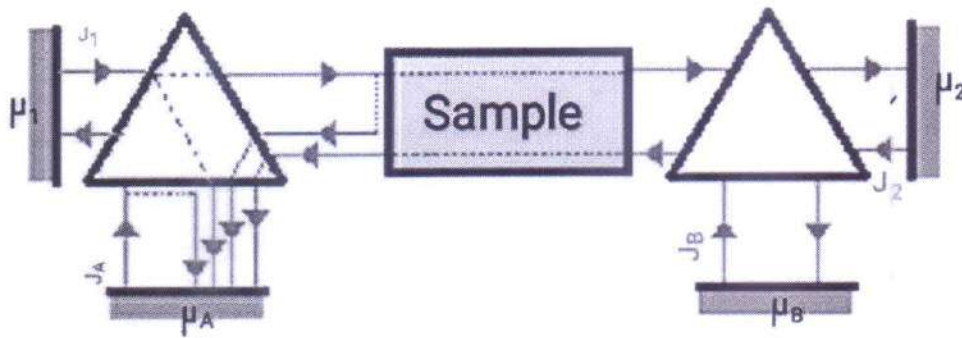


**Fig. 3: Experimental Setup to find Resistance**

After defining the Potentiometer, we go back to our original system (fig.3). The currents ' $J_1$ ' and ' $J_2$ ' are impressed from left and right, respectively. From eq. 4 we get:

$$J_1 = \frac{e}{h} \mu_1, \quad J_2 = \frac{e}{h} \mu_2, \quad J_A = \frac{e}{h} \mu_A, \quad J_B = \frac{e}{h} \mu_B \quad (5)$$

The potentiometers divert a small part of the current from the channel into the reservoirs A & B. This makes in- and outgoing current equal for all reservoir.

Let's first calculate for reservoir A. Here we shall take up-to the first order of  $\sqrt{\varepsilon}$  while calculating current density. So while calculating current amplitude we shall consider up-to  $\sqrt{\varepsilon}$ . From fig.4 it is clear that the transmission amplitude from the left in-going channel (channel 1) to the reservoir A is:

$$\begin{aligned} b_{A1} &= t_{A1}a_1 + t_{AS} \cdot r(E) \cdot t_{S1}a_1 = \sqrt{\varepsilon}e^{i\phi_1}a_1 + \sqrt{\varepsilon} \cdot r(E) \cdot \{1 + O(\varepsilon)\}a_1e^{i\phi_2} \\ &= \sqrt{\varepsilon}e^{i\phi_1}a_1 + r(E) \cdot \{\sqrt{\varepsilon} + O(\varepsilon^{3/2})\}a_1e^{i\phi_2} \approx \sqrt{\varepsilon}\{e^{i\phi_1} + r'(E)e^{i\phi_2}\}a_1, \end{aligned}$$

where  $r(E)$  is the reflection amplitude of the sample. Here we have used the fact that  $\varepsilon \ll T$ . As then reservoir has finite width, an average over the relative paths of the directly transmitted wave to the reservoir and of the reflected wave from the sample has to be taken. So phase average transmission coefficient of the in-coming current density at channel 1 to reservoir A is:

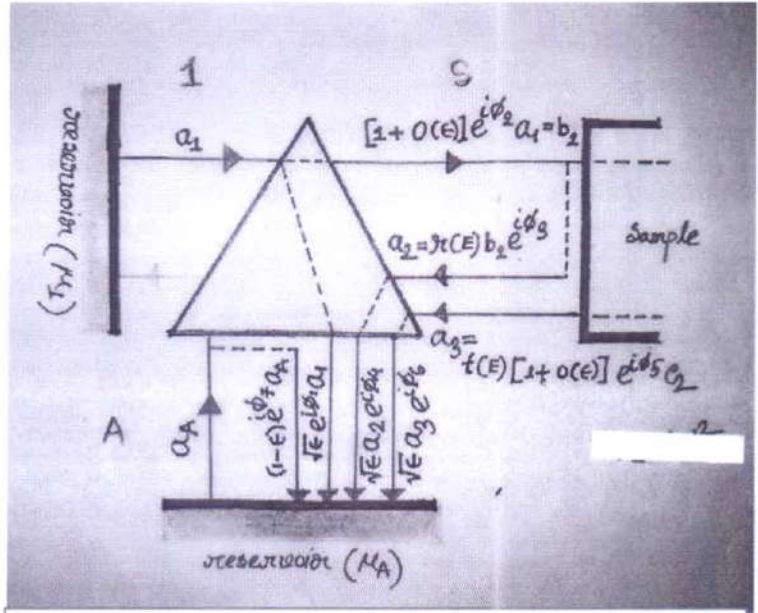


Fig. 4: Detailed analysis of the current components

$$\langle T_{A1} \rangle = \left\langle \frac{|b_{A1}|^2}{|a_1|^2} \right\rangle = \varepsilon \{1 + |r(E)|^2\}, \quad (6)$$

Here we have used the fact that  $\langle e^{i\phi} \rangle = 0$ . So ingoing current at A originating from the external current  $J_1$  is:

$$J_{A1} = \int_{-\infty}^{+\infty} J_1 \langle T_{A1} \rangle \left( -\frac{\partial f}{\partial E} \right) dE = \varepsilon J_1 \int_{-\infty}^{+\infty} \{1 + |r(E)|^2\} \left( -\frac{\partial f}{\partial E} \right) dE, \quad (7)$$

Here  $J_1 = |a_1|^2$ . Similarly the transmission amplitude from the left out-going channel of Reservoir 2 (channel 2) to the reservoir A is:

$$\begin{aligned} b_{A2} &= t_{AS} \cdot t(E) \cdot t_{S2}a_2 = \sqrt{\varepsilon} \cdot t(E) \cdot \{1 + O(\varepsilon)\}a_2e^{i\phi_3}, \\ &= t(E) \cdot \{\sqrt{\varepsilon} + O(\varepsilon^{3/2})\}a_2e^{i\phi_3} \approx \sqrt{\varepsilon} t(E)e^{i\phi_3}a_2, \end{aligned}$$



where  $t(E)$  is the transmission amplitude of the sample. Again after phase averaging the ingoing current at A originating from the external current  $J_2$  is:

$$J_{A2} = \int_{-\infty}^{+\infty} J_2 \langle T_{A2} \rangle \left( -\frac{\partial f}{\partial E} \right) dE = \varepsilon J_2 \int_{-\infty}^{+\infty} |t(E)|^2 \left( -\frac{\partial f}{\partial E} \right) dE. \quad (8)$$

Contribution from the other currents like  $J_B$  in the ingoing current at A can be ignored because this will be  $O(\varepsilon^n)$ ,  $n \geq 1$ . Again contribution from the reflected portion of the outgoing current  $J_A$  is:

$$J_{Ar} = |1 - \varepsilon|^2 J_A \approx (1 - 2\varepsilon) J_A. \quad (9)$$

So the net outgoing current at reservoir A is:  $J_{Ao} = J_{Ar} + J_{A1} + J_{A2}$ . Now the condition for zero net flow ( $J_A = J_{Ao}$ ) through the wall of the reservoir gives:

$$J_A = (1 - 2\varepsilon) J_A + \varepsilon J_1 \int_{-\infty}^{+\infty} \{1 + |r(E)|^2\} \left( -\frac{\partial f}{\partial E} \right) dE + \varepsilon J_2 \int_{-\infty}^{+\infty} |t(E)|^2 \left( -\frac{\partial f}{\partial E} \right) dE. \quad \text{----(10a)}$$

Similarly from reservoir B we get:

$$J_B = (1 - 2\varepsilon) J_B + \varepsilon J_1 \int_{-\infty}^{+\infty} |t(E)|^2 \left( -\frac{\partial f}{\partial E} \right) dE + \varepsilon J_2 \int_{-\infty}^{+\infty} \{1 + |r(E)|^2\} \left( -\frac{\partial f}{\partial E} \right) dE. \quad \text{----(10b)}$$

Using these two eq. with the fact  $(\mu_A - \mu_B) = \delta\mu = \frac{h}{e} (J_A - J_B)$  from eq. 5:

$$\begin{aligned} \frac{e}{h} \delta\mu &= \frac{(J_1 - J_2)}{2} \cdot \int_{-\infty}^{+\infty} \{1 + |r(E)|^2 - |t(E)|^2\} \left( -\frac{\partial f}{\partial E} \right) dE \\ \rightarrow \frac{e}{h} \delta\mu &= (J_1 - J_2) \cdot \int_{-\infty}^{+\infty} |r(E)|^2 \left( -\frac{\partial f}{\partial E} \right) dE, \end{aligned} \quad (11)$$

Here we have used the fact that:  $|r(E)|^2 + |t(E)|^2 = 1$

Now the net current flowing through the sample is the difference between the current flowing from left to right and the current flowing right to left. For a particular energy it becomes:

$$J_E = |t(E)|^2 \cdot |t_{1S}|^2 \cdot J_1 - |t(E)|^2 \cdot |t_{2S}|^2 \cdot J_2 = \{1 + O(\varepsilon)\} \cdot (J_1 - J_2) \cdot |t(E)|^2,$$

So net current through the sample is:  $J = \int_{-\infty}^{+\infty} J_E \left( -\frac{\partial f}{\partial E} \right) dE$ . This gives:

$$J = \{1 + O(\varepsilon)\} \cdot (J_1 - J_2) \cdot \int_{-\infty}^{+\infty} |t(E)|^2 \left( -\frac{\partial f}{\partial E} \right) dE \approx (J_1 - J_2) \cdot \int_{-\infty}^{+\infty} |t(E)|^2 \left( -\frac{\partial f}{\partial E} \right) dE.$$



Using this in eq. 11 we get:

$$\delta\mu = \frac{h}{e} \cdot \frac{\int_{-\infty}^{+\infty} |r(E)|^2 \left(-\frac{\partial f}{\partial E}\right) dE}{\int_{-\infty}^{+\infty} |t(E)|^2 \left(-\frac{\partial f}{\partial E}\right) dE} \cdot J. \quad (12)$$

Now at  $T=0K$ ,  $\left(-\frac{\partial f}{\partial E}\right) = \delta(E)$ . Using this in eq. 12 we get,  $\delta\mu = \frac{h}{e} \cdot \frac{|r(0)|^2}{|t(0)|^2} \cdot J$

Now using this result in eq. 1, we get resistivity  $\rho = \frac{h}{e^2} \cdot \frac{|r(0)|^2}{|t(0)|^2} = \frac{h}{e^2} \cdot \frac{R}{T}$

So resistivity of a 1D system at  $T=0K$  becomes:

$$\boxed{\rho = \frac{h}{e^2} \cdot \frac{R}{T}} \quad (13)$$

#### IV. Basic Formalism: Tight Binding Model

Having found the definition of resistivity, we now have to calculate the  $R$  and  $T$  of the electrons in the disordered system. For this we use here Tight Binding Model. In this model wave-function of electron is considered as a linear superposition of the last orbitals of the atoms i.e. scattering centers.

Let there is a 1D system made of array of atoms with equal spacing ' $d$ '. We have to find the eigen-function of an electron moving in the potential created by this system. Let the Hamiltonian is denoted by  $\hat{H}$ . Let  $\{|n\rangle\}$  be a set of mutually orthogonal kets following the relation  $\hat{t}(d)|n\rangle = |n+1\rangle$ , where  $\hat{t}(d)$  is the translation operator. Let Physically the ket  $|n\rangle$  is the Hilbert space representation of a wave-function peaked at the site of the  $n$ th atom. Though there is some leakage possible into the neighboring sites due to quantum mechanical tunneling.

If  $\hat{H}$  is represented in the  $\{|n\rangle\}$  basis, then the diagonal elements will be

$$\langle n | \hat{H} | n \rangle = E_n,$$

But  $\hat{H}$  is not completely diagonal in  $\{|n\rangle\}$  basis due to the leakage. To simplify the situation, we have *Tight binding approximation*.

■ *Tight binding approximation:*

*The only non-diagonal elements of importance connects nearest neighbors.*

$$\begin{aligned} & E_n, \text{ if } m = n \\ \text{i.e. } \langle m | \hat{H} | n \rangle &= V_{m,n}, \text{ if } m = n \pm 1 \\ & 0, \text{ otherwise.} \end{aligned} \quad (14)$$

So the Hamiltonian becomes,

$$\hat{H} = \sum_{n=-\infty}^{+\infty} E_n |n\rangle \langle n| + \sum_{n=-\infty}^{+\infty} V_{n,n+1} \{ |n\rangle \langle n+1| + |n+1\rangle \langle n| \}$$

$$\text{From this we obtain, } \hat{H}|n\rangle = E_n |n\rangle + V_{n,n-1} |n-1\rangle + V_{n,n+1} |n+1\rangle \quad (15)$$

Now let one eigen-ket of this Hamiltonian be  $|\theta\rangle = \sum a_n |n\rangle$  with energy eigen-value  $\epsilon$ . So using eq. 15 with TISE we get,

$$\begin{aligned} \hat{H}|\theta\rangle &= \epsilon |\theta\rangle, \Rightarrow \sum a_n \hat{H}|n\rangle = \epsilon \sum a_n |n\rangle, \\ \Rightarrow \langle n | (\sum a_n \{ E_n |n\rangle + V_{n,n-1} |n-1\rangle + V_{n,n+1} |n+1\rangle \}) &= \epsilon \sum a_n \langle n | n \rangle \end{aligned}$$

$$\text{Which gives, } \epsilon a_n = E_n a_n + V_{n+1,n} a_{n+1} + V_{n-1,n} a_{n-1}. \quad (16)$$

Here  $a_n$  is the wave-function amplitude of the  $n$ th lattice site,  $V_{n+1,n}$  is the hopping interaction between neighboring sites,  $E_n$  is the on-site energy term,  $\epsilon$  is the energy eigen-value of the Hamiltonian.

## V. Incorporating Disorder

Having defined our basic model we shall now apply it for our specific 1D disordered system. Consider in the 1D system described above, there is some disorder from site  $n=1$  to  $n=N$ . This disorder creates some sort of random potential within that region. Outside that region (i.e. at  $n \geq N, -\infty < n \leq 1$ ) potential is periodic [ $V(x+d) = V(x)$ ]. As a result,  $E_n$  has a constant value outside the disordered region. Inside the region it will take random value depending upon the potential.



■ **Assumption I:**

The site energies  $\{E_n\}$  are assumed to be uncorrelated random variables with an arbitrary probability density  $P(E_n)$ , symmetric around zero for  $1 < n < N$ , and to be identically zero outside the region (Fig.1). Similarly,  $\{V_{n,n+1}\}$  are assumed to be un-correlated random variable for  $1 < n < N$  and outside the region it is constant  $V_0$ .

Thus the system is made of a disordered segment containing  $N$  atoms with length  $(N-1)d$  embedded in a infinite conducting ordered chain.

We have to calculate the resistivity defined by  $\rho = \frac{h}{e^2} \cdot \frac{R}{T}$  and study its nature with disorder size,  $R$  and  $T$  are reflection and transmission coefficient.

**a. Transfer Matrix:**

This is used to find the relation between neighboring sites. From eq.3

$$\begin{pmatrix} a_{n+1} \\ a_n \end{pmatrix} = \begin{pmatrix} \frac{\varepsilon - E_n}{V_{n+1,n}} & \frac{-V_{n-1,n}}{V_{n+1,n}} \\ 1 & 0 \end{pmatrix} \begin{pmatrix} a_n \\ a_{n-1} \end{pmatrix} = p_n \begin{pmatrix} a_n \\ a_{n-1} \end{pmatrix} = \prod_{i=1}^n p_i \begin{pmatrix} a_1 \\ a_0 \end{pmatrix} = P_n \begin{pmatrix} a_1 \\ a_0 \end{pmatrix}, \quad \text{---(17)}$$

Here  $p_n$  is called transfer matrix. With these matrices, once we are given amplitudes of two neighboring sites, those of other sites can be found easily. Here  $P_n = \prod_{i=1}^n p_i \rightarrow P_n = p_n P_{n-1}$ . From this we get the recursive relations as follows:

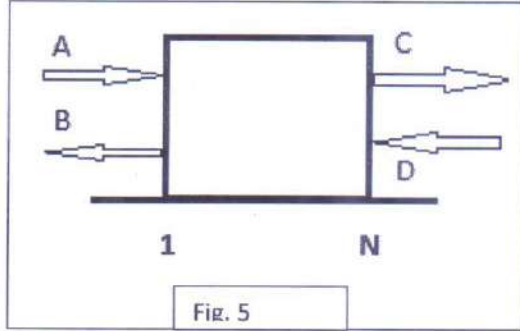
$$P_n^{11} = \frac{\varepsilon - E_n}{V_{n+1,n}} P_{n-1}^{11} - \frac{V_{n-1,n}}{V_{n+1,n}} P_{n-2}^{11}, \quad P_n^{21} = P_{n-1}^{11} \quad (18a)$$

$$P_n^{12} = \frac{\varepsilon - E_n}{V_{n+1,n}} P_{n-1}^{12} - \frac{V_{n-1,n}}{V_{n+1,n}} P_{n-2}^{12}, \quad P_n^{22} = P_{n-1}^{12} \quad (18b)$$

**b. Boundary Condition**

Inside the disordered region, the components of the eigen-function are governed by eq. 18. But outside the region the relations are much simpler due to order. In that region,  $E_n=0$  and  $V_{n+1,n} = V_0, \forall n \in (-\infty, 1] \cup [N, +\infty)$ . This along with the eq. 15 gives: (Appendix II eq. 48)





$$a_n = Ae^{ikdn} + Be^{-ikdn}, -\infty < n \leq 1 \quad (19a)$$

$$= Ce^{ikdn} + De^{-ikdn}, \quad n \geq N$$

$$\epsilon = 2V_0 \cos kd, \quad (19b)$$

Here A and D are amplitude of incident wave from left and right of the disordered region. C, B are the amplitude of scattered wave.

Now we will connect the two boundaries of the random lattice by a transfer matrix defined as,

$$\mathbf{T} \begin{pmatrix} B \\ A \end{pmatrix} = \begin{pmatrix} D \\ C \end{pmatrix} \rightarrow \begin{cases} \mathbf{T}_{11}B + \mathbf{T}_{12}A = D \\ \mathbf{T}_{21}B + \mathbf{T}_{22}A = C \end{cases} \quad (20)$$

Again, let  $(r, t)$  are the reflection and transmission coefficient of the wave coming from left, and that of the wave coming from right be  $(\bar{r}, \bar{t})$ . Then from Fig. 2,

$$\begin{cases} rA + \bar{t}D = B \\ tA + \bar{r}D = C \end{cases} \rightarrow \begin{pmatrix} r & \bar{t} \\ t & \bar{r} \end{pmatrix} \begin{pmatrix} A \\ D \end{pmatrix} = \begin{pmatrix} B \\ C \end{pmatrix} \rightarrow \mathbf{S} \begin{pmatrix} A \\ D \end{pmatrix} = \begin{pmatrix} B \\ C \end{pmatrix}, \quad (21)$$

This  $\mathbf{S}$  matrix is known as scattering matrix. It also connects the two boundaries and helps us to find the resistivity. Comparing eq. 20 and eq. 21, we get:

$$r = -\frac{\mathbf{T}_{12}}{\mathbf{T}_{11}}, \quad t = \frac{\det \mathbf{T}}{\mathbf{T}_{11}} \quad (22)$$

$$\text{Which then gives resistivity } \rho = \frac{R}{T} = \frac{|r|^2}{|t|^2} = \frac{|\mathbf{T}_{12}|^2}{|\det \mathbf{T}|^2}. \quad (23)$$

## VI. Resistivity Calculation

As we are interested in the conduction of electron at  $T \rightarrow 0K$ , we can neglect electron thermal scattering and focus on scattering from intrinsic defects. To do that, we have to find the relation between  $\mathbf{T}$  and  $\mathbf{P}_N$  matrix.

From eq. 19a, applying at  $n = N$ ,

$$\begin{aligned} a_{N+1} &= Ce^{ikd(N+1)} + De^{-ikd(N+1)} \\ a_N &= Ce^{ikdN} + De^{-ikdN} \end{aligned} \quad (24a)$$

which gives,

$$\begin{pmatrix} a_{N+1} \\ a_N \end{pmatrix} = \begin{pmatrix} e^{-ikd(N+1)} & e^{ikd(N+1)} \\ e^{-ikdN} & e^{ikdN} \end{pmatrix} \begin{pmatrix} D \\ C \end{pmatrix} = \begin{pmatrix} e^{-ikd} & e^{ikd} \\ 1 & 1 \end{pmatrix} \begin{pmatrix} e^{-ikdN} & 0 \\ 0 & e^{ikdN} \end{pmatrix} \begin{pmatrix} D \\ C \end{pmatrix} \\ = \Lambda \theta^{-1} \begin{pmatrix} D \\ C \end{pmatrix}. \quad (24b)$$

Similarly applying eq. 19a at  $n = 1$  we get,

$$\begin{aligned} a_1 &= Ae^{-ikd} + Be^{ikd} \\ a_0 &= A + B \end{aligned} \rightarrow \begin{pmatrix} a_1 \\ a_0 \end{pmatrix} = \begin{pmatrix} e^{-ikd} & e^{ikd} \\ 1 & 1 \end{pmatrix} \begin{pmatrix} B \\ A \end{pmatrix} = \Lambda \begin{pmatrix} B \\ A \end{pmatrix}. \quad (25)$$

Now comparing eq. 24b and 25 we get,

$$\left. \begin{aligned} \begin{pmatrix} a_{N+1} \\ a_N \end{pmatrix} &= \mathbf{P}_N \begin{pmatrix} a_1 \\ a_0 \end{pmatrix} = \mathbf{P}_N \Lambda \begin{pmatrix} B \\ A \end{pmatrix} \\ \begin{pmatrix} a_{N+1} \\ a_N \end{pmatrix} &= \Lambda \theta^{-1} \begin{pmatrix} D \\ C \end{pmatrix} \end{aligned} \right\} \rightarrow \begin{pmatrix} D \\ C \end{pmatrix} = \theta \Lambda^{-1} \mathbf{P}_N \Lambda \begin{pmatrix} B \\ A \end{pmatrix} \\ \rightarrow \mathbf{T} \begin{pmatrix} B \\ A \end{pmatrix} = \theta \Lambda^{-1} \mathbf{P}_N \Lambda \begin{pmatrix} B \\ A \end{pmatrix}.$$

Which finally gives,  $\mathbf{T} = \theta \Lambda^{-1} \mathbf{P}_N \Lambda. \quad (26)$

Where  $\theta = \begin{pmatrix} e^{ikdN} & 0 \\ 0 & e^{-ikdN} \end{pmatrix}, \quad \Lambda^{-1} = \frac{1}{\det \Lambda} \begin{pmatrix} 1 & -e^{ikd} \\ -1 & e^{-ikd} \end{pmatrix} \quad (27)$

and,  $\det \Lambda = e^{-ikd} - e^{ikd} = -2i \sin kd = -2i \sqrt{1 - \cos^2 kd} = -i \sqrt{4 - \epsilon^2/V^2}$

Now from eq. 27, it is clear that  $\det \theta = 1, \det (\Lambda^{-1} \Lambda) = 1$ , which gives:

$$\det \mathbf{T} = \det \mathbf{P}_N = \det p_N \cdots \det p_2 \det p_1 = (-1)^N \frac{V_{N,N-1}}{V_0} \frac{V_{N-1,N-2}}{V_{N,N-1}} \cdots \frac{V_{2,1}}{V_{3,2}} \frac{V_0}{V_{2,1}} \\ = (-1)^N$$

This result reduces eq. 23 to,  $\rho = |\mathbf{T}_{12}|^2. \quad (28)$

Multiplying eq. 26 using eq. 27 we get,

$$\mathbf{T}_{12} = \frac{1}{\det \Lambda} e^{ikdN} (e^{ikd} p_N^{11} - e^{-ikd} p_N^{22} + p_N^{12} - e^{ik2d} p_N^{21}) \\ \mathbf{T}_{12}^* = \frac{1}{\det \Lambda^*} e^{-ikdN} (e^{-ikd} p_N^{11} - e^{ikd} p_N^{22} + p_N^{12} - e^{-ik2d} p_N^{21}). \quad (29)$$



Putting this in eq. 28 we get,

$$\rho = |\mathbf{T}_{12}|^2 = \mathbf{T}_{12}^* \mathbf{T}_{12} = \frac{1}{|\det A|^2} \{ (P_N^{11})^2 + (P_N^{22})^2 + (P_N^{12})^2 + (P_N^{21})^2 + 2\cos kd (P_N^{11} - P_N^{22})(P_N^{12} - P_N^{21}) - 4\cos^2 kd P_N^{21} P_N^{12} - 2 \} \quad (30a)$$

$$\rightarrow \rho = \frac{1}{4 - \varepsilon^2/V^2} \{ (P_N^{11})^2 + (P_N^{22})^2 + (P_N^{12})^2 + (P_N^{21})^2 + \frac{\varepsilon}{V_0} (P_N^{11} - P_N^{22})(P_N^{12} - P_N^{21}) - \frac{\varepsilon^2}{V_0^2} P_N^{21} P_N^{12} - 2 \} . \quad (31b)$$

Using eq. 19b in eq. 30a, we get 30b. This expression is very useful for analytical as well as computational analysis of Anderson model. Averaging eq. 30b gives arithmetic mean of resistivity  $\langle \rho \rangle$  in terms of  $\langle P_N^{ij} P_N^{kl} \rangle$  which again can be found from the recursion relation of eq. 18. *Here we take the average for arbitrary diagonal and non-diagonal disorder with  $\varepsilon = 0$ .* This condition makes the calculation easier, though it can also be proved for non-zero energy as well. Using this condition with eq. 18 we get,

$$\rho = \frac{1}{4} \{ (P_N^{11})^2 + (P_N^{22})^2 + (P_N^{12})^2 + (P_N^{21})^2 - 2 \} = \frac{1}{4} \{ (P_N^{11})^2 + (P_{N-1}^{12})^2 + (P_N^{12})^2 + (P_{N-1}^{11})^2 - 2 \} \quad (32)$$

If we define  $F_n = \langle (P_n^{11})^2 \rangle$  and  $f_n = \langle (P_n^{12})^2 \rangle$  then eq. 32 becomes,

$$\langle \rho \rangle = \frac{1}{4} [F_N + F_{N-1} + f_N + f_{N-1}] - \frac{1}{2} \quad (33)$$

Again using  $\varepsilon = 0$  in eq. 18a we get,  $P_n^{11} = \frac{E_n}{V_{n+1,n}} P_{n-1}^{11} - \frac{V_{n-1,n}}{V_{n+1,n}} P_{n-2}^{11}$  (34)

Squaring eq. 34 and taking average we will get the recursion relation of  $F_n$ 's. Here we have to utilize *assumption I*. As  $E_n$ 's probability distribution is symmetric about zero, which gives  $\langle E_n \rangle = 0$ . Again as all  $E_n$ 's and  $V_{n,n+1}$ 's are uncorrelated random variable so their probability distributions are independent of each other. This gives relations like  $\langle \frac{E_n^2}{V_{n,n+1}^2} \rangle = \langle E_n^2 \rangle \langle \frac{1}{V_{n,n+1}^2} \rangle$ . Again from eq. 21 we get  $P_{n-1}^{11}$  depends only on  $E_{n-1} \dots E_1$  and  $V_{n-1,n} \dots V_{1,2}; V_0$ . This makes  $P_{n-1}^{11}; E_n; V_{n+1,n}$  independent random variable. Furthermore if we take all the distributions are similar it will make all these expectation values independent of  $n$ . Then representing  $\langle E_n^2 \rangle = \langle E^2 \rangle$ ,  $\langle \frac{1}{V_{n,n+1}^2} \rangle = \langle \frac{1}{V^2} \rangle$ ,  $\langle V_{n,n+1}^2 \rangle = \langle V^2 \rangle$  we get,



$$\begin{matrix} F_N = \langle E^2 \rangle \langle \frac{1}{V^2} \rangle F_{N-1} + \langle V^2 \rangle \langle \frac{1}{V^2} \rangle F_{N-2} \\ F_{N-1} = F_{N-1} \end{matrix} \rightarrow \begin{pmatrix} F_N \\ F_{N-1} \end{pmatrix} = \begin{pmatrix} \langle E^2 \rangle \langle \frac{1}{V^2} \rangle & \langle V^2 \rangle \langle \frac{1}{V^2} \rangle \\ 1 & 0 \end{pmatrix} \begin{pmatrix} F_{N-1} \\ F_{N-2} \end{pmatrix}$$

Which gives, 
$$\begin{pmatrix} F_N \\ F_{N-1} \end{pmatrix} = \mathbf{R} \begin{pmatrix} F_{N-1} \\ F_{N-2} \end{pmatrix} = \mathbf{R}^{N-2} \begin{pmatrix} F_2 \\ F_1 \end{pmatrix} \quad (35)$$

The eigen-values and normalized eigen-vectors of  $\mathbf{R}$  are found to be:

$$\lambda_{\pm} = \frac{1}{2} \langle E^2 \rangle \langle \frac{1}{V^2} \rangle \pm \sqrt{\frac{1}{4} \langle E^2 \rangle^2 \langle \frac{1}{V^2} \rangle^2 + \langle V^2 \rangle \langle \frac{1}{V^2} \rangle}, \quad u_+ = \begin{pmatrix} 1 \\ 1/\lambda_+ \end{pmatrix}, \quad u_- = \begin{pmatrix} 1 \\ 1/\lambda_- \end{pmatrix} \quad (36)$$

Now expanding initial vector of eq. 35 in eigen-basis as  $\begin{pmatrix} F_2 \\ F_1 \end{pmatrix} = \alpha u_+ + u_- \beta$

we write, 
$$\begin{pmatrix} F_N \\ F_{N-1} \end{pmatrix} = \alpha \lambda_+^{N-2} u_+ + u_- \lambda_-^{N-2} \beta \quad (37)$$

Similarly from eq. 18a and 18b we see that both  $F_n$  and  $f_n$  follows similar relations. So  $f_N$  can also be written as eq. 37. Substituting these in eq. 33 finally gives,

$$\langle \rho \rangle = \frac{1}{4(\lambda_+ - \lambda_-)} \left\{ \left( 1 + \frac{\langle E^2 \rangle}{V_0^2} \right) (\lambda_+^N - \lambda_-^N) + \left( \frac{\langle V^2 \rangle}{V_0^2} + V_0^2 \langle \frac{1}{V^2} \rangle + \langle E^2 \rangle \langle \frac{1}{V^2} \rangle \right) (\lambda_+^{N-1} - \lambda_-^{N-1}) + \langle V^2 \rangle \langle \frac{1}{V^2} \rangle (\lambda_+^{N-2} - \lambda_-^{N-2}) \right\} - \frac{1}{2} \quad (38)$$

### c. Analysis of the Resistivity:

We know always  $\langle E^2 \rangle > 0$  and also from Schwartz inequality  $\langle V^2 \rangle \langle \frac{1}{V^2} \rangle > \langle V^2 \frac{1}{V^2} \rangle = 1$ . Applying this in eq. 36 we get  $\lambda_+ > \langle V^2 \rangle \langle \frac{1}{V^2} \rangle > 1$ . Again  $\lambda_-$  is always negative and also  $\lambda_+ > |\lambda_-|$ . So when  $N \rightarrow +\infty$ , the only dominant term in eq. 38 is  $\lambda_+^N$ . At large  $N$  limit,

$$\langle \rho \rangle \propto \lambda_+^N = e^{N \ln \lambda_+} \quad (39)$$

From eq. 39 it is clear that resistivity grows exponentially with length of disorder region, leading to the localization of wave no matter strong or weak the randomness is.

For diagonal disorder,  $\langle V^2 \rangle \langle \frac{1}{V^2} \rangle = 1$ . But still we have same properties of the Eigen-values which leads to localization.

Another important point to note is that  $\langle \rho \rangle$  only depends on the average values like  $\langle E^2 \rangle, \langle \frac{1}{V^2} \rangle, \langle V^2 \rangle$ . So this result is insensitive to the precise nature of the distribution that these random variables follow.

## VI. Numerical Calculations

From tight Binding Model, Hamiltonian of a electron in the disordered region becomes:

$$\hat{H} = \sum_{n=-\infty}^{+\infty} E_n |n\rangle \langle n| + \sum_{n=-\infty}^{+\infty} V_{n,n+1} \{ |n\rangle \langle n+1| + |n+1\rangle \langle n| \}$$

We have to find the stationary states of these electrons. For this we have to solve the TISE of the electron. The TISE of these electrons with energy  $\epsilon$  becomes:

$$\hat{H}|\theta\rangle = \epsilon|\theta\rangle \quad (1)$$

Where  $|\theta\rangle$  is a eigen state of electron:  $|\theta\rangle = \sum a_n |n\rangle$

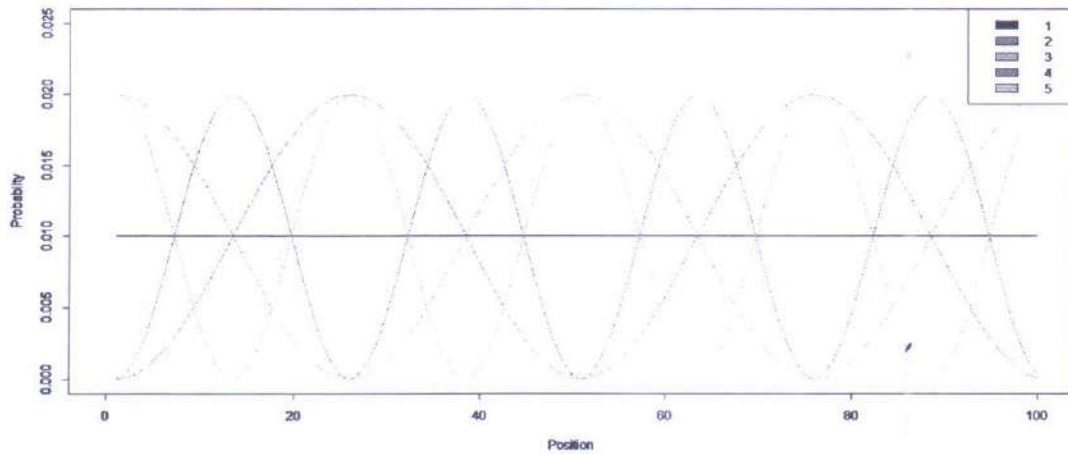
Now in  $\{|n\rangle\}$  basis, eq. 1 can be written as:

$$\begin{pmatrix} E_1 & V_{12} & \cdots & 0 & V_{1,N} \\ V_{12} & E_2 & \cdots & 0 & 0 \\ \vdots & \vdots & \ddots & \vdots & \vdots \\ 0 & 0 & \cdots & E_{N-1} & V_{N-1,N} \\ V_{1,N} & 0 & \cdots & V_{N-1,N} & E_N \end{pmatrix} \begin{pmatrix} a_1 \\ a_2 \\ \vdots \\ a_{N-1} \\ a_N \end{pmatrix} = \epsilon \begin{pmatrix} a_1 \\ a_2 \\ \vdots \\ a_{N-1} \\ a_N \end{pmatrix} \quad (2)$$

So the problem boils down to solving a matrix eigen value equation.

### I. For Disorder-free region:

If there is no disorder, we can take  $V_{n,n+1} = 1$ ,  $E_n = 0 \forall n \in 1(1)N$ , We take  $N=100$ .  $|a_n|^2$  gives the probability of finding the electron at the  $n$ 'th site with energy  $\epsilon$ . Plotting this probability with position ( $n$ ) for first few energy eigen values, we get simple bloch waves. Different colours corresponds to different energy value.

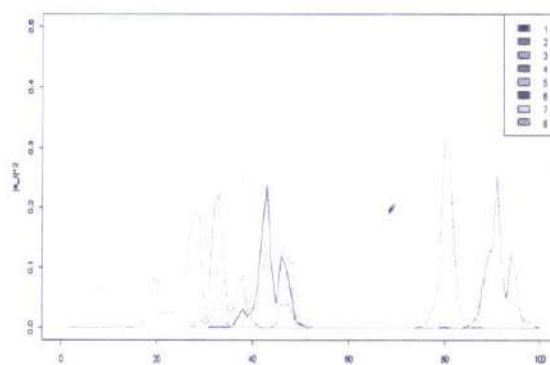
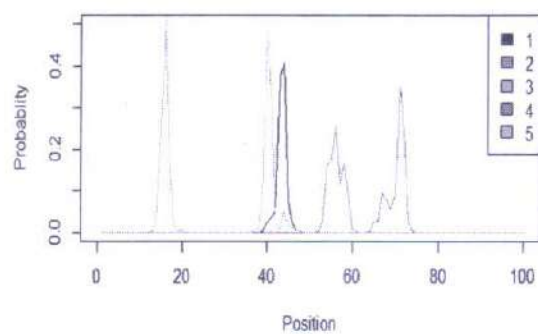


### II. For Disordered System:

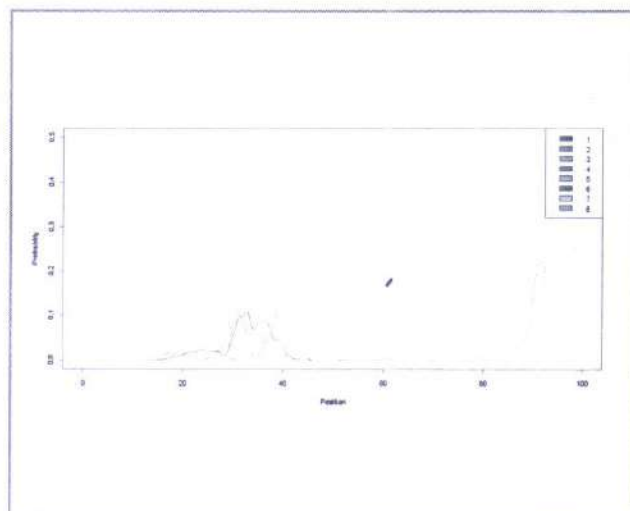
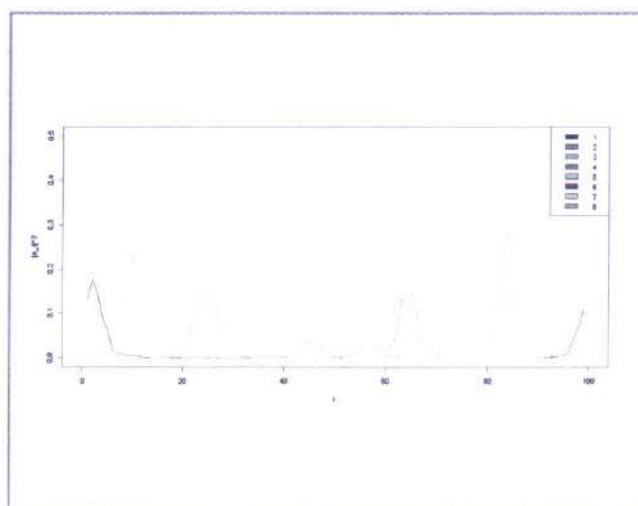
Here we take  $V_{n,n+1} = 1$  and sample  $E_n$  from a random variable with range  $[-W/2, W/2]$  following uniform distribution for all  $n \in 1(1)N$ . Here we take  $N=100$ . Now we do the same calculations for different disorder strength i.e. different  $W$ . Now as the computer is choosing a matrix with random entry, each time it choose a different matrix even though  $W$  is same. This will change the probability density of wave function by some amount. Here we present the result for such two choices of matrix. We are plotting probability density with site number. Different colors corresponds to different energy values of same matrix.

#### a. $W=2.0$ :

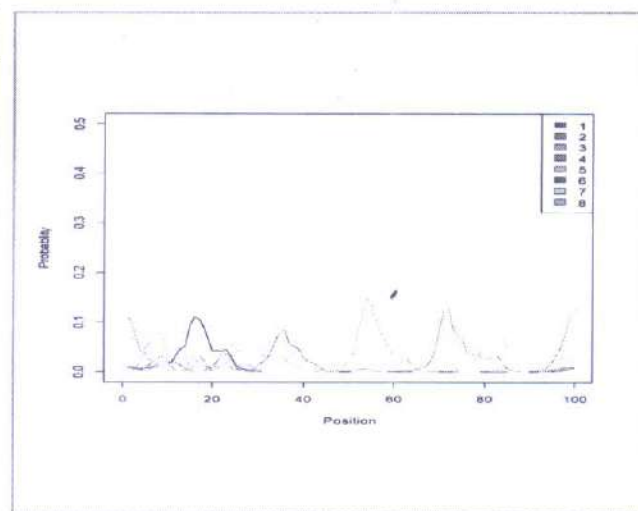
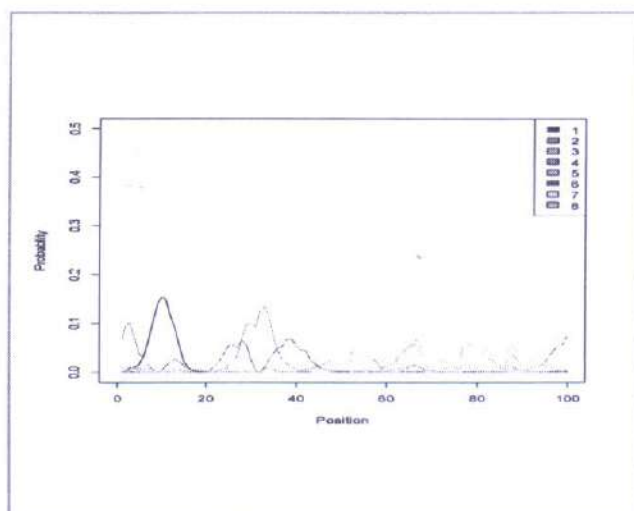




b.  $W=1.0$ :



c.  $W=0.5$ :



*So from the above graphs, it is clear that the electron wavefunction localizes for one-dimensional disordered system. The wave function becomes more and more localizes with the increase of the disorder strength. Moreover for a fixed disorder strength, different choices of the Hamiltonian may chance the degree of localization to some extent but not significantly.*

## VII. Summary

In this project report we have reviewed the 1D Anderson localization using transfer matrix method. It has been found that one-dimensional system shows Anderson localization for any small value of disorder strength. So there is no transition between metal and insulator for one-dimensional system. We have also verified our analytical results through numerical simulations for different disorder strengths.

## Acknowledgement

I would like to thank my project supervisor Dr. Atanu Rajak, Department of Physics, Presidency University, for guiding me throughout the project by showing path to explore the vast subject, by giving valuable suggestions and helping me out with necessary resources. Without his patience, motivation and immense knowledge this reading project would not have been possible. I would like to thank Dr. Sobhan Kr. Sounda, Department of Physics, Presidency University, for recommending me to Dr. A. Rajak for this project. I would like to thank Dr. Malay Purkait, Head of the Department of Physics, Ramakrishna Mission Residential College (Autonomous) Narendrapur, for his continuous support and motivation for this project. I would like to thank my friend Mr. Soham Das, Mr. Rajarshi Chattopadhyay, Mr. Shatanik Bhattacharya, for helping me in learning programming language which was necessary for this project. I am grateful to the faculty and staff of my parent institution Ramakrishna Mission Residential College (Autonomous) Narendrapur for providing me help in many ways and constant encouragement for exploring this subject. Finally, I thank my family members and friends who have given me immense support and motivation for these past months.



### Appendix I

We assume that the potential is not dependent of the momentum of the electron.

So for 1D system,  $E = \frac{p^2}{2m} + V(x)$ . Which gives  $v = \frac{p}{m} = \frac{\partial E}{\partial p}$ .

Again, from the phase space diagram of a 1D system, we get the number of states with energy from  $E$  to  $E+dE$  becomes:  $N(E) dE = 2dp/h = (1/\pi\hbar) \cdot dp$

Which gives:  $N(E) = (1/\pi\hbar) \times \left(\frac{\partial p}{\partial E}\right)$ . Here  $N(E)$  is the density of states

### Appendix II

Eq. 14 defines the Tight Binding Hamiltonian for 1D system. Now outside the disordered region, there is another symmetry condition due to the periodic nature of the potential:  $V_{n+1,n} = V_0, \forall n \in (-\infty, 1] \cup [N, +\infty)$ . This gives the Hamiltonian in the region outside the disordered region as:

$$\langle m | \hat{H} | n \rangle = \begin{cases} E_0, & \text{if } m = n \\ V_0, & \text{if } m = n \pm 1 \\ 0, & \text{otherwise} \end{cases} \quad (40a)$$

$$\text{So we get: } \hat{H} = \sum E_0 |n\rangle\langle n| + \sum V_0 (|n\rangle\langle n+1| + |n+1\rangle\langle n|) \quad (41b)$$

$$\text{Again the translation operator is defined as: } \hat{\tau}(d)|n\rangle = |n+1\rangle \quad (42)$$

First we find properties of the translation operator. From the normalization condition:  $\langle n | n \rangle = \langle n+1 | n+1 \rangle$  which gives,  $\hat{\tau}^\dagger \hat{\tau} = \hat{I}$  (43)

Here  $\hat{\tau}(d) \equiv \hat{\tau}$ . So  $\hat{\tau}$  is unitary. Now acting  $\hat{\tau}^\dagger$  from the left side of eq. 42 we get:  $|n\rangle = \hat{\tau}^\dagger |n+1\rangle$ . Writing it in bra-space, we get:  $\langle n| = \langle n+1| \hat{\tau}$

So in ket-space  $\hat{\tau}$  shifts one step towards right and  $\hat{\tau}^\dagger$  shifts towards left. Now,

$$\begin{aligned} \hat{\tau}^\dagger \hat{H} \hat{\tau} &= \sum_{n=-\infty}^{+\infty} \{ E_0 \hat{\tau}^\dagger |n\rangle\langle n| \hat{\tau} + V_0 (\hat{\tau}^\dagger |n\rangle\langle n+1| \hat{\tau} + \hat{\tau}^\dagger |n+1\rangle\langle n| \hat{\tau}) \} \\ &= \sum_n \{ E_0 |n-1\rangle\langle n-1| + V_0 (|n-1\rangle\langle n| + |n\rangle\langle n-1|) \} = \hat{H} \\ &\rightarrow \hat{\tau}^\dagger \hat{H} \hat{\tau} = \hat{H} \end{aligned} \quad (44)$$

So the Hamiltonian is invariant under translation with a displacement 'd'. Now using eq. 43 with eq. 44, we get:  $[\hat{H}, \hat{\tau}] = 0$  (45)



Here  $\hat{\tau}$  Unitary but not Hermitian. So its eigen-values would be complex numbers with unit modulus. Again eq. 45 tells that  $\hat{H}$  and  $\hat{\tau}$  have simultaneous eigen-states. Let us specifically form a linear combination:

$$|\theta\rangle = \sum_{n=-\infty}^{+\infty} e^{in\theta} |n\rangle \quad (46)$$

$$\text{Now, } \hat{\tau}|\theta\rangle = \sum_n e^{in\theta} \hat{\tau}|n\rangle = \sum_n e^{in\theta} |n+1\rangle = \sum_n e^{i(n-1)\theta} |n\rangle = e^{-i\theta} |\theta\rangle$$

$$\begin{aligned} \text{and, } \hat{H}|\theta\rangle &= \sum_n e^{in\theta} \hat{H}|n\rangle = \sum_n e^{in\theta} (E_0|n\rangle + V_0|n-1\rangle + V_0|n+1\rangle) \\ &= E_0 \sum_n e^{in\theta} |n\rangle + V_0 \sum_n (e^{i(n+1)\theta} + e^{i(n-1)\theta}) |n\rangle = (E_0 + 2V_0 \cos \theta) \sum_n e^{in\theta} |n\rangle \end{aligned}$$

$$\text{Here we had used eq. 15. So we get: } \boxed{\hat{H}|\theta\rangle = (E_0 + 2V_0 \cos \theta)|\theta\rangle} \quad (47)$$

So  $|\theta\rangle$  is a simultaneous eigen-ket of  $\hat{H}$  and  $\hat{\tau}$ . Now comparing with eq. 16 we get,

$$\mathcal{E} = E_0 + 2V_0 \cos \theta, \quad a_n = e^{in\theta} \quad (48)$$

Now we have to find the physical meaning of the parameter  $\theta$ . For this we have to study the position space wave function of the energy eigen-ket. Firstly, let  $|x\rangle$  be a position eigen-ket with eigenvalue 'x'. So by definition of the lattice translation operator,  $\hat{\tau}|x\rangle = |x+d\rangle$ . Now the position space wave function of the lattice translated energy eigen-ket becomes

$$\langle x|\hat{\tau}|\theta\rangle = \langle x-d|\theta\rangle \quad (49a)$$

if we let  $\hat{\tau}$  to act on  $\langle x|$ . If we let  $\hat{\tau}$  to act on  $\hat{\tau}|\theta\rangle$ , we get

$$\langle x|\hat{\tau}|\theta\rangle = e^{-i\theta} \langle x|\theta\rangle \quad (49b)$$

$$\text{Which gives us: } \langle x-d|\theta\rangle = e^{-i\theta} \langle x|\theta\rangle \quad (50)$$

If we take  $\langle x|\theta\rangle = e^{ikx} u(x)$  with  $\theta = kd$  and  $u(x+d) = u(x)$  and putting it in eq. 50, we get:

$$e^{ik(x-d)} u(x) = e^{-ikd} \cdot e^{ikx} u(x) \quad (51)$$

Eq. 51 tells us that  $\langle x|\theta\rangle = e^{ikx} u(x)$  satisfies eq. 50. This condition is known as *Bloch's Theorem*. It tells us that, in position space, energy eigen-ket  $|\theta\rangle$ , which is also a eigen-ket of lattice translation operator, can be written as a plane wave  $e^{ikx}$  times a periodic function  $u(x)$  with periodicity equal to lattice constant.

- 
- [1] Modern Quantum Mechanics Revised Edition, J. J. Sakurai, Addison-Wesley Publishing Company, Inc., 1994
  - [2] A brief introduction to Anderson Localization, Chenguang Guan, Xingyue Guan, Department of Physics, Massachusetts Institute of Technology, May 18, 2019
  - [3] Localization and low temperature transport in disordered one-dimensional systems, Alfred Douglas Stone, Doctorate in Philosophy, Massachusetts Institute of Technology, Jan. 1983.
  - [4] Definition and measurement of the electrical and thermal resistances, H.-L. Engquist and P. W. Anderson, Physical Review B, Volume 24, Number 2, July 1981
  - [5] Fifty years of Anderson localization, Ad Lagendijk, Bart van Tiggelen, and Diederik S. Wiersma, August 2009, Phys. Today 62(8), 24 (2009); doi: 10.1063/1.3206091
  - [6] Observation of the critical regime near Anderson Localization of light, Martin Störzer, Peter Gross, Christof M. Aegerter, and Georg Maret, Phys.Rev. Lett. **96**, 063904



BSC PROJECT

ON

# MEASURING CAPACITANCE VOLTAGE CHARACTERISTICS OF

## ELECTRICAL COMPONENTS USING LCR METER

SUBMITTED BY

SAGNIKGHOSH

Roll No. (PHUG/235/17)

On behalf of RAMAKRISHNA MISSION RESIDENTIAL COLLEGE, NARENDRAPUR,  
KOLKATA: 700103

Duration Of The Project: December 2019 to February 2020

As a B.Sc. project (experimental) under the supervision of,

DR. DEBAMALYA BANNERJEE

ASSISTANT PROFESSOR

DEPARTMENT OF PHYSICS

INDIAN INSTITUTE OF TECHNOLOGY, KHARAGPUR

KHARAGPUR-721302

*DBannerjee*

Signature with Date





**Ramakrishna Mission Residential College (Autonomous)**

**Vivekananda Centre for Research**

**Ramakrishna Mission Ashrama**

(A Branch Centre of Ramakrishna Mission, Belur Math, Howrah-711202)

**Narendrapur, Kolkata - 700 103, West Bengal, India**

A Scientific Industrial Research Organisation, Recognised by DST, Govt. of India

College with Potential for Excellence (CPE), Re-accredited by NAAC - 'A' (CGPA 3.56 out of 4)

---

## **DEPARTMENT OF PHYSICS**

### **Certificate**

This is to certify that Sagnik Ghosh, a student of B.Sc has successfully completed the project of UG curriculum entitled "MEASURING CAPACITANCE VOLTAGE CHARACTERISTICS OF ELECTRICAL COMPONENTS USING LCR METER" in the period from January to May, 2020.

*Malay Purkait*  
.....  
30.06.2020

**Signature Of HOD**

**Dept. of Physics**

**Dr. Malay Purkait**

Associate Prof. & Head

Department of Physics

Ramakrishna Mission Residential College

(Autonomous)

Narendrapur, Kolkata- 700 103 (W.B.)

---

PHONES : 24772201(3lines), 24772205 FAX : 033-24773597 EMAIL : rkmcpur@vsnl.com

WEBSITE : [www.rkmcnarendrapur.org](http://www.rkmcnarendrapur.org)



भारतीय प्रौद्योगिकी संस्थान, खड़गपुर  
खड़गपुर-७२१ ३०२, भारत

Indian Institute of Technology, Kharagpur  
Kharagpur – 721 302, India

Department of Physics

**Dr. Debamalya Banerjee**

*Assistant Professor*

October 2, 2020

IIT, Kharagpur

---

**To whom it may concern**

This is to certify that Mr. Sagnik Ghosh has completed a project titled “Measuring Capacitance Voltage Characteristics of Electrical Components Using LCR Meter” under my supervision in our research lab at IIT Kharagpur during December 2019 through February 2020. His project was focused on measuring the capacitance-voltage (C-V) characteristics using LCR meter and external bias unit. He had measured the C-V characteristics of different types (*i.e.* ceramic, electrolyte and film type) of capacitors. Also he has measured C-V characteristics of a spin coated organic semiconductor thin film. During this time he has used thermal evaporation facility of our lab, alongside other fabrication facilities such as spin coater, heat bath and basic characterization facilities such as source measure unit, LCR meter, DC bias unit, etc.

Sagnik is very sincere and hard working. I wish him best of luck for his future academic career.

(Dr. Debamalya Banerjee)



## ACKNOWLEDGEMENT

---

The success and final outcome of this reading project required a lot of guidance and assistance from many people and I am extremely privileged to have got this all along the completion of my project. All that I have done is only due to such supervision and assistance and I would not forget to thank them.

I would like to express my gratitude to my supervisor and guide **Prof. Dr. Debamalya Bannerjee** for the continuous support in my reading project study and related works, with his patience, immense knowledge and motivation. His guidance helped me in all the time of understanding and writing of this reading project. I could not have imagined having a better advisor and mentor for my reading project study.

I am thankful to and fortunate enough to get constant encouragement, support and guidance from all the **teaching professors of Department of Physics, Ramakrishna Mission Residential College (Autonomous)**, which helped me in successfully completing my project work.

I also thank respected **Swami Bhudevananda Maharaj**, Principal, and **Swami Krishnathananda Maharaj**, Vice Principal, for providing me an opportunity to do the project work in my 6th semester course and giving me all the support and guidance which made me complete the project duly.

I thank my fellow classmates for the stimulating discussions, for the sleepless nights we were working together before deadlines, and for all the fun we have had in the last few months. Also I would like to thank my family; my parents, sister and others for supporting me spiritually throughout writing this project.

Last but not the least, I would like to thank the internal and external project expert not only for their insightful comments and encouragement, but also for helping me to widen my understanding about the topic from various perspectives.

*Sagnik Ghosh*

---

SIGNATURE WITH DATE



## TABLE OF CONTENTS

---

|                                                     |    |
|-----------------------------------------------------|----|
| ACKNOWLEDGEMENT .....                               | 3  |
| MOTIVATIONANDOBJECTIVE .....                        | 4  |
| INSTRUMENTS ANDMETHODOLOGY .....                    | 4  |
| CHALLENGESANDPRECAUTIONS .....                      | 7  |
| C-V MEASUREMENT OFDIFFERENTCAPACITORS .....         | 8  |
| C-V MEASUREMENT OFVARACTORDIODES .....              | 11 |
| C-V MEASUREMENT OF P3HT-PCBMBULKHETEROJUNCTION..... | 13 |
| CONCLUSION.....                                     | 14 |
| REFERENCE.....                                      | 15 |

# MEASURING CAPACITANCE - VOLTAGE CHARACTERISTICS USING LCR METER

---

**Motivation and Objective:** For semiconductor materials, dielectric property is one of the key characteristics. A multitude of semiconductor device and material parameters can be obtained from capacitance voltage (C-V) characteristics like carrier concentrations, carrier lifetime, etc. Of special interest is the Mott-Schottky equation which relates the capacitance to the applied voltage across a semiconductor electrolyte junction. The equation is given by,

$$\frac{1}{C^2} = \frac{2(V + V_{bi})}{A^2 e \epsilon N}$$

where  $e$  is electronic charge,  $N$  is the doping concentration,  $A$  is the surface area and  $V_{bi}$  is the built in potential,  $C$  is capacitance and  $V$  is the applied voltage,  $\epsilon$  is dielectric constant of the semiconductor. Capacitance Voltage profiling is a technique for characterising semiconductor materials and devices in which the applied voltage is varied, and the capacitance is measured as a function of voltage. The depletion region in a semiconductor-semiconductor junction is empty of conducting charges, but contains ions. On varying the applied voltage to the junction it is possible to vary the width of the depletion region. If the width of the depletion region is  $d$ , cross sectional area of the junction is  $A$  and the permittivity is  $\epsilon$ , then capacitance  $C = A\epsilon/d$ . This can be considered as a simple equation to visualise the relation between depletion region width and the capacitance of the junction. Generally, measurements are done by applying a DC bias which can be varied manually and applying a small AC test signal.

Capacitance voltage profiling is widely used by researchers to find various semiconductor parameters. These data are also utilised by engineers to enhance yields and improve device performance. Accurate CV measurements can reveal oxide thickness, oxide charges, contamination from mobile ions, etc.

Here, we have used an LCR meter and a DC bias unit to measure capacitance-voltage characteristics of some of the commercially available capacitors.

A brief introduction to the instruments used in the study is provided below.

## Instruments and Methodology:

### 1) LCRmeter

The instrument that we have used to measure the capacitance-voltage characteristics of different electrical circuit components is called LCR meter. The LCR meter measures the impedance (complex resistance) of the given sample, as well as the current, voltage and phase angles. It then calculates the corresponding LCR values i.e.  $R_s$ ,  $C_s$ ,  $C_p$ ,  $L_s$ ,  $L_p$ , etc. Suitable measurements can be performed by giving a frequency sweep ranging from a few Hertz to few Megahertz. Capacitance vs. frequency curves can be plotted for various samples using this sweep measurement. An LCR meter is ideal for performing direct and precise measurements of inductors, capacitors and resistors using different test frequencies. In the following measurements we have used a LCR meter manufactured by HIOKI. The product code is IM3536A981-03 18-07H. A picture of the same has been provided below.



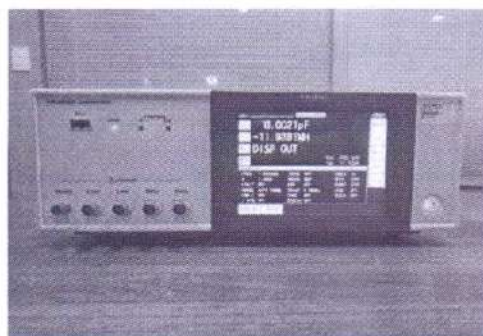


Figure 1: Hioki LCR Meter used in the present study

The different methods adopted in LCR meter are given below:

a) **Two Terminal method:** In this method, the design contacts the measurement target with two terminals. Measured values include wiring resistance and contact resistance and are significantly affected when the measurement target has low resistance (impedance). Stray capacitance also exists between the two cables and measurement signal flows to the stray capacitance as well as the measurement target during measurement at high frequencies and high impedance measurement, contributing a source of error.

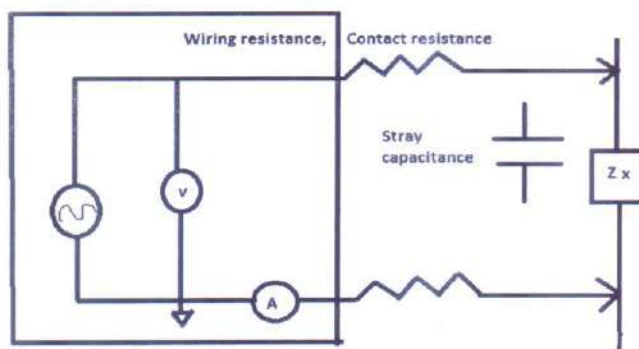


Figure 2: The two terminal circuit diagram

b) **Five Terminal method:** Reduces effects of wiring and contact resistance by using separate cables for signal current and voltage detection. Stray capacitance is reduced by using shielded cables and placing the shielded portion at same potential.

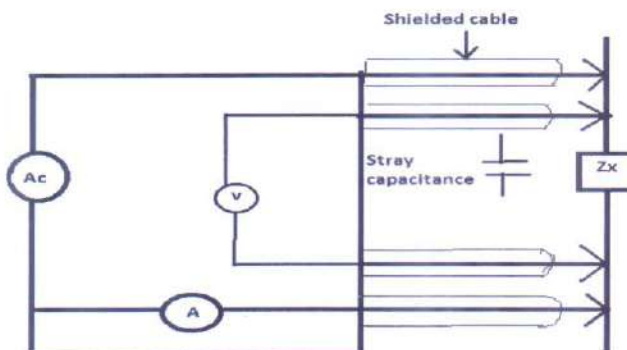


Figure 3: The Five terminal method



c) **Four Terminal pair method:** Reduces effects of magnetic field by using shielded cables and overlapping the cables carrying the current to and from the measurement target.

d) **Automatic Balance Bridge method:** This is a circuit design that is used in many LCR meters as the measurement circuit. The four terminals of the circuit (Hc, Hp, Lp and Lc) are connected to the measurement target.

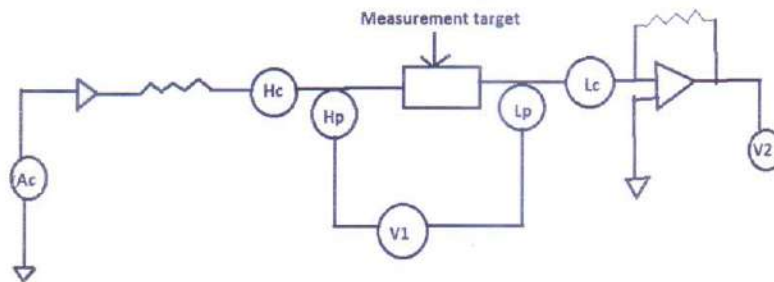


Figure 4: The Automatic balance bridge diagram

Hc: It applies a measurement signal generated with controlled frequency and amplitude to the measurement target. The frequency can be controlled within the range of several milihertz to megahertz and amplitude from 5mv to 5v.

Hp: Detects the measurement targets Hi potential. The detection circuit's input impedance is extremely high which allows accurate detection of the potential without a voltage drop.

Lp: It detects the measurement target's Lo potential.

Lc: Converts the current flowing to the measurement target into a voltage based on the detected resistance and detects the result. Lc terminal's potential is always held to 0v.

**Working formulae for finding parameters from impedance(Z) in LCR meter**

- $Z = V/I$
- $Y(\text{admittance}) = 1/Z$
- $Z_s(\text{series impedance}) = R + jX$ ;  $X = \omega L$  or  $-1/\omega C$
- $|Z_s| = (R^2 + X^2)^{1/2}$
- $|Z_p| = RX/(R^2 + X^2)^{1/2}$

2) **DC Bias Unit:** We have also used a DC bias unit attachment to provide DC voltage to the measurement target. The voltage input can be varied manually. The output of the bias unit is connected to the measurement circuit using a BNC cable. Here we have used a bias unit manufactured by GWINSTEK with the model name PSB-1800M. It is a multi range DC power supply(0-160V).



Figure5: DC voltage supply

## Challenges and precautions during measurement

Unlike much high end and costly instruments like impedance analysers, LCR meters are relatively less sensitive and hence require far greater optimization to get the desired outcomes. One of the foremost challenges is the fluctuations in the Capacitance vs Frequency plots. A suitable AC drive voltage has to be selected for which we get a more or less smooth graph. Given below are a series of plots of C vs F for a varactor diode at different AC voltage drive.

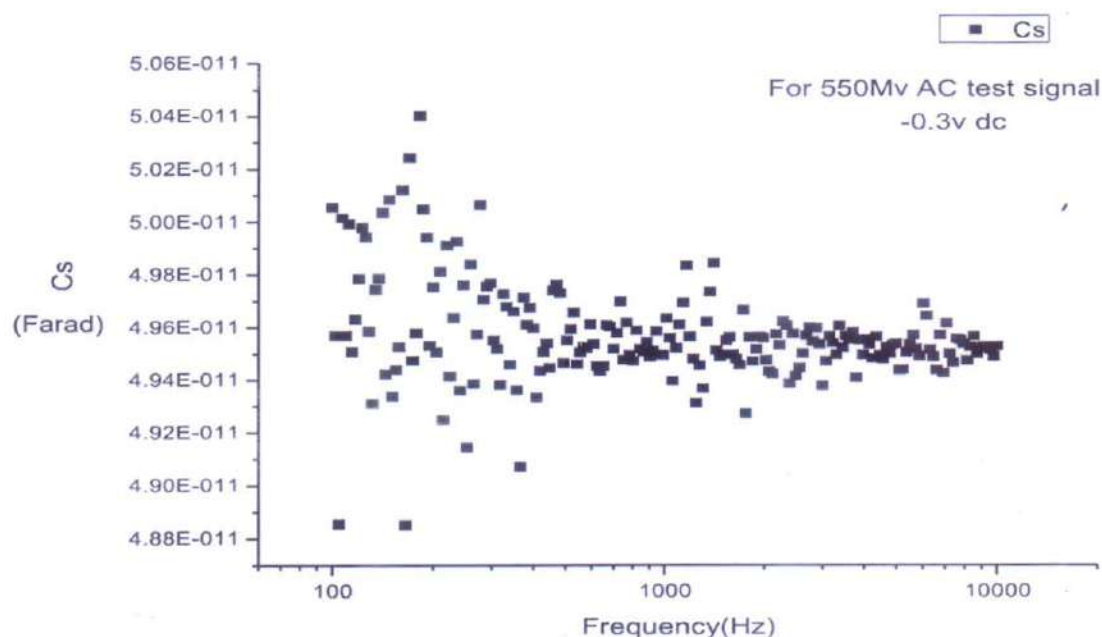


Figure 6: C vs. F plot for 550mV AC test signal at -0.3V dc

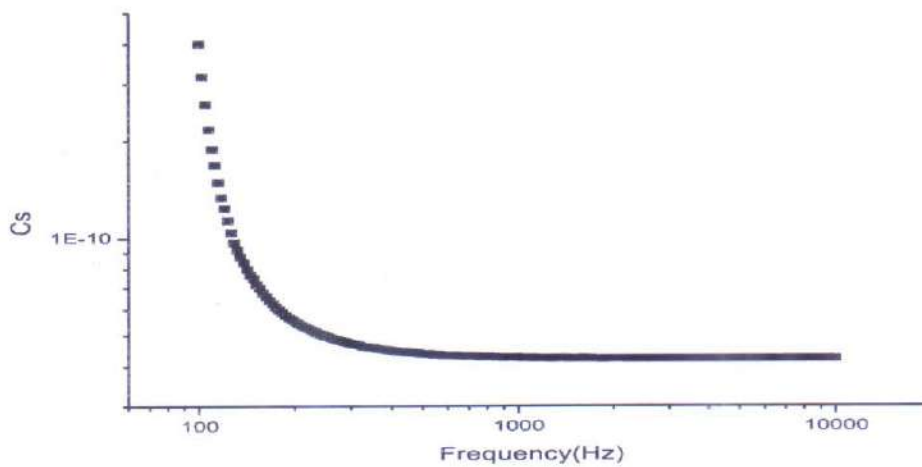


Figure : Capacitance vs. Frequency for 1 v Ac test signal

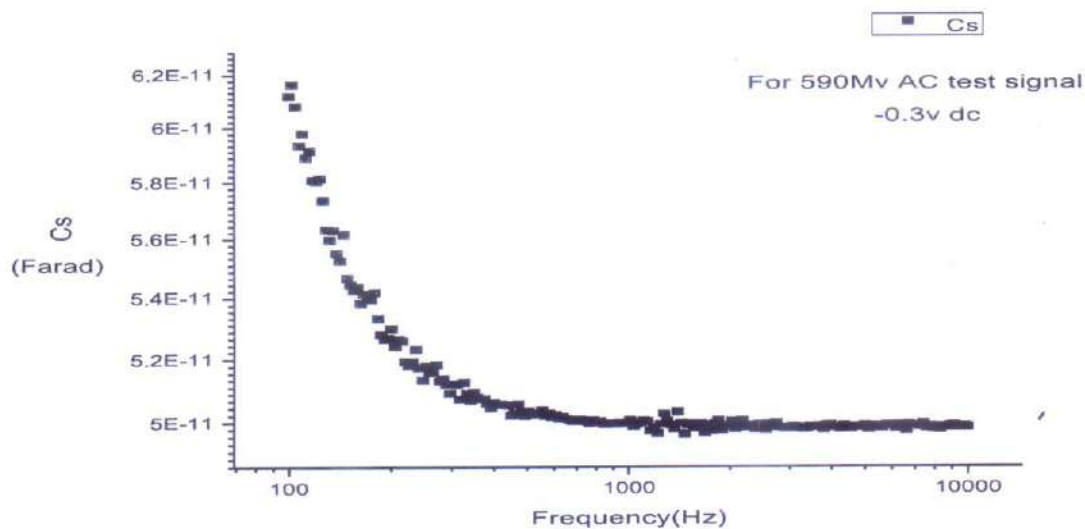


Figure 7: C vs. F plot for 590 mV AC test signal at -0.3V dc

At 550mV Ac test voltage there is large amount of fluctuations in the graph. However, at 800Mv test voltage fluctuations are much less. For 1V ac test voltage we get almost no fluctuations in the plot. Hence all the measurements are performed with 1v Ac test signal.

Another important challenge during the measurement is to keep the measurement contact undisturbed. Disturbing the measurement contact may result in erroneous data.

### C-V measurement of different capacitors

Here, we have conducted measurements on three different types of capacitors. They are ceramic, electrolytic and film capacitors. A brief description of each capacitor has been provided.

The capacitor which has ceramic as its dielectric material is called a ceramic capacitor. It is the most commonly used capacitor in electronic circuits due to its small size and large charge storage capability. Ceramic capacitors have no polarity and can be easily used in ac circuits. Ceramic disc capacitors consist of two conductive discs on each side of a piece of ceramic insulator, one lead attached to each plate, and coated with some inert, waterproof coating of ceramic composition.



Film capacitors use a thin plastic film as the dielectric. They are relatively cheap, stable over time and have low self inductance and equivalent series resistance. Film capacitors have no polarity and hence are suitably used in AC circuits. Typical film capacitors have capacitances ranging from below 1Nf to 30 microfarad. Voltage ratings vary from 50V to above 2Kv.

Electrolytic capacitors are polarised capacitors whose anode or positive plate is made of a metal that forms an insulating oxide layer through anodisation. The oxide layer is the dielectric of the capacitor and a solid, gel or liquid electrolyte covering the surface of the oxide layer acts as the negative plate of the capacitor. Here, an electrolytic capacitor of 100 microfarad has been used.

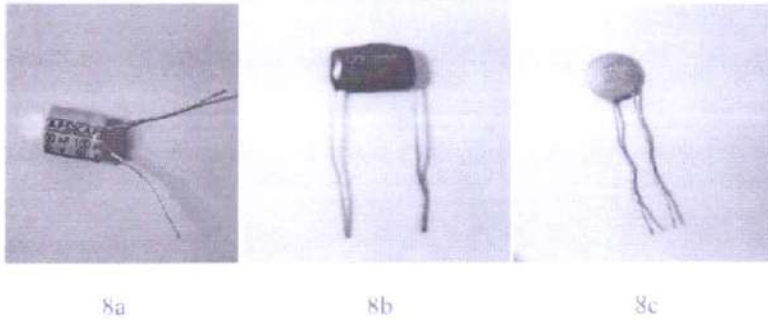


Figure 8: An electrolytic capacitor (9a); A film capacitor (9b); A ceramic capacitor (9c)

1) Apparatus used: A LCR meter, a variable DC voltage source, BNC cables, a ceramic disc capacitor, crocodile clips.

2) Circuit Arrangement: Here, we have used the automatic balance bridge method which is the basic circuit in most LCR meters.

3) Procedure: At first two crocodile clips were attached on either ends of the capacitor which were then connected to the LCR meter using BNC cables. The output of the DC source is attached to the LCR meter to provide DC bias, which can be varied manually. A DC bias was applied to the circuit. A frequency sweep ranging from 100Hz to 10 KHz with a 1V A.C test signal was applied through the LCR meter. Data was recorded for the parameter  $C_s$  (series mode capacitance). The above steps were repeated for different DC voltages ranging from -5 to +5volts.

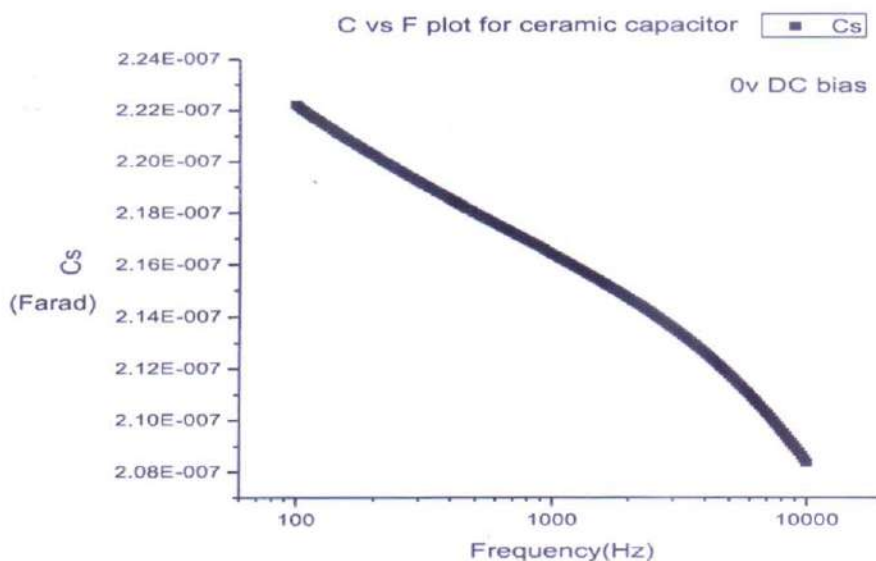


Figure 9: C vs. F plot for ceramic capacitor

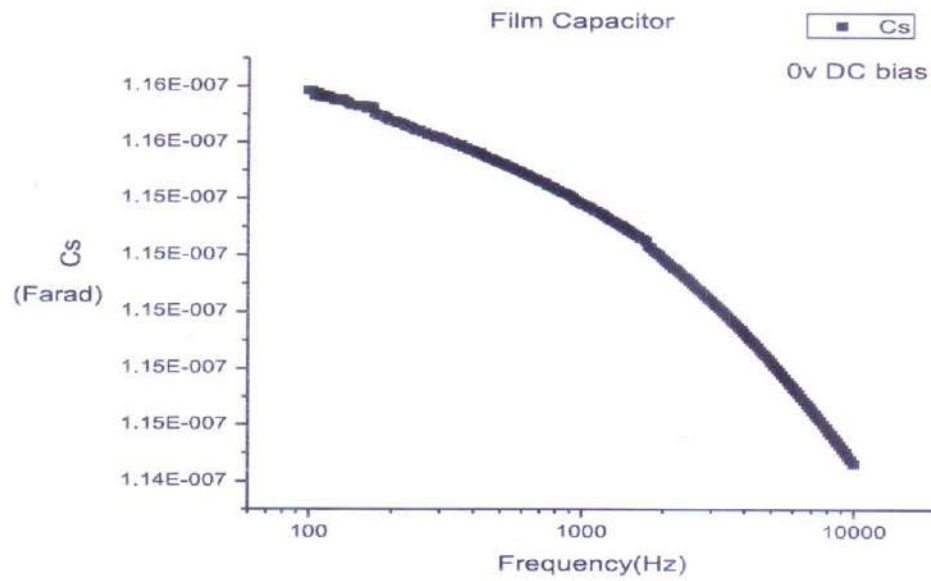


Figure 10: C vs. F plot for Film Capacitor

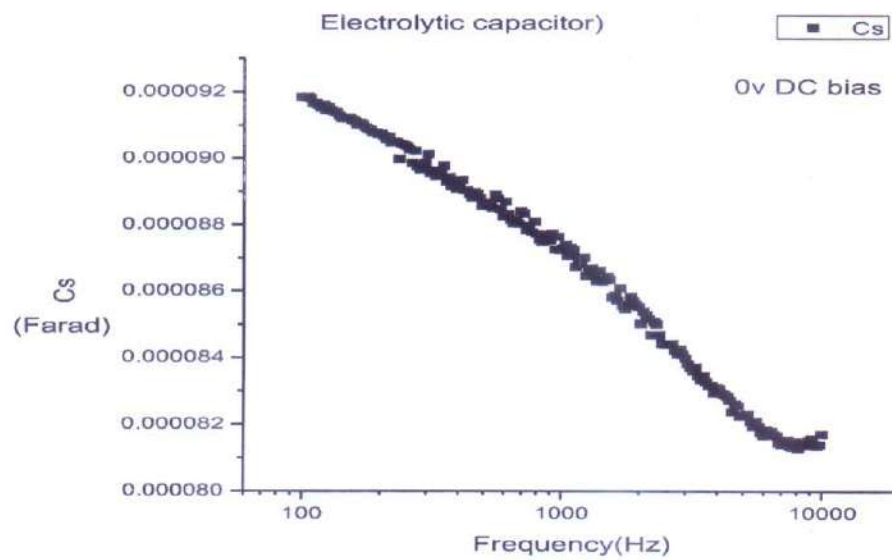


Figure 11: C vs. F plot for Electrolytic capacitor

From the C vs. F plots we can see that electrolytic capacitors have poor stability under frequency change while film capacitors show better stability.

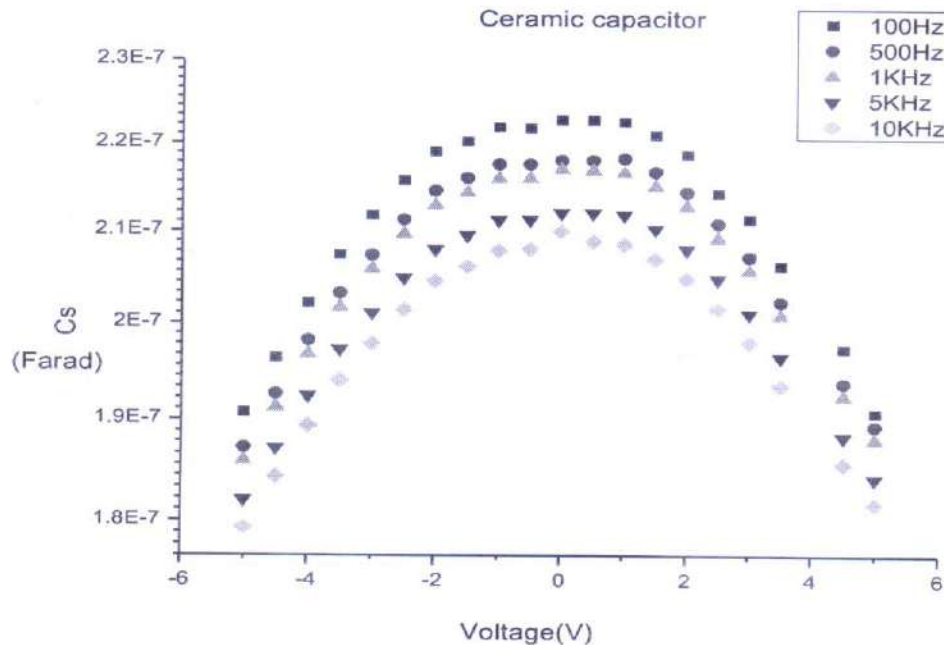


Figure 12: Capacitance vs. Voltage plot for Ceramic Capacitor

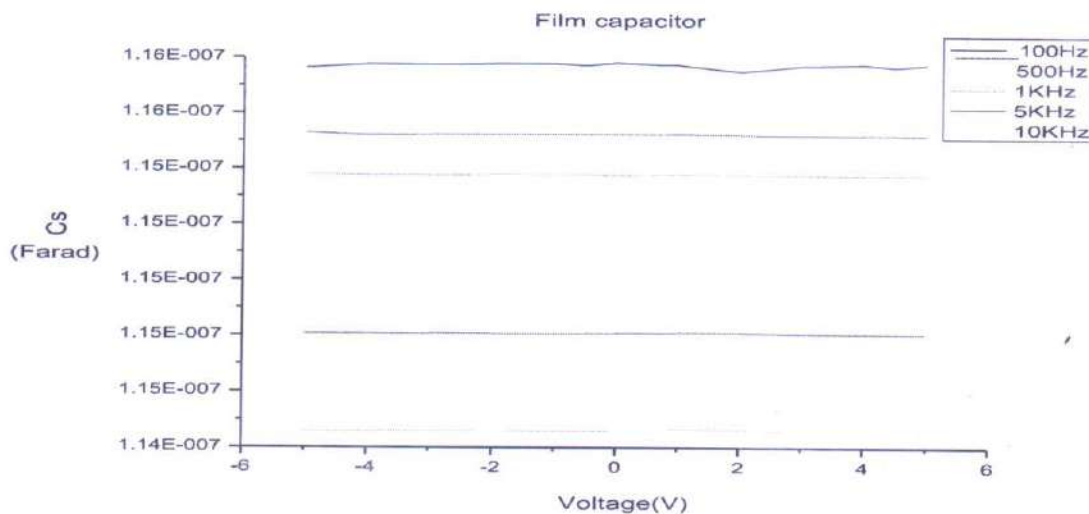


Figure 13: Capacitance vs. Voltage plot for Film Capacitor

**Conclusion:** It is evident that ceramic capacitors have their effective capacitance reduced with increase in DC bias. Ceramic capacitors have dielectrics which are ferroelectric materials. Therefore their polarisation and permittivity varies with applied field and hence capacitance also varies. On increasing the field, capacitance decreases. However, film capacitors show stable capacitance over a long voltage range.

## C-V measurement of varactordiode

Varactor diode is a p-n junction diode whose capacitance varies with the reverse voltage. Here, the depletion region of the junction acts as the dielectric medium and the p and n sides act as the two plates of a parallel plate capacitor. With increase in reverse bias voltage the electron from n-region and holes from p-region



moves away from the junction resulting in the increase of the width of the depletion region. Now capacitance,  $C = AE/d$ , where  $A$  is surface area of the junction,  $E$  is permittivity of the depletion region and  $d$  is the width of the depletion region. So, with increase in width, the capacitance of the diode decreases.

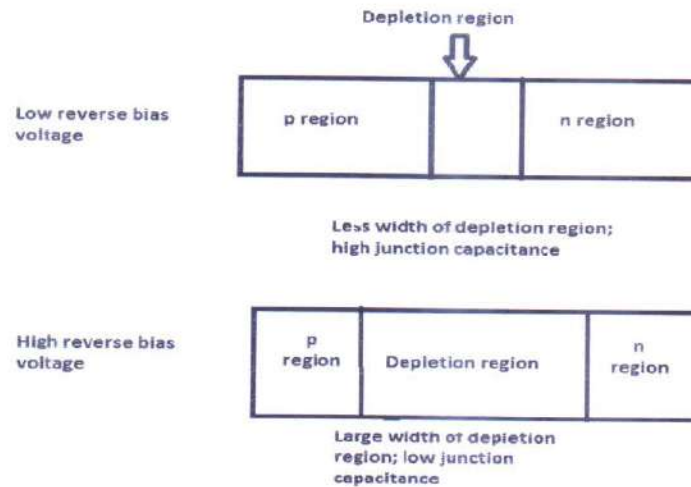


Figure14: Illustration of depletion region and junction capacitance

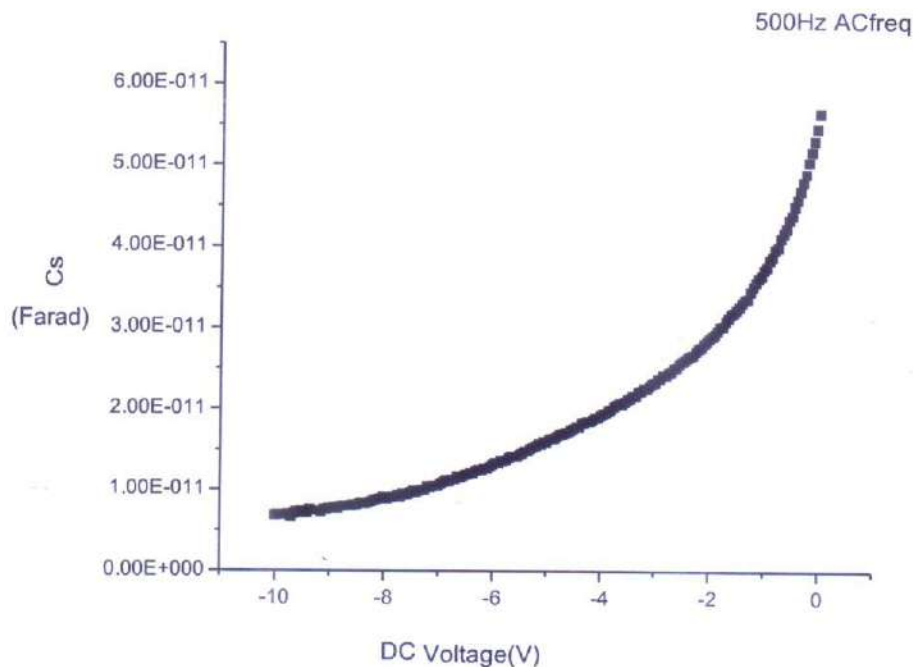


Figure 15: Capacitance vs. Voltage plot for Var5actor Diode

It is evident from the C-V graph of the varactor diode that the junction capacitance decreases with increase in the reverse bias voltage. This feature of a varactor diode provides a way for having a voltage controlled variable capacitance in a circuit. Some utilities of varactor diodes include:

- 1) Used in voltage controlled oscillators. Voltage controlled oscillators are used as FM demodulators or within frequency synthesizers.

2) Varactor diodes can be used in frequency modulators where they are placed across the resonant element within the generator and the audio applied to the diode. So, its capacitance will vary in line with the audio, causing signal frequency to shift up and down in line with the capacitance variations, and hence in line with the audio.

## C -V Measurement of P3HT-PCBM Bulk Heterojunction

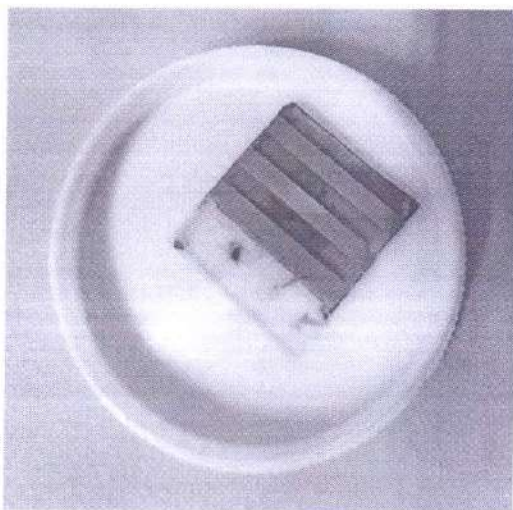


Figure16: The hetero-junction sample used for C-V measurements

We have used a bulk hetero-junction sample for C-V measurements. P3HT and PCBM (from Sigma Aldrich) were dissolved individually in chlorobenzene (20 mg/ml) and stirred for 12 hours. The two solutions were mixed at 1:1 weight ratio and stirred for another 12 hours. Indium Tin Oxide (ITO) coated glass substrate (obtained from Macwin India) was cleared through ultrasonic treatment sequentially in de-ionised water, acetone and isopropyl alcohol for 15 minutes each. A PEDOT-PSS (Sigma Aldrich) layer (hole transport layer) was spin coated onto the patterned ITO at 4000 rpm for 30 seconds and baked at 120°C for 1 hour in a silicone oil bath under vacuum. P3HT-PCBM solution was spin coated onto the PEDOT-PSS layer at 1000 rpm for 60 seconds. The fabricated active layer was annealed at 150°C for 15 minutes in a

silicone oil bath under vacuum. Finally, an Al-electrode was deposited onto the active layer by thermal evaporation through a shadow mask under vacuum pressure of  $5 \times 10^{-6}$  mbar. The active area, defined by the overlap of ITO and Al electrode, was  $6 \text{ mm}^2$ .

P3HT is a  $\pi$ -conjugated polymer, which becomes p-doped when it is exposed to oxygen or air. It is reported from separate measurements that the work function of ITO, HOMO levels of PEDOT-PSS, and those of P3HT lie very close (less than or equal to 0.2 eV) to each other. So ITO/PEDOT-PSS/P3HT interfaces can be considered as ohmic. Hence, the interfacial transport properties in the device will be dominated by the Al/PCMB Schottky junction.

The C-V characteristics of the sample were inspected by the LCR meter at different modulation frequencies ranging from 100 Hz to 10 KHz over the dc voltage range -1V to +1V. Beyond this voltage our sample showed serious damages and the measurements obtained were not reliable.



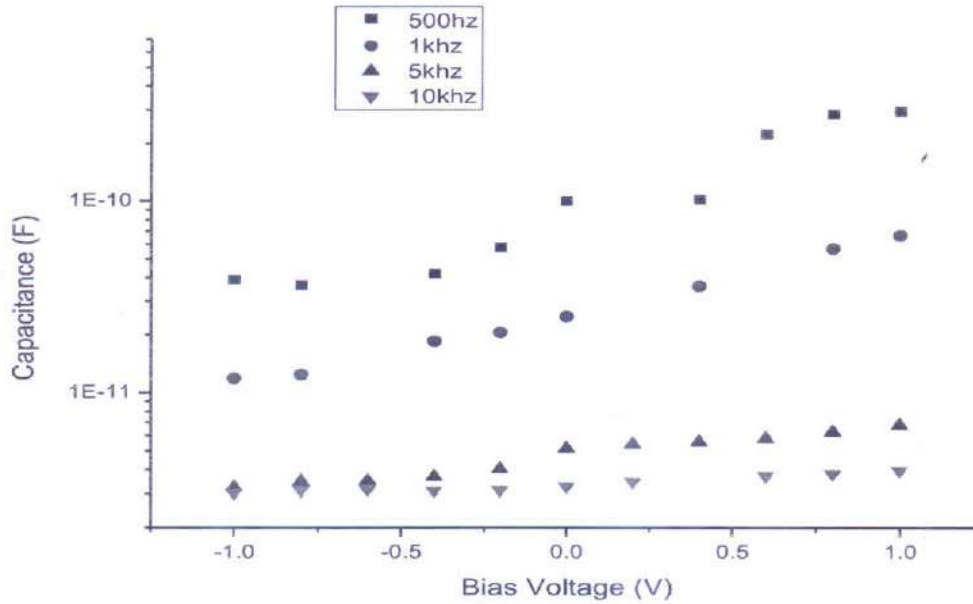


Figure 17: Capacitance vs. Voltage plot

The sample we have used for our measurements is quite old and hence the plot is not perfectly accurate at high modulation frequencies. However, it acts as a good approximation. We can see that on applying reverse bias across the sample, the capacitance value increases slowly with increased bias voltage. As applied dc bias becomes positive we see a rapid increase in the capacitance up to a certain limit. The reverse bias region is drift controlled and the forward bias region is diffusion controlled, up to the maximum value of the capacitance. The peak in C-V occurs due to the competition between the two competing processes of charge carrier transport- drift and diffusion. The position of the peak indicates the transition from diffusion controlled region to the drift controlled region. Active layer/Al junction is a Schottky junction, so it follows the Mott-Schottky relation:

$$\frac{1}{C^2} = \frac{2(V + V_{bi})}{A^2 e \epsilon N}$$

Where  $V$  is the applied bias voltage,  $V_{bi}$  (voltage across the depletion region under thermal equilibrium) represents built-in voltage of sample,  $A$  is the active area of the sample,  $N$  is the carrier concentration,  $e$  is the electronic charge,  $\epsilon$  is the permittivity of the active material.

## CONCLUSION

Thus, from our series of measurements done on different capacitors, varactor diode and a metal semiconductor hetero-junction, we have learnt that capacitance-voltage characteristics reveal crucial information about electronic components. Studying the C-V characteristics of varactor diode, we have gained knowledge about its working and where it can be used to get desired results. Similarly, a



lot of features of different capacitors and metal-semiconductor hetero-junction can be deduced by carefully studying the respective C-V characteristics. The LCR meter is thus an essential and useful device to carry out measurements using an ac test signal as a frequency sweep for a particular dc bias.

## REFERENCES

The following sources have been used as a reference in this reading project:

1. [https://www.hioki.com/en/products/detail/?product\\_key=5824](https://www.hioki.com/en/products/detail/?product_key=5824)HIOKI LCR meter manual, specifications and applications.
2. **Atri Sarkar, Abdulla Bin Rahaman and Debamalya Banerjee on Temperature dependent charge transport studies across thermodynamic glass transition in P3HT: PCBM bulk heterojunction: insight from J-V and impedance spectroscopy.**<https://iopscience.iop.org/journal/0022-3727>Journal of Physics D: Applied Physics, Volume51, Number9.

**RAMAKRISHNA MISSION RESIDENTIAL**  
**COLLEGE (AUTONOMOUS)**  
**NARENDRAPUR, KOLKATA - 700103**



**CALCULATION OF  $I_{ds}-V_{ds}$  CHARACTERISTICS OF ULTRA-THIN FDSOI**  
**MOSFET**

Supervised by : Dr. SOURAV CHATTOPADHYAY  
(Assistant Professor, Department of Physics, RKMRC Narendrapur)  
Project done by : SANTANU MANDAL  
Roll Number : PHUG/177/17  
B.Sc. 6th Semester



**Ramakrishna Mission Residential College (Autonomous)**

**Vivekananda Centre for Research**

**Ramakrishna Mission Ashrama**

(A Branch Centre of Ramakrishna Mission, Belur Math, Howrah-711202)

**Narendrapur, Kolkata - 700 103, West Bengal, India**

A Scientific Industrial Research Organisation, Recognised by DST, Govt. of India

College with Potential for Excellence (CPE), Re-accredited by NAAC - 'A' (CGPA 3.56 out of 4)

---

## **DEPARTMENT OF PHYSICS**

### **Certificate**

This is to certify that Santanu Mandal, a student of B.Sc has successfully completed the project of UG curriculum entitled "**Calculation of  $I_{ds} - V_{ds}$  characteristics of ultra-thin FDSOI Mosfet**" in the period from January to May, 2020.

*Malay Purkait*  
.....  
30.06.2020

**Signature Of HOD**

**Dept. of Physics**

**Dr. Malay Purkait**

Associate Prof. & Head

Department of Physics

Ramakrishna Mission Residential College  
(Autonomous)

Narendrapur, Kolkata-700 103 (W.B.)



## TO WHOM IT MAY CONCERN

This is to certify that SANTANU MANDAL (Roll Number : PHUG/177/17) of B.Sc. 6th Semester student is known to me for three years in the Department of Physics, Ramakrishna Mission Residential College (Autonomous), Narendrapur. He had done this project as a part of B.Sc. 6th Semester Course Curriculum. During the tenure of this project, he has made infrared sensor based burglar alarm and magnetic levitation circuit and studied it's performance.

*Sourav Chattopadhyay*

**Dr. SOURAV CHATTOPADHYAY**  
Assistant professor

Department of Physics Ramakrishna Mission Residential College (Autonomous)  
Narendrapur, Kolkata-103

## **ACKNOWLEDGEMENT**

I acknowledge with pleasure the support of Dr. Sourav Chattopadhyay, Assistant Professor of Department of Physics, Ramakrishna Mission Residential College Narendrapur. Under his supervision, I have completed my project report. I thank Dr. Malay Purkait, H.O.D. of Department of Physics of RKMRC Narendrapur, for supporting me at every step. This project has been very insightful and I consider myself lucky to being a part of it.

*Santanu Mandal*

Santanu Mandal

Roll : PHUG/177/17

## INTRODUCTION

Ultra-thin body and box (UTBB) fully depleted silicon-on-insulator (FD-SOI) MOSFETs are considered as one of the best candidates for control of short channel effects (SCEs) in future sub-28 nm CMOS generations, because they provide process simplicity compared to FinFETs, a threshold voltage control with back gate bias and lower variability phenomena due to random dopant fluctuations.

To exploit the benefits of UTBB FD-SOI MOSFETs with back bias control, an analytical, accurate and fast compact model that describes properly the transistor behavior for a wide range of back bias is required. In previously reported works on compact models of asymmetric independent double-gate MOSFETs, the models are based on numerical techniques, resulting in a poor speed of simulation. Recently, a computationally efficient model has been presented, providing accurate results when the back gate is biased in the reverse and low forward bias range. For the case where a strong forward back bias is applied, a surface potential compact model has been proposed, utilizing complicated equations while fundamental effects (such as velocity overshoot and self-heating) were not considered.

Recently, we developed simple analytical models for the threshold voltage and ideality factor of the front interface for asymmetrical UTBB FD-SOI MOSFETs. In this paper, we have improved our previous model and derive a complete analytical charge-based compact drain current model valid in all regions of operation with back gate control, including the drain-induced barrier lowering (DIBL), channel-length modulation (CLM), saturation velocity, mobility degradation, quantum confinement, velocity overshoot (VO) and self-heating (SH) effects.

## THRESHOLD VOLTAGE

From charge based model it is clear that at threshold voltage, the point with minimum voltage on the conduction channel have carrier density exactly equal to the doping concentration of substrate.

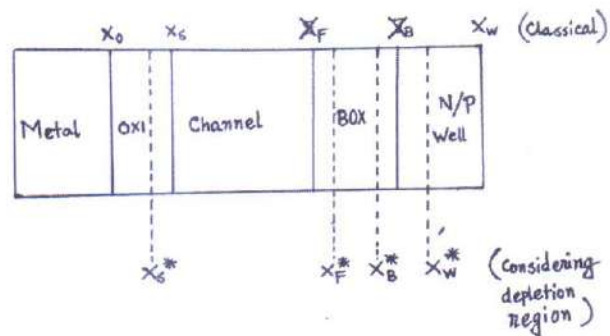
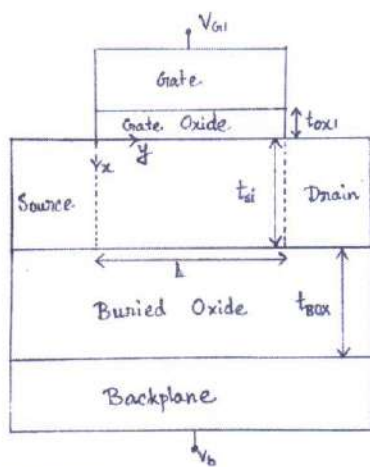
$$n_i e^{\frac{\phi_1(x_c, y_m) + \phi_2(x_c, y_m) V_{tf}}{V_{th}}} = N_a$$

$$V_{tf} = V_{fbf} + \frac{V_T}{\phi_2(x_c, y_m)} \ln \left( \frac{N_a}{n_i} e^{\frac{\phi_1(x_c, y_m)}{V_T}} \right)$$

where  $V_{fbf(b)}$  is the flat-band voltage of the front (back) gate. Which is zero for ideal situation.



## CARRIER CONCENTRATION



To find carrier concentration inside the channel we need to solve 1-D Schrodinger equation and Poisson's equation with proper boundary values.

$$\frac{\partial}{\partial x} \left( \epsilon \frac{\partial \phi(x)}{\partial x} \right) = -\rho(x)$$

Poisson's equation gives

$$\phi(x_0) = V_{G1} - \phi_{ms1} \quad ; \quad \phi(x_w) = V_{G2}$$

With boundary conditions

And 1-D time independent Schrodinger equation is given by

$$-\frac{\hbar^2}{2} \frac{\partial}{\partial x} \left( \frac{1}{m^*(x)} \frac{\partial \psi(x)}{\partial x} \right) + q \phi(x) \psi(x) = E \psi(x)$$

With boundary conditions  $\psi(x_s^*) = \psi(x_F^*) = 0$  ;  $\psi(x_B^*) = \psi(x_w^*) = 0$

Here we simply considered that  $(x_s^* < x < x_F^*)$  and  $(x_B^* < x < x_W^*)$  are two square wells and  $(x_F^* < x < x_B^*)$  a forbidden region in between these two.

$m^*(x)$  = effective mass of carriers inside channel

Now from F.D. statistics it can be calculated that

Electron density 
$$n(x) = \sum_v \frac{m_v}{\pi \hbar^2} g_v K_B T \ln \left( 1 + e^{\frac{E_F - E}{K_B T}} \right) |\psi(x)|^2$$

Similarly for holes 
$$p(x) = \sum_v \frac{m_h}{\pi \hbar^2} g_v K_B T \ln \left( 1 + e^{-\frac{(E_F - E)}{K_B T}} \right) |\psi(x)|^2$$

Total charge density 
$$\rho(x) = q (p(x) - n(x) + N_d - N_a)$$

$$Q_i = \int_{x_s^*}^{x_F^*} \rho(x) dx$$

Integrating above equation we get

$$Q_i(V_{ds}) = C_{oxi} \eta \frac{K_B T}{q} \ln \left( 1 + e^{\frac{V_{ds} - V_T}{\eta K_B T}} \right) \left[ 1 - \frac{\ln \left( 1 + \ln \left( 1 + e^{\frac{V_{ds} - V_T}{\eta K_B T}} \right) \right)}{2 + \ln \left( 1 + e^{\frac{V_{ds} - V_T}{\eta K_B T}} \right)} \right]$$

$$Q_i(V_{ds}) = C_{oxi} \eta \frac{K_B T}{q} LW \left( e^{\frac{V_{ds} - V_T}{\eta K_B T}} \right)$$

LW is Lambert W function.

## MOBILITY OF CARRIERS

From drift-diffusion model

$$I_{ds} = W \mu C_{oxi} V_T q_i \frac{dV_g}{dy}$$

Where  $\mu$  is mobility of carriers. Inside the channel mobility is modified due to various effects such as impurity scattering, rough surface scattering. Mobility decreases rapidly with decrease in temperature when temperature is below a certain cryogenic temperature, when coulomb impurity scattering dominates over phonon scattering. This is experimentally verified by split C-V measurements. Mobility also depends on gate voltage. Hence we apply an empirical formula for mobility

$$\mu = \mu_0 [1 + \theta(V_{GS} + V_T)] \quad \text{where} \quad V_T = \frac{k_B T}{q}$$

Including the carrier saturation velocity and the transversal field effects, the mobility can be approximated as follows

$$\mu = \frac{\mu_{eff}}{1 + \frac{\mu_{eff}}{v_{sat}} \left| \frac{d\phi_s}{dy} \right|} = \frac{\mu_{eff}}{1 + \frac{\mu_{eff} V_T}{v_{sat}} \frac{dq_s}{dy}}$$

Taking into account the entire channel charge distribution instead of the charge sheet approximation, which is not accurate in the moderate inversion region, we can derive the expression for the drain current at any point  $y$  in the channel, based on drift-diffusion transport equation given above

$$I_{ds} = \frac{W \mu_{eff} C_{ox1} V_T^2 \eta}{L + \frac{\mu_{eff} V_T}{v_{sat}} (q_s - q_d)} \left[ \text{poly} \log \left( 2 \left( 1 - e^{\frac{q_s}{\eta}} \right) \right) - \frac{\pi^2}{6} \right]$$

## DRAIN CURRENT CALCULATION

Integration from the source to the drain results in the following drain current equation in terms of the

$$q_i = \frac{q_i}{C_{ox1} V_T}$$

normalized charges at the source ( $q_s$ ) and drain ( $q_d$ ) electrodes.

terms of  $q_s$  and  $q_d$ , in above expression of  $I_{ds}$  the dilogarithm function can be replaced by an equivalent 2<sup>nd</sup> order polynomial expression for compact modeling purpose, obtaining

$$I_{ds} = \frac{W \mu_{eff} C_{ox1} V_T^2}{L_{eff} + \frac{\mu_{eff} V_T}{v_{sat}} (q_s - q_d)} \left[ (q_s - q_d) + \frac{1}{2\eta} (q_s^2 - q_d^2) \right]$$



which constitutes the basic structure of compact drain current models like BSIM. The  $\mu_{eff}$  degradation due to the vertical gate field is expressed in terms of  $q_s$  as

$$\mu_{eff} = \frac{\mu_0}{1 + \theta_1 \frac{q_s}{C_{ox1}} + \theta_2 \left( \frac{q_s}{C_{ox1}} \right)^2}$$

where  $\mu_0$ ,  $\theta_1$  and  $\theta_2$  can be extracted from experimental data at low drain voltage using a modified Y-function method. The parameter  $\theta_2$  is correlated to the surface roughness scattering, while  $\theta_1$  includes phonon scattering and Coulomb scattering. Taking into account the effect of  $R_{sd}$ ,  $\theta_1$  becomes:

$$\theta_1 = \theta_{1,0} + W\mu_0 R_{sd} C_{oxf} / L,$$

In saturation region, based on the channel length shortening  $\Delta L$  due to the CLM effect can be modelled as:

$$\Delta L = \lambda_f \ln \left( 1 + \frac{(V_{ds} - V_{dsat} + 0.05) \tanh(V_{ds} / V_{dsat})^3}{V_E} \right)$$

It should be noted that above equation will lead to an implicit expression for  $V_{dsat}$ . Considering that the second charge term in the brackets of the equation is dominant in the above-threshold region, an explicit expression for  $V_{dsat}$  can be obtained from the relation  $dI_{ds}/dV_{ds} = 0$  yielding

$$V_{dsat} = \sqrt{\left( \frac{V_{sat} L}{\mu_{eff}} \right)^2 + \frac{2q_s V_{th} V_{sat} L}{\mu_{eff}}} - \frac{V_{sat} L}{\mu_{eff}} + \frac{q_s V_{th}}{\eta_f} - q_s V_{th}$$

As  $V_{th}$  is determined at the onset of inversion [9], we found that for a smooth transition from weak to strong inversion, the normalized charge of weak inversion  $q_i = Q_i / C_{oxf} V_{th}$  should be obtained with increasing  $V_{th}$  by  $2.5 * V_{th}$  and the charge terms of strong inversion with increasing  $V_{th}$  by  $5 * V_{th}$ .

In order to further improve the accuracy of the model, we include some other important effects, namely the quantum-mechanical (QMEs), VO and the SH effects. As  $t_{si}$  is scaled down below 10 nm, the splitting of the energy bands has to be considered in the model. Due to this splitting, the lowest energy band rises and the carriers need more energy to occupy it, resulting in an increase of the threshold voltage. Thus, the shift in  $V_{th}$  due to quantum confinement is included in the model considering the work function difference as

$\Delta\phi = \phi_m - \phi_{snew}$ , where  $\phi_{snew}$  the new work function after decreasing  $\phi_s$  by the minimum energy of the lowest conduction sub-band. The shift in  $V_{th}$  due to the quantum confinement according to  $I_{ds}$  equation is, where  $t_{si}$  is expressed in nm. Thus, for  $t_{si} = 7$  nm, the contribution of quantum confinement in  $\Delta\phi$  is about 0.129V.

$$\Delta V_{th} = 0.085 + 2.178 / t_{si}^2$$

Positive  $V_{gb}$  moves the mean channel position deeper away from the front gate interface into the silicon film. This effect is also taken into account by modifying  $\eta_f$  prior to the drain current calculation. The following back gate bias dependent equivalent thicknesses for the front gate oxide and silicon body are applied to  $\eta_f$  in  $I_{ds}$  equation to refine

$$t_{oxf,eq} = t_{oxf} + \frac{\epsilon_{ox}}{\epsilon_{Si}} X_c \quad t_{Si,eq} = t_{Si} - \frac{\epsilon_{ox}}{\epsilon_{Si}} X_c$$

the drain current calculation

In short-channel transistors, in contrast to the classical drift-diffusion models,  $v_{sat}$  in the saturation region can achieve higher values due to non-stationary effects. This phenomenon is known as velocity overshoot (VO), whose contribution is introduced in a simple way

$$v_{sat,vo} = v_{sat} \left( 1 + \frac{2\lambda_w}{L} \right),$$

Due to the thin  $t_{si}$ , the SH effect is expected to be significant in short UTBB FD-SOI devices. Experimental evidence for the presence and importance of SH effects in the investigated FD-SOI transistors has been presented in recent works. Because removal of heat from the channel to the substrate is quick, the temperature rise can be assumed to be uniform throughout the channel given by

$$T - T_o = R_{th} V_{ds} I_{ds}, \quad \text{where} \quad R_{th} = \frac{1}{2W} \sqrt{\frac{t_{ox,h}}{K_{ox} K_{si} t_{si}}}.$$

Once  $T$  is obtained,  $v_{sat}$ ,  $V_{th}$  and  $\mu_{eff}$  have to be recalculated to obtain the drain current at that temperature. For typical temperature rise, the saturation velocity indicates a weak temperature dependence, thus it can be considered constant in our model. Furthermore, it has been demonstrated that in lightly doped UTBB SOI MOSFETs the effect of temperature on the threshold voltage is negligible.

In addition to the mobility reduction due to the vertical gate oxide field as described by the expression of  $\mu_{eff}$ , the carrier mobility decreases with temperature due to increase in phonon scattering. For modeling the SH effect, the effective mobility  $\mu_{eff,sh}$  at  $T$  is approximated in terms of the effective mobility  $\mu_{eff}$  at  $T_o$  as

$$\mu_{eff,sh} \approx \frac{\mu_{eff}}{1 + \frac{r R_{th} V_{ds} I_{ds}}{T_o}}.$$

In the equation of  $I_{ds}$ , substitute  $\mu_{eff}$  with  $\mu_{eff,sh}$  to get a quadratic equation of  $I_{ds}$  solving which we get

$$I_{ds} = \frac{-A_2 + \sqrt{A_2^2 + 4A_1A_0}}{2A_1},$$

$$\text{where } A_0 = \frac{W}{L_{eff}} \mu_{eff} C_{oxf} V_{th}^2 \left[ (q_s - q_d) + \frac{q_s^2 - q_d^2}{2\eta_f} \right],$$

$$A_1 = \frac{r R_{th} V_{ds}}{T_o}, \quad (19b) \quad A_2 = 1 + \frac{V_{th} \mu_{eff}}{v_{sat,vo} L_{eff}} (q_s - q_d)$$

## REFERENCES

1. Characterization and Modeling of 28-nm FDSOI CMOS Technology down to Cryogenic Temperatures

Arnout Beckers, Farzan Jazaeri, Heorhii Bohuslavskyi, Louis Hutin, Silvano De Franceschi, Christian Enz

2. Electrical characterization and modelling of advanced FD-SOI transistors for sub-22nm nodes

Minju Shin

3. Caractérisation et modélisation de UTBB MOSFET sur SOI pour les technologies CMOS avancées et applications en simulations circuits

Thèse soutenue publiquement le 12 Juillet 2017

4. WIKIPEDIA

## ACKNOWLEDGEMENT

I acknowledge with pleasure the support of Dr. Sourav Chattopadhyay, Assistant Professor of Department of Physics, Ramakrishna Mission Residential College Narendrapur. Under his supervision, I have completed my project report. I thank Dr. Malay Purkait, H.O.D. of Department of Physics of RKMRC Narendrapur, for supporting me at every step. This project has been very insightful and I consider myself lucky to being a part of it.



**RAMAKRISHNA MISSION RESIDENTIAL**  
**COLLEGE (AUTONOMOUS)**  
NARENDRAPUR, KOLKATA-700103



**TOPIC: Theory and Analysis of Nanowire Radial p-n**  
**Junction**

Project done by : SAYAK DATTA

Class : B.Sc. 3rd Year (6<sup>th</sup> Semester)

Roll Number : PHUG/015/17

Registration No. : A03-1112-0015-17

Supervised by : Dr. Sourav Chattopadhyay  
(Assistant Professor, Department of Physics, RKMRC Narendrapur)



**Ramakrishna Mission Residential College (Autonomous)**

**Vivekananda Centre for Research**

**Ramakrishna Mission Ashrama**

(A Branch Centre of Ramakrishna Mission, Belur Math, Howrah-711202)

**Narendrapur, Kolkata - 700 103, West Bengal, India**

A Scientific Industrial Research Organisation, Recognised by DST, Govt. of India

College with Potential for Excellence (CPE), Re-accredited by NAAC - 'A' (CGPA 3.56 out of 4)

---

## **DEPARTMENT OF PHYSICS**

### **Certificate**

**This is to certify that Sayak Datta, a student of B. Sc has successfully completed the project of UG curriculum entitled "Theory and Analysis of Nanowire Radial p-n Junction " in the period from January to May, 2020.**

*Malay Purkait*

.....  
30.06.2020.

**Signature Of HOD**

**Dept. of Physics**

**Dr. Malay Purkait**

**Associate Prof. & Head**

**Department of Physics**

**Ramakrishna Mission Residential College**

**(Autonomous)**

**Narendrapur, Kolkata-700 103, (W.B.)**

## To Whom It May Concern

This is to certify that Mr. Sayak Datta (Roll Number : PHUG/015/17) of B.Sc. 6<sup>th</sup> Semester student is known to me for three years in the Department of Physics, Ramakrishna Mission Residential College (Autonomous), Narendrapur. He had done this project as a part of B.Sc. 6<sup>th</sup> Semester Course Curriculum. This is a reading project on the theory and analysis of nanowire radial p-n junction. He had studied this topic sincerely and put in hard work to complete this project.

*Sourav Chattopadhyay*  
20/6/20  
Dr. Sourav Chattopadhyay

Assistant Professor  
Department of Physics  
Ramakrishna Mission Residential College (Autonomous)  
Narendrapur, Kolkata-103



## Acknowledgement

I acknowledge with pleasure the support of Dr. Sourav Chattopadhyay, Assistant Professor of Department of Physics, Ramakrishna Mission Residential College, Narendrapur. Under his supervision and guidance, I have completed my project report. I thank Dr. Malay Purkait, H.O.D. of Department of Physics of RKMRC Narendrapur, for supporting me at every step. I would also like to thank the Physics Department of our college for giving me the opportunity of doing this project. I am really grateful to my parents for their constant support and precise suggestions in completing this project.

This project has been very insightful and I consider myself lucky to be a part of it. Lastly I would like to conclude by saying that this project would not have been completed unless the above honourable people have helped me.

Thank you.

– Sayak Datta

*Sayak Datta*

# **THEORY AND ANALYSIS OF NANOWIRE RADIAL P-N JUNCTION**

## **Abstract**

We have developed a theoretical model for the radial p-n junction in a nanowire (NW) core/shell structure as a new building block for different semiconductor devices. We have calculated the potential distribution across the junction, the depletion layer widths and the capacitance of the radial p-n junction. We have then plotted the current-voltage characteristics from where we studied the behaviour of the proposed model of the radial p-n junction. We have also found the relationship between the depletion width and built-in potential for different core radius of the p-n junction.

## Contents

|                                                                   |      |
|-------------------------------------------------------------------|------|
| 1. Introduction .....                                             | 1-3  |
| i. What is p-n junction? .....                                    | 1    |
| ii. Comparison between planar and radial p-n junction.....        | 1    |
| iii. Characteristics of radial p-n junction.....                  | 2    |
| 2. Methodology .....                                              | 3-6  |
| i. Calculation of potential distribution and depletion width..... | 3    |
| ii. Calculation of junction capacitance.....                      | 6    |
| 3. Results.....                                                   | 6-10 |
| 4. Discussion and Conclusion.....                                 | 11   |
| 5. References.....                                                | 12   |



## **1. INTRODUCTION**

### **i. What is a p-n junction?**

A p-n junction is a boundary or interface between two types of semiconductor materials, p-type and n-type inside a single crystal of semiconductor. When one side of a single-crystal semiconductor is doped with acceptors and the other side is doped with donors, a p-n junction is produced. The p-side contains an excess number of holes and the n-side contains an excess number of electrons. It is thus a two-terminal device and is referred to as a junction diode.

### **ii. Comparison between planar and radial p-n junction:**

A planar p-n junction has so far been used in many electronic devices and has been greatly successful till date. A planar p-n junction has been used for photovoltaic applications such as solar cells, etc. But in some cases a planar p-n junction has been found to be inefficient and there has been a constant need for some new type of geometry for better results. For example, planar solar cell geometries lose efficiency due to current and voltage losses when minority carrier diffusion length decreases. This has led to the idea of giving a new geometry to the conventional solar cells which will prove to be more efficient than the already existing planar structure. Here comes the boon of nanotechnology.

The semiconductor nanowires have the potential to impact many different technologies either through the improved material parameters or by offering a new geometry not possible with bulk or thin film structures. Modern advances in nanotechnology allow to incorporate several material layers with the same or different type of conductivity into a single nanowire (nanorod). Coaxial core/shell nanowire (NW) structures with built-in radial p-n-junctions have been developed recently. This new type of structures represents an important class of nanoscale building blocks with potential for exploring new device concepts, e.g., for photovoltaic applications, field-effect transistors and different semiconductor devices.

The array of NWs in which each wire has a p-n-junction in the radial direction provides an interesting application in the third generation solar cells technology. The advantage of such solar cells is that the directions of light absorption and

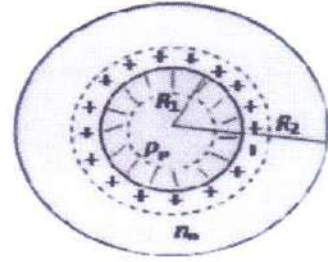
carrier collection can be orthogonal, which allows to provide efficient carrier separation in the radial direction for the optically thick NW arrays, even when the minority carrier diffusion lengths are shorter than the optical absorption length unlike conventional planar solar cells.

Therefore it is an important issue to develop a theoretical model of the nanowire radial p-n junction and a good understanding of the device performance will guide designer to choose the best components for optimization. The model for the nanowire radial p-n junction will be constructed by extending the results obtained from the conventional planar p-n junction geometry.

### iii. Characteristics of Radial p-n junction:

The analytical model of NW p-n coaxial homo-junction consists of a p-type inner “core” with acceptor concentration  $N_A$  and radius  $R_1$ , capped by n-type outer “shell” with donor concentration  $N_D$  and thickness  $(R_2 - R_1)$ . The visualized structure of the radial p-n junction is given alongside.

To neglect the quantum size effects, relatively thick NWs with a diameter of several 100 nm are considered. The radial p-n junction is divided into 4 regions: the quasi-neutral part of the p-core ( $r \leq R_1 - w_p$ ), the depletion part of the p-core (of width  $w_p$ ), the depletion part of the



n-shell (of width  $w_n$ ) and the quasi-neutral part of the n-shell ( $r \leq R_2 - R_1 - w_n$ ).

If the temperature is sufficiently high and all impurities are ionized, the majority charge carriers in the core and shell quasi-neutral regions are:

$p_p = N_A$  for  $r \leq R_1 - w_p$  and  $n_n = N_D$  for  $R_1 + w_n \leq r \leq R_2$ .

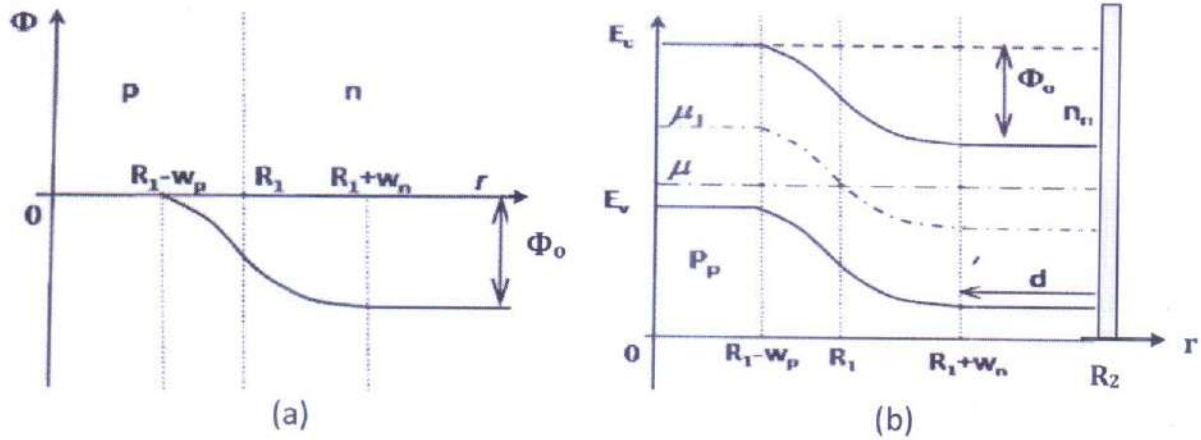
When p-n junction is formed along core/shell interface, a fraction of the electrons pass from the n region into the p region, while the holes, on the contrary, pass from the p region into the n region. The space-charge layers are created on both sides of the core/shell interface and potential energy barrier is established. The electric field arises across the junction and the energy bands bent until the establishment of equilibrium state and the alignment of Fermi energy levels. The built-in potential energy barrier that forms along the p-n junction can be

expressed as: 
$$\phi_0 = kT \ln \frac{n_n p_p}{n_i^2}, \quad \text{-----} \quad (1)$$

where  $kT$  is the thermal energy,  $n_i$  is the intrinsic carrier concentration of the semiconductor. This potential barrier opposes the electron diffusion from the n-type shell to the core and also hole diffusion from the core to the shell such that the



total electron current and the total hole current are both zero at thermal equilibrium. The value of the potential barrier is equal to the height defined by the work function difference of the core and shell which can be represented by the following profile of potential energy and energy band diagram given below:



## 2. METHODOLOGY

### i. Calculation of Potential Distribution and Depletion Region Width:

In order to develop the analytic model for the radial p-n junction, we need to further investigate the characteristics of p-n junction by calculating the potential distribution across the junction and the depletion region width by deriving suitable expressions which can be analyzed as functions of material properties and radius of nanowire (NW).

We know, near the junction or the depletion region, the concentration of mobile charge sharply decreases and the space charge is mainly formed by ionized donors and acceptors. In the depletion region the space charge density can be given as:

$$\rho = \begin{cases} -e \cdot N_A = -e \cdot p_p, & R_1 - w_p \leq r \leq R_1 \\ e \cdot N_D = e \cdot n_n, & R_1 \leq r \leq R_1 + w_n \end{cases} \quad (2)$$

where 'e' is the electron concentration.

We then solve the Poisson equation for the radial p-n junction in cylindrical coordinates to determine the potential distribution across the junction such as follows:

$$\nabla^2 \phi = \frac{e\rho}{\epsilon\epsilon_0} \quad (3)$$

In cylindrical coordinates L.H.S can be written as:

$$\nabla^2 \phi = \frac{1}{r} \frac{\partial}{\partial r} \left( r \frac{\partial \phi}{\partial r} \right) + \frac{1}{r^2} \frac{\partial^2 \phi}{\partial \theta^2} + \frac{\partial^2 \phi}{\partial z^2} \quad (4)$$



Since  $\phi$  is only dependent upon  $r$ , then the required Poisson equation can be written as:

$$\frac{1}{r} \frac{d}{dr} \left( r \frac{d\phi}{dr} \right) = \begin{cases} -\frac{e^2 p_p}{\epsilon \epsilon_0}, & R_1 - w_p \leq r \leq R_1 \\ \frac{e^2 n_n}{\epsilon \epsilon_0}, & R_1 \leq r \leq R_1 + w_n \end{cases} \quad \text{----- (5)}$$

where  $\phi$  is the potential energy of electrons,  $\epsilon$  is the relative permittivity of the semiconductor and  $\epsilon_0$  is the electric constant. The potential reference is chosen at the border of depletion region in the p-type core. Thus the boundary conditions at  $r = R_1 - w_p$  and  $r = R_1 + w_n$  present the variation of potential energy across the junction and the requirement that the radial component of the electric field should be zero outside the space charge/depletion region:

$$\phi(R_1 - w_p) = 0, \quad \left. \frac{d\phi}{dr} \right|_{r=R_1 - w_p} = 0 \quad \text{----- (6)}$$

$$\phi(R_1 + w_n) = -\phi_0, \quad \left. \frac{d\phi}{dr} \right|_{r=R_1 + w_n} = 0 \quad \text{----- (7)}$$

Then the potential can be found out by solving equations (5) – (7) which is as follows:

$$\phi(r) = -\frac{e^2 p_p}{4\epsilon \epsilon_0} \left[ r^2 - (R_1 - w_p)^2 - 2(R_1 - w_p)^2 \ln \frac{r}{R_1 - w_p} \right], \text{ for } R_1 - w_p \leq r \leq R_1$$

$$\text{and } \phi(r) = -\phi_0 + \frac{e^2 n_n}{4\epsilon \epsilon_0} \left[ r^2 - (R_1 + w_n)^2 - 2(R_1 + w_n)^2 \ln \frac{r}{R_1 + w_n} \right],$$

----- (8)

for  $R_1 \leq r \leq R_1 + w_n$ .

The electric field continuity at  $r = R_1$  gives  $n_n (R_1^2 - (R_1 + w_n)^2) = p_p ((R_1 - w_p)^2 - R_1^2)$ , ignoring the charge on the core/shell interface. Then using the above eqn. (8) and demanding the continuity of the potential at the homo-junction interface  $r = R_1$ , we get the following equation for  $w_p$ ,

$$\left( \frac{n_n + p_p}{p_p} - \left( 1 - \frac{w_p}{R_1} \right)^2 \right) \cdot \ln \left( \frac{n_n + p_p}{n_n} - \frac{p_p}{n_n} \left( 1 - \frac{w_p}{R_1} \right)^2 \right) + \left( 1 - \frac{w_p}{R_1} \right)^2 \ln \left( 1 - \frac{w_p}{R_1} \right)^2 =$$

$$\frac{4\epsilon \epsilon_0}{e^2 p_p R_1^2} \phi_0 \quad \text{----- (9)}$$

Now for the given  $n_n$ ,  $p_p$ ,  $\phi_0$  and  $R_1$  the depletion layer widths in the core ( $w_p$ ) and in the shell ( $w_n$ ) can be calculated from the above equations. It has been observed from the above equations that the width of space charge layer in the radial p-n junction is a function of the core radius ( $R_1$ ), which is the manifestation of the classical size effect. Thus for NWs with the same doping level but different radius the depletion layer has different width.

For sufficiently large NW radius (i.e.,  $R_1 \gg w_p$ ), the relationship between depletion width and potential energy  $\phi_0$  can be given by the conventional square root law as follows:  $\sqrt{\frac{2\epsilon\epsilon_0 n_n \phi_0}{e^2 p_p p_p + n_n}}$ . Then from the electric field continuity the

ratio  $w_p/w_n$  can be given as:  $\frac{w_p}{w_n} = \frac{n_n}{p_p} \frac{2 + \frac{w_n}{R_1}}{2 - \frac{w_n}{R_1}}$ , ----- (10)

which depends not only on the doping concentration but also on NW radius.

It can be seen from equation (10) that at equal core and shell doping levels ( $n = p$ ) the depletion width in the core is always larger than in the shell. This is the unique feature of radial p-n junctions unlike planar geometry where the junction is symmetric ( $w_p = w_n$ ) at equal donor and acceptor concentrations. Now to find the depletion widths  $w_p$  and  $w_n$  under the external bias ( $V$ ), we have to replace the built-in energy barrier  $\phi_0$  with  $(\phi_0 - eV)$  in the R.H.S of equation (9). By substituting  $w_p = R_1$  in the same equation we get,

$$\frac{e|V_C|}{\phi_0} = \frac{e^2(n_n + p_p)R_1^2}{4\epsilon\epsilon_0\phi_0} \ln \frac{n_n + p_p}{n_n} - 1 \quad \text{----- (11)}$$

However, even in the absence of external bias for a given core radius  $R_1$  there is a certain ratio of doping concentrations  $n_n$  and  $p_p$  and, hence a certain built-in potential barrier  $\phi_{0c}$  at which the NW core is totally covered by the space charge. From equation (9) we get,

$$\phi_{0c} = \frac{e^2(n_n + p_p)R_1^2}{4\epsilon\epsilon_0} \ln \frac{n_n + p_p}{n_n} \quad \text{----- (12)}$$

For sufficiently long NW, the junction electric field has only radial component and its distribution across the space charge region is different from the conventional p-n junction. It can be found out by differentiating eqn. (8) with respect to  $r$



(i.e.,  $\varepsilon(r) = -\frac{d\phi(r)}{dr}$ ) which may be expressed by the sum of linear and hyperbolic terms such as follows:

$$\varepsilon(r) = \begin{cases} \frac{ep_p}{2\epsilon\epsilon_0} \left( r - \frac{(R_1 - w_p)^2}{r} \right), & R_1 - w_p \leq r \leq R_1 \\ \frac{en_n}{2\epsilon\epsilon_0} \left( \frac{(R_1 + w_n)^2}{r} - r \right), & R_1 \leq r \leq R_1 + w_n \end{cases} \quad (13)$$

The maximum value of this electric field falls at the core/shell interface ( $r = R_1$ ) and is given as,

$$\varepsilon_m = \frac{en_n w_n}{2\epsilon\epsilon_0} \left( 1 + \frac{w_n}{2R_1} \right) = \frac{ep_p w_p}{2\epsilon\epsilon_0} \left( 1 - \frac{w_p}{2R_1} \right) \quad (14)$$

Thus the maximum value of the electric field depends not only on the doping concentration and applied voltage but also on the NW radius.

## ii. Capacitance of Radial p-n Junction:

The p-n- junction barrier capacitance dominates when the applied voltage is reverse-biased or the forward bias is much smaller than the built-in potential. For the given applied voltage the total charge in the depletion region is easy to calculate if  $w_p$  and  $w_n$  are defined from eqn. (9) and (10).

The depletion charge in p-region is defined by the following relationship:

$$Q = ep_p \pi R_1^2 L \left( 1 - \left( 1 - w_p/R_1 \right)^2 \right) \quad (15)$$

Thus for the junction capacitance we get,

$$\begin{aligned} C = \left| \frac{dQ}{dV} \right| &= 2ep_p \pi R_1 L \left( 1 - w_p/R_1 \right) \frac{dw_p}{dV} \\ &= 4\epsilon\epsilon_0 \pi L \cdot \ln \left[ \left( 1 + \frac{n_n w_p}{p_p R_1} \left( 2 - \frac{w_p}{R_1} \right) \right) / \left( 1 - \frac{w_p}{R_1} \right)^2 \right]^{-1} \end{aligned} \quad (16)$$

It is seen from eqn. (16) that the capacitance of nanowire radial p-n junction per unit length is determined by the fundamental constant  $\epsilon_0 (F/m)$ . Thus for NW with length  $L = 10 \mu m$ , the junction capacitance is of the order of  $0.1 fF$ .

## 3. RESULTS

We have been able to calculate the potential distribution across the junction and the depletion region widths of the radial p-n junction and also the corresponding electric field which are the prerequisites for analyzing the performance of the developed theoretical model. Now we have to see whether the aforesaid parameters



give the desired results. Thus we need to study the current-voltage characteristics of the radial p-n junction.

We assume that the core doping level is much higher than that of the shell (i.e.,  $p_p \gg n_n$ ). Since most NWs have the diameter of the order of 100 nm, the thickness of quasi-neutral region in the shell ( $d = R_2 - (R_1 + w_n)$ ) is much smaller than the minority carriers diffusion length  $L_p$ . Thus the NW radial p-n junction, will operate in the short-base diode conditions of the conventional planar diode. In such junctions minority carriers injected from the core to the shell will reach the metallic contact on the external surface of the shell without significant recombination within the volume. We have to consider the standard current transport model where there is an ideal metallic contact, wrapping the shell, such that the built-in potential barrier formed at the metal and shell contact, in both accumulation and depletion modes is not higher than several  $kT$ . These conditions can be written as:

$$p(R_2) - p_n = \Delta p(R_2) = 0, \quad n(R_2) = n_n \quad \text{-----} \quad (17)$$

where  $p(R_2)$  and  $n(R_2)$  are, respectively, the concentrations of holes and electrons at the surface of the shell,  $p_n$  is the minority carrier concentration in the volume of the n-shell. This means that the holes injected from the p-n-junction does not accumulate at the semiconductor-metal interface and freely pass to the metal, recombining there with electrons. Therefore the hole recombination process in n-region can be ignored. So the net electron and hole currents remain constant throughout the n-region:

$$I_p = 2\pi r L_e D_p \left( \frac{e}{kT} E(r) \cdot p(r) - \frac{dp(r)}{dr} \right) = \text{const} \quad \text{-----} \quad (18)$$

$$I_n = 2\pi r L_e D_n \left( \frac{e}{kT} E(r) \cdot n(r) + \frac{dn(r)}{dr} \right) = \text{const} \quad \text{-----} \quad (19)$$

where  $D_p$  and  $D_n$  are the diffusion constants of holes and electrons respectively,  $E(r)$  is the radial component of electric field.

Since the carrier recombination does not take place in the shell, the current density passing through the metal-semiconductor contact is  $\frac{R_2}{R_1}$  times less than the one crossing the core/shell interface. But for the same value of applied voltage and comparatively smaller built-in potential barrier, the current density is much higher than that through the p-n junction. In order to compensate this, the main voltage drop occurs along the radial p-n junction given by:

$$\Delta p(R_1 + w_n) = p_n \left( e^{\frac{eV_1}{kT}} - 1 \right) \quad \text{-----} \quad (20)$$

The minority carriers injected into the n-shell will induce the redistribution of majority carriers, so that they will quickly compensate the charge of minority carriers resulting in an increase of electron concentration as follows:  $\Delta n(r) - n_n = p(r) - p_n = \Delta p(r)$ . Now depending on injection level the concentration of non-equilibrium charge carriers at the depletion layer edge in the n-region can be compared to  $n_n$  or even higher, i.e.,  $\Delta n(R_1 + w_n) = n_n + \Delta p(R_1 + w_n)$ . Therefore the concentration of injected electrons at the end of depletion region in the p-core should be:

$$\Delta n(R_1 - w_p) = n_p \left[ \left( 1 + \frac{\Delta p(R_1 + w_n)}{n_n} \right) e^{\frac{eV_1}{kT}} - 1 \right] \quad \text{-----} (21)$$

Since  $p_p \gg n_n$ , as already stated, the electron current ( $I_n$ ) through the p-n junction is very small compared with the hole current ( $I_p$ ). As the bulk recombination is assumed to be very small, we can consider  $I_n \approx 0$ , then it is easy to find the radial component of electric field in the n-region. Then putting  $I_n = 0$  in

eqn. (19) we get: 
$$E(r) \approx -\frac{kT}{e} \frac{1}{n} \frac{dn}{dr} \quad \text{-----} (22)$$

By substituting eqn. (22) into eqn. (18) and by taking into account the quasi-neutrality of n-region we can express the net hole current as:

$$I_p = -2\pi r L e D_p \left( 2 - \frac{n_n}{n_n + \Delta p(r)} \right) \frac{dp(r)}{dr} \quad \text{-----} (23)$$

Then multiplying equation (23) by  $r^{-1}$  and by integrating it between  $(R_1 + w_n)$  and  $R_2$  for  $I_p = \text{const}$  we get,

$$I_p = \frac{2\pi e D_p p_n L}{\ln(R_2/R_1 + w_n)} \left\{ 2 \left( e^{\frac{eV_1}{kT}} - 1 \right) - \frac{n_n}{p_n} \ln \left[ 1 + \frac{p_n}{n_n} \left( e^{\frac{eV_1}{kT}} - 1 \right) \right] \right\} \quad \text{-----} (24)$$

Using the boundary condition (17) and  $\Delta n(R_1 + w_n) = n_n + \Delta p(R_1 + w_n)$ , we can find the potential drop in quasi-neutral part of the shell as:

$$V_2 = \int_{R_1 + w_n}^{R_1 + w_n + d} E dr = \frac{kT}{e} \ln \left[ 1 + \frac{p_n}{n_n} \left( e^{\frac{eV_1}{kT}} - 1 \right) \right] \quad \text{-----} (25)$$

We know the applied voltage  $V = V_1 + V_2$ . In case of small applied voltages corresponding to the weak injection of holes into the shell (i.e.,  $\Delta p(R_1 + w_n) \ll n_n$ ). So the voltage drop in the shell is very small (i.e.,  $eV_2 \ll kT$  and  $V_1 \approx V$ ), then the junction current can be written as:

$$I_p = \frac{2\pi e D_p p_n L}{\ln(R_2/R_1 + w_n)} \left( e^{\frac{eV}{kT}} - 1 \right) \quad \text{-----} (26)$$



Thus the concentration of non-equilibrium charge carriers decreases in n-region very slowly, logarithmically and not linearly as in conventional planar p-n junction,

$$\Delta p(r) = \Delta p(R_1 + w_n) \frac{\ln R_2/r}{\ln R_2/R_1 + w_n} \quad \text{-----} (27)$$

The depletion width  $w_n$  increases at high reverse biases and therefore the width of quasi-neutral part of the shell decreases, then due to the increase of the hole concentration gradient the junction current, according to eqn. (26), continues to slowly increase instead of becoming saturated, which is a specific feature of devices with planar geometry and thick base.

But if the situation is opposite when high forward bias is applied and the minority carrier injection is enhanced such that  $p(R_1 + w_n) \gg n_n$ , or  $eV_1 \gg kT \ln \frac{n_n}{n_i}$ .

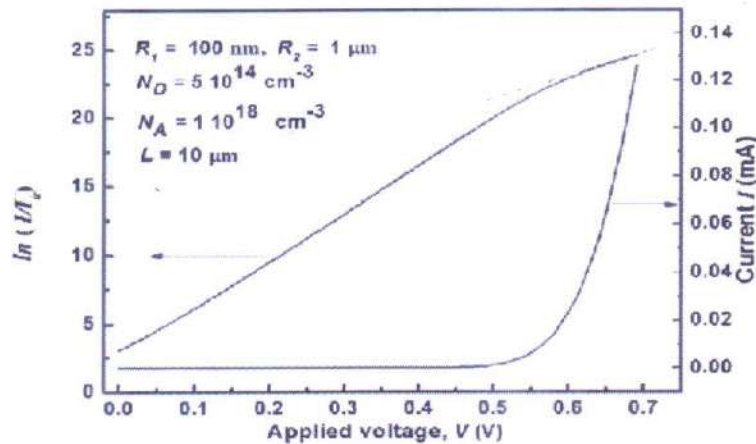
Then from eqn. (25) it follows that the voltage drops on the shell volume and on the junction are:

$$\begin{cases} V_2 = V_1 - \frac{kT}{e} \ln \frac{n_n}{p_n} = \frac{V}{2} - \frac{kT}{2e} \ln \frac{n_n}{p_n} = \frac{V}{2} - \frac{kT}{e} \ln \frac{n_n}{n_i} \\ V_1 = \frac{V}{2} - \frac{kT}{2e} \ln \frac{n_n}{p_n} = \frac{V}{2} + \frac{kT}{e} \ln \frac{n_n}{n_i} \end{cases} \quad \text{-----} (28)$$

Substituting  $V_1$  into eqn. (24), the junction current can be written as:

$$I_p \approx \frac{2\pi e D_p n_i L}{\ln(R_2/R_1 + w_n)} \exp\left(\frac{eV}{2kT}\right) \quad \text{-----} (29)$$

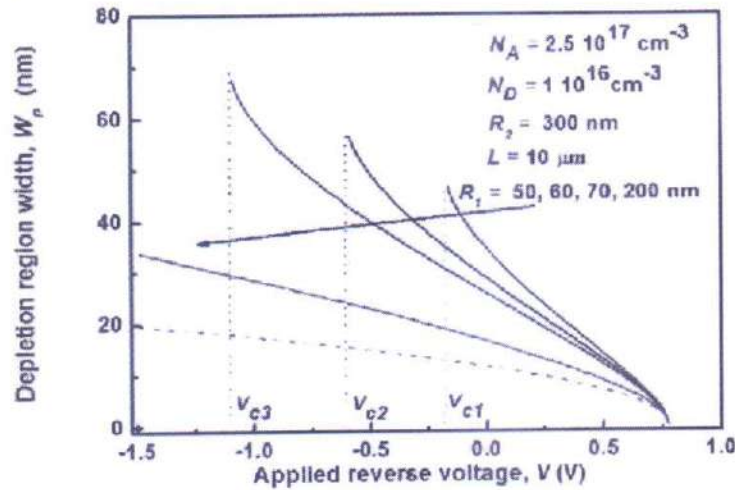
Thus if an applied voltage is in the range  $\frac{2kT}{e} \ln \frac{n_n}{n_i} < V < \frac{2kT}{e} \ln \frac{p_n}{n_i}$ , the main part of the voltage drop occurs on the quasi-neutral region of n-shell and the junction current starts to increase less sharply, proportional to  $\exp\left(\frac{eV}{kT}\right)$  which can be illustrated by the following current – voltage characteristics obtained by solving eqn. (24) and (25):





It can be seen that the slope of  $\ln(I/I_0)$ , where  $I_0 = 2\pi e D_p p_n L$ , decreases almost two times with an increase of applied voltage, which means that the forward current of the NW radial p-n junction starts to increase with significantly reduced slope at high applied voltages.

The depletion region width in the NW core at different core diameters as a function of applied voltage can be plotted as given below:



It can be seen that for a given value of applied voltage, the width of depletion region is smaller for larger radii  $R_1$  and for sufficiently thick NW it tends to the square root dependence on applied voltage which is given by dashed line.

#### **4. DISCUSSION AND CONCLUSION**

In this project we have explored the ability of a radial p-n junction to enable photovoltaic devices to maintain high efficiencies despite low minority-carrier lifetimes. We have also studied the potential benefits of a radial p-n junction over conventional planar geometry. We have derived the required analytical expressions to calculate the width of the depletion layers, the barrier capacitance and the volt-ampere characteristics. This developed theoretical model not only serves a good base for further studies in radial p-n junction but also in various applications such as photovoltaics, etc.

## 5. REFERENCES:

1. D. Chattopadhyay and P. C. Rakshit, *Electronics Fundamentals and Applications*, (New Age International Publishers, 12<sup>th</sup> Edition).
2. S. Petrosyan, A. Yesayan, and S. Nerseyan, *Theory of Nanowire Radial p-n Junction*, (International Journal of Physical and Mathematical Sciences, Vol. 6, No. 11, 2012)
3. B. M. Kayes, *Radial p-n junction, wire array solar cells*, (Conference Record of 33<sup>rd</sup> Photovoltaic Specialists Conference, 2008)



Project Reported On:- Tunneling Current at the interface of Silicon and silicon nanocrystals having ellipsoidal shape in Metal-Oxide-Semiconductor Field-Effect Transistor (MOSFET)

Submitted by:- Soham Maiti

College Roll No:- PHUG/209/17

Project Guided By:- Dr. Sourav Chattopadhyay, Department of Electronics, Ramakrishna Mission Residential College (Autonomous), Narayandrapur



**Ramakrishna Mission Residential College (Autonomous)**

**Vivekananda Centre for Research**

**Ramakrishna Mission Ashrama**

(A Branch Centre of Ramakrishna Mission, Belur Math, Howrah-711202)

**Narendrapur, Kolkata - 700 103, West Bengal, India**

A Scientific Industrial Research Organisation, Recognised by DST, Govt. of India

College with Potential for Excellence (CPE), Re-accredited by NAAC - 'A' (CGPA 3.56 out of 4)

---

## **DEPARTMENT OF PHYSICS**

### **Certificate**

This is to certify that Soham Maiti, a student of B.Sc has successfully completed the project of UG curriculum entitled "Tunneling current at the interface of Silicon and silicon nano-crystals having ellipsoidal shape in MOSFET" in the period from January to May, 2020.

*Malay Purkait*  
.....  
30.06.2020

**Signature Of HOD**

**Dept. of Physics**

**Dr. Malay Purkait**

Associate Prof. & Head

Department of Physics

Ramakrishna Mission Residential College

(Autonomous)

Narendrapur, Kolkata-700 103. (W.B.)

## TO WHOM IT MAY CONCERN

This is to certify that Soham Maity, a final year B.Sc. student (Dept. of physics) of Ramakrishna Mission Residential College, Narendrapur, Kolkata-700103, has successfully completed his B.Sc. project work entitled 'Tunneling current at the interface of silicon and silicon nanocrystals having ellipsoidal shape in Metal-Oxide-Semiconductor Field Effect Transistor (MOSFET)' under my supervision.

Sourav Chattopadhyay  
20/6/20.



### ∴ Acknowledgement :-

I am really grateful to my project guide Dr. Sourav Chattopadhyay . All time , sir helped me to complete the project successfully.

I would like to thank Prof. Amit Ray for helping me in programming . I thanked prof. Malay Purnkait , HOD, Department of physics for giving me the opportunity of doing project.

I am extremely thankful to our Principal Maharaj, Swami Shastrajnananda.

Soham Maiti

Signature of student



### -: Abstract :-

My project is to deal with the tunneling current in MOSFET devices. Actually, in MOSFET device, there is some gate leakage <sup>current</sup> flowing from gate electrode ~~to~~ silicon to gate electrode via dielectric medium (electron is flowing from gate electrode to silicon substrate) by quantum tunneling process. We should reduce this leakage current which is actually unexpected. Because, when device has been switched off, then this current is still flowing. This should be hopped. So, here in this project, we have detailed study about tunneling phenomena (which is ~~due to~~ leakage current) after less dilute inclusion of nanocrystal-silicon in silicon di-oxide dielectric medium.

## Table of Content:-

|                                |       |
|--------------------------------|-------|
| i> Introduction                | 1-2   |
| ii> Theoretical Model          | 3-5   |
| iii> Fowler-Nordheim Tunneling | 6-8   |
| iv> Direct Tunneling           | 8-9   |
| v> Analysis                    | 9-10  |
| vi> References                 | 10-11 |



∴ Tunneling current at the interface of silicon and silicon dioxide partly embedded with silicon nanocrystals having ellipsoidal shape in metal oxide semiconductor structures (MOSFET) :-

Introduction:- Recently, silicon nanocrystals (nc-si) embedded in the silicon dioxide films in MOS structures extensively. Such films can be used as active layers for single electron devices and silicon based light emitting devices<sup>(1,2)</sup>. The applications of single electron devices essentially demand the detailed information of the charge transport mechanism in the nanocrystalline silicon in MOS structures.

Memory devices based on silicon nanocrystals have reportedly being very useful due to the scaling of the gate dielectrics<sup>(3)</sup>. Although there are some relevant works related to the issue. The studies have normally been carried out with memory cell structures with the nanocrystals combined only in a narrow layer embedded in the gate dielectric.

In this article we are concerning about the MOS-structure in MOSFET. The MOS structure is consisting with metal (n<sup>+</sup> polysilicon) situating in gate, silicon dioxide layer used for insulator, then si-substrate. Here we insert some nanocrystal silicon having ellipsoidal shape to change the nature of oxide layer. It makes to vary tunneling current which is very important aspect of memory device application.



Modelling and numerical simulation of the tunneling currents depend on the knowledge of the quantum mechanical transmission probability for an ultrathin barrier. A simplified equivalent effective mass, the dielectric constant and the band gap have been considered to describe tunnelling current due to flow of electron from poly Si gate to silicon substrate via composite gate dielectric.

There are two types of tunneling being observed in MOSFET.

1) Fowler-Nordheim Tunneling

2) Direct tunneling.

Direct tunneling is dominating when the barrier height is greater than applied field and for the FN

tunneling, this incident is totally opposite. The two tunneling phenomenon is dependent of the thickness of the dielectric. As gate oxides are made thinner by successive generations of MOSFET, the FN tunneling have been converted to Direct tunneling.

Basically our aim is to observe the change of gate leakage current impacted by the tunneling incident. This ~~structure~~ leakage current have a crucial role in modern day electronic devices.

This whole structure of MOSFET exhibits memory effect and shows good retention characteristics. Also the article examines the effect of the volume fraction and the crystalline size of the Silicon nanocrystals on the FN tunneling current.

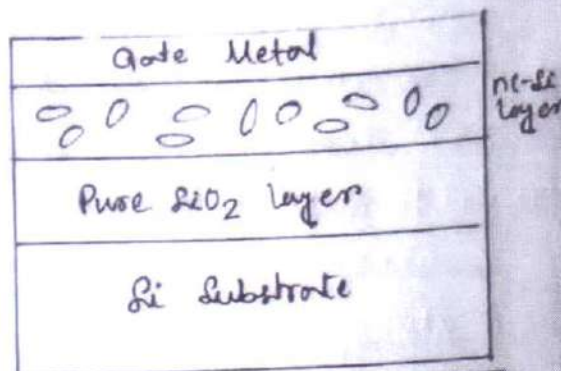


Fig-1:- Schematic diagram of the MOS structure with Composite gate dielectric



### Theoretical Model:-

In a MOS structure, the carriers are confined in a narrow potential well close to silicon surface. When the field is applied, the electrons inside the silicon are emitted in such a way that it tunnel from the quantized levels near the surface through the gate dielectric embedded with silicon nanocrystallites. We have proposed a MOS structure with gate/nc-Si embedded  $\text{SiO}_2$  layer / pure  $\text{SiO}_2$  w/ Si substrate. Here, in  $\text{SiO}_2$  insulator region, the <sup>two</sup> layers has been formed. One is nanocrystal Si embedded  $\text{SiO}_2$  layer, other is pure  $\text{SiO}_2$  layer. The two layers forms series-capacitor inside the MOSFET. We have found the effective dielectric of the given medium.

$$\frac{\epsilon_{ox}}{d_{ox}} = \epsilon_{ox} \quad \frac{\epsilon'_{ox}}{d_{ox}} = C_{ox} \quad \frac{\epsilon'_{nc-sio_2}}{d-d_{ox}} = C_{nc-sio_2} \quad \frac{\epsilon'_{ebb}}{d} = C_{ebb}$$

$$\epsilon'_{ox} = \epsilon_0 \epsilon_{ox}, \quad \epsilon'_{nc-sio_2} = \epsilon_0 \epsilon_{nc-sio_2}, \quad \epsilon'_{ebb} = \epsilon_0 \epsilon_{ebb}$$

Where,  $\epsilon_{ox}, \epsilon_{nc-sio_2}, \epsilon_{ebb}$  is the dielectric constants of the pure  $\text{SiO}_2$ , the nc-Si embedded  $\text{SiO}_2$  and the equivalent dielectric.  $d$  is the total thickness of the gate dielectric.  $d_{ox}$  is the thickness of the pure  $\text{SiO}_2$ .  $\epsilon'_{ox}, \epsilon'_{nc-sio_2}, \epsilon'_{ebb}$  is the permittivity of pure  $\text{SiO}_2$ , the nc-Si embedded  $\text{SiO}_2$  and the equivalent dielectric.

$$\frac{1}{C_{ebb}} = \frac{1}{C_{ox}} + \frac{1}{C_{nc-sio_2}}$$

$$\Rightarrow \frac{d}{\epsilon_0 \epsilon_{ebb}} = \frac{d_{ox}}{\epsilon_0 \epsilon_{ox}} + \frac{d-d_{ox}}{\epsilon_0 \epsilon_{nc-sio_2}}$$

$$\Rightarrow \epsilon_{ebb} = \left[ \frac{d_{ox}}{\epsilon_{ox} d} + \frac{d-d_{ox}}{\epsilon_{nc-sio_2} d} \right]^{-1}$$

— (i) no.



We consider that nc-si crystals <sup>having ellipsoidal structure</sup> has been less diluted in the  $\text{SiO}_2$  insulator. So, here it is less diluted suspensions of nc-si. For this condition, the relation among  $\epsilon_{ox}$ ,  $\epsilon_{nc-si}$ ,  $\epsilon_{nc-siO_2}$  is followed by, (6)

$$1-c = \frac{\epsilon_{nc-si} - \epsilon_{nc-siO_2}}{\epsilon_{nc-si} - \epsilon_{ox}} \left( \frac{\epsilon_{ox}}{\epsilon_{nc-siO_2}} \right)^{3L(1+2L)/(2-3L)} \\ \times \left[ \frac{(1+3L)\epsilon_{ox} + (2-3L)\epsilon_{nc-si}}{(1+3L)\epsilon_{nc-siO_2} + (2-3L)\epsilon_{nc-si}} \right]^{2(3L-1)^2/(2-3L)(1+3L)} \quad \text{--- (6) no.}$$

where,  $c$  is the volume fraction of the nanosilicon. For convenience, we report here the complete expressions of  $L$  for prolate and oblate ellipsoidal particles,

$$L = \begin{cases} \frac{e}{16^3} \left[ 2ep + \ln \frac{e-b}{e+p} \right] & \text{if } e > 1 \text{ (prolate ellipsoids)} \\ \frac{e}{16^3} \left[ \pi - 2eq - 2 \arctan \frac{e}{q} \right] & \text{if } e < 1 \text{ (oblate ellipsoids)} \end{cases} \quad \text{--- (7) no.}$$

where,  $p = \sqrt{e^2 - 1}$ ,  $q = \sqrt{1 - e^2}$

if  $e=1$ , then the (7) no. expressions reduces to the spherical inclusions of nc-si crystals.  $\epsilon_{nc-si}$  is the dielectric constants of the nanocrystalline silicon given by, (7)

$$\epsilon_{nc-si} = \epsilon_{si} - ds(\epsilon_{si} - 1) \quad \text{--- (8) no.}$$

where,  $ds$  is the relative change of dielectric susceptibility which depends on the nanocrystalline diameter.

The barrier height  $\phi_b$  is the difference between conduction band edge of the proposed gate dielectric and the conduction band edge of silicon substrate.

Therefore, barrier height is given by,

$$\phi_b = (\epsilon_{gcb} - \epsilon_{gci})/2 \quad \text{--- (9) no.}$$



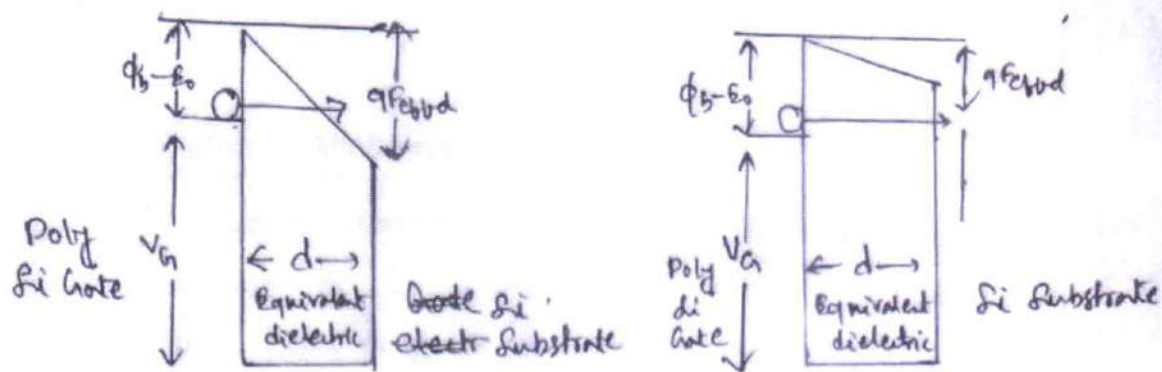


Fig 2- Band structure criteria for (a) FN tunneling (b) direct tunneling

Where,  $E_{gebb}$  is the equivalent band gap of the whole gate dielectric containing pure  $\text{SiO}_2$  layer and nc-Si embedded  $\text{SiO}_2$  layer.  $E_{gsi}$  is the band gap of Si. In the present model, a composite gate dielectric containing these two dielectrics (pure  $\text{SiO}_2$  and  $\text{SiO}_2$  embedded with nc-Si) has been considered.  $E_{gebb}$  can be written as,

$$E_{gebb} = \frac{E_{gox} + E_{gnc-sio_2}}{2} \quad \text{--- (10) no}$$

where,  $E_{gox}$  is the band gap of the pure silicon dioxide and  $E_{gnc-sio_2}$  is the band gap of the silicon dioxide embedded with nc-Si. According to the virtual crystal approximations,  $E_{gnc-sio_2}$  is given by,

$$E_{gnc-sio_2} = E_{gox}(1-C) + E_{gnc-si}C \quad \text{--- (11) no}$$

The  $E_{gnc-si}$  is the band gap of nanocrystalline silicon given by, (8)

$$E_{gnc-si} = E_{gsi} + \frac{C}{d_0^n} \left( \frac{d_m}{d_0} \right)^{n/(n+3)/5}$$

where,  $d_0$  is the mean size of nanocrystals and  $d_m$  is the size for which the maximum occurs in the log-normal distribution,  $n \approx 1.22$ ,  $\frac{d_m}{d_0} \approx 0.7$  (9)



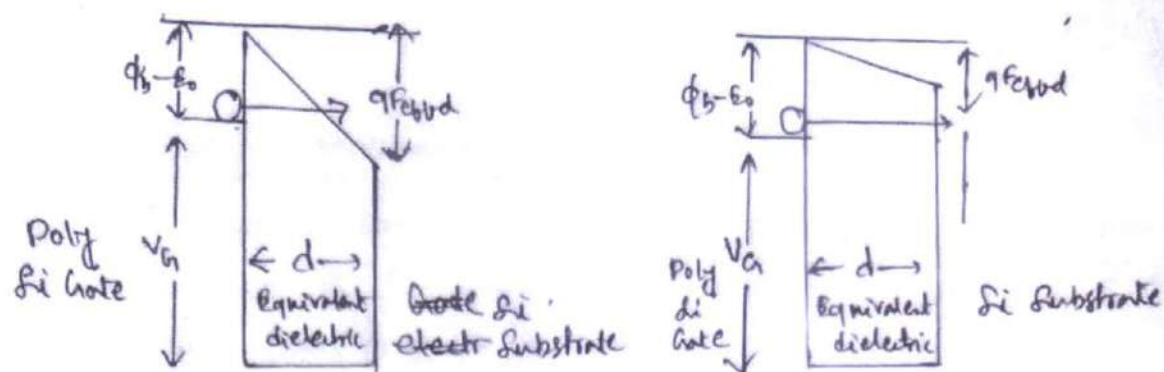


Fig-2- Band structure criteria for (a) FET tunneling (b) direct tunneling

Where,  $E_{gebb}$  is the equivalent band gap of the whole gate dielectric containing pure  $SiO_2$  layer and nc-Si embedded  $SiO_2$  layer.  $E_{gsi}$  is the band gap of Si. In the present model, a composite gate dielectric containing these two dielectrics (pure  $SiO_2$  and  $SiO_2$  embedded with nc-Si) has been considered.  $E_{gebb}$  can be written as,

$$E_{gebb} = \frac{E_{gox} + E_{gnc-sio_2}}{2} \quad \text{--- (10)}$$

where,  $E_{gox}$  is the band gap of the pure silicon dioxide and  $E_{gnc-sio_2}$  is the band gap of the silicon dioxide embedded with nc-Si. According to the virtual crystal approximation,  $E_{gnc-sio_2}$  is given by,

$$E_{gnc-sio_2} = E_{gox}(1-c) + E_{gnc-si}c \quad \text{--- (11)}$$

The  $E_{gnc-si}$  is the band gap of nanocrystalline silicon given by,

$$E_{gnc-si} = E_{gsi} + \frac{c}{d_0^n} \left( \frac{d_m}{d_0} \right)^{n(n+3)/5}$$

where,  $d_0$  is the mean size of nanocrystals and  $d_m$  is the size for which the maximum occurs in the log-normal distribution,  $n \approx 1.22$ ,  $\frac{d_m}{d_0} \approx 0.7$  (9)



### A) Fowler-Nordheim tunneling:-

Fowler-Nordheim injection of electrons in a MOS structure is the high field-induced emission of electrons either from a gate electrode or a degenerate accumulation or inversion layer. The tunneling occurs when the applied voltage  $V > (\phi_b - \phi_s)/q$ . For the strong applied field, the triangular potential barrier arises.

On applying the gate voltage and neglecting the image lowering force, the effective field and the field near the silicon surface are lowered to  $\frac{1}{\epsilon_{bb}}$  and  $\frac{1}{\epsilon_{si}}$  times that in vacuum respectively. Following the linear potential approximation near the silicon surface we have,

$\epsilon_{si} E_{si} = \epsilon_{bb} E_{bb} = F$ , where  $E_{si}$ ,  $E_{bb}$ , and  $F$  are the surface field of silicon.

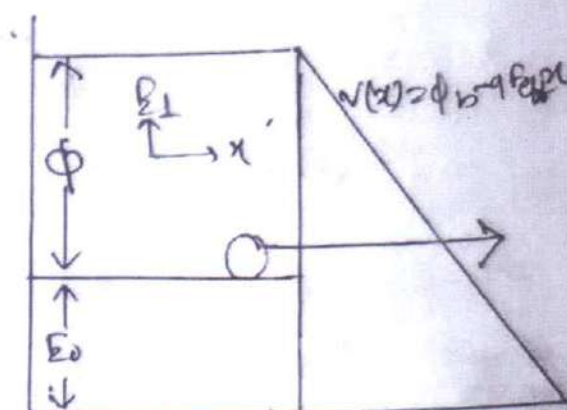


Fig-3-Schematic diagram of FN Tunneling

The Fowler-Nordheim tunneling method expresses the emission current density ( $J_{FN}$ ) in terms of the product of supply function  $N(E_1)$  and transmission coefficient  $D(E_1)$  as following,  $J_{FN} = \int_0^\infty N(E_1) D(E_1) dE_1$  — (i)  
where,  $N(E_1) = \frac{2m_{eff}}{2\pi^2 \hbar^3} \ln \left[ 1 + \exp \left( - \frac{E_0 - E_1}{k_B T} \right) \right]$  — (ii)

where,  $k_B$  is Boltzmann's constant,  $T$  is temperature,  $\hbar$  is reduced plank constant. In quantum mechanics, the transmission coefficient is defined by  $D(E_1) = j_t/j_i$  where transmitted, incident ( $j_t/j_i$ ) probability current density is related to respective wave function ( $\psi_t/\psi_i$ ) by  $j_t/j_i = \frac{i\hbar}{2m_{eff}} \left( \psi_{t,i} \frac{\partial \psi_{t,i}^*}{\partial x} - \psi_{t,i}^* \frac{\partial \psi_{t,i}}{\partial x} \right)$



So, here FET tunneling takes place from a flat planar surface, through an exact triangular barrier given by

$V(x) = \phi_b - q F_{eff} x$ , where  $\phi_b = E_0 + \phi$ , where  $\phi$  is the work function at zero bias ( $F=0$ ). So, Schrödinger equation is, given by,

$$-\frac{\hbar^2}{2m_{eff}} \nabla^2 \psi(x) + V(x)\psi(x) = E_1 \psi(x) \quad \text{--- (i)}$$

$$-\frac{\hbar^2}{2m_{eff}} \nabla^2 \psi(x) + (\phi_b - q F_{eff} x) \psi(x) = E_1 \psi(x)$$

The transmission coefficient of the barrier,

$$D(E_1) = \exp\left(-q \int_{x_1}^{x_2} \sqrt{V(x)} dx\right) \quad \text{--- (ii)}$$

$$V_0(x) = \phi_b - E_1 = \phi_b - q F_{eff} x - E_1 \quad \text{--- (iii)}$$

$$= E_F + \phi - E_1 - q F_{eff} x = V_h - q F_{eff} x \quad \text{--- (iv)}$$

where,  $V_h = \phi + E_F - E_1$  is the zero field height of the potential barrier,  $x_1 = 0, x_2 = \frac{V_h}{q F_{eff}}$ , using the binomial expansion and taking  $\frac{q F_{eff} x}{V_h} \ll 1$ , the above integral is approximated as,

$$\int_{x_1}^{x_2} \sqrt{V_0(x)} dx = \int_{x_1}^{x_2} \sqrt{V_h - q F_{eff} x} dx$$

$$\approx \frac{2}{3} \frac{V_h^{3/2}}{q F_{eff}}$$

Inserting eq<sup>n</sup> (iv) into eq<sup>n</sup> (ii),

$$D(E_1) = \exp\left(-q \frac{2}{3} \frac{V_h^{3/2}}{q F_{eff}}\right) \quad \text{--- (v)}$$

Substituting eq<sup>n</sup> (iv), (v) into (vi), the emission current density can be written as, (10)



$$J_{FNT} = \frac{e m_{eff}}{2\pi^2 \hbar^3} \int_0^\infty \exp\left(-\frac{2}{3} \frac{V_b^{3/2}}{e F_{eff}}\right) \cdot \ln\left[1 + \exp\left(\frac{E_0 - E_1}{k_B T}\right)\right] dE_1$$

$$= \frac{e m_{eff}}{2\pi^2 \hbar^3} \int_0^\infty \exp\left(\frac{2 \sqrt{m_{eff}}}{\hbar} \times \frac{2}{3} \frac{(E_0 + \phi - E_1)^{3/2}}{e F_{eff}}\right) \ln\left[1 + \exp\left(\frac{E_0 - E_1}{k_B T}\right)\right] dE_1$$

So, the FN Tunneling current is,

$$J_{FN} = \frac{e^2 m_{eff}}{2\pi^2 \hbar^3 q_1^2} \frac{1}{0.081} \times \frac{1}{81} \frac{F_{eff}^2}{\phi} \exp\left(-\frac{b_{FN}}{F_{eff}} \phi^{3/2}\right) \quad \text{--- (xv) no.}$$

where  $\phi = \phi_b - E_0$

where,  $b_{FN} = 0.44 \times \frac{3}{2e} q \times 2 \sqrt{\frac{2m_{eff}}{\hbar^2}}$   
equivalent

Here  $m_{eff}$  is the effective mass of the composite dielectric with pure  $SiO_2$  and  $SiO_2$  embedded with the nanosilicon.

Taking the resistance in series of the two layers of the gate dielectric. We have,  $R_{eff} = R_{ox} + R_{nc-sio_2}$

Considering the relaxation time,  $\tau_{ox} = \tau_{nc} = \tau_{eff} = \tau$  ~~--- (xvi) no.~~  
we obtain equivalent effective mass using (xvi) eqn. and

$$m_{eff} = \left[ \frac{m_{ox} d_{ox}}{d} + \frac{m_{nc-sio_2} (d - d_{ox})}{d} \right] \quad \text{--- (xvii) no.}$$

where,  $m_{ox} = 0.5 m$ ,  $m_{nc-sio_2} = 0.37 m$

B) Direct tunneling: The schematic energy band diagram of the direct tunneling is shown in Fig (2b).

The interfacial energy barrier in the direct tunneling regime is no longer triangular but trapezoidal in shape. Such tunneling phenomena dominate when  $V < (\phi_b - E_0)/q$ . When two electrodes are separated by an insulated film, the equilibrium conditions require that the top of the energy gap of the insulator be positioned above the Fermi level of two electrodes. Thus, the action of the insulating film is



From the Simmons's model<sup>(11)</sup>, the tunneling current density through a barrier in the direct tunneling regime is given by,

$$J_D = \left( \frac{e}{4\pi^2 \hbar d} \right) \left\{ (\phi_b - E_0 - \frac{eV}{2}) \exp \left[ - \frac{2(2m_{eff})^{1/2}}{\hbar} \alpha (\phi_b - E_0 - \frac{eV}{2})^{1/2} d \right] \right. \\ \left. - (\phi_b - E_0 + \frac{eV}{2}) \exp \left[ - \frac{2(2m_{eff})^{1/2}}{\hbar} \alpha (\phi_b - E_0 + \frac{eV}{2})^{1/2} d \right] \right\}$$

For the low <sup>field</sup> range, this eqn<sup>n</sup> (11) can be written as,

$$J_D = \frac{[2m_{eff}(\phi_b - E_0)]^{1/2} e q^2 V}{\hbar^2 d} \exp \left[ \frac{2\alpha \sqrt{2m_{eff}(\phi_b - E_0)}}{\hbar} d \right] \quad (xviii)$$

where,  $m_{eff}$  = effective mass of electron,  $d$  is the barrier width,  $\phi_b$  is the barrier height,  $V$  is applied bias and  $\alpha$  is a unitless adjustable parameter that is introduced to modify the single rectangular barrier. The physical meaning of  $\alpha$  is not very well defined. However it may be used to describe the tunneling through either a rectangular barrier. By adjusting the two parameters  $\phi_b$  and  $\alpha$ , one can accordingly modify the direct tunneling in the present model has been calculated as a function of gate voltage.

Analysis:- Here, we have noticed that FI tunneling is dependent of the effective applied field ( $E_{eff}$ ) from (xv) eqn<sup>n</sup>. But direct tunneling is totally independent of effective electric field which is also function of effective dielectric. So, it is also understood that whatever the particle is inserted on the insulator layer. for changing the effective dielectric of the medium, there is no change of direct in respect of effective dielectric.



direct tunneling depends on the barrier height ( $\phi_b$ ), which is also function of equivalent band gap of gate dielectric ( $E_{geff}$ ). This depends on the volume fraction of nc-Si crystal. So, direct tunneling is depending upon the volume fraction in respect of effective band gap ( $E_{geff}$ ) but not effective dielectric ( $\epsilon_{eff}$ ). But FN tunneling depends upon volume fraction ( $\epsilon$ ) in two cases. At low voltage direct tunneling is more dominating than FN tunneling. We have presented in this article analytical model of the gate current due to combination of the direct and FN tunneling in a deep submicron MOS structure.

#### References:-

1. S. Tiwary, P. Rana, H. Hamada, A. Hartstein, Appl. Physics Lett. 68, 1377 (1996).
2. S.H. Choi and R.G. Elliman, Appl. Physics Lett. 75, 968 (1999).
3. T.P. Chen, M.S. Tse, and X. Zeng, Appl. Phys. Lett. 78, 968 (2001).
4. W.Y. Guan, D.M. Kim and M. K. Cho J. Appl. Phys. 86, 3804 (1999).
5. E. Cassan, S. Galdin, P. Dollfus and P. Heato, J. Appl. Phys. 92, 3724 (2002).
6. Stefano Giondano, Journal of Electrostatics 58 (2003) 59-76.
7. C.B. Sun, X.W. Sun, B.K. Tay, S.P. Lau, H.T. Huang and S. Li, J. Physics D-31, 2959 (2001).
8. V. Ranjan, M. Kapoor and V.A. Singh, J. Physics, Condens. Matter 14, 6647 (2002).
9. T. Ando, A.B. Fowler and F. Stern, Rev. Mod.

10. Muhammad Zubair, Yee Sin Ang, and Lay Kee Ang,  
IEEE Transactions on electron devices, accepted  
(in-press), SI: Vacuum Electronics, 2018.

11. J. G. Simmons, J. Appl. Phys. 34, 1793 (1963).

— 0 —



# Study of Gaseous Detectors

B.sc Third Year Project

By

Sourav Mondal  
Roll No- PHUG/021/17  
Reg No- A03 1122 0021 17

Supervised by  
Dr. Amal Sarkar  
Dept. of Physics



Ramakrishna Mission Residential College (Autonomous), Narendrapur  
Kolkata, West Bengal 700103



**Ramakrishna Mission Residential College (Autonomous)**

**Vivekananda Centre for Research**

**Ramakrishna Mission Ashrama**

(A Branch Centre of Ramakrishna Mission, Belur Math, Howrah-711202)

**Narendrapur, Kolkata - 700 103, West Bengal, India**

A Scientific Industrial Research Organisation, Recognised by DST, Govt. of India

College with Potential for Excellence (CPE), Re-accredited by NAAC - 'A' (CGPA 3.56 out of 4)

---

## **DEPARTMENT OF PHYSICS**

### **Certificate**

This is to certify that Sourav Mandal, a student of B.Sc has successfully completed the project of UG curriculum entitled "IoT Based Smart Weather Monitoring system" in the period from January to May, 2020.

Malay Purkait  
.....  
30.06.2020

**Signature Of HOD**

**Dept. of Physics**

**Dr. Malay Purkait**

**Associate Prof. & Head**

**Department of Physics**

**Ramakrishna Mission Residential College**

**(Autonomous)**

**Narendrapur, Kolkata-700 103, (W.B.)**

## Certification

This is to certify that the project entitled "**Study of Gaseous Detectors**" by **Sourav Mandal**, a final year B.Sc student of the Department of Physics, RKMRC, Narendrapur Kolkata, completed his project work under my supervision. I wish him every success in his future.

Supervisor Amal Sarkar.

Dr. Amal Sarkar  
Assistant Professor  
Department of Physics  
RKMRC, Narendrapur  
Kolkata, India - 700103

Date: 26/06/2020

Place: Kolkata

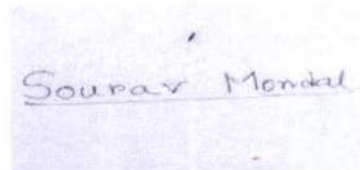


## Declaration

I hereby declare that I have not copied anything from any book or any other resources to complete my project work. I have not used any unauthorized data in this work. I have given all the references from which I have collected information and modified it regarding to the context.

Date: 04/07/2020

Sign

A rectangular box containing a handwritten signature in blue ink that reads "Sourav Mondal".

(Sourav Mondal)

# Contents

|                                                                          |           |
|--------------------------------------------------------------------------|-----------|
| <b>1. Introduction .....</b>                                             | <b>3</b>  |
| 1.1 History and evolution of Gaseous Ionization Detectors .....          | 5         |
| 1.1.1. Working principle of Gaseous Ionization Detectors.....            | 5         |
| 1.2 Types of gas chambers.....                                           | 6         |
| 1.2.1 Ionization Chamber.....                                            | 6         |
| 1.2.2 Proportional Chamber.....                                          | 7         |
| 1.2.3 Geiger Muller counter.....                                         | 8         |
| 1.2. Disadvantages of G-M counter.....                                   | 8         |
| <b>2. Time Projection Chamber.....</b>                                   | <b>8</b>  |
| 2.1 Introduction.....                                                    | 9         |
| 2.2 Constituents of TPC.....                                             | 9         |
| 2.3 Working principle of TPC.....                                        | 10        |
| 2.4 Particle detection in TPC.....                                       | 10        |
| 2.4.1. Momentum measurement.....                                         | 10        |
| 2.4.2. Energy measurement.....                                           | 10        |
| 2.4.3 Calculation of energy from $\frac{dE}{dx}$ plot with momentum..... | 11        |
| 2.4.4. Time resolution in TPC.....                                       | 12        |
| 2.4.5 Energy resolution un TPC.....                                      | 12        |
| 2.5. Experiments ongoing using TPC and their speculations.....           | 13        |
| 2.6. Problems while using TPC.....                                       | 13        |
| <b>3. Gas Electron Multiplier.....</b>                                   | <b>14</b> |
| 3.1. Introduction.....                                                   | 14        |
| 3.2. Structure of Gas Electron multiplier.....                           | 14        |
| 3.2.1. Time projection chamber GEM.....                                  | 14        |
| 3.2.1.1. The Karlsruhe GEM TPC prototype.....                            | 15        |
| 3.2.2. Proportional counter GEM.....                                     | 15        |

|                                              |           |
|----------------------------------------------|-----------|
| 3.3. Working principle of GEM.....           | 16        |
| 3.4. GEM: CMS experiment.....                | 16        |
| 3.5. Multistage Gas Electron Multiplier..... | 17        |
| 3.6. Application.....                        | 18        |
| 3.7. Advantages of GEM.....                  | 18        |
| 3.7.1. Limitations of GEM.....               | 19        |
| <b>4) Summary and Conclusion.....</b>        | <b>20</b> |
| Acknowledgement.....                         | 21        |
| References.....                              | 22        |



## Chapter 1

### Gaseous Ionization Detectors

#### Introduction

The first ionization chamber was made by Pierre Curie in 1895-1900. They were used by Marie and Pierre Curie in their work of extracting the radioactive materials such as radium, polonium, uranium etc. Since then Ion Chambers are widely used among researchers to detect the ionizing particles. As the time passed the structure and working principle of detectors evolved. The most efficient among their category (gm counter, proportional counter etc.) ION CHAMBERS are of great use due to their optimal efficiency. In modern particle accelerators the total energy monitoring has been made easy due to Gaseous Ionization Chambers. This is one of the best radiation detection instruments in particle physics. Generally, two beams from opposite side collide creating a bunch of particles which leave the gas ionized, by applying the electric fields they are accelerated to the receptors called readout pads. Hence, we get the required information about the unknown particle created at vertex.

#### **1.1.1. History and Evolution Gaseous Ionization Detectors**

Nearly 100 years ago, Hans Geiger operated the first gaseous detectors in Manchester, United Kingdom, in 1908. This detector helped to detect the COSMIC RAY. It had a gas-filled space with a cathode and anode. As the ionizing particle went through the gas, electrons drifted towards the anode; discharge propagation and quenching were successfully executed. As time passed, the mechanism of detection has been upgraded over the years. Nowadays, a cylindrical type of gas chamber is used frequently as the anode wire is placed centrally and the inner surface of the cylinder is made negatively charged, which is the cathode. Radiation detection counters were reported in 1932 by Jaffe and in 1945 by Van Heerden. However, radiation detectors that measure ionization, which is analogous to gaseous chambers, emerged only after the late 1950s and early 1960s.

#### **1.1.2. Working principle of gaseous ionization detectors**

Despite their simple basic principle, gas ionization detectors are still used frequently for the detection of ionizing radiation emitted both from radioactive substances and artificial radiation sources. In cylindrical detectors, the anode is situated generally along the axial line, and the walls of the detectors are made cathode. When an ionizing particle is made to go through the gas tube, newly generated electrons and large positive ions migrate to the anode and cathode respectively. The voltage between the anode and cathode is made high enough to terminate the recombination of electrons and ions. Meanwhile, the electrons make collisions with the large gas ions to initiate an avalanche process. But if the voltage

difference between the anode and cathode is increased something interesting happens. Two types of phenomenon are observed i.e.

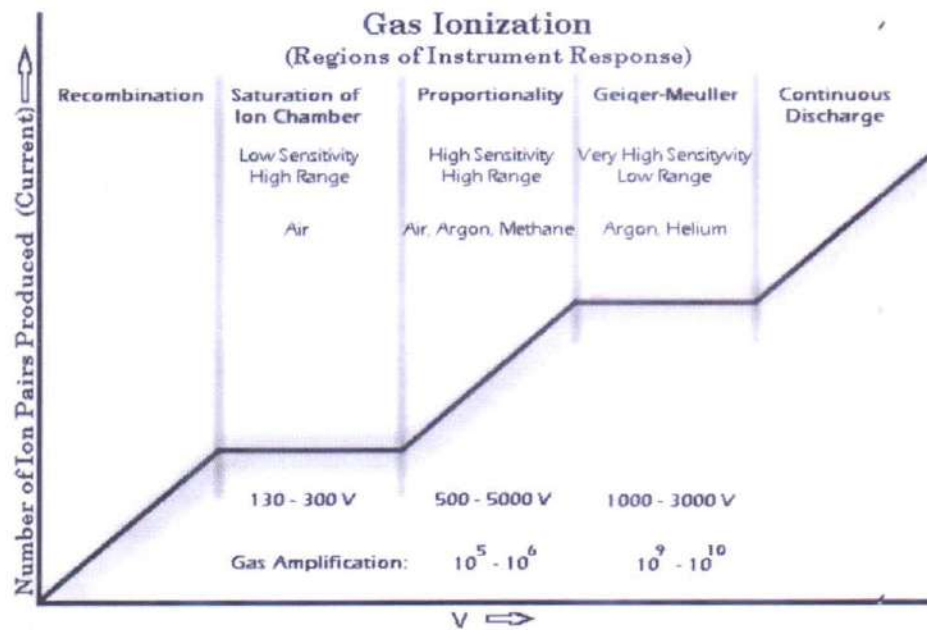


Figure 1: Ion pair production process in gaseous ionization chamber detectors

## 1.2. Types of gas chambers

There are three types of gas chambers in use

1. Ionization Chamber
2. Proportional Chamber
3. G-M Counter

### 1.2.1. Ionization chamber

Primary ionization is a process generally created by direct interaction with incident radiation with the gas. In case of secondary ionization, the voltage between electrode is made high enough that it requires more kinetic energy to produce more electron-ion pairs creating an avalanche [3].

#### Introduction

Ionization chamber collects all charges created by direct ionization within the gas through the application of electric field. At First a radiation interacts with gas and resultant positive ions and dissociated electrons move to electrodes. The output ionization current is then measured by the electrometer circuit which is nothing but a sensitive electric voltmeter with high input impedance.

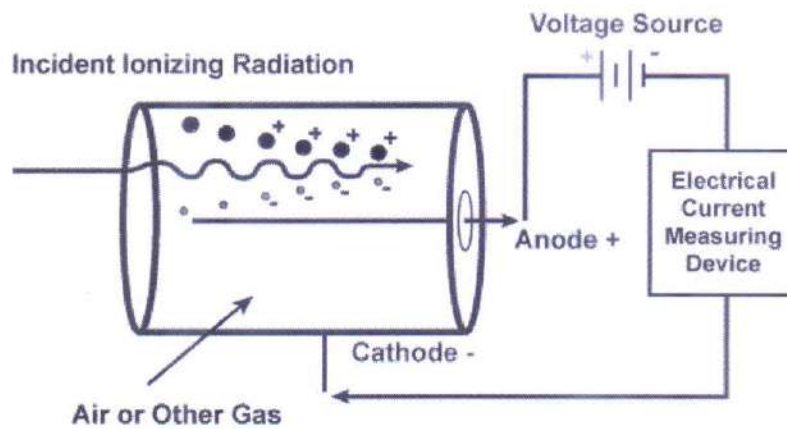


Figure 1.2.1: Schematic Diagram of Ionization chamber

## 1.2.2. Proportional Chamber

### Introduction

In this type of chamber the tube is filled with generally P-10 gas [P-10 gas consists of 90% argon, 10% methane]. As the ionizing particle goes through the chamber it leaves a trail of ion pairs along its trajectory the number of which is proportional to the energy of the particle. The avalanche process occurs at a fraction of millimetres from the anode wire [2]. This is called the "Avalanche Region". Here the multiplication effect of avalanche is considered. In case of cylindrical proportional counter, the multiplication  $M$  is calculated by the following formulae.

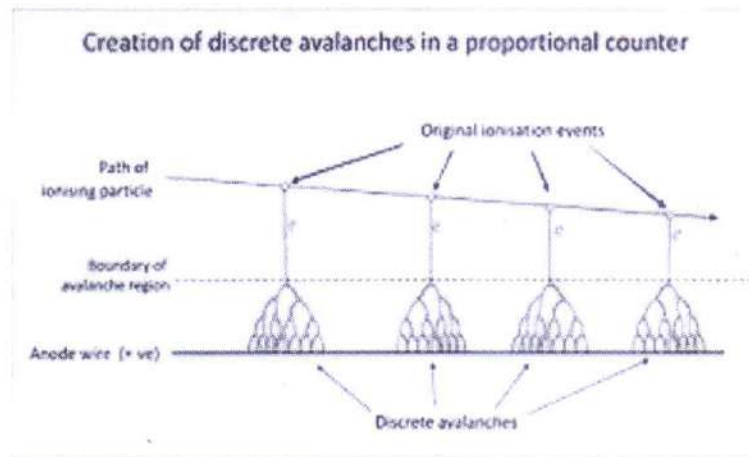


Figure 1.2.2: Schematic diagram of Proportional counter



### 1.2.3. Geiger-Muller Counter-

#### Introduction

The principle mechanism of Geiger-Muller counter is 'Townsend Avalanche'. Townsend noticed that current varies exponentially over ten or more orders of magnitude as distance between two plate is varied. In G-M counter when the electron is ionizing the gas molecules the electron interacts with the potential field of the nucleus and experience deceleration, loses its energy creating photons, this is known as Bream Strolling Effect. This ultra- violet creates their own avalanche in the entire anode. The positive ions accumulate at cathode [1]. During the dead time electrons again recombine with the positive ions.

1. The working formulae given by Townsend is

$$\frac{I}{I_0} = k \exp(\alpha_n * d) \quad (\text{Eqn.1})$$

This is the modified formulae

$$\frac{I}{I_0} = \frac{\exp(\alpha * d)}{1 - \epsilon(\exp(\alpha * d) - 1)} \quad (\text{Eqn.2})$$

$\alpha_n$  = Townsend coefficient

$\epsilon$  = second ionization coefficient

$I$  = current flown in the circuit

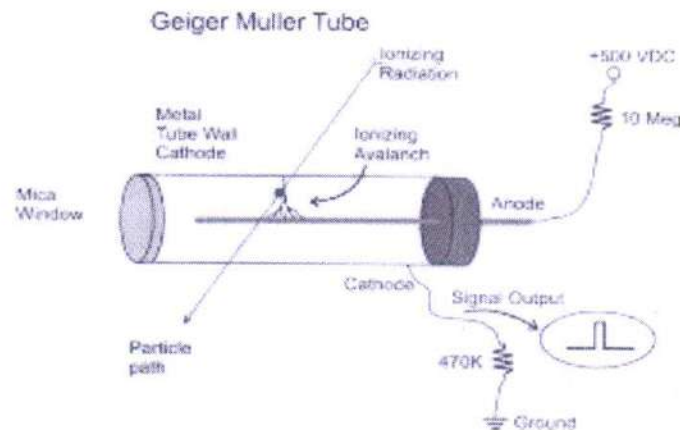


Figure 1.2.3: Schematic diagram of GM counter

#### 1.2.3.1. Disadvantages of GM counter

1. The avalanche of electron dies at one point, so no continuous output signal is obtained.
2. GM counter cannot detect chargeless particle like neutrino.
3. It is inefficient due to its large dead time.

## Chapter 2

### Time Projection Chamber

#### 2.1. Introduction

The **Time Projection Chamber (TPC)** uses both electric field and magnetic field for construction of 3-dimensional particle trajectory. This is one of the widely used gas chambers in modern times, exact calculation of momentum and energy of unknown particle can be measured with great accuracy.

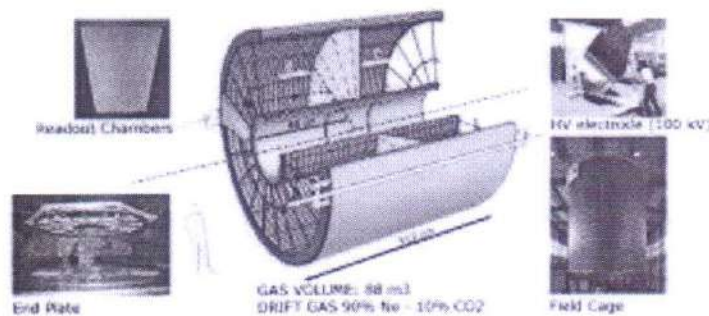


Figure 2.1: ALICE Time Projection Chamber

#### 2.2. Constituents of TPC

1. High Voltage Cathode Plane
2. The Collection Plane
3. Field cage in between the cathode and anode plane

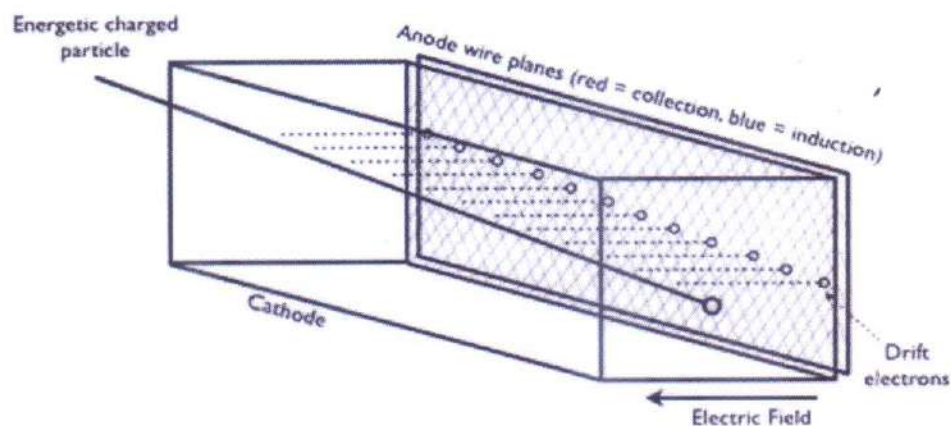


Figure 2.2: Rough sketch of cathode and anode plane in TPC

### 2.3. Working principle of TPC

Each wire in each anode plane is part of an R-C circuit, the wire itself located between the resistors and the capacitors. One end is given bias, and the end to the front-end electronics which amplifies the current. When the electrons drift towards induction plane it induces current in the wire, producing bump in the output current. As the electron moves away from the wire it induces negative current i.e reverse bump. Signals from the collection plane is unipolar, since electrons are collected by the collection plane. 3d arrangements can be analysed by combined 2D projections. While the 2d projections correspond to each anode plane

### 2.4. Particle Detection in Time projection chamber

To detect a particle, we need to know two factors about it

1. The momentum of the particle
2. The energy of the particle

#### 2.4.1. Momentum measurement

IN TPC a magnetic field of order 0.5 tesla and electric field of order 135 volt/m is used. The tube is filled with P 10 gas. Two beams from opposite side is made to collide, the point of collision is called the VERTEX. Along the vertex we consider the z axis, one direction is called the positive z axis and the opposite one is negative z axis, as the result of collision the gas is then ionized, at this point we have three different types of elements inside, one is the electrons, other is the larger positive ions, and the last one is unknown particle created by the collision. By applying the electric field the electrons are then accelerated towards the anode, anode have multiple receptors, the electron received gives the information about the position of the vertex i.e where the collision have been occurred, the unknown charge say positive in nature drifts towards the cathode. As the structure of the detector is of solenoidal type, electrons are collected towards the end, the dimension of the detectors (length=4.2metres, diameter=4 metre) are known and also the time of flight (the time taken by the particle to reach the receptor from vertex) is calculated. That is how we obtain the velocity, also momentum [mass is measured by calibration]

The transverse momentum resolution can be calculated as

$$\sigma\left(\frac{1}{p_t}\right) = \frac{\sigma_{pt}}{p_t^2} \quad (\text{Eqn. 3})$$

$\sigma$  = rms uncertainty

$P$  = track momentum

$\sigma_{pt}$  = transverse momentum resolution.

Using these two formulae we can calculate the transverse momentum resolution.

#### 2.4.2. Energy measurement



The electrons lose its energy along its path. When it reaches the receptors the amount of energy left is measured by DETECTORS. The amount of energy lost i.e.  $\left(\frac{dE}{dx}\right)$  calculated from the mean and deviation of the charge distribution using Truncated Mean Method.

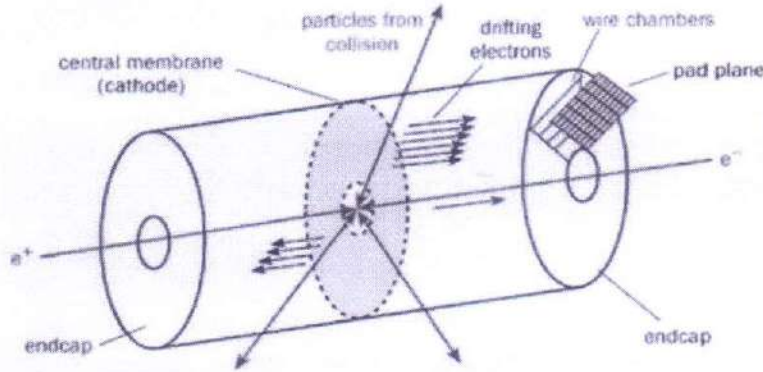


Figure 2.3: PEP 4 TPC showing drift volume, wire chamber and pads

TPC has been successfully operated in LARGE HADRON COLLIDER at CERN, recording collision of two proton and of heavy ions since 2009 with optimal data quality.

### 2.4.3: Calculation of energy using $\frac{dE}{dx}$ plot

The particle while traversing in the gas volume of the detector the energy and momentum transfer do not change the direction of the ionizing particles and the shell electrons are considered to be free and at rest. That is why Bethe- Bloch-Formulae can be applied; which describes the mean energy loss of the particle at a distance  $x$  from the VERTEX-

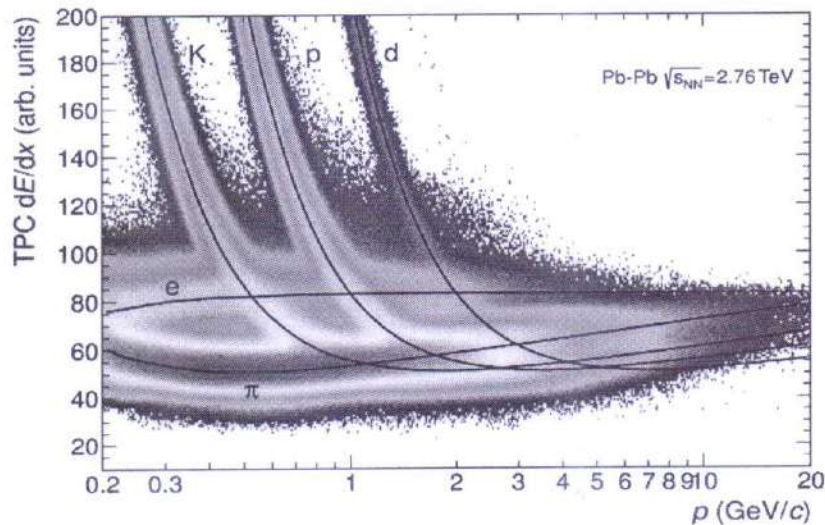


Figure 2.4:  $\frac{dE}{dx}$  plot with momentum

$$\ln M = \ln M = \frac{V}{\ln\left(\frac{b}{a}\right)} \frac{\ln 2}{\Delta V} \left[ \ln\left(\frac{V}{p a \ln\left(\frac{b}{a}\right)}\right) - \ln K \right] \dots \dots \dots (Eq. 4)$$

$e$  = Electron charge

$N$  = Avogadro Number

$z$  = charge of traversing particle in units of  $e$

$m$  = electron mass

$\epsilon$  = dielectric constant of the medium

$I$  = average ionization energy of the absorber

$\delta, C$  = Parameters of the fermi density and shell correction.

The energy loss of a particle is a statistical process, this can be studied using Straggling functions. The function depends on the distance travelled i.e.  $dx$ . In the case of a very thick layer the Central Limit Theorem holds, and it follows gaussian distribution around the mean value. And for the thin layer the distribution can be described by Landau Distribution [4]. In gaseous detectors the layer is usually thin. At high energies the distribution has a long tail which resembles the shape of original Landau Distribution.

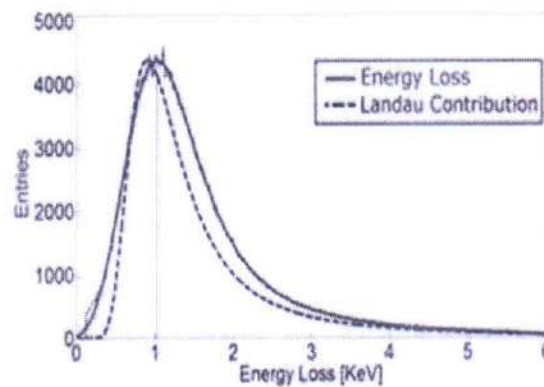


Figure 2.6: Landau distribution of energy loss

For  $kappa < 1$ , it follows the Landau distribution otherwise gaussian. The energy cannot be measured directly. It is noted that electrons produced in primary ionization is proportional to

$n = \frac{dE}{dx} \cdot W^{-1}$ ; energy conservation imposes another constraint that the distribution is not Poisson Distribution. The standard deviation for the number of produced electron is calculated as ; where  $F$  is the Fano factor

#### 2.4.4. Time resolution in TPC

Time resolution means how accurately and quickly a detector can detect two different particles. Generally, a detector with high resolution have a very low dead time, which are those high-resolution detectors. TPC can operate in high time resolution range. In ILD's 3-dimensional track time between two collision is 300ns, 100 events drifting at the same time for a fast gas.

#### 2.4.5. Energy resolution in TPC

A good energy resolution is of great importance for most application of detectors. Two different particles coming in the tracks of TPC with energy 40Kev or higher can easily be detected, TPC is widely used for its optimal energy resolution power.

## **2.5. Experiments ongoing using TPC and their specification**

### **1. The Star and Xenon experiments**

- In the STAR experiment Time Projection chamber is used to detect the signals of possible phase transition.
- The XENON experiment used dual phase TPC which utilizes a liquid xenon with gas chamber on top, particles in this chamber uses scintillations and ionization.

### **2. Liquid argon TPC for ICARUS experiments**

- This experiment is carried out to study neutrino with a direct velocity measurement.

### **3. HARP experiments**

- This experiment was designed to study the hadron pair production in proton-nucleus collision the energy range 1.5GeV/c-15 GeV/c.

### **4. Gem based TPC for LEGS experiments**

- This TPC uses double GEM as the amplification stage at BNL. A peak sensing circuit is used to measure the amplitude and the timing of signal peak from anode pad.

## **2.6. Problems while using TPC**

The main problem in TPC is the positive ion feedback in the drift volume, that is why particles cannot be measured with accuracy, causing large dead time. TPC has space charge and event construction problems.



## Chapter 3

### Gas Electron Multiplier

#### 3.1. Introduction

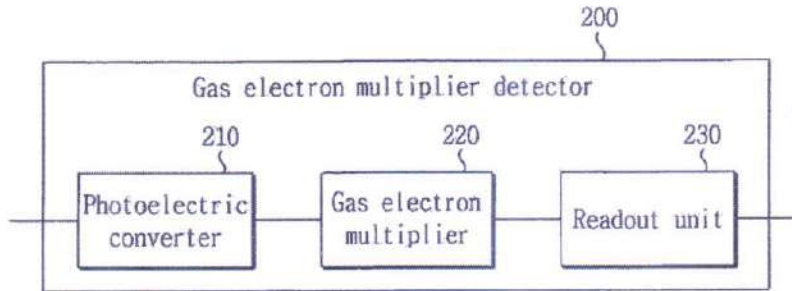


**Figure 3.1:** Gas Electron Multiplier

Gas Electron Multiplier was developed in 1997 by FABIO SAULI for particle physics experiments. The device has spawned many developments and applications over the years. This is a quick overview the status of developments and applications of this detector. A major evolution occurred in 1968 when CERN's Georges Charpak invented the Multi Wire Proportional Chamber (MWPC) which is a gaseous detector outperforming by orders of magnitude. Then came microstrip gas counters introduced by ANTON OED. In this counter a insulating material was taken and on this thin parallel metallic strips alternatively connected as cathode and anode. It provided the ten-fold improvement in the multi-track resolution. Nowadays it is a subject of extensive research in the domain of particle physics.

#### 3.2. Structure of Gas Electron Multiplier

Typical GEM is constructed of 50-70 micrometers thick KAPTON foil clad in copper on both sides. The small holes can be made dimensionally stable. Operation voltage is 1500-400 V placed across the two copper layers. A single electron entering one hole would cause an avalanche of 100-1000 electrons, this is the gain of GEM. There are two separate GEMs.

##### 3.2.1. Time Projection Chamber GEM

## GEM (Gas Electron Multiplier) Structure

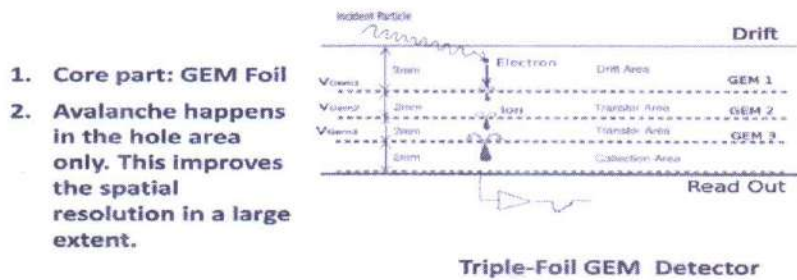


Figure 3.1: Structure of Gas Electron Multiplier

The electrode supply both the drift field and amplification field. A detector with higher drift region can be operated as the Time Projection Chamber. There are many advantages of using GEM in TPC in comparison to wires. The approaching electrons are amplified in the holes and are able to continue their way to endplate. Ions which are built in this amplification process are mostly absorbed on the upper on the upper side of the GEM foil. Here the ion feedback is suppressed. The principle difference between TPC and GEM TPC is that the signal width of the GEM TPC is only given by the transverse diffusion coefficient. On application of magnetic field (4 T) this coefficient can be made smaller. Spatial resolution can be improved by calculating the hit by event in COG (Centre of Gravity) method

### 3.2.1.1. The Karlsruhe GEM-TPC Prototype

In the year 2002 a new GEM-TPC prototype was made in Karlsruhe. It had dimensions (25 X 12.5 cm). It had a double GEM structure and readout system for measuring the drift velocities, diffusion coefficients and the temperature dependence of gains. It consists of a two-resistor chain that are placed outside of the drift volume to ensure no heating in this volume is occurred. Detecting the incident ionized radiation has been quite accurate.

### 3.2.2. Proportional counter GEM

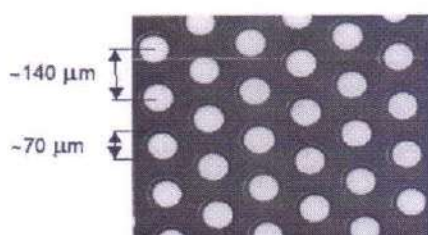
A detector with a smaller drift region can be operated as Proportional Counter. The read-out plane made out of conductive strips can be fabricated with ordinary lithography techniques. They are like 2d strips and grids, hexagonal pads, radial/azimuthal segments etc. and any other readout geometry is possible.



## The Gas Electron Multiplier GEM

A GEM (F. Sauli, 1997) is a thin metal-insulator-metal structure, densely perforated with small holes. A voltage across the metal layers generates a sufficiently strong field within the holes to focus the electrons and multiply them.

The GEM is technically realized at CERN through copper-coating on 50  $\mu\text{m}$  thick kapton (polymer) foil, with chemically etched holes of conical profile. A standard GEM has a hexagonal pattern of 70  $\mu\text{m}$  diameter holes in the metal, 55  $\mu\text{m}$  in the foil, with a pitch of 140  $\mu\text{m}$ .



A 2D readout of strip anodes on the transfer side of the GEM can provide ~ 1 mm spatial resolution.

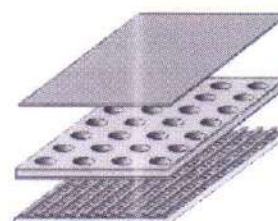
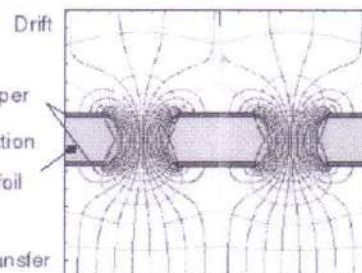


Figure 3.2: Solid state structure of GEM

Proportional chamber using GEM detectors has an increased rate of detection rather than Wired Proportional Chamber. This is due to two factors.

- A short, high field transfer-gaps resulting in fast clearance of ions.
- The screening effect of from the external field due to holes narrow geometry.

Prolonged exposure to radiation causes progressive degradation of performance in gaseous detectors as organic molecules i.e. contaminants are created at same time. GEM detectors are less affected by the deposits on electrodes. In accelerated aging tests no degradation of performance is observed in GEM detectors being exposed to continuous exposure to soft X rays for a long time. The addition of CARBON TETRA FLUORIDE to the gas mixture has improved in the resolution of GEM devices due to strong reactivity of fluorine.[5]

### 3.3 Working principle of GEM

Problems raised while using the MSGC, as in those detectors the electrodes were in contact of high electric fields, as a result a local charge density is created say for example neutron or gamma conversion. Similar problem happened in case of MWPC filled with photosensitive gas. The holes diameter and shape have a direct impact on the long-term stability and performance of the detectors. The real gain of the multiplier is always more than the useful or effective gain defined as the ratio of the detected primary ionization charge. Avalanche multiplication begins in the induction gap. The fraction of ionizing electrons transfers in the GEM foil. Generally, holes are 70 micrometers wide, the whole structure is designed to terminate the back flow to the TPC taking care of the fact the gain of electrodes increases with voltage. Many experiments use double or triple GEM stacks to achieve gains of one million or more.

#### 3.4.1. GEM: CMS experiment



Gas electron Multiplier detectors represent a new muon system in CMS. The GEM chamber will provide additional redundancy and measurement point, allowing a better muon track identification and also wider coverage in the very forward region. The CMS detectors are made of three layers each of which is 50-micron thick copper made polyimide foil. This gas chambers are filled with Ar /CO<sub>2</sub> gas where the primary ionization due to incident muon would occur.

### 3.5. Multistage Gas Electron Multiplier

Several composite grids, mounted within same gas volume, and powered by suitable resistor chain allows to reach large gains, somehow analogous to multi-grid vacuum tube but substantially cheaper and simpler for manufacturing. It operates in strong magnetic field, with only some image distortions.

In micro strip gas chamber's, a serious problem of discharges has been met recently when operated near their maximum gain limit. MSGC can be irreversibly damaged by a discharge initiated by heavily ionizing tracks. GEM grid with moderate pre-amplification would allow to operate the MSGC well below the critical potential for discharge. GEM with its de clustering effect also improves the localization accuracy. The presence of GEM mesh between the main amplification element and the photo cathode reduce the possibility of dangerous **PHOTON FEEDBACK**. The GEM grid can easily be used as controlled gate to prevent ions feedback. The small value of the gating voltage would greatly reduce pick up problems

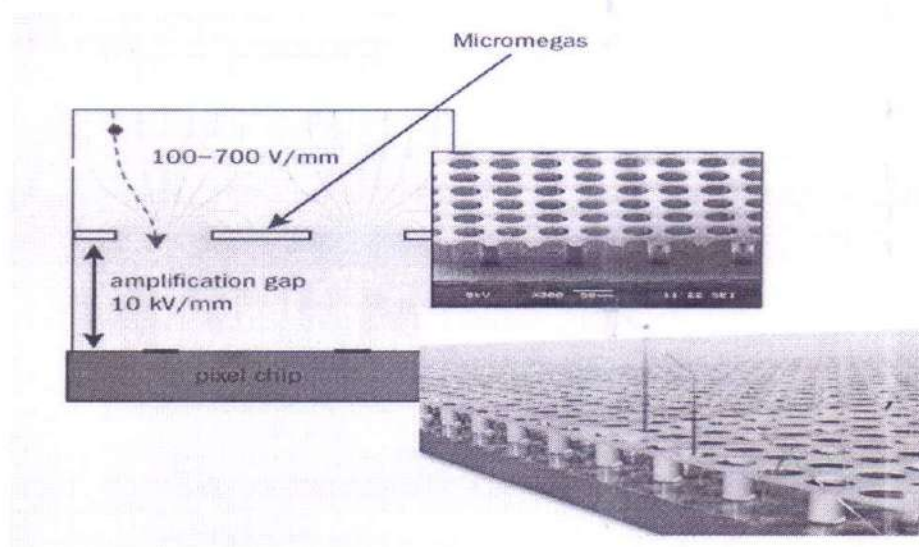


Figure 3: 3-dimensional visualization of GEM

### 3.6. Application

In micro strip gas chambers, a serious problem of discharges has been discovered recently when operated near their maximum gain limit. MSGC can be irreversibly damaged by a discharge initiated by heavily ionizing tracks. GEM grid with moderate pre-amplification would allow to operate the MSGC well below the critical potential for discharge. GEM with its de clustering effect also improves the localization accuracy. The presence of GEM mesh between the main amplification element and the photo cathode reduce the possibility of dangerous Photon feedback.

The GEM grid can easily be used as controlled gate to prevent ions feedback. The small value of the gating voltage would greatly reduce pick up problems. There are several particle physics experiments

where GEM has been used successfully and still in use. The following experiments are using GEM based detectors

- **CERN experiments at the Large Hadron Collider**
- **STAR and Phenix experiment at RHIC**
- **Muon-g2 experiment at Fermilab**
- **Muon Tomography**

There are several future experiments which are planning to use GEM based detectors for particle tracking in their measurements. For example, future Electron Ion Collider (EIC) and fair experiment at GSI.

### **3.7. Advantages of Gas Electron Multiplier**

- a. Safe and non-explosive gas mixture**
- b. High reliability**
- c. High time and position resolution**

Position resolution is defined by the distribution of charge on the readout plane, It is determined by two process one of which is a direct drift of electrons in the electric field and the other one is their random diffusion in in the gas filling the detector. The size of readout granularity was around the 100 micrometre. 2D gaussian charge distribution is obtained in readout plane. To characterize the space resolution of different readout geometry the distribution of residuals between the generated and the reconstructed track position was built, and the width of this distribution was taken to characterize the space resolution. Time resolution can be obtained as some nanoseconds (140-160 ns) in this type of detectors.

#### **A. Flexible detector shape and readout pattern**

Gas Electron Multiplier (GEM) uses composite grid with a rectangular array of pinhole. Between two metal layers there is a non-explosive gas which is ionized incident photons. this type of geometrical structure is very easy to construct. The anode plate or the readout pad is generally made of copper which is easily available and of low cost.

#### **B. High performance at low cost**

The International GEM collaboration is designing the Gas Electron Multiplier such that it gives optimal performance while detecting the incident ionized radiation. It consists a thin metal coated polymer foil with a density of holes. The material used for fabricating the device is easily available and of low cost. Step by step repeated multiplication of avalanche is what gives a better detection system

#### **C. Works in harsh radiation environment**

GEM can operate in harsh radiation environment with losing its optimum quality, though the electrodes of GEM is exposed to radiation for a long-time detection of incident ionizing particles has no discrepancy.

#### **3.7.1. Limitations of Gas Electron Multiplier**

1. Complexity added by gas chamber compared to solid state detectors.
2. Low quantum efficiency compared to solid state detectors.



## References:

- 1) Glenn F Knoll. *Radiation Detection and Measurement*, third edition 2000. John Wiley and sons, ISBN 0-471-07338-5
- 2) G. Charpak and F. Sauli; Sauli, F (1984). "High-resolution Electronic Particle Detectors". *Annual Review of Nuclear Science*. Annual Reviews Inc. **34** (1): 285–350. Bibcode:1984ARNPS..34..285C. doi:10.1146/annurev.ns.34.120184.001441
- 3) Seco, Joao; Clasié, Ben; Partridge, Mike (21 October 2014). "Review on the characteristics of radiation detectors for dosimetry and imaging". *Physics in Medicine and Biology*. **59** (20): R303–R347. Bibcode:2014PMB....59R.303S. doi:10.1088/0031-9155/59/20/R303. PMID 25229250.
- 4) Demonchy, C. E.; Mittag, W.; Savajols, H.; Roussel-Chomaz, P.; Chartier, M.; Jurado, B.; Giot, L.; Cortina-Gil, D.; Caamaño, M.; Ter-Arkopian, G.; Fomichev, A.; Rodin, A.; Golovkov, M. S.; Stepanov, S.; Gillibert, A.; Pollacco, E.; Obertelli, A.; Wang, H. (2007). "MAYA, a gaseous active target". *Nuclear Instruments and Methods in Physics Research Section A: Accelerators, Spectrometers, Detectors and Associated Equipment*. **573** (1–2): 145–148. Bibcode:2007NIMPA.573..145D. doi:10.1016/j.nima.2006.11.025.
- 4) Institut für Kernphysik, Goethe Universität, Max-von-Laue-Str. 1, 60438 Frankfurt am Main, Germany
- 5) The Gas Detectors Development group. <http://gdd.web.cern.ch/GDD/>

## **IoT Based Smart Weather Monitoring system**

*Project Report submitted to the Department of Physics, Ramakrishna Mission Residential College (Autonomous), Narendrapur, Kolkata for the partial fulfilment of the requirements of the degree of*

### **Bachelor of Science (Hons.) in Physics**

Submitted by:

Tridib Bera [Roll No.: PHUG/233/17]

Sourav Mandal [Roll No.: PHUG/118/17]

Semester VI, B.Sc. Physics (Hons.)

University of Calcutta, Kolkata

2020



**Ramakrishna Mission Residential College (Autonomous)**

**Vivekananda Centre for Research**

**Ramakrishna Mission Ashrama**

(A Branch Centre of Ramakrishna Mission, Belur Math, Howrah-711202)

**Narendrapur, Kolkata - 700 103, West Bengal, India**

A Scientific Industrial Research Organisation, Recognised by DST, Govt. of India

College with Potential for Excellence (CPE), Re-accredited by NAAC - 'A' (CGPA 3.56 out of 4)

---

## **DEPARTMENT OF PHYSICS**

### **Certificate**

This is to certify that Sourav Mondal, a student of B.Sc has successfully completed the project of UG curriculum entitled "Study of Gaseous Detectors in the period from January to May, 2020.

*Malay Purkait*

.....

30.06.2020

**Signature Of HOD**

**Dept. of Physics**

**Dr. Malay Purkait**

**Associate Prof. & Head**

**Department of Physics**

**Ramakrishna Mission Residential College**

**(Autonomous)**

**Narendrapur, Kolkata-700 103, (W.B.)**



Mr. Tanmay Biswas


Assistant Professor

Ramakrishna Mission Residential  
College (Autonomous)  
Narendrapur, Kolkata-700103

## CERTIFICATE OF APPROVAL

Date: 1 July, 2020

This is to certify that the project report entitled "**Android Based Smart Body-Temperature Monitoring and Recording System**" has been done under my supervision at the Department of Physics, Ramakrishna Mission Residential College (Autonomous). I also endorse that this work submitted by **Arunabha Mondal** (Reg. No: A03-1112-0113-17) is original and has not been submitted to any other University for the award of any Degree or Diploma. I therefore, recommend the project work for the award of **Bachelor of Science (Honours) in Physics**.

  
(Mr. Tanmay Biswas)

## ACKNOWLEDGEMENT

*The successful completion of the project would not be possible without the help and support of the following people.*

*We would like to take the opportunity to thank and express our gratitude to our project supervisor Mr. Tanmay Biswas (Assistant Professor, Department of Electronics). He did support us at every stage of the project. Every time we would come up with a new idea or modification to the existing project, he would patiently listen and correct our approach and most importantly support our idea.*

*We would also like to thank The Department of Physics, Ramakrishna Mission Residential College (Autonomous) in particular and the college in general for providing us the platform to create and present a project.*

*We would like to thank all the teachers of The Department of Physics whose simplified explanation and continued support in academics made it possible for us to understand the subjects properly and focus on the applicability of the subjects.*

*Last but not the least, we would take the privilege to thank our parents and both our sisters and all our friends for their valuable inputs.*

*We hope that we can build upon the experience and knowledge gathered during the development of this project and make a valuable contribution towards our College.*

*Arunabha Mondal*

Arunabha Mondal

*Subrata Maiti*

Subrata Maiti

## Abstract

The proposed system is an advanced solution for weather monitoring based on Internet of Things (IoT) which provides weather report by mobile messaging system to the farmers of a particular locality. The system deals with monitoring weather and climate changes like temperature, humidity, UV radiation in the air using two sensors (DHT11 and ML8511). These sensors send data to microcontroller which then sends the weather report alert via GSM SIM 800L module to the farmers whose numbers are registered in this module. Frequent periodical updates in results every second showed that the system has no delay in providing the new readings. It provides the particular weather report by mobile messaging system to the registered mobile number. Numerical results are presented and analyzed in this report to validate the theoretical analysis of the whole system taking account of expected data of a whole day including temperature, humidity, and UV index.

## 1. INTRODUCTION

Present day innovations in technology mainly focus on controlling and monitoring of different devices wirelessly over the internet such that the internet acts as a medium for communication between all the devices [8]. And irrespective of spatial disparity, life in contemporary society cannot be imagined without the convenience of wireless weather readings and forecasts. Since the world is changing so fast, weather stations have become urgently important for the safety and progress of human civilization. Here in this project we present a weather station that can prove to be helpful for any place. This weather station is based on IOT (internet of things). It is equipped with environmental sensors used for measurements at any particular place and it reports the users in real time on cloud. To accomplish this, we used Arduino Uno and different environmental sensors like DHT11 and ML8511 ultraviolet light sensor. The sensors constantly sense the weather parameters and keeps on transmitting it to the farmers over massaging system. This project also focuses on the IOT application in the new generation of environmental information and contributes towards the foreseeable shift in the paradigm of environmental monitoring in future [15]. The system has been developed particularly in the view of building smart city by giving the weather update of any particular place like a particular office or room.

### 1.1 Existing System

The existing weather monitoring systems generally use weather stations that use multiple instruments such as thermometers, barometers, wind vanes, rain gauge etc. to measure weather and climate changes [16,17]. Most of these instruments use simple analog technology which is later physically recorded and stored in a data base. This information is later sent to news reporting stations and radio stations where the weather report is given.

### 1.2 Limitations of the Existing System

(i) Existing weather monitoring systems that are used in the field generally consist of unconventional and heavy machinery that consists of numerous moving parts that require constant maintenance and need to be manually monitored and changed frequently [3].



- (ii) Power requirements are one of many major constraints as these instruments are generally sited far from main power supply. This adds to the cost of using such instruments.
- (iii) The use of thermometers to measure external temperature; however accurate is still outdated and constantly needs to be manually checked for any change in temperature.
- (iv) Data that is collected by the instruments needs to be manually transferred from the logger to a laptop or computer via a cable.
- (v) Existing systems consist of large and heavy instruments that occupy a lot of space hence making it difficult to install them in remote location and places which have limited space [16].
- (vi) The instruments used in the existing systems are expensive and add up to the already high cost of installation and maintenance.
- (vii) The current system always faces problems such as delay in warning people about bad weather and sudden changes in the forecast [11].

## 2. PROPOSED SYSTEM

The system proposed is an advanced solution for weather monitoring that uses IoT to make its real time data easily accessible to its user over a very wide range [16]. The system deals with monitoring weather and climate changes like

- (i) Temperature and humidity by using the DHT11 sensor,
- (ii) UV radiation using ML8511 solar sensor

### 2.1 System Architecture

The implemented system consists of an Arduino Uno which is used as the main processing unit for the entire system and all the sensors and devices are connected with the microcontroller. The sensors are operated by the microcontroller to retrieve the data and further process the analysis of the sensor data. The processed data is, then, reported via GSM SIM 800L module to the registered mobile number. The proposed design of the model is shown in Figure 1.

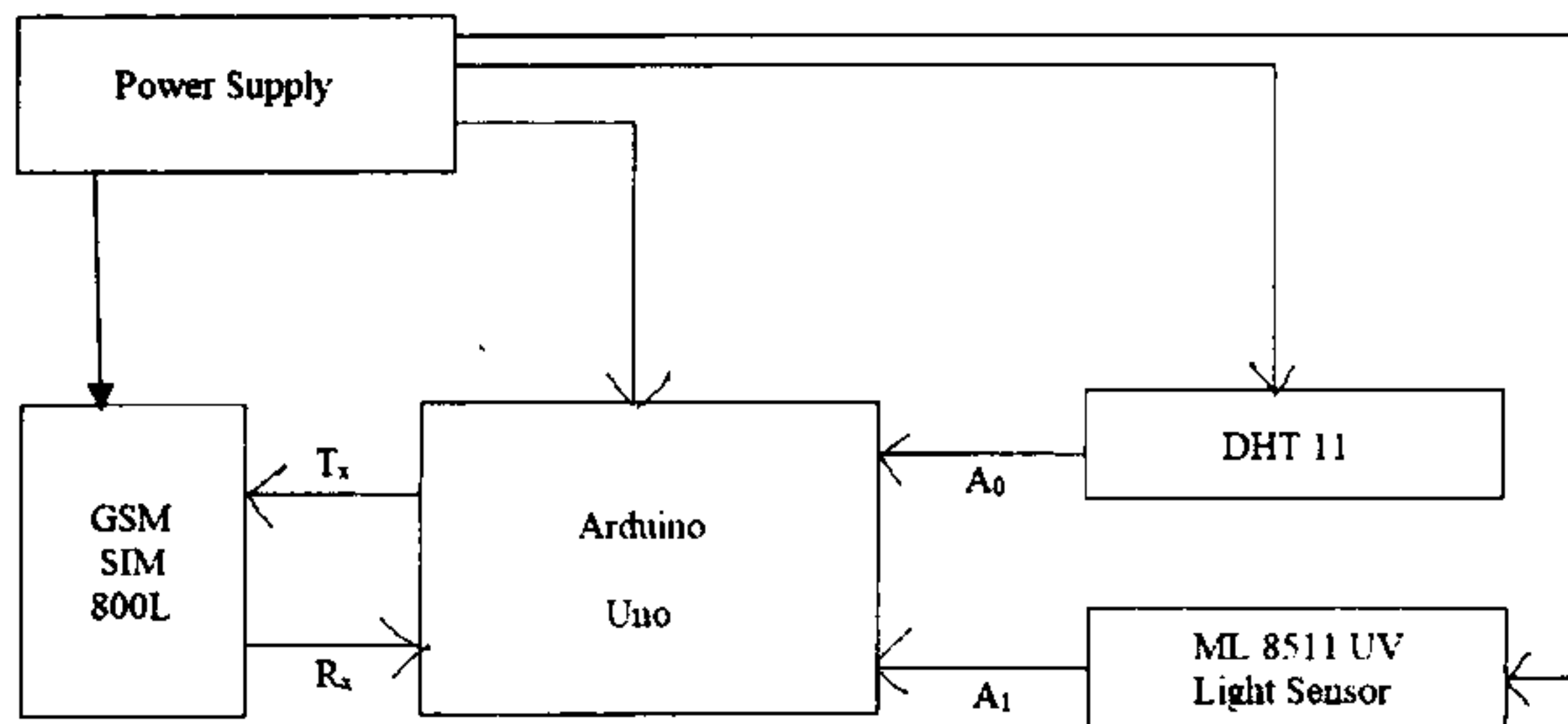


Fig. 1. Proposed Design

### 2.1.1 Arduino UNO

It is an open-source physical computing platform based on a simple micro-controller board, and a development environment for writing software for the board [10]. Arduino can be used to develop interactive objects, taking inputs from a variety of switches and or sensors, controlling a variety of lights, motors, and other physical outputs. The commercially available Arduino Uno board is shown in Figure 2.

- (i) Microcontroller: Microchip ATmega328P
- (ii) Operating Voltage: 5 Volt
- (iii) Input Voltage: 7 to 20 Volts
- (iv) Digital I/O Pins: 14 (of which 6 provide PWM output)
- (v) Analog Input Pins: 6
- (vi) DC Current per I/O Pin: 20 mA
- (vii) DC Current for 3.3V Pin: 50 mA
- (viii) Flash Memory: 32 KB of which 0.5 KB used by bootloader
- (ix) SRAM: 2 KB
- (x) EEPROM: 1 KB
- (xi) Clock Speed: 16 MHz
- (xii) Length: 68.6mm
- (xiii) Width: 53.4 mm
- (xiv) Weight: 25 g



Fig. 2. Arduino UNO

### 2.1.2 DHT11

The DHT11 is a basic, ultra-low-cost digital temperature and humidity sensor. It uses a capacitive humidity instrument and a thermistor to measure the surrounding air, and spits out a digital signal on the data pin (no analog input pins needed) [16]. It is shown in Figure 3.

- (i) Temperature range:  $0^{\circ}\text{C}$ - $50^{\circ}\text{C}$  /  $\pm 2^{\circ}\text{C}$
- (ii) Humidity Range: 20%-95% /  $\pm 2\%$
- (iii) Sampling rate: 1Hz (one reading every second)
- (iv) Body size: 15.5mm\*12mm\*5.5mm
- (v) Operating voltage: 3-5V
- (vi) Max current during measure: 2.5mA

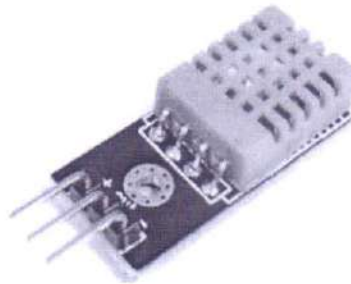


Fig. 3. DHT11

### 2.1.3 ML8511

ML8511 module, shown in Figure 4, is an informal to use ultraviolet light sensor. The ML8511 Sensor works by outputting an analog signal in relation to the amount of detected UV light [7]. This breakout can be very handy in creating devices that warn the user of sunburn or detect the UV index as it communicates to weather conditions.

- (i) Supply Voltage: DC 5V
- (ii) Operating Temperature:  $-20^{\circ}\text{C}$ ~ $70^{\circ}\text{C}$
- (iii) Sensitivity Region: UV-A and UV-B
- (iv) Sensitivity Wave Length: 280-390nm
- (v) Module Size: 30 x 22mm

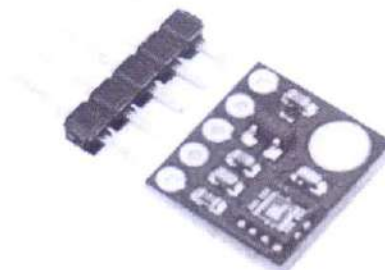


Fig. 4. ML8511



### 2.1.4 SIM800L GSM Module

SIM800L GSM module similar to the one which is on our phone. The GSM module is shown in Figure 5 for further reference and better understanding. Basically, SIM800L module is a small chip that uses serial-communication to communicate with any microcontroller or microprocessor. It has an in-built onboard antenna and an onboard SIM slot for SIM insertion purposes. The SIM800L module has total 12 pins that are used to establish connections with the microcontroller. For simplicity, here I have shared a detailed pinout of the SIM800L and a function of each pin.

**Ring:** This pin is used for indication purpose. It produces an interrupt signal when we receive an SMS or a phone call.

**DTR:** We can call this pin an enable pin. This pin plays an important role in saving electricity. If we turn this pin high, the module enters sleep mode by disabling serial communication and if the pin is turned low, the module turns on. In case, SIM800L is not working, the reason might be that this pin has been accidentally turned high.

**Mic+, Mic-, SPK+ & SPK:** These are the pins where we can connect the microphone and speaker.

**NET:** Here the helical shape antenna can be attached.

**RST:** This pin is used to reset the SIM800L module. If the module is not responding to the AT command, that might be because of a baud rate problem, you can turn this pin high for 100ms to reset the SIM800L.

**VCC and GND:** You can power SIM800L using these pins but the voltage should not be more than 3.3V and Current should not be less than 1A.

**RX and TX:** These pins are used for Serial communication Rx for receiving commands from the controller and Tx for sending out the data.

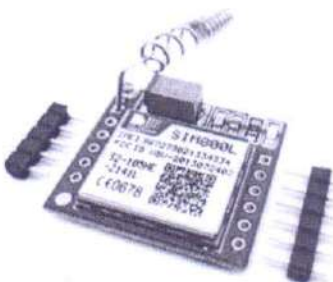


Fig. 5. SIM800L GSM Module

## 4. IMPLEMENTATION

Based on framework shown in figure 7, we have a suitable implementation model that consists of different sensor devices and module. In this implementation model we used Arduino Uno board with GSM SIM800L module, DHT11 and ML8511 sensors as embedded devices for sensing data and sending alert to the farmers. Arduino Uno board consists of analog input pins (A0-A5), digital output

pins (D<sub>0</sub>-D<sub>13</sub>), inbuilt ADC and GSM module that sends alert to the registered numbers. Sensors are connected to Arduino Uno board for monitoring. ADC converts the corresponding sensor readings to its digital value and from that value corresponding environmental parameter is evaluated. The design flow of the proposed system can be seen in Figure 6.

An embedded system for environmental monitoring and its components is shown in figure 7. The embedded device is placed in particular area for testing purpose. DHT11 sensor detects temperature and humidity in that area and ML8511 is the sensor to detect UV light. Once the readings cross the threshold limit, an alert is sent via GSM module to the registered mobile numbers. After successful completion of building the system, and completing analysis on data the threshold values are to be set accordingly for controlling alert purposes.

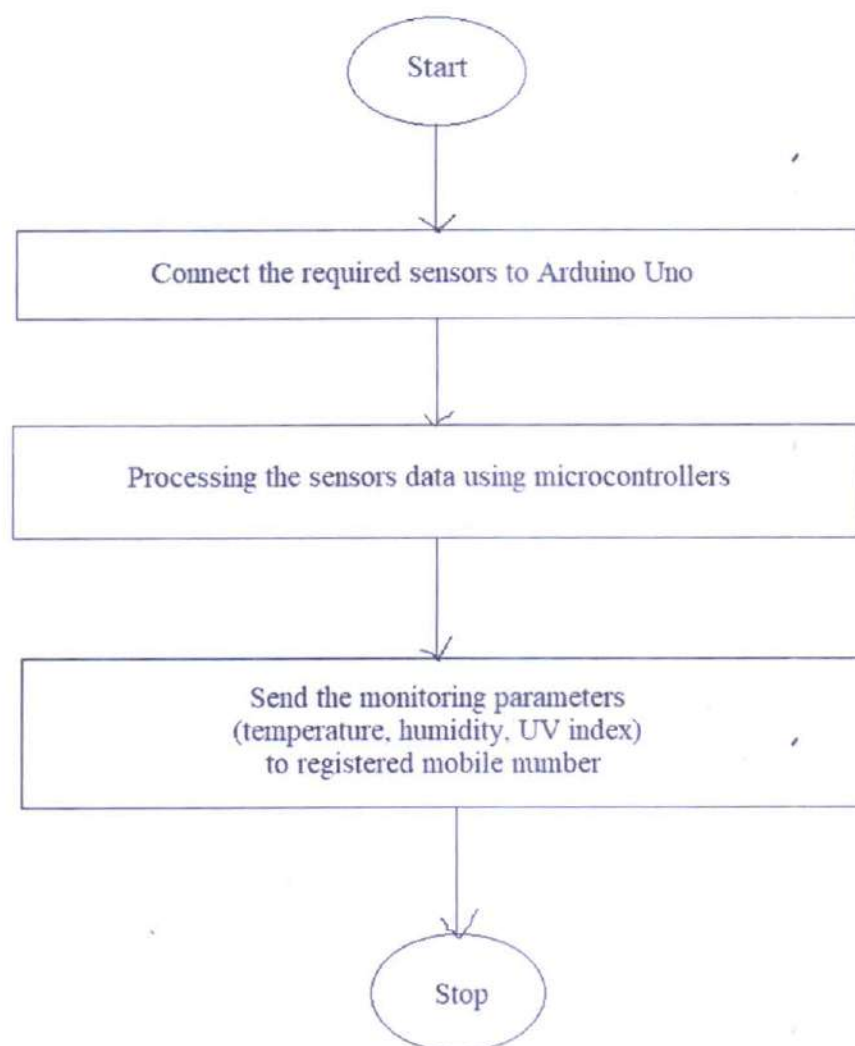


Fig. 6. Flow Chart

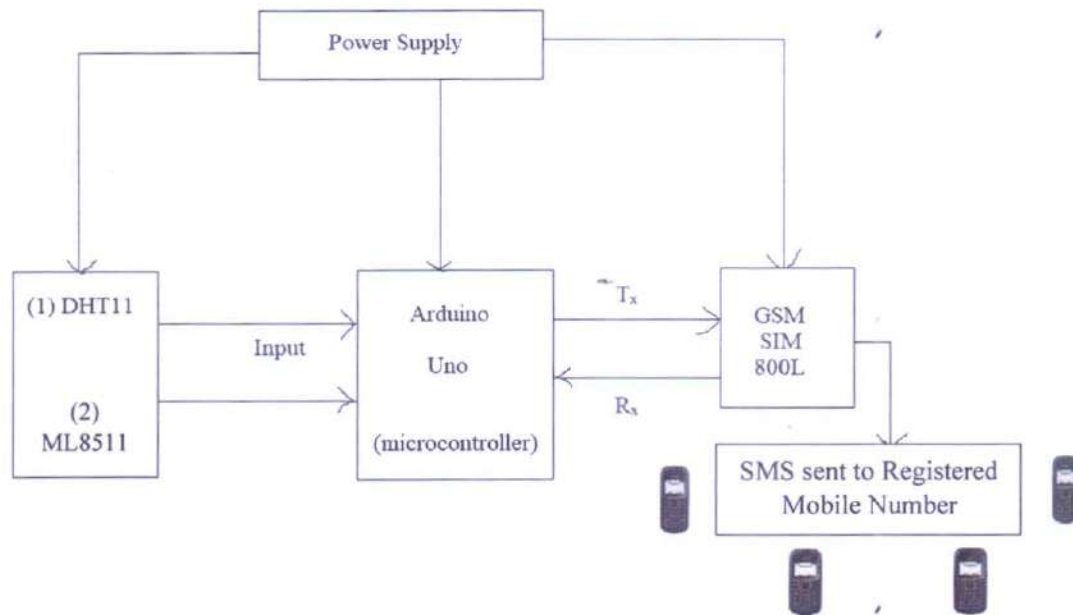


Fig. 7. System Design

### 3. RESULT AND ANALYSIS

Here we can monitor different weather parameters by this system. Various weather parameters observed and collected on June 22, 2020 are tabulated in Table 1 below, for example.

Standard or threshold value of humidity is 90%, temperature is 30°C and UV index is 7 of 10 for cloudy or rainy weather [2]. Accordingly, a messaging system is designed so that if these values are equal to or greater than above mentioned standard values, then a bad-weather alert message is sent to the farmers, as shown in Table 1.

| Sl. No. | Time     | Temperature | Humidity | UV Index | Comparing to the standard weather parameter | Alert Status |
|---------|----------|-------------|----------|----------|---------------------------------------------|--------------|
| 1       | 12:30 am | 28°C        | 94%      | 0 of 10  | temp.<std.; hmd.>std.; UV<std.              | Not sent     |
| 2       | 1:30 am  | 28°C        | 95%      | 0 of 10  | temp.<std.; hmd.>std.; UV<std.              | Not sent     |
| 3       | 2:30 am  | 27°C        | 95%      | 0 of 10  | temp.<std.; hmd.>std.; UV<std.              | Not sent     |
| 4       | 3:30 am  | 27°C        | 96%      | 0 of 10  | temp.<std.; hmd.>std.; UV<std.              | Not sent     |
| 5       | 4:30 am  | 27°C        | 96%      | 0 of 10  | temp.<std.; hmd.>std.; UV<std.              | Not sent     |
| 6       | 5:30 am  | 27°C        | 96%      | 0 of 10  | temp.<std.; hmd.>std.; UV<std.              | Not sent     |



|    |          |      |     |          |                                   |          |
|----|----------|------|-----|----------|-----------------------------------|----------|
| 7  | 6:30 am  | 28°C | 94% | 1 of 10  | temp.<std.; hmd.>std.;<br>UV<std. | Not sent |
| 8  | 7:30 am  | 29°C | 93% | 2 of 10  | temp.<std.; hmd.>std.;<br>UV<std. | Not sent |
| 9  | 8:30 am  | 29°C | 93% | 5 of 10  | temp.<std.; hmd.>std.;<br>UV<std. | Not sent |
| 10 | 9:30 am  | 29°C | 93% | 7 of 10  | temp.<std.; hmd.>std.;<br>UV=std. | Not sent |
| 11 | 10:30 am | 30°C | 92% | 9 of 10  | temp.=std.; hmd.>std.;<br>UV>std. | Sent     |
| 12 | 11:30 am | 31°C | 92% | 10 of 10 | temp.>std.; hmd.>std.;<br>UV>std. | Sent     |
| 13 | 12:30 am | 31°C | 93% | 9 of 10  | temp.>std.; hmd.>std.;<br>UV>std. | Sent     |
| 14 | 1:30 pm  | 31°C | 92% | 8 of 10  | temp.>std.; hmd.>std.;<br>UV>std. | Sent     |
| 15 | 2:30 pm  | 31°C | 90% | 6 of 10  | temp.>std.; hmd.=std.;<br>UV<std. | Sent     |
| 16 | 3:30 pm  | 30°C | 84% | 3 of 10  | temp.=std.; hmd.<std.;<br>UV<std. | Not sent |
| 17 | 4:30 pm  | 30°C | 83% | 1 of 10  | temp.=std.; hmd.<std.;<br>UV<std. | Not sent |
| 18 | 5:30 pm  | 30°C | 85% | 0 of 10  | temp.=std.; hmd.<std.;<br>UV<std. | Not sent |
| 19 | 6:30 pm  | 30°C | 86% | 0 of 10  | temp.=std.; hmd.<std.;<br>UV<std. | Not sent |
| 20 | 7:30 pm  | 29°C | 89% | 0 of 10  | temp.<std.; hmd.<std.;<br>UV<std. | Not sent |
| 21 | 8:30 pm  | 29°C | 91% | 0 of 10  | temp.<std.; hmd.>std.;<br>UV<std. | Not sent |
| 22 | 9:30 pm  | 29°C | 92% | 0 of 10  | temp.<std.; hmd.>std.;<br>UV<std. | Not sent |
| 23 | 10:30 pm | 28°C | 93% | 0 of 10  | temp.<std.; hmd.>std.;<br>UV<std. | Not sent |
| 24 | 11:30 pm | 28°C | 93% | 0 of 10  | temp.<std.; hmd.>std.;<br>UV<std. | Not sent |

Table 1. Result

Practically improved results from data values are determined in the proposed system. These results were expected when the system worked in Howrah, West Bengal in the mid-June (one-day reading). And as discussed before, when the value of any two amongst temperature, humidity and UV index reached or crossed the standard value, an alert was sent.

For example,

According to result table,

At 10:30 am, temperature= 30°C

Humidity= 92%

UV index= 9 of 10

Consequently, an alert was sent at 10:30 am.

## 5. CONCLUSION

To implement this, we need to deploy the sensor devices in the environment for collecting the data and analysing it. Deploying sensor devices in the environment enables us to record real time data. It can cooperate with other objects through the network. Then the collected data and the analysed results are sent to the registered mobile numbers via GSM module. This data will be cooperative for future analysis and can be easily shared with other end-users. This model can be further expanded to monitor the developing cities and manufacturing zones for pollution monitoring. To protect the public health from pollution, this model provides an efficient and low-cost solution for unceasing monitoring of environment.

Here are some suggested additions that can be made to improve the system:

- (i) Powering the device using solar panels.
- (ii) Suspending the device from a weather balloon so that it can be used to record atmospheric parameters at high altitudes and remote and inaccessible areas.
- (iii) Use of a tough exterior cover for the system that will act as a protective cover enabling the device to function in harsh weather conditions.
- (iv) Designing a method to mount the weather monitoring device onto a buoyant platform like a buoy hence enabling the system to measure weather changes over the sea. This data can also be shared to cargo ships and other nautical industries conducting operations within the area.
- (v) Using silica gel to prevent condensation on the exterior cover as condensation might affect the sensors readings.



## REFERENCES

- [1] A. Katyal, R. Yadav, M. Pandey, "Wireless Arduino Based Weather Station" in *International Journal of Advanced Research in Computer and Communication Engineering*, Vol. 5, Issue 4, April, 2016.
- [2] B. S. Rao, K. S. Rao, N. Ome, "Internet of Things (IOT) Based Weather Monitoring system" in *International Journal of Advanced Research in Computer and Communication Engineering*, vo. 5, no. 9, September 2016. <https://ijarcece.com/wp-content/uploads/2016/09/IJARCCCE-66.pdf>. Accessed 22 June, 2020.
- [3] D-Robotics, UK, *DHT11 Humidity & Temperature Sensor datasheet*. [online]. Available: <https://www.droboticsonline.com>. (30/Jul/2010).
- [4] D. V. Sose, A. D. Sayyad, "Weather Monitoring Station: A Review" in *International Journal of Engineering Research and Application*, vol. 6, no. 6, (Part-1) June 2016, pp.55-60.
- [5] F. Hahn, M. Pablo, J. Reyes "Solar Driven Wind Speed Monitoring System Using Wireless or Wired Sensors" in *SciRes, Energy and Power Engineering*, vol. 6, pp. 213-221, 2014.
- [6] G. Mois, T. Sanislav and S. C. Folea, "A Cyber-Physical System for Environmental Monitoring," in *IEEE Transactions on Instrumentation and Measurement*, vol. 65, no. 6, pp. 1463-1471, June 2016. doi: 10.1109/TIM.2016.2526669.
- [7] K. Krishnamurthi, S. Thapa, L. Kothari, A. Prakash, "Arduino Based Weather Monitoring System," in *International Journal of Engineering Research and General Science*, vol. 3, no. 2, pp. 452-8, March-April, 2015. <http://pnrsolution.org/Datacenter/Vol3/Issue2/64.pdf>. Accessed 22 June, 2020.
- [8] K. N. V. Satyanarayana, S. R. N. Reddy, K. N. V. S. Varma & P. K. Raju "Mobile App & IoT Based Smart Weather Station" in *International Journal of Electronics, Communication & Instrumentation Engineering Research and Development*, vol. 7, no. 4, pp. 7-14, Aug 2017. [https://www.academia.edu/35073563/MOBILE\\_APP\\_and\\_IOT\\_BASED\\_SMART\\_WEATHER\\_STATION](https://www.academia.edu/35073563/MOBILE_APP_and_IOT_BASED_SMART_WEATHER_STATION). Accessed 22 June, 2020.
- [9] N. Gahlot, V. Gundkal, S. Kothimbire and A. Thite, "Zigbee Based Weather Monitoring System," in *The International Journal of Engineering and Science (IJES)*, vol. 4, no. 4, pp. 61-66, 2015. <http://www.theijes.com/papers/v4-i4/Version-2/10442061066.pdf>. Accessed 22 June, 2020.
- [10] N. Sabharwal, R. Kumar, A. Thakur, J. Sharma "A Low Cost Zigbee Based Automatic Wireless Weather Station with Gui And Web Hosting Facility" *ICRTEDC*, vol. 1, Special Issue 2, May, 2014.
- [11] S. R. Shinde, A. H. karode and S. R. Suralkar, "IOT Based Environment Monitoring System," in *International Journal of Scientific Research*, vol. 7, no. 2, February 2018. [https://www.worldwidejournals.com/international-journal-of-scientific-research-\(IJSR\)/fileview.php?val=February\\_2018\\_1517574149\\_191.pdf](https://www.worldwidejournals.com/international-journal-of-scientific-research-(IJSR)/fileview.php?val=February_2018_1517574149_191.pdf). Accessed June 22, 2020.
- [13] P. Susmitha, G. Sowmyabala, "Design and Implementation of Weather Monitoring and Controlling System," in *International Journal of Computer Applications* (0975 – 8887)
- [14] Xiamen Amotec Display Co. Ltd, *Specification of LCD Module LCD datasheet Module-sparkfun*. <https://www.sparkfun.com/datasheets/LCD>. (29 Oct, 2008).
- [15] Sarmad Nozad Mahmood and Forat Falih Hasan, "Design of Weather Monitoring System Using Arduino Based Database Implementation," in *Journal of Multidisciplinary Engineering Science and Technology (JMEST)*, vol. 4, no. 4, April 2017. <http://www.jmest.org/wp-content/uploads/JMESTN42352157.pdf>. Accessed June 24, 2020.
- [16] Yashaswi Rahut, Rimsha Afreen, Divya Kamini, "Smart Weather Monitoring System Using IoT".
- [17] Alexandros Zografos, "Wireless Sensor Based Agricultural Monitoring System". 2014. <https://people.kth.se/~maguire/c/DEGREE-PROJECT-REPORTS/140325-Alexandros.Zografos-with-cover.pdf>. Accessed June 24, 2020.



## **IoT Based Smart Weather Monitoring system**

*Project Report submitted to the Department of Physics, Ramakrishna Mission Residential College (Autonomous), Narendrapur, Kolkata for the partial fulfilment of the requirements of the degree of*

## **Bachelor of Science (Hons.) in Physics**

Submitted by:

Tridib Bera [Roll No.: PHUG/233/17]

Sourav Mandal [Roll No.: PHUG/118/17]

Semester VI, B.Sc. Physics (Hons.)

University of Calcutta, Kolkata

2020



**Ramakrishna Mission Residential College (Autonomous)**

**Vivekananda Centre for Research**

**Ramakrishna Mission Ashrama**

(A Branch Centre of Ramakrishna Mission, Belur Math, Howrah-711202)

**Narendrapur, Kolkata - 700 103, West Bengal, India**

A Scientific Industrial Research Organisation, Recognised by DST, Govt. of India

College with Potential for Excellence (CPE), Re-accredited by NAAC - 'A' (CGPA 3.56 out of 4)

---

## **DEPARTMENT OF PHYSICS**

### **Certificate**

This is to certify that Tridib Bera, a student of B. Sc has successfully completed the project of UG curriculum entitled "IoT Based Smart Weather Monitoring system" in the period from January to May, 2020.

*Malay Purkait*

.....  
30.06.2020.

**Signature Of HOD**

**Dept. of Physics**

**Dr. Malay Purkait**

Associate Prof. & Head

Department of Physics

Ramakrishna Mission Residential College

(Autonomous)

Narendrapur, Kolkata-700 103, (W.B.)

**Mr. Tanmay Biswas**

Assistant Professor

Ramakrishna Mission Residential  
College (Autonomous)  
Narendrapur, Kolkata-700103

## **CERTIFICATE OF APPROVAL**

**Date: 1 July, 2020**

This is to certify that the project report entitled "**IoT Based Smart Weather Monitoring System**" has been done under my supervision at the Department of Physics, Ramakrishna Mission Residential College (Autonomous). I also endorse that this work submitted by **Tridib Bera** (Reg. No: A03-1112-0244-17) is original and has not been submitted to any other University for the award of any Degree or Diploma. I therefore, recommend the project work for the award of **Bachelor of Science (Honours) in Physics**.

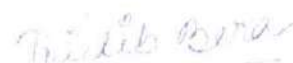
  
(Mr. Tanmay Biswas)



## Acknowledgement

We would like to acknowledge our sincere gratitude to Mr. Tanmay Biswas (Assistant Professor, Department of Physics, Ramakrishna Mission Residential College (Autonomous), Narendrapur, Kolkata) whose continuous guidance, comments and feedback helped us throughout the course of this project work.

We also express our profound thankfulness to our professors and peers at the Department of Physics, and the principal of Ramakrishna Mission Residential College (Autonomous) for their valuable support in making this attempt successful.



Tridib Bera

Registration No. A03-1112-0244-17

## Abstract

The proposed system is an advanced solution for weather monitoring based on Internet of Things (IoT) which provides weather report by mobile messaging system to the farmers of a particular locality. The system deals with monitoring weather and climate changes like temperature, humidity, UV radiation in the air using two sensors (DHT11 and ML8511). These sensors send data to microcontroller which then sends the weather report alert via GSM SIM 800L module to the farmers whose numbers are registered in this module. Frequent periodical updates in results every second showed that the system has no delay in providing the new readings. It provides the particular weather report by mobile messaging system to the registered mobile number. Numerical results are presented and analyzed in this report to validate the theoretical analysis of the whole system taking account of expected data of a whole day including temperature, humidity, and UV index.

## 1. INTRODUCTION

Present day innovations in technology mainly focus on controlling and monitoring of different devices wirelessly over the internet such that the internet acts as a medium for communication between all the devices [8]. And irrespective of spatial disparity, life in contemporary society cannot be imagined without the convenience of wireless weather readings and forecasts. Since the world is changing so fast, weather stations have become urgently important for the safety and progress of human civilization. Here in this project we present a weather station that can prove to be helpful for any place. This weather station is based on IOT (internet of things). It is equipped with environmental sensors used for measurements at any particular place and it reports the users in real time on cloud. To accomplish this, we used Arduino Uno and different environmental sensors like DHT11 and ML8511 ultraviolet light sensor. The sensors constantly sense the weather parameters and keeps on transmitting it to the farmers over massaging system. This project also focuses on the IOT application in the new generation of environmental information and contributes towards the foreseeable shift in the paradigm of environmental monitoring in future [15]. The system has been developed particularly in the view of building smart city by giving the weather update of any particular place like a particular office or room.

### 1.1 Existing System

The existing weather monitoring systems generally use weather stations that use multiple instruments such as thermometers, barometers, wind vanes, rain gauge etc. to measure weather and climate changes [16,17]. Most of these instruments use simple analog technology which is later physically recorded and stored in a data base. This information is later sent to news reporting stations and radio stations where the weather report is given.

### 1.2 Limitations of the Existing System

(i) Existing weather monitoring systems that are used in the field generally consist of unconventional and heavy machinery that consists of numerous moving parts that require constant maintenance and need to be manually monitored and changed frequently [3].

- (ii) Power requirements are one of many major constraints as these instruments are generally sited far from main power supply. This adds to the cost of using such instruments.
- (iii) The use of thermometers to measure external temperature; however accurate is still outdated and constantly needs to be manually checked for any change in temperature.
- (iv) Data that is collected by the instruments needs to be manually transferred from the logger to a laptop or computer via a cable.
- (v) Existing systems consist of large and heavy instruments that occupy a lot of space hence making it difficult to install them in remote location and places which have limited space [16].
- (vi) The instruments used in the existing systems are expensive and add up to the already high cost of installation and maintenance.
- (vii) The current system always faces problems such as delay in warning people about bad weather and sudden changes in the forecast [11].

## 2. PROPOSED SYSTEM

The system proposed is an advanced solution for weather monitoring that uses IoT to make its real time data easily accessible to its user over a very wide range [16]. The system deals with monitoring weather and climate changes like

- (i) Temperature and humidity by using the DHT11 sensor,
- (ii) UV radiation using ML8511 solar sensor

### 2.1 System Architecture

The implemented system consists of an Arduino Uno which is used as the main processing unit for the entire system and all the sensors and devices are connected with the microcontroller. The sensors are operated by the microcontroller to retrieve the data and further process the analysis of the sensor data. The processed data is, then, reported via GSM SIM 800L module to the registered mobile number. The proposed design of the model is shown in Figure 1.

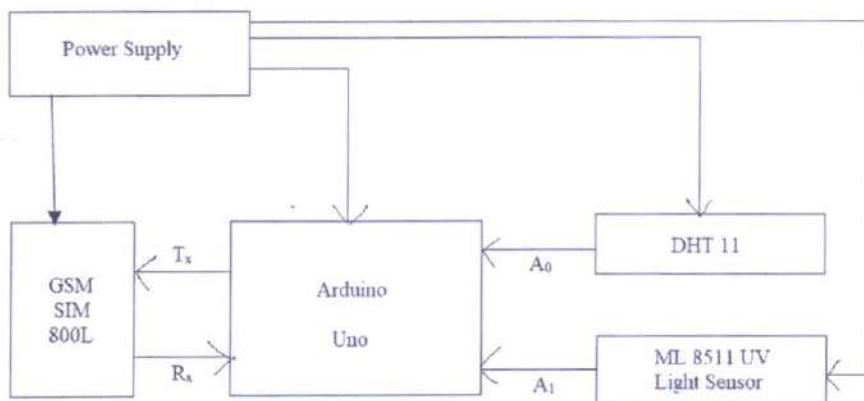


Fig. 1. Proposed Design



### 2.1.1 Arduino UNO

It is an open-source physical computing platform based on a simple micro-controller board, and a development environment for writing software for the board [10]. Arduino can be used to develop interactive objects, taking inputs from a variety of switches and or sensors, controlling a variety of lights, motors, and other physical outputs. The commercially available Arduino Uno board is shown in Figure 2.

- (i) Microcontroller: Microchip ATmega328P
- (ii) Operating Voltage: 5 Volt
- (iii) Input Voltage: 7 to 20 Volts
- (iv) Digital I/O Pins: 14 (of which 6 provide PWM output)
- (v) Analog Input Pins: 6
- (vi) DC Current per I/O Pin: 20 mA
- (vii) DC Current for 3.3V Pin: 50 mA
- (viii) Flash Memory: 32 KB of which 0.5 KB used by bootloader
- (ix) SRAM: 2 KB
- (x) EEPROM: 1 KB
- (xi) Clock Speed: 16 MHz
- (xii) Length: 68.6mm
- (xiii) Width: 53.4 mm
- (xiv) Weight: 25 g



Fig. 2. Arduino UNO

### 2.1.2 DHT11

The DHT11 is a basic, ultra-low-cost digital temperature and humidity sensor. It uses a capacitive humidity instrument and a thermistor to measure the surrounding air, and spits out a digital signal on the data pin (no analog input pins needed) [16]. It is shown in Figure 3.

- (i) Temperature range:  $0^{\circ}\text{C}$ - $50^{\circ}\text{C}$  /  $\pm 2^{\circ}\text{C}$
- (ii) Humidity Range: 20%-95% /  $\pm 2\%$
- (iii) Sampling rate: 1Hz (one reading every second)
- (iv) Body size: 15.5mm\*12mm\*5.5mm
- (v) Operating voltage: 3-5V
- (vi) Max current during measure: 2.5mA

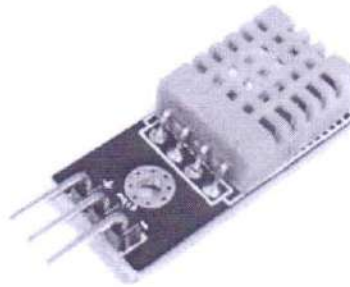


Fig. 3. DHT11

### 2.1.3 ML8511

ML8511 module, shown in Figure 4, is an informal to use ultraviolet light sensor. The ML8511 Sensor works by outputting an analog signal in relation to the amount of detected UV light [7]. This breakout can be very handy in creating devices that warn the user of sunburn or detect the UV index as it communicates to weather conditions.

- (i) Supply Voltage: DC 5V
- (ii) Operating Temperature:  $-20\sim 70^{\circ}\text{C}$
- (iii) Sensitivity Region: UV-A and UV-B
- (iv) Sensitivity Wave Length: 280-390nm
- (v) Module Size: 30 x 22mm

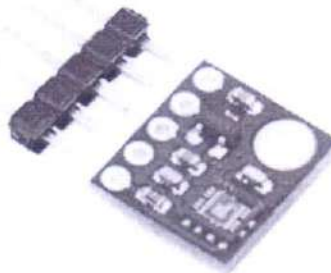


Fig. 4. ML8511

### 2.1.4 SIM800L GSM Module

SIM800L GSM module similar to the one which is on our phone. The GSM module is shown in Figure 5 for further reference and better understanding. Basically, SIM800L module is a small chip that uses serial-communication to communicate with any microcontroller or microprocessor. It has an in-built onboard antenna and an onboard SIM slot for SIM insertion purposes. The SIM800L module has total 12 pins that are used to establish connections with the microcontroller. For simplicity, here I have shared a detailed pinout of the SIM800L and a function of each pin.

**Ring:** This pin is used for indication purpose. It produces an interrupt signal when we receive an SMS or a phone call.

**DTR:** We can call this pin an enable pin. This pin plays an important role in saving electricity. If we turn this pin high, the module enters sleep mode by disabling serial communication and if the pin is turned low, the module turns on. In case, SIM800L is not working, the reason might be that this pin has been accidentally turned high.

**Mic+, Mic-, SPK+ & SPK:** These are the pins where we can connect the microphone and speaker.

**NET:** Here the helical shape antenna can be attached.

**RST:** This pin is used to reset the SIM800L module. If the module is not responding to the AT command, that might be because of a baud rate problem, you can turn this pin high for 100ms to reset the SIM800L.

**VCC and GND:** You can power SIM800L using these pins but the voltage should not be more than 3.3V and Current should not be less than 1A.

**RX and TX:** These pins are used for Serial communication  $R_X$  for receiving commands from the controller and  $T_X$  for sending out the data.

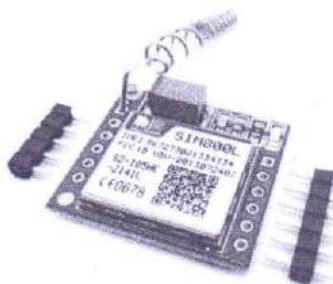


Fig. 5. SIM800L GSM Module

## 4. IMPLEMENTATION

Based on framework shown in figure 7, we have a suitable implementation model that consists of different sensor devices and module. In this implementation model we used Arduino Uno board with GSM SIM800L module, DHT11 and ML8511 sensors as embedded devices for sensing data and sending alert to the farmers. Arduino Uno board consists of analog input pins ( $A_0$ - $A_5$ ), digital output



pins (D<sub>0</sub>-D<sub>13</sub>), inbuilt ADC and GSM module that sends alert to the registered numbers. Sensors are connected to Arduino Uno board for monitoring. ADC converts the corresponding sensor readings to its digital value and from that value corresponding environmental parameter is evaluated. The design flow of the proposed system can be seen in Figure 6.

An embedded system for environmental monitoring and its components is shown in figure 7. The embedded device is placed in particular area for testing purpose. DHT11 sensor detects temperature and humidity in that area and ML8511 is the sensor to detect UV light. Once the readings cross the threshold limit, an alert is sent via GSM module to the registered mobile numbers. After successful completion of building the system, and completing analysis on data the threshold values are to be set accordingly for controlling alert purposes.

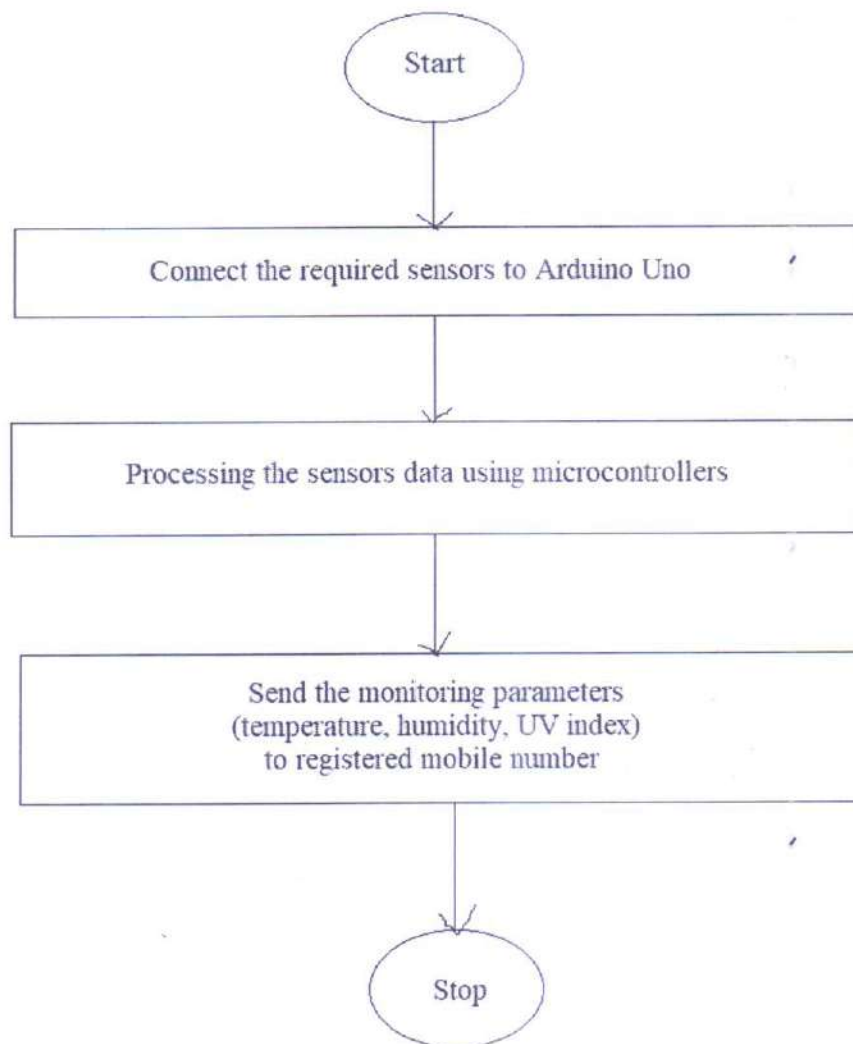


Fig. 6. Flow Chart

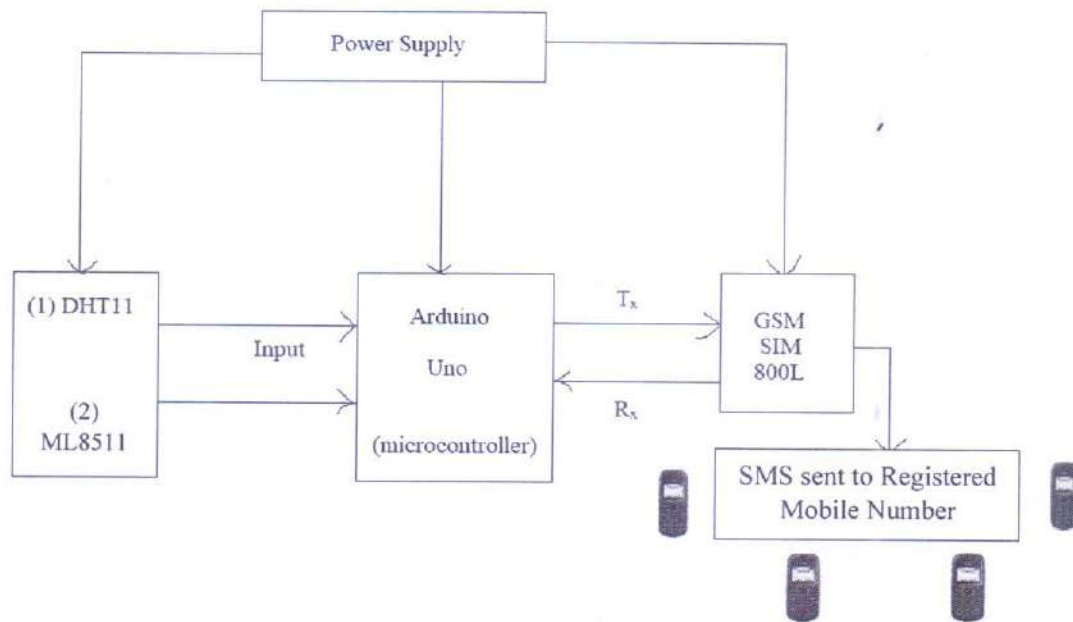


Fig. 7. System Design

### 3. RESULT AND ANALYSIS

Here we can monitor different weather parameters by this system. Various weather parameters observed and collected on June 22, 2020 are tabulated in Table 1 below, for example.

Standard or threshold value of humidity is 90%, temperature is 30°C and UV index is 7 of 10 for cloudy or rainy weather [2]. Accordingly, a messaging system is designed so that if these values are equal to or greater than above mentioned standard values, then a bad-weather alert message is sent to the farmers, as shown in Table 1.

| Sl. No. | Time     | Temperature | Humidity | UV Index | Comparing to the standard weather parameter | Alert Status |
|---------|----------|-------------|----------|----------|---------------------------------------------|--------------|
| 1       | 12:30 am | 28°C        | 94%      | 0 of 10  | temp.<std.; hmd.>std.; UV<std.              | Not sent     |
| 2       | 1:30 am  | 28°C        | 95%      | 0 of 10  | temp.<std.; hmd.>std.; UV<std.              | Not sent     |
| 3       | 2:30 am  | 27°C        | 95%      | 0 of 10  | temp.<std.; hmd.>std.; UV<std.              | Not sent     |
| 4       | 3:30 am  | 27°C        | 96%      | 0 of 10  | temp.<std.; hmd.>std.; UV<std.              | Not sent     |
| 5       | 4:30 am  | 27°C        | 96%      | 0 of 10  | temp.<std.; hmd.>std.; UV<std.              | Not sent     |
| 6       | 5:30 am  | 27°C        | 96%      | 0 of 10  | temp.<std.; hmd.>std.; UV<std.              | Not sent     |

|    |          |      |     |          |                                   |          |
|----|----------|------|-----|----------|-----------------------------------|----------|
| 7  | 6:30 am  | 28°C | 94% | 1 of 10  | temp.<std.; hmd.>std.;<br>UV<std. | Not sent |
| 8  | 7:30 am  | 29°C | 93% | 2 of 10  | temp.<std.; hmd.>std.;<br>UV<std. | Not sent |
| 9  | 8:30 am  | 29°C | 93% | 5 of 10  | temp.<std.; hmd.>std.;<br>UV<std. | Not sent |
| 10 | 9:30 am  | 29°C | 93% | 7 of 10  | temp.<std.; hmd.>std.;<br>UV=std. | Not sent |
| 11 | 10:30 am | 30°C | 92% | 9 of 10  | temp.=std.; hmd.>std.;<br>UV>std. | Sent     |
| 12 | 11:30 am | 31°C | 92% | 10 of 10 | temp.>std.; hmd.>std.;<br>UV>std. | Sent     |
| 13 | 12:30 am | 31°C | 93% | 9 of 10  | temp.>std.; hmd.>std.;<br>UV>std. | Sent     |
| 14 | 1:30 pm  | 31°C | 92% | 8 of 10  | temp.>std.; hmd.>std.;<br>UV>std. | Sent     |
| 15 | 2:30 pm  | 31°C | 90% | 6 of 10  | temp.>std.; hmd.=std.;<br>UV<std. | Sent     |
| 16 | 3:30 pm  | 30°C | 84% | 3 of 10  | temp.=std.; hmd.<std.;<br>UV<std. | Not sent |
| 17 | 4:30 pm  | 30°C | 83% | 1 of 10  | temp.=std.; hmd.<std.;<br>UV<std. | Not sent |
| 18 | 5:30 pm  | 30°C | 85% | 0 of 10  | temp.=std.; hmd.<std.;<br>UV<std. | Not sent |
| 19 | 6:30 pm  | 30°C | 86% | 0 of 10  | temp.=std.; hmd.<std.;<br>UV<std. | Not sent |
| 20 | 7:30 pm  | 29°C | 89% | 0 of 10  | temp.<std.; hmd.<std.;<br>UV<std. | Not sent |
| 21 | 8:30 pm  | 29°C | 91% | 0 of 10  | temp.<std.; hmd.>std.;<br>UV<std. | Not sent |
| 22 | 9:30 pm  | 29°C | 92% | 0 of 10  | temp.<std.; hmd.>std.;<br>UV<std. | Not sent |
| 23 | 10:30 pm | 28°C | 93% | 0 of 10  | temp.<std.; hmd.>std.;<br>UV<std. | Not sent |
| 24 | 11:30 pm | 28°C | 93% | 0 of 10  | temp.<std.; hmd.>std.;<br>UV<std. | Not sent |

Table 1. Result

Practically improved results from data values are determined in the proposed system. These results were expected when the system worked in Howrah, West Bengal in the mid-June (one-day reading). And as discussed before, when the value of any two amongst temperature, humidity and UV index reached or crossed the standard value, an alert was sent.

For example,

According to result table,

At 10:30 am, temperature= 30°C



Humidity= 92%

UV index= 9 of 10

Consequently, an alert was sent at 10:30 am.

## 5. CONCLUSION

To implement this, we need to deploy the sensor devices in the environment for collecting the data and analysing it. Deploying sensor devices in the environment enables us to record real time data. It can cooperate with other objects through the network. Then the collected data and the analysed results are sent to the registered mobile numbers via GSM module. This data will be cooperative for future analysis and can be easily shared with other end-users. This model can be further expanded to monitor the developing cities and manufacturing zones for pollution monitoring. To protect the public health from pollution, this model provides an efficient and low-cost solution for unceasing monitoring of environment.

Here are some suggested additions that can be made to improve the system:

- (i) Powering the device using solar panels.
- (ii) Suspending the device from a weather balloon so that it can be used to record atmospheric parameters at high altitudes and remote and inaccessible areas.
- (iii) Use of a tough exterior cover for the system that will act as a protective cover enabling the device to function in harsh weather conditions.
- (iv) Designing a method to mount the weather monitoring device onto a buoyant platform like a buoy hence enabling the system to measure weather changes over the sea. This data can also be shared to cargo ships and other nautical industries conducting operations within the area.
- (v) Using silica gel to prevent condensation on the exterior cover as condensation might affect the sensors readings.

## REFERENCES

- [1] A. Katyal, R. Yadav, M. Pandey, "Wireless Arduino Based Weather Station" in *International Journal of Advanced Research in Computer and Communication Engineering*, Vol. 5, Issue 4, April, 2016.
- [2] B. S. Rao, K. S. Rao, N. Ome, "Internet of Things (IOT) Based Weather Monitoring system" in *International Journal of Advanced Research in Computer and Communication Engineering*, vo. 5, no. 9, September 2016. <https://ijarccce.com/wp-content/uploads/2016/09/IJARCCCE-66.pdf>. Accessed 22 June, 2020.
- [3] D-Robotics, UK, *DHT11 Humidity & Temperature Sensor datasheet*. [online]. Available: <https://www.droboticsonline.com>. (30/Jul/2010).
- [4] D. V. Sose, A. D. Sayyad, "Weather Monitoring Station: A Review" in *International Journal of Engineering Research and Application*, vol. 6, no. 6, (Part-1) June 2016, pp.55-60.
- [5] F. Hahn, M. Pablo, J. Reyes "Solar Driven Wind Speed Monitoring System Using Wireless or Wired Sensors" in *SciRes, Energy and Power Engineering*, vol. 6, pp. 213-221, 2014.
- [6] G. Mois, T. Sanislav and S. C. Folea, "A Cyber-Physical System for Environmental Monitoring," in *IEEE Transactions on Instrumentation and Measurement*, vol. 65, no. 6, pp. 1463-1471, June 2016. doi: 10.1109/TIM.2016.2526669.
- [7] K. Krishnamurthi, S. Thapa, L. Kothari, A. Prakash, "Arduino Based Weather Monitoring System," in *International Journal of Engineering Research and General Science*, vol. 3, no. 2, pp. 452-8, March-April, 2015. <http://pnrsolution.org/Datacenter/Vol3/Issue2/64.pdf>. Accessed 22 June, 2020.
- [8] K. N. V. Satyanarayana, S. R. N. Reddy, K. N. V. S. Varma & P. K. Raju "Mobile App & IoT Based Smart Weather Station" in *International Journal of Electronics, Communication & Instrumentation Engineering Research and Development*, vol. 7, no. 4, pp. 7-14, Aug 2017. [https://www.academia.edu/35073563/MOBILE\\_APP\\_and\\_IoT\\_BASED\\_SMART\\_WEATHER\\_STATION](https://www.academia.edu/35073563/MOBILE_APP_and_IoT_BASED_SMART_WEATHER_STATION). Accessed 22 June, 2020.
- [9] N. Gahlot, V. Gundkal, S. Kothimbire and A. Thite, "Zigbee Based Weather Monitoring System," in *The International Journal of Engineering and Science (IJES)*, vol. 4, no. 4, pp. 61-66, 2015. <http://www.theijes.com/papers/v4-ij4/Version-2/10442061066.pdf>. Accessed 22 June, 2020.
- [10] N. Sabharwal, R. Kumar, A. Thakur, J. Sharma "A Low Cost Zigbee Based Automatic Wireless Weather Station with Gui And Web Hosting Facility" *ICRTEDC*, vol. 1, Special Issue 2, May, 2014.
- [11] S. R. Shinde, A. H. karode and S. R. Suralkar, "IOT Based Environment Monitoring System," in *International Journal of Scientific Research*, vol. 7, no. 2, February 2018. [https://www.worldwidejournals.com/international-journal-of-scientific-research-\(IJSR\)/fileview.php?val=February\\_2018\\_1517574149\\_191.pdf](https://www.worldwidejournals.com/international-journal-of-scientific-research-(IJSR)/fileview.php?val=February_2018_1517574149_191.pdf). Accessed June 22, 2020.
- [13] P. Susmitha, G. Sowmyabala, "Design and Implementation of Weather Monitoring and Controlling System," in *International Journal of Computer Applications* (0975 – 8887)
- [14] Xiamen Amotec Display Co. Ltd, *Specification of LCD Module LCD datasheet Module-sparkfun*. <https://www.sparkfun.com/datasheets/LCD>. (29 Oct, 2008).
- [15] Sarmad Nozad Mahmood and Forat Falih Hasan, "Design of Weather Monitoring System Using Arduino Based Database Implementation," in *Journal of Multidisciplinary Engineering Science and Technology (JMEST)*, vol. 4, no. 4, April 2017. <http://www.jmest.org/wp-content/uploads/JMESTN42352157.pdf>. Accessed June 24, 2020.
- [16] Yashaswi Rahut, Rimsha Afreen, Divya Kamini, "Smart Weather Monitoring System Using IoT".
- [17] Alexandros Zografos, "Wireless Sensor Based Agricultural Monitoring System". 2014. <https://people.kth.se/~maguire/c/DEGREE-PROJECT-REPORTS/140325-Alexandros.Zografos-with-cover.pdf>. Accessed June 24, 2020.



## ACKNOWLEDGEMENT

My name is Suman Debnath, roll no PHUG/238117.  
This project is about the Time independent  
perturbation Theory. My project guide Dr. Debnath  
Jana. helped me to complete my project. I am  
also grateful to Dr. Malay Purokait, HOD of  
Ramakrishna Mission Residential college, Physics  
Department and the principle Mahara  
Sw. Sastragandanaji.

Date - 4th July 2020.

Reference: Introduction to Quantum Mechanics  
- Griffiths